

21 August 2009 | \$10

Science

China's Origins

 AAAS

Invest Yourself in Citrus Solutions...



Citrus cultivation is threatened by a very serious disease called Citrus Greening or Huanglongbing (HLB). Symptoms are latent, then become lethal. The spread and cause of HLB are associated with a phloem-feeding insect (Asian Citrus Psyllid) and a fastidious bacterium (*Candidatus Liberibacter*).

The Citrus Research and Development Foundation requests proposals focused on comprehensive methods of controlling psyllid transmission of disease.

We also invite proposals of \$100,000 or less to test new methods of disease control made possible using the bacterial genomic sequence recently published at:

<http://www.citrusgreening.org/>

We need the brightest minds to quickly help us find the best solutions. Infectious disease has no boundaries. Neither does first-rate science.

Visit www.fcprac.com for details on awards and simplified program application instructions.



Citrus Research and
Development Foundation, Inc.

WHERE THE BASIC SCIENCE

WORLD MEETS THE WORLD OF MEDICINE

Submit your work to *Science Translational Medicine* today!

This fall, AAAS and *Science* will launch *Science Translational Medicine*, a new journal focused on applications of basic research knowledge that will improve human health.

The goal of *Science Translational Medicine* is simple: to help the scientific community harness decades of progress in research at the basic level and translate these biological discoveries into medical advances. Take this opportunity to have your work recognized in this groundbreaking new journal.

Papers in the following areas will be reviewed and considered for publication:

- Animal & Human Studies
- Applied Physical Sciences
- Behavior
- Bioengineering
- Biomarkers
- Cancer
- Cardiovascular Disease
- Cell Culture
- Chemical Genomics/Drug Discovery
- Data Mining
- Drug Delivery
- Gene Therapy/Regenerative Medicine
- Imaging
- Immunology/Vaccines
- Infectious Diseases
- Medical Informatics
- Medical Nanotechnology
- Metabolism/Diabetes/Obesity
- Neuroscience/Neurology/Psychiatry
- Pharmacogenetics
- Policy
- Toxicology & Pharmacokinetics
- And other interdisciplinary approaches to medicine

To submit your work for consideration, please visit: www.submit2scitranslmed.org



www.ScienceTranslationalMedicine.org

INTEGRATING MEDICINE AND SCIENCE

GE Healthcare

360° Service

"These days, productivity is everything in our business. Knowing that our scientists were losing valuable time due to service-related issues wasn't helping. To solve this problem and improve overall organizational efficiency, we looked at ways we could consolidate by purchasing from fewer suppliers. GE Healthcare was the only company that was happy to manage everything, regardless of the OEM; unbeatable flexibility that allows our teams to focus on what they are best at. Of course, GE Healthcare's track record in healthcare is world-class and it's a real benefit having a company that is happy to manage equipment of all types."

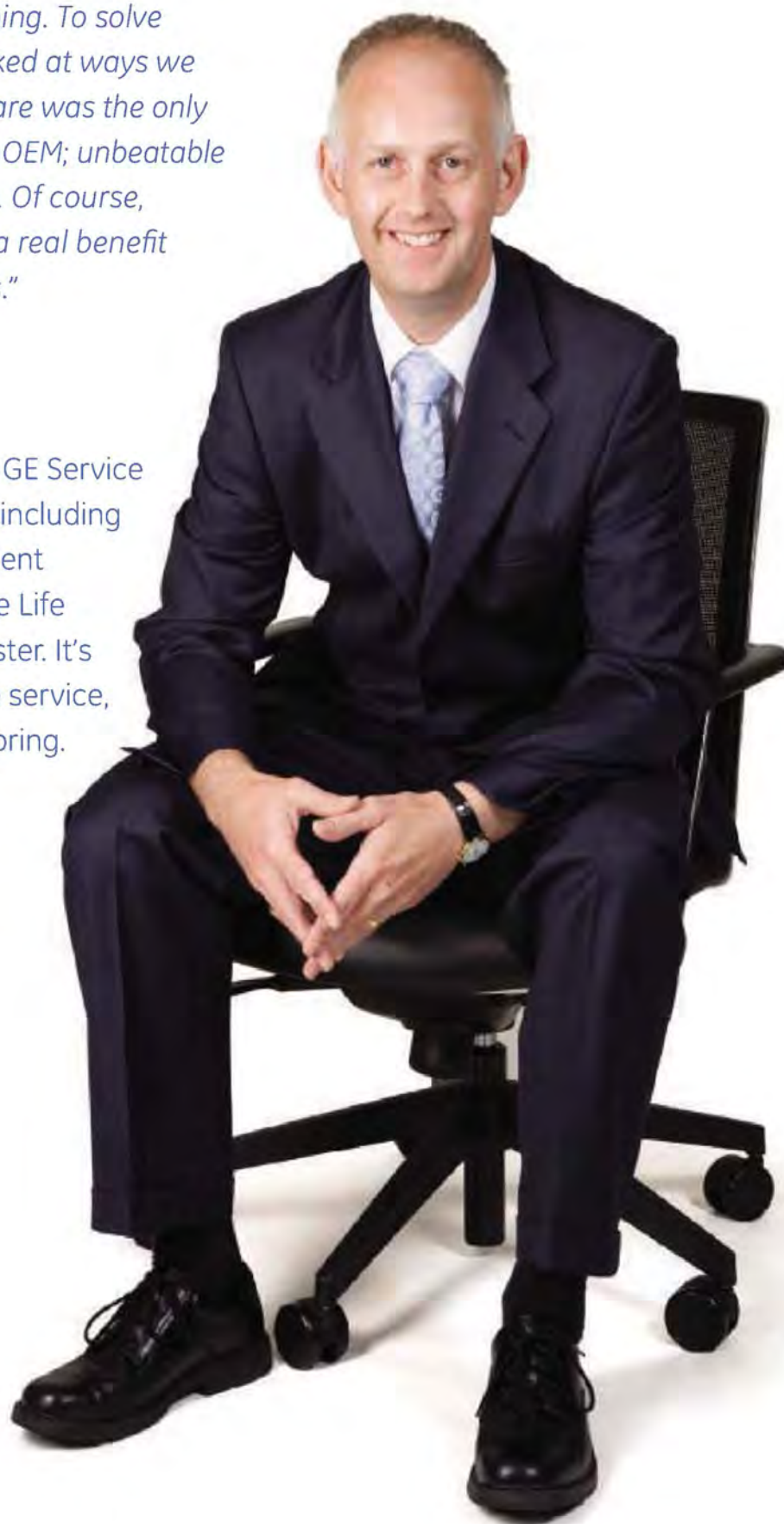
Richard Dickinson, Director of Operations, ERBI Ltd.

Pharmaceutical and biotech companies around the world rely on GE Service to deliver total coverage. From instrument service agreements — including systems from other manufacturers — to asset lifecycle management and facility validation. Now that's service in 360°. At GE Healthcare Life Sciences, our focus is on helping scientists achieve even more, faster. It's a commitment we have in our genes. And all this is backed by the service, support, and investment for the future that being part of GE can bring.

Find out more. Why not talk with us today.

Visit www.gelifesciences.com/360service

| ÄKTA | Amersham | Biacore | IN Cell | Whatman | **GE Service** |



imagination at work

© 2009 General Electric Company – All rights reserved.
First published June 2009

GE Healthcare Bio-Sciences AB, Björkgatan 30, 751 84 Uppsala, Sweden

GE07-09

EDITORIAL

- 920 Globalizing Science Publishing
Wieland Gevers

NEWS OF THE WEEK

- 924 Draft Rule Threatens Fossil Excavations in China
- 925 New Strategy Promises Lasting Resistance to a Rice Plague
>> Report p. 998
- 926 U.S. Energy Agency Stumbles Out of the Blocks
- 927 Rejecting 'Big Science' Tag, Collins Sets Five Themes for NIH
- 927 From *Science's* Online Daily News Site
- 928 Two Steps Forward for Synthetic Biology
>> Science Express Report by C. Lartigue et al.
- 929 From the *Science* Policy Blog

NEWS FOCUS

- 930 **ARCHAEOLOGY IN CHINA**
Beyond the Yellow River:
How China Became China
Founding Dynasty or Myth?
- 936 Archaeologists Raise the Old With the New
Landing the Looters
Go East, Young Archaeologist
- 940 Bridging East and West
Millet on the Move
>> Science Podcast

LETTERS

- 944 Less-Toxic Cigarette Use May Backfire
M. E. Deutsch
NIH Needs a Makeover
S. K. Dey
Keeping Infection at Arm's Length
V. Verhoeven et al.

Make Way for Robot Scientists

R. D. King et al.
Looking to Bacteria for Clues
R. J. Redfield

- 945 Life in Science: Creationists Made Me Do It
P. J. Keeling

946 CORRECTIONS AND CLARIFICATIONS

BOOKS ET AL.

- 947 The Paleobiological Revolution
D. Sepkoski and M. Ruse, Eds.,
reviewed by R. Wood
- 948 Wetware
D. Bray, reviewed by W. F. Marshall

POLICY FORUM

- 949 Energy and Technology Policies for Managing Carbon Risk
A. A. N. Patrinos and R. A. Bradley

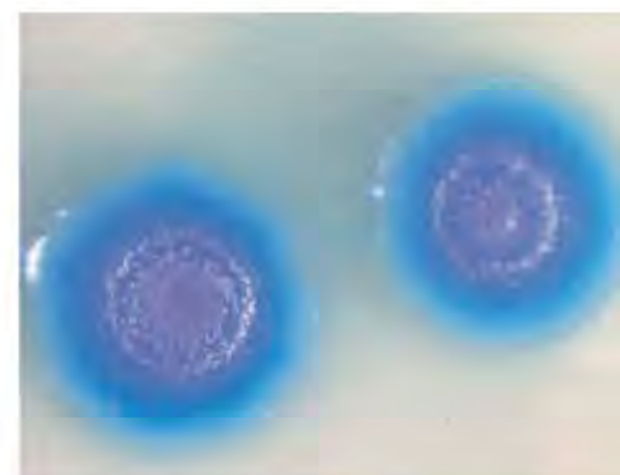
PERSPECTIVES

- 951 Early Solar System Chronology
A. M. Davis
>> Report p. 985
- 952 Coastal Exploitation
T. C. Rick and J. M. Erlandson
- 953 The Yin and Yang of Follicular Helper T Cells
A. Awasthi and V. K. Kuchroo
>> Reports pp. 1001 and 1006
- 955 Risks of Climate Engineering
G. C. Hegerl and S. Solomon
- 957 Is Gas Hydrate Energy Within Reach?
R. Boswell
- 958 More Than Just a Copy
H. Kaessmann
>> Report p. 995

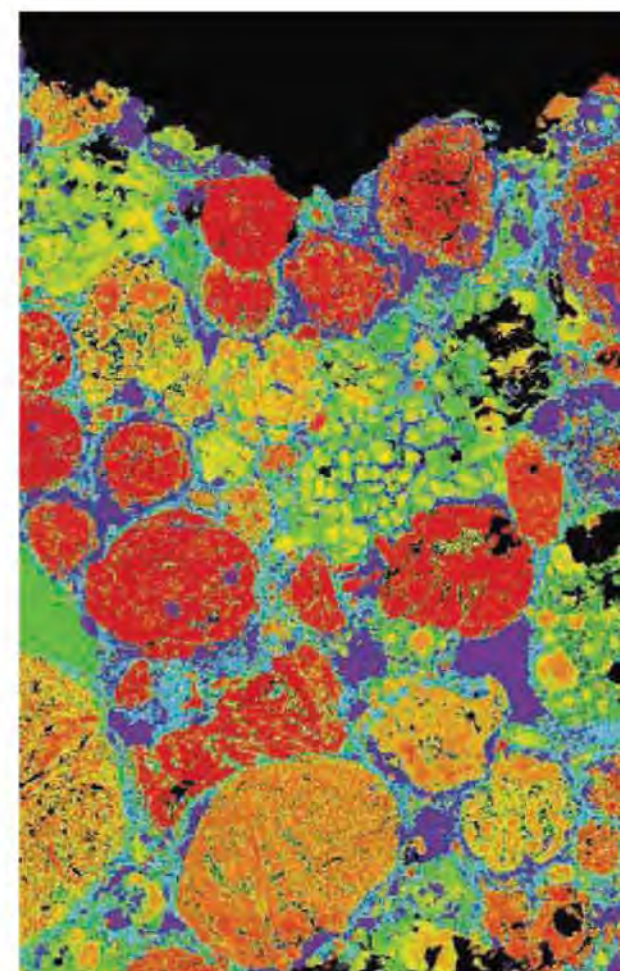
REVIEW

- 960 Structural Plasticity in Actin and Tubulin Polymer Dynamics
H. Y. Kueh and T. J. Mitchison

CONTENTS continued >>



page 928



pages 951 & 985



COVER

This elegantly carved jade face from Liangzhu in southeastern China provides an intriguing glimpse into the beliefs of the people who lived there from 3400 B.C.E. to 2250 B.C.E. As described in a special News Focus section beginning on page 930, discoveries at Liangzhu and other regions far from the traditional heartland of Chinese civilization are revealing surprisingly complex ancient cultures that thrived in far-flung regions of China.

Photo: Liu Bin/Archaeological Institute of Zhejiang Province

DEPARTMENTS

- 918 This Week in *Science*
- 921 Editors' Choice
- 922 *Science* Staff
- 923 Random Samples
- 1021 New Products
- 1022 *Science* Careers

10 Ways to Improve Your Chances of Securing Research Funding



RESEARCH



APPLICATIONS



NETWORKING



HOPING



WISHING



TANTRUM



RABBIT'S FOOT



SLOTS



SELF-FINANCING



JOINING

There are many approaches to securing funding, but not all are effective.

That's why the American Association for the Advancement of Science is committed to offering its members a variety of resources to help them locate the money they need—including an ongoing analysis of R&D budgets and funding, and an extensive directory of funding opportunities. Join us. Together we can make a difference. aaas.org/plusyou

 AAAS + U = Δ



BREVIA

- 964 **Deep-Sea, Swimming Worms with Luminescent "Bombs"**
K. J. Osborn et al.
Several species of deep-sea polychaete worms have been discovered that have a bizarre predator distraction mechanism.
>> *Science Podcast*
- 965 **DICER1 Mutations in Familial Pleuropulmonary Blastoma**
D. A. Hill et al.
A rare form of lung cancer in children is associated with mutational disruption of an enzyme that generates small noncoding RNAs.

RESEARCH ARTICLE

- 966 **Formation of the First Peptide Bond: The Structure of EF-P Bound to the 70S Ribosome**
G. Blaha et al.
Elongation factor P binds to the ribosome so as to position the initiator transfer RNA for the first bond formation.

REPORTS

- 970 **Exploring Dark Matter with Milky Way Substructure**
M. Kuhlen et al.
Simulations reveal that dark matter in our Galaxy could be detected by the Fermi space telescope.
- 973 **Light-Induced Spontaneous Magnetization in Doped Colloidal Quantum Dots**
R. Beaulac et al.
Long-lifetime excited states created by quantum confinement effects enable the light-induced magnetization of a quantum dot.
- 977 **Printed Assemblies of Inorganic Light-Emitting Diodes for Deformable and Semitransparent Displays**
S.-I. Park et al.
Methods to fabricate and assemble inorganic light-emitting diodes provide a route toward transparent, flexible, or stretchable display devices.
- 981 **Visualization of Fermi's Golden Rule Through Imaging of Light Emission from Atomic Silver Chains**
C. Chen et al.
A correlation of photon emission and scanning tunneling microscopy images illustrates a fundamental quantum principle.
- 985 **Homogeneous Distribution of ^{26}Al in the Solar System from the Mg Isotopic Composition of Chondrules**
J. Villeneuve et al.
High-precision isotopic analyses in chondrule minerals validate the use of ^{26}Al as an early solar system chronometer.
>> *Perspective p. 951*

- 988 **Adjoint Tomography of the Southern California Crust**
C. Tape et al.
Analysis of seismic data using a more realistic crustal model reveals detailed variations in density beneath southern California.
- 992 **Bacteriophages Encode Factors Required for Protection in a Symbiotic Mutualism**
K. M. Oliver et al.
A virus endows a bacterial symbiont of an aphid with virulence factors that kill parasitoid wasps.
- 995 **An Expressed *Fgf4* Retrogene Is Associated with Breed-Defining Chondrodysplasia in Domestic Dogs**
H. G. Parker et al.
The short legs that characterize certain dog breeds are associated with a gene that arose recently by RNA-based gene duplication.
>> *Perspective p. 958*
- 998 **Loss of Function of a Proline-Containing Protein Confers Durable Disease Resistance in Rice**
S. Fukuoka et al.
Quantitative trait loci may offer a particularly durable strategy for disease resistance.
>> *News story p. 925*
- 1001 **Bcl6 Mediates the Development of T Follicular Helper Cells**
R. I. Nurieva et al.
- 1006 **Bcl6 and Blimp-1 Are Reciprocal and Antagonistic Regulators of T Follicular Helper Cell Differentiation**
R. J. Johnston et al.
The transcription factors that regulate follicular T helper cell differentiation are identified.
>> *Perspective p. 953*
- 1010 **Structure and Mechanism of a Na^+ -Independent Amino Acid Transporter**
P. L. Shaffer et al.
The structure of the transporter ApcT reveals common architectural principles between proton- and sodium-coupled transporters.
- 1014 **Structures of the Ribosome in Intermediate States of Ratcheting**
W. Zhang et al.
Structures of the *Escherichia coli* 70S ribosome show how the large and small subunits rotate to facilitate protein synthesis.
- 1017 **Dopamine Controls Persistence of Long-Term Memory Storage**
J. I. Rossato et al.
Pharmacological and biochemical analyses reveal that dopamine determines the duration of fear memory storage.

CONTENTS continued >>



page 952



page 988



pages 925 & 998

Rotor-Gene Q — pure detection



- Enjoy a real-time PCR cycler with outstanding thermal and optical performance
- Perform multiple real-time PCR applications and optional high-resolution melting
- Benefit from a variety of state-of-the-art analyses
- Experience unrivaled robustness and minimal maintenance
- Count on reliable results from QIAGEN kits and assays



Discover more at www.qiagen.com/goto/PureDetection.

Sample & Assay Technologies

SCIENCEONLINE

SCIENCEEXPRESS

www.sciencexpress.org

Optimizing Influenza Vaccine Distribution

J. Medlock and A. P. Galvani

Age-related transmission patterns should be incorporated into vaccine distribution policy to minimize the impact of epidemics.

10.1126/science.1175570

>> *Science Podcast*

Creating Bacterial Strains from Genomes That Have Been Cloned and Engineered in Yeast

C. Lartigue et al.

A *Mycoplasma mycoides* genome was engineered in yeast and then transplanted into *Mycoplasma capricolum* cells to produce a new strain.

10.1126/science.1173759

>> *News story p. 928*

Eos Mediates Foxp3-Dependent Gene Silencing in CD4⁺ Regulatory T Cells

F. Pan et al.

A transcription factor required for gene suppression in regulatory T cells is identified.

10.1126/science.1176077

Memory Metamaterials

T. Driscoll et al.

A tunable metamaterial is demonstrated that can remember its switched state.

10.1126/science.1176580

Gold Helix Photonic Metamaterial as Broadband Circular Polarizer

J. K. Gansel et al.

A three-dimensional array of gold nano-helices can polarize light over a wide range of wavelengths.

10.1126/science.1177031

SCIENCENOW

www.sciencenow.org

Highlights From Our Daily News Coverage

Dogs Are No Mind Readers

Fido can't figure out what you're thinking, according to a new study.

Weight Loss for Batteries

Carbon nanofibers wrapped in a silicon shell make for lighter and more powerful rechargeables.

Friends or Acquaintances? Ask Your Cell Phone

Study shows that mobile phone calls accurately reflect people's relationships.

SCIENCESIGNALING

www.sciencesignaling.org

The Signal Transduction Knowledge Environment

RESEARCH ARTICLE: Differential p53-Independent Outcomes of p19^{Arf} Loss in Oncogenesis

Z. Chen et al.

p19^{Arf} signals independently of p53 in prostate cancer associated with the loss of Pten.

RESEARCH ARTICLE: The Plant NADPH Oxidase RBOHD Mediates Rapid Systemic Signaling in Response to Diverse Stimuli

G. Miller et al.

Reactive oxygen species produced by RBOHD mediate rapid, long-distance stress signals in plants.

RESEARCH ARTICLE: Quantitative Phosphoproteomic Analysis of T Cell Receptor Signaling Reveals System-Wide Modulation of Protein-Protein Interactions

V. Mayya et al.

Serine-threonine phosphorylation plays a role in regulating the interactions among proteins involved in T cell responses.

RESEARCH ARTICLE: Mitofusin 2 Inhibits Mitochondrial Antiviral Signaling

K. Yasukawa et al.

A protein that mediates mitochondrial fusion also suppresses innate immune responses to viral infection.

PERSPECTIVE: mTORC1 Phosphorylates the ULK1-mAtg13-FIP200 Autophagy Regulatory Complex

E. Y. Chan

The kinase complex mTORC1 links nutrient availability to autophagy.

PERSPECTIVE: miRNA Regulation Through Ligand Occupancy of a Nuclear Hormone Receptor

A. E. Rougvie

Ligand occupancy of DAF-12 determines whether transcription of *let-7* family miRNAs occurs during *C. elegans* development.

PODCAST

D. K. Han and A. M. VanHook

D. K. Han discusses roles for serine-threonine phosphorylation in T cell signaling.

SCIENCECAREERS

www.sciencecareers.org/career_magazine

Free Career Resources for Scientists

Tooling Up: Myths About Industry Jobs

D. Jensen

There is more common ground between industry and academia than you think.

Independent Postdocs, Part 2: On-the-Ground Experiences

E. Pain

Three postdocs describe their early and successful transitions to research independence.

GrantsNet Funding News

D. Adams

Get the latest weekly compilation of research funding and student support.



SCIENCE SIGNALING

Arabidopsis responding to wounding.



SCIENCE CAREERS

The real story about jobs in industry.

SCIENCEPODCAST

www.sciencemag.org/multimedia/podcast

Free Weekly Show

Download the 21 August *Science* Podcast to hear about optimizing the distribution of influenza vaccines, archaeology in China, bioluminescent deep-sea worms, and more.

ORIGINSBLOG

blogs.sciencemag.org/origins

A History of Beginnings

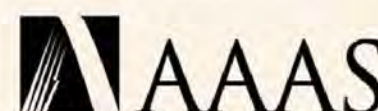
SCIENCEINSIDER

blogs.sciencemag.org/scienceinsider

Science Policy News and Analysis

SCIENCE (ISSN 0036-8075) is published weekly on Friday, except the last week in December, by the American Association for the Advancement of Science, 1200 New York Avenue, NW, Washington, DC 20005. Periodicals Mail postage (publication No. 484460) paid at Washington, DC, and additional mailing offices. Copyright © 2009 by the American Association for the Advancement of Science. The title *SCIENCE* is a registered trademark of the AAAS. Domestic individual membership and subscription (51 issues): \$146 (\$74 allocated to subscription). Domestic institutional subscription (51 issues): \$835; Foreign postage extra: Mexico, Caribbean (surface mail) \$55; other countries (air assist delivery) \$85. First class, airmail, student, and emeritus rates on request. Canadian rates with GST available upon request, GST #1254 88122. Publications Mail Agreement Number 1069624. **Printed in the U.S.A.**

Change of address: Allow 4 weeks, giving old and new addresses and 8-digit account number. **Postmaster:** Send change of address to AAAS, P.O. Box 96178, Washington, DC 20090-6178. **Single-copy sales:** \$10.00 current issue, \$15.00 back issue prepaid includes surface postage; bulk rates on request. **Authorization to photocopy** material for internal or personal use under circumstances not falling within the fair use provisions of the Copyright Act is granted by AAAS to libraries and other users registered with the Copyright Clearance Center (CCC) Transactional Reporting Service, provided that \$20.00 per article is paid directly to CCC, 222 Rosewood Drive, Danvers, MA 01923. The identification code for *Science* is 0036-8075. *Science* is indexed in the *Reader's Guide to Periodical Literature* and in several specialized indexes.



ADVANCING SCIENCE, SERVING SOCIETY

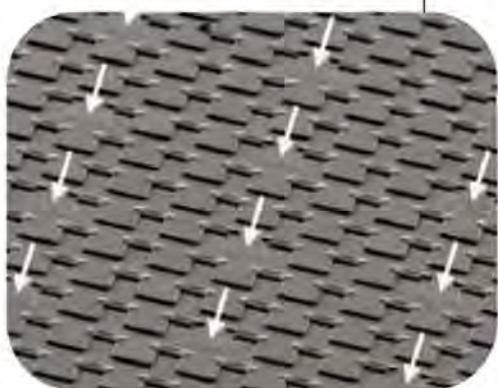
Going Retro >>

In a year celebrating Darwin, the question of how new functional genes arise during evolution is of particular interest. Through a multibreed genetic analysis of the domestic dog, **Parker *et al.*** (p. 995, published online 16 July; see the Perspective by **Kaessmann**) find that the short-legged phenotype that characterizes at least 19 common dog breeds, including the corgi, dachshund, and basset hound, is specifically associated with the expression in developing bone of a gene encoding fibroblast growth factor 4 (*fgf4*), a member of a gene family previously implicated in dwarfism in humans. Interestingly, the culprit *fgf4* gene in dogs has the hallmarks of a "retrogene," a gene that arises when a parental gene is duplicated through an RNA-based copying mechanism.



Bend Me, Stretch Me

In the push toward flexible electronics, much research has focused on using organic conducting materials, including light-emitting diodes (LEDs), because they are more readily processed using scalable techniques. **Park *et al.*** (p. 977) have developed a series of techniques for depositing and assembling inorganic LEDs onto glass, plastic, or rubber. Conventional processing techniques are used to connect the LEDs in order to create flexible, stretchable displays, which, because the active diode material only covers a small part of the substrate, are mostly transparent.



Saturated Magnetism in Photoexcited Nanocrystals

Switching the magnetic state of semiconductors with either an electric field or by light absorption is a key requirement for spintronics, in which devices are based on electronic spin state rather than charge. In semiconductor nanoparticles doped with magnetic ions, excitons can form a spin state, a magnetic polaron, but often the effect is limited to low temperatures (below 30 kelvin) and does not saturate in the absence of an applied magnetic field. **Beaulac *et al.*** (p. 973) report the synthesis of Mn-doped CdSe nanocrystals in which the quantum confinement effects lead to long exciton lifetimes. Photoexcitation results in exchange fields that can exceed

30 Tesla at low temperatures and that persist even up to room temperature in the absence of an applied magnetic field.

Discussing Polymerization Dynamics

Actin and tubulin represent the major components of microfilaments and microtubules, which are responsible for the cytoskeletal framework of cells. Together with their recently discovered bacterial counterparts, the mechanisms of assembly and disassembly of polymers of these proteins are fundamental to our understanding of cytoplasmic organization and motility. **Kueh and Mitchison** (p. 960) review mechanisms of cytoskeleton polymerization dynamics and discuss the relative importance of structural plasticity in regulating polymerization.

Toward Detecting Dark Matter Signals

Dark matter, whose presence has been inferred indirectly through its gravitational effects on luminous matter, is thought to hold galaxies together and may form most of the matter in the universe. Although its nature is still unknown, theoretical models predict that when certain dark matter particles collide, they annihilate, producing gamma rays. Using a numerical simulation of a galaxy the size of the Milky Way, **Kuhlen *et al.*** (p. 970, published online 16 July) investigated the potential signals from dark matter in our galaxy, for the case in which the annihilation rate is boosted by an attractive force

between incident dark matter particles. If this enhancement effect is valid, hundreds of dark matter clumps in our galaxy should be detected by the Fermi Gamma-ray Space Telescope.

Solar Chronometer

The use of the short-lived radioactive isotope ^{26}Al as a precise chronometer of early solar system processes relies on the assumption that it was uniformly distributed in the initial solar accretion disk. **Villeneuve *et al.*** (p. 985; see the Perspective by **Davis**) validate this assumption on the basis of high-precision isotopic analyses of primitive meteoritic materials. Furthermore, chondrules—constituents of the most common type of meteorites and among the first materials to have formed in the solar system—formed episodically over a period of more than one million years.

Crustal Details Revealed

In seismic tomography, a large collection of data representing paths through Earth are inverted to provide an analysis of variation of density in which errors are minimized. Typically, the inversion starts with a simple layered model of the tomographic region. **Tape *et al.*** (p. 988) show how, starting with a three-dimensional model, based on synthetic seismograms, an improved iterative inversion approach can lead to a much more detailed view of a region. Using the rich data for Southern California, the model reveals details of the geologic history of the crust in this region.

Attacks Wasps

The bacterium *Hamiltonella defensa* infects aphids and carries virulence determinants from a bacteriophage virus. **Oliver *et al.*** (p. 992) have

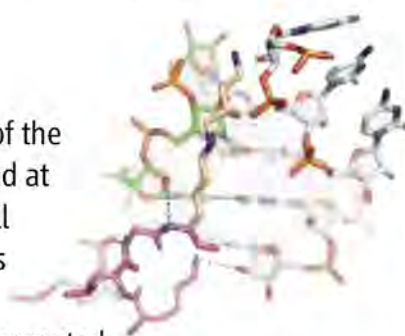
now found that the toxin-bearing phage does not harm the aphid host of the bacterium, but targets the larvae of parasitoid wasps that infest the aphids. If an aphid population is not infested by wasps, the allied bacteriophage is shed by the bacterium, presumably because there is a cost to carrying it. If the wasps then resume their predation, the aphids are no longer protected and succumb to the parasitoid.

Blast-Resistant Rice

The durability of disease resistance for an agricultural crop reflects the extent to which the defense stands up to evolutionary dodges on the part of the pathogen. *Pi21*, which is a quantitative trait locus (QTL) of rice, contributes to a particularly durable resistance to a fungal rice blast disease: Rice plants carrying the resistant allele have been in cultivation for more than a century, and yet the pathogen has been unable to find a way through the defense. **Fukuoka *et al.*** (p. 998; see the news story by **Normile**) have now cloned the responsible *Pi21* QTL allele and were able to separate *Pi21* resistance from tightly linked reductions in grain quality, paving the way for more widespread use of this allele in rice breeding.

Protein Synthesis Initiation Complex

The final step in the initiation phase of protein synthesis is the formation of the first peptide bond, which requires initiator transfer RNA (tRNA) to be bound at the ribosomal P site. Elongation factor P (EF-P) is a protein conserved in all eubacteria that stimulates this initial bond formation. Insight into how this is achieved comes from a structure of *Thermus thermophilus* 70S ribosome bound to EF-P, initiator tRNA, and a short piece of messenger RNA presented by **Blaha *et al.*** (p. 966). EF-P binds between the P and E sites and facilitates proper positioning of initiator tRNA in the P site. A similar mechanism is likely to apply to structurally homologous initiation factors in archaea and eukarya.



T Follicular Helper Cell Differentiation

When B cells respond to an infection, they often require help from CD4⁺ T cells to mount a proper response. It is thought that a subset of CD4⁺ effector T cells, called T follicular helper cells (T_{FH}), performs this function. Several subsets of effector CD4⁺ T cells arise, depending on the type of infection, which have distinct transcriptional programs driving their differentiation. Whether this is also the case for T_{FH} cells has not been clear (see the Perspective by **Awasthi and Kuchroo**). **Nurieva *et al.*** (p. 1001, published online 23 July) and **Johnston *et al.*** (p. 1006; published online 16 July) now demonstrate that the transcription factor Bcl6 is both necessary and sufficient for T_{FH} differentiation and subsequent B cell-mediated immunity, suggesting that it is a master regulator of this lineage. Johnston *et al.* also show that expression of Bcl6 and the transcription factor, Blimp-1, are reciprocally regulated in T_{FH} cells and that, when ectopically expressed, Blimp-1 inhibits T_{FH} development.

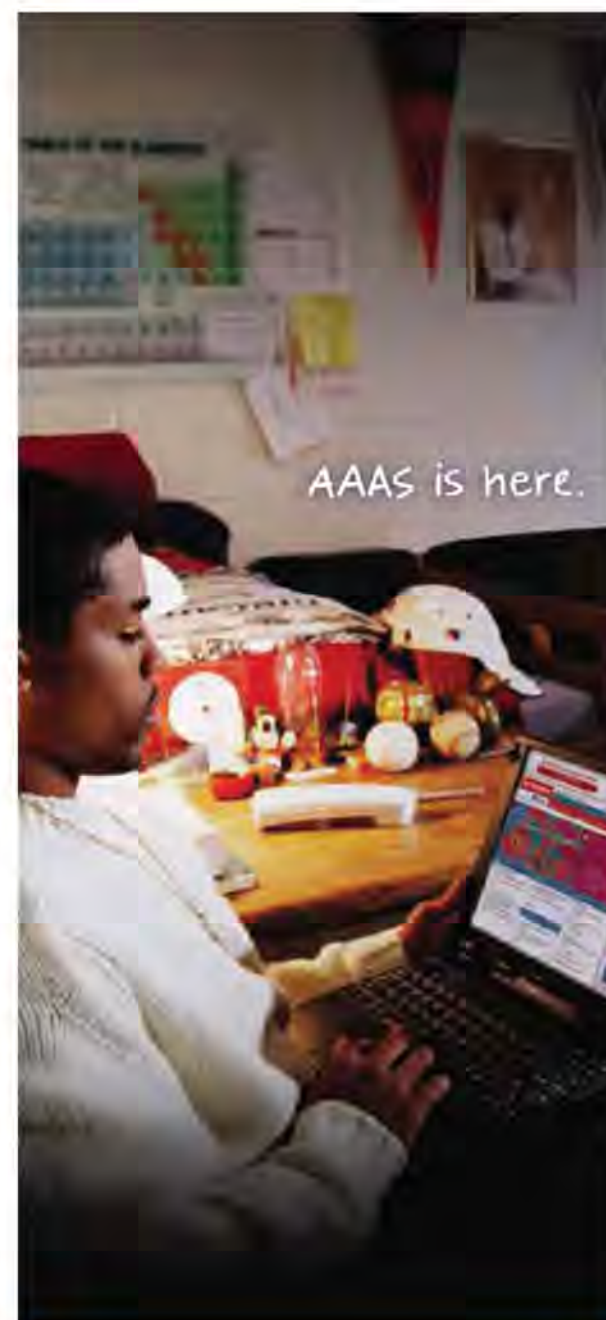
Translational Rearrangements

Conformational changes in the ribosome are required to translocate messenger RNA and transfer RNA (tRNA) during protein biosynthesis. For example, after peptide bond formation, rotation of the large and small subunits results in a hybrid state of tRNA binding—tRNAs are bound respectively in the aminoacyl-tRNA (A) and peptidyl-tRNA (P) sites in the small subunit, but in the P and exit-tRNA (E) sites on the large subunit. **Zhang *et al.*** (p. 1014) now describe x-ray structures of the intact *Escherichia coli* ribosome, either in the apo form or with one or two anticodon stem-loop tRNA mimics bound, which show intermediate states of intersubunit rotation. The structures provide insight into how the interface between the large and small subunits rearranges in discrete steps to reach the hybrid state.

Making Memories Last

How can memory traces persist over days or weeks, despite the short-lived nature and rapid turnover of their molecular substrates? It has recently been reported that, in order to persist, an otherwise rapidly forgotten long-term memory requires BDNF (brain-derived neurotrophic factor) expression in the hippocampus 12 hours post training. **Rossato *et al.*** (p. 1017) now show that this mechanism is gated into action by activation of the ventral tegmental area acting upon dopamine D1 receptors in the hippocampus. Time-limited *N*-methyl-D-aspartate receptor-dependent activity in the ventral tegmental area-hippocampal circuitry underlies the delayed increase in BDNF levels in the hippocampus 12 hours after inhibitory avoidance, a hippocampus-dependent form of learning.

CREDIT: BLAHA ET AL.



HBCU-UP National Research Conference

AAAS partners with NSF to host a national gathering that highlights underrepresented ethnic minorities' undergrad student research to enhance the quality of STEM education. And this is just one of the ways that AAAS is committed to advancing science to support a healthy and prosperous world. Join us. Together we can make a difference.

To learn more, visit:
aaas.org/plusyou/hbcuup



Globalizing Science Publishing

PUBLISHING IN SCIENTIFIC JOURNALS IS THE MOST COMMON AND POWERFUL MEANS TO DISSEMINATE new research findings. Visibility and credibility in the scientific world require publishing in journals that are included in global indexing databases such as those of the Institute for Scientific Information (ISI). Most scientists in developing countries remain at the periphery of this critical communication process, exacerbating the low international recognition and impact of their accomplishments. For science to become maximally influential and productive across the globe, this needs to change.

The economy of electronic publication, open access, and property rights fuel current academic and policy debates about scientific publishing in the industrialized world. The concerns in the developing world (with few ISI-indexed journals) focus on more fundamental questions, such as sustaining local research activity and achieving the appropriate global reach of its science activities.

The essence of the African situation is captured by R. J. W. Tijssen's analysis of publications by African authors,* which was based not only on data from ISI indexing databases, but also on publications not indexed in this system. Surprisingly, half of the South African citations in the indexed ISI literature are to articles in nonindexed, locally published journals. Also, several nonindexed local journals are cited in the ISI system at about the same rate as are indexed journals. The share of indexed articles with at least one author with an African address remains steady at about 1%. About half of the ISI-indexed papers with at least one author with an African address have non-African partners outside of the continent. These figures vary, country by country, sometimes in surprising ways. For example, 85% of the papers published from Mali or Gabon involve collaborations on other continents, versus 39% and 29%, respectively, for South Africa and Egypt, the continent's leading research producers. Thus,

much of the African research system is now highly dependent on collaborations.

How can the global reach and potential impact of scientific research in Africa and other developing countries be optimized? Of primary importance is boosting the quality and quantity of work that is locally published, through measures including review of submissions by peers from within and outside the country, skilled editing, and exploitation of local niches and special research opportunities. A proliferation of journals, short-lived publications, print-only journals, and poor distribution constitutes a picture that must change. A nationally organized project can probably make the biggest difference, with investment by government and research-support agencies, as well as wide participation by local and regional scientific communities.

The work published in local journals must become more visible through search engines and bibliometric tools. An open-source software-based system called Scientific Electronic Library Online (SciELO), in development since 1998 with government support in Brazil, has two major aims. One is to index high-quality local journals, extending beyond the ISI-indexed titles, through a selection based on transparent assessment and performance monitoring. The second aim is to provide free worldwide electronic access to the content of these journals. This system has already revealed the existence of local journals and articles that are highly cited in ISI-indexed journals; it has also revealed journals and articles that have a high impact within the SciELO system itself.†

The SciELO system is now being extended to South Africa, with government support. Extension to other African countries and regions is readily possible with the appropriate program leadership and government support at national and international levels. Few forms of foreign aid would be more likely to yield real and recurrent dividends than the facilitation of a connected system of national and regional, open-access, quality-assured SciELO sites (or similar) throughout Africa, and even more so, across the entire developing world.

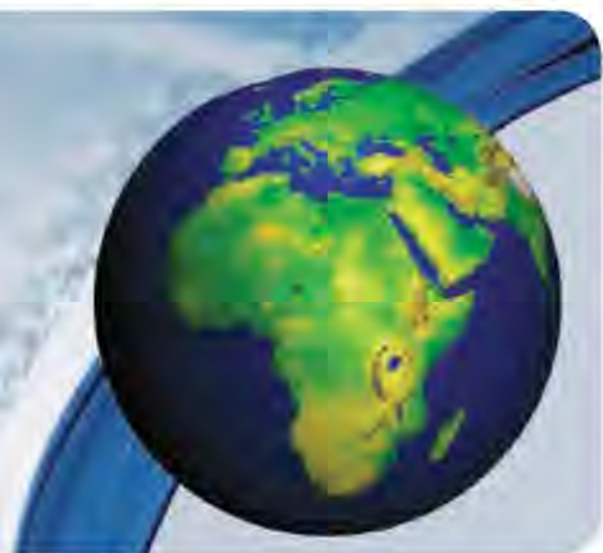
—Wieland Gevers

10.1126/science.1178378

*R. J. W. Tijssen, *Scientometrics* 71, 303 (2007). †R. Meneghini, R. Mugnaini, A. L. Packer, *Scientometrics* 69, 529 (2006).



Wieland Gevers is Emeritus Professor of Medical Biochemistry at the University of Cape Town in South Africa; he was President of the Academy of Science of South Africa from 1998 to 2004.





PLANT SCIENCE

Cereal Mutation

More than 9000 years ago, the domestication of barley began. Today, wild barley carries spikelets with two rows of grains, whereas domesticated barley varieties are found with two or six rows. The latter has a higher protein content and greater fecundity, although the grains of the former are larger and hence yield roughly equal biomass. Six-row varieties are commonly preferred and have been available in northern Africa for thousands of years. A loss-of-function mutation in the gene *Vrs1* produces a six-row morphology.

Archaeological analysis at Qasr Ibrim, a settlement on the boundary of the Nubian and Roman Empires, has shown that two-row barley (shown above) predominates. By analysis of ancient barley samples found at Qasr Ibrim, Palmer *et al.* discovered the same loss-of-function mutation in *Vrs1* and infer that a subsequent and as yet unidentified mutation derived the two-row morphology from the domesticated six-row variety. The agricultural preference for two-row barley hints at a competitive advantage, such as its greater tolerance to drought. That the several cultures that occupied Qasr Ibrim during the past 3000 years all adopted the local two-row barley suggests that this strain is particularly well suited for cultivation at this locale. — PJH

PLoS ONE 4, e6301 (2009).

CHEMISTRY

Gilded Coupling

Contrary to gold's historical reputation as an inert element, increasingly versatile examples of catalysis by nanoparticulate morphologies of the precious metal are emerging. Zhou *et al.* now show that even larger particles of bulk gold (5 to 50 μm in diameter) can promote organic coupling reactions. Carbene precursors such as diazoalkanes ($\text{R}_2\text{C}=\text{N}=\text{N}$, where R is an alkyl group) and 3,3-diphenylcyclopropene react in the presence of this gold powder to form olefins through apparent carbene coupling at the metal surface. Cyclopropanation reactions with added styrene were also observed. The surface morphology affected reactivity: Initially reduced powders (incorporating residual carbon) were less active than the smoother, shinier surfaces that formed after a round of diazo substrate couplings. — PDS

J. Am. Chem. Soc. 131, 10.1021/ja900653s (2009).

EDUCATION

A Matter of Animation

Students of chemistry often have trouble making the connection between macroscopic phenomena they can see and the underlying molecular events operating on a scale too small to visualize directly. Chang *et al.* investigated whether seventh-grade students' understanding of the molecular structure of matter could improve with the help of computer animation software to portray molecular events in familiar processes such as boiling. Specifically, the authors sought to assess the relative efficacies of three approaches: design and interpretation by individual students of animations illustrating chemical phenomena; self-design of animations followed by interactive critiquing sessions with peers in the class; and examination by students of purely teacher-generated animations. Assessments were based on comparative test performance before and after the animation project. Data from 178 students supported significantly greater gains in understanding among students who participated in peer evaluation than among

*Melissa McCartney is a summer intern in *Science's* editorial department.

those who simply prepared animations alone. Thus, including an interactive evaluation component may take more time, but it appears to be time well spent. There was no significant difference in test outcome between the students in the peer-evaluation group and those in the teacher-generated animation group, though the former students did perform slightly better in an assessment of their ability to interpret molecular animations in class. — MM*

Sci. Educ. 93, 10.1002/sce.20352 (2009).

CHEMISTRY

Zooming in on pH

Local acidity plays a central role in many chemical and physiological processes. Molecular-scale tools that can sense or alter the pH of their environment are therefore eagerly sought. Harbuzaru *et al.* present a miniaturized pH sensor operative in the physiologically relevant pH 5 to 7.5 range. The sensor is based on a metal-organic framework material (optical micrograph shown below) that contains strongly photolumi-



nescent trivalent europium ions in two distinct coordination environments. The authors combined this material with a commercial optical fiber in their prototype design. Because only one of the two ion sites is sensitive to pH, the sensor is self-calibrating.

In a similarly directed study, Alibrandi *et al.* show that [1,1,1]cryptand—a cage-like molecule that gradually captures protons from aqueous solution—can be used as a molecular-scale automatic titrator to smoothly vary the pH of a solution through nearly two units over time. Beyond pK_a determinations (which the authors demonstrate), this system may find use in studying phenomena such as the pH-dependent unfolding of proteins. — JFU

Angew. Chem. Int. Ed. 48, 6476; 6332 (2009).

**1200 New York Avenue, NW
Washington, DC 20005**
Editorial: 202-326-6550, FAX 202-289-7562
News: 202-326-6581, FAX 202-371-9227
**Bateman House, 82-88 Hills Road
Cambridge, UK CB2 1LQ**
+44 (0) 1223 326500, FAX +44 (0) 1223 326501

SUBSCRIPTION SERVICES For change of address, missing issues, new orders and renewals, and payment questions: 866-434-AAAS (2227) or 202-326-6417, FAX 202-842-1065. Mailing addresses: AAAS, P.O. Box 96178, Washington, DC 20090-6178 or AAAS Member Services, 1200 New York Avenue, NW, Washington, DC 20005

INSTITUTIONAL SITE LICENSES please call 202-326-6755 for any questions or information

REPRINTS: Author Inquiries 800-635-7181
Commercial Inquiries 803-359-4578

PERMISSIONS 202-326-7074, FAX 202-682-0816

MEMBER BENEFITS AAAS/Barnes&Noble.com bookstore www.aaas.org/bn; AAAS Online Store www.apisource.com/aaas/ code MKB6; AAAS Travels: Betchart Expeditions 800-252-4910; Apple Store www.wapple/eppstore/aaas; Bank of America MasterCard 1-800-833-6262 priority code FAA3YU; Cold Spring Harbor Laboratory Press Publications www.cshlpress.com/affiliates/aaas.htm; GEICO Auto Insurance www.geico.com/landingpage/go51.htm?logo=17624; Hertz 800-654-2200 CDP#343457; Office Depot https://bsd.officedepot.com/portallLogin.do; Seabury & Smith Life Insurance 800-424-9883; Subaru VIP Program 202-326-6417; VIP Moving Services www.vipmayflower.com/domestic/index.html; Other Benefits: AAAS Member Services 202-326-6417 or www.aaasmember.org.

science_editors@aaas.org (for general editorial queries)
science_letters@aaas.org (for queries about letters)
science_reviews@aaas.org (for returning manuscript reviews)
science_bookrevs@aaas.org (for book review queries)

Published by the American Association for the Advancement of Science (AAAS), *Science* serves its readers as a forum for the presentation and discussion of important issues related to the advancement of science, including the presentation of minority or conflicting points of view, rather than by publishing only material on which a consensus has been reached. Accordingly, all articles published in *Science*—including editorials, news and comment, and book reviews—are signed and reflect the individual views of the authors and not official points of view adopted by AAAS or the institutions with which the authors are affiliated.

AAAS was founded in 1848 and incorporated in 1874. Its mission is to advance science, engineering, and innovation throughout the world for the benefit of all people. The goals of the association are to: enhance communication among scientists, engineers, and the public; promote and defend the integrity of science and its use; strengthen support for the science and technology enterprise; provide a voice for science on societal issues; promote the responsible use of science in public policy; strengthen and diversify the science and technology workforce; foster education in science and technology for everyone; increase public engagement with science and technology; and advance international cooperation in science.

INFORMATION FOR AUTHORS

See pages 807 and 808 of the 6 February 2009 issue or access www.sciencemag.org/about/authors

EDITOR-IN-CHIEF **Bruce Alberts**

EXECUTIVE EDITOR

Monica M. Bradford

NEWS EDITOR

Colin Norman

MANAGING EDITOR, RESEARCH JOURNALS **Katrina L. Kelner**

DEPUTY EDITORS **R. Brooks Hanson, Barbara R. Jasny, Andrew M. Sugden**

EDITORIAL SENIOR EDITORS/COMMENTARY Lisa D. Chong, Brad Wible; **SENIOR EDITORS** Gilbert J. Chin, Pamela J. Hines, Paula A. Kiberstis (Boston), Marc S. Lavine (Toronto), Beverly A. Purnell, L. Bryan Ray, Guy Riddihough, H. Jesse Smith, Phillip D. Szurmi (Tennessee), Valda Vinson, Jake S. Yeston; **ASSOCIATE EDITORS** Kristen L. Mueller, Nicholas S. Wigginton, Laura M. Zahn; **RESEARCH ASSOCIATE** Alexis Wynne Mogul; **ONLINE EDITOR** Stewart Willis; **ASSOCIATE ONLINE EDITORS** Robert Frederick, Tara S. Marathe; **WEB CONTENT DEVELOPER** Martyn Green; **BOOK REVIEW EDITOR** Sherman J. Suter; **ASSOCIATE LETTERS EDITOR** Jennifer Sills; **EDITORIAL MANAGER** Cara Tate; **SENIOR COPY EDITORS** Jeffrey E. Cook, Cynthia Howe, Harry Jach, Barbara P. Ordway, Trista Wagoner; **COPY EDITORS** Chris Filiatreau, Lauren Kmec; **EDITORIAL COORDINATORS** Carolyn Kyle, Beverly Shields; **PUBLICATIONS ASSISTANTS** Ramatoulaye Diop, Carlos L. Durham, Joi S. Granger, Jeffrey Hearn, Lisa Johnson, Scott Miller, Jerry Richardson, Jennifer A. Seibert, Brian White, Anita Wynn; **EDITORIAL ASSISTANTS** Emily Guise, Michael Hicks, Patricia M. Moore; **EXECUTIVE ASSISTANT** Sylvia S. Kihara; **ADMINISTRATIVE SUPPORT** Maryrose Madrid; **EDITORIAL FELLOW** Melissa R. McCartney

NEWS DEPUTY NEWS EDITORS Robert Coontz, Eliot Marshall, Jeffrey Mervis, Leslie Roberts; **Contributing Editors** Elizabeth Culotta, Polly Shulman; **NEWS WRITERS** Yudhijit Bhattacharjee, Adrian Cho, Jennifer Couzin, David Grimm, Constance Holden, Jocelyn Kaiser, Richard A. Kerr, Eli Kintisch, Andrew Lawler (New England), Greg Miller, Elizabeth Pennisi, Robert F. Service (Pacific NW), Erik Stokstad; **INTERNS** Michael Torrice, Brittany Johnson, Preyanka Makadia; **CONTRIBUTING CORRESPONDENTS** Dan Charles, Jon Cohen (San Diego, CA), Daniel Ferber, Ann Gibbons, Robert Koenig, Mitch Leslie, Charles C. Mann, Virginia Morell, Evelyn Strauss, Gary Taubes; **COPY EDITORS** Linda B. Felaco, Melvin Gatling, Melissa Raimondi; **ADMINISTRATIVE SUPPORT** Scherraine Mack, Fannie Groom; **BUREAU** New England: 207-549-7755; San Diego, CA: 760-942-3252, FAX 760-942-4979; Pacific Northwest: 503-963-1940 **PRODUCTION DIRECTOR** James Landry; **SENIOR MANAGER** Wendy K. Shank; **ASSISTANT MANAGER** Rebecca Doshi; **SENIOR SPECIALISTS** Steve Forrester, Chris Redwood; **SPECIALIST** Anthony Rosen; **PREFLIGHT DIRECTOR** David M. Tompkins; **MANAGER** Marcus Spiegler; **SPECIALIST** Jason Hillman **ART DIRECTOR** Yael Kats; **ASSOCIATE ART DIRECTOR** Laura Creveling; **SENIOR ILLUSTRATORS** Chris Bickel, Katharine Sutliff; **ILLUSTRATOR** Yana Greenman; **SENIOR ART ASSOCIATES** Holly Bishop, Preston Huey, Nayomi Kevitiyagala; **ART ASSOCIATES** Jessica Newfield, Matthew Twombly; **PHOTO EDITOR** Leslie Blizard

SCIENCE INTERNATIONAL

EUROPE (science@science-int.co.uk) **EDITORIAL: INTERNATIONAL MANAGING EDITOR** Andrew M. Sugden; **SENIOR EDITOR/COMMENTARY** Julia Fahrenkamp-Uppenbrink; **SENIOR EDITORS** Caroline Ash, Stella M. Hurtley, Ian S. Osborne, Peter Stern; **ASSOCIATE EDITOR** Maria Cruz; **LOCUM EDITOR** Helen Pickersgill; **EDITORIAL SUPPORT** Deborah Dennison, Rachel Roberts, Alice Whaley; **ADMINISTRATIVE SUPPORT** John Cannell, Janet Clements, Louise Moore; **NEWS: EUROPE NEWS EDITOR** John Travis; **DEPUTY NEWS EDITOR** Daniel Clery; **CONTRIBUTING CORRESPONDENTS** Michael Balter (Paris), John Bohannon (Vienna), Martin Enserink (Amsterdam and Paris), Gretchen Vogel (Berlin)

ASIA Japan Office: Asca Corporation, Eiko Ishioka, Fusako Tamura, 77 Tenjin-cho, Shinjuku, Tokyo 162-0808, Japan; +81 3 6802 4616, FAX +81 3 6802 4615, inquiry@sciencemag.jp; **ASIA NEWS EDITOR** Richard Stone (Beijing: rstone@aaas.org); **CONTRIBUTING CORRESPONDENTS** Dennis Normile [Japan: +81 (0) 3 3391 0630, FAX +81 (0) 3 5936 3531; dnormile@gol.com]; Hao Xin [China: +86 (0) 10 6307 4439 or 6307 3676, FAX +86 (0) 10 6307 4358; cindyhao@gmail.com]; Pallava Bagla [South Asia: +91 (0) 11 2271 2896; pbagla@vsnl.com]

EXECUTIVE PUBLISHER **Alan I. Leshner**

PUBLISHER **Beth Rosner**

FULFILLMENT SYSTEMS AND OPERATIONS (membership@aaas.org); **DIRECTOR** Waylon Butler; **SENIOR SYSTEMS ANALYST** Nomuna Nyamaa; **CUSTOMER SERVICE SUPERVISOR** Pat Butler; **SPECIALISTS** Latoya Casteel, LaVonda Crawford, Vicki Linton, April Marshall; **DATA ENTRY SUPERVISOR** Cynthia Johnson; **SPECIALISTS** Shirlene Hall, Tarika Hill, William Jones

BUSINESS OPERATIONS AND ADMINISTRATION DIRECTOR Deborah Rivera-Wienhold; **ASSISTANT DIRECTOR, BUSINESS OPERATIONS** Randy Yi; **MANAGER, BUSINESS ANALYSIS** Eric Knott; **MANAGER, BUSINESS OPERATIONS** Jessica Tierney; **FINANCIAL ANALYSTS** Priti Pamnani, Celeste Troxler; **RIGHTS AND PERMISSIONS: ADMINISTRATOR** Emilie David; **ASSOCIATE** Elizabeth Sandler; **MARKETING DIRECTOR** Ian King; **MARKETING MANAGERS** Allison Pritchard, Alison Chandler, Julianne Wielga; **MARKETING ASSOCIATES** Aimee Aponte, Mary Ellen Crowley, Adrian Parham, Wendy Wise; **MARKETING EXECUTIVE** Jennifer Reeves; **DIRECTOR, SITE LICENSING** Tom Ryan; **DIRECTOR, CORPORATE RELATIONS** Eileen Bernadette Moran; **PUBLISHER RELATIONS, eRESOURCES SPECIALIST** Kiki Forsythe; **SENIOR PUBLISHER RELATIONS SPECIALIST** Catherine Holland; **PUBLISHER RELATIONS, EAST COAST** Phillip Smith; **PUBLISHER RELATIONS, WEST COAST** Philip Tsolakidis; **FULFILLMENT SUPERVISOR** Iquo Edim; **FULFILLMENT COORDINATOR** Carrie MacDonald; **MARKETING ASSOCIATE** Mary Lagnaoui; **ELECTRONIC MEDIA: MANAGER** Lizabeth Harman; **PROJECT MANAGER** Trista Snyder; **ASSISTANT MANAGER** Lisa Stanford; **SENIOR PRODUCTION SPECIALISTS** Christopher Coleman, Walter Jones; **PRODUCTION SPECIALISTS** Nichele Johnston, Kimberly Oster

ADVERTISING DIRECTOR, WORLDWIDE AD SALES Bill Moran

PRODUCT (science_advertising@aaas.org); **MIDWEST/WEST COAST/W. CANADA** Rick Bongiovanni: 330-405-7080, FAX 330-405-7081; **EAST COAST/E. CANADA** Laurie Faraday: 508-747-9395, FAX 617-507-8189; **UK/EUROPE/ASIA** Roger Goncalves: TEL/FAX +41 43 243 1358; **JAPAN** Mashy Yoshikawa: +81 (0) 3 3235 5961, FAX +81 (0) 3 3235 5852; **SENIOR TRAFFIC ASSOCIATE** Delandra Simms

COMMERCIAL EDITOR Sean Sanders: 202-326-6430

PROJECT DIRECTOR, OUTREACH Brianna Blaser

CLASSIFIED (advertise@sciencecareers.org); **U.S.: SALES MANAGER** Daryl Anderson: 202-326-6543; **MIDWEST** Tina Burks: 202-326-6577; **EAST COAST** Alexis Fleming: 202-326-6578; **WEST/SOUTH CENTRAL** Nicholas Hintibidze: 202-326-6533; **SALES COORDINATORS** Rohan Edmonson, Shirley Young; **INTERNATIONAL: SALES MANAGER** Tracy Holmes: +44 (0) 1223 326525, FAX +44 (0) 1223 326532; **SALES** Susanne Kharraz, Dan Pennington, Alex Palmer; **SALES ASSISTANT** Lisa Patterson; **JAPAN** Mashy Yoshikawa: +81 (0) 3 3235 5961, FAX +81 (0) 3 3235 5852; **ADVERTISING SUPPORT MANAGER** Karen Foote: 202-326-6740; **ADVERTISING PRODUCTION OPERATIONS MANAGER** Deborah Tompkins; **SENIOR PRODUCTION SPECIALIST/GRAPHIC DESIGNER** Amy Hardcastle; **SENIOR PRODUCTION SPECIALIST** Robert Buck; **SENIOR TRAFFIC ASSOCIATE** Christine Hall

AAAS BOARD OF DIRECTORS **RETIRING PRESIDENT, CHAIR** James J. McCarthy; **PRESIDENT** Peter C. Agre; **PRESIDENT-ELECT** Alice Huang; **TREASURER** David E. Shaw; **CHIEF EXECUTIVE OFFICER** Alan I. Leshner; **BOARD** Alice Gast, Linda P. B. Katehi, Nancy Knowlton, Cherry A. Murray, Julia M. Phillips, Thomas D. Pollard, David S. Sabatini, Thomas A. Woolsey



ADVANCING SCIENCE. SERVING SOCIETY

SENIOR EDITORIAL BOARD

John I. Brauman, *Chair, Stanford Univ.*
Richard Losick, *Harvard Univ.*
Marcia McNutt, *Monterey Bay Aquarium Research Inst.*
Linda Partridge, *Univ. College London*
Michael S. Turner, *University of Chicago*

BOARD OF REVIEWING EDITORS

Adriano Aguzzi, *Univ. Hospital Zürich*
Takuzo Aida, *Univ. of Tokyo*
Joanna Aizenberg, *Harvard Univ.*
Sonia Altizer, *Univ. of Georgia*
David Altshuler, *Broad Institute*
Arturo Alvarez-Buylla, *Univ. of California, San Francisco*
Richard Amasino, *Univ. of Wisconsin, Madison*
Angelika Amon, *MIT*
Meinrat O. Andreae, *Max Planck Inst., Mainz*
Kristi S. Anseth, *Univ. of Colorado*
John A. Bargh, *Yale Univ.*
Cornelia I. Bargmann, *Rockefeller Univ.*
Ben Barres, *Stanford Medical School*
Marisa Bartolomei, *Univ. of Penn. School of Med.*
Facundo Batista, *London Research Inst.*
Ray H. Baughman, *Univ. of Texas, Dallas*
Yasmine Belkaid, *NIAID, NIH*
Stephen J. Benkovic, *Penn State Univ.*
Ton Bisseling, *Wageningen Univ.*
Mina Bissell, *Lawrence Berkeley National Lab*
Peer Bork, *EMBL*
Robert W. Boyd, *Univ. of Rochester*
Paul M. Brakefield, *Leiden Univ.*
Stephen Buratowski, *Harvard Medical School*
Joseph A. Burns, *Cornell Univ.*
William P. Butz, *Population Reference Bureau*
Mats Carlsson, *Univ. of Oslo*
Peter Carmeliet, *Univ. of Leuven, VIB*
Mildred Cho, *Stanford Univ.*
David Clapham, *Children's Hospital, Boston*
David Clary, *Oxford University*
J. M. Claverie, *CNRS, Marseille*
Jonathan D. Cohen, *Princeton Univ.*
Andrew Cossins, *Univ. of Liverpool*

Robert H. Crabtree, *Yale Univ.*
Wolfgang Cramer, *Potsdam Inst. for Climate Impact Research*
F. Fleming Crim, *Univ. of Wisconsin*
William Cumberland, *Univ. of California, Los Angeles*
Jeff L. Dangl, *Univ. of North Carolina*
Stanislas Dehaene, *Collège de France*
Edward DeLong, *MIT*
Emmanouil T. Dermizakis, *Univ. of Geneva Medical School*
Robert Desimone, *MIT*
Claude Desplan, *New York Univ.*
Dennis Discher, *Univ. of Pennsylvania*
Scott C. Donney, *Woods Hole Oceanographic Inst.*
W. Ford Doolittle, *Dalhousie Univ.*
Jennifer A. Doudna, *Univ. of California, Berkeley*
Julian Downward, *Cancer Research UK*
Denis Duboule, *Univ. of Geneva/EPFL Lausanne*
Christopher Dye, *WHO*
Gerhard Ertl, *Fritz-Haber-Institut, Berlin*
Mark Estelle, *Indiana Univ.*
Barry Everitt, *Univ. of Cambridge*
Paul G. Falkowski, *Rutgers Univ.*
Ernst Fehr, *Univ. of Zurich*
Tom Fenchel, *Univ. of Copenhagen*
Alain Fischer, *INSERM*
Scott E. Fraser, *Cal Tech*
Chris D. Frith, *Univ. College London*
Wulfram Gerstner, *EPFL Lausanne*
Charles Godfray, *Univ. of Oxford*
Diane Griffin, *Johns Hopkins Bloomberg School of Public Health*
Christian Haass, *Ludwig Maximilians Univ.*
Steven Hahn, *Fred Hutchinson Cancer Research Center*
Niels Hansen, *Technical Univ. of Denmark*
Dennis L. Hartmann, *Univ. of Washington*
Chris Hawkesworth, *Univ. of Bristol*
Martin Heimann, *Max Planck Inst., Jena*
James A. Hendler, *Rensselaer Polytechnic Inst.*
Ray Hilborn, *Univ. of Washington*
Michael E. Himmel, *National Renewable Energy Lab.*
Kei Hirose, *Tokyo Inst. of Technology*
Ove Hoegh-Guldberg, *Univ. of Queensland*
Brigid L. M. Hogan, *Duke Univ. Medical Center*
Ronald R. Hoy, *Cornell Univ.*
Olli Ikkala, *Helsinki Univ. of Technology*
Meyer B. Jackson, *Univ. of Wisconsin Med. School*

Stephen Jackson, *Univ. of Cambridge*
Steven Jacobsen, *Univ. of California, Los Angeles*
Peter Jonas, *Universität Freiburg*
Barbara B. Kahn, *Harvard Medical School*
Daniel Kahne, *Harvard Univ.*
Gerard Karsenty, *Columbia Univ. College of P&S*
Bernhard Keimer, *Max Planck Inst., Stuttgart*
Elizabeth A. Kellog, *Univ. of Missouri, St. Louis*
Hanna Kokko, *Univ. of Helsinki*
Lee Kump, *Penn State Univ.*
Mitchell A. Lazar, *Univ. of Pennsylvania*
David Lazer, *Harvard Univ.*
Virginia Lee, *Univ. of Pennsylvania*
Olle Lindvall, *Univ. Hospital, Lund*
Marcia C. Linn, *Univ. of California, Berkeley*
John Lis, *Cornell Univ.*
Richard Losick, *Harvard Univ.*
Ke Lu, *Chinese Acad. of Sciences*
Laura Machesky, *CRUK Beatson Inst. for Cancer Research*
Andrew P. MacKenzie, *Univ. of St Andrews*
Raul Madariaga, *Ecole Normale Supérieure, Paris*
Anne Magurran, *Univ. of St Andrews*
Charles Marshall, *Harvard Univ.*
Virginia Miller, *Washington Univ.*
Yasushi Miyashita, *Univ. of Tokyo*
Robert Morris, *Univ. of Edinburgh*
Edvard Moser, *Norwegian Univ. of Science and Technology*
Naoto Nagaosa, *Univ. of Tokyo*
James Nelson, *Stanford Univ. School of Med.*
Timothy W. Nilsen, *Case Western Reserve Univ.*
Helga Nowotny, *European Research Advisory Board*
Eric N. Olson, *Univ. of Texas, SW*
Stuart H. Orkin, *Dana-Farber Cancer Inst.*
Erin O'Shea, *Harvard Univ.*
Elinor Ostrom, *Indiana Univ.*
Jonathan T. Overpeck, *Univ. of Arizona*
John Pendry, *Imperial College*
Reginald M. Penner, *Univ. of California, Irvine*
Simon Philippot, *Univ. of Florida*
Philippe Poulin, *CNRS*
Molly Przeworski, *Univ. of Chicago*
Colin Renfrew, *Univ. of Cambridge*
Trevor Robbins, *Univ. of Cambridge*
Barbara A. Romanowicz, *Univ. of California, Berkeley*
Jens Rostrup-Nielsen, *Haldor Topsøe*

Edward M. Rubin, *Lawrence Berkeley National Lab*
Shimon Sakaguchi, *Kyoto Univ.*
Jürgen Sandkühler, *Medical Univ. of Vienna*
David W. Schindler, *Univ. of Alberta*
Georg Schulz, *Albert-Ludwigs-Universität*
Paul Schulze-Lefert, *Max Planck Inst., Cologne*
Christine Seidman, *Harvard Medical School*
Terrence J. Sejnowski, *The Salk Institute*
Richard J. Shavelson, *Stanford Univ.*
David Sibley, *Washington Univ.*
Joseph Silk, *Univ. of Oxford*
Montgomery Slatkin, *Univ. of California, Berkeley*
Davor Solter, *Inst. of Medical Biology, Singapore*
Joan Steitz, *Yale Univ.*
Elsbeth Stern, *ETH Zürich*
Jerome Strauss, *Virginia Commonwealth Univ.*
Jürg Tschopp, *Univ. of Lausanne*
Derek van der Kooy, *Univ. of Toronto*
Bert Vogelstein, *Johns Hopkins Univ.*
Ulrich H. von Andrian, *Harvard Medical School*
Bruce D. Walker, *Harvard Medical School*
Christopher A. Walsh, *Harvard Medical School*
David A. Wardle, *Swedish Univ. of Agric Sciences*
Graham Warren, *Max F. Perutz Laboratories*
Colin Watts, *Univ. of Dundee*
Detlef Weigel, *Max Planck Inst., Tübingen*
Jonathan Weissman, *Univ. of California, San Francisco*
Sue Wessler, *Univ. of Georgia*
Ellen D. Williams, *Univ. of Maryland*
Ian A. Wilson, *The Scripps Res. Inst.*
Jerry Workman, *Stowers Inst. for Medical Research*
Xiaoliang Sunney Xie, *Harvard Univ.*
John R. Yates III, *The Scripps Res. Inst.*
Jan Zaanen, *Leiden Univ.*
Huda Zoghbi, *Baylor College of Medicine*
Maria Zuber, *MIT*

BOOK REVIEW BOARD

John Aldrich, *Duke Univ.*
David Bloom, *Harvard Univ.*
Angela Creager, *Princeton Univ.*
Richard Sweder, *Univ. of Chicago*
Ed Wasserman, *DuPont*
Lewis Wolpert, *Univ. College London*



THE TELLTALE AMYGDALA

Brain scans of Israeli paramedics suggest that it's possible to predict how well an individual will respond to stress.

Scientists at Tel Aviv University have performed an unusual prospective study to see if they could identify brain differences between emotionally resilient people and those who respond poorly to traumatic events. They recruited 50 18-year-old Israelis, half of them female, who were starting training as paramedics. They scanned them with functional magnetic resonance imaging while flashing photographs of military medical scenes. The recruits were also scored on stress-related symptoms such as anxiety and difficulty sleeping.

Eighteen months later, all the paramedics had been through rough emotional experiences dealing with combat casualties. The scientists, led by brain imager Roe Admon, again put them through the brain-scan experiment. Reporting online 5 August in the *Proceedings of the National Academy of Sciences*, the researchers found that the paramedics who reported the largest increase in stress symptoms had also showed the most activity in the amygdala—the seat of fear in the brain—in the first test.

Co-author Talma Hendler says the amygdala may turn out to be an “a priori biological marker” for factors that make people liable to post-traumatic stress disorder. The study shows that these factors “can be sensitively identified with brain imaging in otherwise healthy subjects,” says psychiatrist Amit Etkin of Stanford University in Palo Alto, California.

of the controls. Among those who thought about something positive that had happened the day before, 65% felt better, and the gratitude and smiling groups came in at 58%. But those in the “acts of kindness” group were no cheerier than the controls—which was “a bit disappointing,” says Wiseman.

Wiseman says in most surveys, about 50% report themselves as happy, 30% unhappy, and the rest don't know. He hasn't yet calculated from this experiment whether the already-happy got happier or whether actions such as gratitude and smiling can pull people up from the dumps.

Hominids' Diverse Tastes

Humans vary genetically in their ability to taste a bitter chemical known as phenylthiocarbamide, which has been compared to bitter flavors in Brussels sprouts, cabbage, and broccoli.

About 75% of people can detect these flavors because they possess a “taster” variant of the *TAS2R38* gene. People without this variant are insensitive to bitter fruits and vegetables. Now Spanish researchers say that analysis of DNA recovered from the bone of a Neandertal in El Sidrón cave in northern Spain reveals that he had both the taster and the nontaster versions of the gene, meaning that the gene



existed 40,000 years ago. That indicates that a common ancestor of Neandertals and *Homo sapiens* must have carried both variants, suggesting that differences in the ability to detect bitterness stretch back at least half a million years, the team reported last week in *Biology Letters*.

“The standard assumption is that these bitter chemicals are bad for us—and thus being a taster would be advantageous,” says anthropological geneticist Anne Stone of Arizona State University in Tempe. But the fact that both variants have survived suggests that some bitter foods may contain advantageous properties, she says. Study director Carles Lalueza-Fox of the Institute of Evolutionary Biology in Barcelona, Spain, adds that the study shows that Neandertals, renowned for their reliance on meat to thrive in frigid habitats, also “had some significant intake of vegetables in their diet.”

Youth Bulge

Twenty percent of the world's population is between the ages of 18 and 24, according to the latest report from the Population Reference Bureau. In sub-Saharan African nations, two-thirds of the population is in that age range. The “youth bulge” won't be abating there anytime soon: In Mali, for example, 50% of women

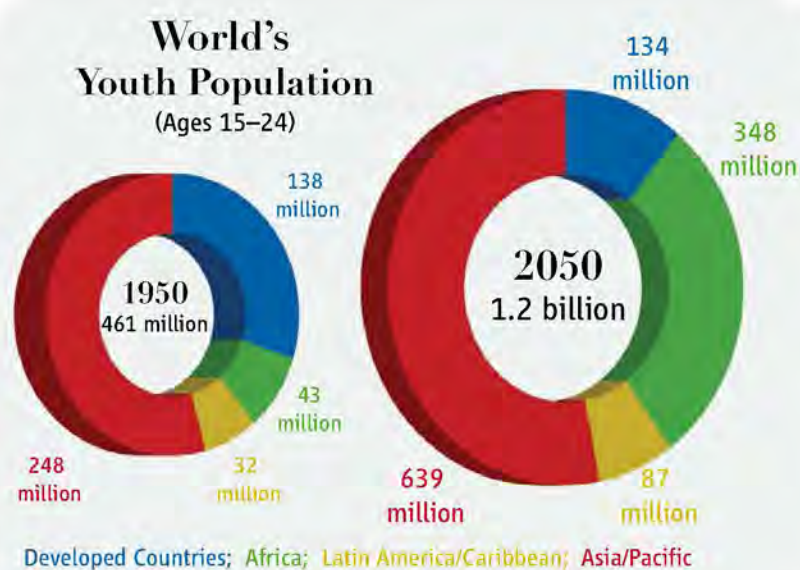
become mothers in their teens, and women's average ideal family size is slightly fewer than six children.

Put on a Happy Face

Helping others is supposed to make you feel good, but there may be surer routes to cheer, according to a U.K. psychologist.

Richard Wiseman of the University of Hertfordshire wants to know how the general public can get happier, so this month he conducted an Internet experiment. He divided his 26,000 respondents—mostly young adults—into five groups. One was a control group. During the 5-day exercise, each of the other groups engaged in one type of upbeat behavior: being kind to others, dwelling on a happy memory, feeling grateful, or smiling.

The results: All groups reported rises in happiness, including 50%





Halcyon dig. Li Chun on a less stressful expedition to Guizhou in 2007, when he discovered *Odontochelys semitestacea*, a missing link in turtle evolution (inset).

PALEONTOLOGY

Draft Rule Threatens Fossil Excavations in China

BEIJING—Li Chun was in high spirits: After 3 months of digging in southwestern China's Guizhou Province, he had unearthed a dozen superb fossil specimens. It was 31 December 2001 and Li, a researcher with the Institute of Vertebrate Paleontology and Paleoanthropology (IVPP) of the Chinese Academy of Sciences here, was returning to his hotel in Xingyi to ring in the New Year. But when Li arrived, police were waiting. They accused the 35-year-old paleontologist of illegal fossil collection and detained him.

Based on Li's notes, which referred to his collaboration with The Field Museum in Chicago, Illinois, investigators accused him of involvement in an international smuggling ring. The police said that Xingyi authorities did not allow valuable specimens out of their control, and they scoffed at Li's claim that IVPP had a permit to collect in Guizhou. IVPP colleagues worked their *guanxi*, or connections, and Li was liberated 10 days later; he was never charged with a crime. The confiscated fossils have since vanished.

Fossil theft and smuggling are rampant in China, and scientists welcome tougher enforcement. But a draft regulation released

this summer, intended to crack down on illicit trade, would impede fieldwork and make paleontologists more vulnerable to the whims of local officials, scientists fear, potentially leading to repeats of Li's harrowing experience. "The draft regulation has aroused considerable panic among research professionals," 12 senior scientists warned in a recent letter to China's State Council. They hope to persuade the council to amend the regulation before it is finalized by the end of this year.

A large share of paleontology's most scintillating recent finds, including remains of feathered dinosaurs and primitive mammals and angiosperms, have come from China. As a result, paleontology is arguably the country's strongest scientific discipline: Since 1999, 65 of 256 papers in *Science* and *Nature* with first authors from mainland China were on paleontology.

But as the discipline has flourished, so has criminal activity. "We are still faced with serious problems in ... fossil destruction, loss, illegal trade, and smuggling," says Xu Shaoshi, minister of land and resources. The draft regulation declares that the state owns all fossils underground or underwater on Chi-

nese territory and bans commercial fossil transactions; violators could face penalties of up to \$73,000 and criminal charges. Individuals and institutions will be allowed to keep fossil collections obtained legally to date. The regulation encourages them to donate their fossils to museums or other public organizations. But no cutoff date is set for such donations—and scientists say that illegal collectors could exploit this loophole to continue their activities.

The biggest controversy is raging over fossil management. The regulation designates the Ministry of Land and Resources as the lead agency on fossil collection and trade and tasks county-level mineral resource bureaus with responsibility for local management. Lumping together fossil excavation and mineral extraction could spur local governments to develop fossil beds into profitmaking ventures. The "core value" of fossils—to promote research and public awareness—is "obviously different from exploitation of mineral resources," says IVPP Director Zhou Zhonghe.

A revised permit system could create new barriers to scientific excavations, says Yin Hongfu, former president of China University of Geosciences in Wuhan. Under the new regulation, the central government's permission would no longer suffice: Researchers would need permits from both the land resources ministry and county-level mineral bureaus. Institutes and universities have petitioned the State Council to grant them blanket

CREDITS: COURTESY CHUN LI; (INSET) CHUN LI ET AL., NATURE 456, 7221 (27 NOVEMBER 2008); REPRINTED BY PERMISSION FROM MACMILLAN PUBLISHERS LTD.



permission to discover, collect, and study fossils. Paleontologists have suggested that the central government set up an interagency expert board to oversee major aspects of fossil discovery and site management. Scientists are also calling for an explicit right to lend, borrow, and swap fossils with overseas partners, under board supervision.

The regulation's fate now rests with the State Council's Legislative Affairs Office.

The final regulation, sources say, is expected to designate an expert board to certify qualifications of excavators and approve digs. The council is considering other amendments as well, including a provision to allow researchers to conduct small-scale digs without a permit.

Such leniency would be a boon for Li and other fieldworkers. Undaunted by his travails, Li has returned to Guizhou several

times and uncovered more prize specimens, including a missing link in turtle evolution that he and colleagues published in *Nature* last year. "I don't object to efforts to overhaul fossil protection," says Li, brushing dirt off a fossilized aquatic reptile in his Beijing lab. "But any regulation should embody respect for research freedom."

—ZHENG YU

Zheng Yu is a writer in Beijing.

PLANT GENETICS

New Strategy Promises Lasting Resistance to a Rice Plague

Having a blast is no fun for farmers. The rice blast fungus *Magnaporthe oryzae* can wipe out hectares at a time. It is "a devastating problem," says Robert Zeigler, a plant pathologist and director general of the International Rice Research Institute (IRRI) in Los Baños, Philippines. IRRI estimates that blast outbreaks can cut yields up to 85%. Fungicides are widely used in developed countries, but in the developing world they "are not a viable economic or logistical option for most farmers," Zeigler says.

Breeders have found genes that provide resistance against rice blast. But plants equipped with these genes produce lower-quality rice, and the fungus has quickly evolved to overcome resistance in as little as 2 years. At last, however, scientists appear to have found a winner. In this issue of *Science* (p. 998), a team led by plant molecular biologist Shuichi Fukuoka of Japan's National Institute of Agrobiological Sciences in Tsukuba describes a novel type of gene that promises lasting resistance without degrading grain taste. "More effective and durable genetic control of rice blast is of major importance," says Jeffrey Ellis, a plant molecular biologist at CSIRO Plant Industry in Canberra, Australia.

Fukuoka's group zeroed in on a blast-resistant cultivar that has been grown in Japan for a century but remains unpopular. The resistance was traced to a quantitative trait

locus (QTL), a DNA stretch containing one or more genes encoding particular characteristics. Unfortunately, QTL *Pi21* was also associated with poor taste.

Fukuoka and colleagues set out to identify the source of resistance in QTL *Pi21*, determine how it works, and see if it could be sepa-

are thought to work by interacting with a single gene in a specific fungal strain, a concept called gene-for-gene response that appears to allow the pathogen to quickly evolve resistance. The *pi21* gene "has a different structure and a different mechanism, so we think it will be more durable," says Fukuoka.

To look at grain quality, the group made numerous crosses of a cultivar carrying QTL *Pi21* and high-quality commercial cultivars. The team found a gene close to *pi21* in the strains with undesirable taste that was missing in tastier crosses. The team has now established the *pi21* gene sans bad-taste gene in commercial cultivars. "The study puts to rest the notion that such resistance comes at a cost to eating quality," Zeigler says.

There are still questions about the gene's effectiveness. The authors note the resistance is "incomplete" compared with previously known resistance genes: Rather than preventing infection, it limits the disease's

spread. Fukuoka's team is working to add additional resistance genes to the mix. Such gene "stacking" is increasingly common in wheat breeding, Ellis says.

The gene's long-term promise could start to become clear as early as next year, when cultivars carrying it enter commercial cultivation in Japan. Zeigler says IRRI plans to soon start testing the gene in tropical rice varieties. The finding, he says, "will certainly help reinvigorate resistance breeding efforts."

—DENNIS NORMILE



Brownout. A newly identified gene variant protects rice (healthy plants in background) from the devastating rice blast fungus (brownish plants in foreground and inset).

rated from the DNA sequence affecting taste. Using map-based cloning in which ever-smaller DNA stretches are examined, they discovered a gene they dubbed *pi21*. By comparing rice varieties, they found that the resistant *pi21* allele, or variant, has two deletions that cause at least partial loss of gene function. The loss curiously enables the plant to defend itself against fungus. In blast-susceptible strains, the *pi21* variant found in most cultivars hinders the rice plant's resistance. The *pi21* gene is unlike previously identified resistance genes, which

ARPA-E FUNDING

U.S. Energy Agency Stumbles Out of the Blocks

The new U.S. Advanced Research Projects Agency–Energy (ARPA-E) is supposed to “disrupt the status quo” by funding “transformational” ideas that will help end the country’s dependence on foreign oil, reduce greenhouse gas emissions, and move the economy toward sustainable energy sources. So far, however, the agency has caused more disruption among scientists than transformation of the U.S. energy sector.

Researchers are grumbling about the way ARPA-E, which is part of the Department of Energy (DOE), is handling its first round of grant proposals. On 27 April, the agency asked for preliminary ideas for spending the first \$150 million of some \$400 million it was given in the president’s stimulus package. The solicitation was a big hit: Researchers submitted 3500 concept papers describing myriad ways to revolutionize every conceivable type of energy technology.

the lack of any feedback. Kosinski noted that “the large number of submissions prevents me from sending you specific comments on the rationale for the decision.” ARPA-E expects to fund fewer than 2% of the 3500 proposals, he added.

“I don’t know whether they think [my proposal] is trash or if I just need to make a better argument,” says Ning Zeng, an atmospheric scientist at the University of Maryland, College Park, who sought funding to test his idea of burying and storing wood as part of an ongoing forest management system to sequester large amounts of carbon. “Maybe they thought it was just too simple an idea.”

Martin Hoffert, a physicist at New York University in New York City who had proposed testing a system of space-based lasers that would beam solar energy to Earth, says he lobbied for the creation of ARPA-E and still believes it can play an important role in

copy of the agency’s guidelines to reviewers, which lays out the procedures. The reviewers were asked to rate each proposal on its scientific merit and relevance to ARPA-E’s mission using a five-point scale from excellent to poor for each category. Reviewers were also asked for a “narrative on the strengths and weaknesses of the application.”

Energy Secretary Steven Chu, an early and vocal advocate of ARPA-E, says he beat the bushes to expand the pool of top-quality reviewers. But with less than a month to vet the proposals, ARPA-E officials were forced to streamline the process. The vast majority of proposals received only two reviews, although Chu says “if one reviewer said [a proposal] was great and another said it was a dog, we had a third reviewer look at it.” Chu told *Science* he believes the process “was as transparent as we could make it.” The deadline for those invited to submit a full

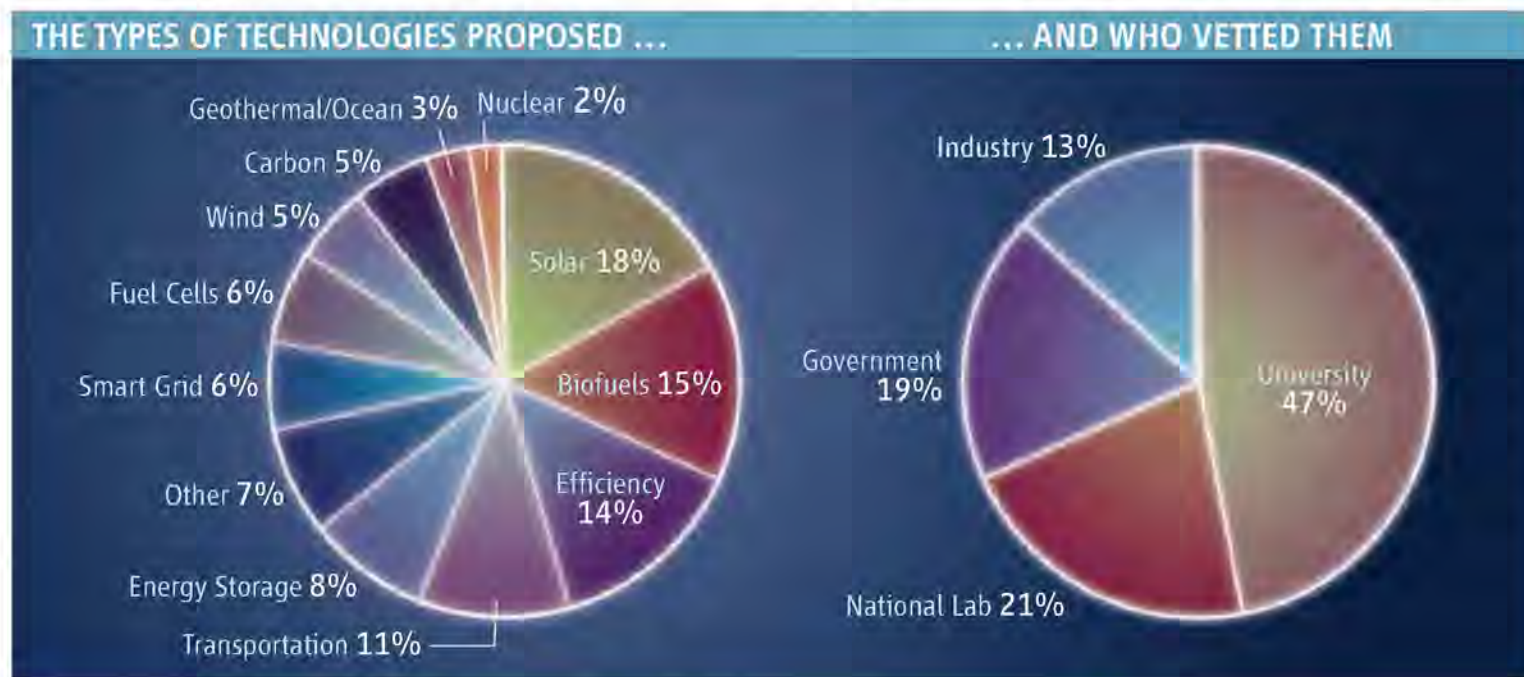
research proposal is 28 August, and the winners will be announced in the fall.

Some scientists are worried that ARPA-E’s shaky start may point to bigger problems down the road. “Some people say ARPA-E should be a very nimble organization, with a focus on short-term technologies that can be scaled up quickly, while others say it’s supposed to support long-term research. We’re all waiting for them to spell it out,” says Michael Lubell, head of public affairs for the Washington, D.C., office of the

American Physical Society. “Everybody wants it to be like DARPA [the Defense Department’s innovative research shop launched after Sputnik that is credited with inventing the Internet and promoting high-performance computing]. But DARPA funds research based on what DOD needs. DOE doesn’t know what is needed—that’s up to the market. You can guess, but you may be wrong.”

Hoffert has a more immediate metric. “I still think ARPA-E is a great idea,” he says. “So let’s see what they fund. If it’s mostly pedestrian ideas, things that DOE already wanted to do, then we’ll know the answer. And a lot of people are worried that’s exactly what will happen.”

—JEFFREY MERVIS



Seeking the best minds. ARPA-E sought out scientists in many sectors to review the 3500 proposals it received.

The outpouring overwhelmed the agency, which until February had no budget and is still operating without a permanent director and with only a skeletal staff. The initial template for submitting the eight-page papers—the first of a two-step process for obtaining funding—proved so cumbersome that it was scrapped, and the deadline was extended by nearly a month. The change ate into a mandate for agencies to spend their stimulus money as quickly as possible.

Last month, all but 200 or so of the applicants received a form letter telling them not to bother submitting a full proposal. “Your concept is unlikely to receive funding,” wrote Acting Deputy Director Shane Kosinski. It wasn’t just the rejection that stung, but also

helping the country move to a low-carbon economy. But he doesn’t like the secrecy surrounding the review process. “This is the type of command-and-control system that is better suited to a classified program,” he says.

The fallout prompted *New York Times* science writer Andrew Revkin to ask in his widely read blog, Dot Earth: “Does this look like an energy quest to you?” He’s also invited scientists to post their rejected concept papers in hopes of stimulating further discussion of their self-identified transformative ideas. (Hoffert and Zeng, among others, accepted the offer.)

A DOE spokesperson said Kosinski declined to discuss how the competition has been managed. But *Science* has obtained a

BIOMEDICAL RESEARCH

Rejecting 'Big Science' Tag, Collins Sets Five Themes for NIH

The new director of the U.S. National Institutes of Health (NIH) laid out his priorities this week, spending his 1st day on the job speaking to his staff and reporters. Physician-geneticist Francis Collins said he plans to emphasize five "themes," including health care reform and translating research into medicine. Collins also sought to allay perhaps the biggest concerns about his nomination last month by President Barack Obama, saying that he will protect investigator-initiated science and that his religious interests will not influence how he runs the agency.

Collins, who in 2008 stepped down after 15 years as director of NIH's genome institute, spoke publicly about his ideas for the first time since his name surfaced as the leading candidate to head the agency. In a town hall meeting with NIH staff, he said he now has an "exciting, daunting, and perhaps the most amazing job that anybody could ever ask for." He assured a large crowd that "the mainstay" of NIH will be the individual investigator; anybody who thinks otherwise "need look no further" than the genome institute's intramural program, where research is "driven by ideas" and where he will keep his lab.

At the same time, large biology projects are one of Collins's five priorities. He will promote high-throughput technologies in areas that are "poised for this kind of approach," such as gene transcription and autism studies. He expects to emphasize translational research, such as a new NIH program to develop drugs for rare diseases. The

three other themes are health care reform, including research comparing treatments, which he said NIH "should embrace"; global health; and "empower[ing] the biomedical research community," which he said includes sustained funding, encouraging young investigators, and funding innovative research.

Collins said that "job one" is dealing with what happens when the \$10.4 billion that NIH received as part of this year's stimulus package runs out in 2011. NIH faces "a perfect storm," he said, partly driven by a flood of more than 20,000 applications for stimulus-funded grants, that could bring record-low success rates if the agency's budget doesn't rise above the current \$30.6 billion. He will argue for more funding by telling Congress that NIH funding stimulates local economies and by emphasizing "themes that clearly resonate." He noted that \$40 billion, which some groups are pushing for, is "within [the] envelope" of what NIH would need to restore losses to inflation since 2003.

Collins also addressed concerns that he said have "graced many pages of the blogosphere," as well as the op-ed page of *The New York Times*, that his evangelical Christian beliefs could influence how he runs NIH. He has resigned from BioLogos, the foundation exploring science and faith that he started. He told reporters that those "personal interests ... will not interfere with the judgments that I will need to make as the director of the NIH."

As for management issues, Collins has chosen to retain Raynard Kington as his principal deputy director. Kington served in that position until becoming acting NIH director after Elias Zerhouni resigned last fall. Collins expects to hold off on finding a permanent director for the alcoholism institute because of an ongoing discussion about whether it should merge with

NIH's drug addiction institute. Asked about NIH's intramural program, he said he is "resistant to the idea that [the program] is in need of some sort of dramatic redo" but is pondering whether to create a pool of intramural money that, like NIH's Common Fund, could be used to fund crosscutting research quickly.

—JOCELYN KAISER



Quick study. NIH Director Francis Collins spent his first day on the job explaining his vision for NIH.

ScienceNOW.org

From *Science's*
Online Daily News Site



Dogs Are No Mind Readers

Despite thousands of years of domestication, dogs have a hard time figuring out what humans are thinking. That's the conclusion of a new study, which shows that dogs continue to trust unreliable people and therefore lack a so-called theory of mind.
<http://bit.ly/3S8YZa>

The Social Life of Your Cell Phone

Your cell phone may know more about your private life than you do, according to a new study of mobile phone calls. This insight opens the door to mining massive data sets from mobile phone call logs, which should allow researchers to test theories on how relationship networks make or break businesses, shape the flow of information, and even affect the course of epidemics.
<http://bit.ly/3HK2sa>

Weight Loss for Batteries

With \$27 billion a year in sales, lithium-ion batteries already dominate the market for rechargeables. But there's always pressure to do better. Now researchers report that they've come up with a way to use nanotechnology to either significantly increase the energy-storage capacity of lithium-ion batteries or reduce their weight while maintaining their current energy content. The new work could lead to everything from lighter laptops to electric cars with a considerably longer range. <http://bit.ly/laG8f>

Neandertals Led Bitter Lives

Humans vary genetically in their ability to taste a bitter chemical known as phenylthiocarbamide, which elicits the same response as bitter flavors in Brussels sprouts, cabbage, and broccoli. A new study finds that our close relatives, Neandertals, also had varied tastes for bitter food, suggesting that differences in the ability to detect bitterness stretch back at least half a million years. <http://bit.ly/gj9Ej>

Read the full postings, comments, and more on sciencenow.sciencemag.org.

GENETIC ENGINEERING

Two Steps Forward for Synthetic Biology

For more than 3 decades, researchers have been engineering microbes with the aim of harnessing these simple creatures to clean up pollution, make drugs, and produce bio-fuels. They have largely been limited to tinkering with individual genes, however. Now, two new developments have brought genetic engineers closer to a major goal: routinely manipulating sets of genes and even whole genomes.

J. Craig Venter of the J. Craig Venter Institute in Rockville, Maryland, and his colleagues have transferred a bacterial genome into yeast, modified that genome, and then put it into a different bacterium within which it drives the microbe's biochemistry and reproduction. They describe this technology in a paper published online this week by *Science* (www.sciencemag.org/cgi/content/abstract/1173759). Independently, George Church of Harvard University and his team have come up with a way to quickly improve entire chemical pathways in bacteria and in a matter of days generate new strains capable of producing useful chemicals. That work was published in the 13 August issue of *Nature*.

"The tools developed by Venter and Church are both major advances in synthetic biology," says Hal Alper, a cellular and metabolic engineer at the University of Texas, Austin.

In 2002, Venter created a stir by announcing that he intended to create life by making a synthetic chromosome and, eventually, a self-replicating organism controlled by this artificial genome. His goal was to determine the minimal genome needed for life and use that as a starting point to create designer organisms that synthesize specific compounds. In early 2007, he and his colleagues showed they could replace one bacterium's genome with the genome from another species (*Science*, 3 August 2007, p. 632) and assumed that they could do the same with a humanmade genome once they had it in hand.

By early 2008, they had built from

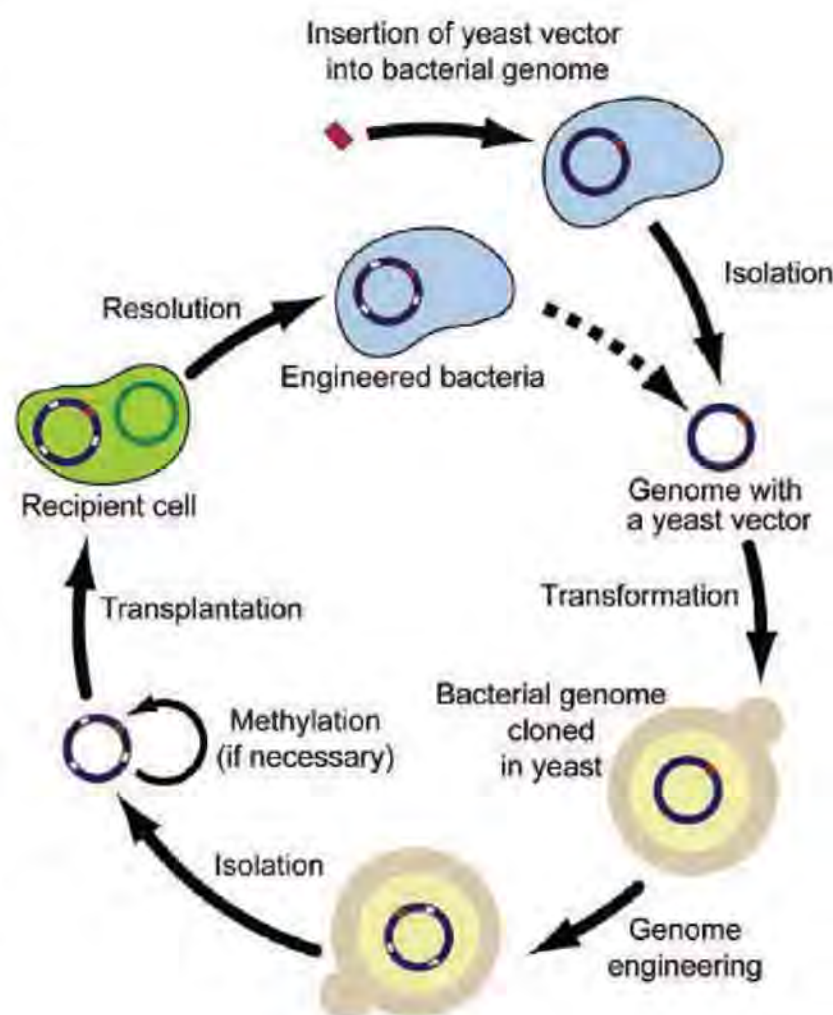
scratch the 580,000-base genome of *Mycoplasma genitalium*, a parasitic bacterium that has the smallest known genome of any free-living organism, using yeast to assemble chemically synthesized pieces of DNA into the complete genome. But when they tried to put the synthetic genome into a bacterium whose own genome had been removed, they were stumped. "When we tried to transplant [the genome], it wouldn't [work]," Venter recalls.

To begin to figure out what went wrong, they decided to put the natural bacterial chromosome into yeast. They also switched to a different mycoplasma that grows faster than *M. genitalium*. They modified the mycoplasma genome by adding yeast DNA, including a centromere, to turn that DNA into a yeast artificial chromosome. The yeast took up the genome and maintained it intact, providing a system they could use to test different ways to make transplantation work, Venter's team reports.

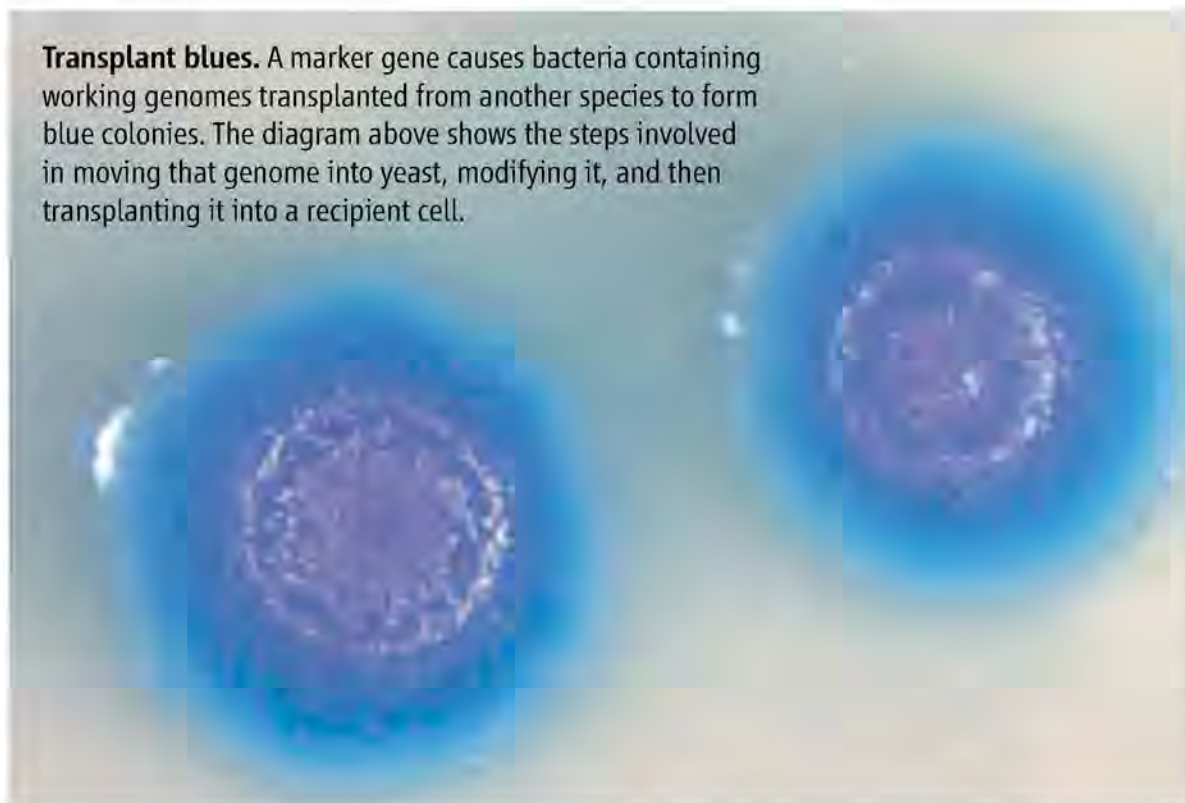
Once the bacterial genome was in the yeast, the researchers deleted a gene that they lacked the technology to delete from the genome when it was still in the bacterium, demonstrating that they could use the genetic tools available for modifying yeast DNA to manipulate the bacterial DNA. That feat is an important step forward, says Alper. "It will now be possible to create de novo function from the ground up, especially in organisms lacking comprehensive genetic tools," he notes. "This approach certainly opens the door for importing and synthesizing functions from novel and natively isolated organisms."

When they tried to transfer the modified genome from yeast into bacterial cells, however, Venter's team hit the same roadblock they encountered when they tried to implant the synthetic mycoplasma genome into bacteria: It didn't work. Venter surmised that proteins called restriction enzymes were short-circuiting the transfer. Bacteria carry these enzymes to defend against foreign DNA; they cut DNA in specific places, effectively destroying it. A bacterium protects its own DNA sequence from enzyme attack by adding methyl side groups to it.

In one experiment, the researchers knocked out the recipient cell's gene for its restriction enzyme. In another experiment, they isolated the



Transplant blues. A marker gene causes bacteria containing working genomes transplanted from another species to form blue colonies. The diagram above shows the steps involved in moving that genome into yeast, modifying it, and then transplanting it into a recipient cell.



CREDITS (TOP TO BOTTOM): C. LARTIGUE ET AL., SCIENCE; J. CRAIG VENTER INSTITUTE



Seeing red. An automated process for adding DNA to bacteria and culturing them sped the evolution of strains that produce high concentrations of a red compound, lycopene, useful as an antioxidant dietary supplement.

bacterial genome from yeast and chemically treated it to methylate its DNA before putting it into the recipient cell.

Their hunch was right. The genome transferred just fine into recipient cells lacking restriction enzymes. And the methylated genome was successfully incorporated even into recipient cells that still had their restriction enzyme gene intact. “This team has shown that they can go from yeast to mycoplasma,” says Church. “The next step is going from synthetic DNA in yeast to mycoplasma. The key advance seems to be methylation.” Venter’s group has yet to try methylating a synthetic genome to see if it can be transplanted effectively.

For Venter, this work clears the way for making a functioning genome from scratch, which he intends to do “as a proof of principle,” he says. But for designing new microbes, his group may not need to create a synthetic genome: By deleting genes from the natural chromosome using the yeast system, they can determine the minimal genome, and they can then add genes at will, he points out.

Church and his colleagues are taking a different route. Rather than focusing on minimal genomes and working up from there to designer microbes, they have come up with a way to fine-tune the workhorse of synthetic biology, *Escherichia coli*. Genetic engineers have long used this bacterium to make insulin and about 100 other human proteins by adding human genes to its genetic repertoire. But making improvements in the production of useful drugs and other substances can be slow and inefficient, says Church.

To remedy that, his team has developed an automated system to add batches of new DNA to bacteria, generate multiple new strains, and select the ones that work best in producing a particular compound—a type of genome editing. Bearing the complicated name of multiplex automated genome engineering (MAGE),

the technology quickly increased the efficiency with which *E. coli* produced lycopene, a useful antioxidant found in tomatoes, carrots, and watermelons, Church and his colleagues reported last week.

First, Church used a computer to design variations of 20 genes that are involved in lycopene synthesis. His team made thousands of 90-base pieces of DNA, changing just a few bases in each piece. These bases are the part of the DNA that is involved in binding to the ribosome, where genetic information is put to use making proteins. The stronger the binding, the more efficient the production of the enzyme coded for that particular gene, and greater efficiency translates into higher production of lycopene. He also silenced four other genes that produce enzymes that siphon off intermediates from the lycopene-production pathway, making production less efficient.

Church added these pieces of DNA to his MAGE system, which uses electrical current to force the DNA pieces into the cells and grows, chills, washes, and resuspends cells in media. The cells keep cycling through growth and DNA-addition steps, resulting in 4 billion genetic variants per day. After 24 hours, the team screened the variants for the reddest colonies—signaling the ones producing the most lycopene—measured the amount of lycopene, and analyzed the variants’ genetic makeup. In 3 days, the experiment yielded strains in which lycopene production increased fivefold, with a better yield than ever before achieved industrially, says Church.

Alper thinks Venter’s and Church’s approaches are complementary, with the latter potentially helping to make newly created genomes better. “This combination would provide a powerful, selective way to edit and improve genomes prior to transplanting [them] back into a host cell,” he notes.

—ELIZABETH PENNISI

ScienceInsider

From the *Science* Policy Blog



Restoring national forests to prepare them for climate change and to protect water resources will be the overarching goal of U.S. forest policy, Tom Vilsack, who heads the U.S. Department of Agriculture, announced 14 August.

The chair of a blue-ribbon panel reviewing the **U.S. human space program** briefed senior Obama Administration science officials on what’s expected to be a frank assessment of NASA’s choices. The panel held its final public hearing on 12 August and has promised to finish its report by the end of this month.

Lower-than-expected inflation rates have **U.K. research councils** considering whether they can legally demand that grantees return some grant money.

The **Smithsonian Institution** has tapped an academic administrator to take over as Under Secretary for Science. Eva Pell, senior vice president for research and dean of the graduate school at Pennsylvania State University, will start in January.

President Barack Obama has awarded the **2009 Presidential Medal of Freedom** to 16 people, including two scientists: geneticist Janet Davison Rowley of the University of Chicago, who identified a chromosomal translocation as a cause of leukemia, and Stephen Hawking of Cambridge University for his work in theoretical physics.

Astronomers are making good progress discovering and **tracking large asteroids** that could hit Earth, but they won’t meet the goal set by Congress without dedicated funding, according to a report released 12 August by the National Academies’ National Research Council.

A decision to fold a long-running center supporting underrepresented minorities and women in engineering into a larger student services office has upset many students and faculty at the **University of California, Berkeley**.

For more science policy news, visit blogs.sciencemag.org/scienceinsider.



Beyond the Yellow River: How China Became China

The cradle of Chinese civilization was long considered to be the region around the middle Yellow River. But ancient and complex cultures from far-flung corners of the modern nation now tell a different story about the origin of Chinese culture

LIANGZHU, CHINA—Three years ago, a farmer who works the lush fields along the meandering Tiaoxi river, 200 kilometers southwest of Shanghai, decided to build a new house. This area around the town of Liangzhu has long been known as a center of Neolithic settlements, so Liu Bin of Zhejiang Province's archaeological institute assembled a team to conduct routine salvage work. But rather than the postholes or earthen floors typically found at such settlements, the team instead encountered a carefully prepared foundation of stone blocks.

The blocks were part of a wall, now dated to 4300 years ago—and it was no simple enclosure. Further excavation revealed a massive perimeter of earth built on stone, with an average width of 50 meters, running in a rough circle for 7 kilometers and surrounded by a wide moat. The farmer lost his house site, but archaeologists gained a new appreciation for the complexity of this ancient culture. The enormous wall enclosed previously discovered earthen platforms, which extend over 30 hectares and are raised 10 meters above the low-lying plain. Although modest in comparison with the pyramids and ziggurats of this era in Egypt and Mesopotamia, the structures required an enormous amount of labor and skill. “To construct these large platforms and walls with simple tools, you would need 10,000 people over 2 years,” Liu estimates.

Even more astonishing than the engineering are the site's location and age. Archaeologists long thought that Chinese civilization was born half a millennium later and 800 kilometers to the north-

west along the central plains of the Yellow River. Wikipedia summarizes the classic view: “Chinese civilization originated in various city-states along the Yellow River in the Neolithic era.” Yet centuries earlier, Liangzhu was at the center of a sophisticated culture that included hundreds of settlements discovered in recent decades, stretching across the flat and fertile expanses as far as Shanghai. With finely worked jade ornaments, elaborate tombs, high platforms, and objects carved in an artistic and distinctive style, the Liangzhu culture appears separate from that of the Yellow River. In fact, goods and styles from this region, such as the fine jades, have been found as far west as the upper reaches of the Yangtze River, 3000 kilometers upstream, and were imitated across China for thousands of years.

Dramatic discoveries like those at Liangzhu have been repeated across China in the past 2 decades, challenging long-held views. From Manchuria in the north, to the Chengdu plain to the west, and to the coastal cities of the south (see map, p. 933), excavations are revealing a host of complex and distinct ancient cultures, each with its own artifacts and traditions. Liangzhu's striking carved faces are one example; other cultures developed enormous bronze statues, large stone ceremonial complexes, and a golden, whirling sun motif.

Yellow River sites like Erlitou remain key to understanding the first true urban centers in China. But other, far-flung cultures also contain the seeds of Chinese traditions. “Before these astonishing

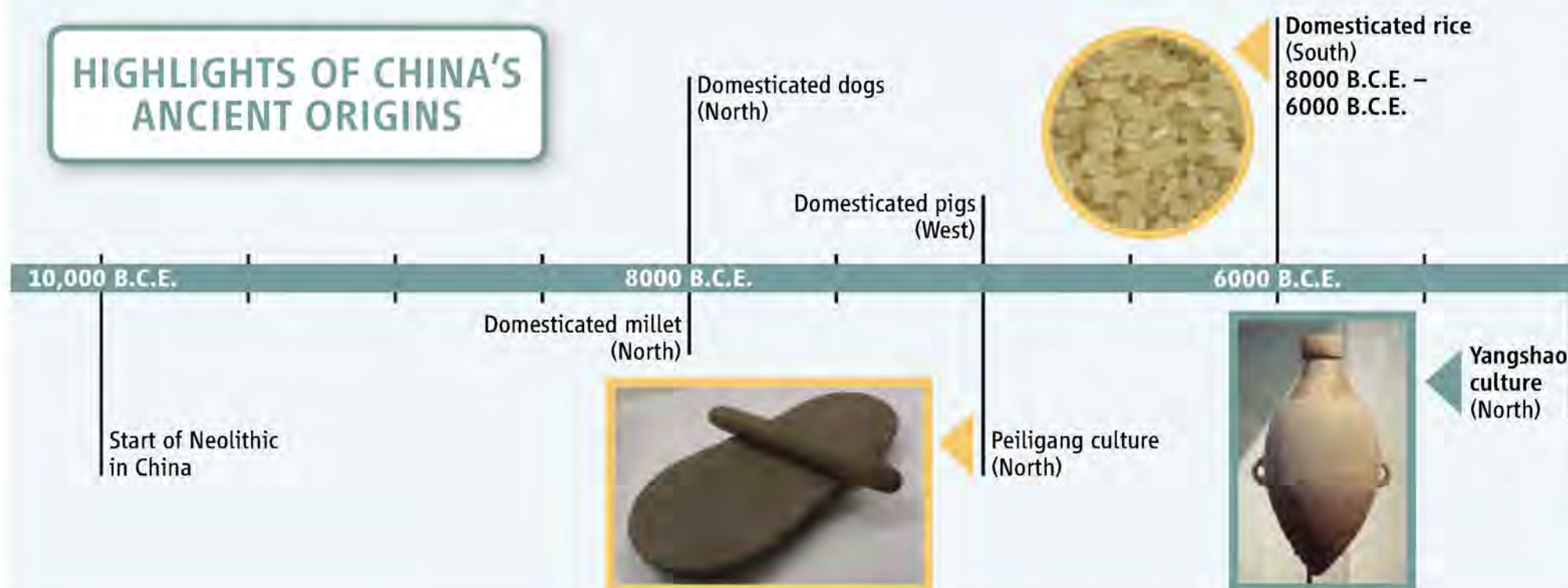
Online

sciencemag.org



Podcast interview
with author

Andrew Lawler.

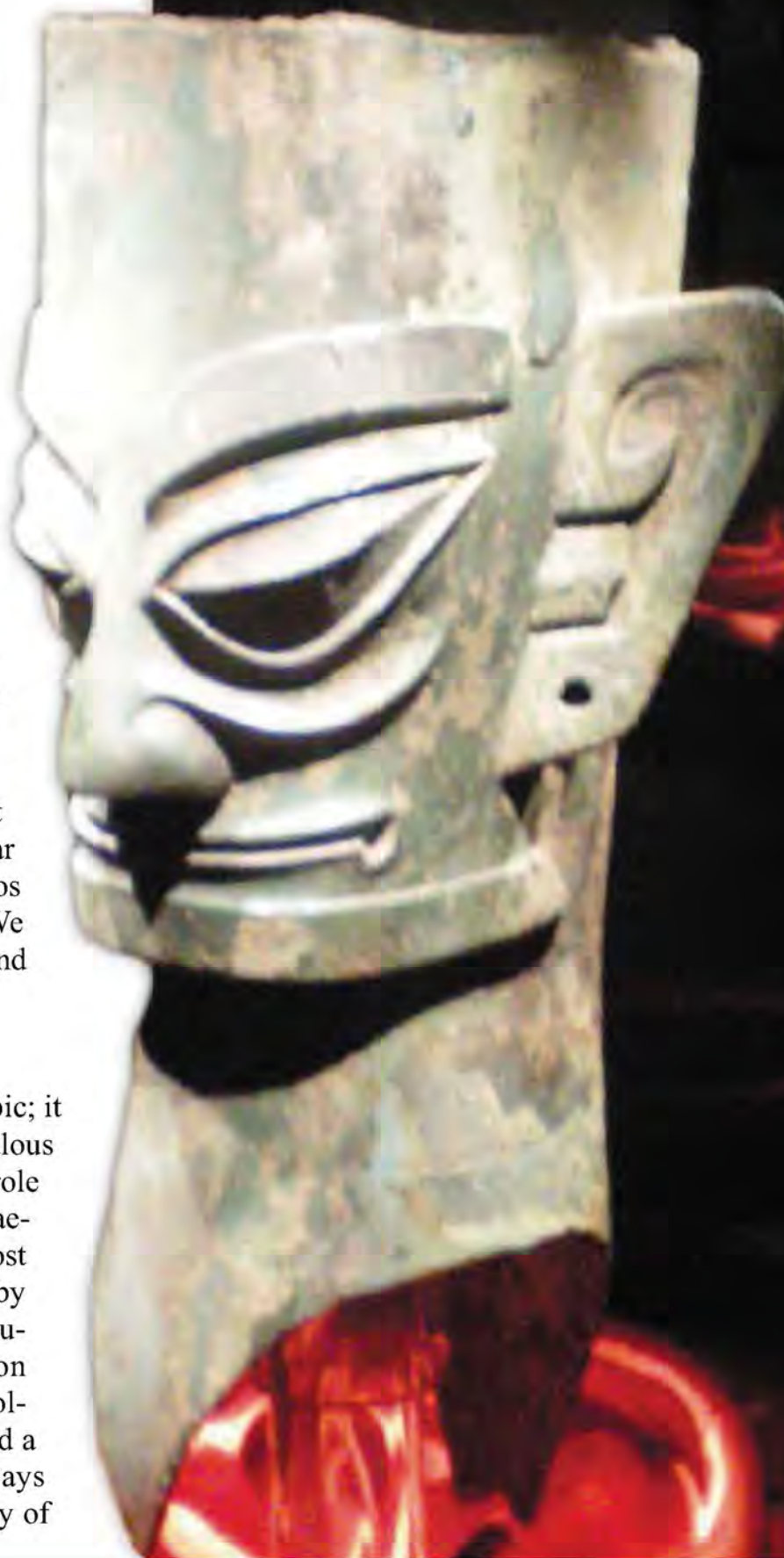


finds, we were focused on the central plains,” says Wang Wei, director of the Institute of Archaeology of the Chinese Academy of Social Sciences in Beijing. “Most of us accepted that the Yellow River was the origin of Chinese civilization. But as we’ve done more research, we have found other cultural areas as numerous as the stars in the sky. ... Now it is clear that the development and expansion of regional centers contributed to the formation of Chinese civilization.” And, he adds, communication and competition among those centers may hold the key to understanding how a common culture emerged.

In 2004, Wang’s institute began coordinating an ambitious multidisciplinary effort to chart this in detail, by providing a more accurate chronology for sites and bringing to bear the latest methods for analyzing the past 25 years of finds. By drawing on researchers across China and collaborating with foreign scientists, Wang hopes to paint a more nuanced and data-driven view of the country’s ancient past while pushing China’s archaeological community toward the forefront of the field. But it is a formidable challenge, says archaeologist Lothar von Falkenhausen of the University of California, Los Angeles, who has long experience in China. “We don’t really know how the interactions took place, and they changed over millennia.”

Want a revolution

How China became China is no mere academic topic; it goes to the very heart of how the world’s most populous and economically vibrant nation sees itself and its role in the world. During much of the 20th century, archaeology was often used as a political tool, first as a boost to national pride in a country that felt dominated by Western powers and Japan. After the 1949 Communist revolution, suggestions that China’s evolution was strongly influenced by Western trade and technology became politically taboo. “Archaeology played a critical role in defining Chinese nationalism,” says Gary Crawford, an anthropologist at the University of



Saving face. These 3000-year-old bronzes of a previously unknown style were recovered from Sanxingdui near Chengdu.



Shang dynasty, Erligang culture (North)

Domesticated chicken (North)

Domesticated horse (North)

Western Zhou dynasty

Hongshan culture (North)

Taoisi (North), Domesticated sheep and wheat (North)

4000 B.C.E.

2000 B.C.E.

1 C.E.

Liangzhu culture (South)

Baodun culture (West)

Bronze Age begins

Erlitou culture (North), Xia dynasty?

Sanxingdui (West)

Eastern Zhou dynasty

Han dynasties



Toronto, Mississauga, in Canada. “But there’s been a real revolution in the profession in the past 20 years.”

That revolution has opened up previously off-limits topics, from the impact of the West (see p. 940) to regional diversity. After decades of isolation, Chinese archaeologists are increasingly setting aside formerly obligatory Marxist theory and drawing on modern techniques in gathering and interpreting data. Regional discoveries and institutes find a warm welcome—and funding—within provincial governments flush with tax revenues and eager to emphasize their unique contributions (see p. 936).

No one doubts that the plains around the middle Yellow River are where Chinese civilization coalesced around the middle of the 2nd millennium B.C.E., during what historians call the Shang dynasty (see timeline, p. 930). Legend speaks of an earlier dynasty called the Xia, but its existence remains controversial (see p. 934). The vast archaeological and textual remains from the Shang reveal an elite with a rich court culture ruling over masses of millet and wheat farmers—the grains of choice in the cooler and drier north. Embroiled in frequent conquests, the Shang people used advanced weaponry such as horse-drawn chariots and took many prisoners from conquered regions. They also practiced human and animal sacrifice, worshipped a supreme god who dominated the forces of nature, and paid homage to their ancestors, who were seen as active participants in family life.

Many of these traditions and technologies echo through the next 3 millennia. The Shang set the stage for the expansion and collapse of central authority that repeatedly characterizes Chinese history. But there have been hints that this single region did not hold the whole story. More than 30 years ago, Su Bingqi of Peking University and K. C. Chang of Harvard University independently suggested that China’s civilization grew out of a complex interweaving of many regional cultures. Recent excavations back up these ideas. Indeed, prehistoric Chinese societies stretched across time and space, from the millet-farming-and-pig-raising Peiligang people in the north starting in 7000 B.C.E., to the 5000 B.C.E. Yangshao people near the Yellow River, who may have first experimented with silk. Many of the symbols of classic Chinese civilization, such as dragon motifs and the use of jade as a magical stone, appear to originate far from the central plains. Two cultures in particular—the Hongshan in the northeast, which flourished from 4500 B.C.E. to 2250 B.C.E., and the Liangzhu, which lasted from 3500 B.C.E. until 2250 B.C.E.—were setting the pace many centuries before the Shang. Indeed, the peoples

of the mid-Yellow River area began to construct their first major settlement, called Taosi, at about the time the older cultures collapsed.

Finely carved jade, for example, first appears about 3500 B.C.E. during the Hongshan culture in today’s Liaoning and Inner Mongolia. There, researchers have found elaborate stone tombs containing numerous jade objects shaped like a phoenix and dragon—animals that later become central symbols in Chinese mythology.

“Jade is like gold in the West,” says archaeologist Elizabeth Childs-Johnson of Old Dominion University in Norfolk, Virginia, who frequently works in China. “It is a major symbol of power” in China from the Neolithic to the modern era. The stone is also hard to work and therefore labor intensive. Whereas copper, bronze, and gold take center stage in the early civilizations of the West, these metals come relatively late to the East. Childs-Johnson argues that

like precious metals in the West, jade production in China acted as a major stimulus for social evolution by defining an elite.

Recent excavations at Hongshan sites such as Niuheliang in the Liao River valley northeast of Beijing have focused mainly on remarkable burial structures and goods, including the jades. Eighteen elite graves dating to the centuries before 3000 B.C.E. have so far been unearthed, one with 20 pieces of carefully carved jade beads, disks, bracelets, hair tubes, and a plaque with fangs. The sacred and burial areas demonstrate “a level of cultural sophistication that is not duplicated elsewhere at this time in early China,” says Childs-Johnson. One partially excavated site near Niuheliang called Chengzishan

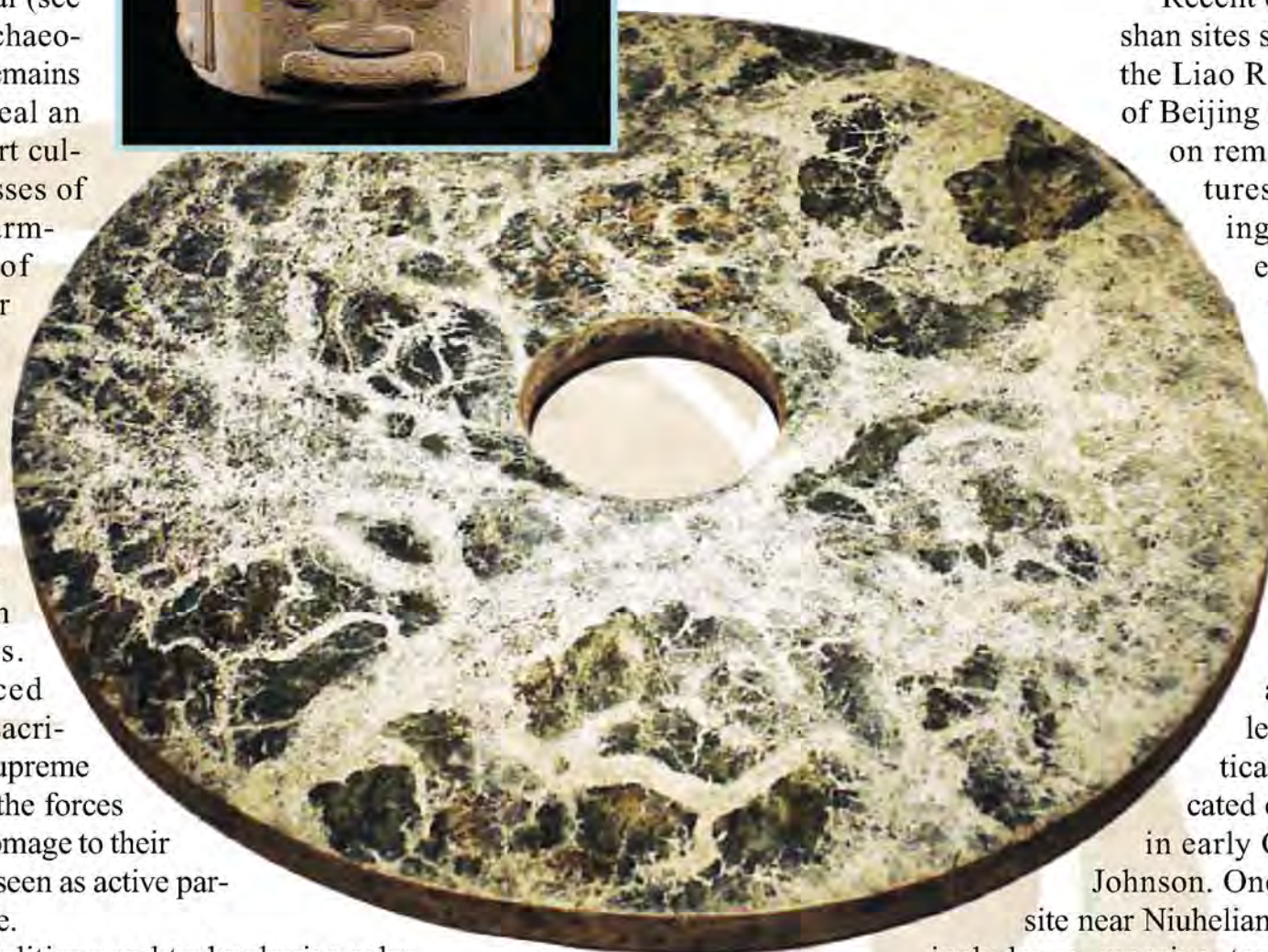
includes a massive temple on a platform 165 meters wide and 900 meters long—nearly half the size of the National Mall in Washington, D.C. Researchers have so far found subterranean rooms, a life-size ceramic head of a female with inlaid nephrite-jade eyes, and sculptures of ox heads and birds.

Archaeologists have also increasingly found the material of daily life among the Hongshan people, including stone tools such as plow tips in standardized shapes; sophisticated kilns that fired black, gray, and red vessels; and unusual red-painted ceramic cylinders that served as building supports. And they say there are undoubtedly large numbers of undiscovered sites in this little-explored region, which Childs-Johnson thinks was “a prominent cultural center and player in the evolution of Chinese civilization.”

Researchers say they are just beginning to piece together the interactions among the Hongshan and other highly complex cultures that developed before the Yellow River culture or were largely independent of it. Was there trade, migration, diffusion, or warfare? Did the later cultures build on the earlier ones, or were they completely



Heaven and Earth. The round bi and square cong used in Liangzhu became enduring Chinese symbols.



independent? New excavations may yield answers soon. “Northeast China is currently a hotbed of active field research that will illuminate both the nature of local cultural developments and long-distance relationships,” says Harvard archaeologist Rowan Flad.

Long-distance contacts among cultures seem likely, but their complexity and extent remain elusive. For example, the Liangzhu culture, which emerged 1000 years later and 2000 kilometers southeast of the Hongshan heartland, may have drawn on the older society’s expertise in jade, but direct evidence is lacking. As early as the 1930s, Liangzhu archaeologists began to uncover numerous and varied jade objects of an even higher quality than those in the northeast.

The Liangzhu people seem to have had military and political concerns with their neighbors, as hinted at by the walls, moats, and stone weapons found more recently. And some 30 excavated large-scale mounds, often with elaborate burials that include jade, ivory, and lacquer, show that there was widespread regional trade, primarily up the Yangtze River. To date, archaeologists have identified nearly 300 settlements in an area of 18,000 square kilometers, says Liu.

The age of many of these early sites, particularly Liangzhu itself, is controversial. New radiocarbon evidence shows that the massive stone and earth wall uncovered by Liu was constructed in the later period, just before Liangzhu’s collapse around 2250 B.C.E., says Wu Xiaohong of Peking University. Whether that huge effort was for defensive purposes or to hold back floods—there is some evidence of climate change—remains uncertain.

Whatever the wall’s purpose and age, Liangzhu itself had a broad influence that touched much of the territory of present-day China. Its products—from jade to pottery—are scattered throughout the north and the east and are found in the western province of Gansu as well as the southwestern province of Sichuan. And the society appears to have imparted religious ideas



that remain quintessentially Chinese. The Liangzhu people created circular disks called *bi*—symbolizing heaven—as well as squarish cylindrical *cong*s—symbolizing earth—at a time when the Yellow River was still relatively sparsely settled. The *bi* and *cong* are widely found in the Yellow River region later and came to be seen as shapes that express the Chinese culture’s mythological understanding of the cosmos.

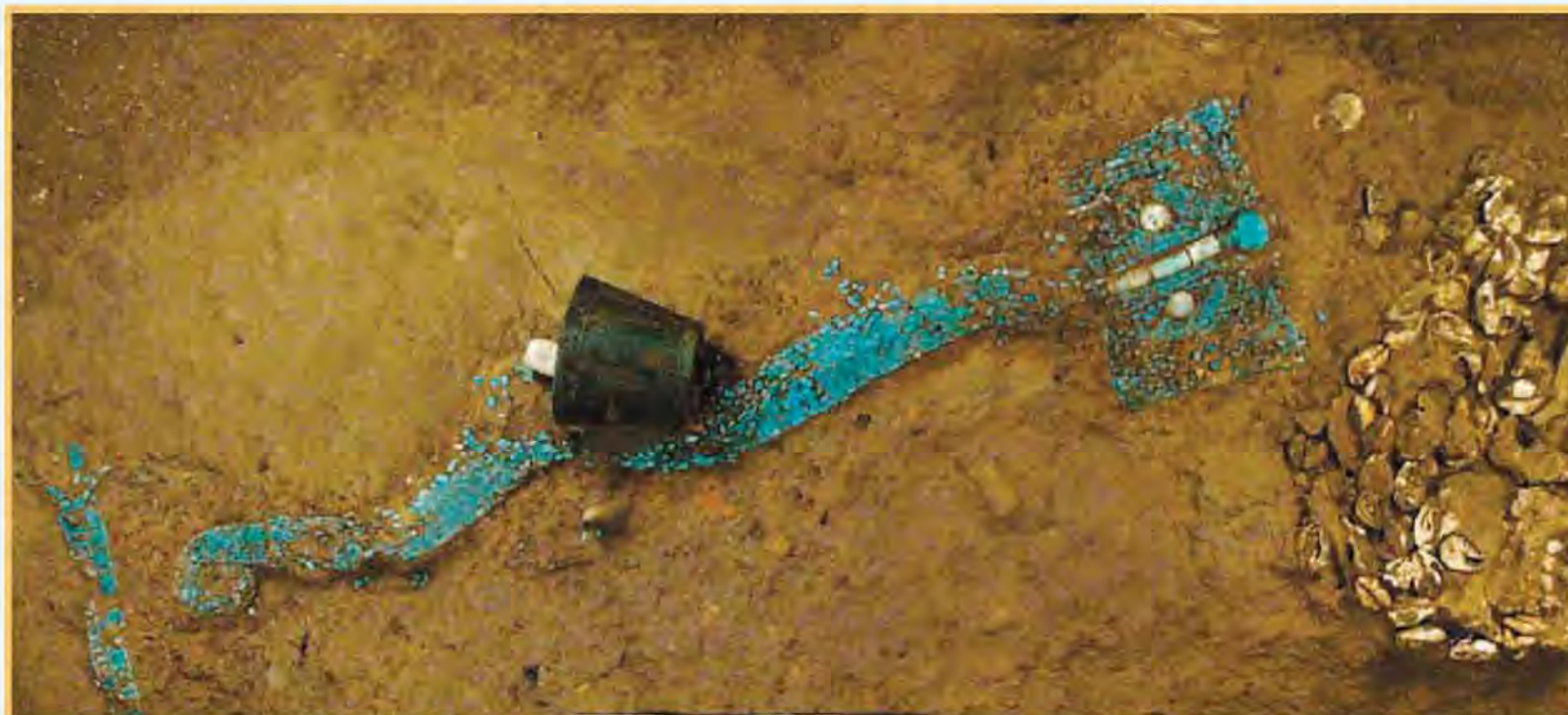


Origin seekers. Beijing’s Wang Wei (*above*) and Liangzhu’s Liu Bin (*below*) see a more complex story of China’s emergence.

Mistaken identity

Although Hongshan and Liangzhu were among the first complex cultures in East Asia, others also clearly contributed elements now considered part of Chinese culture. The first lacquerware and protoporcelain, for example, appear to have emerged in the late Liangzhu period from the middle Yangtze River area, far upstream from Liangzhu itself. And rice, that staple and symbol of Chinese society, was domesticated over a long period of time in the lower reaches of the Yangtze, starting by 7000 B.C.E. or even earlier.

Other regions evolved their own unique cultures, styles, and traditions that did not obviously transfer to what later came to be called Chinese civilization. In 1987, archaeologists working on a 12-kilometer-square site called



Mythical creature? A turquoise dragon found at Erlitou, an important early site in the central plains area of the Yellow River. When discovered in 1959, the settlement was hailed as the capital of the legendary Xia dynasty, which was described in early texts. But recent excavations, coupled with new dating, cast doubt on that claim, as well as on the accuracy of the texts detailing the rise of the Xia.

FOUNDING DYNASTY OR MYTH?

ERLITOU, CHINA—In the 6th century B.C.E., Confucius referred to the ancient Xia dynasty as China's first, based on documents that were old in his day. For generations of Chinese scholars, the Xia was China's initial great flowering of civilization, inaugurating a history that unfolded in methodical fashion from city-state to empire (see main text and timeline, p. 930). But there was no physical evidence for the dynasty's existence, so in 1959 an archaeological team set out to find its seat. Along this marshy section of the Luo River in the central plains of the Yellow River Valley, they uncovered a 300-hectare site dating to roughly the correct period—and promptly hailed it as the long-lost first capital.

But did the Xia, said to have flourished from 2100 B.C.E. to 1600 B.C.E., really exist? New, unpublished dates and excavation data from this modest site challenge its status as the capital of the Xia. "We have proven that Erlitou is the largest and most culturally developed site with the biggest population," says Chen Guoliang, an assistant researcher at the site, standing in a gentle spring rain on the roof of the dig house. "But what it was exactly requires more research."

Until the archaeological finds of the past half-century, most of what we knew of early Chinese history was based largely on ancient texts, which have a status here somewhat comparable to that of the Bible in the West. They provide a detailed account of how the Xia succumbed to the Shang dynasty, which in turn gave over to the Zhou dynasty around 1045 B.C.E. Although the texts were written long after most of the events, digs have confirmed many of the assertions made about the Shang and later eras. But the Xia dynasty has remained elusive, despite the identification of Erlitou as its capital.

During the past decade, Xu Hong of the Institute of Archaeology in Beijing has directed

extensive excavations here, although digging has stopped for now to allow archaeologists to interpret their data and the site has been reburied and planted with wheat. The digs have revealed the details of Erlitou's rise, including a central complex, possibly a palace, in the first phase. Then the settlement grew, the palace area was walled, and a street network was built. A section of road with wagon tracks provides the oldest evidence for wheeled vehicles in China, though whether they were pulled by humans or draft animals is unclear. Many bronze and other precious artifacts, including a spectacular, snakelike turquoise dragon, were apparently made in the palace area and found in large numbers in nearby tombs of the elite. At its peak, as many as 20,000 people may have lived at Erlitou before it slowly faded into obscurity around 1500 B.C.E.

"It looks like a planned city, separated by function, with relatively clustered tombs, workshop areas, pottery workshops near the river, and a clear hierarchy," says Chen. With regular walls surrounding a spacious palace complex near the city center and wide, straight streets, Erlitou's design matches an urban layout that became common throughout China for millennia and is still visible in cities like Beijing, built around the Forbidden City.

Xu's radiocarbon dating of Erlitou to between 1900 B.C.E. and 1500 B.C.E. was later than records indicated for the Xia. Some archaeologists therefore called Erlitou a "late Xia" capital. Now, a larger series of organic samples from the lower layers shift the start date even later—to approximately 1750 B.C.E., says Wu Xiaohong of Peking University, where the samples were recently analyzed. That will make it much more difficult to connect Erlitou with the Xia, which was supposedly ending at the time Erlitou was evolving.

Most younger archaeologists avoid the term Xia altogether. They prefer the term "Erlitou culture" to "Xia dynasty," and its successor "Erligang culture" to "Shang dynasty." Chen explains that "old scholars who graduated before the Cultural Revolution are steeped in a background centered on written Chinese history—and they wanted to solve the 'problem' of the Xia and Shang dynasties by using archaeology to prove their view." He adds that the Cultural Revolution wiped away the traditional lineages of historians, while archaeologists have since embraced Western methods. "Only physical evidence can prove the existence of these two dynasties," he says.

Xu, the excavation chief, criticizes the recent government-funded Xia-Shang-Zhou Chronology Project as "a kind of political propaganda." For him, "archaeology and legendary history are different disciplines." He says that research has been overshadowed for too long by a preoccupation with the dynastic tradition.

As Xu and his team analyze the data from a decade of excavation, they are focusing on how salt production may have been Erlitou's economic driver; such issues are neglected in the written histories. The resulting scenario may be less dramatic than the texts' story of a great storm sent by heaven—complete with 3 days of blood rain—that inaugurated the Xia kingdom, but more convincing to modern archaeologists.

For many researchers, the controversy pitting texts against excavations is a distraction rather than an assault on Confucian learning. Like Near Eastern archaeologists, they are happy to make use of revered ancient texts but do not treat them as revealed truth. "We don't just want to know whether Erlitou is Xia; we want to know the economic and political system. That's what's important," says Ma Xiaolin, vice-director of the Henan Provincial Institute of Cultural Relics and Archaeology in nearby Zhengzhou. "We don't care about the name; we just want a clearer picture."

—A.L.

CREDIT: CHEN GUOLIANG

Sanxingdui, north of the modern city of Chengdu in Sichuan Province in the country's rugged southwest, unearthed a spectacular array of finds. They found eerie bronze and gold masks, a gold scepter, jade ornaments, and massive bronze statues—including a 4-meter-high representation of a tree—from the period around 1200 B.C.E. Sanxingdui is unmentioned in any texts or myths, has no writing of its own, and lies in a remote area; a Tang dynasty poem warns that it is harder to get into Sichuan than heaven. So the evidence of a wealthy and complex culture here stunned both researchers and the Chinese public. Some of the artifacts hinted at connections to Central Asia and far southern China. “The discoveries in the province have forced Chinese archaeologists to completely rethink [Sichuan’s] importance in narratives of prehistoric and early historic China,” says Flad.

A decade later, archaeologists working elsewhere in Sichuan’s Chengdu Plain revealed a culture that appears to have been the predecessor of the Sanxingdui culture, dating to as early as 2500 B.C.E. The largest of these sites, called Baodun, had been mistaken for years for a later Han dynasty settlement. “Nobody believed a city could be from that early period,” recalls Wang Yi, who directs the Chengdu City Institute of Archaeology and Cultural Relics. After confirming the dates, “we realized it was a discovery to rewrite the history of Sichuan and even China.”

The settlements are on a smaller and less complex scale than the cities that emerged 1000 years later on the central plain. But since 1996, a total of eight early walled sites in Sichuan have been pinpointed, ranging in size from 10 to 66 hectares. Wang says the largest contained a population in the thousands, although he declines to be more specific pending further excavations. Many have small houses ringed around larger structures that sit on earthen platforms paved with pebbles. Construction of the walls resembles that down-

Stone Age. The Hongshan people of northeast China created fine jade works like these 5500 years ago.



stream along the middle Yangtze, where other cultures are known to have flourished, but specific trade links remain unclear. Work on Baodun sites has been delayed, because many lie beneath modern towns and villages, and the 2001 discovery of the Jinsha site in Chengdu dating to 1000 B.C.E.—likely a successor to the Sanxingdui culture—forced regional archaeologists to focus their attention and resources there instead. Wang says there are plans to resume digs at Baodun once villages on the site are relocated.

The sophisticated sites in Sichuan, in the northeast, around Liangzhu and elsewhere have made it clear that “the origin of Chinese civilization is scattered all over the present-day country,” says Jiang Weidong, an archaeologist and director of the Liangzhu Museum outside the city of Hangzhou. Weidong thinks that these independent cultures began to link up only sporadically and gradually over many centuries. He notes that in later Chinese history, a half-dozen or so regions periodically reassert their sovereignty and that each of these regions had highly developed prehistoric cultures. For example, in the early centuries B.C.E., the Shu state in today’s Sichuan and the Yue state in the Liangzhu area repeatedly broke away from central control. The serial pattern of Chinese centralization followed by the rise of regional powers may be an artifact of those ancient regional developments, Weidong suggests.

Although not even half-complete, the project to define the origins of Chinese civilization has already laid to rest the notion of an imperial China rising from the central plains of the Yellow River to bestow its gifts on backward hinterlands. Now archaeologists face the challenging task of understanding how the myriad peoples and cultures of the region interacted over several millennia. UCLA’s Von Falkenhausen even suggests that, as a result of this complexity, “the very notion of [a single] Chinese civilization will probably have to be jettisoned.” Chinese scholars say that they will follow the data. “The focus of this project is not to prove the glory of Chinese civilization but to see how it formed,” says Wang. “We want the details.”

—ANDREW LAWLER



Face time. Enigmatic carved visages decorate this jade box from Liangzhu.

CREDITS (TOP TO BOTTOM): LOWE ART MUSEUM/UNIVERSITY OF MIAMI; SMITHSONIAN/FREER GALLERY OF ART; COURTESY OF LIU BIN



Golden days.

New archaeology museums, such as this one in Chengdu, are springing up all over China.

Archaeologists Raise The Old With the New

Researchers work to transform China's development boom from a curse into a blessing for ancient sites

CHENGDU, CHINA—Amid tangles of highways and phalanxes of high rises in this booming capital of Sichuan province, more than 30 hectares of prime urban real estate—three times as large as New York City's Battery Park—is meticulously landscaped around two massive glass, steel, and stone pavilions. But unlike many of the high-rise buildings, this \$75 million, 2-year-old complex is not the modern headquarters of a successful Chinese corporation. Instead, it is a museum paying homage to a 3000-year-old settlement and its surprisingly rich culture, which until recently was completely unknown.

This sprawling ancient site, called Jinsha, lies 1000 kilometers from the traditional center of Chinese civilization along the Yellow River (see p. 934) and deep within a region long assumed to have been a cultural backwater until it was absorbed into the Qin dynasty in the 3rd century B.C.E. In recent decades, however, archaeologists have uncovered astonishing evidence of sophisticated and largely independent cultures in the region dating back to 2500 B.C.E., cultures that are helping to rewrite the origins of Chinese civilization (see p. 930).

A decade ago, Jinsha was still buried. Until its accidental discovery during a construction project, the site was verdant farmland on the outskirts of a city with a mere 5 million people. Today, thanks to savvy archaeologists and their allies in city government, the new Jinsha Site Museum not only offers a welcome haven from urban sprawl but also sets aside a large area for future digs. The excavated

area is covered with a vast glass roof, and a separate building houses state-of-the-art exhibits. Chengdu hotels and department stores proudly sport the site's icon, a gold sun disk surrounded by four birds, as a symbol of the city's unique past.

Jinsha creates a place of beauty, bolsters civic pride, and pulls in tourists—and its success is encouraging other cities to follow suit. “Dozens of local governments have come to see this,” says Zhu Zhangyi, 49, who is now the museum's vice curator. “It has become a model.” Western archaeologists are deeply impressed, too. “The priority is to teach people about their past,” says Gary Crawford of the University of Toronto, Mississauga, in Canada. “They are willing to put real money into that—and we could learn some lessons from that.”

Archaeologists say models such as this are desperately needed in a country developing more rapidly than any other in human history. Half of the world's concrete is poured in China. There are more than

2 million kilometers of highways, double the amount there was in 1986. And cities like Chengdu—which now boasts more than 10 million people and adds a million a year—have mushroomed, eating up land along rivers and on plains typically favored by ancient peoples. The pace of construction threatens to destroy sites ranging from Paleolithic campsites to Han royal tombs, and with them, a treasure trove of data critical for understanding the role of East Asia in early human migrations, animal and plant domestication, and urbanization.

Halting or even slowing development in a society eager to emerge from rural poverty is not possible. Instead, archaeologists



Past protector. Chengdu's Wang Yi saves sites.

CREDITS (TOP TO BOTTOM): A. LAWLER/SCIENCE; COURTESY OF ROWAN FLAD

LANDING THE LOOTERS

In the summer of 1998, a reservoir in a rural area of Hunan in southern China dried up. As the water receded, local farmers found ancient pottery and porcelain from the 10th to 13th century C.E. Song Dynasty, which produced some of the world's finest ceramic art. Within a few weeks, hundreds of looters were openly digging at the site. Despite an outcry from a television reporter and a few cultural-heritage specialists, local officials refused to intervene. It was not until the following February that police arrived to stop the illegal digs, arrest the culprits, and clear the way for a team of archaeologists to save what they could.

In a land chock-full of wealthy tombs and poor farmers, grave robbing is an ancient tradition. But in the past decade, China has tightened its laws against looting, a reflection of changing attitudes toward archaeological treasures (see main text). Now those who destroy the country's past face jail terms and even the death penalty, although no one appears to have actually been executed for looting. Earlier this year, the United States and China agreed to work together to prevent smuggling of looted Chinese antiquities. "The situation in China has improved dramatically in recent years," says Stefan Gruber, a lawyer at the University of Sydney in Australia, who follows the Chinese situation closely.

But he adds that although "the central government has good ideas, the local governments do not necessarily follow their orders." Archaeologist and China expert Lothar von Falkenhausen of the University of California, Los Angeles, remains deeply concerned. "The looters

are absolutely everywhere," he says. "Archaeologists can't keep up, and the looting often takes place with the connivance of local authorities." Von Falkenhausen adds that the new U.S.-China agreement merely shuts American dealers out of a market increasingly driven by wealthy Chinese collectors.

The pace of destruction is difficult to quantify, but it is clearly still taking place. In the northeast, for example, between 4000 and 15,000 tombs from the Neolithic Hongshan culture (see p. 930), which produced rich jades in fantastic animal shapes 5000 years ago, have been damaged or destroyed by looters during the past decade, says He Shuzhong of the National Administration on Cultural Heritage in Beijing. In the southern province of Hubei, 2000-year-old graves filled with jewelry, documents written on bamboo, and other artifacts have been stolen.

"When an archaeological team finally went in, there was nothing left to save," says one archaeologist familiar with the destruction.

In response to such damage, museum and site security has recently improved. At the Yanghai cemetery in the remote western province of Xinjiang, for

Twins. Both plaques are probably from Erlitou, but only one was dug legally.

example, looters who a decade ago helped themselves to jewelry in the 3000-year-old graveyard are now stymied by a high fence, locked gate, and live-in caretaker. Recent high-profile cases, coupled with educational initiatives, are making China's vast population aware that looting is illegal and unpatriotic.

Although strict laws likely dissuade many looters, they can have a perverse effect. Local farmers near Erlitou, one of China's oldest urban centers (see p. 934), now hesitate to bring artifacts found during plowing to archaeologists, perhaps fearing stiff penalties, says Chen Guoliang, an assistant researcher at the site.

Clicking on his laptop in his office at the Erlitou dig house, Chen pulls up several images of similar turquoise-inlaid bronze plaques that appear to be in a style arguably unique to Erlitou.

The use of these elaborate objects remains unclear, and archaeologists are eager to find more in context. But only one was legally excavated from the site. How and when the others were found remains a mystery, though Chen believes that they almost certainly came from Erlitou. Today, the other plaques reside in public and private collections around the world, from the Miho Museum in Japan to Harvard University in the United States. (Many museums have taken at face value claims by sellers that artifacts were legally exported.) Once taken out of their context and sold, says Chen, such artifacts—whose provenance is difficult to verify—no longer have a story about China's heritage worth telling.

—A.L.



are exploring creative ways to collaborate with both government and developers, and using museums like Jinsha's to build popular support for preserving key sites. Thus China's development boom is powering a new wave of archaeological discovery and appreciation even as it threatens sites. Courts are increasingly willing to enforce harsh penalties on looters (see sidebar, this page). And in a dramatic departure from the past, local governments are now willing to lend support and funds to preserve sites. "It was a great fortune we discovered [Jinsha] in 2001," says archaeologist Zhu, who led the team that examined the site just ahead of developers. "If it had been earlier, it would have been impossible to preserve the whole area."

During a recent visit by *Science*, however, archaeologists at several provincial centers also warned that they must race to keep up with the bulldozers and have largely set aside purely academic endeavors in order to rescue sites. The recent economic downturn, rather than easing the pace, has only quickened it, as the central government pumps hundreds of billions of dollars into dams, canals, and highways to stimulate the economy. Says Zhu: "We have to do our best to persuade our government that if it doesn't move aggressively to protect sites, there will be nothing left in 10 or 20 years."

Water over the dam?

The current boom is hardly the first threat to China's past. Qin Shi Huang, the man credited with first unifying China in the 3rd century B.C.E., consolidated the Great Wall and left behind the famous terracotta army in his mausoleum—two of the modern nation's most famous tourist attractions. But he also ordered that evidence of previous rulers be destroyed in order to ensure his importance in history. More than 2 millennia later, China's revolutionary leader Mao Zedong encouraged his people to obliterate "old ways of thinking," triggering the destruction of thousands of ancient buildings and artifacts. During the years of the Cultural Revolution in the late 1960s and early 1970s, archaeological publishing ceased, university courses were restricted to political subjects, and many researchers were forced out of their jobs.

Today, the more insidious threat is not to China's visible past but to the undiscovered sites that lay safely underground until recent development. The most infamous example of this third wave of destruction is the Three Gorges Dam project, which began in 1993 and eventually drowned a 600-kilometer stretch of the middle Yangtze River. The government initially allotted \$37.5 million for archaeological salvage, although archaeologists called for at least \$500 million. The amount was only marginally increased, and sal-

GO EAST, YOUNG ARCHAEOLOGIST

Zhijun Zhao started his career like many promising Chinese students: by studying in the United States with an eye to staying. He got his Ph.D. at the University of Missouri, Columbia, and rose through the academic ranks, acquiring the nickname "Jimmy" and eventually landing a comfortable job at a museum in Kansas City. He also got a coveted green card that put him on the path to U.S. citizenship—all the ingredients of the American dream. "Big houses and cars—I

could have lived the easy life," he muses today.

But instead, in 1999, Zhao made a bold decision. He returned to China and opened a lab at the Institute of Archaeology in Beijing, which at the time lacked many of the modern facilities common at any American university. He was given 5000 yuan—about \$600 at the time—in start-up money. "I spent 4000 yuan on a microscope," Zhao recalls with a laugh. He held on to the green card for a full year.

Zhao's move was a gamble. But today, many Chinese-born scientists educated in the West return to China, says Wang Wei, director of the Beijing institute. Although in the past, that return may have been pushed by difficulties in language, culture, and getting a job overseas, now China is exerting a magnetic pull. As archaeology attracts attention, central and provincial governments are spending more on new facilities and better salaries (see main text). Researchers are drawn home by family ties and professional opportunities. "We want all of our overseas scholars to come back," says Wang. "And we do our best to provide a good environment for researchers."

vage work was not finished before the dam was completed in 2006 (*Science*, 1 August 2008, p. 628). "We may have missed a few sites," says one Chinese archaeologist sheepishly.

Other massive projects have received less publicity but are having a tremendous impact. The \$8 billion South-North Water Transfer Project will divert water from the wetter areas of central and southern China to its thirsty north, through a complex mix of reservoirs, canals, and dams. When complete by 2014 (*Science*, 25 August 2006, p. 1034), the central route—an average of 110 meters wide—will cut across nearly 1300 kilometers, much of it in central Henan Province, which is traditionally considered the homeland of Chinese civilization.

Ma Xiaolin, vice-director of the Henan Provincial Institute of Cultural Relics and Archaeology in Zhengzhou, says work on the canal has uncovered some 340 sites in Henan alone, from Neolithic settlements

The homeward pull is a relatively new phenomenon. With rare exceptions, war and politics isolated China from the outside world between World War II and Mao Zedong's death in 1976. For the most part, archaeological finds made behind the Bamboo Curtain remained unknown in the West, while new theories and methods failed to penetrate into China.

Starting in the 1980s, large numbers of Chinese students, including archaeologists, began to study in

the West. Some stayed, though others tried to keep a toehold in China as well. For example, Tianlong Jiao studied at Harvard University and is now an archaeologist at the Bishop Museum in Honolulu. He moves easily between worlds, doing fieldwork on trade and agriculture in South China and often visiting colleagues at the Beijing institute. But his status as a researcher in both countries may already be an anomaly. "I am probably among the few, if not the only one," he says.

Zhao says he has no regrets about returning to his homeland. His 2008 budget is 1.5 million yuan, or \$220,000, and his modest lab in a Beijing suburb has an enthusiastic staff of mostly young researchers. On a recent weekday,

his team ate lunch together and chatted about work, taking breaks at a Ping-Pong table in a nearby room. Some are specialists in dating ancient wood—dendrochronology—while others analyze spores and pollen to understand paleoenvironments, and another group identifies isotopes in animal bones uncovered in a recent dig. English as well as Chinese textbooks line the walls.

This analytical approach to archaeology marks a radical coming of age for the field in China, where organic material—from human bones to pollen—is still routinely ignored in the search for valuable grave goods. Zhao's example, other archaeologists say, is a powerful motivator for adopting newer techniques. The world is taking notice; a May workshop on archaeological methods in Beijing drew experts from several countries.

Zhao still bemoans the difficulty of getting things done in China, compared with the ease of life in the United States. But he says China's authorities place no restrictions on his work: "Anything related to scientific research is OK." The

energy of his home country is palpable just outside his lab, where new high rises are sprouting all around while a group of elderly women perform their morning tai chi exercises.

Last year, Zhao returned to the United States to give a talk and made a pilgrimage back to Columbia to see his former colleagues. "I was surprised," he says. "Nothing had changed."

In China, you see change every day. There is just more activity and more opportunity."

—A.L.



West to East. Zhijun Zhao returned to China.



Two worlds. Tianlong Jiao keeps a foot in each country.

to Tang Dynasty tombs. Ma says time and funding for salvage work are ample, but there are complications. Archaeologists are now excavating a 2000-year-old king's tomb and have requested that the government alter the canal route. "No decision has been made," says another scientist familiar with the site. "It's a sensitive issue."

That sensitivity reflects the tension between development and preservation. China passed a heritage protection law in 1982, but archaeologists say it was only haphazardly enforced until recently. "In past decades, we were in a very bad position," says Wang Yi, who leads the Chengdu City Institute of Archaeology and Cultural Relics. "Since the first law was passed 27 years ago, we have been fighting against developers. And in the past, local governors were enemies of archaeologists. ... We could not counter a city's development."

But that is changing. In 1997, the government made violations of

cultural heritage laws a criminal act punishable by jail terms and even the death penalty. In Chengdu, the manager of a real-estate company went to jail for 5 years for failing to do archaeological salvage work before construction. “There have been those who destroyed sites and artifacts—but now, if they do, they get in big trouble,” says Wang. “Even government officers don’t dare break this law.”

Hearts and minds

Along with the legal stick comes a carrot. Both the city and provincial government see that development “is not just about an increase in GDP,” asserts Wang. “We have to make this mainstream, so that all branches of government and citizens support archaeology.” He and a growing number of other Chinese researchers are increasingly involved in outreach activities to create a broader constituency for protecting sites. “It is impossible not to lose some sites,” says Wang Wei, director of the Institute of Archaeology in Beijing. “But the public is starting to appreciate the importance of cultural heritage—and that you can move the site of a planned building.”

The archaeologists’ efforts can be seen in a new and surprising phenomenon: multimillion-dollar popular archaeological museums that have opened in recent years across China, sporting three-dimensional movies, elegant restaurants, and exhibits that equal or surpass those in major U.S., European, and Japanese cities. Many, like the Jinsha museum, are on land protected from further development. “For less than \$100 million, the Chengdu municipal government bought a history 1000 years older than it had before,” Zhu says over sushi in the chic museum restaurant.

In another example, last October a gleaming monument of Iranian marble opened outside the southern port city of Hangzhou to celebrate Liangzhu, which started flourishing around 3500 B.C.E. and is one of the oldest major settlements in China. Now 42 hectares around the site have been protected from major development. When a real-estate company sought to buy neighboring land, the government sold it for under market value in exchange for nearly \$24 million for the museum and private-sector expertise in big projects. “This was a real innovation,” says archaeologist Jiang Weidong, director of the Liangzhu Museum, over tea in his sleek Bauhaus-style office.

The exhibit lays out methods of excavation, the evolution of the site, and the day-to-day life of its people 5000 years ago, using cutting-edge artifacts, films, and displays. Visitors can even walk through a recreation of the settlement, showing both the jade-wearing elite—who were buried in elaborate tombs high on earthen platforms—as well as modest tradespeople and rice and millet farmers in wattle-and-daub houses.

Back in Chengdu, archaeologists are also using their facilities to win the hearts and minds of their citizens. After the 2008 Sichuan earthquake, curators at Jinsha opened the grounds to more than 40,000

people who camped out amid fears of aftershocks. To mark the first anniversary of the disaster in May, they waived admission fees and drew an impressive 50,000 citizens. Regular festivals promote the site as a cultural oasis amid the city’s congestion.

Such efforts raise awareness of the nation’s heritage, and plans for park and museum complexes at ancient sites are taking hold all over China, from the 3500-year-old city of Erlitou in the central plains to the ancient Silk Road city of Turfan in the far western province of Xinjiang (see p. 940). In May, a new underwater museum opened along the Yangtze, preserving 1200-year-old poetic inscriptions and measurements of annual high-water levels on rock from the waters impounded



Big dig. A massive new north-south canal threatens hundreds of ancient settlements.

by the Three Gorges Dam. Such museums also provide opportunities for archaeologists themselves, and some scholars who studied abroad are now finding ways to return to China for research or even permanently (see sidebar, p. 938).

Getting the goods

In the rush to modernize, modest prehistoric settlements are at particular risk, although sometimes they can win a reprieve. In Shaanxi province, west of the central plains, for example, construction of a vehicle factory was put on hold after the discovery of an unusually complex, moated, Neolithic site with a line of pottery kilns suggesting specialized handcrafts, dated to a surprisingly early 4000 B.C.E. “The site was preserved, and the provincial government paid dozens of millions of yuan [tens of millions of U.S. dollars] to move the factory,” says Wang Weilin, vice director of the Shaanxi Archaeological Institute.

Wang, whose organization includes 130 archaeologists, says developers pay nearly \$3 million annually to cover the costs of salvage work in his province. But he is particularly concerned about smaller sites without dramatic architecture and artifacts. “We see traces of such sites, but we worry we might not catch up with development,” he says. Harvard University archaeologist Rowan Flad, who is collaborating with Wang, notes that international efforts “are often the only way

that work beyond that of a salvage nature can get done,” because of the time pressures on Chinese institutes.

Smaller, more ancient sites are also at greater risk because they typically lack what Chinese archaeologists privately call “*hao dongxi*,” which can be roughly translated as “goodies” in English. “There is a tendency among some Chinese archaeologists to look for the goodies, that is, the grave goods with artistic merit and which embody China’s cultural heritage,” says Magnus Fiskesjö, an anthropologist at Cornell University. “Fishbones don’t qualify.”

As a result, material with the potential for providing critical data on scientific questions, such as ancient diet, health, and social organization—including fishbones—is often overlooked, particularly during fast-paced salvage digs. Even human bones are often still disposed of rather than analyzed, says Fiskesjö.

That tendency is changing, albeit unevenly. In Zhengzhou, Ma, who studied at La Trobe University in Melbourne, Australia, is eager to show off his labs and storage facilities, which include well-labeled

blue bins of human and animal bones from a host of sites. “Smaller institutes just collect artifacts and throw away the rest,” he says. “We want to focus on new techniques involving plants, animals, and human skeletons and set up databases for each site.” With a healthy \$3 million annual budget, Ma’s institute has the funds to do more detailed research. But the organization is now juggling a dozen excavations, and he expects to conduct more than 30 digs this year alone—90% of which are salvage operations.

Despite—and because of—the pace of development, archaeologists in China appear surprisingly optimistic. “Given the investment from our government, the 21st century will be a golden age for archaeology in Sichuan,” predicts Chengdu’s Wang. With an interested public plus provincial government coffers filled by the economic boom, China is now paying heed to its archaeological treasures in a way that once might have been criticized as a bourgeois luxury. Says Jiang, smiling over green tea in his sun-filled office: “When your granary is full, you pay more attention to ceremony.”

—ANDREW LAWLER



Desert death. A 4000-year-old child mummy peers out of his wooden coffin in Xiaohe cemetery on the edge of the Taklamakan Desert.

ARCHAEOLOGY

Bridging East and West

China’s far west, home to unique ancient cultures, may help reveal how technology and goods flowed from West to East to shape Chinese civilization

YANGHAI, XINJIANG PROVINCE—No place on Earth is farther from an ocean than this dusty spot in the Taklamakan Desert in northwest China. But when archaeologist Lu Enguo recently excavated the sprawling 3000-year-old Yanghai cemetery here, he found a cowrie shell from either the Pacific or the Indian Ocean in the undisturbed tomb of a local shaman. That holy man—his body naturally mummified in the dry climate—was dressed in the style of the Russian steppes, with a headband of gold, a brilliantly colored woven garment, and a ceremonial bronze ax by his side. For him, the wealthy and fertile eastern land called China may have been just a rumor or tall tale.

Yet despite the distance to ancient centers of Chinese culture, Lu, who works for Xinjiang’s archaeology office in nearby Turfan, believes that this remote region may hold the key to understanding early Chinese civilization because of its crucial role in trade. Lu and many of his colleagues argue that as far back as the 3rd millennium B.C.E., during the rise of Mesopotamia, Egypt, and the Indus civilizations, Xinjiang may have served as a critical bridge between East and West, funneling some combination of bronzemaking, wheat domestication, and other technologies toward the incipient Chinese culture. Those technologies may have helped jump-start Chinese urban life along the Yellow and Yangtze rivers in the 2nd millennium B.C.E. (see p. 930).

That is a novel, even radical, idea among Chinese academics, many of whom still see Xinjiang as a distant region that enters history only when a unified China began to assert control in the early centuries B.C.E. Indeed, not so long ago, such discussion of outside influence on China’s origins would have been at best frowned upon and at worst dangerous. “Ten years ago, you could not even say that China adopted anything from the West,” says one Chinese archaeologist. After more than a century of humiliation at the hands of foreigners—both Western and Japanese—China’s leaders in the 20th

CREDIT: XINJIANG CULTURAL RELICS AND ARCHAEOLOGY INSTITUTE

century emphasized the country's indigenous traditions, and archaeologists followed their direction. Now recent discoveries, coupled with the growing self-confidence of a prosperous nation, are challenging the taboo. "Chinese archaeologists still believe China's civilization developed independently," says Wang Wei, director of the Institute of Archaeology in Beijing. "But they also believe that there was important communication with the outside world."

Before the Silk Road

China's contact with that outside world may have come from several directions—from Xinjiang in the northwest, from the steppes to the north, overland through Burma and Yunnan to the south, or around Southeast Asia to the eastern coast. The most direct route from the west to east is here in Xinjiang. For centuries starting in the first century B.C.E., the fabled Silk Road stretched across its deserts and mountains, linking the eastern cities of China with European markets. Roman silver, fine silk, Buddhism, and Islam were passed across its length.

Caves filled with Buddhist images, crumbling caravansaries, and ruined cities still dot the province's dry and rugged landscape.

Today, Xinjiang still retains the hallmarks of a crossroads region. Signs in Arabic script and Russian Cyrillic compete with Chinese characters in the province's capital, Ürümqi, which is closer to Islamabad than it is to Beijing. It is home to ethnic Uighurs—many of whom are Muslim—who traditionally have more in common with their Central Asian brethren than the Han Chinese of the east. Recent ethnic riots in Ürümqi left at least 156 dead and 1000 people injured.

But until the past decade, archaeologists had found little detailed evidence of early human occupation here. Ringed by high mountains, the Taklamakan is one of the world's driest and hottest deserts. So archaeologists and historians assumed that life here was all but impossible until camels were domesticated and deeper wells and other innovations were developed—long after Chinese cities began to flourish thousands of kilometers to the southeast.

Recent excavations have upended that assumption. In the northeastern edge of the desert, archaeologists from 2002 until 2005 excavated an extraordinary cemetery called Xiaohe, which has been radiocarbon-dated to as early as 2000 B.C.E., says Liu Xuetang, a professor at Ürümqi University and former director of Xinjiang's archaeology institute in Ürümqi. A vast oval sand hill covering 25 hectares, the site is a forest of 140 standing poles marking the graves of a long-lost society and environment. The poles, wood coffins, and carved wooden statues with pronounced noses come from the poplar forests of a far cooler and wetter climate.



Forest of graves. These poplar poles from Xiaohe cemetery hint at a wetter climate 4 millennia ago.

A bronze mirror, gold ring, and scatterings of domesticated wheat found in some of the undisturbed tombs show a Central Asian influence. Ox skulls tied to the top of the wooden grave markers show that these animals were sacred. One grave includes a carved wooden snake, the remains of seven real snakes, and a hat made up of small pieces of the ears of sheep, probably serving shamanic purposes common to Central Asia but foreign to eastern China. A tomb of a child holds a pouch with the remains of ephedra, a drug favored by ancient Central Asian pastoralists.

Of 350 tombs, Liu says 190 had been looted and destroyed, but 160 were excavated in the recent digs by a Chinese team. The human remains are eerily well-preserved. Behind the locked doors of the storeroom of the Ürümqi institute, Liu points to a young woman with still-smooth skin and auburn hair, wearing a white wool hat and felt shoes with laces still intact. French and Japanese researchers are helping to analyze the goods and remains at Xiaohe, but that work is still ongoing, he says.

The origins of the Xiaohe culture—which lasted for some 5 centuries, until approximately 1500 B.C.E.—remain obscure. They do not appear to have used pottery, making their connections to other cultures opaque, but there is no evidence that these likely pastoralists were significantly influenced by the Yellow River and other settled cultures to the east. Liu argues that, given their material culture, they probably entered from the north, from present-day Russia, over the Tien Shan mountain range, before 2000 B.C.E. Although no extensive paleoclimate studies have been done, some evidence suggests that the climate became wetter at that time. The poplar



Well-wrapped. One of 30 mummies from Xiaohe buried in airtight ox-hide bags, preserving both skin and cloth.

MILLET ON THE MOVE

What was the most important grain in ancient China? If you said rice, you'd be wrong, according to some archaeologists. It was lowly millet that served as the staple grain that allowed Chinese civilization to flourish in ancient times, says archaeologist Gary Crawford of the University of Toronto, Mississauga, in Canada. "Millet was the principal crop that supported town life," he says. Although rice began to be domesticated in the southeast by 7000 B.C.E. or even earlier, millet was grown all across China in the preurban era, from the north to the southeastern coast.

And whereas important goods and technologies like wheat, bronze, horses, and chariots all flowed from West to East starting some 4000 years ago, perhaps across China's westernmost provinces (see main text), there is now intrigu-

ing evidence that millet traveled the other way. Some researchers say the grain was first domesticated in northern China as early as 8000 B.C.E. and made its way to the Black Sea region of Europe by 5000 B.C.E. If so, it would be a sign of far earlier and extensive connections—going both ways—across the vast Eurasian landmass.

Until this year, the earliest solid evidence of domesticated millet dated to about 6000 B.C.E. from a handful of sites in northern China. But in May, seed cases found at a northeastern site called Cishan in Hebei Province were dated to 8000 B.C.E., according to a paper in the *Proceedings of the National Academy of Sciences* by Houyuan Lu of the Institute of Geology and Geophysics in Beijing and colleagues.

That's the oldest sign yet of this short-season crop, says Crawford, who backs the claim. But others are skeptical. The seed cases are domesticated millet, agrees Zhijun Zhao of the Institute

of Archaeology in Beijing—but the dates are 2000 years older than the Cishan settlement itself, a 400-square-meter site with many storage pits, stone grinders, and sickles. Houyuan counters that his team's dates, done with accelerator mass spectrometry analysis of carbon-14, are solid. "To confirm our results, we rechecked the stratigraphy and obtained additional C^{14} dates from a second C^{14} laboratory," he says. "Previous archaeological excavations in Cishan might be incomplete." Crawford agrees, noting that Cishan was dated back in the 1970s.

Whether the Cishan millet proves to be as old as supporters say, other sites in the region clearly show that millet was grown in significant quantities in northeastern China long before it appears around the Black Sea and in central Europe. Zhao and Crawford, for example, have dated millet at a northeastern Chinese site called Xinglonggou to approximately 5640 B.C.E. Early farmers in the

no longer found in the area is one sign, as is increased snowfall that created channels through the Tarim Basin that contains the Taklamakan. Some lakebed samples in northwest China hint at a warm and wet period between 2800 and 2000 B.C.E., followed by a 1000-year cold and dry spell, says environmental archaeologist Qi Wuyun of the Institute of Archaeology in Beijing. But she adds that further data are needed.

The most important area of settlement may have been an environmentally hostile region on the desert's eastern end called Lop Nur, which China used to conduct nuclear tests. But in ancient times, "the Lop Nur delta was a large oasis hundreds of kilometers in length," Liu says. Preliminary surveys and geological studies suggest a string of settlements along the now-dry Peacock River, which once flowed east and ended in a marshy lake.

Researchers in others parts of Central Asia have found many settlements in similarly marginal climatic zones during the period, such as Gonur in the Kara Kum desert of Turkmenistan. But little archaeological work has been done along the Peacock because of its remoteness, security constraints, and a focus on rescuing sites endangered by development (see p. 936). Increasing aridity by 1500 B.C.E. may have forced the Peacock settlers to revert to a nomadic existence, says Liu. That cycle seems common throughout recorded history in Xinjiang, where small changes in rainfall have a dramatic effect.

Other ancient Xinjiang cemeteries, most from the period starting in 1500 B.C.E., are coming to light and may offer additional clues. At one site in Xiabandi, in the far western end of the province near the Pamir Mountains and adjacent to Kazakhstan, archaeologists found pottery resembling that of the Andronovo pastoralist culture of the steppes. Yet they also found bracelets and earrings that Liu says are in a style common to Gansu, a Chinese province far to the southeast. And to the northwest of Ürümqi, bordering the steppes, Liu excavated a settlement from 1000 B.C.E. with round altars and evidence of horse and sun worship—classic traditions of

Shipshape. Some Xiaohé tombs feature boat-shaped wooden coffins unique to the site.

CREDIT: XINJIANG CULTURAL RELICS AND ARCHAEOLOGY INSTITUTE



region typically planted the crop on the fine and loose soil called loess, which may have been the home of millet's still-unknown wild ancestor. The grain—which can be turned into flour, porridge, or beer—then spread across northern China. It was widely planted in the Yellow River region and



as far southwest as the Chengdu plain, where it became an important staple by 4000 B.C.E.

Millet either diffused from China to Europe or was domesticated independently in each place. Archaeologist Martin Jones of the Univer-

sity of Cambridge in the United Kingdom suspects that the timing of millet's appearance around the Black Sea is no coincidence. Millet can produce seeds quickly—in 45 to 60 days—and the most common variety can survive dry conditions that kill other grains like wheat. So although wheat must have been traded across the steppes, mountains, and deserts that separate China and the Near East, millet could have been passed along by farmers who took up its cultivation across central Asia. Early results from ongoing genetic studies suggest that Chinese and European millets are indeed related, Jones says cautiously. Next year, he hopes to go into the field in Kazakhstan and China's northwest to find millet remains that might connect the dots between north China and the West. "It may seem like looking for a needle in the haystack," says Jones, "but we're going to track down these sites."
—A.L.

steppe pastoralists. But at the same site, he also excavated painted pottery of a type found in the upper Yellow River valley. Such finds offer intriguing but still enigmatic evidence of the links between Central Asian pastoralists and China proper, says Liu.

On the bronze trail

The connection between the steppes and eastern China clearly existed. But did pastoralists such as those buried in Xiaohe carry important technologies like bronze eastward? That idea remains controversial. Bronze technologies in the form of weapons and adornment appear starting in the 3rd millennium B.C.E. across the steppes. The Xinjiang bronzes appear to be slightly earlier than several found in Gansu, to the southeast, and then, not long after, in Erlitou in the mid-Yellow River area. That makes for a neat pattern of diffusion. "But the techniques used in Gansu are more developed than in Xinjiang," notes Liu. And the earliest bronze-casting workshops in the region don't appear until the 4th century B.C.E., adds Lu. "It is not likely these skills were introduced from Xinjiang," he says, standing on the parched ground at the Yanghai cemetery.

Trade with Central Asia likely led to the acquisition of bronzes here—but not necessarily the means to make them, Lu says. He and others increasingly think that bronze technology filtered south from Inner Mongolia, far to the east, and eventually was picked up by peoples along the Yellow River.

But others point out that mold-casting dominates early Chinese metallurgy, and that technology is not used until later in the region between Europe and Central Asia—arguing against a technology transfer. Some scholars argue there was a connection with the West but that the technology then took an independent turn. Evidence for all theories remains thin. "How does it get to Gansu?" asks Chen

Xingcan of the Institute of Archaeology in Beijing. "The route is just not clear."

Whatever the route for bronze, Lu cites another transformative import that he says arrived from the west via the Peacock River valley: wheat. Domesticated first in the Near East 10,000 years ago, wheat is northern China's most important staple today. And at the moment, the oldest domesticated wheat in China seems to be that strewn over bodies before burial at Xiaohe 3000 years ago. "The new term we use is the 'wheat road,'" says Lu.

But other archaeologists in China are not yet convinced. Wheat next turns up in the 1st millennium B.C.E. in northern China, and it's not clear if wheat from Xiaohe made its way there or if diffusion from the west simply stopped in Xinjiang. "We need to find actual wheat fields at Xiaohe," says Xiaohong Wu of Peking University. Some researchers instead see a pattern similar to that of bronze, with wheat coming from the steppes through Inner Mongolia. And a recent find of a few early wheat samples roughly dated to 2000 B.C.E. in the far southeastern province of Fujian raise the possibility of seaborne transfer from the Indus civilization in today's India and Pakistan.

Similar debates revolve around the appearance of domesticated sheep, goats, and cattle in China. Xinjiang sites show evidence of all three in the 2nd millennium B.C.E.—about the time that they appear in central China. But tracing a path of diffusion is difficult, in part because there are few Chinese zooarchaeologists. Everyone agrees that these questions require more extensive exca-

vations in the province as well as better analytical techniques. In a region that retains its position as a continental crossroads, archaeologists are only starting to understand how this bridge between East and West contributed to China's evolution.

—ANDREW LAWLER



Heads up. This tiny wooden face provides a glimpse into the beliefs of the Xiaohe people.

The paleobiology
radiation

947

Ancient effects of humans
on marine ecosystems

952



LETTERS | BOOKS | POLICY FORUM | EDUCATION FORUM | PERSPECTIVES

LETTERS

edited by Jennifer Sills

Less-Toxic Cigarette Use May Backfire

IN THE NEWS OF THE WEEK STORY BY J. COUZIN-FRANKEL AND R. KOENIG ("EXPANDED U.S. DRUG agency to control tobacco," 19 June, p. 1497), Gregory Connolly points out that promoting less-toxic cigarettes has not been shown to reduce tobacco-related death and disease. In fact, promoting the use of cigarettes containing lower levels of nicotine may even increase tobacco-related death and disease.

Of the excess deaths caused by smoking, about 29% have been caused by heart disease and stroke, about 16% by lung cancer, and the rest mostly by assorted other kinds of cancer (1). Many people think of lung cancer as the chief culprit because lung cancer is a relatively rare disease in the absence of smoking, whereas heart disease is quite common. Nonsmokers get lung cancer at about 1/40th the rate of smokers (2), whereas heart disease and stroke are major causes of death in both smokers and nonsmokers (1).

Studies have shown that nicotine addicts smoke until they have absorbed enough nicotine to satisfy their craving (3). This means that they will smoke more cigarettes if the cigarettes contain lower concentrations of nicotine. This, in turn, means that they will be subjected to more of the "tars" (the cancer-causing ingredients of the smoke) in their attempts to get their usual dosage of nicotine (the ingredient responsible for heart disease and stroke). In the end, smokers of low-nicotine cigarettes will remain at the same risk for heart disease and stroke but increase their chances of developing cancer.

MARSHALL E. DEUTSCH

41 Concord Road, Sudbury, MA 01776-2328, USA. E-mail: med41@aol.com

References

1. M. J. Thun *et al.*, *Am. J. Public Health* **85**, 1223 (1995).
2. S. D. Stellman *et al.*, *Cancer Epidemiol. Biomarkers Prev.* **10**, 1193 (2001).
3. N. L. Benowitz *et al.*, *N. Engl. J. Med.* **309**, 139 (1983).



NIH Needs a Makeover

NIH GRANTS ARE COVETED AND LAUDED POSSESSIONS among scientists. They are considered a mark of accomplishment or promise, offered for scientific merit and devoid of politics. Unfortunately, the system that bestows the grants has become tangled and inefficient.

The lack of quality reviewers is a major issue. The guidelines for reviewer selection on the NIH Web site are vague at best (1). We need individuals who are experts in their fields, but there are no specific guidelines as to what defines "expert." These flimsy criteria made it easy to increase the number of reviewers to an astonishing 30,000 (2) in the wake of the stimulus grant deluge, but do not ensure that the reviewers are of high quality. The

Center for Scientific Review is desperate to recruit reviewers and is drafting individuals who have poor records of NIH grant awards or weak publishing histories. How can those individuals be trusted to review grants?

Even without the unprecedented number of grants resulting from the stimulus, it is difficult to recruit and retain adequate numbers of qualified reviewers. (Three to four reviewers are solicited to critique each grant.) Study section reviews are still conducted largely on-site, requiring considerable time investments from reviewing scientists. The NIH should make better use of modern telecommunications technology; the grant discussions could easily be conducted via video/teleconference, freeing up not only time but copious amounts of money spent on travel and lodging.

The newly introduced guidelines for reviewing grant applications also pose a challenge to NIH. Assigned reviewers now summarize the strengths and weaknesses on a grant in "bullet forms," which allow for numerical scores but not detailed comments. A grant is scored in five categories (significance, investigators, innovation, approach, and environment), but a final score on overall merit determines the percentile score for funding determination. It is not yet clear whether individual scores have any bearing on the overall score. Moreover, without detailed comments from the reviewers, an applicant does not have much feedback on how to revise a grant for resubmission. The new system is intended to improve the review process, but requires close monitoring to determine whether it is serving the purpose.

It is time to appoint a strong leader at NIH who has the understanding of a lifetime researcher and the authority to revolutionize the institution. It is imperative that the infrastructure be strengthened immediately to advance biomedical research pursuits. **S. K. DEY**

Department of Reproductive Sciences, Cincinnati Children's Hospital Medical Center, Cincinnati, OH 45229-3039, USA. E-mail: sk.dey@cchmc.org

References

1. National Institutes of Health, Office of Extramural Research, Peer Review Process; www.grants.nih.gov/grants/peer_review_process.htm.
2. M. Wadman, *Nature* **459**, 763 (2009).

Keeping Infection at Arm's Length

IN THEIR REPORT "TOPOGRAPHICAL AND TEMPORAL diversity of the human skin microbiome" (29 May, p. 1190), E. A. Grice *et al.* found that the richest area (in ecological terms) appeared to be the volar forearm, and the antecubital fossa topped the diversity list. This is the exact site physicians use to perform venepuncture, and the results should inform future disinfectant protocol.

Disinfection is often inefficient. When a swabbed venepuncture site is punctured before the antiseptic agent dries (1), the bactericidal effect is compromised. In some cases, official guidelines go so far as to consider cleansing the skin optional (2).

CREDIT: ISTOCK



T cell development

953



Possible impacts
of geoengineering

955

Ineffective disinfection has substantial consequences. Blood culture contamination after venepuncture is relatively common and may lead to false positive cultures and unnecessary antibiotic use and hospital stays (3). Furthermore, bacteria can be introduced in the bloodstream, causing local or systemic infection. Among the bacteria detected in this body region by Grice *et al.* were the *Staphylococcus aureus* species and phyla hosting pathogens that are responsible for the most common causes of bloodstream infection and sepsis (4).

The findings in this report provide grounds for more meticulous disinfection, at least until trials offer us more definitive evidence.

VERONIQUE VERHOEVEN,^{1*}

SERGE BROODHAERS,² BARBARA MICHIELS,¹

SAMUEL COENEN³

¹Centre of General Practice, University of Antwerp, 2610 Antwerp, Belgium. ²Vaccine and Infectious Disease Institute, University of Antwerp, 2610 Antwerp, Belgium. ³Research Foundation—Flanders, University of Antwerp, 2610 Antwerp, Belgium.

*To whom correspondence should be addressed. E-mail: veronique.verhoeven@ua.ac.be

References

1. C. D. Sutton *et al.*, *Ann. R. Coll. Surg. Engl.* **81**, 183 (1999).
2. Protocols and guidelines for GPs: Venepuncture (2007); www.gp-training.net/protocol/nurse/venepunc.htm.
3. G. Suwanpimolkul *et al.*, *J. Infect.* **56**, 354 (2008).
4. K. E. Hodgkin, M. Moss, *Curr. Pharm. Des.* **14**, 1833 (2008).

Make Way for Robot Scientists

IN THEIR 19 JUNE LETTER ("MACHINES FALL short of revolutionary science," p. 1515), P. W. Anderson and E. Abrahams, commenting on our work on the automation of science, state that we are "seriously mistaken about the nature of the scientific enterprise." Their argument seems to be based on two premises: (i) There are two types of science, normal and revolutionary, and normal science "does not contribute very much to the advancement of knowledge." This view dismisses as unimportant the vast bulk of science, and must surely be wrong. (ii) Whereas normal science may be automated, revolutionary science never will be, as there is no possible "mechanism." It is certainly true that revolutionary science cannot currently be automated, and in our Report

("The automation of science," 3 April, p. 85) we described the automatically generated science as "modest...but not trivial." Nevertheless, the inability of some critics to imagine a mechanism does not eliminate the possibility that one exists.

Indeed, the mechanism we propose is the one that has been successfully applied to chess: There is a continuum in player skill, and computers slowly improved with advances in computer hardware and software until they now play at world championship level. We argue that there is a similar continuum in the ability to do science, from what robot scientists can do today, through what most human scientists can achieve, up to the level of a Darwin or Newton.

LIFE IN SCIENCE

Creationists Made Me Do It

I was always a mediocre student, especially in high school. I never really knew what I wanted to do, and nothing seemed to excite me. This changed in my senior year, when a creationist visited my biology class.

On that fateful day, all the science students were herded into the school auditorium, where we listened to a long and richly illustrated lecture describing literal creationism. We were informed that in an effort to "balance" our education, we would soon hear an equally long lecture on evolution. This, like many things I heard that day, turned out to be false. The evolution lecture never materialized. Remarkably, I graduated from senior biology having learned only about creationism.

School had finally gotten my full attention. I wanted to know what we were missing, and why. For the first time in my life, I willingly (eagerly even) picked up my textbook and studiously read it. With growing interest, I realized that evolution made an awful lot of sense, and that I was being hoodwinked by my biology class.

It's hard to overestimate the appeal of rebelling against the system to a teenaged boy, and that day marked the beginning of my path to a career in evolutionary biology. We learned other things in science class that year, too—for example, that all actions have an opposite reaction. For at least one sulky teenager in the small town of Owen Sound, Ontario, it took a creationist to make him into an evolutionary biologist.

EDITOR'S NOTE

This is an occasional feature highlighting some of the day-to-day humorous realities that face our readers. Can you top this? Submit your best stories at www.submit2science.org.

Canadian Institute for Advanced Research, Botany Department, University of British Columbia, Vancouver, BC V6T 1Z4, Canada. E-mail: pkeeling@interchange.ubc.ca

PATRICK J. KEELING

The Physics Nobel Laureate Frank Wilczek has said that the best chess player in the world is "non-human" and that this may well be true for the best physicist in 100 years time (1). Finally, Anderson and Abrahams ignore the possibility of machines and humans working together to do revolutionary science that neither could do alone.

ROSS D. KING,^{1*} JEM ROWLAND,¹

STEPHEN G. OLIVER,² MICHAEL YOUNG,³ WAYNE

AUBREY,¹ EMMA BYRNE,¹ MARIA LIAKATA,¹

MAGDALENA MARKHAM,¹ PINAR PIR,²

LARISA N. SOLDATOVA,¹ ANDREW SPARKES,¹

KENNETH E. WHELAN,¹ AMANDA CLARE¹

¹Department of Computer Science, Aberystwyth University, SY23 3DB, UK. ²Cambridge Systems Biology Centre, Department of Biochemistry, University of Cambridge, Sanger Building, Cambridge CB2 1GA, UK. ³Institute of Biological, Environmental and Rural Sciences, Aberystwyth University, SY23 3DD, UK.

*To whom correspondence should be addressed. E-mail: rdk@aber.ac.uk

References

1. F. Wilczek, *Fantastic Realities: 49 Mind Journeys and a Trip to Stockholm* (World Scientific Publishing, Singapore, 2006), p. 304.



Looking to Bacteria for Clues

IN HIS NEWS FOCUS STORY "ON THE ORIGIN of sexual reproduction" (5 June, p. 1254), C. Zimmer highlights the importance of the phylogenetic perspective championed by John Logsdon, but by considering only eukaryotes he overlooks an important bacterial clue to the evolution-of-sex puzzle.

Until recently, bacteria were thought to be sexual; they have well-characterized processes that cause recombination of chromosomal alleles, and these parasexual processes were assumed to have evolved for recombination in the same way as meiotic sex in eukaryotes. However, a more critical analysis of the genes responsible for the parasexual processes suggests that they did not evolve for sex after all. Instead, the chromosomal recombination they cause appears to arise as unselected effects of related processes, the evolutionary functions of which are well established (1).

The fact that bacteria lack genes evolved for recombination indicates that meiotic sex

must have evolved in eukaryotes to solve a problem that bacteria don't have. Bacteria apparently get whatever recombination they need by accident—why do eukaryotes need so much more?

ROSEMARY J. REDFIELD

Department of Zoology, University of British Columbia, Vancouver, BC V6T 3Z4, Canada. E-mail: redfield@interchange.ubc.ca

Reference

1. R. J. Redfield, *Nat. Rev. Genet.* **2**, 634 (2001).

CORRECTIONS AND CLARIFICATIONS

Letters: "Organics: Evidence of health benefits is lacking" by K. Clancy *et al.* (7 August, p. 676). The title should have been "Organics: Evidence of nutritional superiority is weak."

Policy Forum: "The illusive gold standard in genetic ancestry testing" by S. S.-J. Lee *et al.* (3 July, p. 38). When data were extracted for indexing, the first author's name was incorrectly parsed; her surname is Lee.

News Focus: "The brain collector" by G. Miller (26 June, p. 1634). Henry Molaison died on 2 December, not 8 December, 2008. Also, the credit for the photo of Jacopo Annese should be "Kevin Donley."

Reports: "IL-21 is required to control chronic viral infection" by H. Elsaesser *et al.* (19 June, p. 1569; published online 7 May). The date of receipt was 22 October 2008, not the later date in the original *Science Express* publication. The date has been corrected both online and in print.

News Focus: "Obama moves to revitalize Chesapeake Bay restoration" by E. Stokstad (29 May, p. 1138). The credit for the image on page 1139 should be "Adapted from ECO-CHECK.ORG" (not ECO-CHECK.COM). The link has been corrected online.

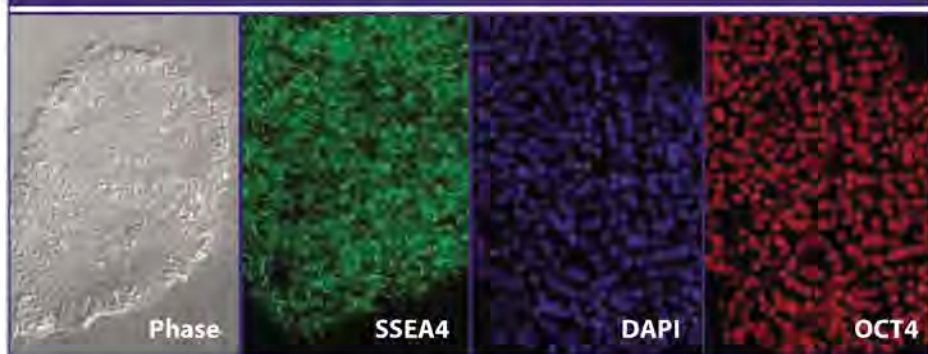
Reports: "Del-1, an endogenous leukocyte-endothelial adhesion inhibitor, limits inflammatory cell recruitment" by E. Y. Choi *et al.* (14 November 2008, p. 1101). The following sentence should be added to the acknowledgments in reference 26: H.F.L. was supported by the German Academy of Sciences (Leopoldina).

Letters to the Editor

Letters (~300 words) discuss material published in *Science* in the previous 3 months or issues of general interest. They can be submitted through the Web (www.submit2science.org) or by regular mail (1200 New York Ave., NW, Washington, DC 20005, USA). Letters are not acknowledged upon receipt, nor are authors generally consulted before publication. Whether published in full or in part, letters are subject to editing for clarity and space.

Advertisement

MEDIA SAVVY.



Human ESCs (H1) show expected morphology and immunofluorescence staining of pluripotency markers

Introducing StemediTM.

Smart research requires a smart approach to tissue culture. You need media that perform like you: intelligently. That's why we've introduced Stemedi, new from Stemgent. First in line is NutriStemTM XF/FF Culture Medium, the only xeno-free complete human ES cell culture medium for

a feeder-free culture system on the market. Use the info link below for the whole story. NutriStem is only the beginning.

MORE www.stemgent.com/ns2



REPROGRAMMING THE REAGENTTM

Developed and manufactured by



BOSTON | www.stemgent.com/sci4 | SAN DIEGO

©2009 by Stemgent, Inc. Stemgent, Reprogramming the Reagent and Stemedi are trademarks of Stemgent, Inc. NutriStem is a trademark of Biological Industries. All rights reserved. Co-developed in collaboration with the Technion R&D Foundation.

Call for Papers

Science Signaling

Science Signaling, from the publisher of *Science*, AAAS, features top-notch, peer-reviewed, original research weekly. Submit your manuscripts in the following areas of cellular regulation:

- Biochemistry
- Bioinformatics
- Cell Biology
- Development
- Immunology
- Microbiology
- Molecular Biology
- Neuroscience
- Pharmacology
- Physiology and Medicine
- Systems Biology

Science Signaling is indexed in CrossRef and MEDLINE

Subscribing to *Science Signaling* ensures that you and your lab have the latest cell signaling resources. For more information visit www.ScienceSignaling.org

Submit your research at:
www.sciencesignaling.org/about/help/research.dtl

Science Signaling



PALEONTOLOGY

Return to the High Table

Rachel Wood

Darwin was deeply concerned by the incomplete nature of the fossil record, as he feared its implications for his theory of natural selection. In the sixth edition of *On the Origin of Species* he famously wrote, "He who rejects this view of the imperfection of the geological record, will rightly reject the whole theory" (1). And from that time until some 40 years ago, paleontology was relegated beyond the fold of evolutionary theory, languishing as a descriptive science: an aid to the dating of geological strata and little else.

The 26 scholarly essays in *The Paleobiological Revolution* document and celebrate the rise of paleobiology—paleontology as a biological science—which established the study of the fossil record as a unique contributor to evolutionary biology. Fossils became considered as once-living organisms with real physiologies and ecologies, populating ancient environments and forming ecosystems that may have no close modern analogs. The new approach was pioneered by Tom Schopf, David Raup, James Valentine, and Stephen Jay Gould among others. Its foundation was the modern synthesis (the union of Mendelian genetics with natural selection to form a coherent theory of evolution) as promoted by George Gaylord Simpson, Ernst Mayr, and Theodosius Dobzhansky. In this volume we find the scientific bones of the paleobiology revolution carefully examined both by historians of science and as personal accounts from many of those who played a part in shaping the transformation. Together they tell the tale, heralded by John Maynard Smith (2), of the return of paleontologists to the "high table" of evolutionary biology.

Paleontology has struggled to secure its place within scientific disciplines because fossils are not amenable to testing hypotheses using the current paradigm of laboratory-based, translational research. Yet only the fossil record can give us insight from the perspective of deep time—that is, how evolutionary patterns are revealed on the grand scale. Paleobiological analysis tells us about the pace and pulse of evolution, the existence of mass extinctions (which could never have been predicted from the modern synthesis

alone), and oddities with profound implications, such as the fact that the first land animals often possessed more than five digits (3). The fossil record provides developmental biology and molecular genetics with a unique evolutionary perspective.

One of the pillars of this revolution was to quantify the fossil record using statistical techniques derived from population biology applied to painstakingly compiled large data sets. Paleobiologists introduced analyses of species diversity, the survivorship of taxa, and rates of evolution and extinction using stochastic modeling and multivariate analysis in order to test many of the questions that they were asking about the nature of evolutionary change.

The paleontological community also started to theorize new evolutionary patterns.

The Paleobiological Revolution

Essays on the Growth of Modern Paleontology

David Sepkoski and Michael Ruse, Eds.

University of Chicago Press, Chicago, 2009.
580 pp. \$65, £45.
ISBN 9780226748610.

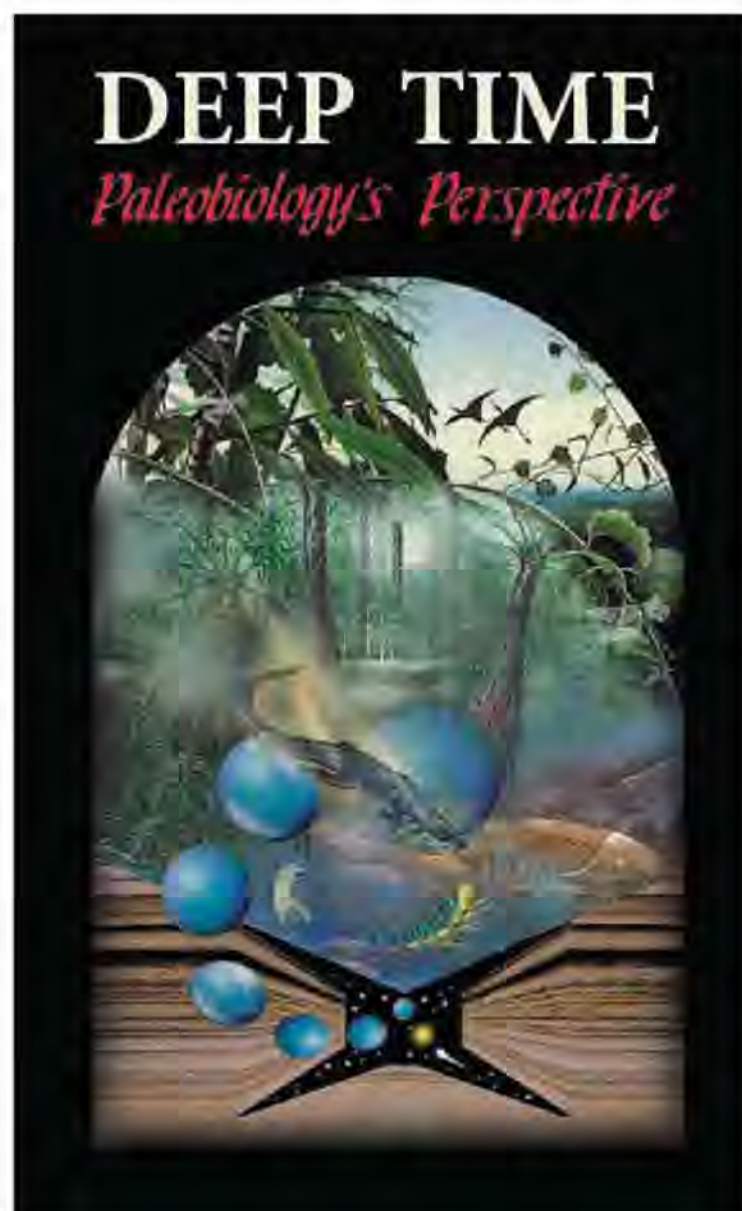
minimal change (stasis) punctuated by geologically rapid speciation events from which transition forms might not be expected to be readily preserved in the fossil record—the infamous theory of punctuated equilibria (4). This had profound ramifications for the modern synthesis.

In turn, work by Steve Stanley considered how species selection might take place within the context of punctuated equilibria. Rather than placing emphasis

on individual selection as the main force driving the history of life on Earth, he suggested that it was the balance between the rates of speciation (origination) and extinction that determines the direction of evolutionary trends. Subsequent years would see the study of genetics shift to the investigation of developmental processes and genome structures that could produce the macroevolutionary change predicted by patterns revealed in the fossil record.

The volume casts a rather unashamedly North American viewpoint on the paleobiological revolution. However, some contributions (including that by Manfred Laubichler and Karl Niklas) argue that crucial to the shift of paleontology from stamp-collecting to theory-generating was the rise of *Palaeobiologie* in 1920s and 1930s Germany. There, paleontologists also attempted to synthesize information gleaned from the fossil record to reveal the tempo of evolutionary change. Indeed, German theorists such as Willi Hennig contributed important methodologies that now form part of the established repertoire of modern paleobiologists.

The powerful integration of evolutionary studies with development, ecology, and paleobiology continues. Developmental biology and the study of phylogeny (the study of the relatedness of taxa) are being combined to understand how genetic modifications are expressed in the morphologies recorded by fossils. Likewise, evolutionary patterns through deep time, particularly radiations and extinctions, are now studied within a



Revolutionaries' journal. *Paleobiology*, founded to promote the integration of paleontology and biology, marked its 25th anniversary with this special volume (5).

The reviewer is at the School of GeoSciences, University of Edinburgh, King's Buildings, West Mains Road, Edinburgh EH9 3JW, UK. E-mail: Rachel.Wood@ed.ac.uk

framework of environmental change increasingly established by the use of geochemical proxies. The fossil and geological records together inform our knowledge of how life, Earth's surface, and the atmosphere have evolved. They also reveal how evolutionary innovations and environmental triggers are often difficult to disentangle as cause or effect. Paleobiology is thus morphing further into geobiology, and the Victorian discipline of geology is fast becoming Earth system science. In many ways then, *The Paleobiological Revolution* presents just a snapshot of a revolution still under way.

References

1. C. Darwin, *On the Origin of Species by Means of Natural Selection* (John Murray, London, ed. 6, 1872).
2. J. Maynard Smith, *Nature* **309**, 401 (1984).
3. M. I. Coates, J. A. Clack, *Nature* **347**, 66 (1990).
4. N. Eldridge, S. J. Gould, in *Models in Paleobiology*, T. J. M. Schopf, Ed. (Freeman, Cooper, San Francisco, 1972), pp. 82–115.
5. *Paleobiology* **26** (4, suppl.) (2000).

10.1126/science.1177946

CELL BIOLOGY

What Is It Like to Be a Cell?

Wallace F. Marshall

Nobody knows where consciousness comes from. In his provocative *Wetware*, cell biologist Dennis Bray presents the view that many features of conscious beings, including learning, knowledge, and awareness, are present within single cells.

Bray lays his foundation by describing the remarkable behaviors of single-celled organisms. He describes how the giant ciliate *Stentor* can not only run through a series of different strategies to avoid a noxious stimulus but also even learn over time which strategies work

and which don't. His other examples include motile bacteria determining the direction of chemical gradients and amoebae actively pursuing swimming prey. He goes on to describe more-complicated cooperative behaviors that groups of cells can perform when they com-

municate and act together. His vivid descriptions paint a clear picture of cells as intelligent agents, continuously sensing their environments, computing the appropriate response, and learning from past mistakes.

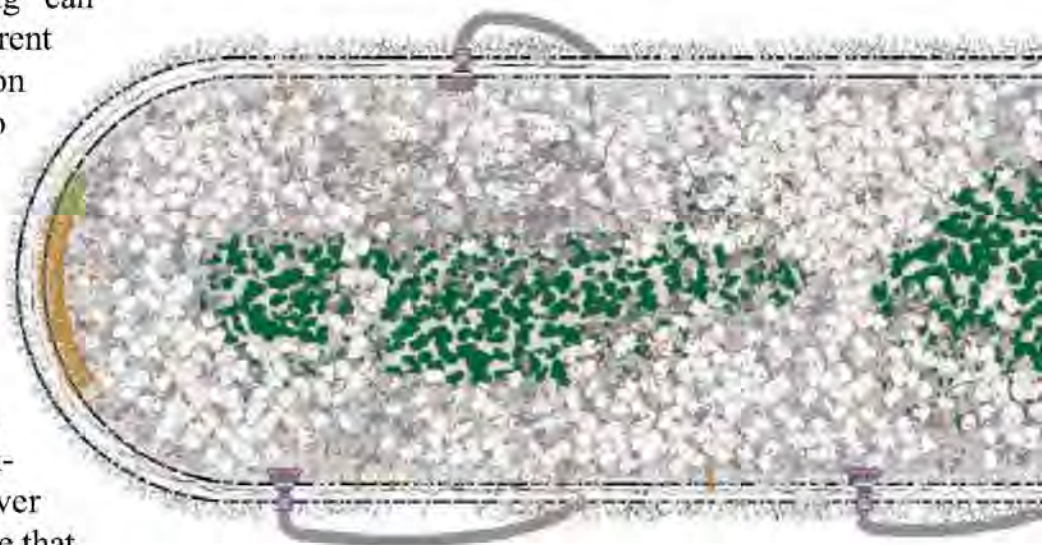
At some level, Bray's argument is that cells are aware because they look aware. Although strictly speaking this is a non sequitur, on the other hand there is strong tradition in psychology of describing all cognition in terms of behaviors. Bray's introduction fits within this behaviorist tradition. But he then moves beyond behaviorism by describing how the biochemical systems that underlie these behaviors resemble neural networks capable of computation and learning. His consideration of computational mechanisms within cells sets a clear agenda for future research into mechanisms of cellular cognition.

Discussions of cognition often degenerate into arguments about terminology. Terms like "knowledge" or "learning" can mean different things to different people. Bray has a clear vision of what these terms mean to him, and he spells them out quite clearly. Nonetheless, sometimes the reader may need to consider whether Bray's use of such terms really matches our intuitive usage. For example, he argues that biochemical pathways are able to "learn" over evolutionary time in the sense that networks that do not perform the correct computation fail to be inherited and that therefore, at the end of the day, the networks implicitly represent some form of "knowledge." Is that really what we mean by "learning"? Suppose we took a thousand horses, asked them what is one plus one, and then shot all those that didn't stomp their hooves twice. Nobody would say that the horses learned how to add. This clearly represents a confusion of levels, in that the unit of learning would be the ensemble of horses, not an individual horse.

What makes a neural network capable of learning isn't the fact that we can kill off all the incorrect networks from some larger ensemble. Rather it is the way the elements and connection weights of a particular existing network can change their function in response to information about the performance of the network. This responsiveness requires plasticity within the system. There is a case to be made that biochemical networks may have such plasticity. Bray touches on this, but in general he shies away from this type of mechanism in favor of a purely evo-

lution-based view of learning. Although the evolution of networks is no doubt very interesting, to say that a cell can learn because its biochemical networks can evolve over many generations seems to deviate from at least the standard usage of "learning."

One of the book's major strengths is Bray's overall unity of vision; another is the way he marshals a breathtaking diversity of fields to make his case. For example, he offers entire chapters on biomimetic robots and synthetic biology. This breadth guarantees that almost every reader, regardless of prior expertise, will learn something new. Generally written at a very accessible level, the book clearly is targeted at the educated lay audience. There is probably a need for a more-technical presentation of Bray's computational view, one that would delve into more details. Although Bray does not attempt that in *Wetware*, he does point out a number of fascinating technical issues



that could provide agendas for entire research labs. For example, he brings up the fact, often missed in discussions of synthetic biology, that mixing of diffusible molecules limits the computational capacity of a system with a fixed number of molecular components, whereas such limitations would be relaxed if the system were not well-mixed. A book written for researchers could provide whole chapters on anomalous diffusion, solid-state biochemical reactions, and so forth. Nevertheless, Bray has already done a great service in making these types of problems explicit.

And that is really the point of *Wetware*: to inspire us to reconsider our basic assumptions about what cells can do. However we choose to interpret words like "think" or "learn," it seems safe to say that most biologists would hold that a cell cannot think, in any sense of the word. After considering Bray's arguments, they will probably be less dismissive of the idea. Whether cells think or not, there is no question that *Wetware* will get the reader thinking.

10.1126/science.1176764

Wetware

A Computer in Every Living Cell

by Dennis Bray

Yale University Press,
New Haven, CT, 2009.
279 pp. \$28, £18.99.
ISBN 9780300141733.

The reviewer is at the Department of Biochemistry and Biophysics, University of California, San Francisco, Mission Bay, 600 16th Street, San Francisco, CA 94158, USA. E-mail: wallace.marshall@ucsf.edu

CREDIT: COURTESY DENNIS BRAY

ENVIRONMENT

Energy and Technology Policies for Managing Carbon Risk

Aristides A. N. Patrinos^{1*} and Richard A. Bradley²

Despite some uncertainties, today's scientific and political consensus is that the level of global emissions of greenhouse gases (GHGs) needs to lead to atmospheric concentrations somewhere between 450 and 500 parts per million (ppm) (1) to avoid serious, if not catastrophic, effects on life and property. Achieving this goal poses some formidable challenges. There is inertia in the climate system (GHGs survive for generations), as well as in GHG-emitting capital investment. Furthermore, every economic sector and country emits. To meet these challenges, a broad range of actions will be required.

Mitigation Policy

To maintain public support for aggressive, cooperative action in achieving such reductions, we must return to and maintain long-term economic growth. Difficult economic times focus public attention on the "here and now" at the expense of the welfare of future generations. For example, the International Energy Agency (IEA) has recently estimated that renewables investment will fall 38% in 2009 (2). Policy frameworks will need to foster economic growth and demonstrate effectiveness to maintain public support. Mitigation policy should therefore emphasize measures that generate near-term reductions but provide incentives for reductions that take longer to accomplish.

The Kyoto Protocol was the first attempt to rein in GHG emissions with a binding agreement. It called for emission reductions in the developed world during the period 2008–12 and has been only marginally successful, mostly because the United States refused to ratify it. Under President Obama, the United States is now reengaging in negotiations with the goal of agreeing on the successor agreement by December 2009 at the international climate meeting in Copenhagen.

One way to encourage reductions is through command-and-control approaches by governments, for example, carbon performance

standards for new power plants. Another approach is to levy a carbon tax, with the revenue devoted to promoting energy efficiency, renewable energy production, and Carbon Capture and Storage (CCS). However, most member governments of the Organization for Economic Cooperation and Development (OECD) have avoided both approaches, preferring a market mechanism.

Many OECD governments, including the European Union (EU), Australia, and New Zealand, have adopted emissions trading for reducing emissions. In contrast to command-and-control approaches, the government's role in cap-and-trade is minimal. Essentially, the government sets a cap on total emissions, and generally, that cap decreases with time. The government also establishes market trading rules and an allowance registry, supervises the distribution of emission allocations to the various emitters, and enforces compliance. The process of staying below the cap is controlled by the "carbon market," where allocations are bought and sold in a way that minimizes costs of compliance. This type of carbon market has been used by several countries that have signed on to the Kyoto Protocol in order to meet their required emission reductions.

The advantage of cap-and-trade is that the marketplace (rather than governments) decides the optimum way to achieve the reductions, which ensures greater innovation and economic efficiency. Reservations about applying cap-and-trade to carbon emissions stem primarily from the concern that compliance costs are highly uncertain and that additional costs for energy may be particularly burdensome in today's economic climate. The recent financial meltdown certainly adds



A bumpy, but hope-filled, road to the Copenhagen meeting.

Elements of a global carbon management strategy have been defined, paving the way to increased international actions to reduce global emissions starting this year.

to the reservations about cap-and-trade. Furthermore, the allocation of emission permits can be contentious, as is setting the appropriate cap.

Some international experience exists. Starting in 2005, the EU established the Emissions Trading Scheme (ETS) and allocated permits to individual countries through a negotiation process. Countries then allocated permits to utilities and major industries. This experiment was not without its problems: The price of emitting a ton of carbon dioxide rose to over 30 euros (€), greatly exceeding the predicted price of 10 €, and then crashed to nearly 0 € because of an oversupply of permits. The current price is about 14 €. On the basis of the ETS experience, the European heads of state struck a deal in December 2008, deciding on 20% emissions reductions

below 1990 levels by 2020.

Another weakness is that sectors that can prove they are facing serious competitive disadvantages (as is claimed by the steel, cement, and aluminum industries) can apply for exemptions to grant up to 100% free emission permits. Nevertheless, initial evidence indicates that the ETS did yield reductions, and the experience of the EU has been an invaluable lesson.

Other countries have either created or are in the process of creating cap-and-trade schemes. Norway is using emissions trading to meet its commitments for the initial Kyoto commitment period. The Norwegian scheme is linked to the EU ETS, allowing for trading between the two systems. Australia and New Zealand are establishing a system with broader GHG and sectoral coverage than the EU ETS.

In the United States, despite success with a cap-and-trade system for controlling sulfur emissions under the Reauthorized Clean

¹Synthetic Genomics Inc., Washington, DC 20024, USA.

²International Energy Agency, Paris, 75739, France.

*Author for correspondence. E-mail: apatrinos@syntheticgenomics.com

Air Act of 1990, carbon trading has only been developed at the state level, through the Regional Greenhouse Gas Initiative (RGGI) and the Western Climate Initiative (WCI). Efforts to pass national trading legislation culminated in the Waxman-Markey Bill that passed the House (H.R. 2454). It sets the goal of reducing emissions by over 80% by 2050. This is critical legislation if 450 to 500 ppm stabilization is to remain a possibility, as the United States is the second largest global emitter of carbon dioxide from energy sources. Other major emitters cannot be expected to adopt aggressive measures in the absence of U.S. action.

Improving Energy Use

A carbon price is essential, but it will not be sufficient to meet climate change goals. In particular, improving the efficient consumption of energy will require use of both voluntary and command-and-control measures to overcome market failures and barriers. The IEA has documented the potential size of some of these market failures as they applied to principal-agent problems (3). One example of these is popularly called the “landlord-tenant” problem. In such cases, energy prices do not unambiguously signal to consumers the changed scarcity of goods, including environmental protection. This could cover in excess of 30% of electricity consumption in the residential sector.

From a climate perspective, this is particularly important, as energy efficiency is the most cost-effective near-term strategy. Given the long time-lags required for many capital investments, energy efficiency improvements offer the possibility of increasing energy services and reducing fossil-fuel use while the existing capital structure is transformed into a low-carbon one. National governments and the international framework developed in Copenhagen will need to provide incentives that fully exploit energy efficiency.

The technology development program will have to be broad in scope and directed at providing cost-effective pathways to markets rather than directing the choice of “key” technologies. The technology program will also have to be much larger than currently being pursued by major economies. There has been only modest response in the size of energy research and development (R&D) funding following the warnings from climate change science. For example, since the 2001 publication of the Third Assessment Report of the Intergovernmental Panel on Climate Change, funding has grown about 8%, whereas in response to the oil shocks of the 1970s, R&D funding grew from 1975 to 1980 by over 60% (4).

The current view is that no successful stabilization of atmospheric CO₂ concentration is possible without extensive applications of CCS (1, 5, 6), given large coal reserves in the United States, China, and other countries. In addition, there will be a need for renewable (e.g., solar, wind, geothermal, and biomass) and low-carbon energy technologies (e.g., nuclear). Fuels derived from lignocellulosic biomass and from algae could be deployed for both transportation needs and the production of power (e.g., in combination with fossil fuels).

Deployment of new and improved energy technologies and of CCS will require rigorous planning, disciplined implementation, and creative incentives. Much can be learned from earlier attempts (e.g., in Europe and in the U.S. states) that used policy tools such as the Renewable Portfolio Standard (RPS) to successfully overcome barriers to the initial use of new renewable technologies.

The *America's Energy Future* (AEF) report (7), recently released by the U.S. National Academy of Sciences, offers a blueprint of how various energy technologies can be compared in terms of cost, supply potential, ability to penetrate the market place, and environmental impacts, including GHG emissions. The AEF paradigm can be applied across countries and regions, leading to optimum combinations of technologies.

Institutional Arrangements

There is no shortage of international organizations. What is in shortage is the institutional mandate and focus on delivery of climate-friendly technologies to the key emitting countries and sectors. Integrating such a broad mandate into a single international organization like the U.N. Framework Convention on Climate Change (UNFCCC) risks creating a cumbersome and inflexible system. Instead, Copenhagen will need to empower new and existing organizations with specific tasks from capacity-building to facilitating cooperative R&D and policy implementation activities.

Existing technology cooperative arrangements like the Carbon Capture Leadership Forum and the International Partnership for a Hydrogen Economy, in addition to IEA Implementing Agreements, will continue to play important roles, and the Asian Pacific Partnership will continue to supplement the UNFCCC. However, new forms of cooperation between nations and between the public and private sectors will be needed to address different technologies and regional and national concerns. As the Consultative Group on International Agricultural Research

played a key role in the green agricultural revolution, a new organization could play a role in adapting energy efficiency and renewable technologies to local circumstances in developing countries. Such regionally oriented approaches may well become part of the international institutional portfolio, as regional and local approaches within the IEA nations have played key roles in fostering renewable energy and energy efficiency. A particularly promising new approach for facilitating energy efficiency policy in the world's largest economies was launched in May 2009 at the G8 ministers' meeting in Rome (8). The International Partnership for Energy Efficiency Cooperation provides, for the first time, a policy-maker consultative forum on energy efficiency where energy efficiency policy experiences can be exchanged among those who can subsequently initiate implementation of the best policy practices.

The road ahead for climate change mitigation is indeed bumpy, and negotiations for the successor to the Kyoto Protocol will be long and difficult. Nevertheless, there is a strong sense that we will emerge with a global agreement to reduce nonrenewable carbon emissions. Such an agreement will certainly empower near-term emission reductions through both market-based and regulatory instruments. It will spur innovation and provide a policy framework that expands the geographic and sectoral application of a carbon market. The agreement will also enhance international cooperation on selected command-and-control instruments to redress market imperfections and to empower existing and new institutions to facilitate international adoption of low-carbon technologies.

References and Notes

1. B. S. Fisher et al., in *Climate Change 2007: Mitigation of Climate Change, Contribution of Working Group III to the Fourth Assessment Report of the Intergovernmental Panel on Climate Change*, 2007, B. Metz et al., Eds. (Cambridge Univ. Press, Cambridge, 2007), pp. 170–250.
2. IEA, *The Impact of the Financial and Economic Crisis on Global Energy Investment: IEA Background paper for the G8 Energy Ministers' Meeting*, Rome, 24 to 25 May 2009 (IEA, Paris, 2009).
3. IEA, *Mind the Gap: Quantifying Principal-Agent Problems in Energy Efficiency* (IEA, Paris, 2007).
4. IEA Energy Technology R&D Statistics Service, funding database (IEA, Paris, 2008); www.iea.org/Textbase/stats/rd.asp.
5. IEA, *Energy Technology Perspectives 2008: Scenarios & Strategies to 2050* (IEA, Paris, 2008).
6. IEA, *World Energy Outlook 2008* (IEA, Paris, 2008).
7. National Academy of Sciences, National Academy of Engineering, National Research Council, *America's Energy Future: Technology and Transformation* (National Academies Press, Washington, DC, 2009).
8. U.S. Department of Energy, press release, 24 May 2009, www.energy.gov/news2009/7420.htm.

10.1126/science.1177603

ASTRONOMY

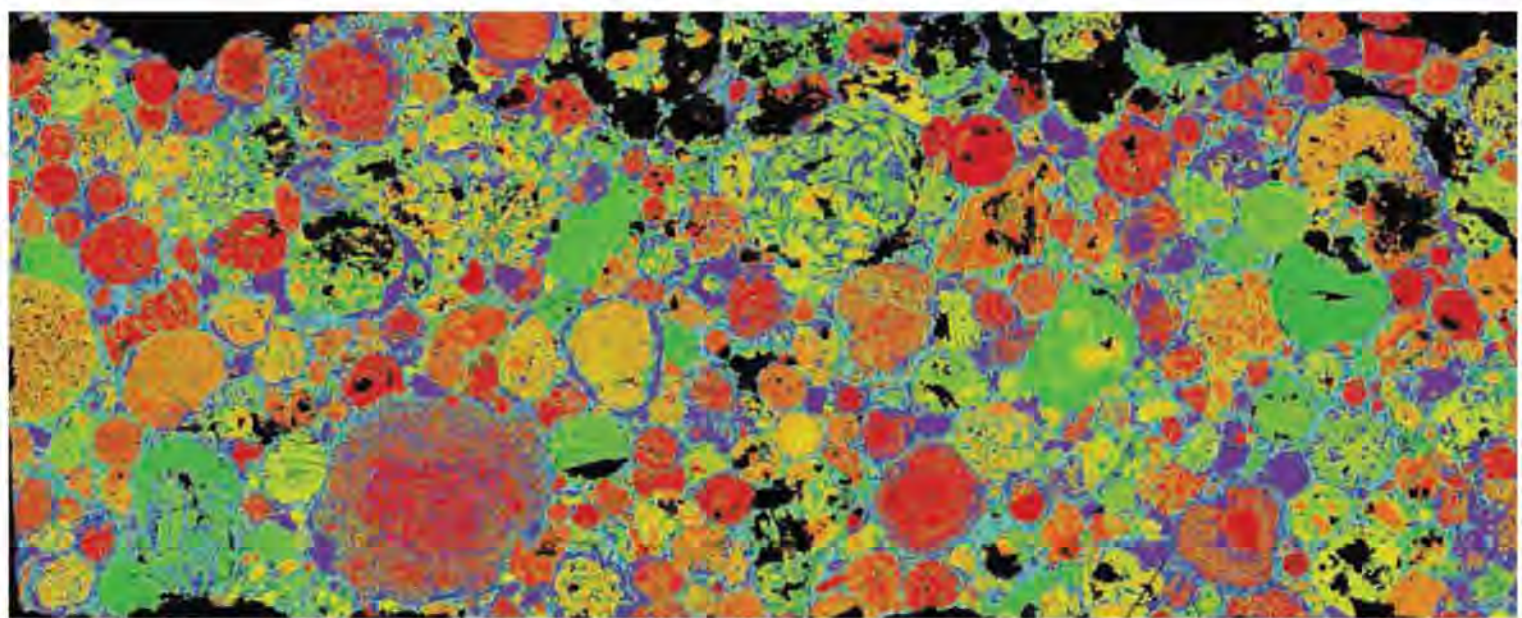
Early Solar System Chronology

Andrew M. Davis

The short-lived radioisotope ^{26}Al (1) has long been used as a relative chronometer of events in the early solar system. However, although much is known about its initial abundance in the early solar system, there remain doubts on applicability of ^{26}Al chronometry, because it is not known whether it was uniformly distributed. On page 985 of this issue, Villeneuve *et al.* (2) report the development of new techniques that allow magnesium isotopic measurements to be made with unprecedented precision. They confirm that $^{26}\text{Al}/^{27}\text{Al}$ was indeed uniform in the early solar system to about the 10% level and find that chondrules formed in discrete events over a time period of more than 1 million years. These data are a major step forward in developing a precise and accurate chronometer, but also raise new questions about early solar system processes.

For ^{26}Al to be useful as a chronometer, the ratio of ^{26}Al to stable ^{27}Al must have been uniform in the solar system before the first solids formed. Because ^{26}Al decays to ^{26}Mg with a half-life of 0.73 million years, all of the early solar system ^{26}Al has decayed by now. The first issue to address is the fact that the source of ^{26}Al is not known. It may have come from a nearby supernova at the time of solar system formation, but it may also have been made in the solar system by particle irradiation from the young Sun (3). If ^{26}Al was injected into the solar system from an external source, it may not have been well mixed within the solar system. If ^{26}Al was made within the solar system, production could have continued for a long period of time, continually injecting fresh ^{26}Al .

Among the most interesting and puzzling discoveries related to the evolution of the solar system is that chondrules, which are the major constituent of the most common type of meteorite, chondrites, are about 2 million years younger than the oldest objects in the



Chemical makeup. Map of the count rate ratio of $\text{Mg}/(\text{Mg}+\text{Fe})$ in a section of the Semarkona LL3.0 chondrite, constructed from magnesium and iron K_α x-ray maps provided by Denton S. Ebel of the American Museum of Natural History. The field of view is 19.2 by 7.8 mm. Type I chondrules are magnesium-rich and almost free of iron, and appear red. Type II chondrules are composed of magnesium and iron silicates and appear in green to orange colors. Fine-grained iron-rich matrix between chondrules is light blue in color, and metal and iron sulfides appear purple. Black denotes cracks and voids.

solar system—refractory calcium- and aluminum-rich inclusions (CAIs), which are also found in chondrites. It remains unclear whether this age difference between the formation of chondrules and CAIs, which is seen in both the ^{26}Al - ^{26}Mg system and by Pb-Pb dating, the only long-lived chronometer with sufficient precision for early solar system events (4), is actually real.

Villeneuve *et al.* have now used secondary ion mass spectrometry to measure magnesium isotopic compositions and Mg/Al ratios in the major phases (olivine, low-calcium pyroxene, and glass) in chondrules from the Semarkona LL3.0 chondrite. They then calculated the $^{26}\text{Al}/^{27}\text{Al}$ ratio at the time of crystallization of each chondrule from the slopes on isochron diagrams. Such measurements have been reported before, but the key feature in their study is the very precise determination of the magnesium isotopic composition that each chondrule had at the time of crystallization. By using high beam currents and paying meticulous attention to detector backgrounds, Villeneuve *et al.* have achieved precisions of 5 parts per million on measurements of the $^{26}\text{Mg}/^{24}\text{Mg}$ ratio in magnesium-rich minerals after correction for instrumental and natural mass-dependent fractionation.

Chondrules in primitive chondrites are of two major types, FeO-poor (type I) and FeO-

rich (type II) (5). To use the ^{26}Al - ^{26}Mg system as a chronometer, each chondrule must have been sufficiently heated during its formation to completely homogenize its magnesium isotopic composition. Libourel *et al.* have shown that glass is not in equilibrium with the minerals present in type I chondrules (6); therefore, Villeneuve *et al.* restricted themselves to type II chondrules. Plotting the initial magnesium isotopic composition at the time of each object's formation against the $^{26}\text{Al}/^{27}\text{Al}$ ratio, they show that Earth, the Semarkona chondrules, and the CAIs are on a single evolution line. The slope of this line is determined by the solar system Al/Mg ratio, an independently determined parameter, and favors the argument that $^{26}\text{Al}/^{27}\text{Al}$ was well mixed in the early solar system. This conclusion is consistent with recent evidence that ^{60}Fe , another short-lived isotope that was present early in solar system history, was also uniformly mixed to at least the 10% level (7).

That $^{26}\text{Al}/^{27}\text{Al}$ was uniform in the early solar system and usable as a chronometer will be reassuring to most in the field. Villeneuve *et al.* also found that the ^{26}Al - ^{26}Mg ages of chondrules cluster, both in their data and earlier work, consistent with chondrules in ordinary chondrites forming in five discrete events spanning more than 1 million years. Ages of chondrules in carbonaceous chondrites also cluster, but occur at different times from those in ordinary chondrites. This clustering raises some important questions.

Chondrites are the most common type of meteorite but come in a number of types (ordinary chondrites, carbonaceous chon-

Department of the Geophysical Sciences, Enrico Fermi Institute and Chicago Center for Cosmochemistry, University of Chicago, Chicago, IL 60637, USA. E-mail: a-davis@uchicago.edu

drites, enstatite chondrites, and R chondrites). There are basically four different populations of chondrules, each associated with a particular type of chondrite (5). If the solar system was well mixed, as the ^{26}Al (2) and ^{60}Fe (7) evidence indicates, how is it that different types of chondrules ended up in different parent bodies when chondrule formation occurred over more than a million years? Data for both ordinary and carbonaceous chondrites indicate clustering in ^{26}Al - ^{26}Mg ages, but in separate sets of events (2). It will

be interesting to extend this record to enstatite and R chondrites. The high-precision techniques introduced by Villeneuve *et al.* should be extended to low Al/Mg phases in CAIs to further establish the solar system magnesium isotopic evolution curve.

References and Notes

1. T. Lee, D. A. Papanastassiou, G. J. Wasserburg, *Geophys. Res. Lett.* **3**, 109 (1976).
2. J. Villeneuve, M. Chaussidon, G. Libourel, *Science* **325**, 985 (2009).
3. F. H. Shu, H. Shang, T. Lee, *Science* **271**, 1545 (1996).

4. Y. Amelin, A. N. Krot, I. D. Hutcheon, A. A. Ulyanov, *Science* **297**, 1678 (2002).
5. E. R. D. Scott, A. N. Krot, in *Meteorites, Planets, and Comets*, A. M. Davis, Ed., Vol. 1, *Treatise on Geochemistry*, 2nd ed. (H. D. Holland, K. K. Turekian, Eds. (Elsevier, Oxford, 2007), pp. 1–72.
6. G. Libourel, A. N. Krot, L. Tissandier, *Earth Planet. Sci. Lett.* **251**, 232 (2006).
7. N. Dauphas *et al.*, *Astrophys. J.* **686**, 560 (2008).
8. This work was supported by the National Aeronautics and Space Administration through grant NNX09AG39G. I am grateful to D. Ebel for providing high-quality elemental maps of the Semarkona meteorite from which the figure was constructed.

10.1126/science.1176730

ANTHROPOLOGY

Coastal Exploitation

Torben C. Rick¹ and Jon M. Erlandson²

The development and spread of agriculture and pastoralism during the past 10,000 years is often seen as the tipping point when humans fundamentally changed our relationship with the natural world. Ancient hunter-gatherers also altered their environments, although the extent to which they did so remains hotly debated (1–3). Hunter-gatherers may have caused major alterations of terrestrial ecosystems, including the use of fire to enhance resource productivity and the translocation of various animals to new regions (3, 4). They are implicated in massive megafaunal extinctions in the Americas and Australia (2, 3). Recent archaeological research from coastal areas shows that they also substantially altered and enhanced marine ecosystems in other ways, some of which obscure the definition of the term “hunter-gatherer.”

Shellfish, fish, and other coastal resources have been harvested by hunter-gatherers for more than 150,000 years, with the earliest evidence found in South Africa (5). Some early hunter-gatherers influenced the size and structure of near-shore shellfish populations by ~23,000 years ago—the earliest evidence for human impacts on marine populations to date (6, 7). Shellfish size reductions intensified during the past 10,000 years as human populations grew and moved into new areas, but the declines documented by 23,000 years ago demonstrate human influence on the structure of near-shore organisms and ecosystems at a very early date—often millennia



Ancient fisheries. In this painting by Henry Wood Elliott from 1872, traditional Aleuts fish in kelp forests of the Aleutian Islands. For centuries or millennia, hunter-gatherers around the world used comparable technologies and techniques to exploit near-shore fisheries.

before the earliest historical accounts.

Ancient exploitation of keystone species by hunter-gatherers also affected the structure and function of near-shore coastal ecosystems. Native American predation of sea otters in California after ~9000 years ago and in the Aleutians ~3000 years ago allowed abalone and sea urchin populations to expand greatly, changing the entire structure of the kelp forest ecosystem. Such “trophic cascades” may have resulted in localized urchin barrens (areas where sea urchin populations are so large that entire kelp forests are depleted) (8, 9). Compared with those seen in contempo-

rary or historical kelp forests, these ancient urchin barrens may have been short-lived or localized, however, with human harvest of urchins replacing the predatory controls once provided by sea otters.

Cod, a keystone species that is depleted in the North Atlantic today, may have been locally overfished by hunter-gatherers in the Gulf of Maine beginning some 3500 years ago, with archaeological data indicating the greatest reduction in larger, older individuals (10). This may have reduced predation pressures on lower trophic level animals, especially medium-sized predators such as floun-

¹Archaeobiology Program, Department of Anthropology, National Museum of Natural History, Smithsonian Institution, Washington, DC 20013, USA. ²Department of Anthropology and Museum of Natural and Cultural History, University of Oregon, Eugene, OR 97403, USA. E-mail: rickt@si.edu; jerland@uoregon.edu

ders, sculpins, and dogfish, a pattern that mirrors changes seen after the recent collapse of cod in the North Atlantic (10). Reductions in top-level predators and increases in medium-sized predators were noted in Gulf of Maine archaeological sites, but unlike the urchin expansions following commercial fisheries, no increase in urchins was identified in the archaeological data, suggesting that these effects were more localized than those of historical commercial fisheries.

Human hunting and fishing in ancient coastal ecosystems thus caused declines in key species, triggered trophic cascades, or reduced the size of prey. However, hunter-gatherers also appear to have improved the productivity of certain resources in some marine ecosystems. For instance, the depletion of sea otters in California waters may have greatly increased the productivity of nearshore shellfish (9). On North America's Northwest Coast, clam gardens—human-made rock walls and terraces—have been reported from the San Juan Islands to Alaska (11). Hunter-gatherers constructed these clam gardens in the low intertidal, expanding and maintaining the area for clams to live and be harvested. The antiquity of clam gardens is poorly documented, but their widespread occurrence suggests that they may span centuries or possibly millennia and likely greatly increased clam yields. This example of mariculture transcends traditional definitions of hunter-gatherers and provides evidence of intentional environmental man-

agement similar to anthropogenic burning in terrestrial landscapes.

Through daily consumption of shellfish and other resources in productive estuaries and marshes, hunter-gatherers also altered coastal ecosystems by depositing vast quantities of shells and other refuse, creating “shell islands” that were often the highest and best drained landforms in the region. Chantuto hunter-gatherers in Mexico created shell mounds 3 to 11 m high that formed islands in the wetlands and were used to process and collect shellfish (12). Similar anthropogenic shell islands have been found along the Gulf of Mexico, the San Francisco Bay, and elsewhere. Constructed above rising postglacial seas, they often form microhabitats of plant and animal communities distinct from much of the surrounding landscape.

These cases of predation pressure, trophic cascades, and landscape modification and management show that hunter-gatherers were important components of coastal ecosystems for millennia. Hunter-gatherer environmental interactions in coastal areas and beyond represent a complex and dynamic continuum—from degradation to active management and enhancement—that blurs the division between the natural and anthropogenic worlds deep into human prehistory.

By the end of the 20th century, humans had “domesticated nature,” leaving few if any truly wild places on Earth (13). However, emerging evidence suggests that hunter-gath-

ers altered many coastal and island ecosystems long before historical accounts of early European explorers provide evidence for phenomenal abundance compared with modern marine ecosystems (14). This increasing antiquity of human alteration of marine and terrestrial environments provides important baselines or benchmarks for the long-term management, restoration, and sustainability of Earth's ecosystems.

References

1. R. Hames, *Annu. Rev. Anthropol.* **36**, 177 (2007).
2. P. S. Martin, *Twilight of the Mammoths: Ice Age Extinctions and the Rewilding of America* (University of California Press, Berkeley, 2005).
3. D. K. Grayson, *J. World Prehist.* **15**, 1 (2001).
4. R. L. Lyman, *Evol. Anthropol.* **15**, 11 (2006).
5. C. W. Marean *et al.*, *Nature* **449**, 905 (2007).
6. M. C. Stiner, *Proc. Natl. Acad. Sci. U.S.A.* **98**, 6993 (2001).
7. T. E. Steele, R. G. Klein, *Archaeofauna* **17**, 63 (2008).
8. D. G. Corbett *et al.*, in *Human Impacts on Ancient Marine Ecosystems: A Global Perspective*, T. Rick, J. Erlandson, Eds. (Univ. of California Press, Berkeley, 2008), pp. 43–75.
9. J. M. Erlandson *et al.*, in *Proceedings of the Sixth California Islands Symposium*, D. Garcelon, C. Schwemm, Eds. (Institute for Wildlife Studies, Arcata, 2005), pp. 9–21.
10. B. J. Bourque, B. J. Johnson, R. S. Steneck, in *Human Impacts on Ancient Marine Ecosystems: A Global Perspective*, T. Rick, J. Erlandson, Eds. (Univ. of California Press, Berkeley, 2008), pp. 165–185.
11. J. Williams, *Clam Gardens: Aboriginal Mariculture on Canada's West Coast* (New Star Books, Vancouver, 2006).
12. B. Voorhies, *Coastal Collectors in the Holocene: The Chantuto People of Southwest Mexico* (University Press of Florida, Gainesville, 2004).
13. P. Kareiva, S. Watts, T. Boucher, *Science* **316**, 1866 (2007).
14. J. B. C. Jackson *et al.*, *Science* **293**, 629 (2001).

10.1126/science.1178539

IMMUNOLOGY

The Yin and Yang of Follicular Helper T Cells

Amit Awasthi and Vijay K. Kuchroo

The human immune system can harness an arsenal of lymphocytes called CD4⁺ T cells, in an adaptive response to infection by a variety of pathogens, including parasites, bacteria, and fungi. Once activated, CD4⁺ T cells can differentiate into subsets of helper T cells [T_H1, T_H2, T_H17, regulatory T (T_{reg}), and follicular T (T_{FH})], whose effector functions include secreting the cytokines necessary for clearing pathogens and inducing inflammatory responses. Each helper T cell subtype

is also critical for helping B lymphocytes produce pathogen-specific antibodies (1). Until now, master transcription factors have been identified that regulate the generation of helper T cell lineages except for T_{FH} cells. On pages 1006 and 1001 of this issue, Johnston *et al.* (2) and Nurieva *et al.* (3), and a study by Yu *et al.* (4), report that the transcription factor Bcl6 is a master transcription factor that controls the generation of T_{FH} cells. However, Bcl6 must work against another transcription factor, Blimp-1, to promote this differentiation process.

Although distinct from other helper T cells, similarities between T_{FH} and other helper T cell lineages have been suggested (5, 6). For

The balanced expression of two transcription factors controls the development of a subset of T cells that support B cell maturation.

instance, like T_H17 cells, T_{FH} cells produce high amounts of the cytokine interleukin-21 (IL-21). This cytokine drives a feed-forward amplification loop for T_H17 generation (7, 8). Mice lacking IL-21 or the IL-21 receptor not only fail to produce T_H17 cells (7, 8), but are also defective in T_{FH} cell development and antibody isotype switching, and lack germinal centers, the regions in lymph nodes where final B cell maturation takes place (9, 10).

Despite similarities with other helper T cells, T_{FH} cells appear to be a distinct lineage of T cell. Each helper T cell subset expresses a lineage-specific master transcription factor: T_H1 cells express T-bet, T_H2 cells express

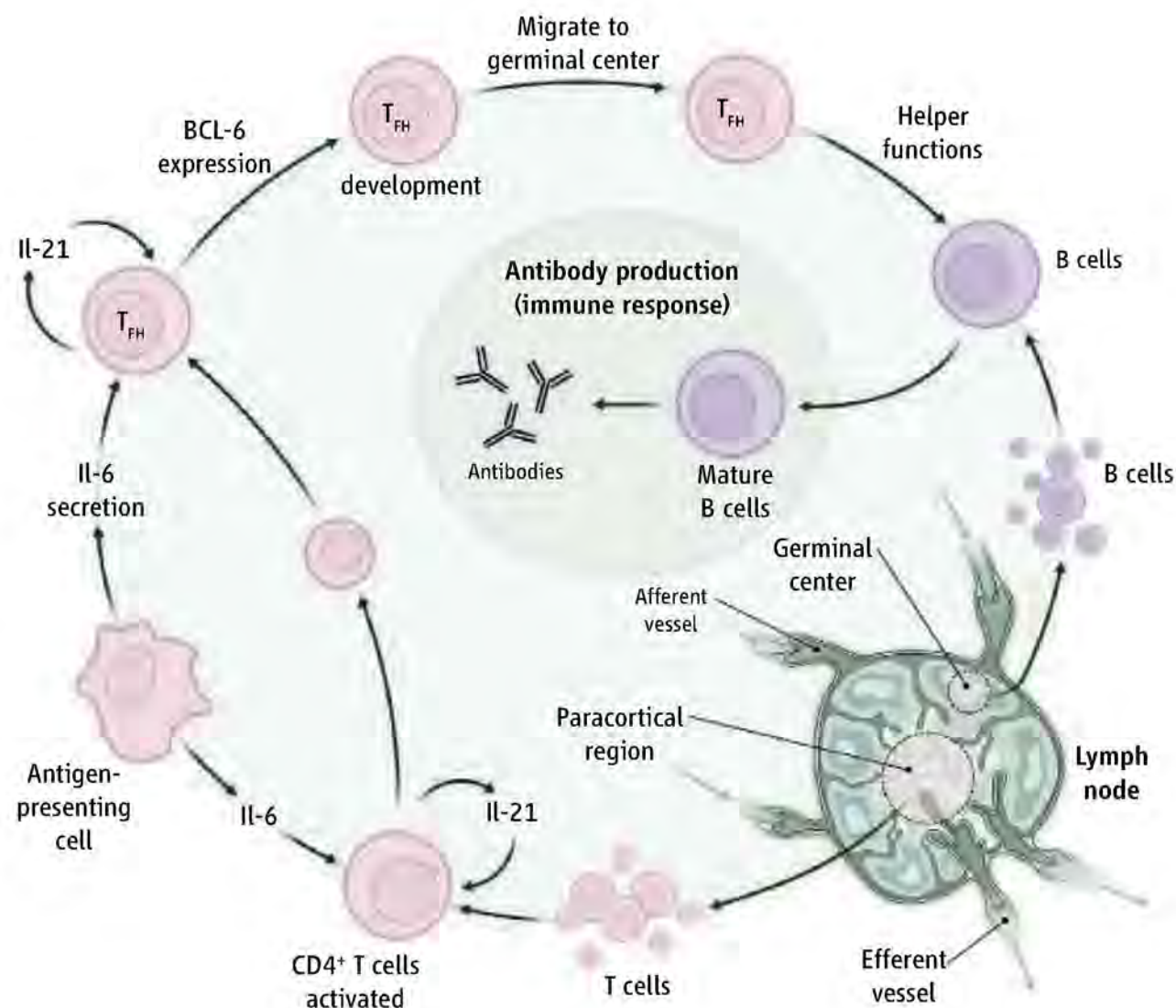
Center for Neurologic Diseases, Brigham and Women's Hospital, Harvard Medical School, Boston, MA 02115, USA.
E-mail: vkuchroo@rics.bwh.harvard.edu

GATA-3, T_H17 cells express ROR γ t, and T_{reg} cells express Foxp3. However, none of these transcription factors are highly expressed in T_{FH} cells. Indeed, microarray analysis revealed a molecular signature for T_{FH} cells that includes expression of the transcription factor Bcl6 in both mice and humans (11). By contrast, other helper T cell subsets do not express high amounts of this transcription factor. Bcl6 is also expressed in maturing B cells found in the germinal centers. Bcl6-deficient mice lack germinal centers and consequently, fail to produce mature B cells and memory B cells (which produce antibodies when they re-encounter specific antigens in subsequent infections). However, a specific function of Bcl6 in the generation of T_{FH} cells has not been clear.

Johnston *et al.* and Nurieva *et al.* show that Bcl6 expression in mouse T_{FH} cells is greater than that in activated $CD4^+$ T cells. Both studies demonstrate that overexpression of Bcl6 in $CD4^+$ T cells induces the generation of T_{FH} cells. Using different experimental approaches, Johnston *et al.* show that overexpression of Bcl6 in $CD4^+$ T cells that were engineered to respond to lymphocytic choriomeningitis virus (LCMV) promoted T_{FH} differentiation in mice upon infection with the virus. Nurieva *et al.* show that both IL-6 and IL-21 induced Bcl6 expression in $CD4^+$ T cells, as well as their differentiation into T_{FH} cells in mice. Overexpression of Bcl6 in $CD4^+$ T cells also induced the expression of the IL-6 receptor, IL-21 receptor, and CXCR5 (a receptor for the chemokine CXCL13), hallmarks of T_{FH} cells. The expression of these receptors makes T_{FH} cells responsive to their respective ligands and helps them localize to germinal centers. This presumably facilitates T_{FH} cell support of B cell maturation, in which B cells rapidly divide and undergo antibody isotype switching (3).

Interestingly, like T_{FH} cells, generation of T_H17 cells is also induced by the cytokines IL-6 and IL-21 (12). However, in the case of T_H17 cells, transforming growth factor- β must also be present, whereas for T_{FH} cells, Nurieva *et al.* found that this growth factor inhibited Bcl6 expression and thus blocked T_{FH} cell development (12, 3). Similar to T_H17 cells, the ability of IL-6 to promote T_{FH} cell differentiation depends on the action of IL-21 on these cells as well—mice lacking IL-21 or the IL-21 receptor have a defect in the induction of Bcl6 expression in response to IL-6 and therefore do not generate T_{FH} cells. Both Johnston *et al.* and Nurieva *et al.* show that $CD4^+$ T cells that lack Bcl6 cannot differentiate into T_{FH} cells, and exhibit decreased expression of the IL-6 and T receptor, the IL-21 receptor, and CXCR5.

Bcl6 is apparently not required for the



Differentiation pathway. Human and mouse follicular helper T cells (T_{FH}) arise from activated $CD4^+$ T cells that express the transcription factor Bcl6. T_{FH} cells then support B cell development and antibody production in response to pathogen infections.

development in other T_H cell lineages, including T_H1 , T_H2 , and T_H17 cells (3, 4). In fact, Bcl6 overexpression in developing cells of these lineages blocked a key effector function—producing cytokines. Yu *et al.* further show that Bcl6 expression in differentiated T_H1 and T_H17 cells prevented the master transcription factors of these cell types from binding to target DNA encoding cytokines; thus, IL-17 and interferon- γ were not produced (4). In addition to binding to and blocking these master transcription factors, Bcl6 repressed the expression of miR-17-92, a microRNA that represses the expression of CXCR5, which is essential for the generation of T_{FH} cells.

But for Bcl6 to have these effects, it must shut off the function of another transcription factor. Johnston *et al.* identified the transcription factor Blimp-1 as an antagonist of Bcl6. Blimp-1 expression decreases in T_{FH} cells, raising the possibility that Bcl6 underlies this reduction, thereby enhancing the generation of T_{FH} cells. Indeed, overexpression of Blimp-1 in $CD4^+$ T cells blocked the expression of Bcl6 and generation of T_{FH} cells (2). Moreover, deletion of Blimp-1 in LCMV-specific $CD4^+$ T cells substantially enhanced their differentiation into T_{FH} cells in mice upon viral infection, further supporting a reciprocal role of Bcl6 and Blimp-1 in T_{FH} cell production (2).

As for B cells, both Nurieva *et al.* and Johnston *et al.* show that mice lacking Bcl6 have defective germinal centers and, as a result, have reduced antibody production. Similarly, overexpression of Bcl6 in $CD4^+$ T cells increased the frequency of maturing B cells found in germinal centers with an increased concentration of circulating antibodies in mice.

Because T_{FH} cells localize in the B cell-rich zones of the lymph node (primary and secondary follicles) (see the figure), it is possible that interaction between T cells and B cells is essential for generating T_{FH} cells. Johnston *et al.* elegantly demonstrate this by showing that the complete absence of B cells in mice results in failed differentiation of T_{FH} cells. However, overexpression of Bcl6 in LCMV-specific $CD4^+$ T cells bypasses the requirement of LCMV-specific B cells for generating T_{FH} cells (2). These observations suggest that a cooperative T cell–B cell interaction is essential for inducing Bcl6 expression in T cells, and (once induced) Bcl6 is sufficient to promote T_{FH} cell generation.

These three studies answer the long-standing question of the transcriptional requirements for generating T_{FH} cells. Bcl6 is the master transcription factor for this differentiation process, but even more important, the balance between Bcl6 and Blimp-1 expression is

a critical determinant of T_{FH} cell generation. It will be interesting to see how different environmental cues affect the balance between these two transcriptional antagonists.

Uncontrolled generation of T_{FH} cells could be fatal, causing systemic autoimmunity by increasing antibody production. Therefore, expression of Blimp-1 may help maintain tolerance by inhibiting Bcl6 expression and the differentiation of T_{FH} cells. But if Bcl6 suppresses the generation of T_{H1} and T_{H17} cells by binding to their master transcription factors, then how are B cells stimulated to produce antibodies in response to interferon- γ and IL-17, the cytokines that these T cell subtypes secrete? One possibility is that B cells are induced to make these antibodies by T_{H1} and T_{H17} cells, instead of T_{FH} cells, outside of germinal centers (13). Alternatively, differentiating T_{H1} , T_{H2} , and T_{H17} cells may express low amounts of Bcl6, which might allow them to acquire the T_{FH} cell phenotype and induce B

cells to make these antibodies. Johnston *et al.* show that a T cell–B cell interaction is essential for Bcl6 expression in activated $CD4^+$ T cells, which in turn could initiate differentiation into T_{FH} cells. It might be possible that activated T_{H1} , T_{H2} , and T_{H17} cells express Bcl6 upon interaction with B cells, causing them to become T_{FH1} , T_{FH2} , and T_{FH17} cells. They could then affect antibody production by B cells through the cytokines they produce.

The transcription factor cMaf also plays an essential role in generating T_{FH} cells (14). cMaf primarily activates IL-21 expression in $CD4^+$ T cells, and thus provides an autocrine growth factor for T_{FH} cell development (15). Bcl6 and cMaf may synergize to generate T_{FH} cells by regulating the expression of critical factors such as IL-21, the IL-21 receptor, and CXCR5. The balance among the transcription factors in the differentiation of T_{FH} cells, particularly between Bcl6 and Blimp-1, could be exploited in various

autoimmune and infectious diseases.

References and Notes

1. L. J. McHeyzer-Williams, M. G. McHeyzer-Williams, *Annu. Rev. Immunol.* **23**, 487 (2005).
2. R. J. Johnston *et al.*, *Science* **325**, 1006 (2009); published online 16 July 2009 (10.1126/science.1175870).
3. R. I. Nurieva *et al.*, *Science* **325**, 1001 (2009); published online 23 July 2009 (10.1126/science.1176676).
4. D. Yu *et al.*, *Immunity* 10.1016/j.immuni.2009.07.002 (2009).
5. N. Fazilleau *et al.*, *Immunity* **30**, 324 (2009).
6. A. G. Zaretsky *et al.*, *J. Exp. Med.* **206**, 991 (2009).
7. T. Korn *et al.*, *Nature* **448**, 484 (2007).
8. R. Nurieva *et al.*, *Nature* **448**, 480 (2007).
9. R. I. Nurieva *et al.*, *Immunity* **29**, 138 (2008).
10. A. Vogelzang *et al.*, *Immunity* **29**, 127 (2008).
11. T. Chtanova *et al.*, *J. Immunol.* **173**, 68 (2004).
12. T. Korn, E. Bettelli, M. Oukka, V. K. Kuchroo, *Annu. Rev. Immunol.* **27**, 485 (2009).
13. J. M. Odegard *et al.*, *J. Exp. Med.* **205**, 2873 (2008).
14. A. T. Bauquet *et al.*, *Nat. Immunol.* **10**, 167 (2009).
15. C. Pot *et al.*, *J. Immunol.* **183**, 797 (2009).
16. We thank J. Hulin and A. C. Anderson for their critical reading of this manuscript.

10.1126/science.1178752

CLIMATE CHANGE

Risks of Climate Engineering

Gabriele C. Hegerl¹ and Susan Solomon²

As the risks of climate change and the difficulty of effectively reducing greenhouse gas emissions become increasingly obvious, potential geoengineering solutions are widely discussed. For example, in a recent report, Blackstock *et al.* explore the feasibility, potential impact, and dangers of shortwave climate engineering, which aims to reduce the incoming solar radiation and thereby reduce climate warming (1). Proposed geoengineering solutions tend to be controversial among climate scientists and attract considerable media attention (2, 3). However, by focusing on limiting warming, the debate creates a false sense of certainty and downplays the impacts of geoengineering solutions.

Discussions of “dangerous” levels of interference with the climate system often use warming as a proxy for the seriousness of greenhouse gas-induced climate change. However, climate change impacts are driven not only by temperature changes, but also by change in other aspects of the climate system, such as precipitation and climate extremes. If

geoengineering studies focus too heavily on warming, critical risks associated with such possible “cures” will not be evaluated appropriately. Here, we present an example illustrative of the need for greater emphasis not only on possible benefits but also on the risks of geoengineering—in particular, the risks already suggested by observations of climate system change.

Carbon dioxide increases cause a reduction in outgoing longwave radiation, thus changing the heat balance of the planet. Several proposed geoengineering solutions aim to avoid the resulting energy imbalance that will lead to warming by reducing incoming solar radiation. This may be achieved by, for example, increasing the number of atmospheric reflecting particles in the stratosphere or by placing reflecting “mirrors” outside the atmosphere. These measures are indeed expected to reduce the projected warming (1, 2). Blackstock *et al.* focus on this particular example of geoengineering, with the rationale that it may allow rapid action to be taken if a threat of catastrophic climate change emerges. Such emerging threats could, for example, be rapidly disintegrating ice sheets, or warming that is more rapid than expected (4). One of the attractions of shortwave climate engineering is the effectiveness and rapidity with which

Observations indicate that attempts to limit climate warming by reducing incoming shortwave radiation risk major precipitation changes.

it could reduce warming, but it is also connected with considerable risks.

It is clear that reducing incoming shortwave radiation would lead to decreases in temperature. Volcanic eruptions in the 20th century led to substantial coolings that occurred within months after the eruption and lasted several years (5, 6). Strong volcanic eruptions have in the past led to anomalously cold conditions: The year without a summer (1816) noted in North America and Europe followed the eruption of Tambora in Indonesia the year before, which was the largest volcanic event observed in recent centuries (5). However, volcanic eruptions also affect precipitation (7). The 1991 eruption of Mount Pinatubo led to substantial decreases in global stream flow and to increases in the incidence of drought (see the figure) (8). An analysis of 20th-century observations indicates that volcanic eruptions caused detectable decreases in global land precipitation (9, 10). The reason is that with reduced incoming shortwave radiation and surface cooling, less energy is available for evaporation.

Greenhouse gas increases also influence precipitation, through two mechanisms: directly through reducing outgoing longwave radiation, and indirectly through warming (11–13). Warming increases evaporation, thus

¹Grant Institute, Kings Buildings, West Mains Road, Edinburgh EH9 3JW, UK. ²National Oceanic and Atmospheric Administration, Earth System Research Laboratory, 325 Broadway R/CSD, Boulder, CO 80305–3337, USA. E-mail: gabi.hegerl@ed.ac.uk; susan.solomon@noaa.gov

A Pinatubo aerosols as seen from the space shuttle Atlantis

making more water available globally for precipitation. However, because greenhouse gases reduce outgoing longwave radiation, they also reduce the effectiveness with which the atmosphere radiates out latent heat of condensation. This reduces precipitation. The net result of the two mechanisms is a relatively small increase in global precipitation in the early stages of greenhouse warming simulations (12).

The 20th-century climate record shows the different effects of shortwave and longwave forcing on temperature and on precipitation. Global surface temperature responds in a quite straightforward way to changes in the energy budget, irrespective of whether shortwave or longwave radiation changes are involved. Thus, temperatures in the latter part of the 20th century were dominated by anthropogenic warming (interspersed with short-term cooling after volcanic eruptions) (14). In contrast, precipitation reacts more strongly to reductions in incoming shortwave radiation, such as volcanic eruptions or shortwave climate engineering, than to reductions in outgoing longwave radiation associated with greenhouse gas forcing. Thus, global land precipitation changes over the 20th century correlate with model-simulated precipitation changes, largely because both show decreases in precipitation after volcanic eruptions (9, 12). In contrast, greenhouse gas-induced precipitation changes so far are smaller on the global land average (10, 15).

Models have been able to capture the patterns of precipitation changes with greenhouse warming (14, 15) but appear to underestimate the magnitude of precipitation changes over the 20th century in response to both shortwave and longwave forcing. Patterns of precipitation changes over the 20th century already show contributions by human influences (15). The observed precipitation patterns with latitude were qualitatively captured in the average change simulated by multiple climate models, but the magnitude of simulated changes was

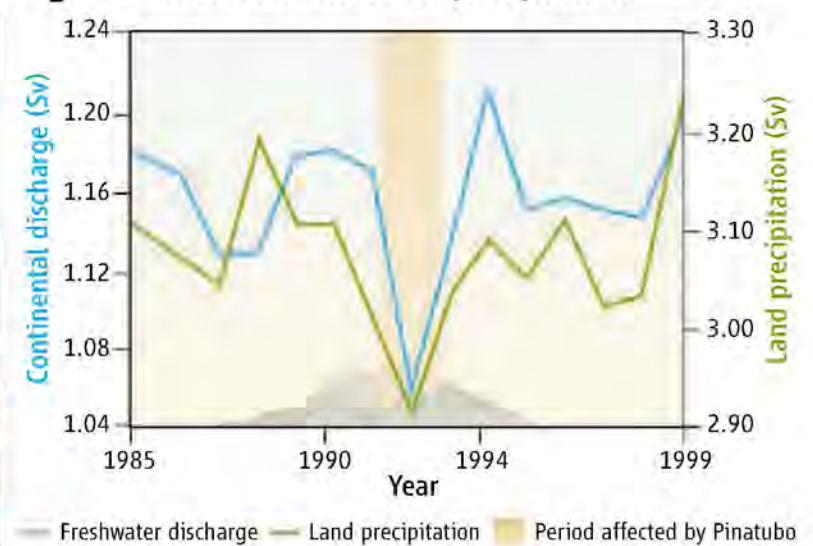
Aerosol effects. The eruption of Mount Pinatubo in June 1991 led to aerosol layering in the stratosphere (A) and to global reductions in precipitation (B). Optically thick layers of stratospheric aerosol cause the dark layers seen in the photo in (A), taken from the space shuttle on 11 August 1991. The data in (B) are averaged over the annual water year (October through September values); $1 \text{ Sv} = 10^6 \text{ m}^3/\text{s}$. Aerosol inserted into the stratosphere as part of geoengineering solutions may have similar effects on precipitation.

significantly underestimated. Similarly, the observed global land precipitation response to volcanic forcing over the 20th century was much stronger than that simulated by present climate models (9, 10).

Satellite data also suggest that climate models underestimate the magnitude of forced changes and of variations in precipitation extremes (16, 17). Although these data are limited (13), they all suggest that precipitation changes are being underestimated. Missing external forcings (such as by absorbing aerosols) or errors in observations could contribute to the discrepancy between observations and model simulations. However, until these discrepancies are fully resolved, models cannot reliably predict how shortwave engineering can target precipitation and temperature simultaneously (18), implying that very large risks are associated with any such geoengineering scheme.

Some models suggest a large degree of cancellation between changes in warming and in precipitation in a shortwave climate-engineered world (18). However, models have been shown to have problems simulating past precipitation variability as well as trends. Furthermore, the combination of a strong greenhouse effect with a reduction of incoming radiation could have substantial effects on regional precipitation (19), including reductions that would rival those of past major droughts (20). Geoengineered changes in the environment could thus lead not only to “winners and losers” but even to conflicts over water resources (19) and the potential for migration and instability, making shortwave climate engineering internationally very controversial.

Blackstock *et al.* call for a study phase, during which the possible impacts of geoengineering options could be investigated.

B Pinatubo effects on precipitation

This is clearly necessary, and optimism about a geoengineered “easy way out” should be tempered by examination of currently observed climate changes. Climate change is about much more than temperature change, and using temperature alone as a proxy for its effects represents an inappropriate risk to the health of our society and to the planet.

References

1. J. J. Blackstock *et al.*, *Climate Engineering Responses to Climate Emergencies* (Novim, 2009), available at <http://arxiv.org/pdf/0907.5140>.
2. P. J. Crutzen, *Clim. Change* **77**, 211 (2006).
3. A. Robock, *Bull. At. Sci.* **64**, 14 (2008).
4. G. A. Meehl *et al.*, in *Climate Change 2007: The Fourth Scientific Assessment*, S. Solomon *et al.*, Eds. (Cambridge Univ. Press, Cambridge, 2007), pp. 747–845.
5. A. Robock, *Rev. Geophys.* **38**, 191 (2000).
6. G. C. Hegerl *et al.*, *Geophys. Res. Lett.* **30**, 1242 (2003).
7. A. Robock, Y. Liu, *J. Clim.* **7**, 44 (1994).
8. K. E. Trenberth, A. Dai, *Geophys. Res. Lett.* **34**, L15702 (2007).
9. N. P. Gillett, A. J. Weaver, F. W. Zwiers, M. F. Wehner, *Geophys. Res. Lett.* **31**, L12217 (2004).
10. F. H. Lambert, N. P. Gillett, D. A. Stone, C. Huntingford, *Geophys. Res. Lett.* **32**, L18704 (2005).
11. J. F. B. Mitchell, C. A. Wilson, W. M. Cunningham, *Q. J. R. Meteorol. Soc.* **113**, 293 (1987).
12. M. R. Allen, W. J. Ingram, *Nature* **419**, 223 (2002).
13. F. H. Lambert, A. R. Stine, N. Y. Krakauer, J. C. H. Chang, *Eos* **89**, 193 (2008).
14. G. C. Hegerl *et al.*, in *Climate Change 2007: The Fourth Scientific Assessment*, S. Solomon *et al.*, Eds. (Cambridge Univ. Press, Cambridge, 2007), pp. 663–745.
15. X. Zhang *et al.*, *Nature* **448**, 461 (2007).
16. F. J. Wentz, L. Ricciardulli, K. Hilburn, C. Mears, *Science* **317**, 233; published online 30 May 2007.
17. R. P. Allan, B. J. Soden, *Science* **321**, 1481; published online 7 August 2008.
18. K. Caldeira, L. Wood, *Philos. Trans. R. Soc. London Ser. A* **366**, 4039 (2008).
19. A. Robock, L. Oman, G. L. Stenchikov, *J. Geophys. Res.* **113**, D16101 (2008).
20. G. T. Narisma, J. A. Foley, R. Licker, N. Ramankutty, *Geophys. Res. Lett.* **34**, L06710 (2007).

10.1126/science.1178530

ENGINEERING

Is Gas Hydrate Energy Within Reach?

Ray Boswell

Technological advances have opened up natural gas resources that were previously unobtainable, including deep-water areas (depths >305 m) and unconventional resources, such as coal-bed methane, and gas in shale, that do not readily release their gas to wells. The next resource poised to be delivered is gas hydrates, which form from methane and water at low temperatures and moderate pressures. Gas hydrates occur in permafrost (1), but most of this vast resource occurs in marine sediments on the outer continental shelves (2). Physical barriers posed by Arctic and deep-water settings, as well as a lack of proven extraction methods, have made them an unexploited resource. However, a series of international field programs in the last 5 years, in conjunction with experimental studies and numerical simulations, show that it should be possible to extract the most favorable gas hydrates—those enclosed in sandy sediments that lay at the apex of the gas hydrate resource pyramid (see the figure)—with existing technologies.

Although recent estimates continue to range over nearly two orders of magnitude (3), the global resource of methane in gas hydrate deposits is commonly cited as 20,000 trillion m³ (2). For comparison, annual natural gas use in the United States is just over 600 billion m³. The carbon stored in gas hydrates may have profound implications for global carbon cycling (4) and climate change (5). However, it is the potential of gas hydrate to become a major energy resource that is the primary driver for the rapidly accelerating international investment in gas hydrate research, especially by countries with limited hydrocarbon resources.

Until the late 1990s, marine gas hydrates were thought to exist primarily in low-permeability, unconsolidated muds. In typical samples, the gas hydrates filled only 10% of the available pore space (6), so although the deposits were

large, they were lean in gas content. Gas hydrates were also known to occur as large, solid mounds directly on the sea floor, often in association with sea-floor seeps hosting unique benthic marine life (7). Because neither of these settings is readily compatible with existing oil and gas production methods, initial production concepts, often invoking mining approaches, faced daunting environmental and economic challenges.

However, the prospects for production from marine gas hydrates greatly improved in 1999, when researchers in Japan discovered extensive gas hydrate deposits in sand reservoirs off the shore of southeastern Japan (8). What made these deposits attractive for gas extraction is their permeability, which appears to enable gas hydrate to accumulate to very high concentrations (typically 60 to 90% of the pore space). In addition, the permeability present in sand reservoirs may be the key to producing methane from gas hydrate reservoirs with existing drilling and production technologies.

This new focus on the most prospective gas hydrate deposits brings a highly

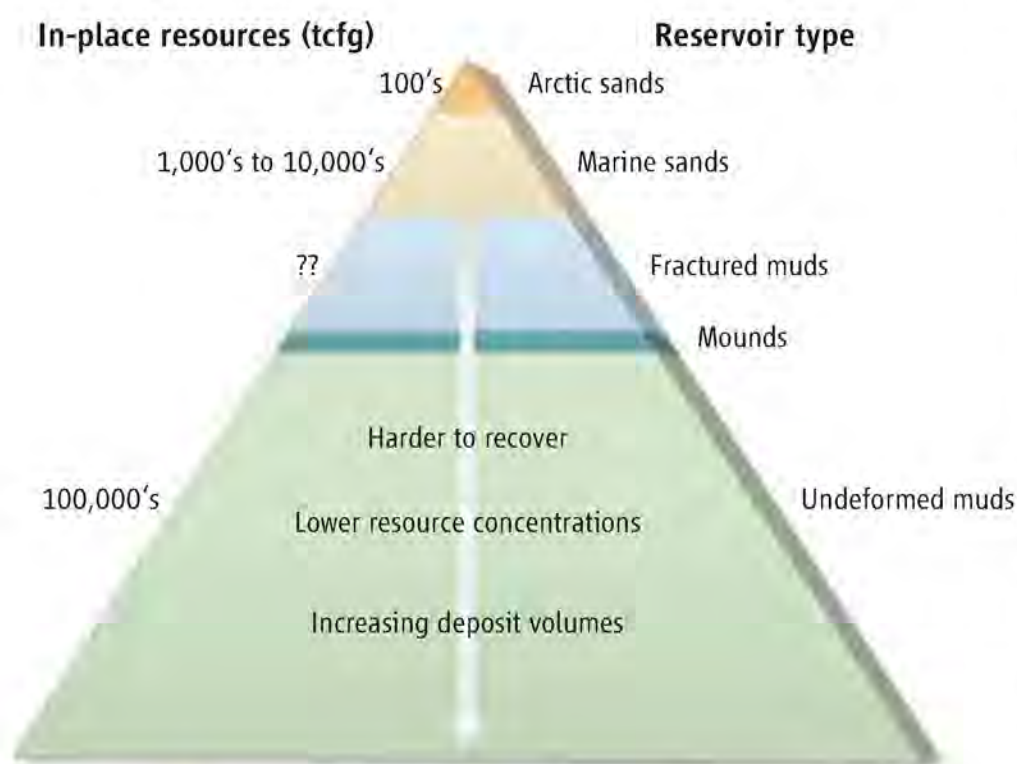
A new focus of the most recoverable gas hydrate deposits is shortening the timeline for the future production of natural gas from this vast resource.

improved perspective and exploration rationale to the study of gas hydrate resources. Unlike the vast but highly dispersed marine gas hydrates in mud, the sand bodies contain discrete and isolated reservoirs that are richly concentrated. Furthermore, these reservoirs are commonly buried many hundreds of meters below the sea floor and enclosed in a matrix of impermeable sediments that help to prevent the escape of released methane. Therefore, the most prospective gas hydrate deposits are also those that are most effectively buffered from environmental change.

There remain two major near-term challenges that will likely determine whether these sand-enclosed gas hydrates are an exploitable resource. The first is to determine the extent of gas hydrates in sand reservoirs in the marine environment. In the United States, the Minerals Management Service recently estimated that more than 190 trillion m³ of gas exist in gas hydrate-bearing sand reservoirs in the northern Gulf of Mexico (9). This estimate needs to be further confirmed by drilling, but initial results are encouraging.

A 21-day expedition to the Gulf of Mexico, completed in April 2009, discovered multiple occurrences of highly saturated gas hydrates in sand reservoirs at two of three sites drilled (10).

The second challenge is whether such deposits yield gas at the rates necessary to make expensive deep-water production commercially viable. The most promising production method reduces pressure in the well bore. Water in the formation moves toward the well, causing a region of reduced pressure to spread rapidly throughout the formation. Reduced pressure initiates gas hydrate dissociation and methane release. The viability of this approach was confirmed during a 6-day production test com-



The gas hydrate resource pyramid. The various components of the total gas hydrate resource are arranged, with those most readily recovered at the top. Current research, focusing on sand-hosted gas hydrates at the top of the pyramid, shows large potential resources that are recoverable with existing technology. These findings may provide insight into the nature and resource potential of the more challenging resources that occur at the base of the pyramid. Current best estimates of resource volumes are in trillions of cubic feet of gas (tcfg); 100 ft³ = 2.83 m³. [Modified from (18)]

National Energy Technology Laboratory, 3610 Collins Ferry Road, Morgantown, WV 26507, USA. E-mail: ray.boswell@netl.doe.gov

pleted in April 2008 by the governments of Japan and Canada at the Mallik site in the Canadian Northwest Territories (11). Numerical simulations (12) show that production based primarily on reducing pressure by pumping could release methane at rates that make commercial production feasible in certain settings. Another production possibility enabled by sand reservoirs is the injection of carbon dioxide (CO₂), which has the potential to displace methane from at least half of the hydrate structure cavities (13) and also leave the CO₂ sequestered within the hydrate structure. Initial studies of these two approaches have been encouraging (12, 14), but extended production tests of both methods are needed. Such testing, currently in the planning stages for sites in Alaska, will be needed to help prepare for marine production tests, which are still several years away.

The new focus on sandy deposits enables the first assessments of resource volumes that are recoverable with existing technology (15). These resource volumes are substantially smaller than those that have previously framed the gas hydrate resource debate. However, these new estimates, which indicate volumes of hundreds of trillions of cubic meters, are still substantial, are more firmly grounded in scientific information obtained in the field, and are far

more relevant to the energy resource issue.

This focus does not mean that the larger resource at the bottom of the pyramid will always be out of reach. Recently, gas hydrate deposits more than 150 m thick were discovered in fine-grained sediments offshore India (16) and Korea (17). The typically low filling of the pore space by gas hydrate is substantially augmented in these deposits by pervasive networks of gas hydrate-filled veins and fractures. The total resource represented by these fractured clay reservoirs is not yet known, but could be substantial. However, a number of engineering challenges must be overcome to enable production from such unconsolidated and practically impermeable sediments.

Exploitation of even the most promising gas hydrate reservoirs requires substantial technological and economic hurdles to be overcome. However, many of these issues, such as geomechanical complications caused by the unconsolidated nature of sand in the reservoirs, are now being successfully addressed in existing oil and gas fields. Solving these issues would provide a new and potentially vast global resource to meet mid- and long-term energy demands. Gas hydrates may offer an important “bridging” fuel that will help ease the transition to the sustainable energy supplies of the future.

References

1. T. Collett, *Am. Assoc. Pet. Geol. Bull.* **77**, 793 (1993).
2. K. A. Kvenvolden, *Chem. Geol.* **71**, 41 (1988).
3. T. Collett, A. Johnson, C. Knapp, R. Boswell, *Am. Assoc. Petrol. Geol. Mem* **89**, 1 (2009).
4. G. R. Dickens, *Earth Planet. Sci. Lett.* **213**, 169 (2003).
5. D. Archer, *Biogeosciences* **4**, 521 (2007).
6. C. Paull *et al.*, *Proceedings of the Ocean Drilling Program, Initial Reports* (College Station, TX, 1996), vol. 4.
7. C. R. Fisher *et al.*, *Naturwissenschaften* **87**, 184 (2000).
8. Y. Tsuji *et al.*, *Resource Geol.* **54**, 3 (2004).
9. M. Frye, Minerals Management Service Report 2008-004; www.mms.gov/revaldiv/GasHydrateFiles/MMS2008-004.pdf.
10. www.netl.doe.gov/technologies/oil-gas/futuresupply/methanehydrates/2009gomjip/index.html.
11. K. Yamamoto, S. Dallimore, U.S. Department of Energy—National Energy Technology Laboratory, *Fire in the Ice. Methane Hydrate Newsletter*, Summer 2008, pp. 1–5; www.netl.doe.gov/mh/HMNewsSummer08/.
12. G. J. Moridis *et al.*, www.netl.doe.gov/technologies/oil-gas/publications/Hydrates/reports/G308_SPE114163_Feb08.pdf.
13. J. Stevens *et al.*, *Proceedings of the 6th International Conference on Gas Hydrates*, Vancouver, BC, Canada, 6 to 10 July 2008, paper 5635; www.netl.doe.gov/mh/NT06553_StevensEtAl/.
14. M. D. White, B. P. McGrail, paper presented at the Offshore Technology Conference, Houston, TX, 5 to 8 May 2008.
15. T. S. Collett *et al.*, *U. S. Geol. Survey Fact Sheet* 2008-3073.
16. T. S. Collett *et al.*, *Proceedings of the 6th International Conference on Gas Hydrates*, Vancouver, BC, Canada, 6 to 10 July 2008, paper 5365; hdl.handle.net/2429/1035.
17. K. Park *et al.*, U.S. Department of Energy—National Energy Technology Laboratory, *Fire in the Ice. Methane Hydrate Newsletter*, Spring 2008, pp. 6–9; www.netl.doe.gov/mh/HMNewsSpring08/.
18. R. Boswell, T. Collett, DOE-NETL *Fire in the Ice. Methane Hydrate Newsletter*, Summer 2006, p. 5; www.netl.doe.gov/mh/FITIO6_Pyramid/.

10.1126/science.1175074

GENETICS

More Than Just a Copy

Henrik Kaessmann

How do new gene functions arise? The importance of gene duplication for the emergence of new gene functions, and hence for the origin of evolutionary innovations, was already recognized in the early 1930s by geneticists J. B. S. Haldane (1) and H. J. Muller (2), and later popularized by S. Ohno (3). In this view, the occurrence of a second copy of a gene provides unique raw material for evolutionary diversification: One of the two duplicate gene copies is preserved to maintain the original gene function, whereas the other is free to accumulate mutations, potentially yielding a gene with new functional properties. A large body of data has provided incontestable support for this early hypothesis (4). On page 995 in this issue

(5), Parker *et al.* provide a new paradigm for gene duplication with implications regarding the evolution of new gene functions.

Until recently, DNA-mediated gene duplication was considered the main underlying mechanism—that is, duplication occurs by recombination of chromosomal segments containing the gene during meiosis (cell divisions that occur during the production of gametes) (see the figure). But gene duplication can also occur through a process called retroposition or retroduplication (6), in which a mature messenger RNA (mRNA) that is transcribed from a gene is then “reverse transcribed” into a complementary DNA copy, which gets inserted into the genome (see the figure). Unlike the parental “source” gene, which contains introns, a “retrocopy” that is produced from a mature mRNA (in which introns have been spliced out) contains only the parental exons. These intronless retrocopies were long

Several dog breeds owe their short legs to a gene duplication event based on reverse transcription of RNA.

thought to be doomed to decay and were routinely classified as processed pseudogenes because of the expected lack of regulatory elements and the presence of deleterious mutations in many copies. Nevertheless, individual functional retrocopies (so-called retrogene) have been discovered since the late 1980s (7), and the genomics era facilitated their discovery and characterization on a larger scale. Often their functions were found to be related to the germ line, but retrogene were also shown to affect other functions, such as in the courtship behavior of flies (6).

Parker *et al.* provide a new example of a retrogene with important functional consequences. The authors aimed to uncover the molecular basis of the short-, curved-leg trait (chondrodysplasia) that is characteristic of several common dog breeds such as the dachshund. In fact, leg length is a primary aspect of interbreed variation and is therefore particu-

Center for Integrative Genomics, University of Lausanne, Genopode Building, CH-1015 Lausanne, Switzerland. E-mail: henrik.kaessmann@unil.ch

larly interesting to study. Through a detailed genetic association study of a large number of dogs representing all major breeds, Parker *et al.* identified a mutation that consistently occurred with the trait—a duplicate copy of the gene encoding fibroblast growth factor 4 (*fgf4*). This duplicate copy displayed a coding sequence identical to that of its parental source gene, but with all the hallmarks of a typical retrogene, such as the lack of introns and the presence of a poly(A) (polyadenylate) tail, reflecting its origination from an *fgf4* mRNA.

How did the emergence of this retrogene lead to such a dramatic trait? Parker *et al.* show that the retrogene encoding *fgf4* is specifically transcribed in the developing humerus bone of fetal chondrodysplastic dogs, in a manner similar to that of its parental source gene, although the precise location

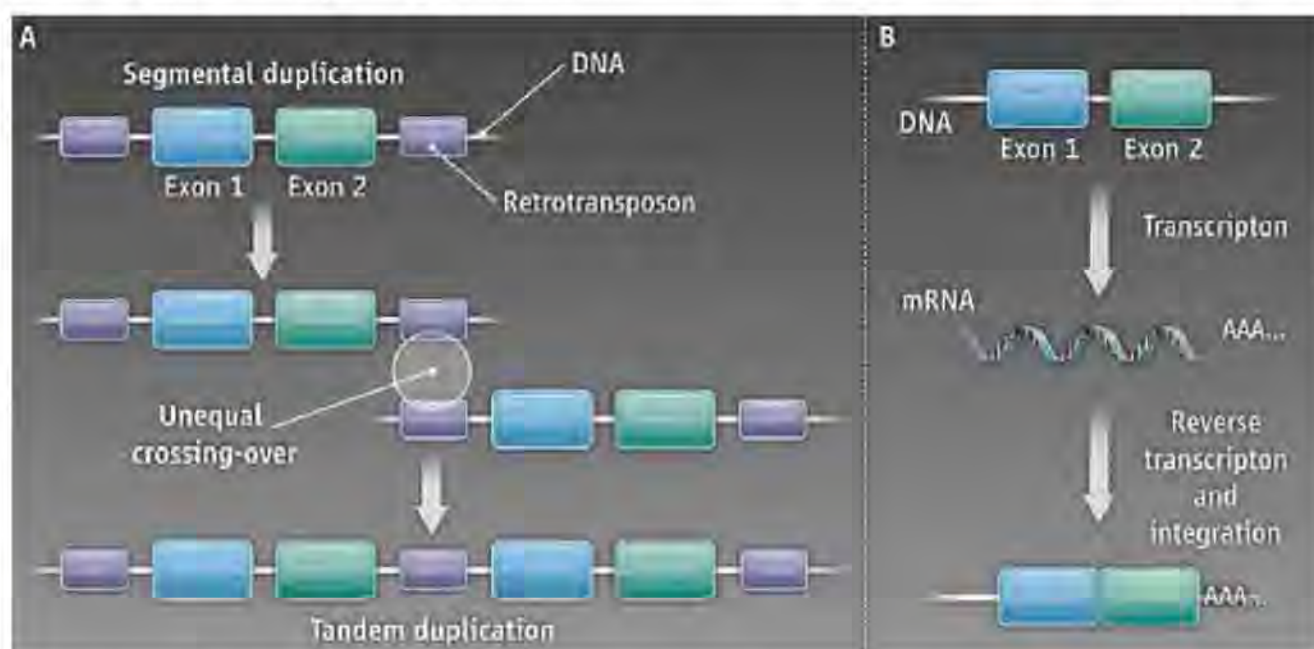
regulatory element located in its 3'-untranslated region, which is identical to that of its parental source gene, and thus appears to be directly inherited from its source gene.

The study by Parker *et al.* is the first description of a retrogene that defines a population- and species-specific morphological trait. The authors further determined that there is substantially reduced genetic variation in the region containing the retrogene. This reflects the strong selective pressure imposed by breeders that has led to permanence, or fixation, of this rare mutational event in short-legged dogs. The study also provides another compelling example (11) of how the genetic study of a domestic animal such as the dog can uncover the nature of mutations underlying dramatic alterations of physical characteristics. Following in the tradition of Darwin, who intensely studied

promoters in the genome (6), thus explaining why a large fraction of retrogenes has become functional and/or transcribed (6, 13). For example, many retrogenes directly hitchhike on the regulatory sequences of other genes into which they insert, often fusing to at least part of the "host" gene's exons (6). The *TRIM5-CypA* fusion gene is an intriguing example of such a scenario. A retroposed copy of the *CypA* gene, which encodes a protein that binds to the protein shell (capsid) that surrounds certain retroviruses, integrated independently into an antiviral defense gene, *TRIM5*, in both a New World monkey (14) and an Old World monkey (15). Thus, the retroposition event twice created a highly similar gene in primates that more efficiently restricts HIV-1 and other retroviruses than does the ancestral *TRIM5* gene. Like the *fgf4* retroposition event reported by Parker *et al.*,

the *TRIM5-CypA* case illustrates that rare retroposition events may be (repeatedly) fixed in a species or population during evolution, provided that selective pressures are sufficiently strong.

It is also noteworthy that even apparently decayed retrocopies (retropseudogenes) that may not have obtained regulatory elements soon after their reemergence, and therefore eventually lost their coding capacity, do not necessarily represent evolutionary dead-ends. Indeed, it was recently found that mammalian retropseudogenes seem to frequently have evolved the capacity to encode small interfering RNAs, important for the regulation of their parental source genes (16, 17).



Making copies. (A) Gene duplication may occur through unequal crossing-over of duplicated chromosomes harboring the gene during meiotic cell divisions in the germ line. This recombination is mediated by, for example, homologous retrotransposable elements that flank the gene. (B) In mammals, the enzymatic machinery necessary for retroposition of a gene (reverse transcriptase and endonuclease) is acquired from LINE1 retrotransposons (7).

and timing of expression are uncertain. In humans, inappropriate expression of FGF4 causes a form of dwarfism resembling chondrodysplasia (8), suggesting a similar molecular basis for the short-legged trait in dogs.

How did the *fgf4* retrogene obtain regulatory sequences that drive its expression in chondrocytes? It seems that the promoter might be derived from a long interspersed nuclear element (LINE); that is, the *fgf4* retrogene inserted into a retrotransposable element downstream of the endogenous promoter of the retrotransposon. This is consistent with observations that retrogenes (6, 9), and genes in general (10), may acquire regulatory elements from nearby retrotransposons. Interestingly, the tissue specificity and temporal pattern of expression of the *fgf4* retrogene can at least partly be explained by a

domestication to derive general evolutionary principles (12), this study is a timely tribute to the 200th anniversary of his birth this year.

Why did this retrogene and several others described recently (6) evolve these intriguing new functions? Perhaps this is a mere coincidence, but it was previously suggested that the properties of retrogenes might make them prone to evolve new functions (6), although, a priori, the initial lack of a promoter upon duplication makes them less likely to become transcribed (and hence functional) than DNA duplicates. Yet if, fortuitously, retrogenes acquire regulatory elements, they might be more likely to evolve new expression patterns (and hence new functional roles) compared to DNA duplicates.

In addition to retrotransposons, there are various other potential sources of retrogene

References

1. J. B. S. Haldane, *Am. Nat.* **67**, 5 (1933).
2. H. J. Muller, *Genetics* **17**, 237 (1935).
3. S. Ohno, *Evolution by Gene Duplication* (Springer-Verlag, Berlin, 1970).
4. G. C. Conant, K. H. Wolfe, *Nat. Rev. Genet.* **9**, 938 (2008).
5. H. G. Parker *et al.*, *Science* **325**, 995; published online 16 July 2009.
6. H. Kaessmann, N. Vinckenbosch, M. Long, *Nat. Rev. Genet.* **10**, 19 (2009).
7. J. R. McCarrey, K. Thomas, *Nature* **326**, 501 (1987).
8. W. A. Horton, G. P. Lunstrum, *Rev. Endocr. Metab. Disord.* **3**, 381 (2002).
9. D. M. Zaiss, P. M. Kloetzel, *J. Mol. Biol.* **287**, 829 (1999).
10. C. Feschotte, *Nat. Rev. Genet.* **9**, 397 (2008).
11. N. B. Sutter *et al.*, *Science* **316**, 112 (2007).
12. C. Darwin, *The Variation of Animals and Plants Under Domestication* (Murray, London, 1868).
13. N. Vinckenbosch, I. Dupanloup, H. Kaessmann, *Proc. Natl. Acad. Sci. U.S.A.* **103**, 3220 (2006).
14. D. M. Sayah, E. Sokolskaja, L. Berthou, J. Luban, *Nature* **430**, 569 (2004).
15. W. E. Johnson, S. L. Sawyer, *Immunogenetics* **61**, 163 (2009).
16. O. H. Tam *et al.*, *Nature* **453**, 534 (2008).
17. T. Watanabe *et al.*, *Nature* **453**, 539 (2008).

10.1126/science.1178487

Structural Plasticity in Actin and Tubulin Polymer Dynamics

Hao Yuan Kueh^{1,2*} and Timothy J. Mitchison^{1†}

Actin filaments and microtubules polymerize and depolymerize by adding and removing subunits at polymer ends, and these dynamics drive cytoplasmic organization, cell division, and cell motility. Since Wegner proposed the treadmilling theory for actin in 1976, it has largely been assumed that the chemical state of the bound nucleotide determines the rates of subunit addition and removal. This chemical kinetics view is difficult to reconcile with observations revealing multiple structural states of the polymer that influence polymerization dynamics but that are not strictly coupled to the bound nucleotide state. We refer to these phenomena as “structural plasticity” and discuss emerging evidence that they play a central role in polymer dynamics and function.

Pioneering observations of cell division using polarization microscopy showed that protein polymers in the cell undergo rapid exchange with soluble subunits and can generate force by subunit addition (polymerization) and loss (depolymerization) (*1*). Subsequent work revealed that polymerization dynamics of actin filaments, microtubules, and their prokaryotic cousins indeed play central roles in diverse physiological processes, including cell shape control, cell motility, and chromosome segregation (*2–4*). Understanding the mechanisms by which these cytoskeletal polymers polymerize and depolymerize is critical for understanding how they spatially organize the cell and promote motility. The field of cytoskeletal polymer research has traditionally adopted a chemical kinetics view of polymerization dynamics, which posits that the chemical state of the subunit-bound nucleotide uniquely controls association and dissociation rates of polymer subunits. Accumulating evidence has questioned the purely chemical kinetics view and points to an important role for structural plasticity in modulating polymer dynamics. Structural plasticity, defined here as change in the structural state of a polymer without change in the chemical state of its bound nucleotide, is likely to play a major role in modulating polymer behavior in cells. A full understanding of polymerization dynamics will require its integration with chemical kinetics. Here, we review the basic structural and biochemical properties of actin and tubulin, as well as models for their polymerization dynamics that are rooted in chemical kinetics theory. We then review evidence for the existence of structural plasticity in

these cytoskeletal polymers and discuss implications for their dynamics inside cells.

End-Dependent Dynamics and Nucleotide Hydrolysis

In eukaryotes, both actin and tubulin assemble into multistranded, polar polymers. Actin filaments consist of two strands that intertwine to form a double-helical structure. Microtubules, the polymers of tubulin, usually consist of 13 parallel strands (or protofilaments) that associate laterally to form a sheetlike lattice. Along the microtubule length, this sheet curves around and closes on itself, giving rise to a hollow tubular structure. The structures of prokaryotic actin and tubulin relatives are currently a topic of intense investigation (*5*). Multistranded polymer architecture has two important consequences: It provides mechanical strength, and it largely restricts

subunit association and dissociation to polymer ends, because subunits at ends make fewer contacts with neighbors. This end-independence enables cells to control the assembly of long (micron-scale) polymers by using localized (nanometer-scale) biochemical reactions at polymer ends, which allows the precise spatial control of polymerization necessary for cell polarity and motility.

Actin and tubulin subunits, as well as their prokaryotic relatives, bind nucleotide triphosphate (NTP), adenosine triphosphate (ATP) for actin, and guanine triphosphate (GTP) for tubulin, and they polymerize preferentially in their NTP-bound form. Shortly after polymerization, subunits hydrolyze NTP to nucleotide diphosphate (NDP), releasing phosphate (P_i) and retaining NDP in the polymer. The resultant NDP-bound polymer is weaker than an NTP-bound polymer and consequently depolymerizes, which releases individual subunits for another round of polymerization and depolymerization. In this scheme, the free energy of NTP hydrolysis does not catalyze polymerization per se, but instead drives depolymerization, enabling polymers to undergo continuous nonequilibrium turnover in cells. This turnover, then, allows polymers to assemble in some places in the cell while disassembling in others and to perform mechanical work by pushing or pulling, or by bending in the case of FtsZ, a bacterial tubulin homolog that helps divide the bacterial cell in two at the end of the cell cycle (*6*). Understanding how polymers use the energy of nucleotide hydrolysis to promote turnover and to perform mechanical work is a central theme in cytoskeleton research.

The Chemical Kinetics View of Polymerization Dynamics

While work in the 1960s and 1970s demonstrated a role for NTP hydrolysis in actin and tubulin

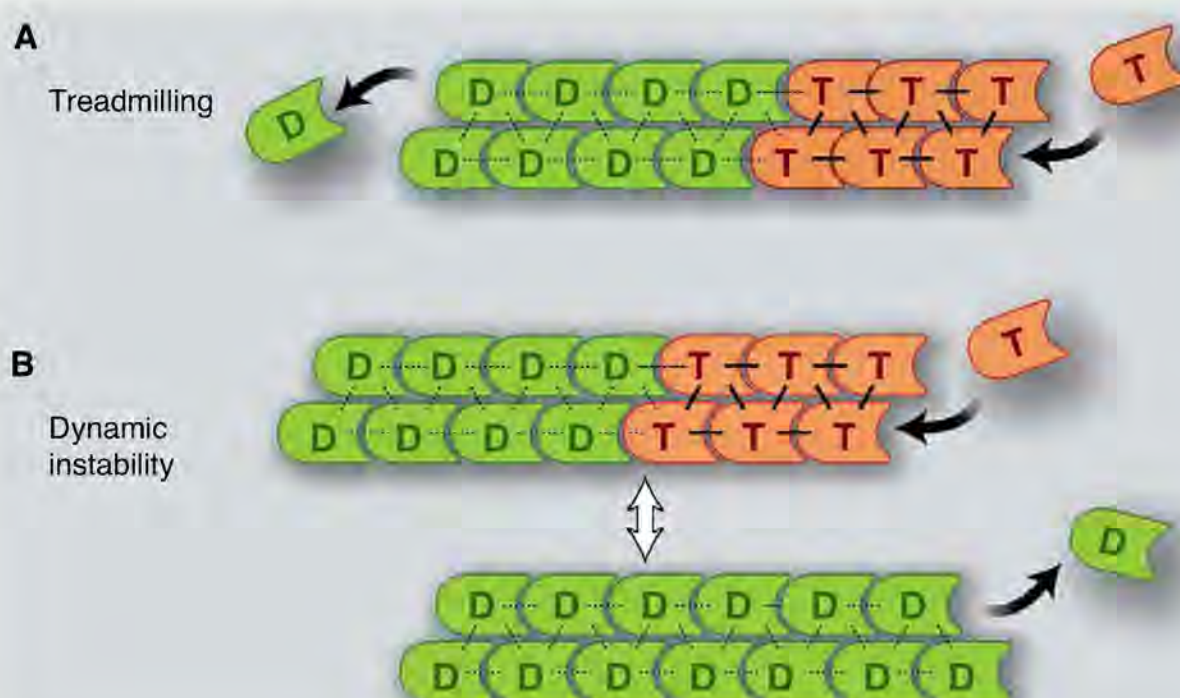


Fig. 1. Classical chemical kinetics models of polymerization dynamics. T, NTP-bound subunit (orange); D, NDP-bound subunit (green). (A) Treadmilling. Arrows indicate NTP-subunit association (right), and NDP-subunit dissociation from the opposite end (left). (B) Dynamic instability. Arrows at polymer ends indicate NTP-subunit association (top) and NDP-subunit dissociation (bottom). Bidirectional arrow indicates reversible transitions of the polymer between growing and shrinking states.

¹Department of Systems Biology, Harvard Medical School, Boston, MA 02215, USA. ²Graduate Program in Biophysics, Harvard University, Cambridge, MA 02139, USA.

*Present address: Division of Biology, California Institute of Technology, Pasadena, CA 91125, USA.

†To whom correspondence should be addressed. E-mail: timothy_mitchison@hms.harvard.edu

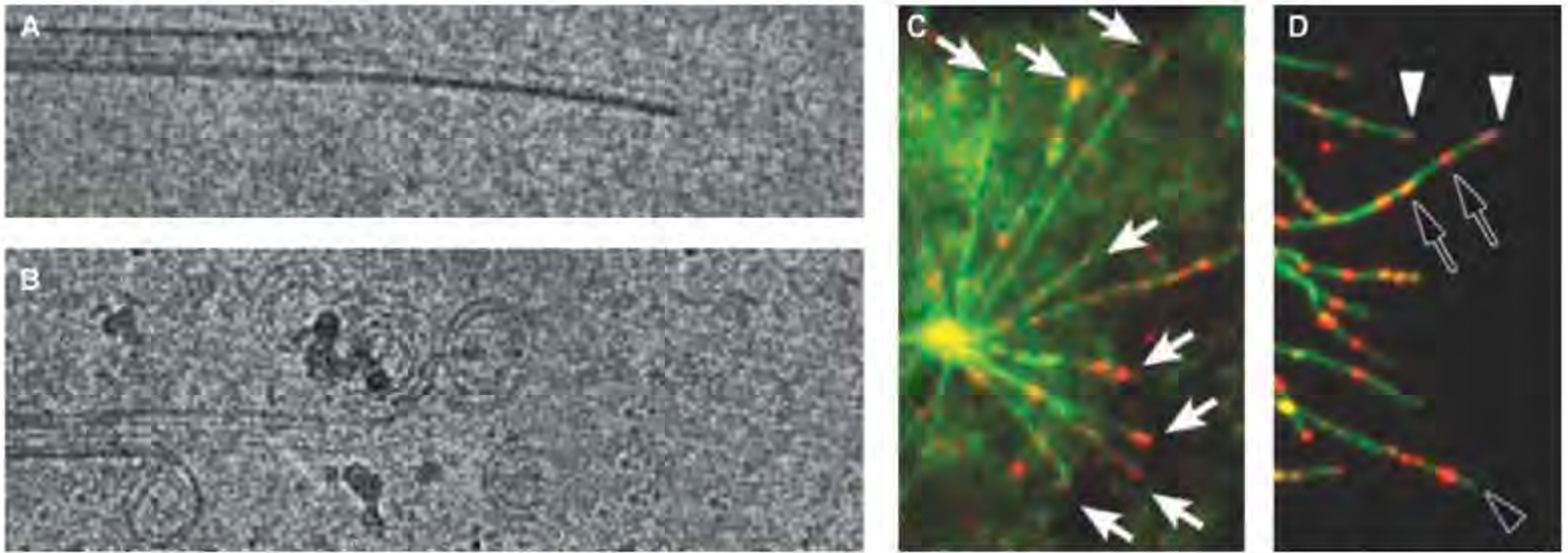


Fig. 2. Microtubule structural plasticity. (A) Cryo-EM images of a growing microtubule end showing a curved, open sheet. (B) Cryo-EM image of a shrinking microtubule end showing outwardly curled protofilaments. (C and D) Localization of microtubule segments with a stable lattice structure, recognized by a recombinant antibody. (C) Pure tubulin microtubules (green) growing from a centrosome stained with an antibody that recognizes a stable structural state of

the microtubule lattice (red). Note staining of growing tips (white arrows). (D) Microtubules in a cell (green) stained with the antibody (red). Note tip staining, presumably on growing microtubules (white arrowhead); lack of tip staining, presumably on shrinking microtubules (empty arrowhead); and internal segments recognized by the antibody (empty arrows). [(A) and (B) courtesy of T. Hyman, MPI Dresden; (C) and (D) adapted from (26)]

polymerization, how exactly NTP hydrolysis could drive polymer turnover remained unclear. A solution was proposed in Wegner's influential treadmilling theory for actin turnover (7). At the heart of this theory was the concept that the chemical state of the nucleotide bound to a subunit influences its association and dissociation rates at the polymer end. In the broad sense, NTP-bound subunits preferentially associate at ends, whereas NDP-bound subunits preferentially dissociate from ends. In conjunction with polarity-dependent rate constants, this concept gives rise to a mode of polymer turnover where actin filaments grow from one end while shrinking from the other (Fig. 1A). In the Wegner model, treadmilling is driven by hydrolysis of polymer-bound ATP, which allows ADP-bound subunits to dissociate preferentially from one polymer end while ATP-bound subunits are associating preferentially onto the other. This model of polymer turnover was first tested in solutions of actin (7) and was later confirmed and extended by direct observations of single filaments using time-lapse imaging (8).

After Wegner's work, microtubules were also proposed to treadmill (9); but later it was found that their dominant kinetic behavior is dynamic instability, where individual ends alternate between bouts of growth and shrinkage (10). Dynamic instability was initially rationalized using a chemical kinetics model, where a lag between tubulin subunit association and subsequent GTP hydrolysis was proposed to generate a cap of GTP-bound tubulin that stabilizes growing ends (Fig. 1B, top). Loss of the cap by GTP hydrolysis initiates depolymerization (Fig. 1B, bottom). A similar model was proposed recently to account for the dynamic instability of ParM, a prokaryotic actin relative, whose polymerization generates pushing force to segregate plasmids (11).

Models based purely on chemical kinetics, like those in Fig. 1, continue to dominate the polym-

erization dynamics field, in part because they employ simple kinetic equations that can successfully rationalize a lot of experimental data and account for observed polymer behaviors. However, these models are becoming increasingly difficult to reconcile with studies revealing multiple structural states of microtubules and actin filaments that strongly influence dynamics, but are not strictly coupled to the chemical state of the bound nucleotide—i.e., structural plasticity. These studies do not invalidate the chemical kinetics viewpoint, but they demand a more sophisticated analysis that takes structural plasticity into account.

Structural Plasticity in Microtubule Dynamics

For microtubules, multiple structural states at polymer ends have long been observed. Early negative-stain electron microscopy (EM) images of microtubules coated with associated proteins showed that depolymerizing ends are frayed, inconsistent with depolymerization by simple reversal of polymerization (12, 13). Later, rapid freezing and cryo-EM of pure tubulin microtubules revealed relatively straight open sheets extending from the ends of growing microtubules (Fig. 2A), and frayed, outward-curling protofilaments at the ends of shrinking microtubules (Fig. 2B) (14, 15). These images began to transform our view of microtubule polymerization dynamics from one dominated by chemical kinetics (the GTP-cap view) to one dominated by structural transitions at polymer ends. Outward curling of protofilaments in shrinking microtubules may reflect a more bent conformation of the GDP-tubulin subunit compared with a straighter GTP subunit, as seen in structural studies (16, 17). An alternative view suggests that GTP and GDP subunits may be similarly bent in solution and that subunits straighten only after their incorporation into growing microtubules (18, 19). In the cur-

rent, structural plasticity-based view of dynamic instability (20–22), GTP tubulin subunits add to open sheets at the end of growing microtubules, perhaps straightening during addition. A few seconds later, the sheet closes into a tube. Sheet closure may be facilitated in cells by microtubule tip-binding proteins, such as EB1 (23), which can modulate the rates of transition between growing and shrinking states. However, it is still unclear how tip-binding proteins modulate chemical or structural dynamics at microtubule ends. At some point after polymerization—we do not know exactly when—GTP is hydrolyzed and phosphate released. The resulting GDP protofilaments prefer to be curved outward, either because their GDP-tubulin subunits are more stable in the bent conformation (19) and/or because they make weaker interactions with neighbors (18). The preference of GDP protofilaments for an outwardly curved configuration causes mechanical stress to accumulate in the microtubule lattice. As the microtubule keeps growing, this stress cannot be released, because protofilaments are trapped in the straight configuration by interactions with their neighbors. However, stress makes the lattice fragile. If a crack develops between protofilaments at the end, it allows protofilaments to peel apart and curl outward, finally releasing the stored free energy from GTP hydrolysis. The force of outward curling causes the crack to propagate down the microtubule, releasing stress and triggering depolymerization as it travels. This stress storage-crack propagation model provides a structural explanation for how ends can persist in growing or shrinking states. It differs from a GTP-cap model in that depolymerization is initiated not by hydrolysis of GTP bound to terminal tubulin subunits (Fig. 1B), but by crack formation between neighboring protofilaments near the polymer end. It has interesting implications for how depoly-

erizing microtubules in the mitotic spindle might pull on attached chromosomes during chromosome segregation. A number of recent models suggest that the outward curling of protofilaments directly generates pulling forces that, through different coupling mechanisms, are transduced from the tip of the depolymerizing microtubule to the attached chromosome (20–22, 24).

Although microtubule dynamics are dominated by behavior at ends, structural plasticity in the middle of microtubules may also regulate dynamics in important ways. The polymer lattice places strong constraints on subunit conformation, but comparative EM of microtubules with bound GDP versus GMPCPP (a GTP analog) showed that their lattices differ subtly, with the intersubunit spacing ~ 0.4 nm shorter along the microtubule axis in GDP microtubules (25). Recently, an antibody was generated that recognizes a stable state of the microtubule lattice present in microtubules stabilized by GMPCPP or the drug taxol, but not in unstable GDP-bound microtubules (26). This antibody stained segments a few hundred nanometers long at the plus ends of growing microtubules, both with pure tubulin (Fig. 2C) and in cells (Fig. 2D), consistent with the classical GTP-cap model (Fig. 1), but not ruling out alternative models positing structural plasticity at ends. It was intriguing that the antibody also stained short segments in the middle of cellular microtubules (Fig. 2D), which were shown to act as reflecting boundaries to bouts of depolymerization. Whether these stable internal segments contain GTP-tubulin (a chemical kinetics view) or GDP-tubulin in an alternative, stable structural state of the lattice (a structural plasticity view) remains to be determined. The stable-state antibody is an exciting new probe that will stimulate interest in studying the mechanisms of structural plasticity in regulating microtubule dynamics.

Structural Plasticity in Actin Dynamics

The structure of the actin filament was first determined by fitting a high-resolution crystal structure of an actin monomer into a filament model to fit x-ray fiber diffraction data from an oriented actin gel (27, 28), and was recently refined with improved versions of these methods (29). This canonical double-helical structure is supported by numerous mutagenesis and EM studies (30). However, EM studies are increasingly showing that the actin helix can exhibit multiple structural states and can transition between states in a highly cooperative manner (31). When pure actin filaments were analyzed by EM within ~ 2 min of polymerization, they were found to exhibit several different structural states, including some where individual subunits were substantially tilted away from the canonical helical orientation (32, 33). After aging in solution for 2 hours, filaments mostly adopted the canonical helical structure (Fig. 3, A and B) (33). The chemical kinetics view predicts that newly polymerized filaments are more stable than aged filaments, because they contain a larger proportion of bound ATP (or

ADP-P_i, the chemical state after hydrolysis but before phosphate release) (34, 35). However, the EM structures seem to contradict this view, because the tilted state present in young filaments appears to have less-stable intersubunit contacts compared with the canonical helical state in aged filaments (36). We directly compared the stability of young and aged pure actin filaments using single-filament imaging and kinetic assays in bulk solution (37) and found that newly polymerized filaments depolymerized faster than aged filaments, inconsistent with the chemical kinetics view, but consistent with EM structural observations. Time-dependent switching from fast to slow depolymerization was seen by live imaging of single filaments (Fig. 3C, blue-green transition). Less frequently, aged, stable filaments reverted back to the unstable, fast-shrinking state (Fig. 3C, green-red transition). The majority of aged filaments were in a slowly shrinking state, and this state

dominated bulk depolymerization kinetics measured in solution (37). In light of EM data, we hypothesize that time-dependent stabilization arises from cooperative and reversible transitions of actin filaments from a disordered or tilted state in young filaments, which depolymerizes rapidly, to the canonical helical structure in older filaments, which depolymerizes slowly.

Structural plasticity appears to be an important determinant of polymerization dynamics for pure actin, but is it important in cells, where dynamics are regulated by many other proteins? Among the most important dynamics regulators are proteins in the actin-depolymerizing factor (ADF)-cofilin family, which promote actin turnover in diverse eukaryotic cells (38). ADF-cofilins selectively bind ADP-actin filaments and catalyze their depolymerization (39, 40), consistent with a chemical kinetics view of their function. A number of different mechanisms have been reported by

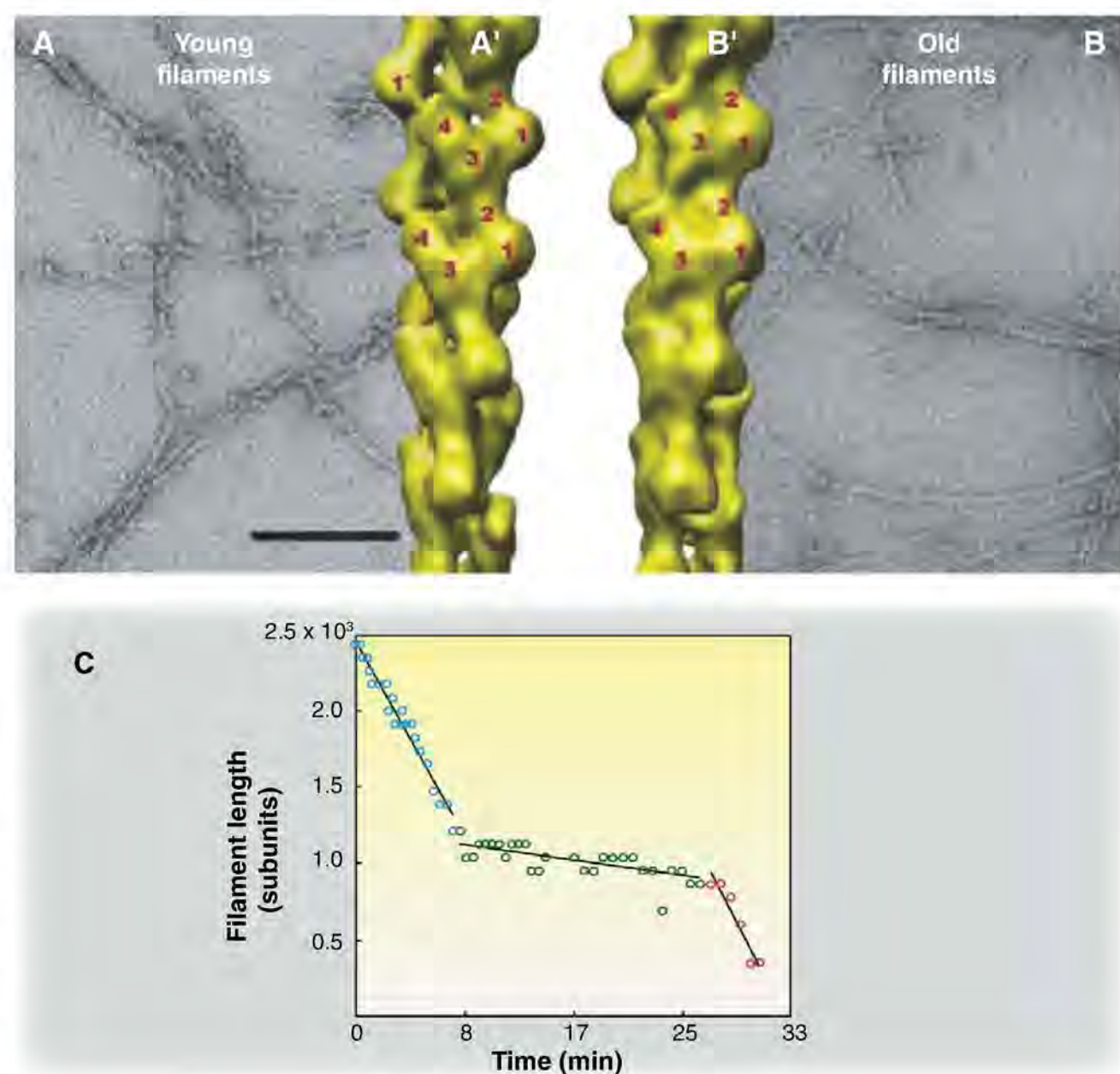


Fig. 3. Actin filament structural plasticity. (A) Negative-stain EM images of pure actin filaments 2 min after initiation of polymerization. Note ragged appearance. (A') Three-dimensional (3D) reconstruction of cryo-EM images of actin filaments, revealing a structural state in which subunits (numbered) are tilted $\sim 30^\circ$ relative to the canonical helix. This state is enriched in newly polymerized filaments. (B) EM image of actin filaments aged for 2 hours. Note regular appearance. (B') 3D reconstruction of Cryo-EM images of actin filaments, revealing a canonical helical state. This canonical state is enriched in aged filaments. Scale bar, 100 nm in both EM images. (Images courtesy of A. Orlova and E. Egelman, University of Virginia. Reconstructions courtesy of V. Galkin, A. Orlova, and E. Egelman, University of Virginia.) (C) Length versus time trace for a single fluorescently labeled actin filament depolymerizing in buffer. [Adapted from (37) ©2008 National Academy of Science, U.S.A.]. Filament switches from fast to slow depolymerization, and then back to fast. We propose that these switches are caused by spontaneous structural transitions, possibly between those shown in (A) and (B).

which ADF-cofilins promote filament turnover: acceleration of subunit loss from ends (37, 40), severing of filaments away from ends (41), and disassembly of long filament segments in abrupt bursts, a pathway observed in the presence of cofactors Aip1 and coronin (42). These alternative depolymerization pathways are difficult to explain from a pure chemical kinetics viewpoint, but structural plasticity begins to reconcile them. Binding of ADF-cofilin is known to induce, or stabilize, alternative structures of the actin filament that can be both hypertwisted (43) and tilted (33, 36). The tilted state induced by ADF-cofilin was similar to that seen in the young filaments of pure actin, so ADF-cofilin binding can be thought of as “rejuvenating” aged, stable filaments (33). Alternative depolymerization pathways can then be viewed as consequences of ADF-cofilin-induced structural transitions that weaken the filament. Because ADF-cofilin binding is promoted by ATP hydrolysis and phosphate release, these proteins may restore time-dependent destabilization to a polymer where structural plasticity promotes time-dependent stabilization.

The concept that binding proteins influence actin dynamics by exploiting intrinsic structural plasticity of the filament may extend to other proteins; recent EM work showed that binding of fimbrin, a cross-linking protein, induces changes in filament internal structure (44). We hypothesize that tropomyosin, a coiled-coil protein that binds cooperatively along the filament and antagonizes cofilin binding (45), might function by inducing (or stabilizing) the more ordered, canonical helical state. Even end-binding proteins might function in part by inducing structural changes in the filament. Two barbed-end binding proteins, formins and gelsolin, both nucleate filaments with altered internal structures (46, 47). If diverse actin-binding proteins take advantage of intrinsic structural plasticity of the filament to promote their own cooperative binding and to regulate interaction of the filament with other proteins, then we expect a rich variety of higher-order behaviors to emerge, which could promote diversity in structure and function of cellular actin assemblies.

Future Directions

For both microtubules and actin filaments, the case for structural plasticity regulating dynamics is strong. We now need to determine exactly how these multiple structural states of the polymer influence dynamics; how they interconvert; and how they influence, or are influenced by, the chemical kinetics of nucleotide hydrolysis. We can then integrate structural data with chemical kinetics into full models of polymerization dynamics. For microtubules, relatively simple chemical kinetics models have so far sufficed to account for dynamic instability behavior in cells (48, 49). As we seek to model complex assemblies, to understand how microtubules pull on chromosomes, and to elucidate mechanisms of proteins that regulate polymerization dynamics, we will need models that integrate structural transitions with GTP hydroly-

sis kinetics. To achieve this, we will need to learn exactly when nucleotide hydrolysis and phosphate release occur at growing microtubule plus ends; how these chemical events relate to sheet growth and tube closure; and how tip-binding proteins, such as EB1, influence and are influenced by structural and chemical transitions. For actin, the field continues to rely on chemical kinetics models that neglect structural plasticity (50, 51), despite the EM data. As we seek to understand local regulation of actin turnover in cells, as well as how actin and its binding proteins function at the systems level, we will need to understand better how filament structure influences dynamics and the extent to which filament-binding proteins control dynamics by modulating filament structure. For both microtubules and actin filaments, we will need probes that recognize different structural states of the polymer in cells. Antibodies that recognize specific structural states of the polymer are a promising start (26, 52, 53), but a more general solution may come from binding factors that have evolved to recognize different chemical or structural states.

For prokaryotic relatives of tubulin and actin there are many outstanding questions, including in most cases, basic descriptions of polymer architecture, dynamics, and biological function. Once these have been answered, we can go on to investigate possible roles of structural plasticity. A purely chemical kinetics model for dynamic instability of ParM filaments was recently proposed (11), but alternate models, which take into account the observed structural plasticity of ParM filaments (54), may be worth considering. Prokaryotes apparently lack motor proteins and possess a much smaller complement of polymer-binding proteins, which make their cytoskeletal systems apparently simpler than those in eukaryotes. Will prokaryotic polymers consequently be more, or less, complicated in terms of their structure and dynamics? Given the diversity of tubulin and actin relatives among prokaryotes, it seems likely that we will see entirely new polymer structures and dynamics, where both nucleotide chemistry and structural plasticity are put to new uses.

References and Notes

1. S. Inoue, H. Sato, *J. Gen. Physiol.* **50** (suppl.), 259 (1967).
2. T. D. Pollard, G. G. Borisy, *Cell* **112**, 453 (2003).
3. T. J. Mitchison, E. D. Salmon, *Nat. Cell Biol.* **3**, E17 (2001).
4. N. A. Dye, L. Shapiro, *Trends Cell Biol.* **17**, 239 (2007).
5. E. H. Egelman, *Curr. Opin. Struct. Biol.* **13**, 244 (2003).
6. M. Osawa, D. E. Anderson, H. P. Erickson, *Science* **320**, 792 (2008).
7. A. Wegner, *J. Mol. Biol.* **108**, 139 (1976).
8. I. Fujiwara, S. Takahashi, H. Tadokuma, T. Funatsu, S. Ishiwata, *Nat. Cell Biol.* **4**, 666 (2002).
9. R. L. Margolis, *Proc. Natl. Acad. Sci. U.S.A.* **78**, 1586 (1981).
10. T. Mitchison, M. Kirschner, *Nature* **312**, 237 (1984).
11. E. C. Garner, C. S. Campbell, R. D. Mullins, *Science* **306**, 1021 (2004).
12. M. W. Kirschner, R. C. Williams, M. Weingarten, J. C. Gerhart, *Proc. Natl. Acad. Sci. U.S.A.* **71**, 1159 (1974).
13. E. M. Mandelkow, E. Mandelkow, *J. Mol. Biol.* **181**, 123 (1985).

14. E. M. Mandelkow, E. Mandelkow, R. A. Milligan, *J. Cell Biol.* **114**, 977 (1991).
15. D. Chretien, S. D. Fuller, E. Karsenti, *J. Cell Biol.* **129**, 1311 (1995).
16. T. Muller-Reichert, D. Chretien, F. Severin, A. A. Hyman, *Proc. Natl. Acad. Sci. U.S.A.* **95**, 3661 (1998).
17. H. W. Wang, E. Nogales, *Nature* **435**, 911 (2005).
18. L. M. Rice, E. A. Montabana, D. A. Agard, *Proc. Natl. Acad. Sci. U.S.A.* **105**, 5378 (2008).
19. R. M. Buey, J. F. Diaz, J. M. Andreu, *Biochemistry* **45**, 5933 (2006).
20. M. I. Molodtsov, E. L. Grishchuk, A. K. Efremov, J. R. McIntosh, F. I. Ataullakhanov, *Proc. Natl. Acad. Sci. U.S.A.* **102**, 4353 (2005).
21. J. R. McIntosh *et al.*, *Cell* **135**, 322 (2008).
22. E. L. Grishchuk *et al.*, *Proc. Natl. Acad. Sci. U.S.A.* **105**, 6918 (2008).
23. B. Vitre *et al.*, *Nat. Cell Biol.* **10**, 415 (2008).
24. S. Westermann *et al.*, *Nature* **440**, 565 (2006).
25. A. A. Hyman, S. Salser, D. N. Drechsel, N. Unwin, T. J. Mitchison, *Mol. Biol. Cell* **3**, 1155 (1992).
26. A. Dimitrov *et al.*, *Science* **322**, 1353 (2008).
27. W. Kabsch, H. G. Mannherz, D. Suck, E. F. Pai, K. C. Holmes, *Nature* **347**, 37 (1990).
28. K. C. Holmes, D. Popp, W. Gebhard, W. Kabsch, *Nature* **347**, 44 (1990).
29. T. Oda, M. Iwasa, T. Aihara, Y. Maeda, A. Narita, *Nature* **457**, 441 (2009).
30. E. Reisler, E. H. Egelman, *J. Biol. Chem.* **282**, 36133 (2007).
31. A. Orlova, E. Prochniewicz, E. H. Egelman, *J. Mol. Biol.* **245**, 598 (1995).
32. M. O. Steinmetz, K. N. Goldie, U. Aebi, *J. Cell Biol.* **138**, 559 (1997).
33. A. Orlova *et al.*, *Proc. Natl. Acad. Sci. U.S.A.* **101**, 17664 (2004).
34. C. Combeau, M. F. Carlier, *J. Biol. Chem.* **263**, 17429 (1988).
35. T. D. Pollard, *J. Cell Biol.* **103**, 2747 (1986).
36. V. E. Galkin, A. Orlova, N. Lukyanova, W. Wriggers, E. H. Egelman, *J. Cell Biol.* **153**, 75 (2001).
37. H. Y. Kueh, W. M. Brieher, T. J. Mitchison, *Proc. Natl. Acad. Sci. U.S.A.* **105**, 16531 (2008).
38. S. K. Maciver, P. J. Hussey, *Genome Biol.* **3**, reviews3007 (2002).
39. L. Blanchoin, T. D. Pollard, *J. Biol. Chem.* **274**, 15538 (1999).
40. M. F. Carlier *et al.*, *J. Cell Biol.* **136**, 1307 (1997).
41. E. Andrianantoandro, T. D. Pollard, *Mol. Cell* **24**, 13 (2006).
42. H. Y. Kueh, G. T. Charras, T. J. Mitchison, W. M. Brieher, *J. Cell Biol.* **182**, 341 (2008).
43. A. McGough, B. Pope, W. Chiu, A. Weeds, *J. Cell Biol.* **138**, 771 (1997).
44. V. E. Galkin, A. Orlova, O. Cherepanova, M. C. Lebart, E. H. Egelman, *Proc. Natl. Acad. Sci. U.S.A.* **105**, 1494 (2008).
45. S. Ono, K. Ono, *J. Cell Biol.* **156**, 1065 (2002).
46. G. Papp *et al.*, *Biophys. J.* **91**, 2564 (2006).
47. E. Prochniewicz, Q. Zhang, P. A. Janmey, D. D. Thomas, *J. Mol. Biol.* **260**, 756 (1996).
48. F. Verde, M. Dogterom, E. Stelzer, E. Karsenti, S. Leibler, *J. Cell Biol.* **118**, 1097 (1992).
49. I. A. Vorobjev, V. I. Rodionov, I. V. Maly, G. G. Borisy, *J. Cell Sci.* **112**, 2277 (1999).
50. M. Bindschadler, E. A. Osborn, C. F. Dewey Jr., J. L. McGrath, *Biophys. J.* **86**, 2720 (2004).
51. D. Vavylonis, Q. Yang, B. O'Shaughnessy, *Proc. Natl. Acad. Sci. U.S.A.* **102**, 8543 (2005).
52. E. H. Egelman, *Nat. Rev. Mol. Cell Biol.* **4**, 621 (2003).
53. C. A. Schoenenberger *et al.*, *J. Struct. Biol.* **152**, 157 (2005).
54. A. Orlova *et al.*, *Nat. Struct. Mol. Biol.* **14**, 921 (2007).
55. We thank E. Egelman and S. Dumont for insightful comments on this manuscript, as well as B. Brieher, D. Needleman, and other members of the Mitchison lab for discussions. This work was supported by NIH grant GM 23928. H.Y.K. is a Howard Hughes Medical Institute predoctoral fellow.

10.1126/science.1168823

Deep-Sea, Swimming Worms with Luminescent "Bombs"

Karen J. Osborn,^{1*} Steven H. D. Haddock,² Fredrik Pleijel,³ Laurence P. Madin,⁴ Greg W. Rouse¹

By using remotely operated vehicles, we have collected specimens of seven species of hitherto unknown swimming annelid worms in deep waters of northeast and western Pacific Ocean (1). Specimens range in length from 18 to 93 mm and propel themselves with fans of long bristles that form swimming paddles (Fig. 1 and movie S1). Five species have four pairs of lateral, ellipsoidal organs on anterior segments that produce brilliant green bioluminescence when autotomized. All species were found between 1863-m and 3793-m depths; four live close to the seafloor (movie S2), whereas the other three are found as far as 444 m above the seafloor and are holopelagic (movie S3). Two of the demersal species were observed at densities as high as six per cubic meter. All are excellent swimmers, moving both forward and backward with use of long (at least eight-segment wavelength) metachronal waves originating posteriorly (movie S1).

These species form a previously unknown monophyletic group of acrocirrids, worms generally living in seafloor sediments. *Swima* n. gen. are swimming Acrocirridae that lack eyes and possess more than 30 long, spinous chaetae per parapodium [supporting online material (SOM) text]. The genus is typified by *Swima bombiviridis* n. sp. [holotype,

SIO-BIC (Scripps Institution of Oceanography–Benthic Invertebrate Collection) A1282, fig. S1; paratypes, SIO-BIC A1281, A1283, A1284, and A1634 to A1638], which is distinguished by its transparent foregut and greater than 15% uncorrected cytochrome oxidase I (COI) distance from all other *Swima* species. This new clade is not closely related to either of the two previously known pelagic cirratuliforms (2) and so represents a third and separate invasion of the pelagic realm within Cirratuliformia (Fig. 1E).

Green bioluminescence occurs in all the "bomb"-bearing species tested for luminosity. The luminescent structures are colloquially termed bombs because they suddenly burst into light when released by the animal, glowing intensely for many seconds then slowly diminishing. Similar autotomy of bioluminescent structures is thought to be a defensive behavior, distracting a predator while the animal escapes, and has been documented in a brittle star (3) and a squid (4). Bioluminescence for defense and reproduction is well known in many polychaetes (SOM text).

Histological study indicates the bombs are simple, fluid-filled structures with minimal internal organization, consisting of two small, central chambers and two minute, hemolymph-filled chambers on opposite poles. Both positional

homology and morphological similarities support bombs as homologous to the segmental branchiae in *Swima* species lacking bombs and other Acrocirridae (fig. S2, A to D).

The discovery of a clade of large, active, deep-sea annelids with unique morphology, bioluminescence, and high biomass emphasizes our limited knowledge of deep-sea pelagic and demersal communities.

References and Notes

1. Materials and methods are available as supporting material on Science Online.
2. K. J. Osborn, G. W. Rouse, *Mol. Phylogenet. Evol.* **49**, 386 (2008).
3. D. Deheyn *et al.*, *J. Mar. Biol. Assoc. U. K.* **80**, 179 (2000).
4. S. L. Bush *et al.*, *Biol. Bull.* **216**, 7 (2009).
5. Research supported by Scripps Institution of Oceanography, University of California President's Postdoctoral Fellowship, David and Lucile Packard Foundation, National Oceanic and Atmospheric Administration, WHOI, and the National Geographic Society. All GenBank and voucher accession numbers are listed in table S1.

Supporting Online Material

www.sciencemag.org/cgi/content/full/325/5943/964/DC1

Materials and Methods

SOM Text

Figs. S1 and S2

Table S1

Movies S1 to S3

18 February 2009; accepted 2 June 2009

10.1126/science.1172488

¹Scripps Institution of Oceanography, La Jolla, CA 92093, USA. ²Monterey Bay Aquarium Research Institute (MBARI), Moss Landing, CA 95039, USA. ³Department of Marine Ecology – Tjärnö, University of Göteborg, SE 452 96 Strömstad, Sweden. ⁴Woods Hole Oceanographic Institution (WHOI), Woods Hole, MA 02543, USA.

*To whom correspondence should be addressed. E-mail: kjosborn@ucsd.edu

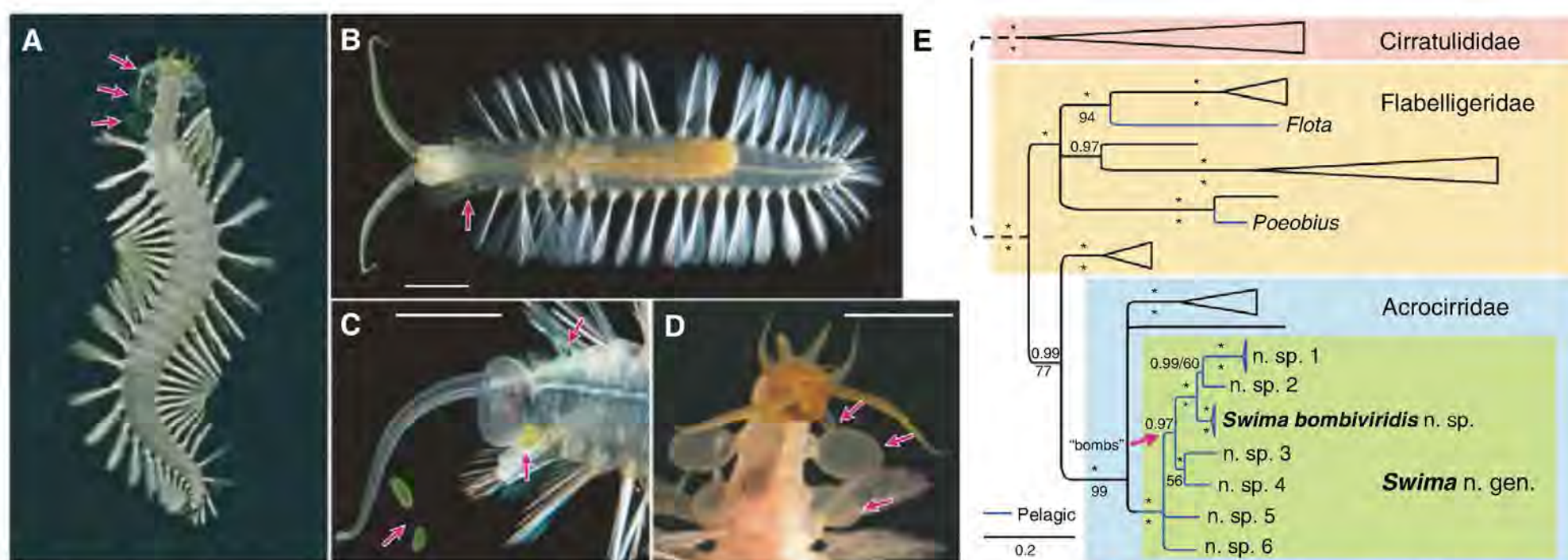


Fig. 1. (A) Video frame grab of a *Swima* sp. 3. Arrows indicate bombs throughout. [Credit: MBARI, 2006] (B) *Swima bombiviridis* n. gen. n. sp., dorsal view; note seven bombs. Scale bars indicate 5 mm. (C) Ventral view of *Swima* sp. 1 with three attached and two autotomized bombs. [Credit: Casey Dunn, 2007] (D) Ventral view of *Swima* sp. 3 showing three pairs of attached bombs. (E) Ninety-five percent majority rule consensus tree from

Bayesian analyses of five concatenated genes from cirratuliform annelids, showing *Swima* n. gen. as part of Acrocirridae. Blue branches indicate three separate pelagic lineages. Note that Flabelligeridae is paraphyletic. Support indicated as posterior probabilities above nodes and bootstraps from a parsimony analysis below. Asterisks indicate 1.0 or 100% support, respectively (detail, fig. S2).

DICER1 Mutations in Familial Pleuropulmonary Blastoma

D. Ashley Hill,^{1,2*} Jennifer Ivanovich,¹ John R. Priest,² Christina A. Gurnett,¹ Louis P. Dehner,¹ David Desruisseau,¹ Jason A. Jarzembowski,³ Kathryn A. Wikenheiser-Brokamp,⁴ Brian K. Suarez,¹ Alison J. Whelan,¹ Gretchen Williams,^{2,5} Dawn Bracamontes,^{1,2} Yoav Messinger,^{2,5} Paul J. Goodfellow¹

Pleuropulmonary blastoma (PPB) is a rare pediatric tumor of the lung that arises during fetal lung development and is often part of an inherited cancer syndrome [Online Mendelian Inheritance in Man (OMIM) 601200]. PPBs contain both epithelial and mesenchymal cells. Early in tumorigenesis, cysts form in lung airspaces, and these cysts are lined with benign-appearing epithelium. Mesenchymal cells susceptible to malignant transformation reside within the cyst walls and form a dense “cambium” layer beneath the epithelial lining. In a subset of patients, overgrowth of the mesenchymal cells produces a sarcoma, a transition that is associated with a poorer prognosis (1). The natural history of PPBs is consistent with a multistep genetic model of tumor progression (2).

About 20% of children with PPB have a family history of neoplasia, especially cystic nephroma of the kidney and rhabdomyosarcoma (3). We mapped the PPB locus to chromosome 14q with a family-based linkage study on four families with inherited predisposition to PPB (4) (figs. S1 and S2). Of 72 genes within the 7-Mb region of interest, *DICER1* was an attractive candidate because of its role in lung development. *DICER1* encodes a ~218-kD ribonuclease (RNase) III endonuclease that participates in the generation of small RNAs [microRNAs (miRNAs) and small interfering RNAs (siRNAs)] (5). miRNAs negatively regulate gene expression and have been implicated in multiple biological processes including stem cell maintenance, organogenesis, and oncogenesis. Conditional loss of *Dicer1* in the developing mouse lung results in cystic airways, disruption of branching morphogenesis, and mesenchymal expansion that resembles the early stage of PPB (6).

We identified heterozygous germline mutations in *DICER1* by sequencing genomic DNA

from affected members in each of 11 families (four included in the linkage study and seven additional families) (Fig. 1A, fig. S3, and table S1). In 10 of these families, the mutations result in proteins truncated proximal to the two carboxy-terminal RNase III functional domains in *DICER1* (Fig. 1B) and thus likely cause loss of function. The missense mutation [Leu¹⁵⁸³→Arg¹⁵⁸³ (L1583R)] detected in the 11th family (family C) affects an evolutionarily conserved amino acid, and the nonpolar to polar change was neither a previously reported sequence variant [National Center for Biotechnology Information Single Nucleotide Polymorphism (NCBI SNP) database Build 128], nor was it detected in 360 cancer-free

controls tested by Pyrosequencing (QIAGEN, Incorporated, Valencia, CA).

Apart from PPB-associated tumors in a subset of family members, the majority of obligate carriers with *DICER1* mutations are phenotypically normal, suggesting that loss of one *DICER1* allele is compatible with normal development and insufficient for tumor formation. Mice haploinsufficient for *Dicer1* also show no overt phenotypic abnormalities (7). *DICER1* immunohistochemistry of PPB tumors suggests expression from the wild-type allele is lost in tumor-associated epithelium in six of the seven families harboring PPBs with a residual epithelial cystic component but is retained in the mesenchymal tumor cells (Fig. 1C and fig. S5). *DICER1* is normally present in lung bronchial and alveolar epithelium throughout life. The areas of absent staining in the tumor epithelium were segmental in most cases but were clearly evident in areas overlying cambium layers. The genetic basis for this altered expression in epithelium is unknown, but the phenotype recapitulates that seen in the *Dicer1*^{−/−} mice. Interestingly, the tumor-associated epithelial cells lacking *DICER1* expression appeared to be normally differentiated.

On the basis of the loss of *DICER1* protein expression specifically in lung epithelium overlying PPB, we hypothesize that PPB may arise through a novel mechanism of non-cell-autonomous cancer initiation. Conceivably, loss of *DICER1* in developing lung epithelium alters miRNA-dependent regulation of diffusible growth factors that promote mesenchymal cell proliferation. Whether and how *DICER1* haploinsufficiency in the mesenchymal cells contributes to pathogenesis remain open questions.

References and Notes

1. D. A. Hill et al., *Am. J. Surg. Pathol.* **32**, 282 (2008).
2. J. R. Priest et al., *Cancer* **80**, 147 (1997).
3. J. R. Priest et al., *J. Pediatr.* **128**, 220 (1996).
4. Materials and methods are available as supporting material on Science Online.
5. D. P. Bartel, *Cell* **116**, 281 (2004).
6. K. S. Harris, Z. Zhang, M. T. McManus, B. D. Harfe, X. Sun, *Proc. Natl. Acad. Sci. U.S.A.* **103**, 2208 (2006).
7. S. Morita et al., *PLoS One* **4**, e4212 (2009).
8. The authors (D.A.H., P.J.G., J.R.P., and Y.M.) have filed a patent related to this work.

Supporting Online Material

www.sciencemag.org/cgi/content/full/1174334/DC1

Materials and Methods

SOM Text

Figs. S1 to S5

Tables S1 to S5

References

31 March 2009; accepted 17 June 2009

Published online 25 June 2009;

10.1126/science.1174334

Include this information when citing this paper.

¹Washington University Medical Center, St. Louis, MO 63110, USA. ²The International Pleuropulmonary Blastoma Registry, Children's Hospitals and Clinics of Minnesota, Minneapolis, MN 55404, USA. ³Children's Hospital of Wisconsin, Milwaukee, WI 53201, USA. ⁴Cincinnati Children's Hospital Medical Center, Cincinnati, OH 45229, USA. ⁵Children's Hospitals and Clinics of Minnesota, Minneapolis, MN 55404, USA.

*To whom correspondence should be addressed. E-mail: dashill@cnmc.org

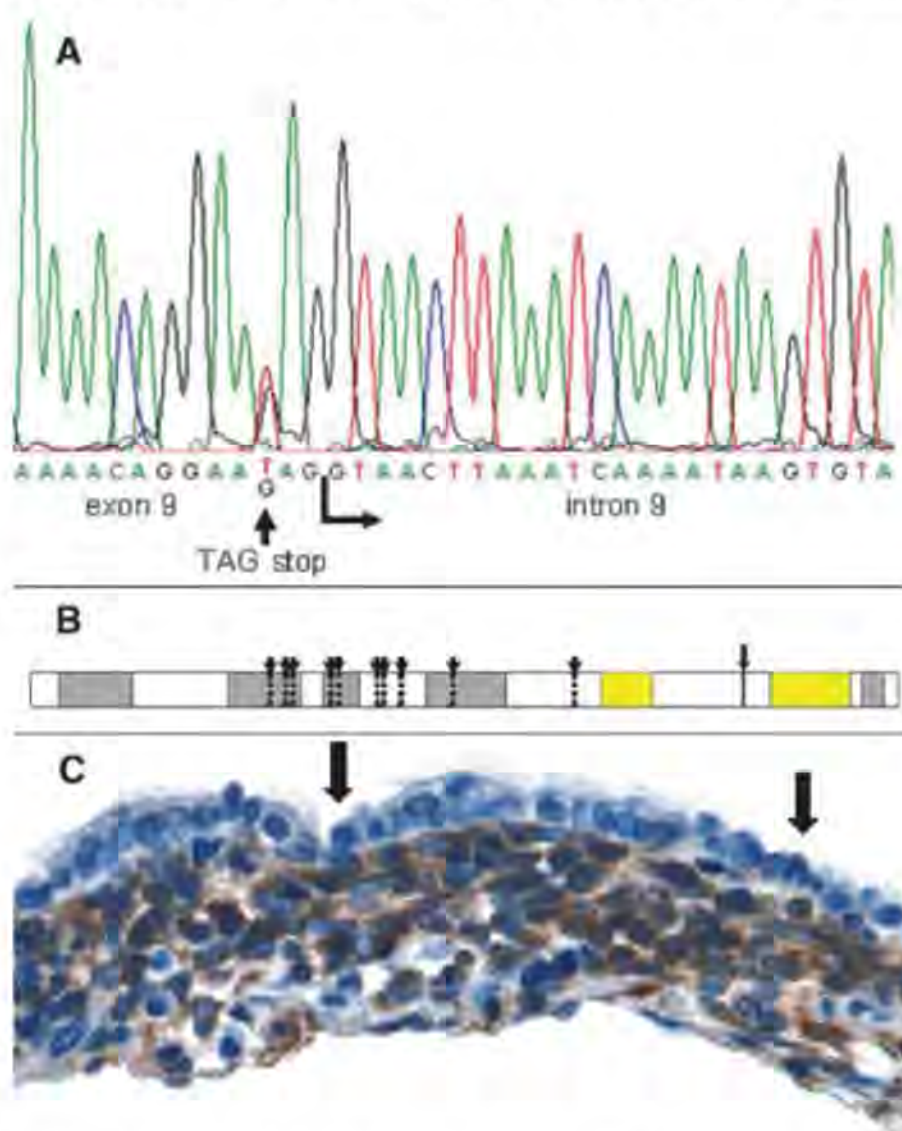


Fig. 1. Germline *DICER1* mutations and *DICER1* protein expression in PPB. (A) *DICER1* sequence alteration in one of the families in the linkage study. (B) Schematic of *DICER1* protein showing the locations of *DICER1* mutations in the 11 PPB families. Vertical dotted lines with arrows indicate truncating mutations or insertions or deletions in 10 families, all occurring proximal to the RNase III domains (yellow). The larger arrow with the solid line marks the missense mutation, which occurs between the RNase III domains. (C) *DICER1* protein is not detectable in benign-appearing tumor-associated epithelium (arrows) but is present in the mesenchymal tumor cells forming the underlying cambium layer (anti-*DICER1* with brown chromogen and hematoxylin counterstain; original magnification 400×).

Formation of the First Peptide Bond: The Structure of EF-P Bound to the 70S Ribosome

Gregor Blaha,^{1*} Robin E. Stanley,^{1*} Thomas A. Steitz^{1,2,3†}

Elongation factor P (EF-P) is an essential protein that stimulates the formation of the first peptide bond in protein synthesis. Here we report the crystal structure of EF-P bound to the *Thermus thermophilus* 70S ribosome along with the initiator transfer RNA *N*-formyl-methionyl-tRNA_i (fMet-tRNA_i^{fMet}) and a short piece of messenger RNA (mRNA) at a resolution of 3.5 angstroms. EF-P binds to a site located between the binding site for the peptidyl tRNA (P site) and the exiting tRNA (E site). It spans both ribosomal subunits with its amino terminal domain positioned adjacent to the aminoacyl acceptor stem and its carboxyl terminal domain positioned next to the anticodon stem-loop of the P site-bound initiator tRNA. Domain II of EF-P interacts with the ribosomal protein L1, which results in the largest movement of the L1 stalk that has been observed in the absence of ratcheting of the ribosomal subunits. EF-P facilitates the proper positioning of the fMet-tRNA_i^{fMet} for the formation of the first peptide bond during translation initiation.

Elongation factor P (EF-P) is encoded by the *efp* gene in *Escherichia coli* (1) and is conserved in all eubacteria (2, 3). Previous studies suggest that EF-P is essential for cell viability in *E. coli* (1). Despite its stimulatory effects on peptide bond formation between ribosome-bound initiator transfer RNA *N*-formyl-methionyl-tRNA_i (fMet-tRNA_i^{fMet}) and puromycin (4) and *N*-acetyl-Phe tRNA^{Phe}-primed poly(U)-directed poly(Phe) synthesis (5), EF-P is not a required component of minimal in vitro translation systems (6). EF-P is present in the cell at about 0.1 copies per ribosome, a ratio similar to that of the initiation factors (7, 8). EF-P binds stoichiometrically to each of the ribosomal subunits and to the 70S ribosome. The ratio of bound EF-P to polysomes declines with the size of polysomes, consistent with its involvement in the initial stages of protein synthesis (9). The crystal structure of EF-P revealed that the protein is composed of three β -barrel domains and has an overall L shape, reminiscent of a tRNA (10). The only known function of EF-P is a stimulatory effect in vitro on the formation of the first peptide bond.

Archaea and eukarya have a factor, known as eukaryotic translation initiation factor 5A (eIF5A, previously called eIF4D), that shares sequence and structural similarity with the first two domains of EF-P (10). Like EF-P, eIF5A stimulates the formation of peptide bonds between initiator tRNA and puromycin in vitro but has no effect on the rate of poly(U)-dependent

poly(Phe) synthesis (11). eIF5A is the only protein known to contain hypusine, an amino acid derived from lysine through posttranslational modification by deoxyhypusine synthase and deoxyhypusine hydroxylase (12). The hypusine modification has been identified in all analyzed archaea and eukarya but not in any eubacteria (2). However, a recent mass spectrometric analysis of endogenous EF-P from *E. coli* indicates a possible modification with a molecular mass of 143 daltons (9). Putative deoxyhypusine synthase-related genes have also been identified in several eubacterial species, although not in *E. coli* or *Thermus thermophilus* (13).

Alignments of the sequences of eIF5A from several species reveal that the residues surrounding the lysine residue that is modified to hypusine are extremely well conserved (12). In yeast, a K51R mutation in eIF5A, in which lysine at position 51 is replaced by arginine (14), not only inhibits hypusine formation but also cannot rescue eIF5A knockouts (15) and has reduced affinity for the ribosome (16). In addition, both eIF5A and deoxyhypusine synthase are essential in yeast (12). Like EF-Ps, the in vivo role of eIF5A in translation is still poorly understood; however, eIF5A has been linked to many other roles in the cell [reviewed in (12)].

Here, we present the crystal structure of EF-P bound to the 70S ribosome along with the initiator tRNA and a short fragment of mRNA. EF-P binds to the 70S ribosome at a site located between the binding sites for the peptidyl tRNA (P site) and the exiting tRNA (E site) and appears to stabilize the positioning of the fMet-tRNA_i^{fMet} in the P site.

Overview of the structure. Crystals of the *T. thermophilus* 70S ribosome with bound mRNA, initiator tRNA, and EF-P diffracted to 3.5 Å resolution (17). The structure was determined by molecular replacement by using a pub-

lished model of the 70S ribosome with the tRNA and mRNA ligands removed (18). A difference electron density map calculated with the use of $F_{\text{obs}} - F_{\text{calc}}$ amplitudes showed density for the initiator tRNA, mRNA, and EF-P, as well as density arising from movement of the L1 stalk. The initiator tRNA, mRNA, EF-P, and the repositioned L1 stalk were built, and the model was refined to an $R_{\text{work}}/R_{\text{free}}$ of 25.2/30.2%.

Contrary to recent biochemical studies that were interpreted to suggest that EF-P binds to the aminoacyl tRNA-binding site (A site) (9), and despite its resemblance to a tRNA, EF-P does not bind to the ribosome in a classical tRNA-binding site, but rather binds at a distinct position that is adjacent to the P-site tRNA, between the P and E sites. The L1 stalk also undergoes a major conformational change that positions the ribosomal protein L1 in the E site to interact with EF-P (Fig. 1). EF-P spans both ribosomal subunits and contacts the initiator tRNA near the anticodon stem-loop on the 30S subunit, the D-loop, and the acceptor stem on the 50S subunit (Fig. 1). Domain I of EF-P binds next to the acceptor stem of the initiator tRNA in the P site, and domain III of EF-P binds adjacent to the anticodon stem-loop of the P-site tRNA and partially overlaps the E site. Domain II of EF-P is sandwiched between domains I and II of the ribosomal protein L1. As previously noted, domain II of EF-P has an OB fold, which is characteristic for many oligonucleotide-binding proteins (10). However, the majority of its surface is negatively charged and does not interact with tRNA, but rather fits into a positively charged pocket of L1 (Fig. 2).

The initiator tRNA bound in the P site displays the same conformation as that observed in the P-site tRNA of the 2.8 Å resolution structure of the *T. thermophilus* 70S ribosome with bound mRNA and tRNAs, which is distorted when compared with that of the crystal structure of unliganded yeast tRNA^{Phe} (18). The superposition of the P-site tRNA from our structure onto that of the 2.8 Å resolution structure yields a root mean square deviation of less than 1.0 Å for the entire phosphate backbone; thus, even though EF-P binds adjacent to the tRNA, it does not induce any significant conformational changes.

Interactions near the peptidyl transferase center (PTC). A loop of domain I of EF-P makes numerous interactions with the CCA end of the acceptor stem of the initiator tRNA. The conserved arginine-lysine (R32) residue that is modified to hypusine in eukaryotes lies at the tip of this positively charged loop, and residues Q26 and K29 are within hydrogen-bonding distance of the 2' hydroxyl groups of the G70 and A72 (Fig. 3). There are also additional likely hydrogen bonds between the amide nitrogens of G31 and R32 to the phosphate of A73 and the sugar of C74, respectively (Fig. 3). R32 is close to the PTC, and in one copy of the asymmetric unit, it interacts with C75 of the tRNA and the phosphates of C2064 and C2065 of the 23S ribosomal

¹Departments of Molecular Biophysics and Biochemistry, Yale University, New Haven, CT 06520, USA. ²Department of Chemistry, Yale University, New Haven, CT 06520, USA. ³Howard Hughes Medical Institute, Yale University, New Haven, CT 06520-8114, USA.

*These authors contributed equally to this work.

†To whom correspondence should be addressed. E-mail: thomas.steitz@yale.edu

RNA (rRNA) (Fig. 4). Another residue in this loop, K29, which is well conserved in both EF-P and eIF5A, is within hydrogen-bonding distance of the ribose of G2253 in the P-loop of the 23S rRNA (Fig. 4). Residues Q28, K36, and H27 of EF-P are also within possible hydrogen-bonding distances of 2594, 2597, and 2254 of the 23S rRNA, respectively. All these interactions suggest that EF-P may play a role in correctly positioning the P-site tRNA or providing additional stabilization of the initiator tRNA in the P site. It appears that EF-P has an indirect, rather than direct, effect on peptide bond formation, because neither the initiator tRNA in the P site nor the PTC has its conformation altered by the presence of EF-P.

Even though residue R32 in *T. thermophilus* is close to the PTC, it is still too distant to par-

ticipate directly in peptide bond formation. However, in eukaryotes, the corresponding hypusine residue has a much longer side chain than either arginine or lysine and, therefore, could extend closer to the active site (Fig. 4). It was previously suggested that the hypusine modification could stabilize the initiator tRNA in the P site (2). Because initiator tRNAs in eukaryotes are not formylated, perhaps the hypusine modification replaces the function of the formyl group of the aminoacylated initiator tRNA (19). This is further supported by in vitro experiments that show that eIF5A lacking hypusine does not stimulate methionyl-puromycin synthesis, but after in vitro modification to hypusine, the stimulatory effect is fully restored (20). Aside from its recognition by initiation factor IF2, the role of formylation of the initiator tRNA in

eubacteria is unclear, as not all eubacteria require the formylase gene to support growth (21).

Interactions of domain III with the 30S subunit at the P- or E-site gate. Domain III of EF-P is well conserved in eubacteria, binds next to the anticodon stem-loop of the initiator tRNA, and partially occupies the E site of the small ribosomal subunit (Fig. 1). A loop of domain III extends toward the mRNA; however, its tip is disordered in both complexes of the asymmetric unit, which prevented us from drawing any conclusions about possible interactions between EF-P and the mRNA. Because domain III contacts only the small ribosomal subunit and is missing from eIF5A, eIF5A must bind specifically to the 60S subunit and does not span both ribosomal subunits.

The interactions made by domain III may help to prevent premature movement of the initiator tRNA to the E site. Residues Y180 and R183 of domain III stabilize the A-minor interactions between two G-C base pairs in the anticodon stem-loop of the initiator tRNA and the bases of residues A1339 and G1338 of the 16S rRNA (Fig. 5). Because these A-minor interactions have to break during translocation, A1339 and G1338 have been proposed to function as a “gate” between the P and E sites (18). These interactions of EF-P may enhance this gate and stabilize the fMet-tRNA^{fMet} in the P site. Although domain III is missing from eIF5A, we cannot exclude the possibility that its function is provided by another protein in eukaryotes.

Movement of the L1 stalk. The L1 stalk is a highly dynamic component of the 50S subunit and consists of three helices from the 23S rRNA (H76 to H78) and the ribosomal protein L1. Although *E. coli* lacking L1 is viable, ribosomes lacking L1 display only about 50% of the activity of wild-type ribosomes in vitro (22), which can be fully restored by adding purified L1 (23). The flexibility of the L1 stalk presumably accounts for its being disordered in most high-resolution structures of the ribosome. Only in the *T. thermophilus* 70S structures with bound tRNAs is the majority of the stalk ordered, seemingly because its interaction with the tRNA bound in the E site fixes the position of the rRNA of the L1 stalk (18, 24, 25). The superposition of the 23S rRNA from the E site-bound 70S structures of *T. thermophilus* with the 23S rRNA of both the *Deinococcus radiodurans* large ribosomal subunit and the *E. coli* 70S reveals a 30° rotation of the L1 stalk toward the E site upon binding of a tRNA into the E site [reviewed in (26)].

An even larger movement of the L1 stalk has been observed by cryo-electron microscopy (cryo-EM) studies of ribosomes with stalled EF-G or eEF2. These complexes capture the ribosome in a ratcheted state, in which the small ribosomal subunit is rotated counterclockwise with respect to the large ribosomal subunit. The guanosine triphosphatase-associated center of the large ribosomal subunit changes its confor-

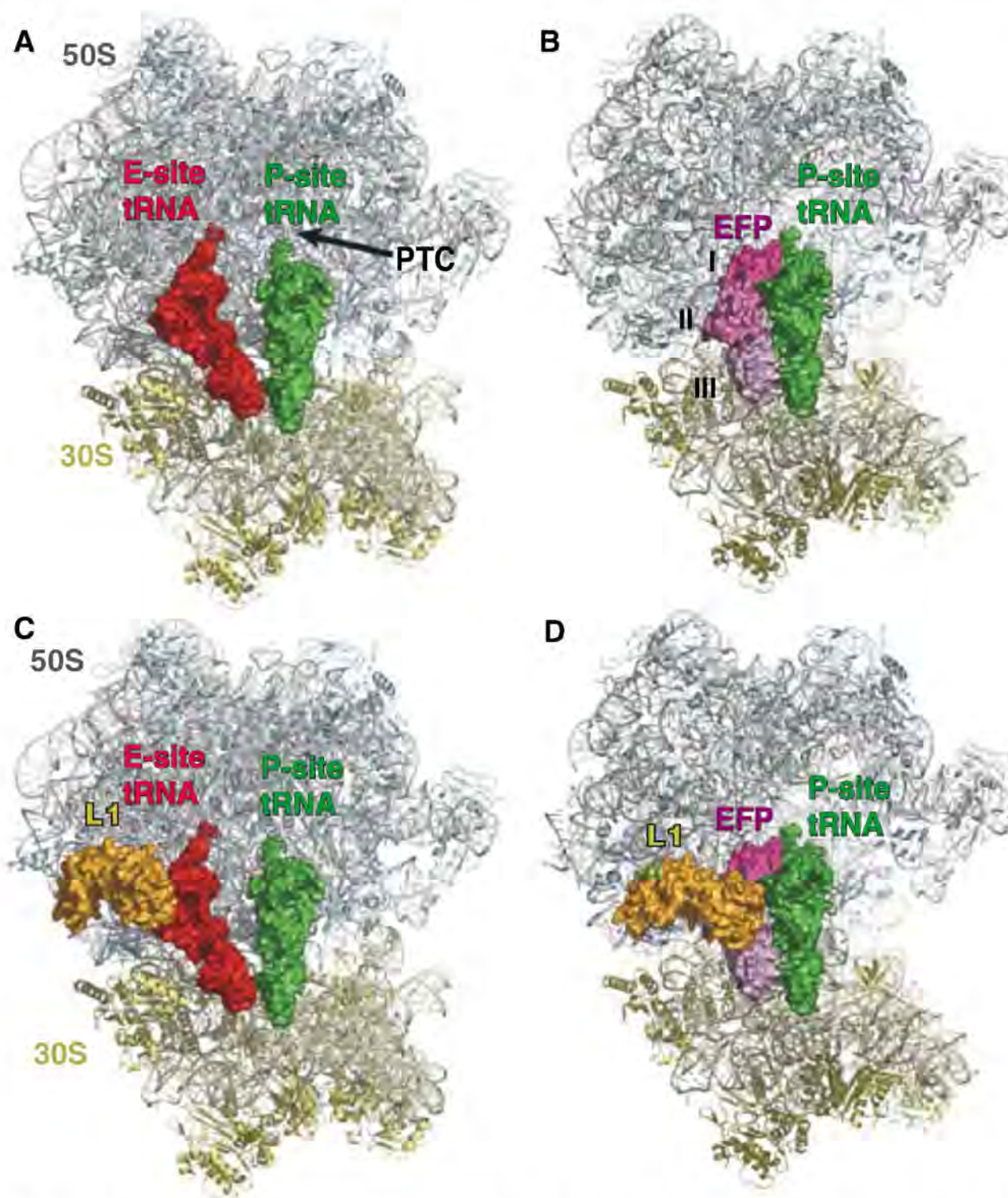


Fig. 1. The structure of EF-P bound to the ribosome. (A) Overview of the E- and P-site tRNAs bound to the 70S ribosome [coordinates were taken from the Protein DataBank (PDB) ID 2j00 and 2j01]. The 50S subunit is colored gray, the 30S subunit is colored yellow, the E-site tRNA is shown in red, and the P-site tRNA is shown in green as a surface representation. Portions of the 70S ribosome were omitted for clarity. (B) Overview of EF-P and P-site tRNA-binding in the 70S ribosome. The 50S, 30S, and P-site tRNA are colored as in (A), and EF-P is shown as a surface representation in shades of magenta to indicate the different domains (I, II, and III) of the protein. (C) Same as (A), but the ribosomal protein L1 is also shown as a surface representation in gold. (D) Same as (B), but L1 is also shown as a surface representation in gold, illustrating the large movement of L1 from its location in (C).

mation, and the L1 stalk dramatically moves toward the E site. The L1 stalk movement is larger than the 30° motion observed between the different crystal structures. The additional motion, about the base of helix H76 of the 23S rRNA, enables the L1 stalk to interact with a tRNA bound in the hybrid P/E position, which suggests an active role for the L1 stalk in tRNA translocation and release of the E site-bound tRNA (27–29).

The structure of the 70S ribosome with EF-P bound exhibits the largest movement of the L1 stalk seen in a crystal structure (Fig. 6 and movie S1). Its movement into the E site in the presence of EF-P is even larger than that observed in the structure of *T. thermophilus* 70S ribosome with a tRNA bound in the E site. Without any disruption of the protein-RNA interface, the L1 stalk is bent and rotated at helix H76 to reposition the ribosomal protein L1 into the E site. With the exception of the repositioning of the L1 stalk, no other major conformational change is observed within the ribosome. The slight differences in the orientation of the subunits compared with the 2.8 Å structure of the *T. thermophilus* 70S ribosome with bound mRNA and tRNA (18) are within the variations seen between the two structures of the 70S ribosome in the asymmetric unit.

The observed movement of the L1 stalk in the EF-P complex with the 70S ribosome appears relevant to the stalk movement associated with translocation. Both cryo-EM and single-molecule studies suggest that the L1 stalk reaches all the way to the P-site tRNA in its P/E hybrid state before translocation concurrent with the counter-clockwise rotation of the small ribosomal subunit (28, 30–32). This interaction between the stalk and the P-site tRNA persists through translocation of the tRNA to the E site until its release from the ribosome. The rRNA of the L1 stalk interacts with bases at the ends of the T- and D-loops of the E-site tRNA (18). If the same interactions exist between the stalk and the P-site tRNA, the stalk would have to move even farther into the E site than is observed in our EF-P-bound 70S ribosome structure in order to reach the P site or hybrid P/E site tRNA, which may only be achievable with the ratchet motion. The motion of the L1 stalk toward the E site seen in our structure clearly is not coupled to the counter-clockwise rotation of the small subunit, as has been observed during translocation, perhaps because the distance it moves is less and it interacts through protein L1, rather than the stalk rRNA.

Because EF-P is completely buried within the ribosome, the L1 stalk must move to allow its dissociation and to make the E site accessible for the translocation of the initiator tRNA. Previous biochemical experiments have demonstrated that the initiator tRNA has a lower propensity to move into the P/E hybrid state than deacylated elongator tRNAs and that the rate of EF-G catalyzed translocation of the initiator tRNA^{Met} is slower (by several factors) than with the elongator tRNA^{Met} (31, 33). Release of EF-P

Fig. 2. The interaction interfaces between EF-P, L1, and the initiator tRNA. **(A)** Ribosomal protein L1 (gold), the P-site tRNA (green), and the mRNA (cyan) are shown as cartoon representations, and EF-P is illustrated as an electrostatic surface, with negatively charged patches displayed in red and positively charged patches within contact of the P-site tRNA displayed in blue. **(B)** Same as in (A) but rotated 240° with EF-P (magenta) shown as a cartoon representation and the ribosomal protein L1 shown as an electrostatic surface, illustrating the charge complementarity between the interface of EF-P and L1.

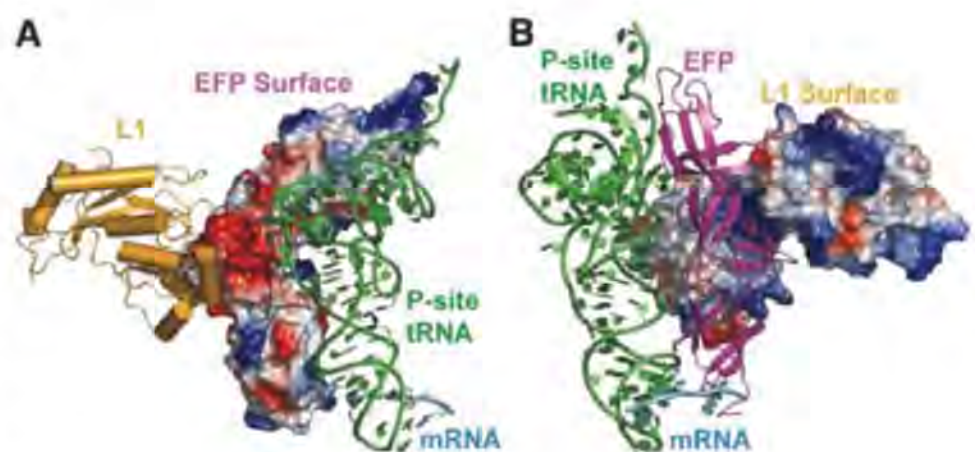
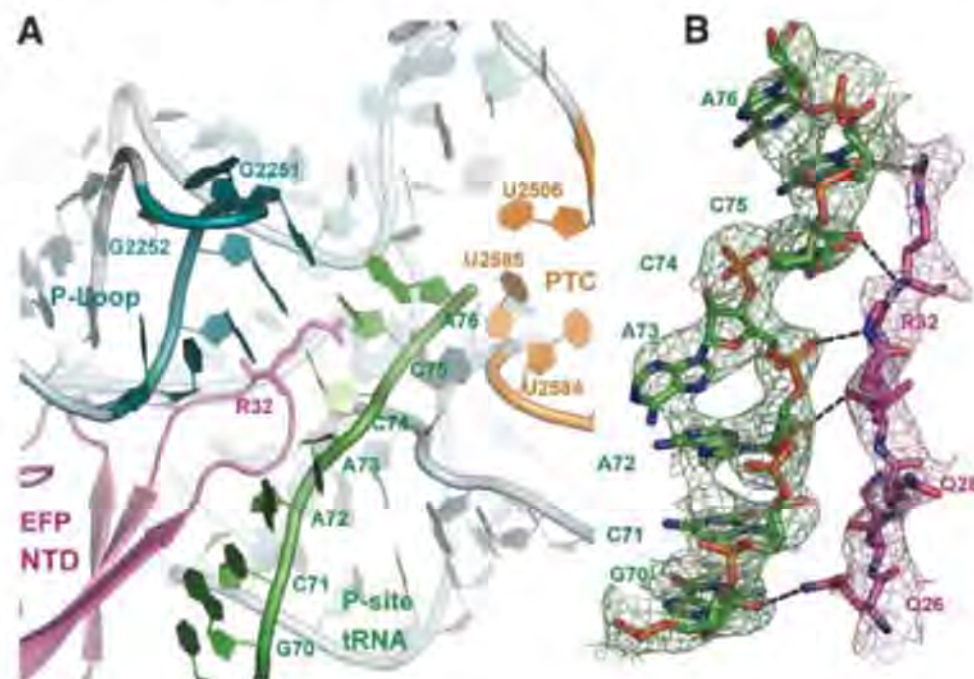


Fig. 3. Interactions near the PTC. **(A)** Overview of the N-terminal domain (NTD) of EF-P and its interactions near the PTC of the large ribosomal subunit. The 23S rRNA is colored gray, with the exception of the P-loop (bluish green) and residues making up the PTC (orange). EF-P is colored magenta, and the acceptor arm of the P-site tRNA is shown in green. EF-P approaches the PTC of the 50S subunit but is too distant to participate directly in catalysis. **(B)** Unbiased difference Fourier map showing the density for the acceptor arm of the P-site tRNA (green) and the loop of the NTD of EF-P containing the R32 residue. Potential hydrogen bonds between the side chains of EF-P and the tRNA are shown as black dashes.



Unbiased difference Fourier map showing the density for the acceptor arm of the P-site tRNA (green) and the loop of the NTD of EF-P containing the R32 residue. Potential hydrogen bonds between the side chains of EF-P and the tRNA are shown as black dashes.

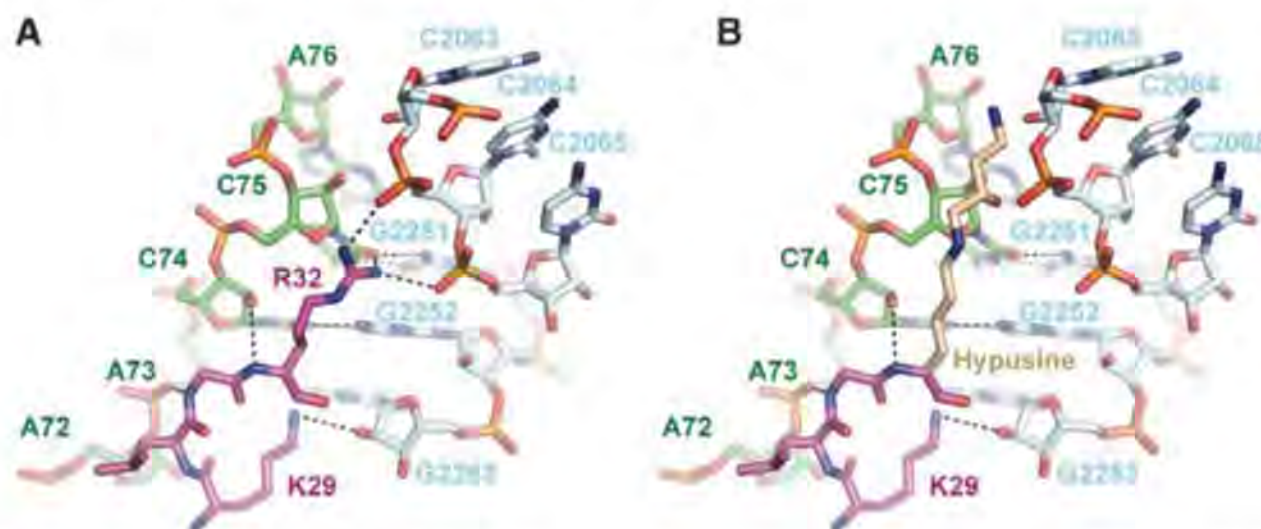


Fig. 4. Hypusine homology model. **(A)** Close-up view of the interactions between R32 and K29 of EF-P (magenta) with the CCA end of the tRNA (green) and the 23S rRNA (light blue). Putative hydrogen bonds of R32 with the ribose of C75 and the phosphate of C2064, as well as of K29 with the ribose of G2253, are shown as black dashes. Hydrogen bonds of C74 with G2552 and of C75 with G2251 are also shown. **(B)** R32 was replaced by a hypothetical model structure of hypusine (light brown). In an elongated conformation, the hypusine side chain could reach into the PTC.

from the ribosome could be before or coupled with the EF-G catalyzed translocation of the deacylated initiator tRNA into the E site.

Correct positioning of the initiator tRNA. The 3.5 Å resolution structure of EF-P bound to the 70S ribosome in complex with the initiator

tRNA provides a structural basis for understanding the role that EF-P plays in promoting the formation of the first peptide bond, the final step in the initiation phase of protein synthesis. During initiation, only the initiator tRNA, which is distinctly different from elongator tRNAs [reviewed

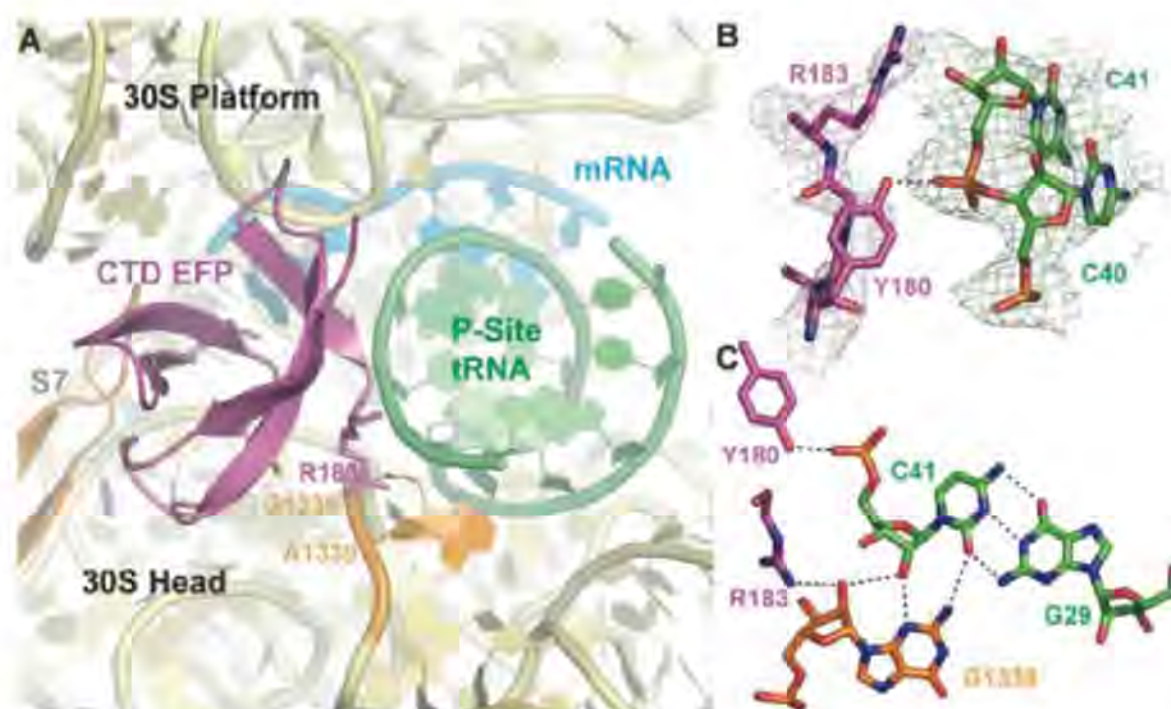


Fig. 5. Interactions between EF-P and the 30S subunit. **(A)** Overview of the interactions made by the P-site tRNA (green) and C-terminal domain of EF-P (magenta) with the small ribosomal subunit (rRNA, yellow; S7 protein, brown). The two key bases of the small ribosomal subunit that act as a gate between the P and E sites are colored orange. **(B)** Unbiased difference Fourier map showing the density for the terminal residues of EF-P and C39-C41 of the initiator tRNA. Potential hydrogen bonds between R183 and Y180 and the tRNA are illustrated as black dashes. **(C)** R138 of EF-P stabilizes the type II A-minor interaction between G1338 and the C41-G29 base pair of the tRNA. Putative hydrogen bonds are shown as black dashes.

in (34)], occupies the P site and no deacylated tRNA is bound in the E-site tRNA. All the interactions between EF-P and the fMet-tRNA_i^{fMet} are not specific for the initiator tRNA; this suggests that EF-P binding to the ribosome is not restricted to the initiator tRNA, consistent with previous biochemical data (5). A recent publication concludes that eIF5A also forms nonspecific contacts with tRNAs in yeast, because it stimulates the first, as well as subsequent, peptidyl-transfer reactions during protein synthesis (20). In our current structure, the positions of the domains 1 and 2 of EF-P that are homologous to eIF5A exclude the simultaneous binding of eIF5A and a tRNA in the E site.

The structure presented here suggests that a major role of EF-P is to help correctly orient the entire P-site tRNA and to restrict the mobility of the aminoacyl arm in order to facilitate peptide bond formation. Similar functions have been attributed to ribosomal proteins L16 and L27 for the correct positioning of the A-site tRNA (35). Although ribosomes lacking L16 are severely impaired in peptide bond formation (36), the first peptide bond formation can still be stimulated by EF-P (37). The interactions observed between L16 and the A-site tRNA suggest that it stabilizes the binding of the A-site tRNA (35). The presence of L27 stimulates the reaction of puromycin with fMet-tRNA_i^{fMet} by the same magnitude as EF-P (38); however, in contrast to EF-P, L27 also affects all subsequent peptidyl transfer reactions. Ribosomes lacking L27 are impaired in binding of the A-site tRNA (38), and removal of even just the first three amino acids reduces the rate of peptide bond formation (39). The high-resolution structure of the 70S ribosome with tRNAs bound in the A and P sites reveals interactions between

the N terminus of L27 and the CCA tail of both the P- and A-site tRNAs (35). The N-terminal residues of L27 are disordered in the structure presented here, perhaps because of the absence of an A-site tRNA. The stabilization of the CCA tail of the A-site tRNA by the N terminus of L27 could explain the increased affinity of the A site for aminoacylated tRNA in the presence of L27, as well as the stimulatory effect of L27 on protein synthesis (38). Similarly, the stabilization of the CCA tail of the P-site tRNA by EF-P could explain the increased puromycin reactivity of fMet-tRNA_i^{fMet}. Whether this stabilization function is subsequently taken up by the nascent polypeptide chain is unknown.

The initiation of translation in eubacteria is a multistep process that involves the formation of several intermediate complexes with different compositions and conformations (40). Structures of initiation complexes derived from cryo-EM studies have revealed that, during the process of initiation, the fMet-tRNA_i^{fMet} adopts several different conformations on both the 30S subunit and the 70S ribosome before finally reaching its proper position in the P/P state (40–42). By stabilizing the P/P state of the initiator tRNA, EF-P could shift initiation toward the first elongation step of protein translation.

Conclusions. The structure of the EF-P complex with the 70S ribosome reveals the detailed interactions between EF-P and the 70S ribosome, initiator tRNA, and the ribosomal protein L1. The essential role of EF-P in the cell may be to correctly position the fMet-tRNA_i^{fMet} in the P site for the first step of peptide bond formation by making several interactions with the backbone of the tRNA. Because eIF5A shows high structural similarity to EF-P, the conclusions drawn for

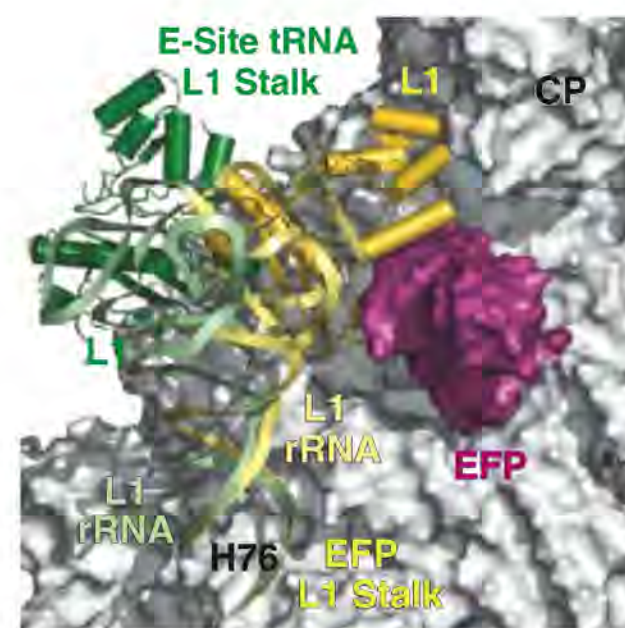


Fig. 6. Movement of the L1 stalk. The L1 stalk from the structure of the 70S ribosome with bound EF-P is shown in gold, and the 70S structure from *T. thermophilus* 70S ribosome with a bound E-site tRNA (PDB ID 2j01) is shown in green. The superposition was based on the entire 23S rRNA between the 70S structures, excluding the L1 stalk. The large ribosomal subunit (gray) and EF-P (magenta) are shown as surface representations. CP indicates the central protuberance of the large ribosomal subunit.

EF-P likely also apply to eIF5A's role in the rate enhancement of the formation of the first peptide bond in eukarya.

References and Notes

1. H. Aoki, K. Dekany, S. L. Adams, M. C. Ganoza, *J. Biol. Chem.* **272**, 32254 (1997).
2. N. C. Kyrpides, C. R. Woese, *Proc. Natl. Acad. Sci. U.S.A.* **95**, 224 (1998).
3. M. C. Ganoza, M. C. Kiel, H. Aoki, *Microbiol. Mol. Biol. Rev.* **66**, 460 (2002).
4. B. R. Glick, M. C. Ganoza, *Proc. Natl. Acad. Sci. U.S.A.* **72**, 4257 (1975).
5. M. C. Ganoza, H. Aoki, *Biol. Chem.* **381**, 553 (2000).
6. Y. Shimizu *et al.*, *Nat. Biotechnol.* **19**, 751 (2001).
7. J. R. Cole, C. L. Olsson, J. W. Hershey, M. Grunberg-Manago, M. Nomura, *J. Mol. Biol.* **198**, 383 (1987).
8. G. An, B. R. Glick, J. D. Friesen, M. C. Ganoza, *Can. J. Biochem.* **58**, 1312 (1980).
9. H. Aoki *et al.*, *FEBS J.* **275**, 671 (2008).
10. K. Hanawa-Suetsugu *et al.*, *Proc. Natl. Acad. Sci. U.S.A.* **101**, 9595 (2004).
11. R. Benne, M. L. Brown-Luedi, J. W. Hershey, *J. Biol. Chem.* **253**, 3070 (1978).
12. C. F. Zanelli, S. R. Valentini, *Amino Acids* **33**, 351 (2007).
13. C. Brochier, P. Lopez-Garcia, D. Moreira, *Gene* **330**, 169 (2004).
14. Single-letter abbreviations for the amino acid residues are as follows: A, Ala; C, Cys; D, Asp; E, Glu; F, Phe; G, Gly; H, His; I, Ile; K, Lys; L, Leu; M, Met; N, Asn; P, Pro; Q, Gln; R, Arg; S, Ser; T, Thr; V, Val; W, Trp; and Y, Tyr.
15. J. Schnier, H. G. Schwelberger, Z. Smit-McBride, H. A. Kang, J. W. Hershey, *Mol. Cell. Biol.* **11**, 3105 (1991).
16. D. L. Jao, K. Y. Chen, *J. Cell. Biochem.* **97**, 583 (2006).
17. Materials and methods are available as supporting material on Science Online.
18. M. Selmer *et al.*, *Science* **313**, 1935 (2006).
19. J. W. Hershey, Z. Smit-McBride, J. Schnier, *Biochim. Biophys. Acta* **1050**, 160 (1990).
20. P. Saini, D. E. Eyler, R. Green, T. E. Dever, *Nature* **459**, 118 (2009).
21. D. T. Newton, C. Creuzenet, D. Mangroo, *J. Biol. Chem.* **274**, 22143 (1999).
22. A. R. Subramanian, E. R. Dabbs, *Eur. J. Biochem.* **112**, 425 (1980).
23. G. Sander, *J. Biol. Chem.* **258**, 10098 (1983).

24. A. Korostelev, S. Trakhanov, M. Laurberg, H. F. Noller, *Cell* **126**, 1065 (2006).
25. M. M. Yusupov *et al.*, *Science* **292**, 883 (2001).
26. A. Korostelev, H. F. Noller, *Trends Biochem. Sci.* **32**, 434 (2007).
27. C. M. Spahn *et al.*, *Cell* **118**, 465 (2004).
28. M. Valle *et al.*, *Cell* **114**, 123 (2003).
29. S. R. Connell *et al.*, *Mol. Cell* **25**, 751 (2007).
30. S. R. Connell *et al.*, *Nat. Struct. Mol. Biol.* **15**, 910 (2008).
31. P. V. Cornish *et al.*, *Proc. Natl. Acad. Sci. U.S.A.* **106**, 2571 (2009).
32. J. Fei, P. Kosuri, D. D. MacDougall, R. L. Gonzalez Jr., *Mol. Cell* **30**, 348 (2008).
33. S. Dorner, J. L. Brunelle, D. Sharma, R. Green, *Nat. Struct. Mol. Biol.* **13**, 234 (2006).
34. B. S. Laursen, H. P. Sorensen, K. K. Mortensen, H. U. Sperling-Petersen, *Microbiol. Mol. Biol. Rev.* **69**, 101 (2005).
35. R. M. Voorhees, A. Weixlbaumer, D. Loakes, A. C. Kelley, V. Ramakrishnan, *Nat. Struct. Mol. Biol.* **16**, 528 (2009).
36. V. G. Moore, R. E. Atchison, G. Thomas, M. Moran, H. F. Noller, *Proc. Natl. Acad. Sci. U.S.A.* **72**, 844 (1975).
37. H. Aoki, S. L. Adams, M. A. Turner, M. C. Ganoza, *Biochimie* **79**, 7 (1997).
38. I. K. Wower, J. Wower, R. A. Zimmermann, *J. Biol. Chem.* **273**, 19847 (1998).
39. B. A. Maguire, A. D. Beniaminov, H. Ramu, A. S. Mankin, R. A. Zimmermann, *Mol. Cell* **20**, 427 (2005).
40. A. Simonetti *et al.*, *Cell. Mol. Life Sci.* **66**, 423 (2009).
41. G. S. Allen, A. Zavialov, R. Gursky, M. Ehrenberg, J. Frank, *Cell* **121**, 703 (2005).
42. A. Simonetti *et al.*, *Nature* **455**, 416 (2008).
43. We thank the staff at the Advanced Photon Source beamline 24-ID and at the National Synchrotron Light Source beamline X29 for help during data collection and the staff at the Center for Structural Biology facility at Yale University for computational support. We also thank I. Lomakin for providing us with methionyl-tRNA synthetase (MetRS) and U. L. RajBhandary

and K. H. Nierhaus for the overexpression plasmids of methionyl-tRNA formyltransferase (MTF) and the initiator tRNA, respectively. This work was supported by NIH grant GM22778 (to T.A.S.). The coordinates for both copies of the 70S in the asymmetric unit have been deposited in the Research Collaboratory for Structural Bioinformatics Protein Data Bank with accession numbers 3HUW, 3HUX, 3HUY, and 3HUZ. T.A.S. owns stock in and is on the advisory board of Rib-X Pharmaceuticals, Inc., which does structure-based drug design targeted at the ribosome.

Supporting Online Material

www.sciencemag.org/cgi/content/full/325/5943/966/DC1

Materials and Methods

Table S1

References

Movie S1

4 May 2009; accepted 2 July 2009

10.1126/science.1175800

REPORTS

Exploring Dark Matter with Milky Way Substructure

Michael Kuhlen,^{1*} Piero Madau,² Joseph Silk³

The unambiguous detection of dark matter annihilation in our Galaxy would unravel one of the most outstanding puzzles in particle physics and cosmology. Recent observations have motivated models in which the annihilation rate is boosted by the Sommerfeld effect, a nonperturbative enhancement arising from a long-range attractive force. We applied the Sommerfeld correction to Via Lactea II, a high-resolution *N*-body simulation of a Milky Way-sized galaxy, to investigate the phase-space structure of the galactic halo. We found that the annihilation luminosity from kinematically cold substructure could be enhanced by orders of magnitude relative to previous calculations, leading to the prediction of gamma-ray fluxes from as many as several hundred dark clumps that should be detectable by the Fermi satellite.

In the standard cold dark matter (CDM) paradigm of structure formation, a weakly interacting massive particle (WIMP) with a mass m_χ of 100 GeV to 10 TeV ceases to annihilate when the universe cools to a temperature of $T_f \sim m_\chi/20$, about 1 ns after the Big Bang. A thermally averaged cross section at freeze-out of $\langle\sigma v\rangle_0 \approx 3 \times 10^{-26} \text{ cm}^3 \text{ s}^{-1}$ results in a relic abundance consistent with observations (1). Perturbations in the dark matter density are amplified by gravity after the universe becomes matter-dominated, around 10,000 years after the Big Bang; the smallest structures (“halos”) collapse early, when the universe is very dense, and merge to form larger and larger systems over time. Today, galaxies like our own Milky Way are embedded in massive, extended halos of dark matter that are very lumpy, teeming with self-bound substructure (“subhalos”) that survived this hierarchical assembly process (2–4). Indirect detection of high-energy antipar-

ticles and gamma rays from dark matter halos provides a potential “smoking gun” signature of WIMP annihilation (5). The usual assumption—that WIMP annihilation proceeds at a rate that does not depend, in the nonrelativistic $v/c \ll 1$ limit, on the particle relative velocities—implies that the primary astrophysical quantity determining the annihilation luminosity today is the local density squared. WIMP annihilations still occur in the cores of individual substructures, but with fluxes that are expected to be dauntingly small. The latest calculations show that only a handful of the most massive galactic subhalos may, in the best case, be detectable in gamma rays by the Fermi satellite (6, 7).

The Sommerfeld enhancement, a velocity-dependent mechanism that boosts the dark matter annihilation cross section over the standard $\langle\sigma v\rangle_0$ value (8–11), may provide an explanation for the experimental results of the PAMELA satellite reporting an increasing positron fraction in the local cosmic ray flux at energies between 10 and 100 GeV (12), as well as for the surprisingly large total electron and positron flux measured by the ATIC and PPB-BETS balloon-borne experiments (13, 14). Very recent Fermi (15) and HESS (16) data appear to be inconsistent with the ATIC and

PPB-BETS measurements, but still exhibit departures with respect to standard expectations from cosmic ray propagation models. Although conventional astrophysical sources of high-energy cosmic rays, such as nearby pulsars or supernova remnants, may provide a viable explanation (17–19), the possibility of galactic dark matter annihilation as a source remains intriguing (20–22). In this case, cross sections a few orders of magnitude above what is expected for a thermal WIMP are required (23).

The Sommerfeld nonperturbative increase in the annihilation cross section at low velocities is the result of a generic attractive force between the incident dark matter particles that effectively focuses incident plane-wave wave functions. The force carrier may be the W or Z boson of the weak interaction (10), $m_\phi = 80$ to 90 GeV/ c^2 , or a lighter boson, $m_\phi \sim 1$ GeV/ c^2 , mediating a new interaction in the dark sector (11, 24). Upon introduction of a force with coupling strength α , the annihilation cross section is shifted to $\langle\sigma v\rangle = S\langle\sigma v\rangle_0$, where the Sommerfeld correction S disappears ($S = 1$) in the limit $v/c \rightarrow 1$ (thus leaving unchanged the weak-scale annihilation cross section during WIMP freeze-out in the early universe). When $v/c \ll \alpha$, $S \approx \pi\alpha c/v$ (“ $1/v$ ” enhancement), but S levels off to $S_{\text{max}} \approx 6\pi\alpha m_\chi/m_\phi$ at $v/c \approx 0.5 m_\phi/m_\chi$ because of the finite range of the interaction. For specific parameter combinations—that is, when $m_\chi/m_\phi \approx n^2/\alpha$ (where n is an integer)—the Yukawa potential develops bound states, and these give rise to large, resonant cross-section enhancements where S grows approximately as $1/v^2$ before saturating (25).

The Sommerfeld effect connects dynamically the dark sector and the astrophysically observable sector. Because the typical velocities of dark matter particles in the Milky Way today are on the order of $v/c \sim 10^{-3}$, the resulting boost in the annihilation rate may provide an explanation for the puzzling galactic signals. Relative to particles in the smooth halo component, the Sommerfeld correction preferentially enhances the annihilation luminosity of cold, lower-velocity dispersion substructure, as emphasized in (10, 26, 27). Detailed

¹School of Natural Sciences, Institute for Advanced Study, Princeton, NJ 08540, USA. ²Department of Astronomy and Astrophysics, University of California, Santa Cruz, CA 95064, USA. ³Department of Physics, University of Oxford, Oxford OX1 3RH, UK.

*To whom correspondence should be addressed. E-mail: mkq@ias.edu

knowledge of the full phase-space density of dark matter particles in the Milky Way is thus necessary to reliably compute the expected signals.

Here, we used the Via Lactea II cosmological simulation—a high-precision calculation of the assembly of the galactic CDM halo—for a systematic investigation of the impact of Sommerfeld-corrected models on present and future indirect dark matter detection efforts. Via Lactea II uses just over 1 billion particles with mass of 4100 solar masses (M_\odot) to follow, with a force resolution of 40 pc, the formation of a $1.9 \times 10^{12} M_\odot$ Milky Way-sized halo and its substructure from redshift $z = 104$ to the present (28–30) (Fig. 1A). The smooth halo particles, whose velocity dispersions are set by the global potential, typically have three-dimensional velocity dispersion $\sigma > 100 \text{ km s}^{-1}$. Particles in self-bound subhalos dominate at lower-velocity dispersions. The total mass fraction of particles with $\sigma < 5 \text{ km s}^{-1}$ is 1%. We calculated the Sommerfeld enhancement factors S on a particle-by-particle basis by averaging $S(v)$ over a Maxwell-Boltzmann distribution of relative velocities with one-dimensional velocity dispersion given by $\sqrt{2/3}\sigma$ (25) (Fig. 1, C and D).

The large Sommerfeld boost expected for $v/c \sim 10^{-4}$ to 10^{-5} makes cold subhalos more promising sources of annihilation gamma rays than the higher-density but much hotter region around the galactic center (Fig. 2). In Sommerfeld-enhanced models, substructures are much more clearly visible, and can even outshine the galactic center when the cross section is close to resonance and saturates at low velocities. Furthermore, baryonic processes will tend to heat up the galactic center and dim its Sommerfeld boost, and thereby increase the relative detectability of subhalos. Dark matter halos are not isothermal and have lower-velocity dispersions in the center (25). In addition to an overall increase in the annihilation rate, this “temperature inversion” leads to a relative brightening of the center at the expense of the diffuse flux from the surrounding region (Fig. 3). The subhalo exhibits its own population of subclumps, also Sommerfeld-enhanced.

To address quantitatively the detectability of Sommerfeld-enhanced subhalos by the Fermi Gamma-ray Space Telescope, we converted the annihilation flux calculated from our simulation (31) into a predicted gamma-ray flux and compared it to the expected backgrounds. We investigated two different classes of particle physics models (Table 1):

1) Models motivated by Lattanzi and Silk (LS) (10), in which the force carrier is the conventional weak force gauge boson, the W or Z particle, and the mass of the dark matter particle is $> \sim 4 \text{ TeV}$. We chose four representative values of m_χ and α that lie increasingly close to a $S \sim 1/v^2$ resonance. In these models, the main source of gamma rays is the decay of neutral pions that are produced in the hadronization of the annihilation products.

2) Models in which the annihilation is mediated by a new dark sector force carrier ϕ (11). The choice of parameters (m_χ , m_ϕ , α) follows Meade, Papucci, and Volansky (MPV) (32) and

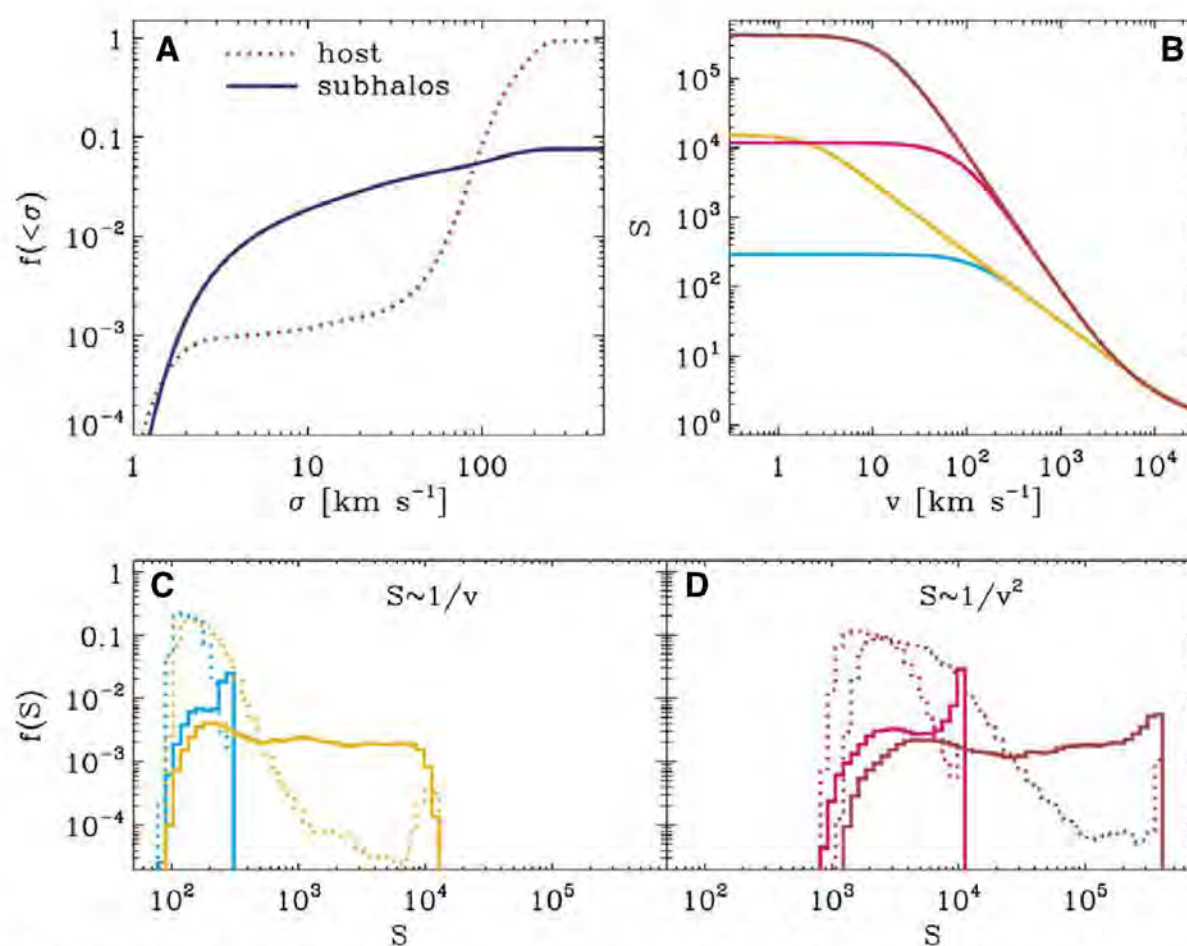


Fig. 1. (A) Distribution of velocity dispersion for Via Lactea II particles within 400 kpc. The dispersions are calculated from the nearest 32 neighbors of each particle. (B) Sommerfeld enhancement factor as a function of velocity for four representative models, exhibiting $S \sim 1/v$ behavior (cyan and orange curves) and $S \sim 1/v^2$ behavior (magenta and brown), and high (cyan and magenta) versus low (orange and brown) saturation velocities. (C and D) Corresponding distributions of S factors for Via Lactea II particles.

Fig. 2. All-sky maps (in a Mollweide projection) of the Sommerfeld-enhanced annihilation surface brightness ($\int_{\text{los}} \rho^2 S dl$) from all Via Lactea II dark matter particles within 400 kpc. The observer is located at 8 kpc from the halo center along the host halo’s intermediate principal axis. (A) No Sommerfeld enhancement. (B) $S \sim 1/v$, saturated at $\sim 1 \text{ km s}^{-1}$. (C) $S \sim 1/v^2$, saturated at $\sim 5 \text{ km s}^{-1}$. The maps have been normalized to give the same total smooth host halo flux.

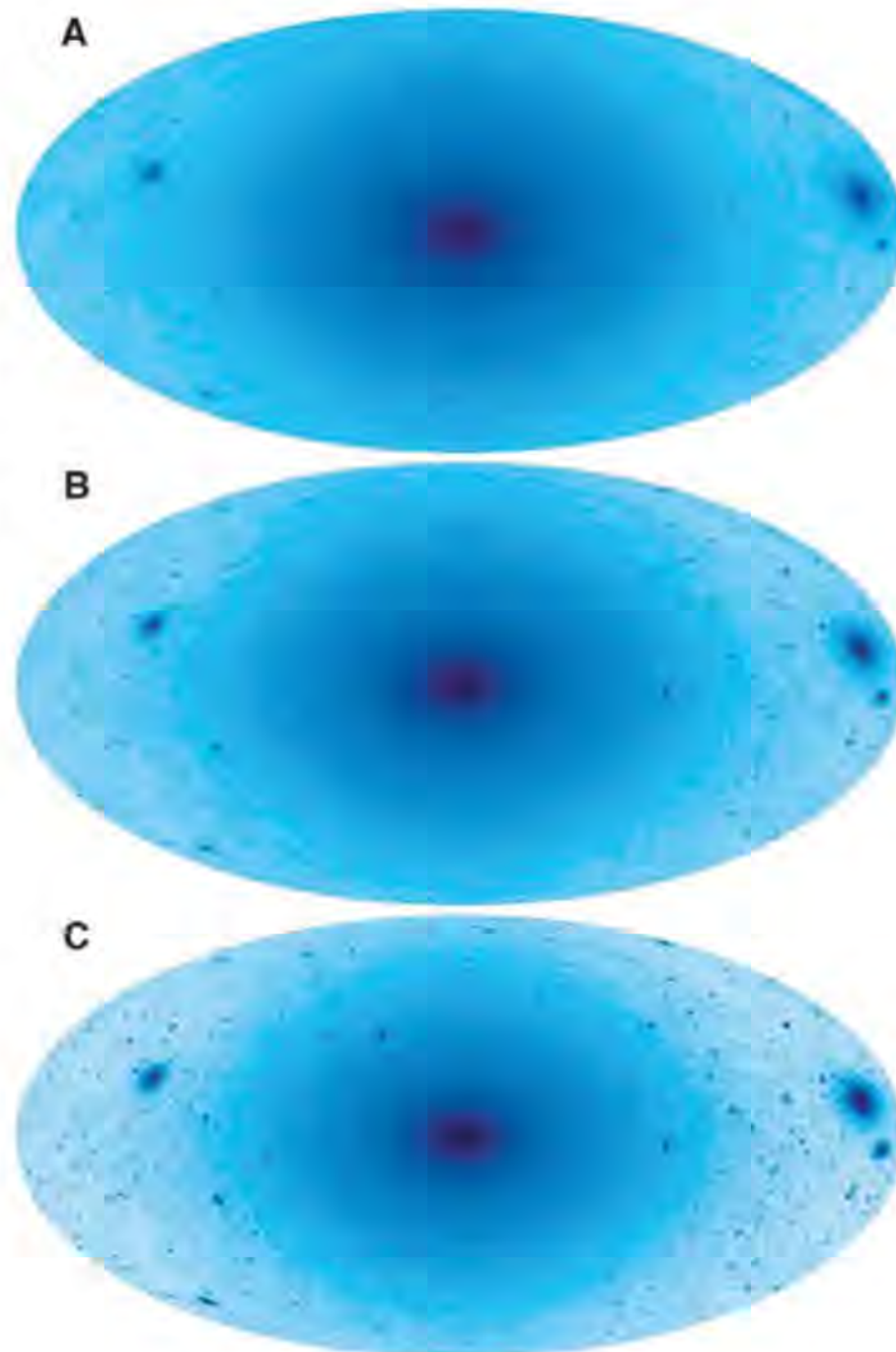


Fig. 3. Annihilation rate maps (projections of $\rho^2 S$ out to the tidal radius) of one of the most massive ($M \sim 2 \times 10^9 M_\odot$) subhalos in Via Lactea II, for the same models as in Fig. 2. The images have not been normalized. Relative to the $S = 1$ case (A), the total luminosity is a factor of 2200 higher for $S \sim 1/v$ (B) and a factor of 160,000 higher for $S \sim 1/v^2$ (C).

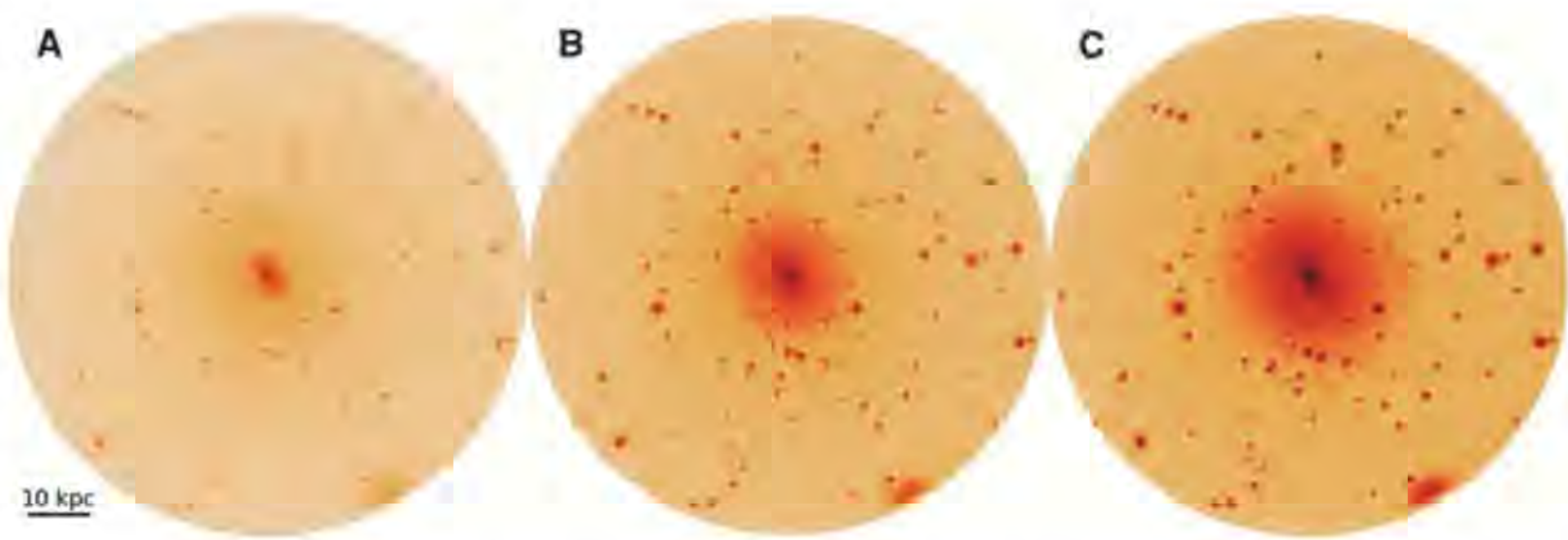


Table 1. Summary of the models used to assess subhalo detectability with Fermi. Particle physics parameters are m_χ , the mass of the dark matter particle; m_ϕ , the mass of the force carrier; and α , the coupling constant. The two rightmost columns show S_{max} , the maximum Sommerfeld enhancement obtained, and the saturation velocity v_{sat} , defined as the velocity at which S reaches 90% of S_{max} .

Model	m_χ (TeV)	m_ϕ (GeV)	$\alpha \times 100$	S_{max}	v_{sat} (km s^{-1})
LS-1	4.30	90	3.307	1,500	80
LS-2	4.45	90	3.297	12,000	28
LS-3	4.50	90	3.288	70,000	12
LS-4	4.55	90	3.281	430,000	4.7
MPV-1a	1.0	0.2	4.000	3,000	7.4
MPV-1b	1.0	0.2	3.739	16,000	2.4
MPV-2a	0.25	0.2	4.000	480	40
MPV-2b	0.25	0.2	4.500	40,000	3.3

Table 2. Numbers of subhalos that would be detected with $>5\sigma$ significance by Fermi after 1, 2, 5, and 10 years in orbit, for different Sommerfeld-enhanced dark matter particle models. The two rightmost columns show \tilde{D} , the median distance, and \tilde{M}_{sub} , the mass of the detectable clumps after 5 years in orbit.

Model	Years in orbit				\tilde{D} (kpc)	\tilde{M}_{sub} (M_\odot)
	1	2	5	10		
LS-1	12	19	29	38	24	1.4×10^7
LS-2	72	99	167	244	42	9.5×10^6
LS-3	225	311	457	583	56	6.2×10^6
LS-4	410	528	730	919	66	4.9×10^6
MPV-1a	5	7	12	15	16	9.8×10^7
MPV-1b	9	14	25	36	25	4.4×10^6
MPV-2a	12	18	29	38	24	1.4×10^7
MPV-2b	187	254	397	518	55	4.5×10^6

satisfies constraints from recent HESS measurements of the galactic center (33) and the galactic ridge (34), as well as the PAMELA measurement of the local positron fraction above 10 GeV (12) and the ATIC (13) and PPB-BETS (14) measurements of the total ($e^+ + e^-$) flux above 100 GeV. Models MPV-1a and MPV-1b incorporate all three constraints; models MPV-2a and MPV-2b incorporate only the HESS and PAMELA data. The suffixes a and b denote models away from and close to resonance, respectively, thereby covering both $S \sim 1/v$ and $S \sim 1/v^2$ behavior. The data favor a light force carrier, $m_\phi \approx 200$ MeV, and the gamma rays then originate as final-state radiation (internal bremsstrahlung) accompanying the decay of the ϕ s into e^+e^- pairs.

The magnitude of the relativistic cross section was fixed to the standard value of $\langle\sigma v\rangle_0 = 3 \times 10^{-26} \text{ cm}^3 \text{ s}^{-1}$. Gamma-ray spectra are shown in fig. S2.

We determined the Fermi detection significance by summing the annihilation photons from all the pixels in our all-sky maps covering a given subhalo, and comparing the result to the square root of the number of background photons from the same area. We counted a subhalo as “detectable” if it had a total signal-to-noise ratio greater than 5 (Table 2). The numbers are quite large, implying that individual subhalos should easily be detected by Fermi if Sommerfeld enhancements are important. Even in the most conservative cases (MPV-1a and MPV-2a), around 10 or

more subhalos should be discovered after 5 years of observation. Indeed, on the basis of all models considered here, Fermi should be able to accumulate enough flux in its first year of observations to detect several dark matter subhalos at more than 5σ significance; if so, this would open the door to studies of nongravitational dark matter interactions. The central brightening discussed above results in a smaller angular extent of a given subhalo’s detectable region: The stronger the Sommerfeld enhancement, the fewer pixels exceed the detection threshold. Nonetheless, for all models considered here, the majority of detectable subhalos would be resolved sources for Fermi.

Another question of interest is whether Sommerfeld-corrected substructure would lead to a strong boost in the local production of high-energy positrons, arising from dark matter annihilation in subhalos within a diffusion region of a few thousand parsecs from Earth, as well as of antiprotons within a correspondingly larger diffusion region. The local dark matter distribution at the Sun’s location appears quite smooth in the highest-resolution numerical simulations to date (28, 30, 35). Tidal forces efficiently strip matter from subhalos passing close to the galactic center and often completely destroy them. Further substructure depletion may be expected from interactions with the stellar disk and bulge. In the Via Lactea II simulation, the mean number of $>10^5 M_\odot$ subhalos within 1 kpc of the Sun is only 0.04, and one must reach 3 times this distance to find one clump on average. Without the Sommerfeld effect, this dearth of nearby substructure leads to a local annihilation boost of less than 1%, and at most 20% in the rare case of a nearby clump, as found in a statistical approach (36). The picture changes with Sommerfeld enhancement. The low-velocity dispersion of cold substructure leads to a greatly increased luminosity relative to the hotter smooth component. For typical $1/v$ models, subhalos resolved in our simulation within 2 kpc contribute on average about half as much luminosity as the smooth component, and up to 5 times as much in rare cases. If the Sommerfeld enhancement is resonant ($S \sim 1/v^2$), then these subhalos dominate by a factor of 20 on average and by as much as a factor of 200 in rare cases.

References and Notes

1. G. Jungman, M. Kamionkowski, K. Griest, *Phys. Rep.* **267**, 195 (1996).
2. A. Klypin, A. V. Kravtsov, O. Valenzuela, F. Prada, *Astrophys. J.* **522**, 82 (1999).
3. B. Moore *et al.*, *Astrophys. J.* **524**, L19 (1999).
4. J. Diemand, M. Kuhlen, P. Madau, *Astrophys. J.* **657**, 262 (2007).
5. J. Silk, M. Srednicki, *Phys. Rev. Lett.* **53**, 624 (1984).
6. M. Kuhlen, J. Diemand, P. Madau, *Astrophys. J.* **686**, 262 (2008).
7. L. Pieri, G. Bertone, E. Branchini, *Mon. Not. R. Astron. Soc.* **384**, 1627 (2008).
8. J. Hisano, S. Matsumoto, M. M. Nojiri, *Phys. Rev. Lett.* **92**, 031303 (2004).
9. J. March-Russell, S. M. West, *Phys. Lett. B* **676**, 133 (2009).
10. M. Lattanzi, J. Silk, *Phys. Rev. D* **79**, 083523 (2009).
11. N. Arkani-Hamed, D. P. Finkbeiner, T. R. Slatyer, N. Weiner, *Phys. Rev. D* **79**, 015014 (2009).
12. O. Adriani *et al.*, <http://arxiv.org/abs/0810.4995> (2008).
13. J. Chang *et al.*, *Nature* **456**, 362 (2008).
14. S. Torii *et al.*, <http://arxiv.org/abs/0809.0760> (2008).
15. A. A. Abdo *et al.*, *Phys. Rev. Lett.* **102**, 181101 (2009).
16. HESS Collaboration (F. Aharonian *et al.*), <http://arxiv.org/abs/0905.0105> (2009).
17. S. Profumo, <http://arxiv.org/abs/0812.4457> (2009).
18. N. J. Shaviv, E. Nakar, T. Piran, <http://arxiv.org/abs/0902.0376> (2009).
19. D. Malyshev, I. Cholis, J. Gelfand, <http://arxiv.org/abs/0903.1310> (2009).
20. L. Bergström, J. Edsjö, G. Zaharijas, <http://arxiv.org/abs/0905.0333> (2009).
21. P. Meade, M. Papucci, A. Strumia, T. Volansky, <http://arxiv.org/abs/0905.0480> (2009).
22. M. Kuhlen, D. Malyshev, *Phys. Rev. D* **79**, 123517 (2009).
23. M. Cirelli, M. Kadastik, M. Raidal, A. Strumia, *Nucl. Phys. B* **813**, 1 (2009).
24. The "dark sector" of our universe consists of dark matter, dark energy, and possibly additional dark forces.
25. See supporting material on Science Online.
26. B. E. Robertson, A. R. Zentner, *Phys. Rev. D* **79**, 083525 (2009).
27. J. Bovy, *Phys. Rev. D* **79**, 083539 (2009).
28. J. Diemand *et al.*, *Nature* **454**, 735 (2008).
29. P. Madau *et al.*, *Astrophys. J.* **689**, L41 (2008).
30. M. Zemp *et al.*, *Mon. Not. R. Astron. Soc.* **394**, 641 (2009).
31. Even at the extremely high resolution of Via Lactea II, the cuspy subhalo centers are often not sufficiently well resolved to give accurate central surface brightnesses. We corrected the centers according to an analytical model that has been calibrated to our numerical simulations (25).
32. P. Meade, M. Papucci, T. Volansky, <http://arxiv.org/abs/0901.2925> (2009).
33. F. Aharonian *et al.*, *Phys. Rev. Lett.* **97**, 221102 (2006).
34. F. Aharonian *et al.*, *Nature* **439**, 695 (2006).
35. M. Vogelsberger *et al.*, *Mon. Not. R. Astron. Soc.* **395**, 797 (2009).
36. J. Lavalley, Q. Yuan, D. Maurin, X. Bi, *Astron. Astrophys.* **479**, 427 (2008).
37. Supported by NASA grant NNX08AV68G (P.M.) and by the William L. Loughlin Fellowship at the Institute for Advanced Study (M.K.). This work would not have been possible without the expertise and invaluable contributions of all the members of the Via Lactea Project team. We thank M. Lattanzi, S. Profumo, N. Arkani-Hamed, N. Weiner, P. Meade, and T. Volansky for enlightening discussions; D. Shih for help with the Sommerfeld enhancement calculations; and M. Papucci for providing gamma-ray spectra.

Supporting Online Material

www.sciencemag.org/cgi/content/full/1174881/DC1

SOM Text

Figs. S1 to S6

References

13 April 2009; accepted 8 July 2009

Published online 16 July 2009;

10.1126/science.1174881

Include this information when citing this paper.

Light-Induced Spontaneous Magnetization in Doped Colloidal Quantum Dots

Rémi Beaulac,¹ Lars Schneider,² Paul I. Archer,¹ Gerd Bacher,² Daniel R. Gamelin^{1*}

An attractive approach to controlling spin effects in semiconductor nanostructures for applications in electronics is the use of light to generate, manipulate, or read out spins. Here, we demonstrate spontaneous photoinduced polarization of manganese(II) spins in doped colloidal cadmium selenide quantum dots. Photoexcitation generates large dopant-carrier exchange fields, enhanced by strong spatial confinement, that lead to giant Zeeman splittings of the semiconductor band structure in the absence of applied magnetic fields. These internal exchange fields allow spontaneous magnetic saturation of the manganese(II) spins to be achieved at zero external magnetic field up to ~50 kelvin. Photomagnetic effects are observed all the way up to room temperature.

Future spintronics and spin-photonics technologies will require a portfolio of techniques for manipulating spins in semiconductor nanostructures (1). One approach is to tailor magnetic exchange interactions between charge carriers and embedded magnetic impurity ions within the semiconductor (1–3), which can lead to the formation of a magnetically ordered state, the so-called magnetic polaron (1, 4). Among the most notable phenomena yet discovered in diluted magnetic semiconductors (DMSs) is the so-called excitonic magnetic polaron (EMP) (Fig. 1A) (5–14), in which charge carrier photoexcitation initiates magnetic polaron formation. EMPs are greatly enhanced by exciton spatial localization (4, 14), a notion that has motivated numerous investigations into epitaxial DMS nanostructures (8, 10–13). Despite more than 40 years of magnetic polaron

studies (15) and its recent renaissance because of its implications for quantum information processing (16, 17) and ferromagnetism in semiconductors (18), EMP signatures have still only been observed below ~30 K, too cold for most practical applications. Furthermore, the experimental exchange fields of only a few tesla contrast with theoretical predictions of exchange fields on the order of 100 T and above (4, 19); magnetic saturation has not been achieved experimentally without the use of strong external magnetic fields at cryogenic temperatures. The data obtained to date thus suggest that EMPs are a low-temperature phenomenon too weak to support spontaneous magnetic saturation.

Recently, chemical syntheses have opened alternative routes to doped semiconductor nanostructures complementary to epitaxially grown materials (Fig. 1, B and C); their spherical zero-dimensional geometries provide even greater exciton spatial confinement than in quantum-well heterostructures or self-assembled quantum dots (QDs), and they can be purified, processed, and incorporated into device architectures with the use

of techniques traditionally associated only with molecular species (20–22). Until very recently, however, available colloidal Mn²⁺-doped semiconductor nanocrystals suffered from exciton quenching by rapid energy transfer to Mn²⁺ after nanocrystal photoexcitation (23). This energy transfer is faster than Mn²⁺ spin reorientation, and it hinders EMP formation (12, 24). Colloidal Mn²⁺:CdSe QDs can now be prepared so that their excitonic photoluminescence (PL) (Fig. 1D) is not quenched by energy transfer to Mn²⁺ because their excitonic energy levels can be tuned to lie below all Mn²⁺ electronic excited states (22, 23). The elimination of QD → Mn²⁺ energy transfer allows the observation of excitonic PL with 10 K decay times of $\tau_{\text{em}} \sim 100$ ns (25). Previous magnetic circular dichroism and magnetic circularly polarized luminescence experiments have already demonstrated that these long-lived excitons coexist with strong Mn²⁺-exciton magnetic exchange coupling (23).

Here, we demonstrate spontaneous photoinduced polarization of Mn²⁺ spins in colloidal doped CdSe nanocrystals. Very large effective internal magnetic fields were observed that lead to complete magnetization of the nanocrystals in the absence of an external magnetic field at temperatures up to ~50 K, with signatures of photomagnetization observable up to room temperature. These large spin effects can be attributed to the strong zero-dimensional exciton confinement achieved in colloidal doped nanocrystals.

We examined the PL of colloidal Mn²⁺:CdSe DMS QDs as a function of temperature and time (26). Representative variable-temperature PL results are shown in Fig. 1D for diameter $d = 4.3$ nm, 4.5% Mn²⁺:CdSe QDs. Even at room temperature, the excitonic PL maximum shifts to lower energy as the temperature is lowered, in stark contrast with the Varshni-like temperature dependence that is typically observed with colloidal CdSe QDs (27) and other semiconductors, in which the PL energy

¹Department of Chemistry, University of Washington, Seattle, WA 98195–1700, USA. ²Werkstoffe der Elektrotechnik and Center for Nanointegration Duisburg-Essen, Universität Duisburg-Essen, 47057 Duisburg, Germany.

*To whom correspondence should be addressed. E-mail: gamelin@chem.washington.edu

increases approximately linearly with decreasing temperature in the range of 100 to 300 K and then plateaus. For comparison, Fig. 1E shows PL data for undoped CdSe QDs prepared and measured in an identical fashion. The absorption spectra of the Mn^{2+} :CdSe and undoped CdSe QDs both follow Varshni-like temperature dependence (Fig. 1F), as does the PL of the undoped CdSe QDs.

The data in Fig. 1D thus indicate a PL Stokes shift (ΔE , representing shift of the excitonic PL maximum from the excitonic absorption maximum at the same temperature) for the Mn^{2+} :CdSe QDs that increases with decreasing temperature, starting already at room temperature (Fig. 1F). This anomalous temperature dependence reflects stabilization of the exciton by Mn^{2+} through a mechanism that is strongly temperature dependent. In epitaxial DMSs, a similar anomalous temperature dependence has been observed at $T < \sim 30$ K that reflects partial Mn^{2+} spin alignment in the effective exchange field (B_{eff}) of the exciton (11, 12). The largest B_{eff} observed in such measurements has been ~ 3.5 T (11).

The data from Fig. 1F are replotted in Fig. 2A as ΔE versus $1/T$ (where T is temperature), along with similar data for two other colloidal Mn^{2+} :CdSe QD samples of different diameters. The resulting plots all show a clear $1/T$ dependence of ΔE at high temperatures (Curie regime) that saturates at temperatures below ~ 50 K. As in previous analyses (11, 12, 24), we fit these data to a simple isotropic $S = 5/2$ Brillouin function (Eq. 1) to estimate the effective exchange field (B_{eff}) acting on the paramagnetic Mn^{2+} ions within the nanocrystals. In Eq. 1, the Mn^{2+} g factor $g_{\text{Mn}} = 2.00$, $\mu_B =$ Bohr magneton, $k =$ Boltzmann constant, and C is a scaling constant proportional to the number of Mn^{2+} per QD (see below). B_{eff} is thus determined by the curvature of the data set, not its height. As illustrated in Fig. 2B, the data from Fig. 1F are reproduced well with $B_{\text{eff}} \approx 75$ T (solid red line). This value of B_{eff} is more than one order of magnitude greater than those reported previously. For comparison, the dashed lines in Fig. 2B show the behavior expected from Eq. 1 for various values of B_{eff} . As detailed below, B_{eff} here is a phenomenological value with contributions from two major sources, but it is nevertheless extraordinarily large in these colloids.

$$\Delta E = C \left\{ \frac{(2S+1)}{2S} \coth \left[(2S+1) \left(\frac{g_{\text{Mn}} \mu_B B_{\text{eff}}}{2kT} \right) \right] - \frac{1}{2S} \coth \left(\frac{g_{\text{Mn}} \mu_B B_{\text{eff}}}{2kT} \right) \right\} \quad (1)$$

All samples show similar saturation of ΔE with temperature. Figure 2C plots B_{eff} versus $1/V_{\text{QD}}$ from analysis of the data in Fig. 2A using Eq. 1, where V_{QD} is the Mn^{2+} :CdSe QD volume. These data yield a straight line that intersects the origin, demonstrating a strong influence of nanocrystal diameter on B_{eff} . The exceptionally large values of B_{eff} shown in Fig. 2, compared with those of self-assembled DMS QDs or bulk DMSs (7, 11, 12, 24), can be attributed to increased ex-

citon spatial confinement within these colloidal Mn^{2+} :CdSe QDs, with B_{eff} increasing by $\sim 50\%$ upon reduction of the QD diameter from 5.0 to 4.3 nm.

All of these colloidal Mn^{2+} :CdSe QDs show saturation persisting as high as ~ 50 K ($1/T \approx 0.02 \text{ K}^{-1}$). The signature EMP temperature dependence of ΔE is even still clearly observed in all samples up to room temperature ($1/T \approx 0.003 \text{ K}^{-1}$) (26). Spontaneous magnetic saturation under the exchange field of an exciton has never been reported in any EMP study. In all previous investigations, B_{eff} induces only partial

magnetization but is insufficient to completely align the Mn^{2+} spins, even at liquid helium temperatures. For example, B_{eff} of 3.5 T induces only 75% magnetization at 5 K and only 10% magnetization at 50 K (Fig. 2B) (11).

A more detailed picture of these EMPs is obtained from time-resolved PL (TRPL) measurements. Figure 3, A and B, shows TRPL data for doped and undoped CdSe QDs measured at 5 K. The Mn^{2+} :CdSe QDs show a large PL redshift within the first few nanoseconds after the laser pulse. The entire PL band shifts in a similar way with time. Relaxation dynamics on

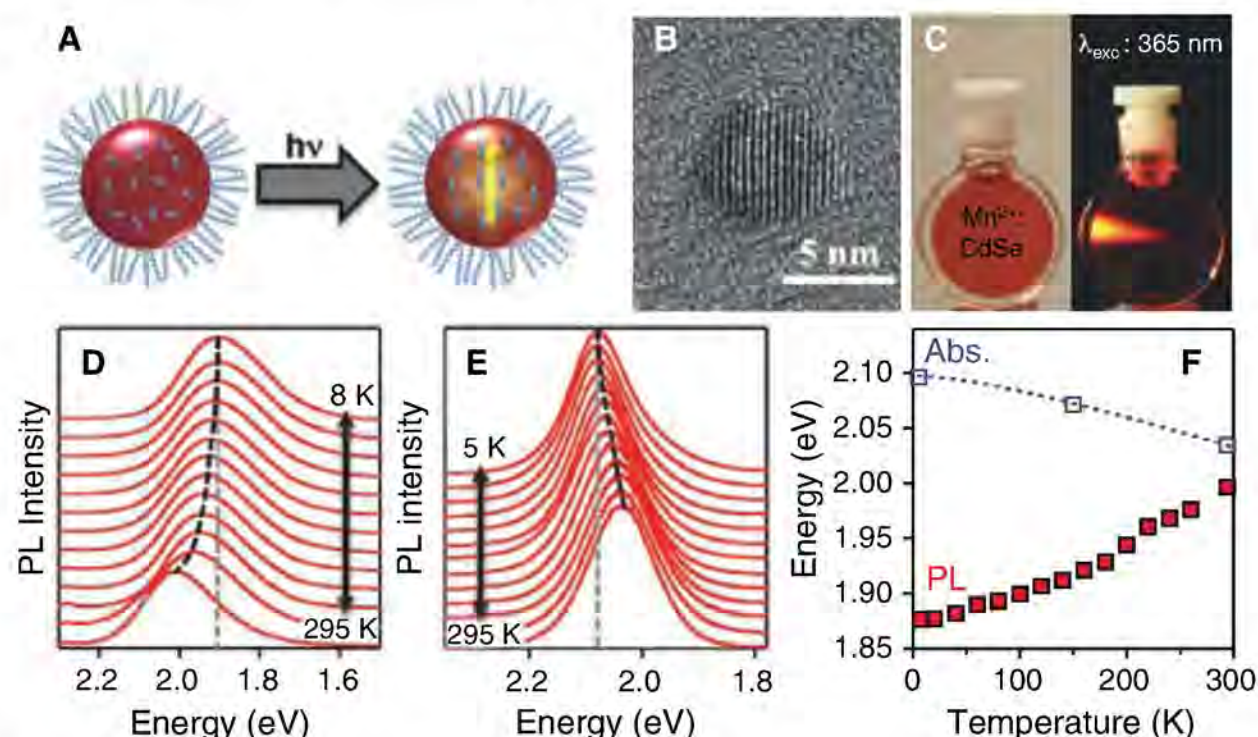


Fig. 1. Colloidal Mn^{2+} :CdSe QDs and their continuous-wave PL. (A) Schematic illustration of photo-induced magnetization of magnetic impurities in the effective magnetic field of a confined exciton. Blue arrows indicate Mn^{2+} dopant spins, the yellow arrow indicates the exciton, and the blue curly lines indicate surface capping ligands. (B) Transmission electron microscopy image of an isolated colloidal Mn^{2+} :CdSe QD. (C) Photograph of a colloidal Mn^{2+} :CdSe QD suspension in ambient room light and in the dark with unfocused laser irradiation. Variable-temperature continuous-wave PL spectra of colloidal (D) $d = 4.3$ nm 4.5% Mn^{2+} :CdSe and (E) undoped $d = 4.0$ nm CdSe QDs at different temperatures. From top to bottom: 5 [in (E)], 8, 30, 50, 70, 100, 120, 150, 170, 200, 225, 250, 275, and 295 K. (F) Absorption and PL peak maxima for $d = 5.0$ nm 4.2% Mn^{2+} :CdSe QDs. The PL of the undoped QDs follows Varshni-like behavior, but for the Mn^{2+} :CdSe QDs, it decreases in energy with decreasing temperature. See (26) for experimental details.

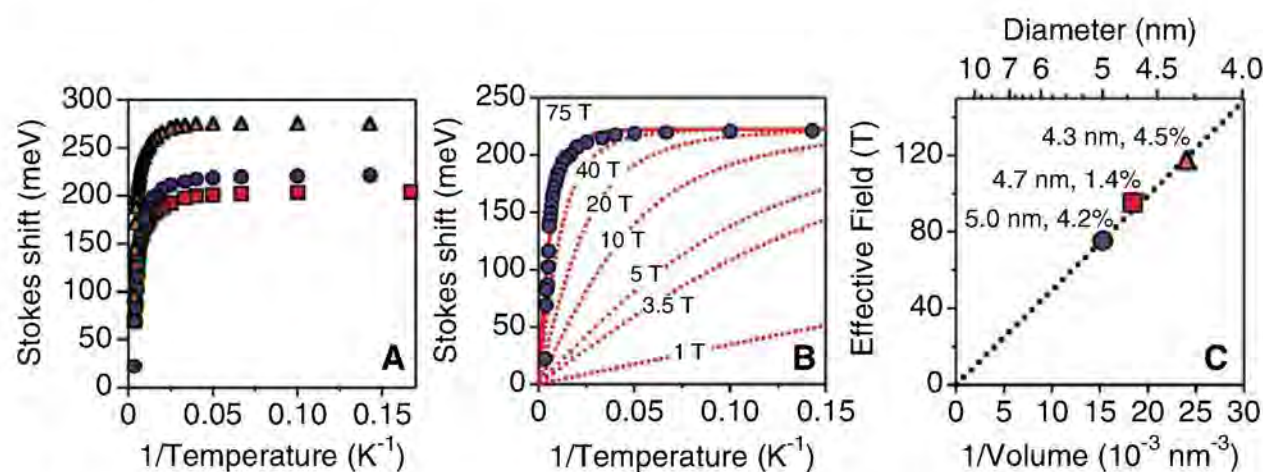


Fig. 2. Analysis of continuous-wave PL Stokes shifts. (A) PL Stokes shifts versus $1/T$ for three separate Mn^{2+} :CdSe QD samples of different diameters (red triangles, $d = 4.3$ nm, 4.5% Mn^{2+} ; red squares, $d = 4.7$ nm, 1.4% Mn^{2+} ; and blue circles, $d = 5.0$ nm, 4.2% Mn^{2+}). (B) Fit of the $d = 5.0$ nm 4.2% Mn^{2+} :CdSe QD Stokes shifts to a modified $S = 5/2$ Brillouin function (Eq. 1) with B_{eff} as the only floating variable, from which B_{eff} of 75 T is estimated (solid red line). The dashed lines illustrate other values of B_{eff} , including 3.5 T, the largest B_{eff} recorded from analogous data for epitaxially grown QDs (11). (C) B_{eff} values obtained from fitting the data in part (A), plotted versus the inverse QD volumes ($1/V_{\text{QD}}$). All reported Mn^{2+} concentrations are actual incorporated concentrations (26).

several different time scales are evident from these data. A very fast relaxation of ~ 50 meV (less than ~ 10 ps) can be seen from the difference between absorption and $t = 0$ PL energies (Figs. 1C and 3C). A similar fast Stokes shift is observed in the undoped CdSe QDs of Fig. 3A, and continuous-wave PL measurements also show Stokes shifts of 50 to 80 meV for the same undoped nanocrystals. Similar Stokes shifts have been described for other undoped colloidal CdSe nanocrystals (~ 25 to 95 meV) and attributed to relaxation among exciton fine-structure levels (28, 29). This shift is not related to the EMP, and thus, we do not consider it further.

The two dominant relaxation processes in the Mn^{2+} :CdSe QDs can be seen more clearly in Fig. 3C, where the 5 K PL maximum is plotted versus time. A fast relaxation of ~ 100 meV is observed within a few hundreds of picoseconds [similar to EMP formation times reported previously ($\tau_{\text{mp}} \sim 50$ to 250 ps) (6, 10, 12, 13)], followed by a slow relaxation over several nanoseconds that converges to the continuous-wave Stokes shifts at long times. The fast relaxation accounts for approximately half of the total continuous-wave Stokes shift and is attributed to EMP formation. The TRPL data also allow the temperature dependence of this EMP formation energy (E_{mp}) to be analyzed. For comparison with Fig. 1F, Fig. 3D illustrates the PL energies measured at $t = 0, 1$, and 13 ns after the laser pulse for the same particles as described by

Fig. 1F. Plotting the 1-ns Stokes shifts versus $1/T$ yields a Brillouin-like saturation magnetization curve (Fig. 3E) similar to that of the total continuous-wave Stokes shift (Fig. 2B). Fitting this curve to Eq. 1 yields best-fit parameters of $B_{\text{eff}} \approx 40$ T and $\Delta E = 80$ meV, which can now be associated with magnetic polaron formation (i.e., $B_{\text{eff}} \approx B_{\text{mp}}$, $\Delta E \approx E_{\text{mp}}$), as in previous studies.

The expected temperature dependence of E_{mp} can also be estimated from Eq. 1 and previously reported parameters, with no fitting. EMP formation is primarily the result of kinetic $e_{\text{VB}}^- - \text{Mn}^{2+}$ exchange, which is typically about four to six times stronger than the $e_{\text{CB}}^- - \text{Mn}^{2+}$ interaction. B_{mp} can thus be described in terms of the isotropic mean-field $e_{\text{VB}}^- - \text{Mn}^{2+}$ exchange energy ($N_0\beta$) with the use of Eq. 2 (9). Here, V_{ex} is the exciton localization volume, and N_0 is the cation density.

$$B_{\text{mp}} \approx \frac{|N_0\beta|}{2\mu_{\text{B}}g_{\text{Mn}}} \cdot \frac{1}{N_0V_{\text{ex}}} \quad (2)$$

Because of the large surface confinement potential, V_{ex} is substantially smaller than V_{QD} . An infinite spherical potential-well calculation yields $V_{\text{ex}} = 23.2 \text{ nm}^3$ for $d = 5 \text{ nm}$ CdSe QD. From Eq. 2 and $N_0\beta = -1.3 \text{ eV}$ (4), a value of $B_{\text{mp}} \approx 14 \text{ T}$ is calculated. In addition, the magnitude of E_{mp} can be calculated. The prefactor from Eq. 1 is $C \approx \frac{1}{2}|x_{\text{eff}}N_0\beta S|$, where x_{eff} is the effective

Mn^{2+} concentration and $S = \frac{5}{2}$, again neglecting the weak $e_{\text{CB}}^- - \text{Mn}^{2+}$ interaction. At saturation, a value of $E_{\text{mp}} \approx 68 \text{ meV}$ is calculated, assuming all Mn^{2+} contribute (i.e., $x_{\text{eff}} = 0.042$). The predicted temperature dependence of ΔE calculated from Eq. 1 using just these values is depicted in Fig. 3E, alongside the 1-ns PL data. The predicted curve agrees reasonably well with experiment, supporting assignment of this fast relaxation as EMP formation, but it also reveals that the isotropic EMP model alone is not sufficient to explain the data. In particular, the greater-than-predicted Stokes shifts observed at elevated temperatures indicate a contribution to the 1-ns data from the slower relaxation process that is also observed in Fig. 3, C and D, which is not accounted for in Eqs. 1 and 2.

The additional slow relaxation (several tens of millielectron volts) takes place with a time constant τ_{slow} of ~ 2 to 20 ns (Fig. 3, C and D). A similar slow EMP relaxation has occasionally been observed in other DMSs and attributed to various possible effects, from exciton localization to inter-system crossing (10, 30), but its precise origin is uncertain. Regardless of its origin, this component is associated with the EMP because it is not observed in undoped CdSe QDs and because it shows a similar Brillouin-like saturation at low temperatures. We favor an interpretation in which τ_{slow} arises from EMP directional reorientation within a potential energy surface that is warped by anisotropy. The time scale of this relaxation is similar to that of EMP reorientation by an applied magnetic field in $\text{Cd}_{1-x}\text{Mn}_x\text{Te}$ epilayers ($\tau \sim 2 \text{ ns}$) (7). The EMP anisotropy energy is similar to those observed in $\text{Cd}_{1-x}\text{Mn}_x\text{Te}$ digital quantum-well structures (8) and predicted for unstrained $\text{Cd}_{1-x}\text{Mn}_x\text{Te}$ (31), in both cases originating from the anisotropy of the hole effective mass. The analogy between anisotropic magnetic polarons and single-molecule magnets has also been described theoretically (17). In our samples, the hexagonal crystal field anisotropy of wurtzite CdSe probably dominates this surface warping, but nanocrystal shape anisotropy is also expected to contribute substantially. This anisotropy model accounts for the time scale of the slow relaxation, as well as the observation that the total EMP stabilization energy at long times (more than $\sim 140 \text{ meV}$, see Figs. 2A and 3A) exceeds what would be possible in the isotropic limit (Fig. 3E).

τ_{slow} is slower than the typical exciton recombination times of self-assembled DMS QDs ($\tau_{\text{em}} \sim 300$ to 600 ps at 2 K) (12), suggesting that EMP relaxation magnitudes in those materials may be limited by their relatively fast exciton recombination kinetics. In contrast, $\tau_{\text{em}} \sim 100 \text{ ns}$ at 10 K and $\tau_{\text{em}} \sim 30 \text{ ns}$ at room temperature for these colloidal DMS QDs (25), allowing EMP relaxation dynamics to be probed in the absence of competing recombination processes, even at elevated temperatures. This exceptionally long τ_{em} is itself also important, because it suggests that the dark-bright formalism used to describe exciton fine-structure splittings in undoped QDs (28) may still be applicable in these Mn^{2+} :CdSe QDs,

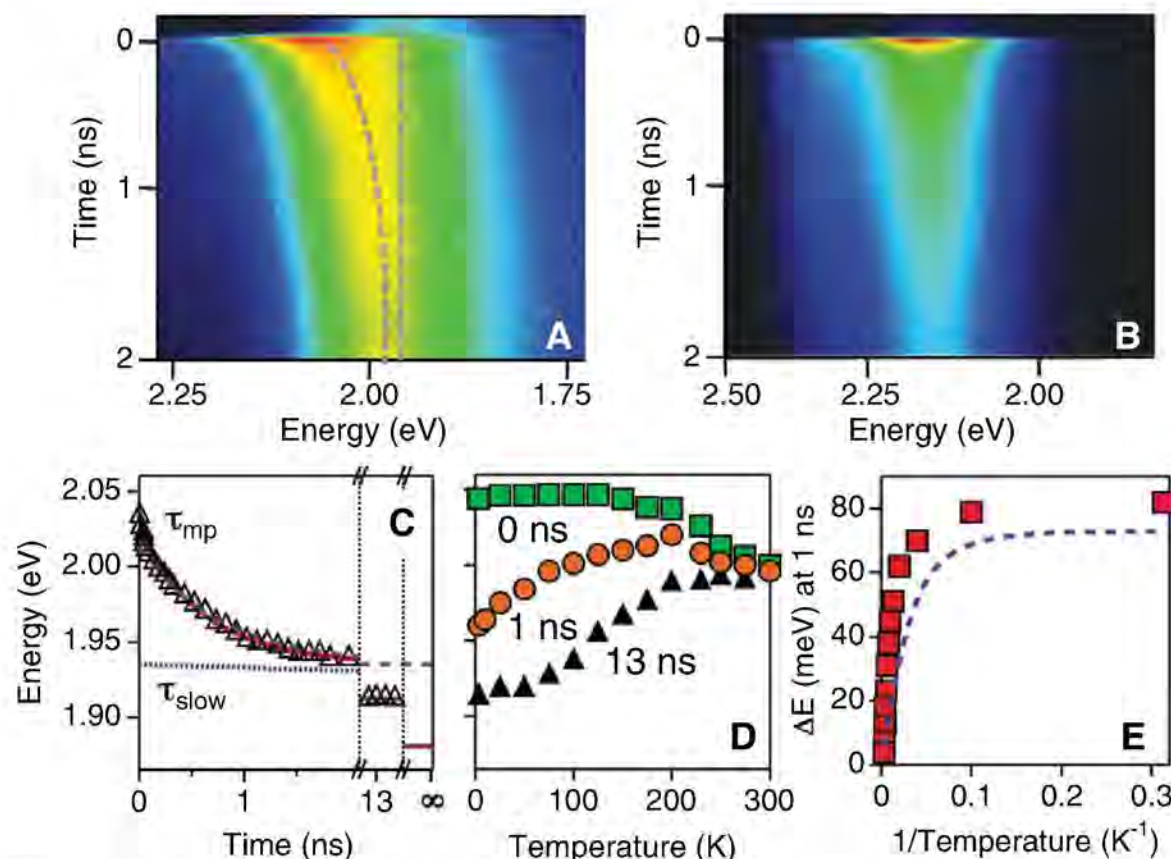


Fig. 3. TRPL data. TRPL spectra for (A) $d = 5.0 \text{ nm}$ 4.2% Mn^{2+} :CdSe and (B) undoped $d = 4.0 \text{ nm}$ CdSe QDs at cryogenic temperatures. The vertical dashed line indicates the PL energy 13 ns after the laser pulse. The Mn^{2+} :CdSe QD PL shows a large red shift after the laser pulse, whereas the CdSe QD PL shows only a small red shift. (C) 5-K PL energy maximum versus time for the same Mn^{2+} :CdSe QDs, emphasizing EMP formation ($\tau_{\text{mp}} \approx 50$ to 500 ps, blue line with long dashes) and reorientation ($\tau_{\text{slow}} \approx 2$ to 20 ns, blue line with short dashes) time scales of the multi-exponential decay. The PL energy converges to that observed in continuous-wave measurements (1.88 eV, $t = \infty$). The red line shows a fitted tri-exponential decay ($\tau_1 = 10 \text{ ps}$, $\tau_2 = 570 \text{ ps}$, $\tau_3 = 20 \text{ ns}$) for illustration. Vertical dotted lines indicate timeline discontinuities. (D) Mn^{2+} :CdSe QD PL maximum versus temperature, measured $\sim 0, 1$, and 13 ns after the laser pulse. (E) Mn^{2+} :CdSe QD PL Stokes shift at 1 ns versus $1/T$. The dashed line shows the predicted temperature dependence calculated from Eqs. 1 and 2 with the reported value of $N_0\beta$, as described in the text. This calculation yields $B_{\text{mp}} = 14 \text{ T}$ and $E_{\text{mp}} = 68 \text{ meV}$.

despite the strong Mn^{2+} -exciton exchange coupling. In colloidal CdSe QDs, these long τ_{em} arise from confinement-enhanced electron-hole exchange interactions (28), and thus they have the same ultimate origin as the exceptionally large B_{mp} values shown in Figs. 2 and 3.

The conclusions presented above are summarized in Fig. 4. Figure 4A shows a plot of energy versus magnetization in a magnetic analog of the single-configurational-coordinate (SCC) diagrams typically used to represent electron-nuclear reorganization after photoexcitation. Much like the SCC diagrams, this magnetic coordinate diagram is valid to the extent that magnetic effects are slow relative to electronic transitions. In this diagram, the DMS QDs in their dark-adapted state reside at $\langle S_\phi \rangle \approx 0$, having only small magnetization fluctuations around zero and no time-averaged magnetization. Photoexcitation generates an excited state that is unstable with respect to magnetization along a random direction ϕ , defined by some combination of the direction of spontaneous Mn^{2+} fluctuation magnetization at the instant of photoexcitation and the initial hole spin orientation, and results in spontaneous relaxation either to the right or to the left of $\langle S_\phi \rangle = 0$ in Fig. 4A via magnetization of the Mn^{2+} sublattice. Magnetic saturation is reached

only if B_{mp} is sufficiently large, and even then only if τ_{mp} is sufficiently fast compared with exciton recombination (τ_{em}). This spontaneous magnetization takes place within a few hundred picoseconds and is followed by slower directional reorientation of the entire EMP (with $\tau_{\text{slow}} > 2$ ns) within a potential energy surface warped by anisotropy. Figure 4B illustrates such a warped surface for the case of axial anisotropy, where ϕ represents the initial magnetization direction, and θ and ϵ represent the two unique magnetization orientations.

The competition among concurrent excited-state magnetization and exciton recombination dynamics is summarized schematically in Fig. 4C. Upon exciton recombination, the system returns vertically to a nonequilibrated ground state having $|\langle S_\phi \rangle| > 0$, and it thermalizes slowly back to $\langle S_\phi \rangle \approx 0$ with $\tau_{\text{MnSLR}} \sim 0.1 \mu\text{s} - \text{ms}$ (where τ_{MnSLR} is the Mn^{2+} spin-lattice relaxation time constant) (6, 13). If the system is excited again before ground-state thermalization, the excited state is already displaced relative to $\langle S_\phi \rangle = 0$ because the excitation occurs vertically; such spin accumulation has been observed previously (32). In the present experiments, the average time between excitation events ($>100 \mu\text{s}$) greatly exceeds the estimated Mn^{2+} spin-lattice relaxa-

tion time ($\tau_{\text{MnSLR}} \sim 0.1 \mu\text{s}$) (13), and spin accumulation is not anticipated.

Future investigation into these and related DMS QDs can be anticipated to reveal new possibilities for spin manipulation in semiconductor nanostructures. In particular, the combination of such strong photomagnetic effects with colloidal processability may now allow incorporation of new spin effects like EMPs (which were previously accessible only in epitaxial DMSs) into molecular devices via spin-coat processing, self-assembly, or other related "soft" chemical techniques that have become mainstays of nanotechnology.

References and Notes

1. T. Dietl, D. D. Awschalom, M. Kaminska, H. Ohno, Eds., *Spintronics*, vol. 82 (Academic Press, Amsterdam, 2008).
2. Y. Léger, L. Besombes, J. Fernández-Rossier, L. Maingault, H. Mariette, *Phys. Rev. Lett.* **97**, 107401 (2006).
3. R. C. Myers *et al.*, *Nat. Mater.* **7**, 203 (2008).
4. J. K. Furdyna, J. Kossut, Eds., *Diluted Magnetic Semiconductors*, vol. 25 (Academic Press, New York, 1988).
5. J. H. Harris, A. V. Nurmikko, *Phys. Rev. Lett.* **51**, 1472 (1983).
6. D. D. Awschalom, J. Warnock, S. von Molnár, *Phys. Rev. Lett.* **58**, 812 (1987).
7. I. A. Merkulov *et al.*, *JETP Lett.* **62**, 335 (1995).
8. R. Fiederling *et al.*, *Phys. Rev. B* **58**, 4785 (1998).
9. K. V. Kavokin, I. A. Merkulov, D. R. Yakovlev, W. Ossau, G. Landwehr, *Phys. Rev. B* **60**, 16499 (1999).
10. Y. Oka *et al.*, *J. Lumin.* **83-84**, 83 (1999).
11. A. A. Maksimov *et al.*, *Phys. Rev. B* **62**, R7767 (2000).
12. J. Seufert *et al.*, *Phys. Rev. Lett.* **88**, 027402 (2002).
13. T. Dietl, P. Peyla, W. Grieshaber, Y. Merle d'Aubigné, *Phys. Rev. Lett.* **74**, 474 (1995).
14. A. K. Bhattacharjee, C. Benoit à la Guillaume, *Phys. Rev. B* **55**, 10613 (1997).
15. T. Kasuya, A. Yanase, *Rev. Mod. Phys.* **40**, 684 (1968).
16. D. Loss, D. P. DiVincenzo, *Phys. Rev. A* **57**, 120 (1998).
17. J. Fernández-Rossier, R. Aguado, *Phys. Status Solidi C* **3**, 3734 (2006).
18. J. M. D. Coey, M. Venkatesan, C. B. Fitzgerald, *Nat. Mater.* **4**, 173 (2005).
19. D. M. Hoffman *et al.*, *Solid State Commun.* **114**, 547 (2000).
20. J. D. Bryan, D. R. Gamelin, *Prog. Inorg. Chem.* **54**, 47 (2005).
21. D. J. Norris, A. L. Efros, S. C. Erwin, *Science* **319**, 1776 (2008).
22. R. Beaulac, P. I. Archer, S. T. Ochsenbein, D. R. Gamelin, *Adv. Funct. Mater.* **18**, 3873 (2008).
23. R. Beaulac *et al.*, *Nano Lett.* **8**, 1197 (2008).
24. G. Bacher *et al.*, *Appl. Phys. Lett.* **79**, 524 (2001).
25. R. Beaulac, P. I. Archer, J. van Rijssel, A. Meijerink, D. R. Gamelin, *Nano Lett.* **8**, 2949 (2008).
26. Materials and methods are available as supporting material on Science Online.
27. T. J. Liptay, R. J. Ram, *Appl. Phys. Lett.* **89**, 223132 (2006).
28. A. L. Efros, M. Rosen, *Annu. Rev. Mater. Sci.* **30**, 475 (2000).
29. T. J. Liptay, L. F. Marshall, P. S. Rao, R. J. Ram, M. G. Bawendi, *Phys. Rev. B* **76**, 155314 (2007).
30. M. C. Debnath *et al.*, *J. Appl. Phys.* **87**, 6457 (2000).
31. T. L. Linnik, Y. G. Rubo, V. I. Sheka, *JETP Lett.* **63**, 222 (1996).
32. T. Gurung, S. Mackowski, G. Karczewski, H. E. Jackson, L. M. Smith, *Appl. Phys. Lett.* **93**, 153114 (2008).
33. We thank the U.S. NSF (Presidential Early Career Award for Scientists and Engineers, DMR-0239325), the Dreyfus Foundation, the Sloan Foundation, the Natural Sciences and Engineering Research Council of Canada postdoctoral fellowship program (to R.B.), and the Deutsche Forschungsgemeinschaft (project SFB 445) for financial support.

Supporting Online Material

www.sciencemag.org/cgi/content/full/325/5943/973/DC1
Materials and Methods

Fig. S1

References

2 April 2009; accepted 2 July 2009
10.1126/science.1174419

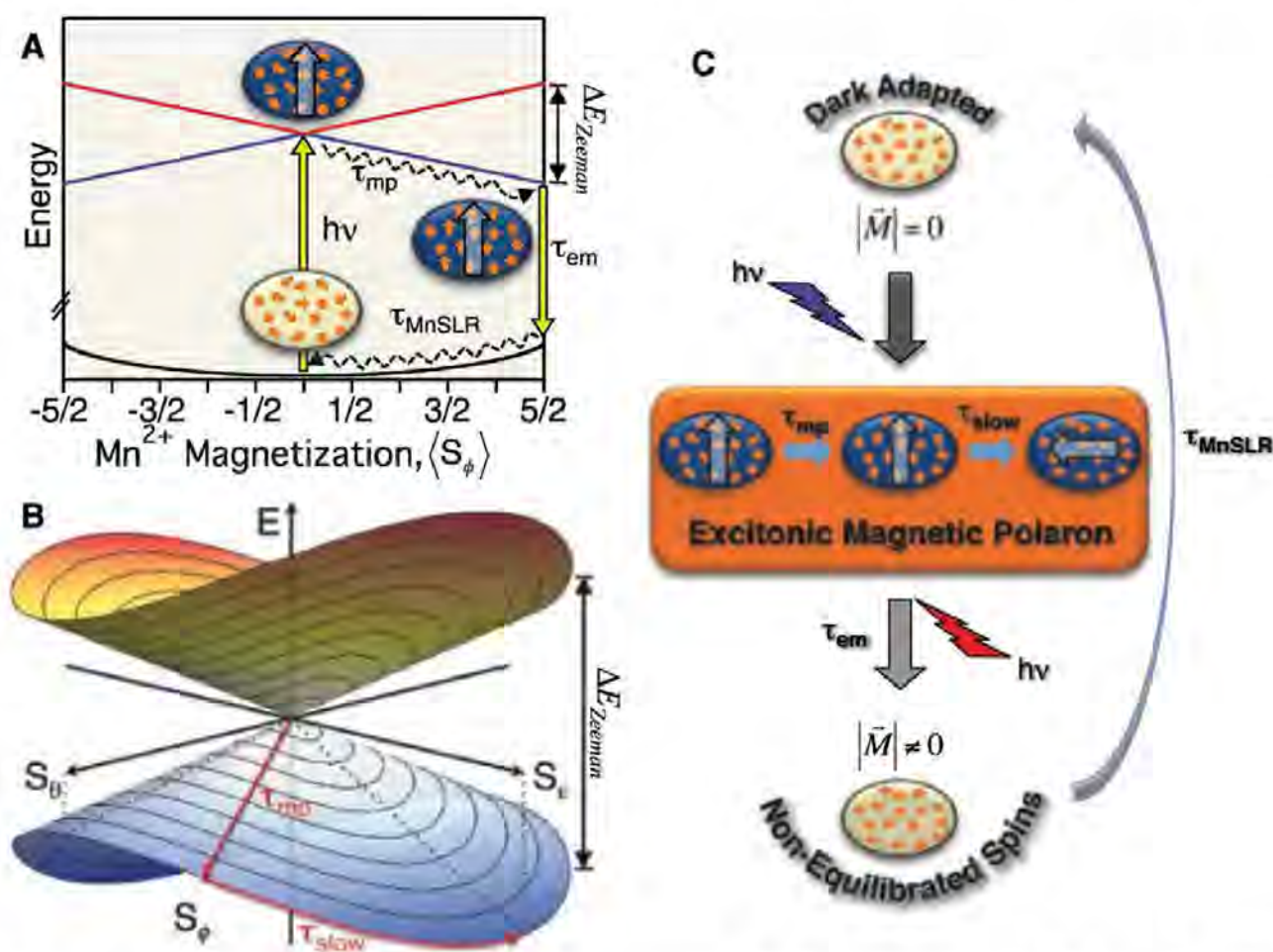


Fig. 4. Competition among dynamic relaxation processes. (A) Magnetic coordinate diagram illustrating spontaneous Mn^{2+} magnetization under the exchange field of the exciton, oriented along a random initial coordinate ϕ . The orange and blue lines represent the upper and lower Zeeman components, respectively, of the lowest excitonic level. Magnetization occurs with τ_{mp} and competes with τ_{em} . After exciton recombination (with τ_{em}), the Mn^{2+} spin sublattice relaxes back to zero net magnetization with τ_{MnSLR} . ΔE_{Zeeman} , the total excitonic Zeeman splitting energy; h , Planck's constant; ν , frequency. (B) Schematic illustration of the effect of anisotropy on the excited-state potential energy surfaces described in (A) for a hypothetical case of axial anisotropy, where θ and ϵ represent the two unique magnetization orientations. The orange and blue surfaces represent the upper and lower Zeeman components, respectively. Lower-symmetry anisotropies will cause more ruffling. (C) Schematic summary of all competing dynamics within (B). Photoexcitation of a dark-adapted Mn^{2+} :CdSe QD initiates EMP formation. Fast relaxation occurs with τ_{mp} along a random initial direction ϕ and is followed by slow reorientation toward ϵ with τ_{slow} to minimize total energy. These kinetics are in competition with τ_{em} . After recombination, the system returns to its dark-adapted form with τ_{MnSLR} .

Printed Assemblies of Inorganic Light-Emitting Diodes for Deformable and Semitransparent Displays

Sang-Il Park,^{1*} Yujie Xiong,^{1*†} Rak-Hwan Kim,^{1*} Paulius Elvikis,² Matthew Meitl,³ Dae-Hyeong Kim,¹ Jian Wu,⁴ Jongseung Yoon,¹ Chang-Jae Yu,¹ Zhuangjian Liu,⁵ Yonggang Huang,^{4,6} Keh-chih Hwang,⁷ Placid Ferreira,² Xiuling Li,⁸ Kent Choquette,⁸ John A. Rogers^{1,2‡}

We have developed methods for creating microscale inorganic light-emitting diodes (LEDs) and for assembling and interconnecting them into unusual display and lighting systems. The LEDs use specialized epitaxial semiconductor layers that allow delineation and release of large collections of ultrathin devices. Diverse shapes are possible, with dimensions from micrometers to millimeters, in either flat or “wavy” configurations. Printing-based assembly methods can deposit these devices on substrates of glass, plastic, or rubber, in arbitrary spatial layouts and over areas that can be much larger than those of the growth wafer. The thin geometries of these LEDs enable them to be interconnected by conventional planar processing techniques. Displays, lighting elements, and related systems formed in this manner can offer interesting mechanical and optical properties.

Display devices represent ubiquitous, central components of nearly all consumer electronics technologies. Organic light-emitting diodes (OLEDs) are rapidly emerging as an attractive alternative to backlit liquid crys-

tals due to their comparatively high refresh rates, contrast ratios, power efficiencies, and capacity for vibrant color rendering (*1, 2*). Inorganic light-emitting diodes (ILEDs) can also form displays, with properties such as brightness, lifetime, and

efficiency that can exceed those possible with OLEDs (*3, 4*). These displays exist, however, only in ultralarge-area, low-resolution formats (square meters; billboard displays), limited by processing and assembly procedures that do not scale effectively to small ($< \sim 200 \mu\text{m}$ by $200 \mu\text{m}$), thin ($< \sim 200 \mu\text{m}$) light emitters or to dense, high-pixel count arrays. An ability to replace existing

¹Departments of Materials Science and Engineering, Beckman Institute, and Frederick Seitz Materials Research Laboratory, University of Illinois at Urbana-Champaign, 1304 West Green Street, Urbana, IL 61801, USA. ²Department of Mechanical Science and Engineering, University of Illinois at Urbana-Champaign, 1206 West Green Street, Urbana, IL 61801, USA. ³Semprius, Durham, NC 27713, USA. ⁴Department of Civil and Environmental Engineering, Northwestern University, Evanston, IL 60208, USA. ⁵Institute of High Performance Computing, 1 Fusionopolis Way, 16-16 Connexis, Singapore 138632. ⁶Department of Mechanical Engineering, Northwestern University, Evanston, IL 60208, USA. ⁷Department of Engineering Mechanics, Tsinghua University, Beijing 100084, China. ⁸Department of Electrical and Computer Engineering, University of Illinois at Urbana-Champaign, 1206 West Green Street, Urbana, IL 61801, USA.

*These authors contributed equally to this work.

†Present address: School of Engineering and Applied Science, Washington University, St. Louis, MO 63130, USA.

‡To whom correspondence should be addressed. E-mail: jrogers@uiuc.edu

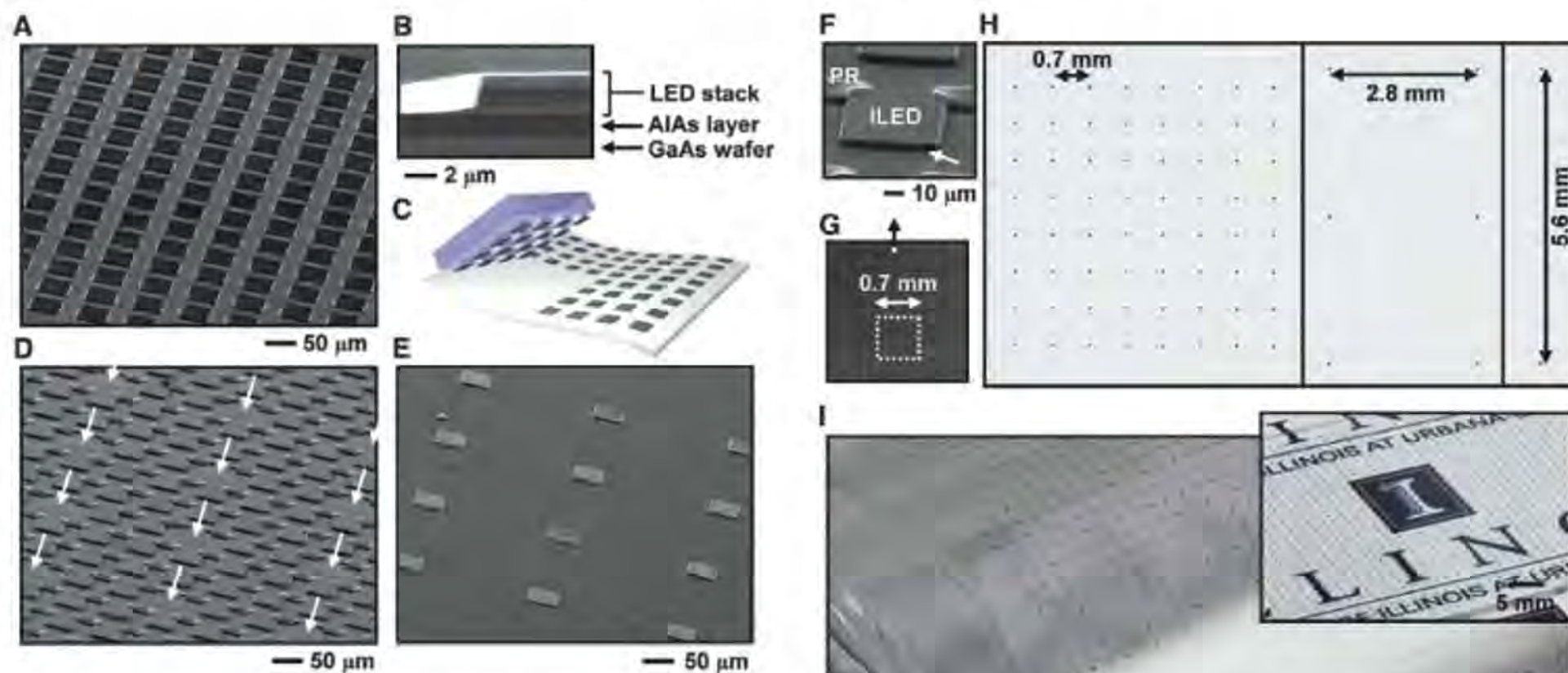


Fig. 1. (A) SEM image of a square array of AlInGaP LED structures ($50 \mu\text{m}$ by $50 \mu\text{m}$) created by vertical, patterned etching through an epitaxial multilayer stack grown on a GaAs wafer. (B) Cross-sectional SEM view of one of these structures, showing the LED semiconductor layers (quantum wells, as well as cladding, spreading, and contact layers) on a sacrificial epilayer of AlAs. (C) Schematic illustration of a printing-based assembly method for transferring collections of LEDs (gray) released from the GaAs wafer to a target substrate (shown here as a flexible sheet). (D) SEM image of the GaAs wafer after removing a set of LEDs (indicated by white arrows) with a stamp. (E) SEM image of a region of the target substrate printed with this stamp. (F) Angled-view SEM image of an individual LED (i.e., ILED) from the array in (D). A pair of “breakaway” photoresist (PR) anchors at the two far corners of the device holds it above the GaAs wafer in the suspended configuration of a diving board, for ease of liftoff with a stamp. The white arrow points to the region of removed AlAs. (G) SEM image of a dense collection of such devices on a piece of a GaAs wafer. The black arrow and white dot indicate, roughly, the region of this chip that corresponds to the image of (F).

(H) Optical image of a target substrate printed with sparse arrays of devices at different spacings, derived from the chip shown in (G). (I) Large-scale collection of ILEDs (1600 devices, in a square array with pitch of 1.4 mm) printed onto a thin, flexible sheet of plastic, shown here wrapped onto a cylindrical glass substrate (main panel). The inset shows a similar collection of ILEDs (1600 devices, in a square array with pitch of 1.4 mm) printed onto a plate of glass. For these cases, relatively large ILEDs were selected for ease of viewing; devices with dimensions of (E) are invisible at this magnification.

methods for fabricating ILEDs (i.e., wafer sawing, serial pick-and-place, wire bonding, and packaging on a device-by-device basis) and for incorporating them into displays (i.e., robotic assembly into tiles followed by interconnection using large quantities of bulk wiring) with those that more closely resemble the planar, batch processing of OLEDs would greatly expand the application opportunities. Examples include not only ILED displays for desktop monitors, home theater systems, and instrumentation gauging, but also, when implemented in flexible or stretchable forms, wearable health monitors or diagnostics and biomedical imaging devices. In microscale sizes, such ILEDs can also yield semitransparent displays, with the potential for bidirectional emission characteristics, for vehicle navigation, heads-up displays, and related uses.

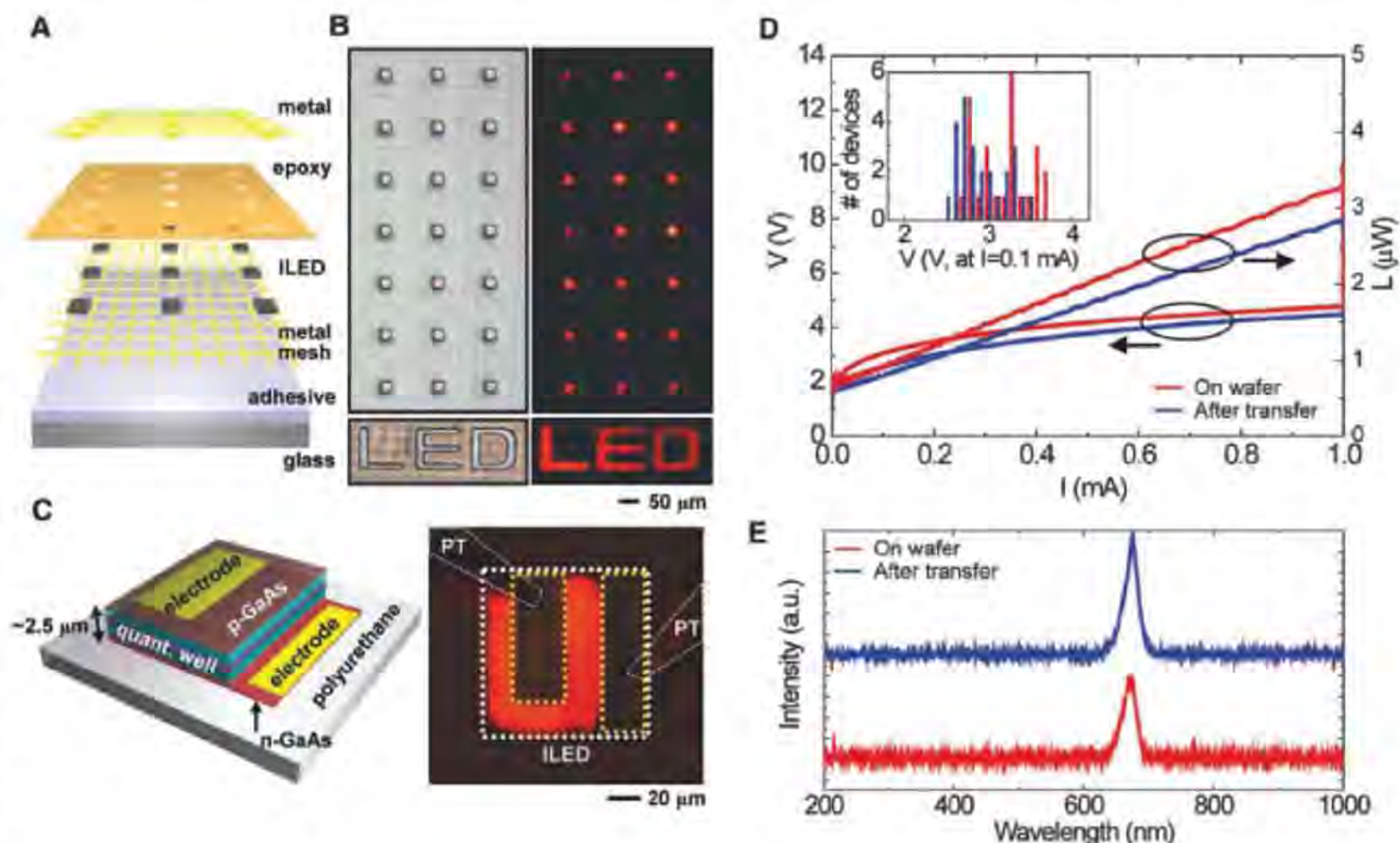
We present routes to create ultrathin, ultra-small ILEDs in flat or “wavy” geometries and to assemble them into addressable arrays using scalable processing techniques, on substrates ranging from glass to plastic and rubber. The strategy involves four key components: (i) epitaxial semiconductor multilayers designed for lateral delineation and release from a source wafer to yield isolated arrays of ILEDs, each of which remains tethered to the wafer by polymeric “breakaway” anchor structures; (ii) printing techniques for manipulating the resulting ILEDs in schemes that enable formation of large-scale arrays on foreign substrates and in arbitrary spatial layouts; (iii) planar processing methods for

establishing electrical interconnects to the devices, in direct or matrix addressable configurations; and (iv) integration strategies capable of yielding ILED displays in flexible or stretchable formats and with conventional, semitransparent, or bidirectional emission characteristics. Certain aspects build on previously reported procedures for etching and manipulating epitaxial semiconductor layers (5–11) and for fabricating flexible and stretchable electronics (12, 13).

Figure 1 presents essential aspects of the first two of the components [see supporting online material (SOM) for details]. The epitaxial semiconductor layers include AlInGaP quantum well structures (6-nm-thick $\text{In}_{0.56}\text{Ga}_{0.44}\text{P}$ wells, with 6-nm-thick barriers of $\text{Al}_{0.25}\text{Ga}_{0.25}\text{In}_{0.5}\text{P}$ on top and bottom), cladding films (200-nm-thick layers of $\text{In}_{0.5}\text{Al}_{0.5}\text{P}:\text{Zn}$ and $\text{In}_{0.5}\text{Al}_{0.5}\text{P}:\text{Si}$ for the p and n sides, respectively), spreaders (800-nm-thick layers of $\text{Al}_{0.45}\text{Ga}_{0.55}\text{As}:\text{C}$ and $\text{Al}_{0.45}\text{Ga}_{0.55}\text{As}:\text{Si}$ for the p and n sides, respectively), and contacts (5-nm-thick layer of GaAs: C and 500-nm-thick layer of GaAs:Si for the p and n sides, respectively), for a total thickness of $\sim 2.523\text{ }\mu\text{m}$, all grown on AlAs (1500-nm-thick layer of $\text{Al}_{0.96}\text{Ga}_{0.04}\text{As}:\text{Si}$) on a GaAs substrate (fig. S1). The AlAs can be removed by etching with hydrofluoric (HF) acid, in procedures that do not alter the overlying layers or the underlying substrate. The process for defining the ILEDs first involves forming a pattern of vertical trenches through the epitaxial layers by inductively coupled plasma reactive ion etching through a mask of

SiO_2 defined photolithographically (fig. S2). This step determines the lateral geometries of the devices (fig. S2). Figure 1, A and B, shows top and cross-sectional scanning electron microscope (SEM) images collected after this etching process for a representative case, where the device islands in Fig. 1 are $50\text{ }\mu\text{m}$ by $50\text{ }\mu\text{m}$. Creating a pattern of photoresist posts (i.e., “breakaway” anchors) located at two of the four corners of each island, followed by immersion in concentrated HF, leads to the undercut release of an organized array of ILEDs. The anchors hold the devices in their lithographically defined locations to prevent lift-off into the etching bath, even after complete undercut (fig. S2). Next, an automated printing tool (fig. S3) brings a soft elastomeric stamp with features of relief embossed onto its surface into aligned contact with a selected set of these ILEDs. Peeling the stamp away fractures the photoresist anchors and leaves the devices adhered via Van der Waals interactions to the raised regions of relief. Figure 1, C and D, shows schematic illustrations of the printing process and an SEM image of an array of anchored ILEDs on the source wafer after one cycle of printing (fig. S4). The white arrows in Fig. 1D highlight the collection of ILEDs removed by this process, corresponding to every third device along the two orthogonal axes of the square array. Figure 1E provides an SEM image of these devices printed onto a glass substrate. The engineering design of the breakaway anchors is such that they are sufficiently robust to hold the ILEDs in their

Fig. 2. (A) Exploded view schematic illustration of an array of ILEDs contacted by a metal mesh (bottom; n contacts) and a metal film (top; p contacts). A thin adhesive layer of PDMS facilitates printing onto the glass substrate. A photopatterned layer of epoxy on top of the devices prevents shorting of the top film to the bottom mesh. (B) Optical micrographs of an array of ILEDs (top: $25\text{ }\mu\text{m}$ by $25\text{ }\mu\text{m}$, square geometries; bottom: characters “LED”) in their off state with frontside illumination (left) and in their on state without illumination (right). (C) Schematic illustration of an ILED with integrated ohmic contacts (left) and optical image of an operating device (right), showing uniform emission characteristics at all regions not directly blocked by the contacts or probe tips. The areas delineated by yellow and white dashed boxes correspond to the contact electrodes and the device periphery, respectively. The regions labeled “PT” correspond to the probe tips used to evaluate the device operation. (D) Current-voltage-emission characteristics of a



representative device before undercut etching on the GaAs wafer, and after transfer printing onto a polyurethane-coated glass slide. The inset provides a histogram of the bias voltages needed to produce currents of 0.1 mA in a collection of devices. (E) Spectral characteristics of emission for a typical device on the wafer and after transfer printing.

lithographically defined locations during the undercut etching and drying processes but sufficiently fragile to enable high-yield liftoff during printing. Three key design aspects are the use of (i) a pair of anchors on the same side of each ILED, to yield, after undercut, suspended, “diving board” layouts (Fig. 1F) that enable transfer of torques large enough to fracture the photoresist upon peel-back of the stamp; (ii) stamps with relief structures that are slightly smaller than the ILEDs and are offset from the centers of the devices to maximize these torques and also to minimize overlap with the anchors; and (iii) photoresist structures that fracture more readily than the semiconductor material. This type of anchoring scheme (i.e., heterogeneous anchoring) is much more efficient in active materials utilization and versatile in design choices than corresponding methods demonstrated previously for transistors (12) and solar cells (14), where peripheral parts of the devices themselves serve as the anchors (i.e., homogeneous anchoring). Conventional wafer dicing and pick-and-place

methods are not suitable for devices with the thicknesses and dimensions in the range reported here, due to challenges associated with wafer utilization, device fragility, and size. Such techniques also lack the high-throughput, parallel operation of the type of printing methods described above.

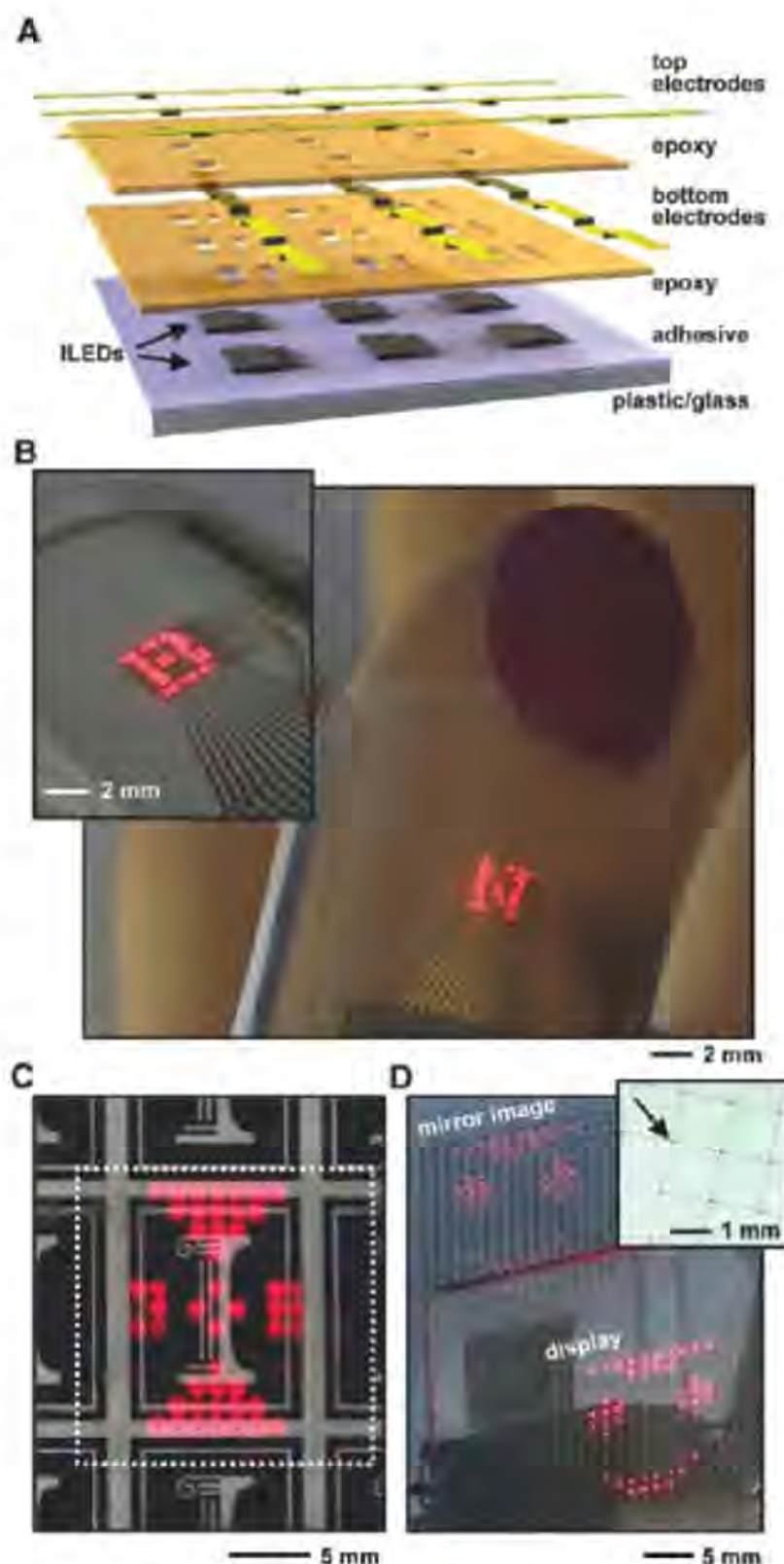
Figure 1G shows a micrograph of a densely packed array of anchored, undercut ILEDs on a source wafer. Figure 1H shows sparse assemblies of these devices formed by printing in a step-and-repeat fashion from this wafer to a glass substrate, coated with a thin ($\sim 10\ \mu\text{m}$) layer of poly(dimethylsiloxane) (PDMS) to promote dry, conformal adhesion (details are in the SOM). As examples of high yields, large areas, and compatibility with plastic substrates, Fig. 1I presents images of collections of ILEDs printed onto a thin sheet of polyethylene terephthalate (PET, $50\ \mu\text{m}$ thick), shown as wrapped around a cylindrical glass support (1600 devices, in a square array with pitch of $1.4\ \text{mm}$; radius of cylinder $\sim 25\ \text{mm}$) and onto a plate of glass (inset; 1600 devices, in a square array with pitch of

$1.4\ \text{mm}$). The overall fabrication yields, including delineation and undercut of the ILEDs and subsequent printing of them onto the target substrates, were 100% in both cases. The devices were selected to have sizes (i.e., $250\ \mu\text{m}$ by $250\ \mu\text{m}$) large enough to be visible in the images; those with sizes of Fig. 1D are too small to be seen clearly at these scales.

Establishing electrical connections to these printed ILEDs yields lighting elements or addressable displays. The small thickness ($\sim 2.5\ \mu\text{m}$) of the devices enables the use of conventional thin-film processing, thereby providing a route to displays and related devices that is simpler, more scalable, and applicable to much smaller pixel geometries than established wire bonding and packaging techniques. To demonstrate the most basic scheme, we printed a collection of devices onto a thin, metal mesh on a transparent substrate, to form bottom contacts, and then established separate top contacts using a planar lithographic process (fig. S5). Figure 2, A and B, shows an exploded view schematic illustration and optical micrograph of an array of small, square devices ($\sim 25\ \mu\text{m}$ by $25\ \mu\text{m}$), as well as those with shapes that spell “LED.” The results indicate bright emission, even out to the edges of the devices, consistent with the relatively low surface recombination velocity in AlInGaP materials (15, 16). For improved performance, ohmic contacts can be implemented by using established metallization and annealing schemes (17, 18). One strategy involves additional processing on the source wafer to yield released devices with integrated ohmic contacts, suitable for printing and interconnection even on low-temperature substrates such as plastic or rubber. An alternative is to use low-temperature approaches to establish the ohmics directly on such substrates. For this work, we pursued the second strategy, using processes that involve temperatures below 175°C (see SOM for details and fig. S6 for transmission-line model analysis of the contact resistances). Figure 2C shows the layout of an ILED with ohmic contacts printed onto a thin layer of polyurethane on a glass substrate, and an optical micrograph of emission from a directly probed device. Figure 2, D and E, presents electrical and optical characteristics of a set of such devices, recorded on the wafer before undercut etching and after printing. The processing in this case used a passivation scheme to eliminate moderate degradation in performance associated with the HF etching step on unprotected devices (fig. S7). The resulting current-voltage-emission behavior of the printed devices is comparable to that of the devices on the wafer (see SOM for processing details and for statistics on devices with two different sizes).

Figure 3A provides a schematic illustration of an interconnect scheme for passive matrix addressing. Photolithography and electron beam evaporation define patterned metal electrodes [Ti ($20\ \text{nm}$)/Au ($300\ \text{nm}$)] that connect p and n contacts (nonohmic for the cases of Figs. 3 and 4) of devices in common columns and rows, respec-

Fig. 3. (A) Schematic illustration of a planar scheme for interconnecting a printed array of ILEDs in a passive matrix layout. Coordinated control of voltages applied to the row and column electrodes allows operation in a passive matrix display mode. (B) Images of a flexible display that incorporates a 16 by 16 array of ILEDs in the layout shown in (A), on a sheet of plastic (PET), wrapped around the thumb of a mannequin hand (main panel; human scale; radius $\sim 8\ \text{mm}$) and a cylindrical glass tube (inset; radius $\sim 12\ \text{mm}$). External interface to control electronics occurs through ribbon cables bonded to column and row electrodes that emerge from the periphery of the display. (C) Image of a comparatively large, semi-transparent display that uses a similar layout but with a sparse array of ILEDs on a glass substrate. The camera is focused on the paper in the background; the white dashed box illustrates the perimeter of the active region of the display. (D) Image of a similar device (bottom right) displaying a different pattern in front of a mirror (upper left), to illustrate the bidirectional emission property. In this system, the ILEDs represent only $\sim 0.8\%$ of the total area. The inset shows a magnified view of a region of the display in its off state, to illustrate the small areal coverage of the devices. The black arrow points to one of the ILEDs, which is barely visible at this magnification.



tively. Two spin-cast, photopatterned layers of epoxy (1.2 μm thick) provide openings to these contacts; the top layer electrically separates the column and row electrodes at their crossing points. Connecting terminal pads at the ends of these electrode lines to external computer control systems via ribbon cables that use anisotropic conductive films (ACFs) enables passive matrix addressing (see SOM and fig. S8 for details). Figure 3B shows images of a small display that uses this design, formed on a thin sheet of plastic (PET, 50 μm thick) with a layer of a photocurable polyurethane as an adhesive. The ILEDs have dimensions of 100 μm by 100 μm and are configured into a 16 by 16 square array. The yields on the individual pixels for the case of Fig. 3B are 100%; at the level of the display, one column and two rows do not function, due to breaks in the contacts to the ACF ribbon cable [fig. S9; see SOM and fig. S10 for an example of similar display with even smaller ILEDs (50 μm by 50 μm)]. Such systems can be bent to radii of curvature of ~ 7 mm, with no observable degradation, even for several hundred cycles of bending (fig. S11). Analytical calculation shows that even at the minimum bend radius investigated here, the maximum strain in the ILED is 0.21%, with a somewhat smaller strain (0.19%) in the quantum well region (see SOM for details). Analysis using literature parameters to determine the dependence of the bandgap on strain (19–22) suggests changes in emission wavelength of ~ 2.4 nm for the smallest bend radius (see SOM for details).

As shown in Fig. 1, step-and-repeat printing can yield systems that cover areas much larger than those of the constituent ILEDs or the source wafer. One important outcome is the ability to form displays that can offer an effectively high level of transparency, where only the ILEDs (and the electrodes, if they are not made with transparent conductors) are opaque. Figure 3, C and D, shows examples of a 16 by 16 array, formed on glass. Here the area of the display is ~ 325 mm²; the cumulative area of all the ILEDs is only ~ 2.5 mm², corresponding to less than $\sim 1\%$ of the display area. Figure 3C illustrates the operation of such a system positioned above a sheet of paper with printed logos; the focus of the image is on the paper, thereby illustrating a practical level of transparency for application in a heads-up display, for example. Figure 3D shows the same device (lower right), operating in front of a mirror (upper left) to demonstrate bidirectional emission characteristics. The inset provides a magnified view of a region of this display, in its off state to show the small sizes of the ILEDs compared to the unit cells. These layouts are critically important for many applications, due to the efficient utilization of the LED material, for reduced cost. For the examples shown, we achieved $\sim 98\%$ yields on the individual devices, and $\sim 80\%$ yields on the interconnections, limited by breaks in the metal lines and failed contacts to the ACF ribbon cable (fig. S12).

The devices and integration methods reported here are compatible with strategies to produce

stretchable electronics (12, 13), thereby providing a route to conformable displays and lighting systems of the type that might be interesting for integration with the human body and other curvilinear, deformable surfaces, all of which demand more than simple bending (e.g., Fig. 3B). Figure 4A shows an example of a stretchable ILED with the shape of a ribbon. This device was formed by transfer printing and bonding to a prestrained, rubber substrate of PDMS. Relaxing the prestrain creates a device with a “wavy,” sinusoidal profile; this structure responds elastically to applied strain with a physics similar to that of an accordion bellows (12, 23) to yield a stretchable ILED device. The top panels provide finite element simulation of the mechanics of the system in compressed (left) and stretched (right) configurations. The results indicate maximum strains in the ILED and the quantum well region of 0.36 and 0.053%, respectively (see SOM for details). The bottom panels show optical micrographs in the off (top) and on (bottom) states, with and without external illumination, respectively, in configurations similar to those illustrated in fig. S18A. The emission characteristics show no noticeable change in color with applied strain or associated changes in device geometry from “wavy” to flat (see SOM and figs. S13 and S14 for details). This observation is consistent with a calculated change in emission wavelength of less than ~ 0.7 nm based on our computed strain values and analysis similar to that performed for the flexible display (see SOM for details).

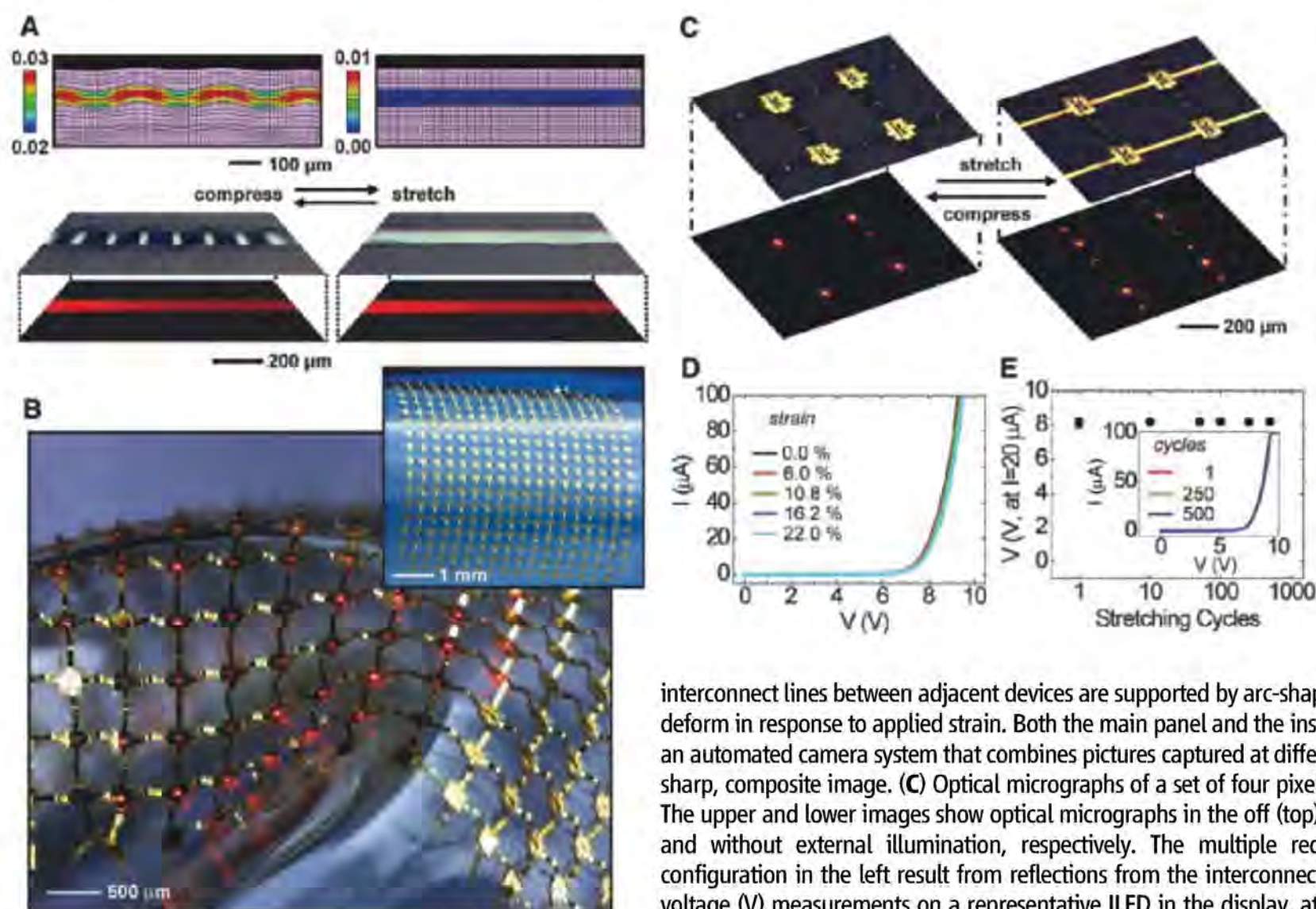


Fig. 4. (A) Color plots of the strain distributions (in percent) at the quantum well region and the corresponding finite element mesh used for simulation (top) and optical micrographs (bottom) of a stretchable ILED on a rubber substrate in unstrained and strained states. The bottom panels show optical micrographs in the off (top) and on (bottom) states, with and without external illumination, respectively. (B) Passive matrix, stretchable ILED display that uses a noncoplanar mesh configuration, on a rubber substrate. Here,

interconnect lines between adjacent devices are supported by arc-shaped bridge structures that can deform in response to applied strain. Both the main panel and the inset images were collected with an automated camera system that combines pictures captured at different focal depths to provide a sharp, composite image. (C) Optical micrographs of a set of four pixels in the display shown in (B). The upper and lower images show optical micrographs in the off (top) and on (bottom) states, with and without external illumination, respectively. The multiple red spots in the case of the configuration in the left result from reflections from the interconnection bridges. (D) Current (I)–voltage (V) measurements on a representative ILED in the display, at different applied strains. (E)

Voltage (V) needed to generate a current of 20 μA measured after stretching cycles to 500 times at an applied strain of 22%. The inset shows the I–V behavior after these cycling tests. These devices have relatively high turn-on voltages, due to the use of nonohmic contacts.

The “wavy” strategy of Fig. 4A can accommodate only a relatively modest range of applied strains (i.e., up to a few percent, for the designs reported here). A path to displays with high levels of stretchability uses non-coplanar mesh designs adapted from schemes reported for integrated circuits (13). Figure 4B presents optical micrographs of such a system, composed of a 16 by 16 square array of ILEDs bonded to a PDMS substrate and interconnected by electrodes supported by arc-shaped bridges, with a fraction of the pixels turned on (overall yield >80%) (see SOM and fig. S15 for details). The shapes of these bridges change in response to deformations of the display, in a way that isolates the ILEDs from any significant strains (figs. S16 and S17). In particular, calculation shows that for strains of 24%, as defined by the change in separation between inner edges of adjacent device islands, the maximum strains in the ILED and quantum well are only 0.17 and 0.026%, respectively. The computed change in emission wavelength is less than ~0.3 nm (see SOM for details). Figure 4C provides optical micrographs of four pixels in this display, in their off and on states, with (top) and without (bottom) external illumination, respectively, in compressed and stretched configurations. The images show the expected reduction in the heights of the arc-shaped bridges that lie in the direction of the applied tensile force (i.e., along the interconnects that run from lower left to upper right), together with an increase in the heights of the bridges in the orthogonal direction, due to the Poisson effect. This mechanical response is fully elastic—the bending-induced strains in the interconnects are small, the strains in the ILEDs are negligible, and the strain in the PDMS is well within its linear response regime. The data in Fig. 4, D and E, are consistent with this mechanics, as are the associated mechanics calcu-

lations. In particular, the current-voltage characteristics of a typical device do not change in a measurable way for applied strains up to ~22%, and we observe no degradation on cycling up to a few hundred times (500 times). Recent work demonstrates the use of smaller collections of large, conventional ILEDs in deformable devices that use different designs (24, 25).

The schemes reported here for creating thin, small inorganic LEDs and for integrating them into display and lighting devices create design options that are unavailable with conventional procedures. The planar processing approaches for interconnect resemble those that are now used for organic devices and, for example, large-area electronics for liquid crystal displays, thereby conferring onto inorganic LED technologies many of the associated practical advantages. In large-area, high-pixel count systems (e.g., 1 million pixels per square meter), the ability to use LEDs with sizes much smaller than those of the individual pixels is critically important to achieve efficient utilization of the epitaxial semiconductor material, for reasonable cost. The minimum sizes of devices reported here are limited only by the resolution and registration associated with manual tools for photolithography.

References and Notes

1. S.-C. Lo, P. L. Burn, *Chem. Rev.* **107**, 1097 (2007).
2. F. So, J. Kido, P. Burrows, *MRS Bull.* **33**, 663 (2008).
3. D. A. Gaul, W. S. Rees Jr., *Adv. Mater.* **12**, 935 (2000).
4. S. Nakamura, G. Fasol, *The Blue Laser Diode: GaN Based Light Emitters and Lasers* (Springer, New York, 1997).
5. E. Yablonovitch, D. M. Hwang, T. J. Gmitter, L. T. Florez, J. P. Harbison, *Appl. Phys. Lett.* **56**, 2419 (1990).
6. H. X. Jiang, S. X. Jin, J. Li, J. Shaky, J. Y. Lin, *Appl. Phys. Lett.* **78**, 1303 (2001).
7. M. Konagai, M. Sugimoto, K. Takahashi, *J. Cryst. Growth* **45**, 277 (1978).
8. E. Yablonovitch, T. Gmitter, J. P. Harbison, R. Bhat, *Appl. Phys. Lett.* **51**, 2222 (1987).

9. C. Camperi-Ginestet, M. Hargis, N. Jokerst, M. Allen, *IEEE Trans. Photon. Tech. Lett.* **3**, 1123 (1991).
10. C. Carter-Coman, R. Bicknell-Tassius, A. S. Brown, N. M. Jokerst, *Appl. Phys. Lett.* **70**, 1754 (1997).
11. M. A. Meitl *et al.*, *Nat. Mater.* **5**, 33 (2006).
12. D. Y. Khang, H. Jiang, Y. Huang, J. A. Rogers, *Science* **311**, 208 (2006).
13. D.-H. Kim *et al.*, *Proc. Natl. Acad. Sci. U.S.A.* **105**, 18675 (2008).
14. J. Yoon *et al.*, *Nat. Mater.* **7**, 907 (2008).
15. M. Tamura *et al.*, *Jpn. J. Appl. Phys.* **37**, 3576 (1998).
16. E. F. Schubert, *Light-Emitting Diodes* P. 43, (Cambridge Univ. Press, Cambridge, UK, 2003).
17. C. L. Chen *et al.*, *Appl. Phys. Lett.* **48**, 535 (1986).
18. G. Stareev, *Appl. Phys. Lett.* **62**, 2801 (1993).
19. D. P. Bour *et al.*, *IEEE J. Quantum Electron.* **30**, 593 (1994).
20. F. H. Pollak, *Surf. Sci.* **37**, 863 (1973).
21. M. Chandrasekhar, F. H. Pollak, *Phys. Rev. B* **15**, 2127 (1977).
22. S. H. Pan *et al.*, *Phys. Rev. B* **38**, 3375 (1988).
23. H. Jiang *et al.*, *Proc. Natl. Acad. Sci. U.S.A.* **104**, 15607 (2007).
24. D. S. Gray, J. Tien, C. S. Chen, *Adv. Mater.* **16**, 393 (2004).
25. F. Axisa, F. Bossuyt, T. Vervust, J. Vanfleteren, *2nd Electronics System-integration Technology Conference (ESTC 2008)*, 1387, Greenwich, UK, 1 to 4 September 2008.
26. We thank T. Banks for help with processing using facilities at the Frederick Seitz Materials Research Laboratory; S. Mikael, V. Malyarchuk, H. C. Ko, and S.-G. Koo for assistance with display operating interface; J. D. Sulkin for help with current-voltage-emission measurement; A. P. Le for help with measurement of emission spectra; and C. Conway, Z. Johnson, and H.-S. Kim for help with photography. This material is based on work supported by Ford Motor Company, the NSF (grant DMI-0328162), and the U.S. Department of Energy, Division of Materials Sciences (Award No. DE-FG02-07ER46471), through the Materials Research Laboratory and Center for Microanalysis of Materials (DE-FG02-07ER46453) at the University of Illinois at Urbana-Champaign. S.-I. Park and R.-H. Kim thank Samsung for doctoral fellowships.

Supporting Online Material

www.sciencemag.org/cgi/content/full/325/5943/977/DC1
Materials and Methods
Figs. S1 to S19
References

1 May 2009; accepted 1 July 2009
10.1126/science.1175690

Visualization of Fermi's Golden Rule Through Imaging of Light Emission from Atomic Silver Chains

Chi Chen,¹ C. A. Bobisch,² W. Ho^{1,2*}

Atomic-scale spatial imaging of one-dimensional chains of silver atoms allows Fermi's golden rule, a fundamental principle governing optical transitions, to be visualized. We used a scanning tunneling microscope (STM) to assemble a silver atom chain on a nickel-aluminum alloy surface. Photon emission was induced with electrons from the tip of the STM. The emission was spatially resolved with subnanometer resolution by changing the tip position along the chain. The number and positions of the emission maxima in the photon images match those of the nodes in the differential conductance images of particle-in-a-box states. This surprising correlation between the emission maxima and nodes in the density of states is a manifestation of Fermi's golden rule in real space for radiative transitions and provides an understanding of the mechanism of STM-induced light emission.

The scanning tunneling microscope (STM), which is based on the tunneling effect, has been used to visualize various quantum

phenomena in real space, including the quantum corral (1), quantum mirage (2), and particle-in-a-box states (3, 4). All of these demonstrations in-

involved the localization of the electron density of states in confined nanostructures. Light emission from the STM junction reveals a different kind of quantum phenomenon that involves the optical transitions and inelastic electron tunneling (IET) processes in single molecules (5, 6) and nanostructures (7). Furthermore, photon intensity imaging with atomic resolution has been demonstrated (8–10). The spatial resolution in these optical experiments originates from the precision of the STM in injecting electrons in a confined space, although the emitted photons are collected in the far field. This atomic-scale optical detection can reveal aspects of the molecules and nanostructures that are hidden when probed with other techniques.

Imaging of STM light emission has not yet been directly correlated with the underlying elec-

¹Department of Chemistry, University of California, Irvine, CA 92697, USA. ²Department of Physics and Astronomy, University of California, Irvine, CA 92697, USA.

*To whom correspondence should be addressed. E-mail: wilsonho@uci.edu

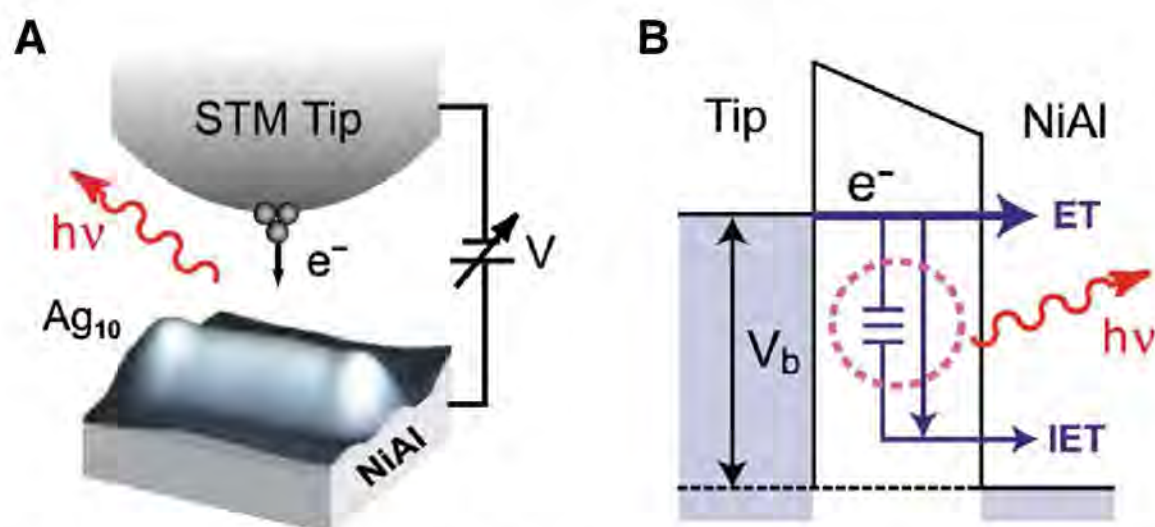


Fig. 1. (A) Illustration of Ag_{10} chain in the tunnel junction, assembled on the $\text{NiAl}(110)$ substrate. The Ag_{10} topography shown in the figure was taken at a bias of 2.8 V and tunneling current of 1 nA. (B) Schematic representation of photon emissions from two coupled IET processes, involving an electronic transition in resonance with the excitation of plasmon modes in the junction. The radiative decay of plasmons is detected as photons in the far field. In the resonant coupling, the plasmons oscillate at the same frequency as the light emitted in the transition between two electronic states of the Ag_{10} chain.

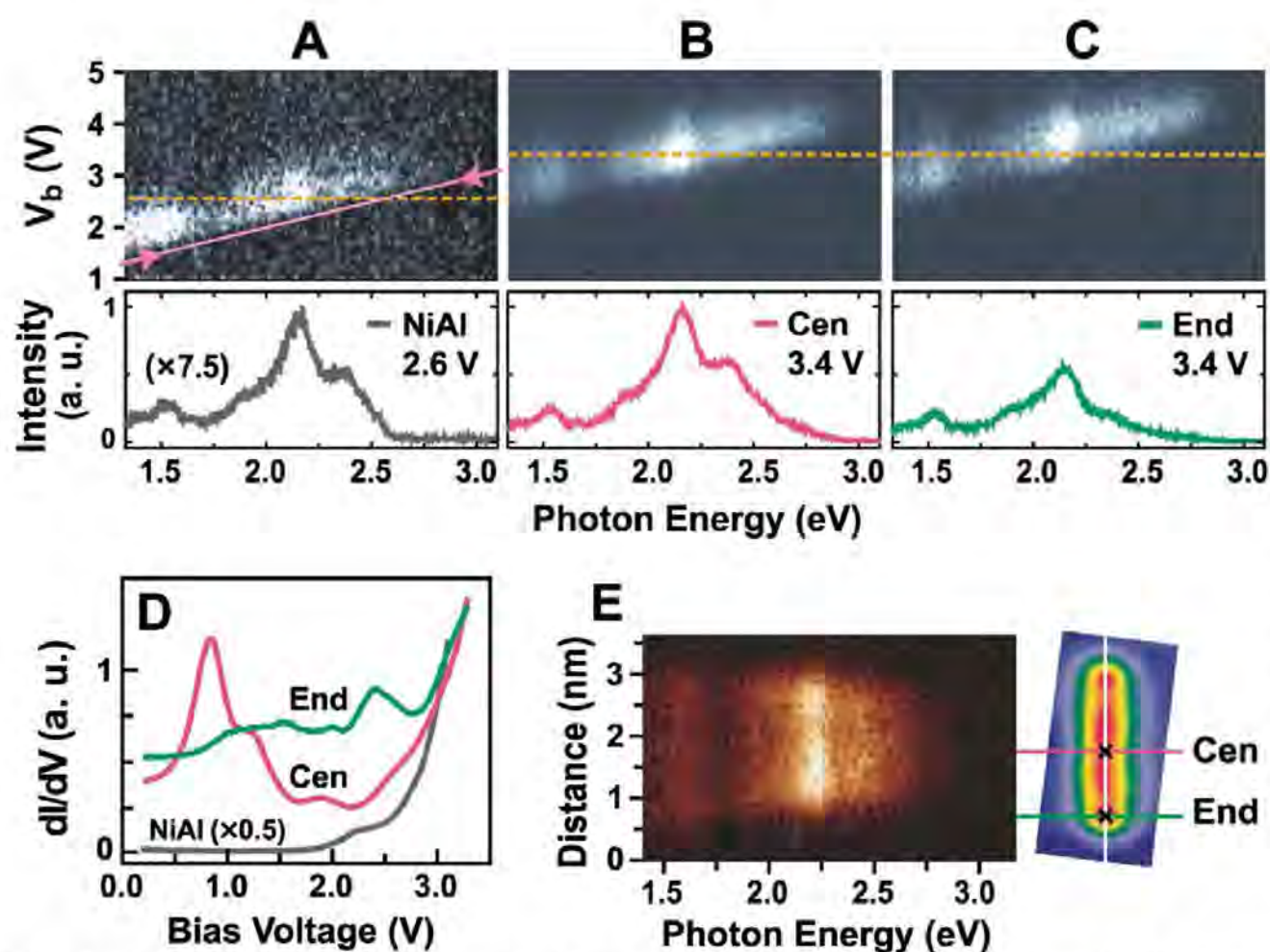


Fig. 2. (A to C) Excitation mappings and spectra taken over the NiAl substrate (A), the center (Cen) (B), and end (End) (C) of Ag_{10} , as indicated in the right panel of (E). (Upper panels) Excitation mappings are composed of a series of spectra taken with bias voltages from 1.0 to 5.0 V at 0.05-V intervals. The horizontal dashed lines (orange) represent the bias voltage for the bottom spectra. The quantum cutoff for substrate emission is shown as the solid line (magenta) in (A). (Lower panels) Spectra at the center [red (B)] and end [green (C)] of Ag_{10} at 3.4-V sample bias compared to the spectrum of the NiAl substrate [gray (A)] at 2.6 V. All spectra were accumulated for 20 s. (D) dI/dV spectra recorded at the center and end of the chain and over the NiAl substrate. At lower bias voltages ($V_b < 2.8$ V), the measured LDOS are mostly dominated by the Ag_{10} . At higher biases, the signal from the NiAl substrate surpasses that of Ag_{10} . (E) (Left) Emission intensity map composed of 96 spectra (1-s accumulation time each) taken along the center line of Ag_{10} chain (white line). (Right) Topographical image of Ag_{10} chain (7° rotation from vertical). The image size is 1.8 nm \times 3.6 nm. Both panels in (E) were recorded at 3.4 V and 6 nA. The positions for spectra taken over the chain (Cen, End) are indicated on the topographic image. The position for spectra taken over the NiAl substrate is outside the range of this image. All spectra shown here and used for photon images are raw data from the spectrometer without grating efficiency correction.

tronic structure of the adsorbate. The connection between the photon yield and the density of states remains to be further clarified. Even though the IET mechanism was proposed by Nazin *et al.* (7), the mechanisms of these radiative transitions and the fundamental selection rules have not been well understood. Here, we describe a system in which the interaction between the initial and final states that give rise to well-defined light emission arises via coupling through the momentum operator.

Here, we report photon imaging of optical transitions from atomic Ag chains to reveal the underlying physical principles and a direct visualization of Fermi's golden rule in real space (11). We manipulated Ag atoms on a $\text{NiAl}(110)$ substrate into one-dimensional (1D) chains following the method described in (3). An atomic chain serves as a model system to realize particle-in-a-box electronic states both in energy and in space. These electronic states could be visualized as a series of differential conductance (dI/dV) images that have different numbers of nodes and anti-nodes (4). This spatial distribution of local density of states (LDOS) dominates the probabilities of radiative electronic transitions in the spatial imaging of the emitted light. The experimental visualization of Fermi's golden rule serves to elucidate one of the fundamental principles in quantum mechanics.

Single Ag atoms were produced by field emission of the Ag tip on a clean NiAl surface and were characterized by dI/dV spectroscopy (7). Every Ag atom exhibits a single peak at 2.1 to 2.2 V in the dI/dV spectrum, which can be easily distinguished from other atoms (Ni or Al) on the surface. After the addition of each Ag atom to the chain, dI/dV spectra along the chain were recorded to characterize the electronic states at each chain length. Results are presented here for the representative case of Ag_{10} , which is the longest chain that was built in this experiment (Fig. 1A).

Photon emission from the STM junction occurs through radiative decay of localized surface plasmons that are excited by IET processes (5, 12, 13). These junction plasmons decay as broadband emission with multiple peaks. Their spectral shape is primarily determined by the structure of the STM tip apex at the nanometer scale and also by the dielectric properties of both the tip and substrate (14). A schematic illustration of radiative emission in the tunneling process is shown in Fig. 1B.

When electrons tunnel through the junction, both elastic tunneling (ET) and IET are possible. The IET channel can be observed when it couples to the excitation of other physical quantities such as molecular vibrations, substrate phonons, plasmons, or electronic transitions. For example, if the IET couples to a vibrational mode, it can be measured through a change in the conductance (dI/dV) as the voltage across the tunneling gap passes through the value V_ω corresponding to the vibrational energy $eV_\omega = \hbar\omega$,

where e is the charge of an electron, \hbar is Planck's constant divided by 2π , and ω is angular frequency (15).

In our experimental case, the IET process could be observed because of the coupling with plasmon modes and electronic transitions. Unlike the ET process, which probes the LDOS only at the applied bias voltage, the IET channel involves both the initial and final LDOS of the inelastic process. The IET efficiency is determined by two factors: The first factor involves the radiative transition between the initial and final states in the tunneling process, and the second factor is that the coupling to the plasmon modes in the junction leads to field enhancement of the radiation field. However, no direct experimental evidence could test this IET process, especially when its analysis required the interpretation of local variations in photon intensity imaging (16).

The radiative emission of plasmons can be characterized by "excitation mapping" (Fig. 2, A to C, upper panels), which reveals the spectral structures of the plasmon emission that shift with the bias voltage. From the spectral evolution of the substrate with increasing bias (Fig. 2A, upper panel), two main emission bands were resolved from the tip–NiAl junction; one was in the visible spectrum and the other lies in the near-infrared. The highest photon energy detected was 2.95 eV, even with higher biases. This is strong evidence for the plasmon emission mechanism. If the emission is through different mechanisms (i.e., hot electron and hole recombination), then higher-energy photons should be emitted as the bias is increased.

When the Ag₁₀ chain was in the junction, the emission spectral features of the tip–Ag₁₀–NiAl junction remained similar to that of tip–NiAl junction;

no additional mode was observed (Fig. 2, B and C, bottom panels). This observation is distinct from theoretical predictions of localized plasmon modes of free atomic chains (17). Because the length of Ag₁₀ from the topographic image is 3.2 to 3.4 nm, depending on the bias, it may be too confined to support localized plasmon modes (18).

Although no new plasmon mode was found, the spectral shape and intensity were affected by the presence of the Ag₁₀ chain. First, the overall intensity was enhanced with Ag₁₀ in the junction (~7.5 times stronger at the center) as compared with bare NiAl (comparing Fig. 2B to 2A). Second, the relative intensity of the visible band was enhanced over the near-infrared band, comparing the upper panels of Fig. 2B and 2C with Fig. 2A, especially the mode at $h\nu = 2.2$ eV, where h is Planck's constant and ν is frequency. The introduction of Ag₁₀ in the junction changed the final state of inelastic electron tunneling from that around the Fermi level of NiAl to states of the Ag₁₀ chain. Thus, the bias for IET excitation of the same plasmon modes was up-shifted by about 0.8 V at the center and by 1.1 V toward the end of the chain (Fig. 2, B and C, upper panels), compared to NiAl (Fig. 2A, upper panels). This up-shift in the excitation bias and the invariance of the plasmon modes have also been observed for light emissions from molecular adsorbate on the metal surface (7, 19).

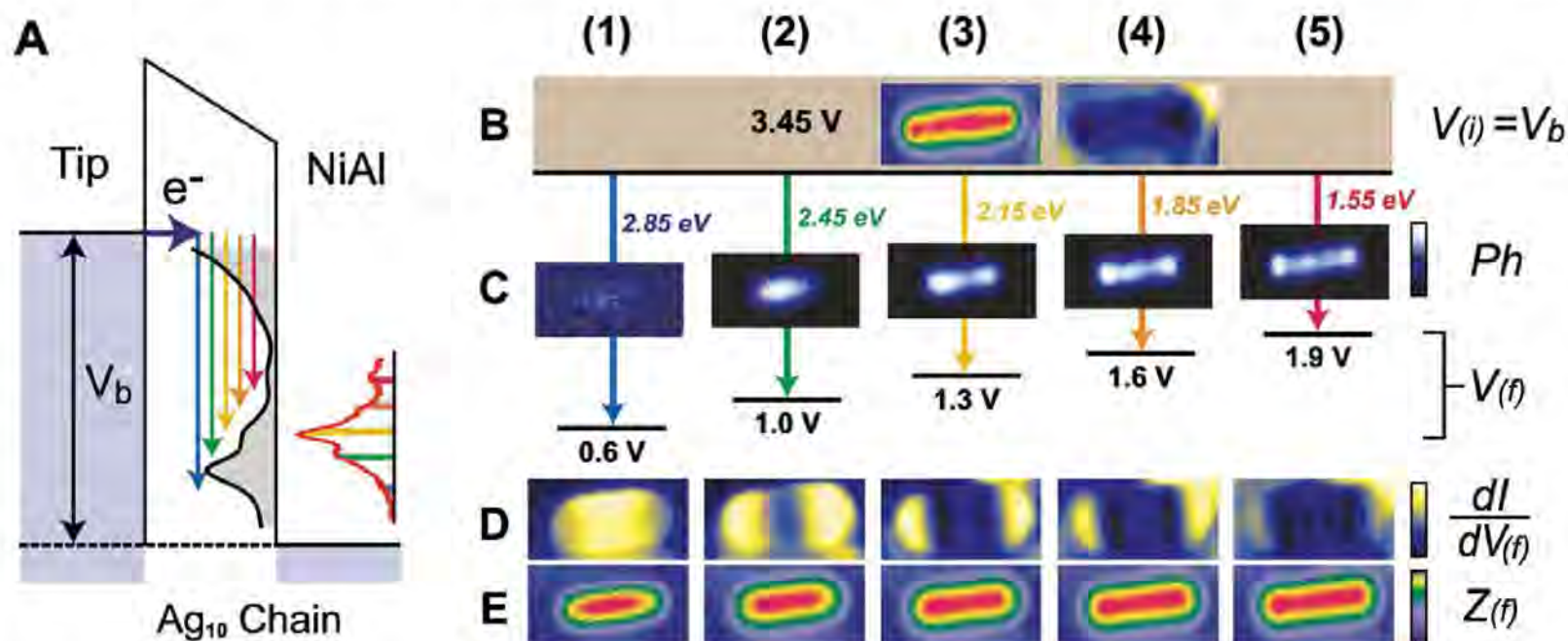
An additional ~0.3 V is required to excite the same plasmon modes at the end as compared to the center of the Ag₁₀ chain. This up-shift in excitation energy has its origin in the dI/dV spectra shown in Fig. 2D, where lower-energy states dominate in the central part of Ag₁₀, whereas higher-energy states populate preferentially toward the ends of the chain. This variation of LDOS

of Ag₁₀ also occurs in atomic Au and Pd chains (3, 4, 20), leading to a difference in their spectral intensity at the same bias. For example, as shown in the bottom panels of Fig. 2, B and C, the overall intensity around $h\nu = 2.4$ eV is higher at the center than at the ends for a bias of 3.4 V. If the dashed line in Fig. 2C is shifted up by 0.3 V, then the spectrum becomes similar to that of 3.4 V at the center. Qualitatively, the shift of the excitation bias with chain position follows the same trend as the shift in dI/dV (7). However, the quantitative relation of these two shifts is complex, because the electronic states at the ends of the chain involve a dramatic transition from Ag₁₀ to NiAl.

Clear contrasts in emission intensities along Ag₁₀ were obtained by plotting a series of spectra for different positions along the chain to yield a 2D intensity contour (Fig. 2E, left panel). Comparison with the corresponding topography (Fig. 2E, right panel) shows that the photon emission is confined within the chain. For lower photon energies ($h\nu < 1.7$ eV), the emission is distributed throughout the chain. For higher photon energies, the emission intensity is seen to spatially narrow toward the center. In addition, the distribution along Ag₁₀ is not uniform in intensity and contains emission maxima and minima. Roughly, the number of maxima decreases from three or four to one as photon energy increases. The observed emission pattern and change in the number of maxima suggest a close connection between the optical transition and the particle-in-a-box properties of Ag₁₀.

This connection between dI/dV and photon images is revealed in Fig. 3 for decreasing photon energies. The oscillating electron densities for the different final states, $dI/dV_{(f)}$, are shown horizontally in Fig. 3D. The number of maxima and minima (nodes) in the $dI/dV_{(f)}$ images

Fig. 3. (A) Schematic representation of radiative transitions in Ag₁₀. Electrons undergo transitions between the Ag chain states (black curve, dI/dV at center of Ag₁₀), and the corresponding photon emission spectrum is shown (red curve, emission at the center of Ag₁₀). The horizontal arrow indicates the injection of a tunneling electron. Five vertical arrows of different colors show transitions into the LDOS of Ag₁₀. **(B)** Topography (left) and simultaneous dI/dV image (right) at 3.45 V, which is the initial state of all the transitions shown below. **(C)** Photon emission (Ph) for different energies from transitions between the same initial state $V_{(i)}$ to five different final states at $V_{(f)}$. The photon images shown here are 3.6 nm × 1.8 nm (96 × 48 pixels) and accumulated under 6-nA tunneling current and 1-s spectral accumulation at each pixel. The range for the integrated intensity is ±0.2 eV. (As an example, we integrated the spectrum at each pixel from 1.28 to 1.32 eV for the photon image at 1.3 eV.) The photon images show zero, one, two, three, and four maxima as the photon energy decreases from 2.85 to 1.55 eV. Each photon image is displayed over the full range of intensity for the shown palette, so the intensities cannot be



compared from one to another. **(D)** $dI/dV_{(f)}$ images for the five final states showing zero, one, two, three, and four nodes (dark bands) for the ground state and first, second, third, and fourth excited states of the particle in a box. The positions of the emission maxima coincide with the nodes in $dI/dV_{(f)}$ images. **(E)** Topographic images $Z_{(f)}$ of the Ag₁₀ chain at biases corresponding to different final states $V_{(f)}$. The images of this chain yield a length of 2.9 to 3.4 nm, with the variation due to the dependence of the image on bias voltage. Images for (B), (D), and (E) have the same size: 3.9 nm × 1.95 nm (64 × 32 pixels), taken at 1-nA tunneling current.

increases with the energy of the states [$eV_{(f)}$]. The ends of Ag_{10} appear as two bright lobes due to the enhancement of edge effects during dI/dV imaging (4). As the bias $V_{(f)}$ increases, sequential $dI/dV_{(f)}$ images could be predominantly assigned to the ground, first, second, third, and fourth excited states (Ψ_1 , Ψ_2 , Ψ_3 , Ψ_4 , and Ψ_5 , respectively) of this 1D particle-in-a-box system. At each chosen bias voltage, the density does not correspond to a pure state and is a weighted sum of nearby states (3). The voltages are chosen to reveal the dominance of one state exhibiting zero,

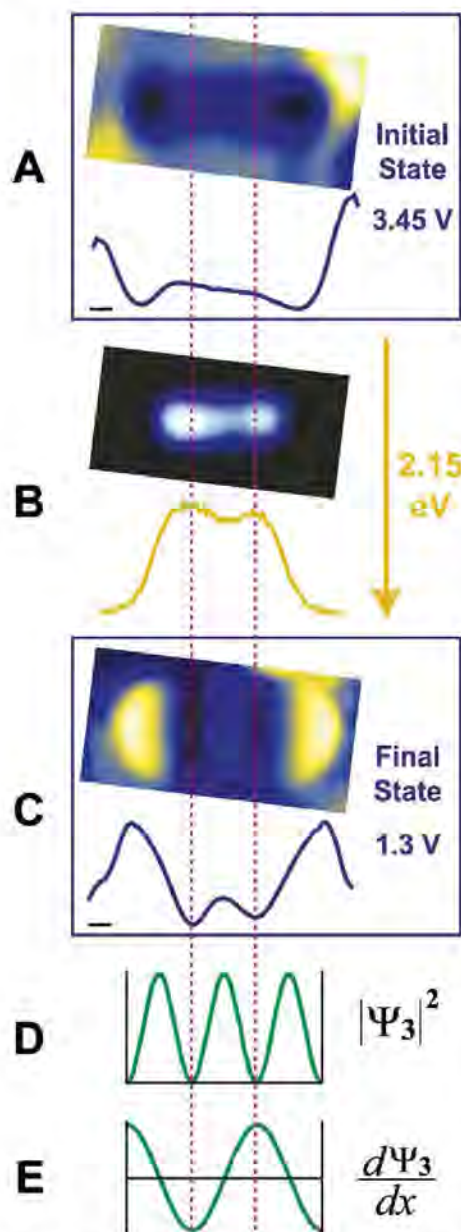


Fig. 4. (A and C) dI/dV images and cross-sectional line cuts of the initial state (3.45 V) and final state (1.3 V). (B) Photon image and its cross-sectional line cut at $h\nu = 2.15$ eV. (D and E) All images and cross-sectional line cuts are aligned (the two vertical dashed lines) with the electron density (D) and derivative (E) of Ψ_3 , the wave function for the second excited state of the 1D particle in a box with infinite walls.

one, two, three, or four nodes in $dI/dV_{(f)}$. As expected, separations between the nodes become smaller for higher-energy states. When the bias voltage is higher than 2.8 V, dI/dV is dominated by the NiAl states (Fig. 2D), and its fine structures are smeared out. For example, at 3.45 V (Fig. 3B), the profile of Ag_{10} is still discernible, but oscillating patterns can no longer be identified.

The role of the spatially oscillating electronic states of Ag_{10} in the optical transitions is determined from imaging of the photon emission. Photon imaging of different emission energies at a fixed bias of 3.45 V allows the investigation of final-state effects and is shown schematically in Fig. 3A. Not every final state could be probed, because of the limited photon detection window of the charge-coupled device (1.3 to 3.0 eV) and spectral range of the plasmon modes. For 3.45-V bias, final states from Ψ_1 to Ψ_5 can be accessed. With emission energies from 2.85 to 1.55 V, photon images show zero (nearly no signal), one, two, three, and four bright maxima (Fig. 3C). A comparison with the corresponding final-state $dI/dV_{(f)}$ images (Fig. 3D) reveals that the number of emission maxima is equivalent to the number of nodes. Furthermore, the distributions of emission maxima directly coincide with the positions of nodes in $dI/dV_{(f)}$ images. The entire emission spectrum was recorded at each pixel of the x - y image. The different images in Fig. 3C correspond to integrated energy slices within each spectrum. These results are consistent for different chain lengths, scanning directions, and biases. We can completely exclude any influence on the photon emission images from feedback or tip movement (7, 8).

The probability of tunneling (both ET and IET) depends on the magnitude of the LDOS. The photon images should reflect the LDOS of the initial state (Fig. 3B) and the final state (Fig. 3D). However, the observed maxima in the photon images do not match the spatial distribution of high LDOS in the initial- or final-state dI/dV images.

To explain this mismatch, the tunneling process needs to be integrated with the optical transition. The rate of transition w_{if} between two states $|i\rangle$ and $|f\rangle$ from Fermi's golden rule (21) is given by

$$w_{if} = \frac{2\pi}{\hbar} |U_{if}|^2 \delta(E_f - E_i \pm \hbar\omega) \quad (1)$$

$$U_{if} = \frac{eA_0}{2mc} \mathbf{\epsilon} \cdot \langle i | \mathbf{p} | f \rangle \quad (2)$$

where E_i and E_f are the energy of the initial and final states $|i\rangle$ and $|f\rangle$, respectively, and ω is the angular frequency of the emitted light. The matrix element U_{if} represents the radiative transition between the two states, in which $A_0\mathbf{\epsilon} = \mathbf{A}$ is the vector potential. The spatial dependence of the matrix element is given by

$$u_{if}(\vec{r}) \propto \Psi_i(\vec{r}) \hat{\mathbf{p}} \Psi_f(\vec{r}) \quad (3)$$

The Ag_{10} eigenstates are well described by the 1D particle-in-a-box wave functions. The mo-

mentum operator can be replaced by the position representation

$$u_{if}(x) \propto \Psi_i(x) \frac{d}{dx} \Psi_f(x) \quad (4)$$

From this equation, it is seen that the maximum emission occurs at positions where the derivative of the wave function is maximum (that is, momentum is largest).

The high-energy initial state $\Psi_i(x)$ can be considered as having weak spatial variations in the interior of the chain, because the higher particle-in-a-box states mix with the high density of smoothly varying substrate states (Fig. 2D). Thus, the symmetry of emission pattern is determined by $\frac{d\Psi_f(x)}{dx}$; that is, the derivative of the final state in the range of energies where the density of substrate states is low. In the case of Ag_{10} , we observe maxima of emission at nodes of the dI/dV images (Fig. 3). For example, in Fig. 4, the cross-sectional line cuts of the initial state (3.45 V), photon intensity at $h\nu = 2.15$ eV, and the final state (1.3 V) are aligned with the electron density $|\Psi_3|^2$ and derivative of the wave function $\frac{d\Psi_3}{dx}$ of the ideal Ψ_3 . The final state at 1.3 V shows two nodes correspond to minima in $|\Psi_3|^2$ and extrema in $\frac{d\Psi_3}{dx}$ (Fig. 4, D and E). There are, in total, four extrema in $\frac{d\Psi_3}{dx}$: two at the nodes and two at the ends. However, photon emission is observed only at the nodes. These results are consistent with Fermi's golden rule, because the matrix element contains not only the derivative of the final state $\frac{d\Psi_f}{dx}$ but also the overlap with the initial state $\Psi_i(x)$. The LDOS for the initial state $\Psi_i(x)$ vanish at the ends for a particle in a box with infinite walls and are nearly zero for the Ag_{10} chain (Fig. 4A). The rapid rise in LDOS outside the chain in Fig. 4A is associated with the NiAl substrate states (Fig. 2D). At high bias values, the Ag_{10} states no longer maintain their distinct particle-in-a-box characters because of strong mixing with the NiAl states.

The Ag_{10} chain is adsorbed on the metallic NiAl(110) substrate. Along the [110] direction, NiAl has a band gap that is responsible for the low differential conductance (dI/dV) up to ~ 2.0 V bias voltage (Fig. 2D) (22). The troughs on the surface provide a template for constructing the 1D Ag chains. Because of the band gap, the particle-in-a-box states are weakly coupled to the substrate states and remain distinct for states below ~ 2.0 V. The radiative process is shown schematically in Fig. 1B, where the intensity of the detected light is enhanced, arising from the coupling of the electronic transition for the plasmon modes in the junction. When the coupling is in resonance, light detected in the far field is enhanced. Such a plasmon-enhanced field is quite general and is determined at the atomic scale in the present experiment. Thus, the use of a Ag tip is preferred over other tips such as W that have strongly damped plasmons. The plasmon modes are revealed by the spectra in the bottom panels of Fig. 2, A to C. The intensity of the radiative plasmon decay does not exhibit spatial variations away from surface inhomogeneities.

The observed spatial and spectral variations in the photon imaging of the Ag chain (Figs. 3C and 4B) are dominated by the LDOS of the Ag₁₀ chain, as described by Eq. 4, and coupling to the plasmons serves to strengthen the emitted light intensity. Because of the relative spatial uniformity of the initial state, the emitted light intensity is highlighted by the gradient of the final state, $\frac{dP_f}{dx}$. In (7), the data led to the conclusion that light emission is caused by the coupling of the initial state $|i\rangle$ and final state $|f\rangle$ via the IET process, $\langle i|\mathbf{V}|f\rangle$, where \mathbf{V} is the interaction potential. In our experiment, it is refined by Fermi's golden rule, in which $|i\rangle$ and $|f\rangle$ are connected by the momentum operator \mathbf{p} , as $\langle i|\mathbf{p}|f\rangle$. This refinement and the association of \mathbf{V} with \mathbf{p} are not revealed by spectroscopy at discrete points as in (7). The transition still goes through the same initial and final states, but the momentum operator in the matrix element gives rise to the seemingly surprising spatial images.

Although only results from Ag₁₀ are presented here, the correspondence between nodes and emission maxima was also observed for Ag₂ through Ag₉. The wave functions for the particle-in-a-box-like atomic chains are simple and exhibit distinct features in energy and space, most notably the nodal structures. By varying the bias

voltage to control tunneling electrons and the radiative transition in inelastic tunneling, the STM is used to obtain spatially and spectrally resolved photon images that lead to direct visualization of Fermi's golden rule, one of the fundamental principles in quantum mechanics. In addition, these results reveal the basic mechanisms underlying optical phenomena at the nanoscale, where light fields with wavelengths much greater than the dimension of the radiator are enhanced by coupling to plasmons.

References and Notes

1. M. F. Crommie, C. P. Lutz, D. M. Eigler, *Nature* **363**, 524 (1993).
2. H. C. Manoharan, C. P. Lutz, D. M. Eigler, *Nature* **403**, 512 (2000).
3. N. Nilius, T. M. Wallis, W. Ho, *Science* **297**, 1853 (2002).
4. T. M. Wallis, N. Nilius, W. Ho, *Phys. Rev. Lett.* **89**, 236802 (2002).
5. X. H. Qiu, G. V. Nazin, W. Ho, *Science* **299**, 542 (2003).
6. S. W. Wu, G. V. Nazin, W. Ho, *Phys. Rev. B* **77**, 205430 (2008).
7. G. V. Nazin, X. H. Qiu, W. Ho, *Phys. Rev. Lett.* **90**, 216110 (2003).
8. R. Berndt *et al.*, *Phys. Rev. Lett.* **74**, 102 (1995).
9. R. Berndt *et al.*, *Science* **262**, 1425 (1993).
10. G. Schull, M. Becker, R. Berndt, *Phys. Rev. Lett.* **101**, 136801 (2008).
11. The details of this experiment are available as supporting material on Science Online.
12. R. Berndt, J. K. Gimzewski, P. Johansson, *Phys. Rev. Lett.* **67**, 3796 (1991).

13. P. Johansson, R. Monreal, P. Apell, *Phys. Rev. B* **42**, 9210 (1990).
14. K. Meguro, K. Sakamoto, R. Arafune, M. Satoh, S. Ushioda, *Phys. Rev. B* **65**, 165405 (2002).
15. B. C. Stipe, M. A. Rezaei, W. Ho, *Science* **280**, 1732 (1998).
16. R. Berndt, J. K. Gimzewski, *Phys. Rev. B* **48**, 4746 (1993).
17. J. Yan, Z. Yuan, S. Gao, *Phys. Rev. Lett.* **98**, 216602 (2007).
18. S. A. Maier, H. A. Atwater, *J. Appl. Phys.* **98**, 011101 (2005).
19. G. Hoffmann, L. Libioulle, R. Berndt, *Phys. Rev. B* **65**, 212107 (2002).
20. N. Nilius, T. M. Wallis, W. Ho, *J. Phys. Chem.* **109**, 20657 (2005).
21. G. C. Schatz, M. A. Ratner, *Quantum Mechanics in Chemistry* (Dover, New York, 2002), chap. 4 and 5.
22. S. C. Lui, M. H. Kang, E. J. Mele, E. W. Plummer, D. M. Zehner, *Phys. Rev. B* **39**, 13149 (1989).
23. Supported by the Chemical Science, Geo- and Bioscience Division, Office of Science, U. S. Department of Energy, under grant DE-FG02-04ER1595, and by the Alexander von Humboldt Foundation through a Feodor Lynen Fellowship to C.A.B. We thank R. Wu, D. L. Mills, P. Chu, Y. Jiang, and N. Ogawa for inspiring discussions.

Supporting Online Material

www.sciencemag.org/cgi/content/full/325/5943/981/DC1
Materials and Methods
Fig. S1

6 April 2009; accepted 26 June 2009
10.1126/science.1174592

Homogeneous Distribution of ²⁶Al in the Solar System from the Mg Isotopic Composition of Chondrules

Johan Villeneuve,^{1*} Marc Chaussidon,¹ Guy Libourel^{1,2}

The timing of the formation of the first solids in the solar system remains poorly constrained. Micrometer-scale, high-precision magnesium (Mg) isotopic analyses demonstrate that Earth, refractory inclusions, and chondrules from primitive meteorites formed from a reservoir in which short-lived aluminum-26 (²⁶Al) and Mg isotopes were homogeneously distributed at $\pm 10\%$. This level of homogeneity validates the use of ²⁶Al as a precise chronometer for early solar system events. High-precision chondrule ²⁶Al isochrons show that several distinct chondrule melting events took place from ~ 1.2 million years (My) to ~ 4 My after the first solids condensed from the solar nebula, with peaks between ~ 1.5 and ~ 3 My, and that chondrule precursors formed as early as $0.87^{+0.19}_{-0.16}$ My after.

Models of the evolution of the early solar system rely on knowledge of the precise time scales for the physical and chemical processes that occurred in the early accretion disk and led to the formation of calcium-aluminum-rich inclusions (CAIs) and chondrules, which are the building blocks of

primitive meteorites (chondrites). Short-lived ²⁶Al [half-life ($T_{1/2}$) = 0.73 million years (My)] is possibly the most accurate chronometer for the first few million years of solar system history, provided that it was homogeneously distributed in the disk. Previous studies of various meteoritic components showed that ²⁶Al was widespread in the disk, but its level of homogeneity has never been quantified precisely. From numerous mineral ²⁶Al isochrons in CAIs, a canonical value of $\sim 5 \times 10^{-5}$ was inferred for the initial ²⁶Al/²⁷Al ratio [hereafter (²⁶Al/²⁷Al)₀] when CAIs crystallized (*1*). This value is slightly lower than $5.23 (\pm 0.13) \times 10^{-5}$, which was determined from the bulk ²⁶Al isochron of

Allende CAIs (*2*) [used in our work instead of $5.85 (\pm 0.05) \times 10^{-5}$ (*3*)], which indicates that the crystallization of CAIs followed closely after (50,000 years at most) the condensation of their precursors. The bulk ²⁶Al isochron precisely defines an initial Mg isotopic composition ($\delta^{26}\text{Mg}^*_0$) for CAI precursors of -0.040 ± 0.029 per mil (‰) (*2*). If ²⁶Al and Mg isotopes were homogeneously distributed in the inner solar system, then CAIs $\delta^{26}\text{Mg}^*_0$ can be taken as the initial Mg isotopic composition of the solar system when ²⁶Al/²⁷Al was $5.23 (\pm 0.13) \times 10^{-5}$. Any object that formed later (when ²⁶Al/²⁷Al < 5.23×10^{-5}) must be characterized by a more radiogenic $\delta^{26}\text{Mg}^*_0$ value. The increase of $\delta^{26}\text{Mg}^*_0$ is a function of the Al/Mg ratio of the reservoir in which the object, or its precursors, resided before the last melting event. Al-rich and ferromagnesian chondrules from unequilibrated ordinary chondrites (UOCs) and carbonaceous chondrites (CCs) show mineral ²⁶Al isochrons with (²⁶Al/²⁷Al)₀ < 2×10^{-5} (*4–12*); that is, much lower than that of CAIs. Because the $\delta^{26}\text{Mg}^*_0$ of chondrules has never been precisely determined, the data from chondrules cannot be compared to those of CAIs nor to the theoretical Mg isotope growth curve calculated for the solar nebula for a homogeneous distribution of ²⁶Al and Mg isotopes.

We developed high-precision analysis of Al and Mg isotopes using the Centre de Recherches Petrographiques et Geochimiques (CRPG)–CNRS Cameca ion microprobe (ims 1270) to determine precisely (even for low Al/Mg ratios)

¹Centre de Recherches Petrographiques et Geochimiques (CRPG)–Nancy Université–CNRS, UPR 2300, 15 Rue Notre-Dame des Pauvres, Boite Postale 20, 54501 Vandoeuvre-lès-Nancy, France. ²Ecole Nationale Supérieure de Géologie (ENSG)–Nancy Université, Rue du Doyen Marcel Roubault, Boite Postale 40, 54501 Vandoeuvre-lès-Nancy, France.

*To whom correspondence should be addressed. E-mail: johanv@crpg.cnrs-nancy.fr

both the slope [from which comes access to $(^{26}\text{Al}/^{27}\text{Al})_0$] and the intercept ($\delta^{26}\text{Mg}^*_0$) of mineral ^{26}Al isochrons in chondrules. We performed multicollection analyses of ^{24}Mg , ^{25}Mg , ^{26}Mg , and ^{27}Al using four Faraday cups (figs. S1 and S2) (13) in the major silicate phases (olivine, low-Ca pyroxene, and mesostasis) of 15 chondrules [three type I (FeO-poor), 11 type II (FeO-rich), and one Al-rich] from the LL3.0 UOC Semarkona. A typical external reproducibility of $\pm 0.005\%$ (2σ) can be obtained for $\delta^{26}\text{Mg}^*$ in magnesium silicate standards (fig. S2) (13). In chondrules, internal errors (2σ) for $\delta^{26}\text{Mg}^*$ were $\pm 0.015\%$ to $\pm 1.98\%$, depending on Mg content (table S1).

The 14 ferromagnesian chondrules show well-resolved mineral isochrons (two examples are shown in Fig. 1, with the remainder shown in fig. S4), with $(^{26}\text{Al}/^{27}\text{Al})_0$ ranging from $1.619 (\pm 0.167) \times 10^{-5}$ to $3.023 (\pm 1.240) \times 10^{-6}$ and $\delta^{26}\text{Mg}^*_0$ values ranging from $-0.0185 (\pm 0.0140)\%$ to $0.0047 (\pm 0.0098)\%$ for Sem-Ch138, Sem-Ch83, and Sem-Ch121, respectively (table S1). Because most Mg-rich olivines in type I chondrules might not have crystallized from the chondrule melt (14, 15), it is theoretically not correct to calculate an isochron between olivine and glass in Sem-Ch2. The $(^{26}\text{Al}/^{27}\text{Al})_0$ for Sem-Ch2 can, however, be determined precisely (fig. S4). The Al-rich chondrule (Sem-Ch4) shows constant ^{26}Mg excesses [$\delta^{26}\text{Mg}^* = 0.098 (\pm 0.016)\%$,

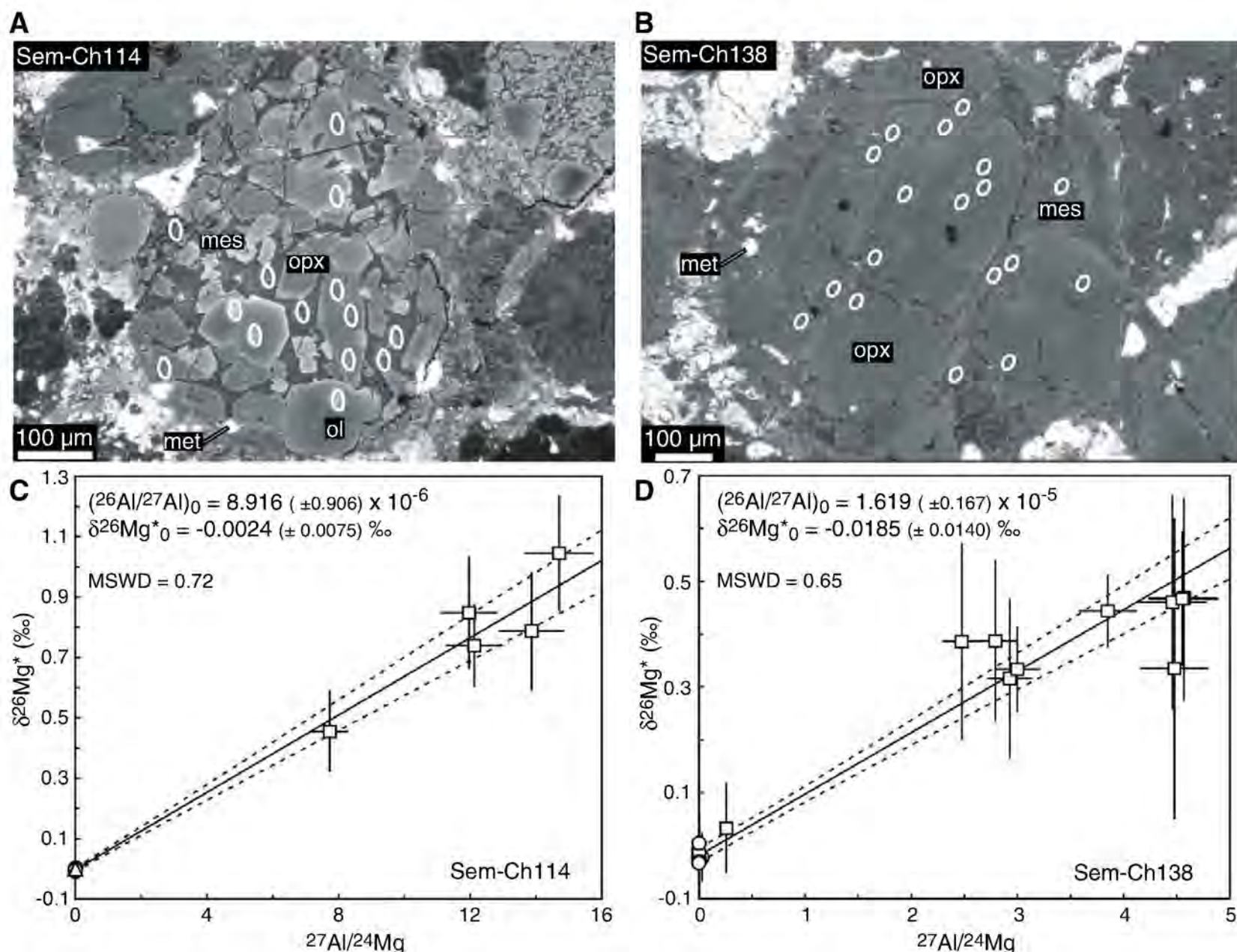
fig. S4] that are not correlated with Al/Mg ratio but would indicate that the last melting event occurred at least 4 My after CAIs; that is, when $(^{26}\text{Al}/^{27}\text{Al})_0 < 10^{-6}$.

Because of their high precision, the present chondrule Al-Mg data can be compared to the growth curve calculated for Mg isotopes in the solar nebula, assuming a simple closed-system evolution (Fig. 2). If ^{26}Al and Mg isotopes were homogeneously distributed in the nebula, any chondrule formed at a given time t , from precursors extracted from the nebula at that time, must have $(^{26}\text{Al}/^{27}\text{Al})_0$ and $\delta^{26}\text{Mg}^*_0$ identical to those of the nebula growth curve at time t . The present ferromagnesian chondrules do plot, within errors, on the solar nebula growth curve, on which Earth also plots (Fig. 2), implying a homogeneous distribution of ^{26}Al and Mg isotopes in the inner solar nebula at the time of formation of CAIs. The clustering of chondrule data along the solar nebula growth curve implies a relative heterogeneity of $\sim 10\%$ (that is, $\pm 0.5 \times 10^{-5}$ for $^{26}\text{Al}/^{27}\text{Al}$ ratios and $\pm 0.004\%$ for $\delta^{26}\text{Mg}^*$, fig. S5). However, this is an upper bound, because part of the chondrule variability may be due to the following: (i) different closed-system evolution paths for up to ~ 1 My with bulk $^{27}\text{Al}/^{24}\text{Mg}$ slightly different from chondritic ratio and (ii) the possible presence within chondrule precursors of CAI-type material. One-million-year-old CAIs would have a bulk

$\delta^{26}\text{Mg}^*$ of $\sim 0.42\%$ (for a bulk $^{27}\text{Al}/^{24}\text{Mg}$ of 2), implying that their fraction in chondrule precursors could not be higher than $\sim 1\%$ (that is, $0.004/0.42$). Finally, it can be seen from Fig. 2 that the bulk ^{26}Al isochron for CAIs with $(^{26}\text{Al}/^{27}\text{Al})_0 = 5.85 (\pm 0.05) \times 10^{-5}$ and $\delta^{26}\text{Mg}^*_0 = -0.0317 (\pm 0.0038)\%$ (3) is not consistent with a homogeneous distribution of ^{26}Al , because that conclusion would imply a positive terrestrial $\delta^{26}\text{Mg}^*$ value of $\sim 0.015\%$ (16), and is not consistent with most of our chondrule data.

The ^{26}Al and Mg isotopic homogeneity of the solar system inferred from our data are not in conflict with the existence of supracanonical $^{26}\text{Al}/^{27}\text{Al}$ ratios (up to 7×10^{-5}) (17) or of large $\delta^{26}\text{Mg}^*$ variations in hibonites (up to 4%) (18). A variability of $\pm 0.5 \times 10^{-5}$ for $^{26}\text{Al}/^{27}\text{Al}$ ratio simply implies that the fraction of components having supra-canonical ratios within CAIs and chondrules precursors was less than $\sim 7\%$. Similarly, a variability of $\pm 0.004\%$ for $\delta^{26}\text{Mg}^*$ implies that the fraction of hibonite-type material was less than $\sim 0.1\%$. In such a homogeneous accretion disk, the composition of the Al-rich chondrule can be simply understood as the result of an earlier extraction of its precursors from the nebula followed by a protracted closed-system evolution until the last melting event. A closed-system evolution model based on the bulk $^{27}\text{Al}/^{24}\text{Mg}$ ratio of the Al-rich chon-

Fig. 1. (A and B) Back-scattered electron image of two Semarkona type II chondrules: porphyritic olivine-pyroxene chondrule Sem-Ch114 and porphyritic pyroxene chondrule Sem-Ch138 (white circles show ion probe spots). The major mineral phases are olivine (ol), low-Ca pyroxene (opx) surrounded by glassy mesostasis (mes), and a few Fe-Ni metal grains (met). **(C and D)** Isochron diagrams obtained from 14 and 18 ion probe analyses, respectively (open circles are for low-Ca pyroxene, open triangles for olivine, and the open square for mesostasis, plotted with 2σ error bars) (fig. S4, table S1) (13).



drule (determined at 0.70 from chemical mapping by secondary electron microscopy) implies that its precursors were extracted from the nebula $\sim 0.87^{+0.19}_{-0.16}$ My after CAIs (Fig. 2). This could have happened earlier if the precursors did not remain as a closed system for Al and Mg and if,

for example, Mg was added to the precursors by condensation, as has been proposed for Al-rich chondrules (19). For the ferromagnesian chondrules, which have $^{27}\text{Al}/^{24}\text{Mg}$ ratios close to the chondritic ratio (0.10 to 0.23 for our 13 chondrules), it is not possible to identify an early ex-

traction of their precursors (for example, 1 My earlier) from the present data (with an error of ± 0.01 to $\pm 0.02\%$ on $\delta^{26}\text{Mg}^*$), because their evolution in a closed system before melting would overlap, within errors, with the solar nebula growth curve.

Because ^{26}Al and Mg isotopes are homogeneously distributed in the inner solar system (within approximately $\pm 10\%$), different values of $(^{26}\text{Al}/^{27}\text{Al})_0$ among chondrules imply the existence of individual melting events at different times; for example, $\sim 1.77^{+0.66}_{-0.47}$ My between chondrule Sem-Ch138 and chondrule Sem-Ch83 (table S1). Our data can be used, in conjunction with data from previously published chondrules $(^{26}\text{Al}/^{27}\text{Al})_0$ (table S2), to investigate whether several major melting episodes can be identified or whether chondrule formation was a continuous process. Because data precision is variable, to make a meaningful comparison between all the data, we calculated a probability density distribution that sums the Gaussian distributions $f(^{26}\text{Al}/^{27}\text{Al})_{0,\sigma}$ calculated for each chondrule. The distribution of the 14 ferromagnesian Semarkona chondrules clearly shows five distinct episodes (Fig. 3) at 1.2, 1.6, 2.1, 2.4, and 2.9 My after CAIs [taking $(^{26}\text{Al}/^{27}\text{Al})_0$ for CAIs of 5.23×10^{-5}] (2). These five episodes are consistent with the $(^{26}\text{Al}/^{27}\text{Al})_0$ measured previously in 11 other Semarkona chondrules (Fig. 3 and table S2) (8, 10, 12); the two most prominent peaks in the distribution are at 2.1 and 2.4 My. Four other episodes of chondrule formation at 1.9, 2.2, 2.6, and 4.3 My can be tentatively identified considering all the available data for UOCs and CCs (Fig. 3 and table S2) (4–7, 9, 11). A Kolmogorov-Smirnov statistical test applied to these distributions confirms that the differences shown in Fig. 3 are statistically significant: The probability for the age distributions to be different between UOC and CC chondrules is 99%. In addition, even with only 25 chondrules, the age distribution of Semarkona chondrules is statistically the same as that of UOC chondrules (82%). Available Pb-Pb ages [from 0.6 (± 1.6) My to 5.8 (± 1.0) My after CAIs] (20–23) are consistent with ^{26}Al ages but not sufficiently precise to identify specific episodes of chondrule formation. The possible existence of a limited number of melting events over a few million years is a fundamental constraint to consider in models of chondrule formation.

The large scatter in the age distribution of chondrules (Fig. 3)—with $\sim 10\%$ of all chondrules formed between 0 and 1.5 My after CAIs, $\sim 40\%$ formed between 1.5 and 2.1 My, $\sim 40\%$ formed between 2.1 and 2.8 My, and $\sim 10\%$ formed beyond 2.8 My after CAIs—can be interpreted in two opposite ways: (i) the peak intensities reflect different magnitudes of chondrule formation at specific times and thus the major episodes of chondrule formation (for UOCs and CCs) would have taken place ~ 1.5 to ~ 3 My after CAIs; or (ii) the variable peak intensities reflect the poor efficiency of chondrule preserva-

Fig. 2. Solar system growth curve (solid line) of Mg isotopes anchored by the $(^{26}\text{Al}/^{27}\text{Al})_0$ and $\delta^{26}\text{Mg}^*$ of bulk CAIs [red square, $5.23 (\pm 0.13) \times 10^{-5}$ and $-0.040 (\pm 0.029)\%$] (2) and calculated for a chondritic $^{27}\text{Al}/^{24}\text{Mg}$ ratio of 0.101 (30). The green field corresponds to the growth curve that could be calculated from the bulk CAIs isochron of $5.85 (\pm 0.05) \times 10^{-5}$ and $-0.0317 (\pm 0.0038)\%$ (green square) (3). All ferromagnesian chondrules (colored diamonds) plot on the solar nebula growth curve and define an error envelope (in red) at $\pm 0.5 \times 10^{-5}$ for $^{26}\text{Al}/^{27}\text{Al}$ ratios and $\pm 0.004\%$ for $\delta^{26}\text{Mg}^*$ (red arrows). Type I Sem-Ch2 is not shown, because its $\delta^{26}\text{Mg}^*$ cannot be determined precisely (fig. S4). The steep solid line (and its blue error envelope) show how a model age can be calculated for the extraction from the nebula of the precursors of the Al-rich chondrule (blue diamond) using its bulk $^{27}\text{Al}/^{24}\text{Mg}$ ratio of 0.7. Two sigma error bars are shown.

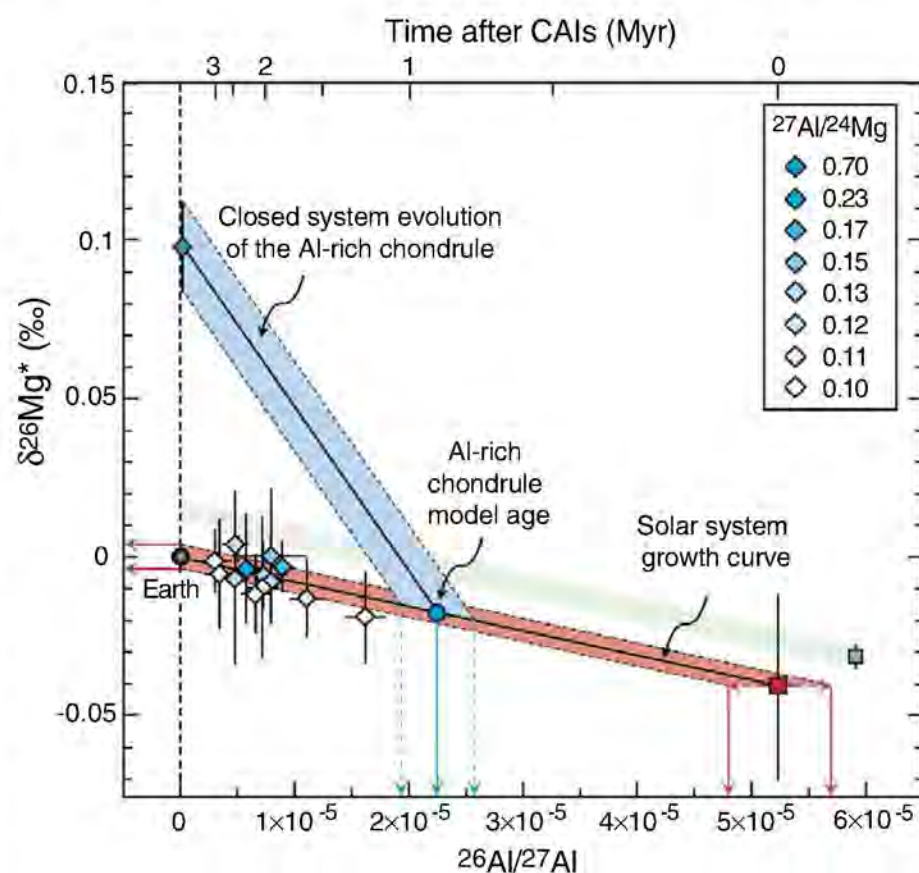
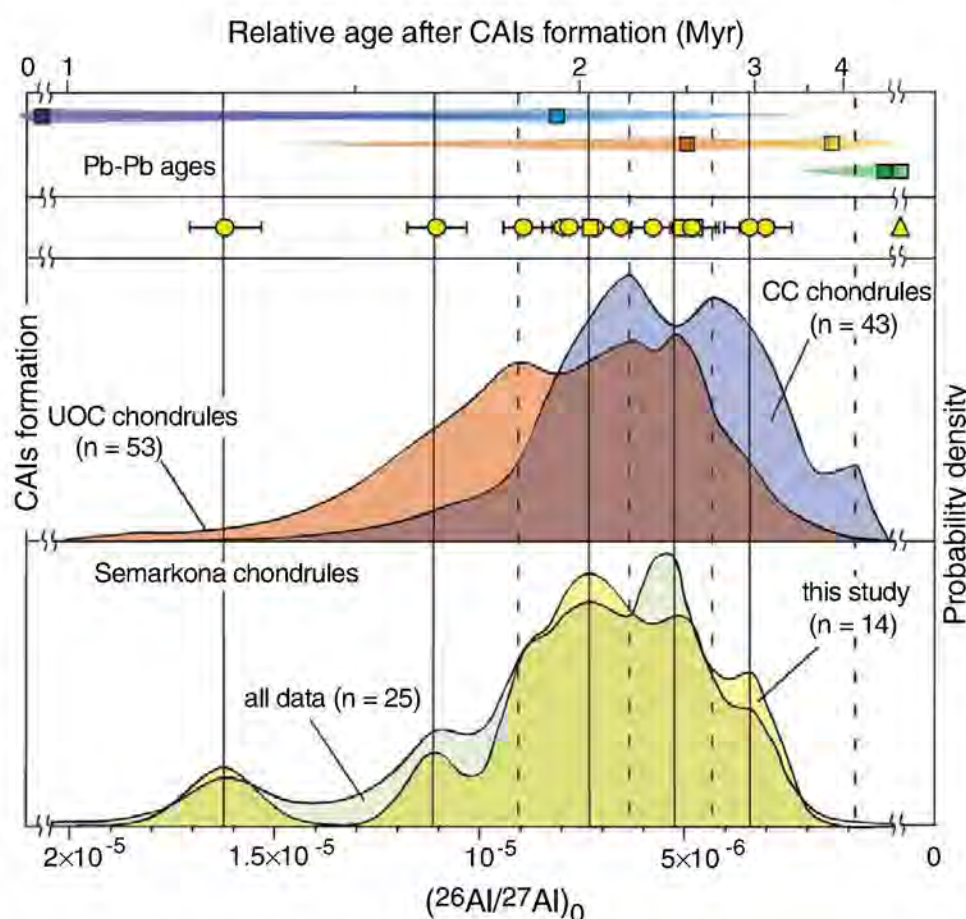


Fig. 3. $(^{26}\text{Al}/^{27}\text{Al})_0$ and corresponding relative ages after the formation of CAIs (2) determined for the 15 Semarkona chondrules (yellow squares for type I chondrules, yellow circles for type II chondrules, and yellow triangle for the Al-rich chondrule) compared with previous analyses of chondrules in the least-equilibrated ordinary and carbonaceous chondrites. Curves show probability density functions (n = number of data points in the distribution) of $(^{26}\text{Al}/^{27}\text{Al})_0$ in our Semarkona chondrules (yellow), all Semarkona chondrules (green), CC chondrules (blue), and UOC chondrules without our data (red). All data are available in table S2. Vertical solid lines show peaks that are present in Semarkona chondrules and often in UOC chondrules. Dotted lines show peaks that are present only in UOC chondrules and CC chondrules. The upper window corresponds to absolute Pb-Pb ages calculated from CV Allende chondrules (23) (dark and light blue squares), CR Acfer chondrules (20) (red and yellow squares), and CB Gujba (21) chondrules (dark and light green), depending on assumed age for CAIs (either 4567.2 ± 0.6 My or 4568.5 ± 0.5 My) (20, 22). One sigma error bar is shown.



tion in the accretion disk before the accretion of UOC and CC parent bodies. In the later scenario, chondrites would be enriched in chondrules formed shortly before accretion (which was constrained for H4 UOC at $^{26}\text{Al}/^{27}\text{Al} \approx 2 \times 10^{-7}$ from the metamorphic cooling of the parent body) (24). Although there is no evidence to favor one of these two extreme hypotheses over the other, it is obvious from the Al-rich chondrule that its precursors were extracted from the nebula $\sim 0.87^{+0.19}_{-0.16}$ My after CAIs and that they remained isolated in the nebula for up to ~ 3 My before chondrule formation. The presence of chondrules of different origins and different ages in the same few cubic centimeters of Semarkona is consistent with astrophysical models of the disk. Radial mixing by turbulence can efficiently distribute solids within 10 astronomical units in several tens of thousands of years, as long as these solids are small (millimeter or centimeter size) and are coupled to the gas (25), but the rate of destruction of these solids by accretion either by the Sun or by forming planetesimals is unknown. The observed age distribution (Fig. 3) does not exclude an early intense period (~ 1 My after CAIs or even before) of chondrule formation (or extraction of chondrule precursors), as was suggested by high $^{26}\text{Al}/^{27}\text{Al}$ inferred from bulk analyses of chondrules (26–28).

Our results imply the following: (i) that ^{26}Al was efficiently homogenized (within $\sim \pm 10\%$) in the inner solar system, (ii) that no substantial ^{26}Al (in excess of $^{26}\text{Al}/^{27}\text{Al} = 5 \times 10^{-5}$) was produced in the disk after time “zero” as defined by the bulk isochron of CAIs, and (iii) that the ^{26}Al - ^{26}Mg systematic has a chronological significance. Nebular models do predict an efficient

homogenization of ^{26}Al at $\sim \pm 10\%$ in the case of an external seeding of the accretion disk with ^{26}Al injected by a nearby supernova (29). In the case of the production of ^{26}Al by irradiation, it is not clear that such a level of homogeneity can be reached, unless most of the irradiated material is evaporated before time zero.

References and Notes

- G. J. Macpherson, A. M. Davis, E. K. Zinner, *Meteoritics* **30**, 365 (1995).
- B. Jacobsen *et al.*, *Earth Planet. Sci. Lett.* **272**, 353 (2008).
- K. Thrane, M. Bizzarro, J. A. Baker, *Astrophys. J.* **646**, L159 (2006).
- T. Kunihiro, A. E. Rubin, K. D. McKeegan, J. T. Wasson, *Geochim. Cosmochim. Acta* **68**, 2947 (2004).
- K. Nagashima, A. N. Krot, M. Chaussidon, *Meteorit. Planet. Sci.* **42**, A115 (2007).
- N. Sugiura, A. N. Krot, *Meteorit. Planet. Sci.* **42**, 1183 (2007).
- E. Kurahashi, N. T. Kita, H. Nagahara, Y. Morishita, *Geochim. Cosmochim. Acta* **72**, 3865 (2008).
- I. D. Hutcheon, R. Hutchison, *Nature* **337**, 238 (1989).
- S. S. Russell, G. Srinivasan, G. R. Huss, G. J. Wasserburg, G. J. MacPherson, *Science* **273**, 757 (1996).
- N. T. Kita, H. Nagahara, S. Togashi, Y. Morishita, *Geochim. Cosmochim. Acta* **64**, 3913 (2000).
- S. Mostefaoui *et al.*, *Meteorit. Planet. Sci.* **37**, 421 (2002).
- N. G. Rudraswami, J. N. Goswami, B. Chattopadhyay, S. K. Sengupta, A. P. Thapliyal, *Earth Planet. Sci. Lett.* **274**, 93 (2008).
- Materials and methods are available as supporting material on Science Online.
- G. Libourel, A. N. Krot, *Earth Planet. Sci. Lett.* **254**, 1 (2007).
- M. Chaussidon, G. Libourel, A. N. Krot, *Geochim. Cosmochim. Acta* **72**, 1924 (2008).
- M. Chaussidon, M. Gounelle, *C. R. Geosci.* **339**, 872 (2007).
- E. D. Young *et al.*, *Science* **308**, 223 (2005).
- M.-C. Liu, K. D. McKeegan, A. M. Davis, *Lunar Planet. Sci. XXXVII*, 2428 (2006).
- H. Nagahara, N. T. Kita, K. Ozawa, Y. Morishita, *Geochim. Cosmochim. Acta* **72**, 1442 (2008).
- Y. Amelin, A. N. Krot, I. D. Hutcheon, A. A. Ulyanov, *Science* **297**, 1678 (2002).
- A. N. Krot, Y. Amelin, P. Cassen, A. Meibom, *Nature* **436**, 989 (2005).
- A. Bouvier *et al.*, *Geochim. Cosmochim. Acta* **71**, 1583 (2007).
- Y. Amelin, A. Krot, *Meteorit. Planet. Sci.* **42**, 1321 (2007).
- E. Zinner, C. Gopel, *Meteoritics* **27**, 311 (1995).
- D. Bockelee-Morvan, D. Gautier, F. Hersant, J. M. Hure, F. Robert, *Astron. Astrophys.* **384**, 1107 (2002).
- A. Galy, E. D. Young, R. D. Ash, R. K. O’Nions, *Science* **290**, 1751 (2000).
- M. Bizzarro, J. A. Baker, H. Haack, *Nature* **431**, 275 (2004).
- M. Bizzarro, J. A. Baker, H. Haack, *Nature* **435**, 1280 (2005).
- A. P. Boss, *Astrophys. J.* **660**, 1707 (2007).
- K. Lodders, *Astrophys. J.* **591**, 1220 (2003).
- We gratefully thank C. Rollion-Bard, D. Mangin, and M. Champenois for their implication and expertise in ion probe techniques; J. Ravaux and A. Kohler for their help with SEM analysis; and J. Marin and P. Burnard for their attentive rereading. Constructive comments by three anonymous reviewers and fruitful discussions with F. Robert and M. Gounelle were highly appreciated and greatly improved this manuscript. This work was funded by L’Agence Nationale de la Recherche grant ANR-08-BLAN-0260-02 T-Tauri, Chem, and European Research Council grant ERC 226846 Cosmochemical Exploration of the first two Million Years of the Solar System (CEMYSS). This is CRPG publication number 2001.

Supporting Online Material

www.sciencemag.org/cgi/content/full/325/5943/985/DC1

Materials and Methods

Figs. S1 to S5

Tables S1 to S2

References

23 March 2009; accepted 19 June 2009

10.1126/science.1173907

Adjoint Tomography of the Southern California Crust

Carl Tape,^{1*} Qinya Liu,² Alessia Maggi,³ Jeroen Tromp⁴

Using an inversion strategy based on adjoint methods, we developed a three-dimensional seismological model of the southern California crust. The resulting model involved 16 tomographic iterations, which required 6800 wavefield simulations and a total of 0.8 million central processing unit hours. The new crustal model reveals strong heterogeneity, including local changes of $\pm 30\%$ with respect to the initial three-dimensional model provided by the Southern California Earthquake Center. The model illuminates shallow features such as sedimentary basins and compositional contrasts across faults. It also reveals crustal features at depth that aid in the tectonic reconstruction of southern California, such as subduction-captured oceanic crustal fragments. The new model enables more realistic and accurate assessments of seismic hazard.

The objective of seismic tomography is to produce detailed three-dimensional (3D) images of Earth’s interior by minimizing the differences between simulated (or “synthetic”) seismograms and recorded (or “observed”) seismograms. Seismic tomography has been successful in producing images of Earth’s interior, such

as large-scale variations in the mantle (1, 2), subducting slabs (3), and mantle plumes (4). These tomographic studies adopt a simple 1D (layered) reference model (5), which allows for computationally inexpensive procedures within the minimization problem. Highly accurate numerical methods, such as the spectral-element method

(SEM), may now be used to compute synthetic seismograms at regional and global scales, allowing tomographers to start the minimization procedure with more realistic 3D initial models and simulations (6–9). We demonstrated in this study that these numerical methods may be exploited within the minimization problem by using adjoint methods (10–12). We refer to this procedure as “adjoint tomography” (13).

Southern California provides an excellent setting for the two-fold objective of fitting seismograms and characterizing the crust. The station coverage (fig. S2A), especially in the Los Angeles region, is one of the densest in the world. A detailed 3D seismological model of the southern California crust has been constructed from a

¹Seismological Laboratory, California Institute of Technology, Pasadena, CA 91125, USA. ²Department of Physics, University of Toronto, Ontario M5S 1A7, Canada. ³Institut de Physique du Globe, Université de Strasbourg, 67084 Strasbourg, France.

⁴Department of Geosciences and Program in Applied and Computational Mathematics, Princeton University, Princeton, NJ 08544, USA.

*To whom correspondence should be addressed. E-mail: carltape@gps.caltech.edu

variety of seismic data sets (15). Several different approaches have been used to determine earthquake source parameters (16). Finally, an accurate wave propagation code, using the SEM, has been applied to simulate seismic wave propagation in the region (15), with recent modifications to facilitate an inverse problem (17).

We wanted to use an initial seismological Earth model that produces the maximum number of measurements for a given set of earthquakes. Hence, we began with a 3D model (14, 15) rather than a standard 1D layered model for southern California. The initial model was provided by the Southern California Earthquake Center

(SCEC) and contains results from several different data sets: seismic reflection and industry well-log data to constrain the geometry and structure of major basins, receiver function data to estimate the depth to the Mohorovicic discontinuity (Moho), and local earthquake data to obtain the 3D background wave-speed structure. The model is described in terms of shear wave speed (V_S) and bulk sound speed (V_B), which can be combined to compute compressional wave speed, $V_P^2 = (4/3)V_S^2 + V_B^2$. We extended the simulation region of (15) westward, so as to include the Coast Ranges (fig. S1). We also implemented a more recent version of the background model

(18, 19), and we obtained density (ρ) by empirically scaling V_P (20). Topography and bathymetry are included, and stations in the simulations are situated at their proper elevations.

In our inversion method, we measured frequency-dependent travel-time differences between simulated and recorded seismic waveforms (16, 21). This involves measuring both body waves and surface waves on all three components (vertical, radial, and transverse), whenever possible. The inversion required examination of 52,000 three-component seismograms of 143 crustal earthquakes. We use an adjoint method to compute the gradient of the misfit function to obtain each update to the tomo-

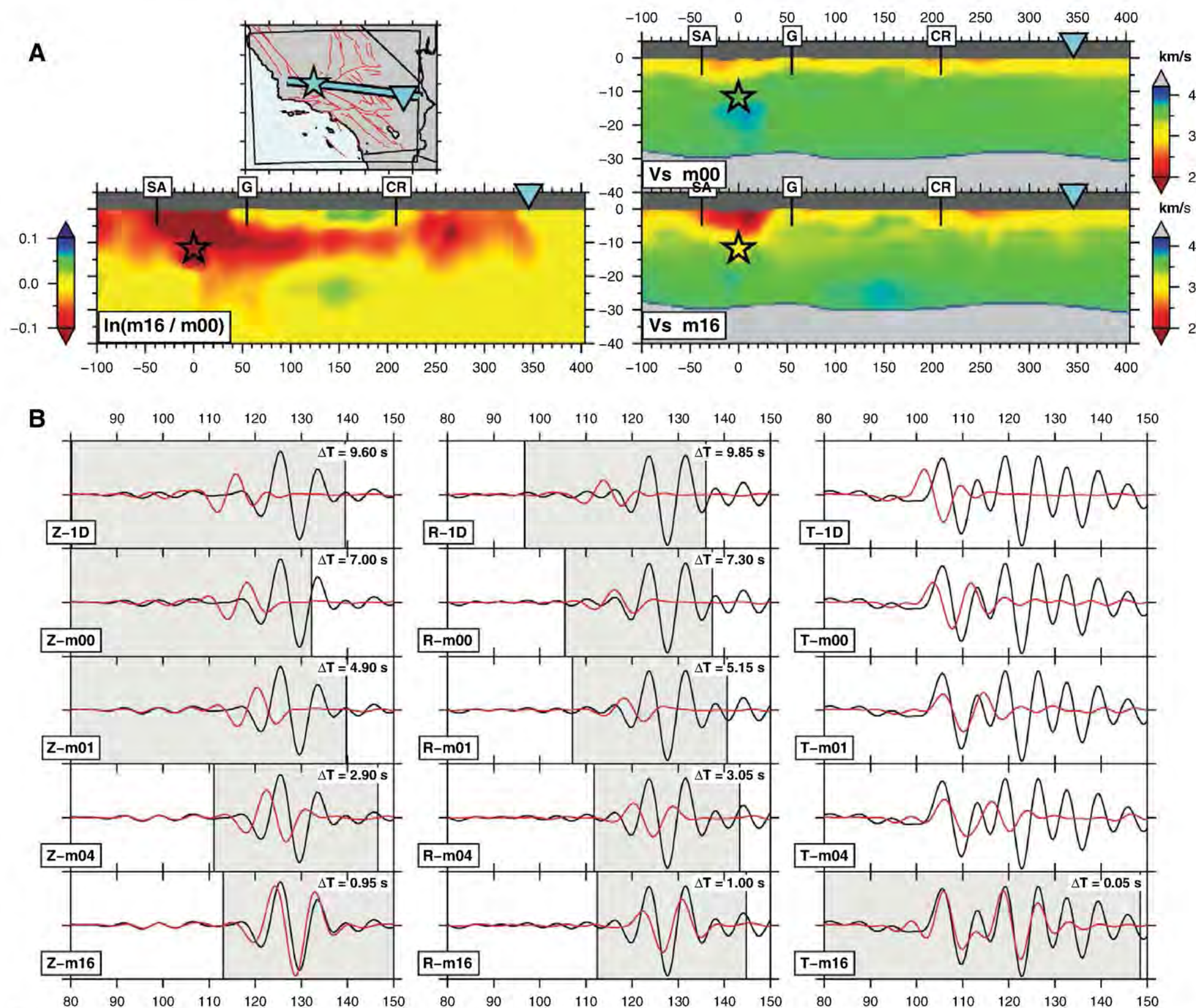


Fig. 1. Iterative improvement of a three-component seismogram. (A) Cross section of the V_S tomographic models for a path from a M_w 4.5 earthquake (stars) on the White Wolf fault to station DAN (triangles) in the eastern Mojave Desert. Vertical exaggeration is 3.0. Upper right is the initial 3D model, m_{00} ; lower right is the final 3D model, m_{16} ; and lower left is the difference between the two, $\ln(m_{16}/m_{00})$. Faults labeled for reference are San Andreas (SA), Garlock (G), and Camp Rock (CR). (B) Iterative three-component seismogram

fits to data for models m_{00} , m_{01} , m_{04} , and m_{16} . Also shown are synthetic seismograms computed for a standard 1D model (table S1). Synthetic seismograms (red) and recorded seismograms (black), filtered over the period range 6 to 30 s. Left column, vertical component (Z); center column, radial component (R); right column, transverse component (T). Inset " ΔT " label indicates the time shift between the two windowed records that provides the maximum cross-correlation (16, 21).

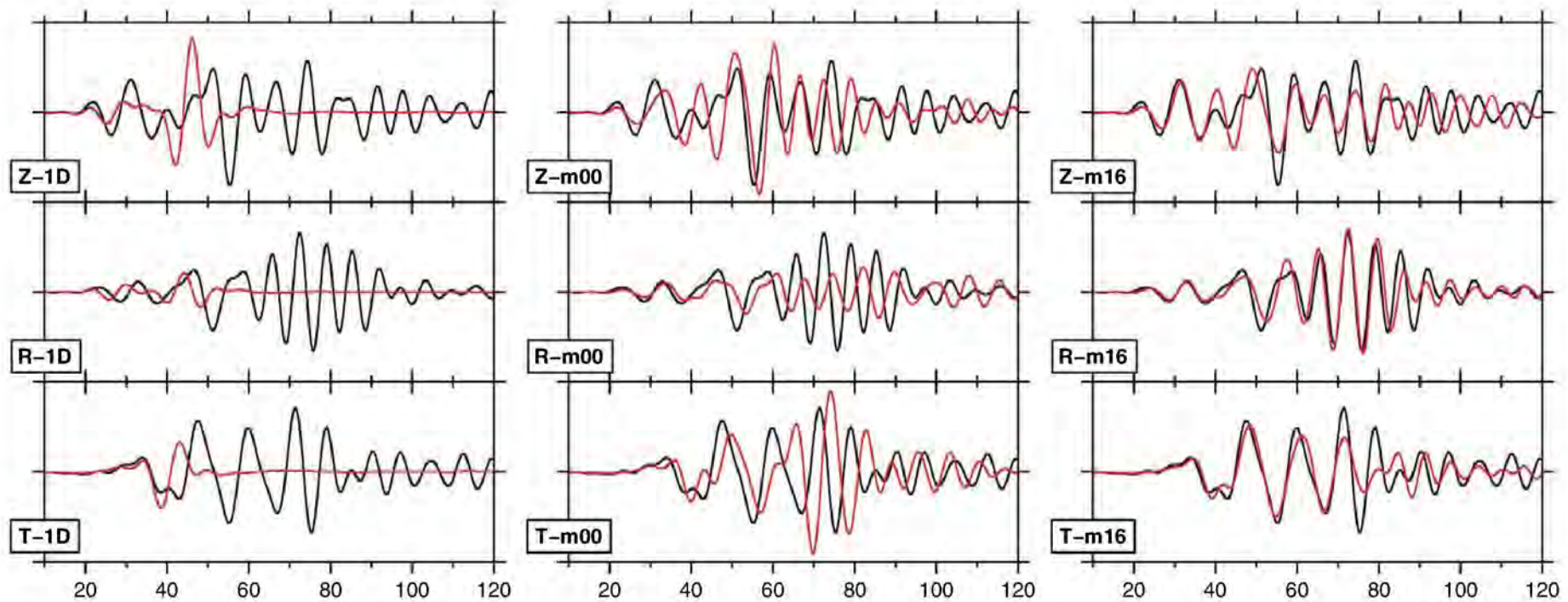


Fig. 2. Synthetic seismograms (red) and recorded seismograms (black) for the period range 6 to 30 s for a path from an earthquake beneath Chino Hills (M_w 5.4, depth 14.2 km), east of the Los Angeles basin, to station STC.CI (distance 137.1 km), within the Ventura basin. Synthetic seismograms are generated

using a 1D layered model, the initial 3D model (m_{00}), and the final 3D model (m_{16}) for all three components: vertical (Z), radial (R), and transverse (T). This earthquake was not used in the tomographic inversion, i.e., it is one of the “extra” earthquakes analyzed in Fig. 3.

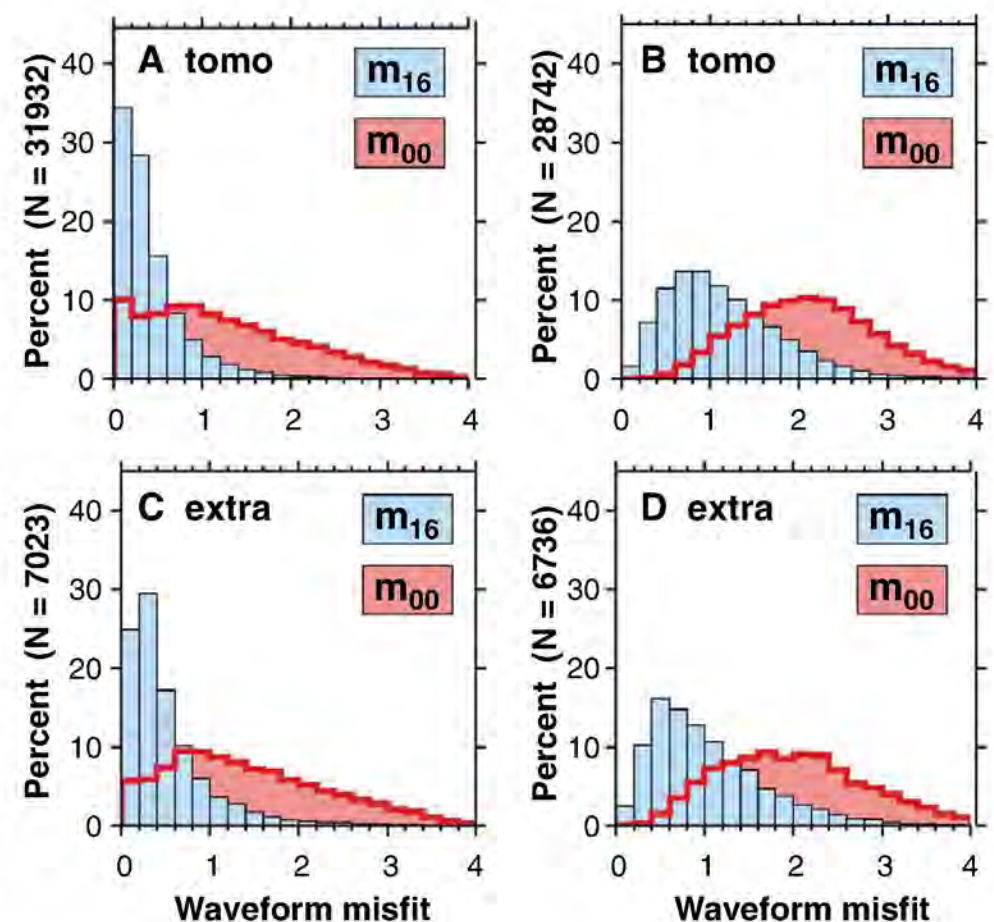
graphic model. Our inversion variables are V_S and V_B . The topography of primary interfaces (Moho and basement surface) is fixed, anisotropy is not permitted, and attenuation does not change.

We present our new crustal model on both relative and absolute scales (8). First, the update to the seismological model (the relative scale) reveals the changes to the initial SCEC model that are required by the data. We compute the update as $\ln(m_{16}/m_{00})$, where m_{16} is the sixteenth iteration from the initial model m_{00} . Second, the seismological model itself reveals the absolute model parameters (e.g., wave speed in units of km/s) and is more relevant for geologic and geodynamic interpretations. All cross sections discussed below are of V_S models (m_{00} and m_{16}). The V_S model is better resolved than the V_B model (fig. S9).

Figure 1 shows the iterative improvement from m_{00} to m_{16} of a single three-component seismogram. The initial travel-time difference (or “time shift”) for the Rayleigh wave in the 1D model is 9.60 s on the vertical component (Z) and 9.85 s on the radial component (R). In the initial SCEC model (m_{00}), the Rayleigh wave time shift is 7.00 s (Z) and 7.30 s (R). After 16 iterations, the time shifts are 0.95 s (Z) and 1.00 s (R). The evolution of the transverse component is more dramatic, because there is virtually no energy between 110 s and 140 s in the SCEC model, and thus there is no time shift to identify. After 16 iterations, the time shift is 0.05 s, and the synthetic transverse-component seismogram captures the main shape of the waveform up to 130 s. Using the technique of (17), we determined that the waveform from 100 to 112 s is a wave reverberating between the surface and the Moho, whereas the waveform after 112 s is a Love wave.

The tomographic update, $\ln(m_{16}/m_{00})$, contains three principal features (Fig. 1A). First, there is the addition of the southern San Joaquin basin

Fig. 3. Waveform misfit analysis for the initial and final tomographic models. The analysis is performed for 143 earthquakes used in the inversion (A and B, “tomo”), as well as for 91 additional earthquakes not used in the inversion (C and D, “extra”). See expanded version in fig. S3. (A) Waveform difference misfit values (16, section S2) for windows used in the inversion. (B) Waveform difference misfit values for full seismograms containing at least one measurement window. (C and D) Same as (A) and (B), but for the set of extra earthquakes.



(22), marked as a -35% (slow) anomaly [with respect to (19)] immediately above the earthquake source. The basin resonates, influencing the Love wave observed after 112 s. Second, the V_S of the western Mojave is increased in the upper 3 km, decreased in the depth range 5 to 15 km, and increased in the depth range 18 to 26 km. Third, east of the Camp Rock fault, there is a -10% change in wave speed, probably associated with Quaternary volcanism (23, 24). Only through multiple iterations is it possible to isolate the locations and amplitudes of these changes.

Fits were also improved within the region containing the higher-resolution basin models (14). In Fig. 2, the seismic wavefield interacts with the Los Angeles and Ventura basins before reaching

station STC. The SCEC model captures the resonance, duration, and approximate amplitude of the observed seismogram, but the final 3D model is markedly better. In particular, the fits for the amplitudes are improved, even though amplitude differences are not built into the misfit function. This demonstrates that the 3D structural changes to the initial model induce additional focusing and amplification of the seismic wavefield.

Our overall assessment of the misfit reduction from the initial SCEC model to the final model is based on 12,583 different paths (such as Fig. 1) that capture 61,673 time windows for measurement (table S2). This assessment cannot be based simply on a travel-time misfit function, because there are many seismic waveforms in the final

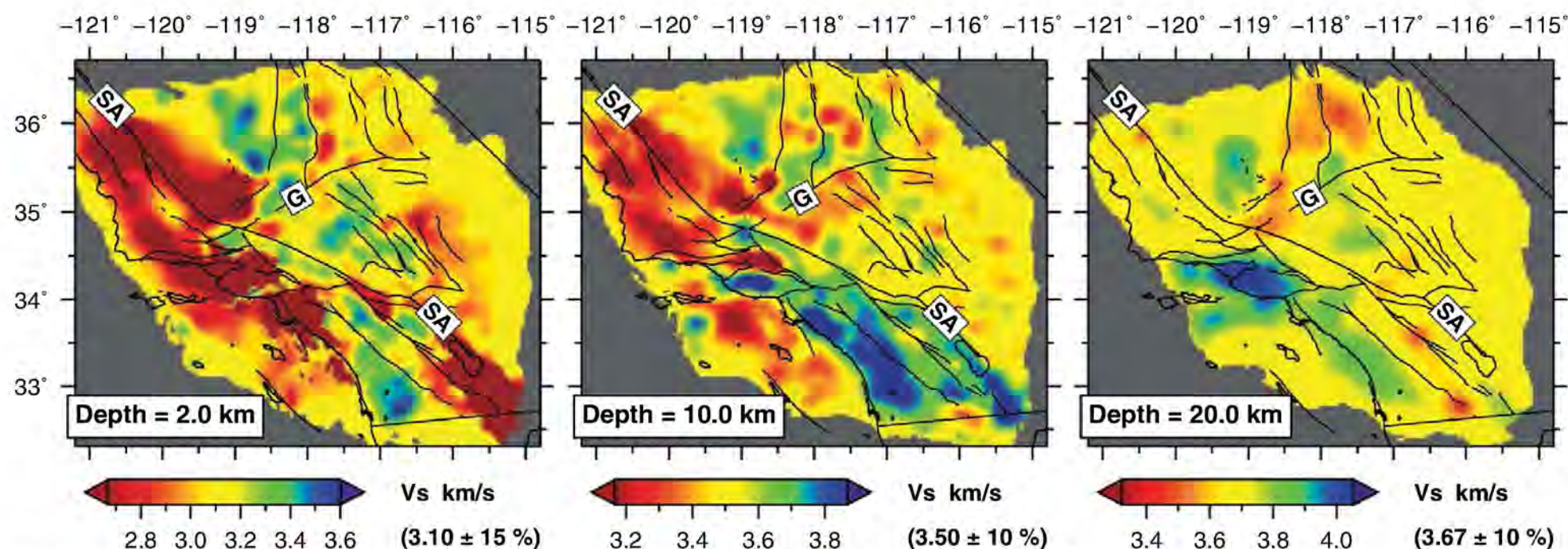


Fig. 4. Horizontal cross sections of V_s tomographic model m_{16} at depths of 2, 10, and 20 km. See fig. S1 for locations of major features; Garlock (G) and San Andreas (SA) faults are labeled for reference.

model that do not have a measurable travel-time difference in the initial model (e.g., Fig. 1B). Thus, to facilitate a direct comparison between the two models, we compute a simple waveform difference using the time windows that were selected for the final model for the 143 earthquakes used in the tomographic inversion (Fig. 3A).

We also consider a separate set of 91 earthquakes that was not used in the tomographic inversion. An earthquake not used in the tomographic inversion—or any future earthquake, for that matter—may be used to independently assess the misfit reduction from m_{00} to m_{16} . The reduction in waveform difference misfit for the extra earthquakes is almost the same as it is for the earthquakes used in the inversion (Fig. 3). This result provides validation for the tomographic model and suggests that future earthquakes will see the same misfit reduction. We also compute waveform differences for the entire seismogram (Fig. 3, B and D), including information outside our measurement windows. We observe a reduction of misfit that is essentially the same for the two sets of earthquakes, and less than that observed for the individual windows.

The travel-time differences in the final model have a standard deviation of less than 1 s for the entire data set (fig. S4). In other words, given an adequate location, origin time, and focal mechanism for any earthquake in southern California with moment magnitude (M_w) between 3.5 and 5.5, we expect most travel-time differences computed using our crustal model to be ≤ 1 s for seismic records at periods of 2 to 30 s.

Our model shows reductions in wave speed due to both compositional and thermal features. Consider the earthquake in Fig. 1A. Above the source is the southern San Joaquin sedimentary basin (22), and east of the Camp Rock fault (and north of 34.3°N) there is higher heat flow (25), likely related to Quaternary volcanism. West of the Camp Rock fault, slow wave speeds and high heat flow are not observed at the surface,

nor is volcanic activity. Horizontal cross sections (Fig. 4) reveal lateral variations in the new crustal model. At 2 km depth, large-scale slow (< 2.8 km/s) regions show several known Neogene basins (fig. S1).

The fastest regions (> 3.5 km/s) are in the Peninsular Ranges west of the Elsinore fault and in the Sierra Nevada west of the Kern Canyon fault (26). The eastern front of the Sierra Nevada is marked by an eastward step in wave speed from about 3.5 to 2.8 km/s, and the Coso geothermal region and the sedimentary fill in Owens Valley and Indian Wells Valley account for the slower wave speeds. We attribute the slow (2.9 km/s) wave speeds in the eastern Mojave to Quaternary volcanism.

At 10 km depth (Fig. 4), some of the basins are no longer visible (e.g., Los Angeles and the Salton trough), and a striking pattern of wave speeds west of the San Andreas fault is evident. The Peninsular Ranges and a mafic layer beneath the Salton trough (27) form a fast (3.8 km/s) region that is separated by the San Andreas fault from slower (3.4 km/s) regions to the northeast.

The 50-km scale variations in wave speeds along the longitudinal line 119°W illuminate, from north to south, the western Sierra Nevada (fast), the southern San Joaquin basin (slow), the San Emigdio Mountains (fast), the Ventura basin (slow), the Santa Monica Mountains (fast), and the Santa Monica basin (slow). Wave speeds in the Coast Ranges are slowest (3.1 km/s) east of the San Andreas (28) and along the coast, and are somewhat faster (3.4 km/s) in between, where Mesozoic granitic and sedimentary rocks are exposed at the surface. The northwestern Mojave is slow (3.3 km/s) compared with faster (3.6 km/s) material in the southern Sierra Nevada, across the Garlock fault.

At 20 km depth (Fig. 4), the most striking feature is the fast wave-speed (4.1 km/s) region beneath the Ventura–Santa Barbara basin and the Santa Monica Mountains, also observed in fig.

S10A. This region coincides with the surface expression of the western Transverse Ranges block (WTRB) (fig. S1), bound to the north by the Santa Ynez fault and to the south by the Malibu Coast fault. We interpret this feature as subduction-captured Farallon oceanic crust, on top of which the WTRB rotated clockwise by more than 90° from a position near the Peninsular Ranges (3.8 km/s) (29). It is possible that the WTRB crustal anomaly is related to upper-mantle anomalies observed below this region (30).

The heterogeneity in the crust (Fig. 4) strongly influences seismic wave propagation from moderate earthquakes ($M_w = 3.5$ to 5.5), such as those in this study. Using the new crustal model, we simulated the details of earthquake ground motion at periods of 2 s and longer for hundreds of different paths in southern California. By beginning to fit complex propagation paths for moderate earthquakes, we provide hope for accurately simulating larger—and damaging—earthquakes that may occur in the future (31). An improved crustal model will also enable better location of earthquakes and identification of faults. Applied at the crustal scale, spectral-element and adjoint methods provide a valuable tool for improving seismic hazard assessment.

References and Notes

1. J. H. Woodhouse, A. M. Dziewonski, *J. Geophys. Res.* **89**, 5953 (1984).
2. B. Romanowicz, *Annu. Rev. Earth Planet. Sci.* **31**, 303 (2003).
3. S. P. Grand, R. D. van der Hilst, S. Widiyantoro, *GSA Today* **7** (no. 4), 1 (1997).
4. R. Montelli *et al.*, *Science* **303**, 338 (2004).
5. A. Dziewonski, D. Anderson, *Phys. Earth Planet. Inter.* **25**, 297 (1981).
6. D. Komatitsch, J. Ritsema, J. Tromp, *Science* **298**, 1737 (2002).
7. V. Akçelik *et al.*, *Proc. ACM/IEEE Supercomputing SC2003 Conference (SC'03)*, 15 to 21 November 2003, Phoenix, AZ.
8. P. Chen, L. Zhao, T. H. Jordan, *Bull. Seismol. Soc. Am.* **97**, 1094 (2007).
9. A. Fichtner, B. L. N. Kennett, H. Igel, H.-P. Bunge, *Geophys. J. Int.* **175**, 665 (2008).

10. A. Tarantola, *Geophysics* **49**, 1259 (1984).
11. O. Talagrand, P. Courtier, *Q. J. R. Meteorol. Soc.* **113**, 1311 (1987).
12. J. Tromp, C. Tape, Q. Liu, *Geophys. J. Int.* **160**, 195 (2005).
13. C. Tape, Q. Liu, J. Tromp, *Geophys. J. Int.* **168**, 1105 (2007).
14. M. P. Süss, J. H. Shaw, *J. Geophys. Res.* **108**, 2170 (2003).
15. D. Komatitsch *et al.*, *Bull. Seismol. Soc. Am.* **94**, 187 (2004).
16. Additional details are available as supporting material on Science Online.
17. Q. Liu, J. Tromp, *Bull. Seismol. Soc. Am.* **96**, 2383 (2006).
18. E. Hauksson, *J. Geophys. Res.* **105**, 13875 (2000).
19. G. Lin, P. M. Shearer, E. Hauksson, C. H. Thurber, *J. Geophys. Res.* **112**, B11306 (2007).
20. T. M. Brocher, *Bull. Seismol. Soc. Am.* **95**, 2081 (2005).
21. A. Maggi, C. Tape, M. Chen, D. Chao, J. Tromp, *Geophys. J. Int.* **178**, 257 (2009).
22. E. D. Goodman, P. E. Malin, *Tectonics* **11**, 478 (1992).
23. P. Luffi, J. B. Saleeby, C.-T. A. Lee, M. N. Ducea, *J. Geophys. Res.* **114**, B03202 (2009).
24. Quaternary and Tertiary volcanic rocks lie predominantly east of the northwest-striking faults of (from north to south) Gravel Hills–Harper, Harper Lake, Camp Rock, and Emerson.
25. J. L. Bonner, D. D. Blackwell, E. T. Herrin, *Bull. Seismol. Soc. Am.* **93**, 2333 (2003).
26. N. M. Shapiro, M. Campillo, L. Stehly, M. H. Ritzwoller, *Science* **307**, 1615 (2005).
27. G. S. Fuis, W. D. Mooney, J. H. Healy, G. A. McMechan, W. J. Lutter, *J. Geophys. Res.* **89**, 1165 (1984).
28. F. Bleibinhaus, J. A. Hole, T. Ryberg, G. S. Fuis, *J. Geophys. Res.* **112**, B06315 (2007).
29. C. Nicholson, C. C. Sorlien, T. Atwater, J. C. Crowell, B. P. Luyendyk, *Geology* **22**, 491 (1994).
30. E. D. Humphreys, R. W. Clayton, *J. Geophys. Res.* **95**, 19,725 (1990).
31. K. B. Olsen *et al.*, *Geophys. Res. Lett.* **33**, L07305 (2006).
32. Seismic waveforms were provided by the Southern California Earthquake Data Center (SCEC), the Northern California Earthquake Data Center (NCEC), the Incorporated Research Institutions for Seismology (IRIS), and the University of Nevada Reno. All earthquake simulations were performed on the CITerra Dell cluster at the Division of Geological and Planetary Sciences of the California Institute of Technology. M. Sambridge suggested using a source subspace projection method to compute the tomographic model update. We acknowledge support by the National Science Foundation under grant EAR-0711177. This research was supported by the Southern California Earthquake Center. SCEC is funded by NSF Cooperative Agreement EAR-0106924 and U.S. Geological Service Cooperative Agreement 02HQAG0008. The SCEC contribution number for this paper is 1261. The Fortran90 software packages SPECFEM3D and FLEXWIN are available for download at www.geodynamics.org.

Supporting Online Material

www.sciencemag.org/cgi/content/full/325/5943/988/DC1

SOM Text

Figs. S1 to S9

Tables S1 to S5

References

22 April 2009; accepted 29 June 2009

10.1126/science.1175298

Bacteriophages Encode Factors Required for Protection in a Symbiotic Mutualism

Kerry M. Oliver,^{1*} Patrick H. Degnan,² Martha S. Hunter,³ Nancy A. Moran²

Bacteriophages are known to carry key virulence factors for pathogenic bacteria, but their roles in symbiotic bacteria are less well understood. The heritable symbiont *Hamiltonella defensa* protects the aphid *Acyrtosiphon pisum* from attack by the parasitoid *Aphidius ervi* by killing developing wasp larvae. In a controlled genetic background, we show that a toxin-encoding bacteriophage is required to produce the protective phenotype. Phage loss occurs repeatedly in laboratory-held *H. defensa*-infected aphid clonal lines, resulting in increased susceptibility to parasitism in each instance. Our results show that these mobile genetic elements can endow a bacterial symbiont with benefits that extend to the animal host. Thus, phages vector ecologically important traits, such as defense against parasitoids, within and among symbiont and animal host lineages.

Invertebrate animals are frequently infected with heritable symbionts, which can spread and persist within host populations by providing benefits to the host organism. For example, terrestrial arthropods that feed exclusively on vertebrate blood or plant sap require nutrients supplied by microbial associates to complete dietary needs (1). Recent work has also revealed that inherited symbionts can benefit diverse invertebrate hosts by providing protection against a range of natural enemies, including pathogens, predators, and parasitoid wasps (2).

In the aphid *Acyrtosiphon pisum*, infection with the inherited gammaproteobacterial symbiont *Hamiltonella defensa* confers protection against an important natural enemy, the para-

sitoid wasp *Aphidius ervi* (3). Female wasps deposit an egg into the aphid hemocoel, which develops within the living aphid before pupating and eventually killing the aphid host (Fig. 1A). Aphids infected with *H. defensa*, however, survive and reproduce when wasps are killed before completing development (4). Bioassays have revealed that levels of protection conferred by different strains of *H. defensa* can vary substantially (5). In the absence of parasitism, *H. defensa* is not required for aphid survival and reproduction, yet surveys of aphid populations in North America and Europe have found that significant proportions of pea aphids (40 to 70%) may be infected and that a wide variety of other aphid species also carry this symbiont (4, 6–8), which appears to confer protection in aphids other than *A. pisum* (9). In experimental populations, the proportion of *H. defensa*-infected aphids increased rapidly under pressure from parasitoid wasps, indicating that defensive benefits probably contribute to the spread of *H. defensa* in natural populations (10). The proportion of infected aphids decreased in the ab-

sence of parasitism, which suggests costs to infection that limit the spread of *H. defensa* (10).

In bacteria, including some symbionts and intracellular pathogens, lateral exchange of genetic material is typically mediated by mobile genetic elements, including transposons, plasmids, and bacteriophages (11). Such elements can introduce functions that may benefit multiple partners in a symbiotic interaction when their interests are aligned (12). *H. defensa* are frequently infected with a lysogenic lamdoid bacteriophage called *A. pisum* secondary endosymbiont (APSE) (12–14). Several lines of evidence link APSE to the protective phenotype. First, variants of APSE have been identified among strains of *H. defensa*, and each encodes homologs of toxins that are known (or suspected) to target eukaryotic tissue (12, 13). For example, phage variant APSE-2 contains a homolog of cytolethal distending toxin (*cdtB*) (12), and aphids infected with APSE-2—carrying *H. defensa* are moderately protected from parasitism (~40% *A. ervi* mortality) (3, 5). APSE-3 encodes a tyrosine-aspartic acid repeat (YD-repeat)-containing protein, which also appears to be a toxin (13). Strains of *H. defensa* carrying APSE-3 were each found to confer high levels of protection (>85% *A. ervi* mortality) (5). The hypothesis that APSE and associated toxins are involved in aphid protection was bolstered by the results of a multi-locus study that found that the highly protective strains of *H. defensa* that carry APSE-3 are identical at 10 bacterial chromosomal markers to a third strain that lacks APSE and confers very little protection (5, 13).

The *H. defensa* chromosome contains virulence factors, including RTX (repeats in toxin) toxins, that could contribute additional protective mechanisms (12, 15). Therefore, despite analyses that showed a correlation between level of protection and presence of APSE, previous evidence could not exclude the hypothesis that variation on the *H. defensa* chromosome is the basis for the

¹Department of Entomology, University of Georgia, Athens, GA 30602, USA. ²Department of Ecology and Evolutionary Biology, University of Arizona, Tucson, AZ 85721, USA. ³Department of Entomology, University of Arizona, Tucson, AZ 85721, USA.

*To whom correspondence should be addressed. E-mail: kmoliver@uga.edu

observed variation in protection to aphids. To separate effects arising from the phage, bacterial, and aphid genomes, we established *A. pisum* lines consisting of the same aphid genotype, infected with the same strain of *H. defensa*, with or without APSE (16). This possibility was presented when polymerase chain reaction (PCR) screening of the APSE P45 and *H. defensa* 16S ribosomal RNA genes revealed that some individual aphids of an *A. pisum* clone (called A1A → 5A, where A1A refers to the strain of *H. defensa*, and 5A indicates the aphid clonal background) had spontaneously lost the phage (APSE-3), retaining only *H. defensa*. We established sublines of clone A1A → 5A from single parthenogenetic females, and individuals in initial generations from each subline consistently tested either positive (now called A1A⁺ → 5A) or negative for APSE (now A1A⁻ → 5A).

We verified the absence of APSE in our A1A⁻ → 5A line by conducting several tests. First, PCR designed to detect phage genes, including conserved genes and the YD-repeat toxin gene, did not yield amplicons in the A1A⁻ → 5A strain. Second, we could not amplify fragments spanning the junction of the integrated phage genome and the integration site (13), which indicated that the phage is not integrated in line A1A⁻ → 5A. Finally, a restriction digest of

whole, isolated *H. defensa* chromosomes from A1A⁺ → 5A and A1A⁻ → 5A lines was subjected to pulsed-field gel electrophoresis. A subsequent Southern hybridization was performed, in which DNA was transferred from the gel to a nylon membrane and exposed to a digoxigenin-labeled probe of a fragment of the APSE P45 gene [as in (17)]. In the A1A⁻ → 5A line, in contrast to A1A⁺ → 5A, we did not detect the probe-bound ~40-kb fragment corresponding to APSE, demonstrating that the phage was indeed absent (fig. S1).

Using three experimental lines: (i) A1A⁺ → 5A, (ii) A1A⁻ → 5A, and (iii) 5A (aphids lacking *H. defensa*), all of which share the same aphid genotype, we conducted parasitism bioassays to compare levels of parasitism and determine the contribution of the phage to the protective phenotype. Aphids of line A1A⁺ → 5A were highly resistant to parasitism by *A. ervi*; infection reduced successful wasp development by 90% compared with uninfected control line 5A (Fig. 1B) [analysis of variance (ANOVA), $F_{1,37} = 241.1$, $P < 0.0001$]. This protection, however, was completely lost in *A. pisum* line A1A⁻ → 5A. Aphids of this line, infected with the same *H. defensa* strain but lacking APSE, suffered lethal parasitism that was ~10-fold higher than that of aphids of their phage-carrying

counterparts (ANOVA, $F_{1,44} = 396.5$, $P < 0.0001$) and not significantly different from rates observed in the *H. defensa*-free control line 5A (ANOVA, $F_{1,38} = 0.58$, $P = 0.45$). These results demonstrate that required factors encoding the defensive properties attributed to this strain of *H. defensa* are located on the bacteriophage APSE-3 chromosome.

We used diagnostic PCR to screen a total of 13 *H. defensa*-infected, clonal lines of *A. pisum* maintained in the laboratory for the presence of APSE. Of the eight lines originally collected from Logan, Utah, USA, in 2003 (5 years before screening), we found that all lines retained infection with *H. defensa*, but none carried APSE (Table 1). Six of the eight *H. defensa* strains had previously carried APSE-3 (13) (Table 1), and past parasitism assays showed that some of these phage-bearing strains of *H. defensa* conferred high levels of protection against *A. ervi* (5). Most *H. defensa*-infected pea aphids in field populations also appear to contain APSE; we found that 17 out of 24 *H. defensa*-infected females carried APSE in the Utah population. Thus, in stark contrast to *H. defensa* infection in aphid lines, which is extremely stable under laboratory conditions, some phage infections are lost over time (Table 1). In laboratory lines collected at different localities and dates, retention of APSE is variable, possibly

Fig. 1. (A) Photograph of *A. ervi* parasitizing *A. pisum*. [Photo credit: Alex Wild] **(B)** Effect of APSE presence on the percentage of *A. pisum* successfully parasitized by the parasitoid wasp *A. ervi*. Aphid line 5A is uninfected with *H. defensa*, line A1A⁺ → 5A is the same *A. pisum* clone infected with *H. defensa* carrying bacteriophage APSE-3, and line A1A⁻ → 5A is the same *A. pisum* clone infected with the same strain of *H. defensa* but lacking phage APSE-3. **(C)** Effect of APSE on percentage of different *A. pisum* clonal lineages successfully parasitized by *A. ervi*. Numbers above columns refer to the total number of aphids counted as alive or parasitized. *** $P < 0.0001$.

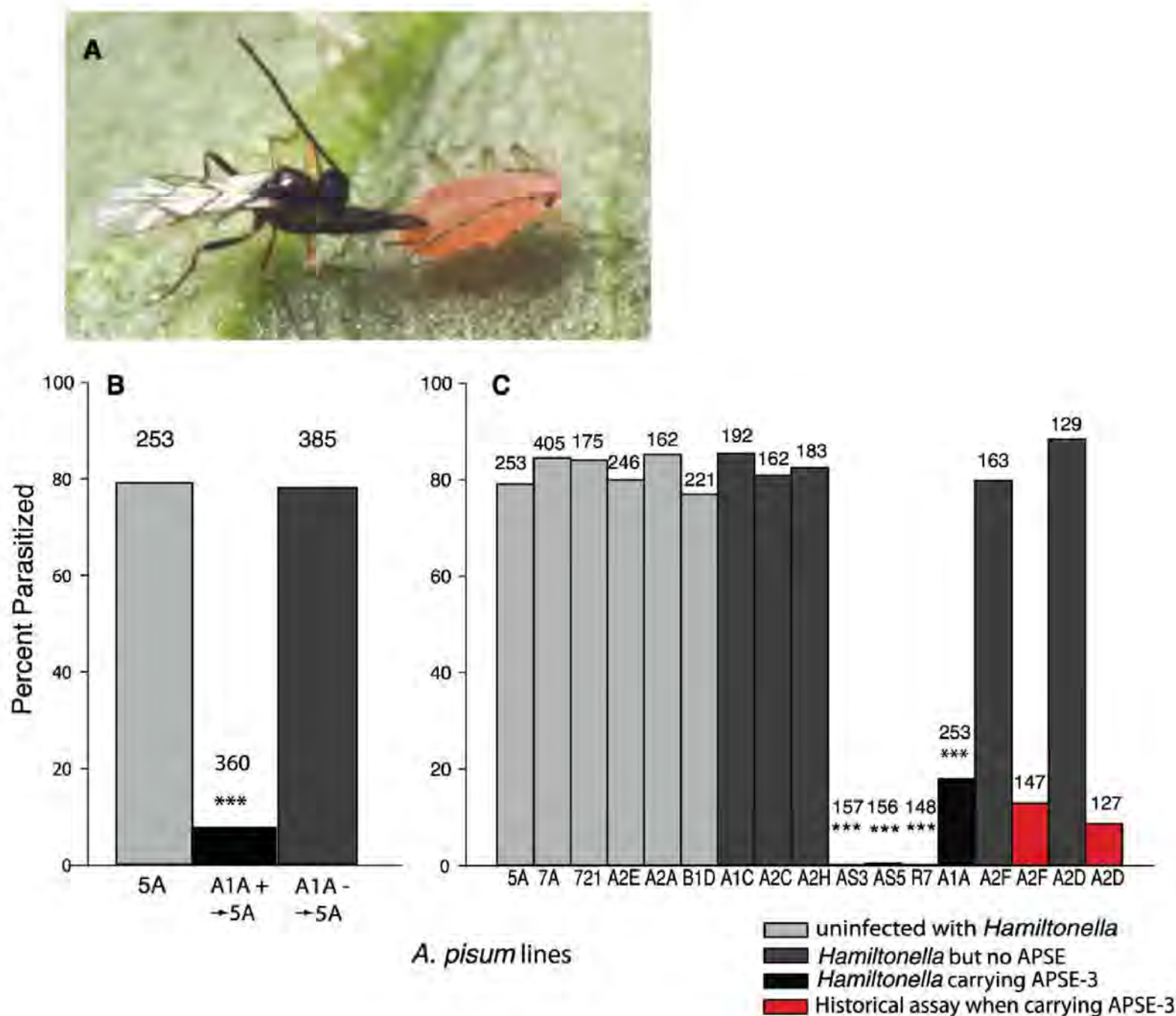


Table 1. Phage loss in *H. defensa*–infected *A. pisum* lines. Each *A. pisum* line is maintained in small cages on *Vicia faba*, either in duplicate or triplicate. Sublines were PCR screened for APSE in 2008 (16) and were found to be either all positive (+), all negative (–), or mixed (+/–). Loss of APSE-3 occurred in all six lines collected and maintained since 2003 and previously determined to carry APSE. It is unclear if lines A1C and A2C carried APSE-3 at the time of collection and subsequently lost the phage, or if they lacked APSE at the time of collection. N/A, not applicable.

<i>A. pisum</i> line	APSE in 2008	APSE in past	Phage variant and toxin	Collection year and location
82B → 5A	+	+	APSE-2 CdtB	New York, USA, 2000
A1A → 5A	+/–	+	APSE-3 YD-repeat	Utah, USA, 2003
A1A	+/–	+	APSE-3 YD-repeat	Utah, USA, 2003
A2D	–	+	APSE-3 YD-repeat	Utah, USA, 2003
A2F	–	+	APSE-3 YD-repeat	Utah, USA, 2003
A2F → 5A	–	+	APSE-3 YD-repeat	Utah, USA, 2003
A2H	–	+	APSE-3 YD-repeat	Utah, USA, 2003
A1C	–	unknown	N/A	Utah, USA, 2003
A2C	–	unknown	N/A	Utah, USA, 2003
AS3	+	+	APSE-3 YD-repeat	Utah, USA, 2007
AS5	+	+	APSE-3 YD-repeat	Utah, USA, 2007
AS5	+	+	APSE-3 YD-repeat	Utah, USA, 2007
R7	+	+	APSE-3 YD-repeat	Utah, USA, 2007

due in part to variation in the rate of spontaneous loss of APSE. Within an individual aphid carrying *H. defensa* and APSE, only some symbiont chromosomes carry an integrated phage (13); therefore, phage loss from some descendant aphid lines probably reflects a simple stochastic process through which only phage-free *H. defensa* infect certain progeny. Loss of the phage and its corresponding protective phenotype potentially explains why *H. defensa* frequencies do not approach fixation in nature, even though *H. defensa* is widespread in surveyed populations (6–8) and APSE is common in sampled *H. defensa* strains [e.g., (12, 17)].

To determine whether loss of the phage generally corresponds to loss of the protective phenotype, we conducted parasitism assays among a range of clones that were uninfected with *H. defensa*, infected with *H. defensa* and carrying APSE-3, or infected with *H. defensa* and lacking the phage. We found that all *H. defensa*–free lines are highly susceptible to parasitism, all APSE-3–carrying strains of *H. defensa* confer high levels of protection, and that the loss of the phage results in the loss of protection in every instance (Fig. 1C). Also included are results of historical assays; though they are not directly comparable, these results demonstrate that two of the same *H. defensa* strains (A2F and A2D) conferred high levels of protection when known to carry phages (Fig. 1C). These correlative results, in conjunction with the experimental evidence presented above, provide strong evidence that bacteriophages are generally required for the bulk of protection conferred to *A. pisum* by infection with *H. defensa*. Thus, *A. pisum* requires toxin-bearing viruses infecting their inherited bacterial symbionts for protection against a common natural enemy.

We performed reverse transcription quantitative PCR to estimate transcript levels of the YD-

repeat protein associated with APSE-3 relative to a highly expressed bacterial gene *dnaK*. We found that transcript levels of this putative toxin were ~2.8-fold as high ($n = 8$ aphids, mean = 2.75 ± 0.57 SE) as those of *dnaK*. A previous study found that the toxin homolog (*cdtB*) associated with APSE-2 is also constitutively expressed at high levels (12). The facts that APSE is required for protection and that APSE toxin homologs are highly expressed strongly suggest a role for phage-associated toxins in the protective mechanism. However, further work is needed to determine if protection results solely from the direct action of phage-encoded factors or from a combination of factors located on both bacterial and phage chromosomes.

There are examples of bacteriophage-encoding virulence factors for pathogens, such as Shiga toxin (*stx*) in *Escherichia coli* (18) and cholera toxin in *Vibrio cholerae* (19). Here, we report the first instance of phage encoding the factors directly underlying a mutualistic symbiosis. Whereas obligate symbionts, such as *Buchnera aphidicola*, have greatly reduced and static genomes, with no evidence of ongoing horizontal gene transfer, facultative inherited symbionts, including *Wolbachia*, have been found to carry several mobile elements (14, 20–22). Our results show that mobile genetic elements can endow a bacterial symbiont with beneficial functions that extend to the eukaryotic host. In our system, the evolutionary interests of phages, bacterial symbionts, and aphids are all aligned against the parasitoid wasp that threatens them all. The phage is implicated in conferring protection to the aphid and thus contributes to the spread and maintenance of *H. defensa* in natural *A. pisum* populations.

In general, phages offer considerable potential as vectors of rapid functional change within and among diverse bacterial lineages associated

with eukaryotic hosts (23). Ecologically important traits, such as defensive functions, encoded by phages may in turn facilitate invasion of new host lineages by bacteria. The presence of these labile elements increases the potential rate of evolutionary responses of hosts and bacterial symbionts in the evolutionary arms race between insects and their natural enemies.

References and Notes

1. A. E. Douglas, *Funct. Ecol.* **23**, 38 (2009).
2. K. M. Oliver, N. A. Moran, in *Defensive Mutualism in Microbial Symbiosis*, J. F. White, M. S. Torres, Eds. (Taylor & Francis, London, 2009), pp. 129–148.
3. K. M. Oliver, J. A. Russell, N. A. Moran, M. S. Hunter, *Proc. Natl. Acad. Sci. U.S.A.* **100**, 1803 (2003).
4. K. M. Oliver, N. A. Moran, M. S. Hunter, *Proc. R. Soc. London Ser. B Biol. Sci.* **273**, 1273 (2006).
5. K. M. Oliver, N. A. Moran, M. S. Hunter, *Proc. Natl. Acad. Sci. U.S.A.* **102**, 12795 (2005).
6. J. C. Simon *et al.*, *Proc. R. Soc. London Ser. B Biol. Sci.* **270**, 1703 (2003).
7. S. Haynes *et al.*, *Appl. Environ. Microbiol.* **69**, 7216 (2003).
8. J. A. Russell, A. Latorre, B. Sabater-Muñoz, A. Moya, N. A. Moran, *Mol. Ecol.* **12**, 1061 (2003).
9. C. Vorburger, C. Sandrock, A. Gouskov, L. E. Castañeda, J. Ferrari, *Evolution* **63**, 1439 (2009).
10. K. M. Oliver, J. Campos, N. A. Moran, M. S. Hunter, *Proc. R. Soc. London Ser. B Biol. Sci.* **275**, 293 (2008).
11. S. R. Bordenstein, W. S. Reznikoff, *Nat. Rev. Microbiol.* **3**, 688 (2005).
12. N. A. Moran, P. H. Degnan, S. R. Santos, H. E. Dunbar, H. Ochman, *Proc. Natl. Acad. Sci. U.S.A.* **102**, 16919 (2005).
13. P. H. Degnan, N. A. Moran, *Appl. Environ. Microbiol.* **74**, 6782 (2008).
14. F. van der Wilk, A. M. Dullemans, M. Verbeek, J. van den Heuvel, *Virology* **262**, 104 (1999).
15. P. H. Degnan, Y. Yu, N. Sisneros, R. A. Wing, N. A. Moran, *Proc. Natl. Acad. Sci. U.S.A.* **106**, 9063 (2009).
16. Materials and methods are available as supporting material on Science Online.
17. P. H. Degnan, N. A. Moran, *Mol. Ecol.* **17**, 916 (2008).
18. A. D. O'Brien *et al.*, *Science* **226**, 694 (1984).
19. M. K. Waldor, J. J. Mekalanos, *Science* **272**, 1910 (1996).
20. A. J. Clark, M. Pontes, T. Jones, C. Dale, *J. Bacteriol.* **189**, 2949 (2007).
21. S. Masui, S. Kamoda, T. Sasaki, H. Ishikawa, *J. Mol. Evol.* **51**, 491 (2000).
22. H. Ogata *et al.*, *PLoS Genet.* **2**, e76 (2006).
23. H. Ochman, J. G. Lawrence, E. A. Groisman, *Nature* **405**, 299 (2000).
24. We thank E. Huang, J. Campos, A. Reedy, and N. Ferguson for providing technical assistance; A. Wild for providing the photograph in Fig. 1; and E. Evans for collecting *A. pisum* in Utah. This project was supported by the National Research Initiative of the U.S. Department of Agriculture Cooperative Research, Education, and Extension Service, grant 2006-35302-17307 to K.M.O. and M.S.H., and NSF grant 0313737 to N.A.M. K.M.O. also received support from NIH training grant 1K12 GM00708, and P.H.D. was supported by an NSF Integrative Graduate Education and Research Traineeship fellowship in comparative genomics (NSF 0654435).

Supporting Online Material

www.sciencemag.org/cgi/content/full/325/5943/992/DC1
Materials and Methods
SOM Text
Fig. S1
Table S1
References
3 April 2009; accepted 10 July 2009
10.1126/science.1174463

An Expressed *Fgf4* Retrogene Is Associated with Breed-Defining Chondrodysplasia in Domestic Dogs

Heidi G. Parker,¹ Bridgett M. VonHoldt,² Pascale Quignon,¹ Elliott H. Margulies,³ Stephanie Shao,¹ Dana S. Mosher,¹ Tyrone C. Spady,¹ Abdel Elkahoul,¹ Michele Cargill,^{4*} Paul G. Jones,⁵ Cheryl L. Maslen,⁶ Gregory M. Acland,^{7,8} Nathan B. Sutter,⁸ Keiichi Kuroki,⁹ Carlos D. Bustamante,¹⁰ Robert K. Wayne,² Elaine A. Ostrander^{1†}

Retrotransposition of processed mRNAs is a common source of novel sequence acquired during the evolution of genomes. Although the vast majority of retroposed gene copies, or retrogenes, rapidly accumulate debilitating mutations that disrupt the reading frame, a small percentage become new genes that encode functional proteins. By using a multibreed association analysis in the domestic dog, we demonstrate that expression of a recently acquired retrogene encoding fibroblast growth factor 4 (*fgf4*) is strongly associated with chondrodysplasia, a short-legged phenotype that defines at least 19 dog breeds including dachshund, corgi, and basset hound. These results illustrate the important role of a single evolutionary event in constraining and directing phenotypic diversity in the domestic dog.

The domestic dog is arguably the most morphologically diverse species of mammal, and theories abound regarding the source of its extreme variation (1). Two such

theories rely on the structure and instability of the canine genome, either in an excess of rapidly mutating microsatellites (2) or an abundance of overactive short interspersed nuclear elements (SINEs) (3), to create increased variability from which to select for new traits. Another theory suggests that domestication has allowed for the buildup of mildly deleterious mutations that, when combined, create the variation observed in the domestic dog (4). The notion of gene duplication as a major cause of morphologic diversity has received little attention.

The majority of phenotypic variation in domestic dogs is found among, rather than within, the over 350 recognized domestic dog breeds. One aspect of interbreed variation is leg length, with some of the most striking short-legged breeds displaying limb morphology characteristic of chondrodysplasia, also known as short-limbed or disproportional dwarfism (table S1). The trait is a primary requirement in the American Kennel Club (AKC) breed standard for over a dozen domestic breeds including

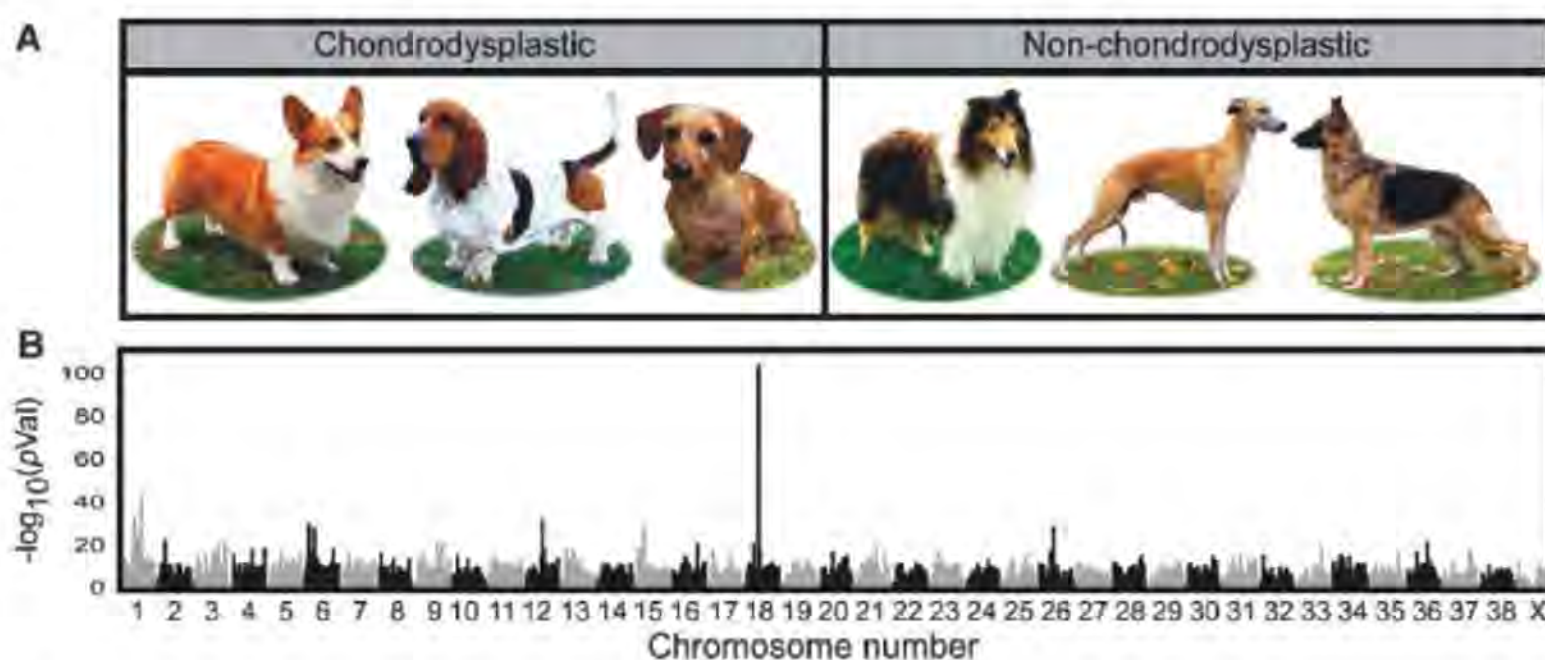
dachshund, Pekingese, and basset hound, where it was found to be dominant and allelic on the basis of arranged crosses (5). The phenotype primarily affects the length of the long bones, with growth plates calcifying early in development, thus producing shortened bones with a curved appearance (Fig. 1A) (6, 7).

To identify the genetic foundations of breed-defining phenotypes such as canine chondrodysplasia, we developed a multibreed approach for mapping fixed canine traits. A total of 835 dogs from 76 distinct breeds that provided maximal coverage of phenotypic variation were genotyped by using the Affymetrix version 2.0 single-nucleotide polymorphism (SNP) chip (8, 9). Chondrodysplastic breeds, or cases, were defined on the basis of specific morphologic criteria set forth in each breed standard (8, 10) and comprised 95 dogs from eight breeds. The control or nonchondrodysplastic group included 702 dogs from 64 breeds lacking the above features (Fig. 1A and table S1).

Single-marker analysis revealed a strong association [odds ratio (OR) = 33.54] between a SNP on chromosome 18 (CFA18) at base position 23,298,242 (CanFam2) and the chondrodysplasia phenotype ($\chi^2 = 437$; $P = 9 \times 10^{-104}$ uncorrected; Fig. 1B). The second best peak of association was found at position 23,729,786; 431 kb telomeric to the first, with a P value of 2×10^{-57} . Because the P values are inflated because of population structure (4% of P values were less than 10^{-7}), we also performed independent Mann-Whitney U tests on the distribution of allele frequencies within the chondrodysplastic and control breeds. The two SNPs on CFA18 retained the strongest association with P values of 1.15×10^{-5} and 2.74×10^{-5} , respectively. The best haplotype across the chromosome spanned the five SNPs beginning at position 23,298,242 and ending at position 23,729,786 (uncorrected P value = 1.9×10^{-111}) (table S1).

Because registered members of a breed are expected to meet specific morphologic criteria, we hypothesized that breed-defining traits such as chondrodysplasia would be under strong

Fig. 1. Results of a whole-genome association analysis for chondrodysplasia across 72 breeds of dog. (A) Examples of breeds used as cases (Pembroke Welsh corgi, basset hound, and dachshund pictured) and controls (collie, whippet, and German shepherd dog) in this analysis. [Photos credit: Mary Bloom, AKC] (B) Alternating shades of gray and black designate the chromosomal boundaries. The two highest peaks are found on chromosome 18 at bases 23,298,242 and 23,729,786 in CanFam2 assembly (16). The peaks are less than 0.5 Mb apart and appear merged in the graph.



selective pressure. We compared heterozygosity in 139 cases and 173 controls genotyped at an additional 64 SNPs that spanned the associated region (table S2) and observed 125 kb (23,320,831 to 23,445,875) in which the cases displayed considerably lower amounts of heterozygosity than the controls did, indicative of a selective sweep (case average = 1.9%, control = 19.6%, $P = 6 \times 10^{-6}$, paired t test) (11–14).

We sequenced 54 amplicons in 44 dogs from 20 breeds (9 case and 11 control) with the goal of (i) identifying additional SNPs, (ii) identifying causative mutations, and (iii) finding the smallest haplotype shared among chondrodysplastic breeds (table S3). Of the 123 SNPs we identified, 50 formed a single continuous homozygous haplotype in all 26 chondrodysplastic dogs tested, covering about 24 kb (23,422,559 to 23,446,056) (Fig. 2A). A portion of the 3' untranslated region (3'UTR) of semaphorin 3c (*sema3c*), a putative thioredoxin domain containing one (*txndc1*) pseudogene, and two evolutionarily conserved sequences are contained within the shared haplotype (Fig. 2B).

An insert of about 5 kb starting at position 23,431,136 (fig. S1) was found by tiling polymerase chain reaction (PCR) amplicons across the homozygous region. This insert was present in all dogs from the original eight breeds and 11 of 12 additional breeds that fit at least two of the three chondrodysplastic criteria (175 dogs from 19 breeds) (8). Seven of the 175 short-legged dogs were heterozygous for the insert (table S4). The insert was not found in 204 medium- to long-legged dogs from 41 breeds that do not display the trait (table S4).

Although the insertion was unambiguously associated with chondrodysplasia, the initial analysis did not address whether the position of the insert or its specific content was causative. We therefore sequenced the insert with use of an Illumina Genome Analyzer (Illumina, Incorporated, San Diego, California). A library was first created from a gel-extracted long-range PCR product that spanned the entire insert from two unrelated chondrodysplastic dogs (dachshund and Scottish terrier). The sequence data were assembled by using Velvet algorithms (15). BLAT analysis (16) revealed a single contig with complete alignment at 100% identity to fibroblast growth factor 4 (*FGF4*), which is located on CFA18 at position 51,439,516; about 30 Mb from the insert.

With use of Sanger sequencing with primers designed from the annotated *FGF4* gene sequence together with the sequence surrounding the insertion site (table S5), we demonstrated that the insert contained a conserved *fgf4* retrogene. Neither the introns nor the upstream promoter sequences of the gene were present in the insert; however, all exons were present, with no alterations in the coding sequence, as well as the 3'UTR and polyadenylate [poly(A)] tail characteristic of retrotransposition of processed mRNA (Fig. 3).

Fig. 2. Observed heterozygosity in chondrodysplastic (red) and nonchondrodysplastic (black) breeds within the associated region on chromosome 18. **(A)** Graph of observed heterozygosity (H_o) across a 34-kb region on CFA18. Each point is the average H_o at one marker across all individuals within the group. The x axis shows the position on chromosome 18. The lines, red for chondrodysplastic and black for nonchondrodysplastic, show the trend in heterozygosity across the region by LOWESS (locally weighted least squares) best fit to the data. The average H_o for controls across the 24-kb homozygous region is 0.10. **(B)** Schematic of the region that is homozygous and identical in chondrodysplastic breeds. Gene 1 is a pseudogene similar to thioredoxin domain containing 1 (*txndc1*). Gene 2 is the 3' end of semaphorin 3c (*sema3c*). The green boxes labeled putative regulatory regions are conserved in both sequence and context in all mammals for which genome data are available. A 5-kb insertion (red rectangle) was found within the fourth LINE between the two putative regulatory elements. The insertion contains an *fgf4* retrogene. Arrangement of genes and conserved regions are per the CanFam2 assembly (16).

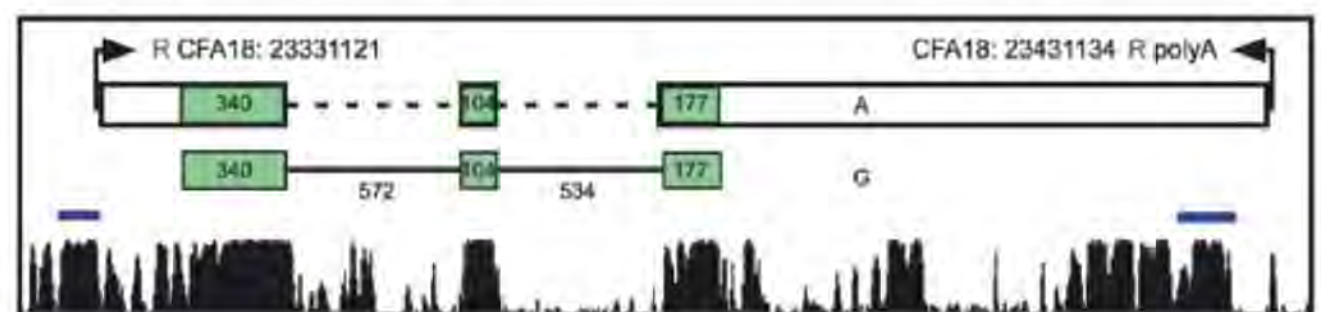
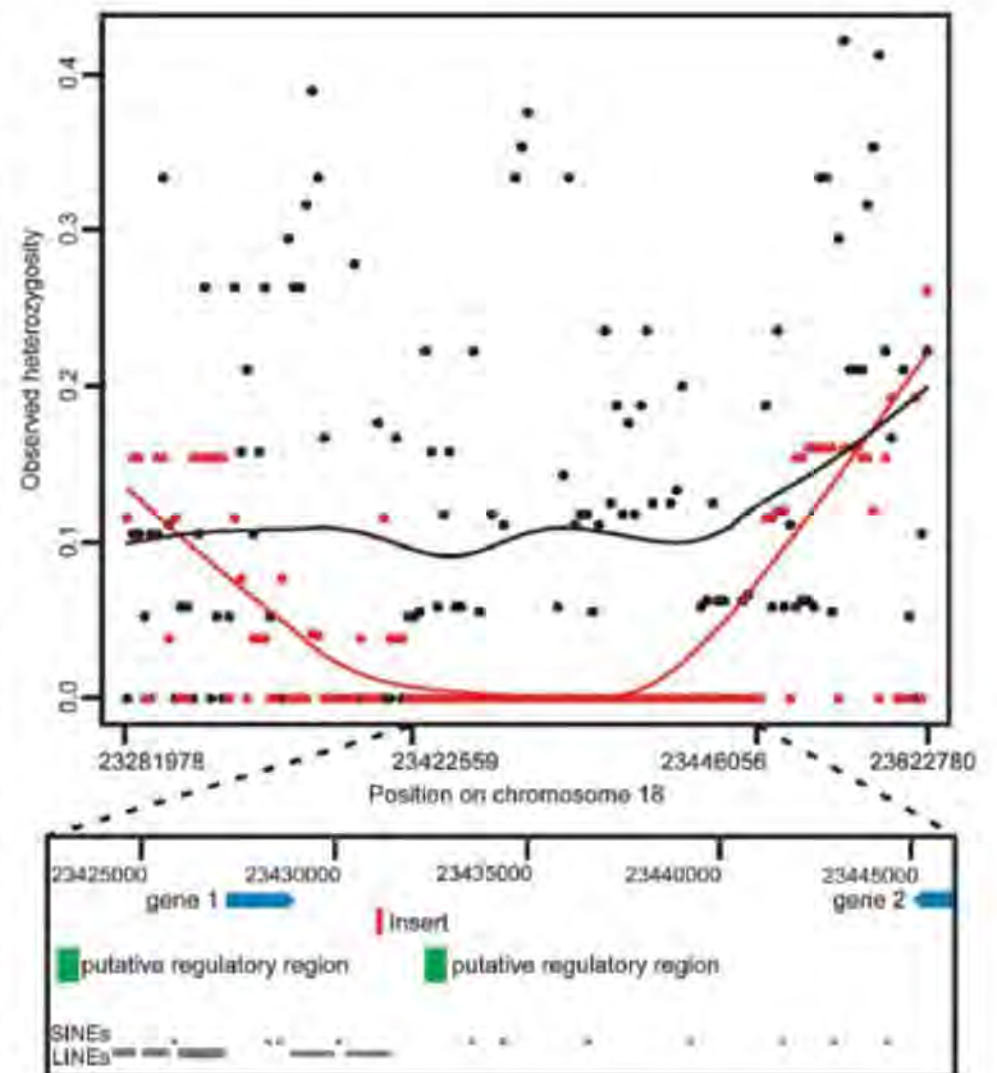


Fig. 3. Comparison of insert to source *FGF4* gene. The first row displays the alignment of the insert sequence to the source *FGF4* sequence. *FGF4* has three coding exons represented by the green boxes on the graph; begins at CFA18 position 51,439,420; and ends at position 51,441,146. All three exons are present in the insert, which aligns between positions 51,439,178 and 51,442,902. The insert includes 242 bases upstream of the start site and 1756 bases downstream of the stop codon followed by a poly(A) repeat. A 13-base sequence (AAGTCAGACAGAG) derived from the insert site, indicated by a blue R on the figure, is repeated at both ends of the insert. The second line shows the coding sequence of *FGF4* with the size of the exons and introns labeled. Alignment of the mouse promoter and enhancer sequences are indicated by the blue lines directly above the dog, human, mouse, and rat conservation track shown at the bottom of the figure (16) (Transcriptional Regulatory Element Database, <http://rulai.cshl.edu/cgi-bin/TRED/tred.cgi?process=home>) (35). Coding sequence is predicted on the basis of sequence similarity of translated proteins (accession no. XM_540801, www.ncbi.nlm.nih.gov).

To determine whether the retrogene was expressed, we searched for retrogene-specific sequences in complete cDNA of chondrodysplastic dogs. A single base at a position syntenic to chr18:51441601, 455 base pairs (bp) distal to the coding sequence of *FGF4*, differed between the retrogene and the source gene, with the former displaying an A nucleotide and the latter a

G, in all samples tested. Both A and G alleles were detected in cDNA generated from articular cartilage of the long bones of chondrodysplastic dogs (Fig. 4A), whereas only the G allele was detected in cDNA and genomic DNA samples from nonchondrodysplastic dogs (Fig. 4B).

Gene duplication through retrotransposition differs from a tandem duplication that may

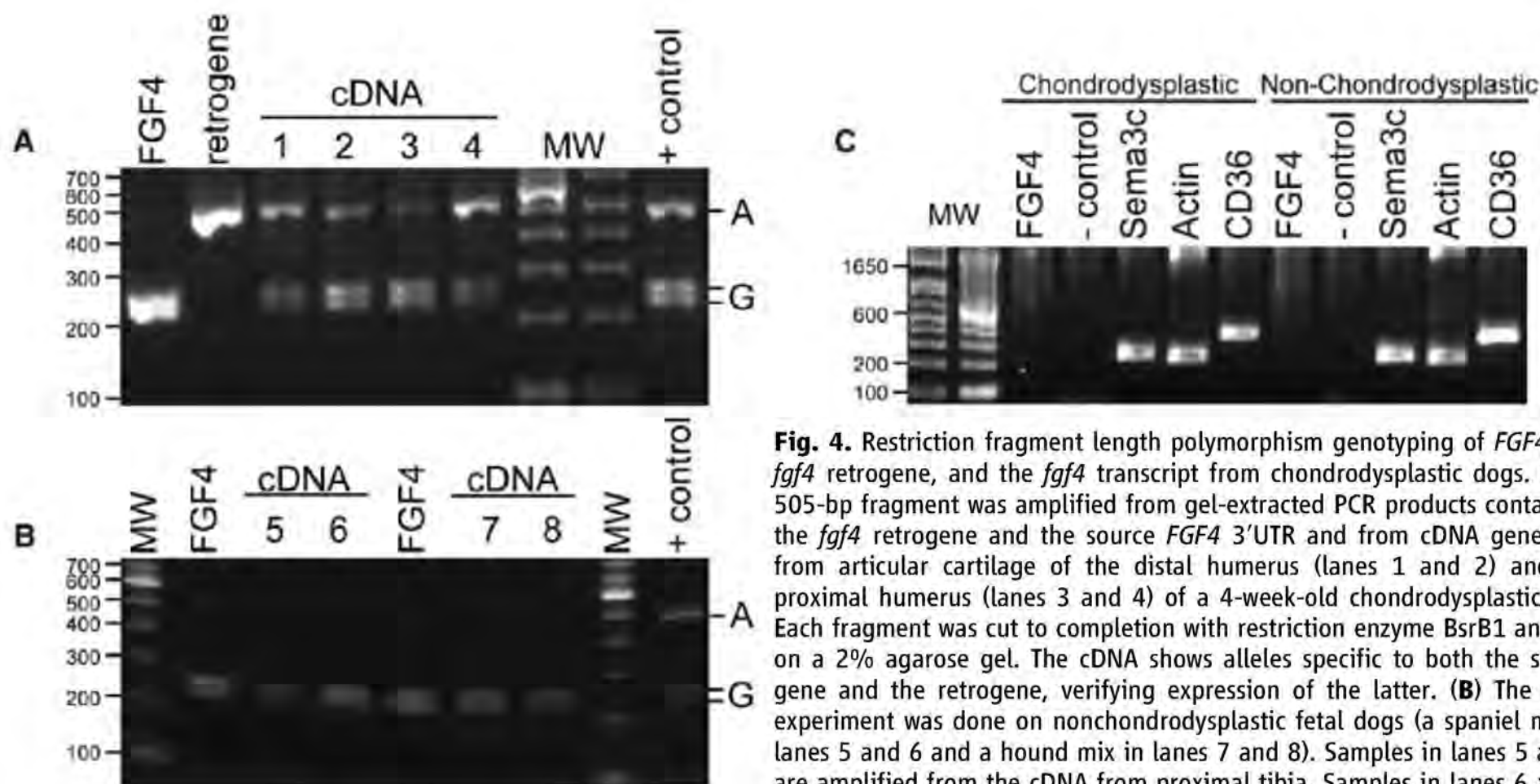


Fig. 4. Restriction fragment length polymorphism genotyping of *FGF4*, the *fgf4* retrogene, and the *fgf4* transcript from chondrodysplastic dogs. **(A)** A 505-bp fragment was amplified from gel-extracted PCR products containing the *fgf4* retrogene and the source *FGF4* 3'UTR and from cDNA generated from articular cartilage of the distal humerus (lanes 1 and 2) and the proximal humerus (lanes 3 and 4) of a 4-week-old chondrodysplastic dog. Each fragment was cut to completion with restriction enzyme BsrB1 and run on a 2% agarose gel. The cDNA shows alleles specific to both the source gene and the retrogene, verifying expression of the latter. **(B)** The same experiment was done on nonchondrodysplastic fetal dogs (a spaniel mix in lanes 5 and 6 and a hound mix in lanes 7 and 8). Samples in lanes 5 and 7 are amplified from the cDNA from proximal tibia. Samples in lanes 6 and 8 are from cDNA from distal femur. Genotypes from the source gene and cDNA are identical because no other copy of *FGF4* is present. **(C)** Genes were amplified in cDNA from articular cartilage from the proximal humerus in an adult chondrodysplastic (shih tzu) and a nonchondrodysplastic (Siberian husky) dog. Although RNA amounts were low in these tissues, expression of *CD36* and *Sema3C* was readily detected. However, expression of neither the source *FGF4* nor the *fgf4* retrogene could be detected.

simply double the gene dosage (17) because the retrogene must acquire a new promoter, likely with a different expression profile, in order to be active. To accomplish this, retrogenes often “borrow” contextual regulatory elements (18). We therefore assessed the expression of thrombospondin receptor (*CD36*) and *Sema3c* genes, which are upstream and downstream of the insert. A PCR-based assay on cDNA from the articular cartilage of fetal and neonatal dogs revealed expression of both genes in the growing limb (fig. S2). Further examination of expression in cartilage tissues from adult dogs shows that, although the surrounding genes were expressed, neither the source *FGF4* gene nor the *fgf4* retrogene were still expressed (Fig. 3C). The finding that the retrogene neither follows the expression pattern of neighboring genes nor is ubiquitously expressed implies that it has a specific time-sensitive role. The retrogene is inserted in the middle of a long interspersed nuclear element (LINE) with both LINEs and SINEs upstream (Fig. 2B). These transposable elements likely provide the regulatory machinery necessary to promote expression of the *fgf4* retrogene (19) with localization and temporal control coming from the intact 3'UTR (20).

We hypothesize that atypical expression of the *FGF4* transcript in the chondrocytes causes inappropriate activation of one or more of the fibroblast growth factor receptors such as *FGFR3*. An activating mutation in *FGFR3* is responsible for >95% of achondroplasia cases, the most common form of dwarfism in humans, and 60 to 65% of hypochondroplasia cases, a

human syndrome that is more similar in appearance to breed-defining chondrodysplasia [reviewed in (21)]. *FGF4* induces the expression of sprouty genes, which interfere with the ubiquitin-mediated degradation of the FGF receptors including *FGFR3*, and overexpression of the sprouty genes can cause chondrodysplastic phenotypes in both mice and humans (22, 23).

The chondrodysplastic breeds were developed in many different countries for a variety of occupations (10). On the basis of genomic analysis of population structure, they do not share a recent common ancestry (24, 25). However, because we find a common haplotype of 24 kb surrounding the *fgf4* retrogene in 19 short-legged breeds, it is likely the chondrodysplastic phenotype arose only once, before the division of early dogs into modern breeds. Thereafter, the retrogene and its associated phenotype were both maintained and propagated by breeders for purposes specific to each breed.

To further explore the origin of the *fgf4* retrogene, we compared haplotypes from the source gene, the retrogene, and the insertion site in both dogs and their wild progenitor, the gray wolf. The ancestor of all chondrodysplastic breeds would have needed to carry both a source gene with the rare haplotype found in the retrogene and the 24-kb haplotype that defines the insertion site (fig. S3 and table S6). This combination was not found in any of the dogs that we tested but was identified in wolves from Europe and the Middle East, supporting fossil evidence that these populations contributed to the early development of the dog (26, 27).

Although retrogenes are recognized as an important source of novel functional elements found between recently diverged species (28–30), little is known about the relation between retrotransposition and phenotypic variation within species (30, 31). We have found a single retrotransposition event producing a conserved, expressed retrogene that has strongly focused the evolutionary direction of morphological change in the dog because at least 12% of American breeds share a common phenotype and the retrogene. This retrogene is actively segregating within the species, has a coding sequence that is identical to that of the source gene, and to the best of our knowledge is the only example of a functional retrogene found in morphologically distinct populations of a single species that is actively maintained by selection. If such rare mutational events or “sports,” as Charles Darwin referred to them in *The Origin of Species* (32), happen only in the evolution of domestic animals, then these systems may be less informative for understanding the origin of evolutionary novelty in wild species. However, if the molecular phenomenon we have observed represents a class of genomic change associated with dramatic phenotypic evolution, such as that characteristic of adaptive radiation (18, 33, 34), then such genetic changes might be keystone molecular innovations.

References and Notes

1. R. K. Wayne, E. A. Ostrander, *Trends Genet.* **23**, 557 (2007).
2. J. W. Fondon 3rd, H. R. Garner, *Proc. Natl. Acad. Sci. U.S.A.* **101**, 18058 (2004).
3. E. F. Kirkness et al., *Science* **301**, 1898 (2003).

4. F. Cruz, C. Vila, M. T. Webster, *Mol. Biol. Evol.* **25**, 2331 (2008).
5. C. R. Stockard, *The Genetic and Endocrinic Basis for Differences in Form and Behavior* (Wistar Institute of Anatomy and Biology, Philadelphia, 1941).
6. S. Heuertz *et al.*, *Eur. J. Hum. Genet.* **14**, 1240 (2006).
7. N. Palmer, in *Pathology of Domestic Animals*, K. V. F. Jubb, P. C. Kennedy, N. Palmer, Eds. (Academic Press, San Diego, CA, 1993), vol. 1.
8. Materials and methods are available as supporting material on Science Online.
9. C. Drogemuller *et al.*, *Science* **321**, 1462 (2008).
10. American Kennel Club, *The Complete Dog Book: Official Publication of the American Kennel Club* (Howell Book House, New York, ed. 19, 1998).
11. K. L. Simonsen, G. A. Churchill, C. F. Aquadro, *Genetics* **141**, 413 (1995).
12. C. Colby, S. M. Williams, *Genetics* **140**, 1129 (1995).
13. N. B. Sutter *et al.*, *Science* **316**, 112 (2007).
14. J. P. Pollinger *et al.*, *Genome Res.* **15**, 1809 (2005).
15. D. R. Zerbino, E. Birney, *Genome Res.* **18**, 821 (2008).
16. <http://genome.ucsc.edu>
17. N. H. C. Salmon Hillbertz *et al.*, *Nat. Genet.* **39**, 1318 (2007).
18. N. Vinckenbosch, I. Dupanloup, H. Kaessmann, *Proc. Natl. Acad. Sci. U.S.A.* **103**, 3220 (2006).
19. C. Feschotte, *Nat. Rev. Genet.* **9**, 397 (2008).
20. D. Fraidenraich, R. Lang, C. Basilico, *Dev. Biol.* **204**, 197 (1998).
21. W. A. Horton, G. P. Lunstrum, *Rev. Endocr. Metab. Disord.* **3**, 381 (2002).
22. G. Minowada *et al.*, *Development* **126**, 4465 (1999).
23. C. Guo *et al.*, *Cell. Signal.* **20**, 1471 (2008).
24. H. G. Parker *et al.*, *Genome Res.* **17**, 1562 (2007).
25. H. G. Parker *et al.*, *Science* **304**, 1160 (2004).
26. M. Germonpre *et al.*, *J. Archaeol. Sci.* **36**, 473 (2009).
27. M. V. Sablin, G. A. Khlopachev, *Curr. Anthropol.* **43**, 795 (2002).
28. J. Brosius, *Genetica* **107**, 209 (1999).
29. A. C. Marques, I. Dupanloup, N. Vinckenbosch, A. Reymond, H. Kaessmann, *PLoS Biol.* **3**, e357 (2005).
30. H. Kaessmann, N. Vinckenbosch, M. Long, *Nat. Rev. Genet.* **10**, 19 (2009).
31. S. Ohno, *Semin. Cell Dev. Biol.* **10**, 517 (1999).
32. C. R. Darwin, *The Origin of Species by Means of Natural Selection* (John Murray, London, 1872).
33. E. Betran, Y. Bai, M. Motiwale, *Mol. Biol. Evol.* **23**, 2191 (2006).
34. J. Rohozinski, C. E. Bishop, *Proc. Natl. Acad. Sci. U.S.A.* **101**, 11695 (2004).
35. T. Nowling, C. Bernadt, L. Johnson, M. Desler, A. Rizzino, *J. Biol. Chem.* **278**, 13696 (2003).
36. We thank D. Babcock and C. Degnin for technical assistance, J. L. Cook for help with tissue identification and acquisition, L. Niswander for thoughtful discussions, and E. Giniger for careful reading of the manuscript. We gratefully acknowledge the dog owners who provided samples, the American Kennel Club–Canine Health Foundation, Affymetrix Corporation, and the Intramural Program of the National Human Genome Research Institute. Funded by NSF grants 0733033 (R.K.W.) and 516310 (C.D.B.) and NIH grants 5R01EY006855 and 1R24GM082910 (G.M.A.) and 1R01GM83606 (C.D.B.).

Supporting Online Material

www.sciencemag.org/cgi/content/full/1173275/DC1

Materials and Methods

Figs. S1 to S3

Tables S1 to S6

References

9 March 2009; accepted 24 June 2009

Published online 16 July 2009;

10.1126/science.1173275

Include this information when citing this paper.

Loss of Function of a Proline-Containing Protein Confers Durable Disease Resistance in Rice

Shuichi Fukuoka,^{1*} Norikuni Saka,² Hironori Koga,³ Kazuko Ono,¹ Takehiko Shimizu,⁴ Kaworu Ebana,¹ Nagao Hayashi,⁵ Akira Takahashi,⁵ Hirohiko Hirochika,⁶ Kazutoshi Okuno,⁷ Masahiro Yano¹

Blast disease is a devastating fungal disease of rice, one of the world's staple foods. Race-specific resistance to blast disease has usually not been durable. Here, we report the cloning of a previously unknown type of gene that confers non-race-specific resistance and its successful use in breeding. *Pi21* encodes a proline-rich protein that includes a putative heavy metal-binding domain and putative protein-protein interaction motifs. Wild-type *Pi21* appears to slow the plant's defense responses, which may support optimization of defense mechanisms. Deletions in its proline-rich motif inhibit this slowing. *Pi21* is separable from a closely linked gene conferring poor flavor. The resistant *pi21* allele, which is found in some strains of *japonica* rice, could improve blast resistance of rice worldwide.

The use of resistance genes (*R* genes) that confer race-specific resistance is a cost-effective strategy for the control of disease in crops. *R* genes are a key component of disease

resistance and often are associated with a hypersensitive response (HR), according to the gene-for-gene concept (1). Most *R* genes cloned in plants contain conserved gene structures (2), and mutation of the pathogen effectors that trigger *R* gene-mediated resistance leads to a loss of resistance, suggesting a substantial vulnerability of this defense mechanism (3). In contrast, resistance controlled by quantitative trait loci (QTLs) is usually non-race-specific (4), and its durability might be a consequence of decreased selective pressure for pathogens to overcome host resistance. Despite the importance of resistance QTLs in crops, their molecular basis remains largely unknown, except *Lr34* and *Yr36*, which house genes that differ structurally from previously reported *R* genes (5, 6).

The resistance to blast disease caused by *Magnaporthe oryzae* conferred by QTLs in rice

(*Oryza sativa* L.) lacks HR, yet it restricts the development of lesions (7). Some cultivars carrying resistance QTLs, such as the *Pi21* locus (8), have maintained resistance throughout a century of cultivation. However, the cointroduction of resistance and undesirable agricultural traits, including grain characteristics from donors, has prevented the use of potential genetic resources for the development of elite cultivars for the past 80 years (9). The causes of the troublesome association have long been debated and could include either tight linkage of genes that control independent traits, known as "linkage drag," or pleiotropic effects of the target gene on other traits (10). Such factors pose penalties on crop production, yet research on the cost to agricultural crops is limited (10). To identify the molecular basis of *Pi21*-mediated resistance and to settle the long-term debate about the cause of associated undesirable characteristics, we undertook map-based cloning of *pi21*, a recessive allele conferring resistance to rice blast.

Leaves of AA-*pi21*, a near-isogenic line (NIL) carrying *pi21* in the genetic background of a susceptible cultivar, had smaller lesions than did the susceptible cultivar (AA) in both a field evaluation and a greenhouse inoculation test (Fig. 1, A and B, and figs. S1A and S2). The resistant *pi21* allele had a consistent effect against all 10 of the widely distributed races of *M. oryzae* studied, although the resistance was incomplete as compared with that triggered by *R* genes (Fig. 1C). Histological examination showed that cells infected with a virulent race were still alive and intact in both AA and AA-*pi21* 40 hours after inoculation (Fig. 1D and table S1), in contrast to those infected with an avirulent race, which induces *R* gene-dependent hypersensitive cell death (table S1). However, cytoplasmic granules, the first sign of cell death, were frequently observed in AA-*pi21* 96 hours after inoculation (Fig. 1E).

¹QTL Genomics Research Center, National Institute of Agrobiological Sciences, Kannondai 2-1-2, Tsukuba, Ibaraki 305-8602, Japan. ²Mountainous Region Agricultural Research Institute, Aichi Agricultural Research Center, Inahasi, Toyota, Aichi 441-2513, Japan. ³Bioproduction Sciences, Ishikawa Prefectural University, Suematsu 1-308, Nonoichi-machi, Ishikawa 921-8836, Japan. ⁴Institute of the Society for Techno-Innovation of Agriculture, Forestry and Fisheries, Ippaizuka, Tsukuba, Ibaraki 305-0854, Japan. ⁵Division of Plant Sciences, National Institute of Agrobiological Sciences, Kannondai 2-1-2, Tsukuba, Ibaraki 305-8602, Japan. ⁶Division of Genome and Biodiversity Research, National Institute of Agrobiological Sciences, Kannondai 2-1-2, Tsukuba, Ibaraki 305-8602, Japan. ⁷Graduate School of Life and Environmental Sciences, University of Tsukuba, Tennohdai 1-1-1, Tsukuba, Ibaraki 305-8572, Japan.

*To whom correspondence should be addressed. E-mail: fukusan@affrc.go.jp

The rate of penetration of hyphae into host cells in AA-*pi21* did not differ from that in AA (Fig. 1F), but the rate of invasion of hyphae from penetrated

cells into adjacent cells, as an indicator of hyphal growth, was significantly lower in AA-*pi21* (Fig. 1G), which is consistent with the observations in

the greenhouse inoculation test (fig. S1, A and B). These observations suggest that *pi21* confers non-race-specific resistance, which is possibly associated with a slow induction of resistance (11). The resistant *pi21* allele did not affect resistance to other fungal and bacterial pathogens (fig. S1, C and D).

By means of high-resolution mapping, we delimited the *Pi21* locus to a 1705-base pair (bp) region containing a single gene, Os04 g0401000 (Fig. 2, A to C, and fig. S3, A and B). The deduced amino acid sequence forms a protein containing a heavy metal-transport/detoxification protein domain in the N-terminal region (fig. S4), implying that metal transport by *Pi21* might be associated with defense as previously reported (12, 13). Comparing the 1705-bp region among two susceptible and one resistant cultivars, we identified seven nucleotide polymorphisms, two of which were located in the open reading frame associated with the phenotype (Fig. 2C and table S2). The resistant *pi21* allele had deletions of 21 and 48 bp from one susceptible *Pi21* allele and of 12 and 48 bp from the other allele in the proline-rich region (fig. S4A).

Transforming a 4.7-kb genomic fragment containing the candidate gene from the resistant cultivar into the susceptible cultivar did not confer resistance, whereas transforming the susceptible *Pi21* allele into AA-*pi21* increased susceptibility to blast in T_1 progeny (table S3). These results suggest that the susceptible allele negatively regulates resistance and that the resistant allele carries a loss-of-function mutation. We confirmed that suppression of susceptible *Pi21* expression by means of RNA interference (RNAi) increased resistance (Fig. 3, A to C), providing evidence that a gene that encodes a protein with a heavy metal-transport/detoxification protein domain (fig. S6) has a role in plant defense. T_2 plants that showed increased susceptible *Pi21* expression also showed enhanced susceptibility to the virulent race, but

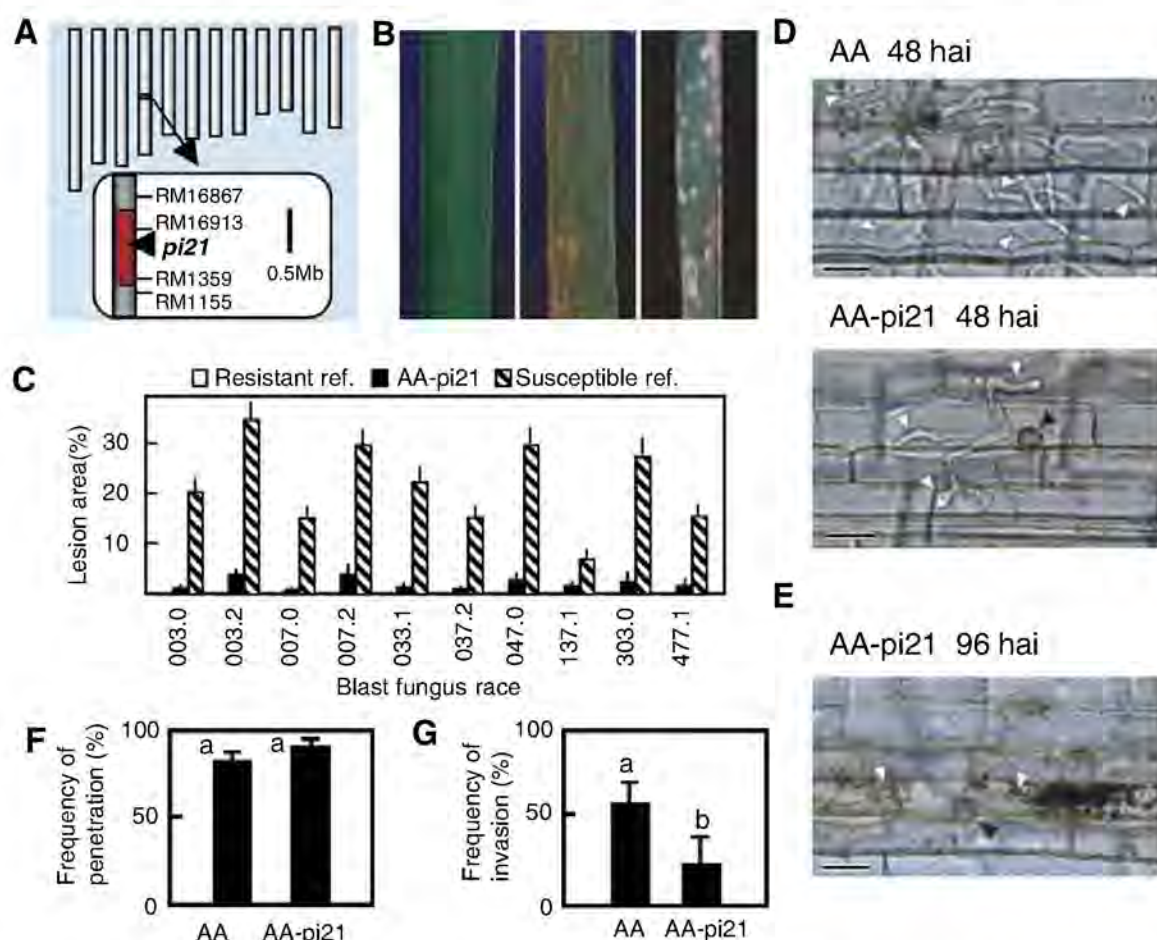
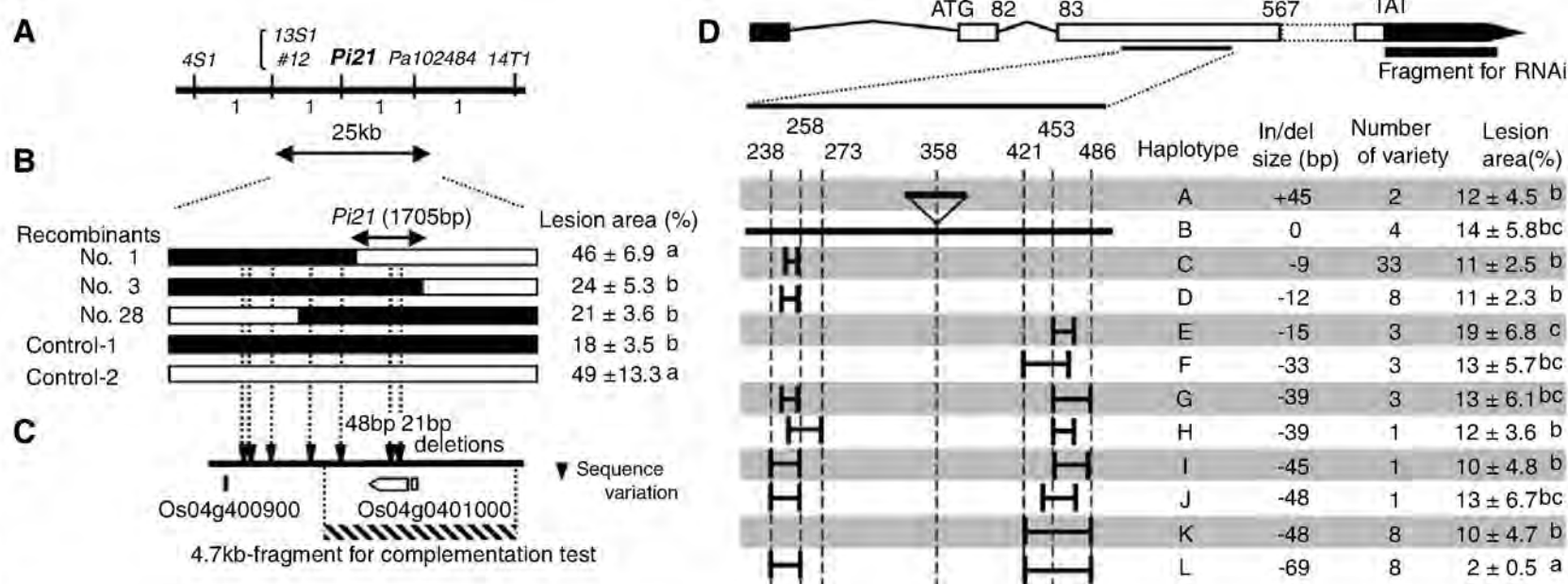


Fig. 1. Phenotypic characterization of the resistant *pi21* allele. (A) Chromosome map of NIL AA-*pi21*. Open boxes indicate chromosomes from susceptible cultivar Aichiasahi (AA); the red box indicates chromosomes from donor cultivar Owarihatamochi. (B) Diseased leaves of 60- to 70-day-old plants from the field evaluation for resistance to blast: Owarihatamochi (left), AA-*pi21* (middle), and AA (right). (C) Lesion area of 30-day-old plants, each inoculated with one of 10 races of blast. The lesion area of the resistant reference was near 0 for all races tested. (D) Infected cells 48 hours after inoculation: AA (top) and AA-*pi21* (bottom). (E) Infected cells 96 hours after inoculation (AA-*pi21*). Black triangles indicate appressoria; white triangles indicate invading hyphae. Scale bars, 20 μ m. Cells challenged by avirulent races are shown in fig. S1E. (F) Frequency of successful penetration of hyphae into cells 48 hours after inoculation. (G) Frequency of invasion of hyphae from penetrated cells into adjacent cells 48 hours after inoculation; a and b are significantly different according to Student's *t*-test ($P = 4.9 \times 10^{-4}$). In (D) to (G), leaf sheath epidermal tissue of 48-day-old plants and blast race 007.0 are shown. Bars in (C), (F), and (G) indicate SE.

Fig. 2. Genetic and physical maps of *Pi21*.

(A) Genetic map produced from 1014 F_2 plants of AA crossed with AA-*pi21*. Numbers below the horizontal line indicate recombinants between *Pi21* and flanking markers. (B) Additional genetic mapping of *Pi21* and progeny testing. Recombinants between marker loci 12 and *Pa102484* were selected from 2703 F_2 plants in which resistant and susceptible alleles from Kasalath segregated. Black bars indicate homozygous resistant; white bars indicate homozygous susceptible. (C) Physical map around *Pi21*. The arrowheads above the horizontal line indicate positions of sequence variations between Owarihatamochi (resistant allele) and Aichiasahi and Kasalath (susceptible alleles). Open boxes represent genes described in the Rice Annotation Project Database (RAP-DB). The hatched box represents the fragment used for the complementation test. (D) Natural



variations in *Pi21*. Indels in *Pi21* identify 12 haplotypes among cultivated rice. The size difference of each haplotype from Nipponbare is shown. The average lesion areas in backcrossed lines carrying the respective *Pi21* haplotypes are indicated. The cultivars used as donors are listed in table S4. The lesion area data in (C) and (D) followed by different letters differ significantly according to Tukey's post hoc test at 5%.

these plants all showed resistance with clear HR against an avirulent race (Fig. 3, D to F), suggesting the involvement of *Pi21* in basal resistance.

We identified 12 variants (haplotypes A to L) in a set of cultivars that represent the genetic variation within cultivated rice (14) on the basis

of insertion-deletion polymorphisms at three positions in a proline-rich region (Fig. 2D and table S4). The resistant *pi21* allele carrying 18- and 48-bp deletions (haplotype L) was found only in *japonica* rice, possibly originating from additional deletion mutation in haplotype K (Fig. 2D and figs. S4B

and S5). We developed a series of backcrossed lines, each possessing one of the *Pi21* haplotypes in the genetic background of a susceptible cultivar, and evaluated their blast resistance (Fig. 2D). Only the line carrying haplotype L showed improved resistance to blast; the rest showed similar susceptibility to the recipient cultivar. Thus, we hypothesized that the defect in *pi21* function is due to the deletion of both the 18- and 48-bp sequences, which house the consensus motif sequence PxxPxxP (fig. S4B), the “core motif” for protein-protein interaction in multicellular organisms (15, 16). A proline-rich protein was suggested to be involved in a defense mechanism of human neutrophils, possibly through competitive inhibition of protein-protein interaction of the proline-rich motif and its counterpart (17). A similar scenario may operate in *pi21*-mediated resistance. Because most rice cultivars carry susceptible *Pi21* alleles (Fig. 2D), the *Pi21* gene is a component associated with susceptibility that can be replaced with the resistant *pi21* allele.

We monitored gene expression in resistant and susceptible lines challenged by either a virulent or an avirulent race of *M. oryzae*. The transient decrease at 3 to 6 hours after the inoculation of all plants implies that *Pi21* responds to stress resulting from inoculation or from incubation in a humidity chamber so as to promote infection (fig. S7A). Plants with the resistant *pi21* allele showed a higher expression of pathogenesis-related genes 3 to 6 hours after inoculation with the virulent race than did plants with the susceptible *Pi21* allele, but not with the avirulent race. This implies that *Pi21*

Fig. 3. Molecular characterization of *Pi21*. (A) Lesions of RNAi lines (AND14 and AND19) 7 days after inoculation with virulent blast race 007.0; T₁ Aichiasahi plants carrying an RNAi construct or an empty vector were used. (B) Lesion areas of empty vector control, RNAi lines, and AA-*pi21* 7 days after inoculation (fig. S2). (C) Reverse transcription polymerase chain reaction (RT-PCR) analysis of *Pi21* in RNAi lines. (D) Lesions of *Pi21*-overexpressing transgenic lines 7 days after inoculation with virulent or avirulent races of blast. Shown are 30-day-old plants of empty vector control, two independent T₃ lines (7-2 and 10-2) carrying multiple copies of the susceptible *Pi21* allele in AA-*pi21* (derived from independent T₀ plants), and Aichiasahi. (E) Lesion area of susceptible *Pi21*-introduced transgenic lines 7 days after inoculation. F₁ of AA crossed with AA-*pi21* is also shown. (F) RT-PCR analysis of *Pi21* in *Pi21*-introduced transgenic lines. In (C) and (F), total RNA was isolated from 24-day-old plants 1 week before the inoculation test. Bars in (B) and (E) indicate SE, and those indicated by different letters differ significantly according to Tukey's post hoc test at 5%.

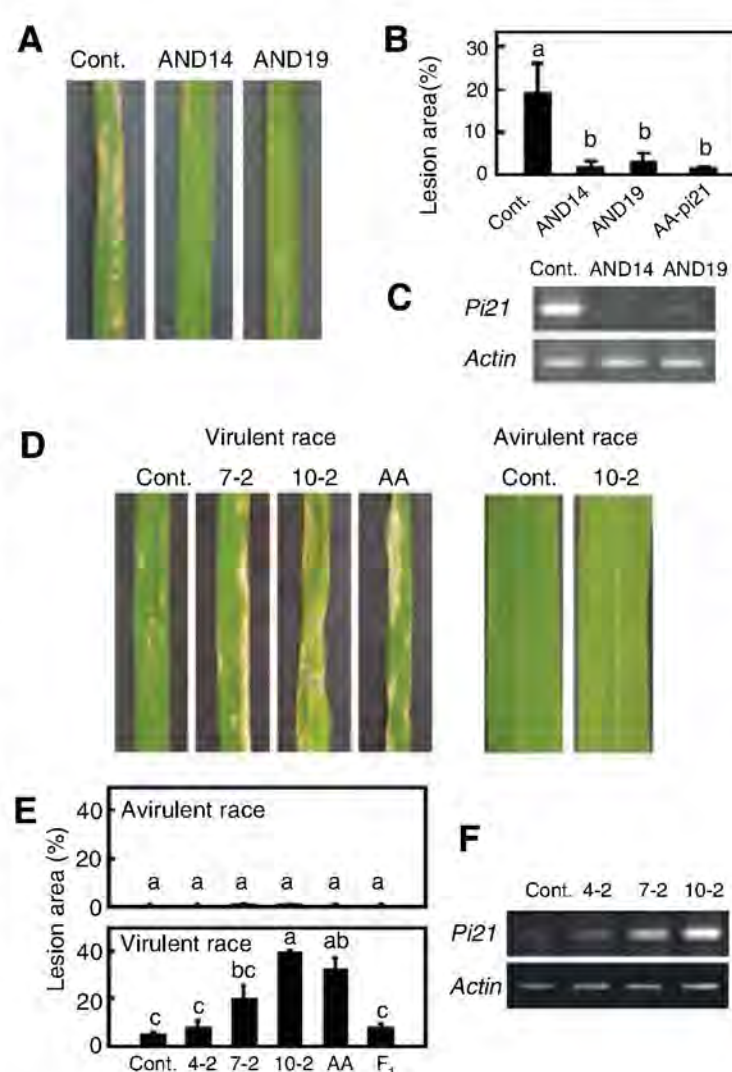
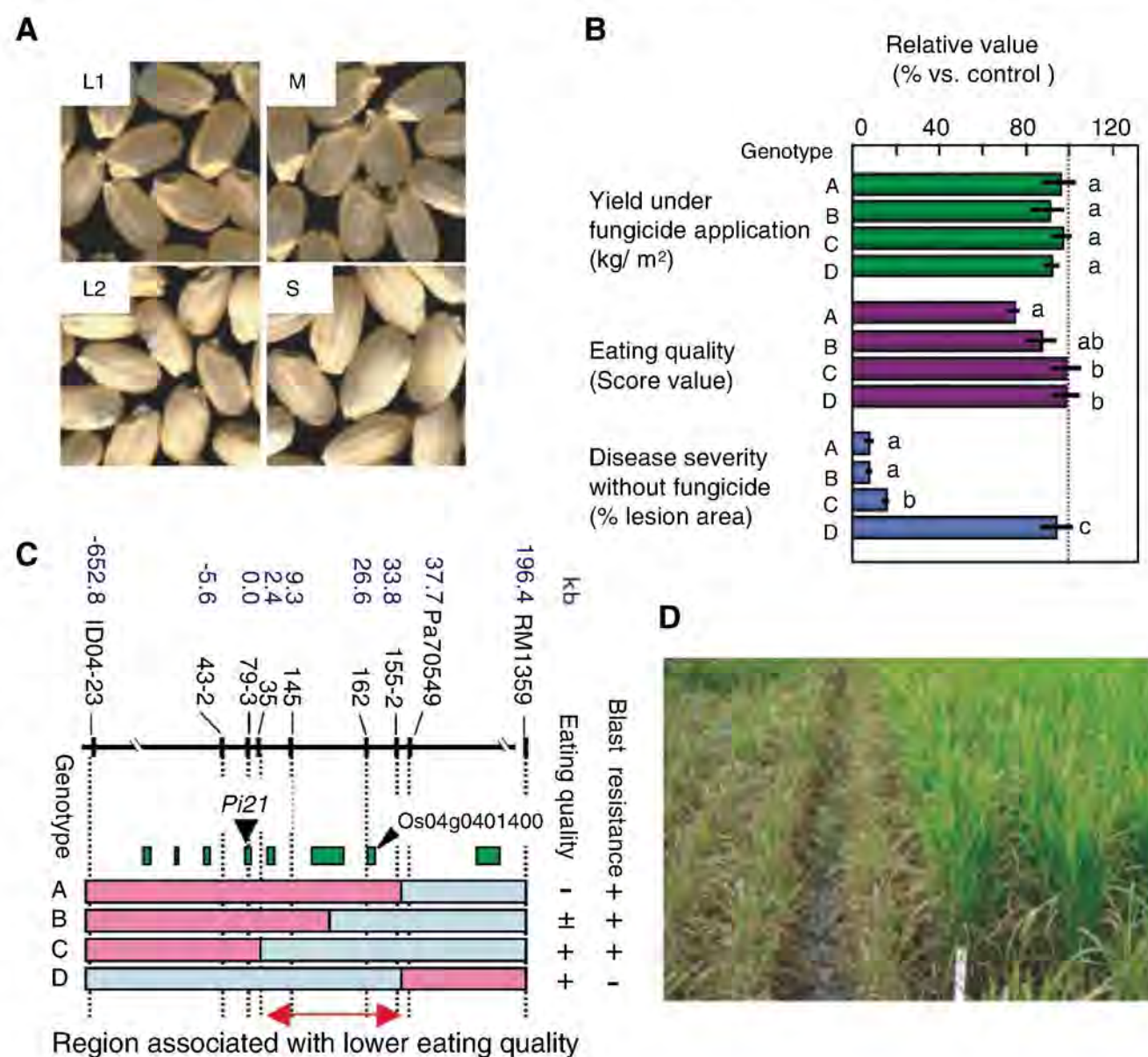


Fig. 4. Successful introduction of resistant *pi21* allele into an elite cultivar. (A) Hulled seed of backcrossed line carrying susceptible *Pi21* allele (L1) and resistant *pi21* allele (L2) in the genetic background of elite rice cultivar Mineasahi. L2 and the donor parent (S) show poor grain quality, which is characterized by a chalky appearance as compared with that of L1 and the recurrent parent (M). (B) Agronomic traits of progeny; the chromosomal structure of each genotype is shown in (C). Bars followed by the same letters are not significantly different according to Tukey's post hoc test at 5%. (C) Map of genomic region associated with eating quality. Physical distance from the *Pi21* locus is shown in kilobases. Pink indicates chromosomes from donor (Sensho); blue indicates chromosomes from recipient elite cultivar (Koshihikari). Phenotype classes are indicated as + (favorable), – (not favorable), and ± (intermediate) and are based on the data in (B). The green boxes indicate positions of genes in RAP-DB. (D) Field trial showing severe infection by blast. (Left) Recurrent parent Koshihikari. (Right) Line carrying the resistant *pi21* allele with improved eating quality (genotype C).



has a role in early response to a virulent race (fig. S7B). Cytoplasmic localization of resistant and susceptible Pi21–green fluorescent protein (GFP) fusion protein accorded with the absence of a nuclear localization signal in the gene sequences (fig. S8).

We introduced the resistant *pi21* allele into an elite cultivar in order to see its effect on other agronomic traits. The plants carrying *pi21* showed undesirable grain characteristics (Fig. 4A and fig. S9), confirming the strong association between blast resistance and poor eating quality that might be contributed by the lower stickiness and hardness of cooked rice. The eating quality of plants carrying the elite cultivar's chromosomal sequence from a point less than 2.4 kb downstream of the *Pi21* locus was equivalent to that of the elite cultivar, and the plants showed a high level of blast resistance (Fig. 4, B to D). In contrast, plants carrying the donor chromosomal sequence up to 37 kb downstream of the *Pi21* locus showed inferior eating quality (Fig. 4, B and C); this sequence carries a gene, Os04 g0401400 (LOC_Os04 g32890), that is highly expressed only at seed maturation, according to the Rice Functional Genomic Express Database. These results clearly show that the resistant *pi21* allele does not penalize agronomic traits and that the cause of the association is tight linkage with genes that cause undesirable effects. A promising line with improved blast resistance (genotype C in Fig. 4) has been evaluated in the field at several locations. Negative regulators of defense, such as *pi21*, may reduce yield owing to constitutive activation of defense responses and

other secondary effects, as barley *Mlo* does (10, 18). However, our data imply that the slow induction of defense by *pi21* will contribute to pathogen control without penalty on yield and other agronomic traits.

Incompleteness, as well as non-race specificity, may be a component of durable resistance. Two QTLs for disease resistance cloned so far in wheat confer resistance that is dependent on temperature or growth stage (5, 6). The response in resistant *pi21* plants after pathogen attack is not as fast or as strong as the *R* gene response. This slower induction of defense may be another type of incompleteness that may contribute to the durability of a plant's resistance. The durability of a resistance gene needs to be proved when cultivars carrying that gene alone maintain prolonged resistance under natural field conditions (19). Monitoring of a newly released cultivar obtained from our study will provide further evidence to confirm or deny the durability of *pi21*-mediated resistance.

Reference and Notes

1. H. H. Flor, *Annu. Rev. Phytopathol.* **9**, 275 (1971).
2. G. B. Martin, A. J. Bogdanove, *Annu. Rev. Plant Biol.* **54**, 23 (2003).
3. M. H. Joosten, T. J. Cozijnsen, *Nature* **367**, 384 (1994).
4. J. E. Parlevliet, *Annu. Rev. Phytopathol.* **17**, 203 (1979).
5. S. G. Krattinger, E. S. Lagudah, *Science* **323**, 1360 (2009).
6. D. Fu, C. Uauy, *Science* **323**, 1357 (2009).
7. A. Ezuka, *Rev. Plant Prot. Res.* **5**, 1 (1972).
8. S. Fukuoka, K. Okuno, *Theor. Appl. Genet.* **103**, 185 (2001).
9. N. Saka, *Plant Prod. Sci.* **9**, 3 (2006).
10. J. K. Brown, *Curr. Opin. Plant Biol.* **5**, 339 (2002).

11. H. Koga, K. Dohi, *Physiol. Mol. Plant Pathol.* **64**, 67 (2004).
12. M. Stein, J. Dittgen, *Plant Cell* **18**, 731 (2006).
13. G. Liu, D. L. Greenshields, *J. Cell Sci.* **120**, 596 (2007).
14. Y. Kojima, K. Ebana, *Breed. Sci.* **55**, 431 (2005).
15. T. Pawson, *Nature* **373**, 573 (1995).
16. L. J. Ball, R. Kuhne, *Angew. Chem. Int. Ed. Engl.* **44**, 2852 (2005).
17. J. Shi, C. R. Ross, *Proc. Natl. Acad. Sci. U.S.A.* **93**, 6014 (1996).
18. R. Buschges, K. Hollricher, *Cell* **88**, 695 (1997).
19. R. Johnson, *Annu. Rev. Phytopathol.* **22**, 309 (1984).
20. We thank the Commonwealth Scientific and Industrial Research Organization Division of Plant Industry, Canberra, for providing the gene-silencing vector; M. Inoue, S. Kudo, and T. Kato for assistance in field blast-resistance tests; H. Ochiai for assistance in the *Xoo* resistance test; H. Kuwahara for assistance in the sheath blight-resistance test; Y. Yoshioka for assistance in image analysis; T. Izawa, E. Minami, E. Kato, and D. Vaughan for helpful comments; S. Konishi and T. Ando for marker-assisted selection; I. Endo for field evaluation of the *pi21*-introduced breeding line; and K. Shimamoto for critical reading of the manuscript. This work was supported by grants from the Ministry of Agriculture, Forestry and Fisheries of Japan (MP1103b, MP1132, QT4004, GB1004, QTL2002, and RGB1101). DNA Databank of Japan accession codes are AB430852, AB430853, and AB430854. Elements of this work are the subject of National Institute of Agrobiological Sciences patent application WO/2007/000880.

Supporting Online Material

www.sciencemag.org/cgi/content/full/325/5943/998/DC1

Materials and Methods

SOM Text

Figs. S1 to S9

Tables S1 to S8

References

29 April 2009; accepted 2 July 2009

10.1126/science.1175550

Bcl6 Mediates the Development of T Follicular Helper Cells

Roza I. Nurieva,* Yeonseok Chung, Gustavo J. Martinez, Xuexian O. Yang, Shinya Tanaka, Tatyana D. Matskevitch, Yi-Hong Wang, Chen Dong*

A fundamental function of CD4⁺ helper T (T_H) cells is the regulation of B cell–mediated humoral immunity. Development of T follicular helper (T_{FH}) cells that provide help to B cells is mediated by the cytokines interleukin-6 and interleukin-21 but is independent of T_H1, T_H2, and T_H17 effector cell lineages. Here, we characterize the function of Bcl6, a transcription factor selectively expressed in T_{FH} cells. Bcl6 expression is regulated by interleukin-6 and interleukin-21. Bcl6 overexpression induced T_{FH}-related gene expression and inhibited other T_H lineage cell differentiation in a DNA binding–dependent manner. Moreover, Bcl6 deficiency in T cells resulted in impaired T_{FH} cell development and germinal center reactions, and altered production of other effector T cell subsets. Our data thus illustrate that Bcl6 is required for programming of T_{FH} cell generation.

A critical function of CD4⁺ helper T (T_H) cells is to provide “help” to B cells, especially in the germinal center structures where activated B cells proliferate and undergo

antibody affinity maturation. Recently, T follicular helper (T_{FH}) cells have been characterized by their expression of chemokine (C-X-C motif) receptor 5 (CXCR5) (1–3). We, as well as others, recently reported that T_{FH} cell development is mediated by interleukin (IL)–6 or IL-21 but is independent of T_H1, T_H2, and T_H17 cells (4, 5).

The B cell lymphoma 6 (Bcl6) transcription factor is selectively expressed by T_{FH} cells (2, 3). Bcl6 was previously shown to be inhibitory to

T_H2 responses by blocking signal transducer and activator of transcription 6 (STAT6) binding to DNA (6, 7), whereas Bcl6-deficient mice developed multiorgan inflammatory diseases, enhanced immunoglobulin E (IgE) production, and defective germinal center reaction (6, 8). It is not clear whether the germinal center defect in these mice is caused by lack of proper T and/or B cell function because Bcl6 is also expressed by germinal center B cells (9). To analyze the function of Bcl6 in T_{FH} cells, we activated naïve CD4⁺ T cells (CD44^{low}CD62L^{high}CD25[–]) from C57BL/6 mice with antibodies to CD3 and CD28 in the presence or absence of various cytokines for 1 or 2 days, and Bcl6 mRNA expression was assessed by real-time reverse transcription polymerase chain reaction (RT-PCR) analysis (10). Treatment with IL-6 or IL-21 significantly up-regulated Bcl6 expression, which was strongly inhibited by the addition of exogenous transforming growth factor beta (TGFβ) (Fig. 1A). These results correlate with our previous observations that IL-6 or IL-21 alone induces T_{FH} cell development and Bcl6 expression, whereas treatment, together with TGFβ, promotes T_H17 differentiation instead (4). To determine whether IL-21 is necessary for IL-6–induced Bcl6 expression, we activated naïve wild-type and IL-21– or IL-21 receptor (IL-21R)–deficient CD4⁺ T cells in the presence of IL-6. IL-21– and

Department of Immunology, M. D. Anderson Cancer Center, Houston, TX 77030, USA.

*To whom correspondence should be addressed. E-mail: rnurieva@mdanderson.org (R.I.N.); cdong@mdanderson.org (C.D.)

IL-21R-deficient T cells showed significantly reduced expression of Bcl6 (fig. S1).

We next assessed whether overexpression of Bcl6 promoted T_{FH} cell development in the absence of exogenous cytokines. Bcl6 overexpression led to increased expression of endogenous Bcl6 mRNA as well as IL-21R, IL-6R, and CXCR5 mRNA, similar to cells treated with IL-6 or IL-21 (Fig. 1B and fig. S2A). Interestingly, IL-21 expression was not up-regulated by Bcl6 overexpression.

Bcl6 has multiple zinc finger (ZF) domains, and the mutation of two of these (ZF3 and ZF5) was previously shown to abolish DNA binding but not nuclear localization (11). We thus assessed the function of Bcl6 with a mutation in either domain in the induction of T_{FH}-specific genes. ZF3 and ZF5 mutations completely abrogated the ability of Bcl6 to up-regulate endogenous Bcl6, IL-21R, and CXCR5 expression, whereas the ZF3 exhibited less efficient inhibition of IL-6R expression than ZF5 (Fig. 1C). Thus, the regulation of T_{FH} gene expression by Bcl6 appears to depend largely on its ability to bind DNA.

We then assessed whether Bcl6 overexpression antagonizes the differentiation of other T_H lineage cells. We first overexpressed Bcl6 in cells undergoing T_H17 differentiation in the presence of TGF β and IL-6. We found that Bcl6 overexpression induced endogenous Bcl6 expression and also moderately increased the expression of CXCR5, IL-21R, and IL-6R (Fig. 2A); however, the expression of these genes was significantly lower than that induced by Bcl6 under neutral conditions or in T_{FH} cells (Fig. 1B). Bcl6 also inhibited IL-17 protein expression when measured by intracellular staining, as well as IL-17 and IL-17F mRNA expression, in a DNA binding-dependent manner (Fig. 2, A and B). In contrast, ROR γ t or IL-21 expression was not affected by Bcl6. We further analyzed whether Bcl6 might influence ROR γ t-dependent transcription using a luciferase reporter driven by the IL-17 gene promoter and the conserved noncoding sequence 2 (CNS2) element (12). Wild-type Bcl6, but not the DNA-binding mutants ZF3 and ZF5, strongly inhibited ROR γ t-induced luciferase activity (Fig. 2C). Thus, similar to Foxp3, Bcl6 inhibits ROR γ t function but not its expression. Unlike Foxp3 (13), however, Bcl6 function appears to be dependent on its binding to DNA.

In addition to T_H17 cells, we also analyzed the effect of Bcl6 in developing T_H1 and T_H2 cells and found that overexpression of Bcl6 increased endogenous Bcl6 expression and CXCR5 (Fig. 2D and fig. S2, B and C). Bcl6, but not ZF3 and ZF5 mutants, also significantly inhibited the expression of T_H1 (IFN γ and T-bet) and T_H2 (IL-4 and GATA3) genes (Fig. 2, D and E, and fig. S2, B and C). Together, these data suggest that Bcl6 autoregulates its own expression. Moreover, Bcl6 not only induces T_{FH} gene expression in

neutral conditions, similar to IL-6 or IL-21, but also inhibits the differentiation of other T_H lineage cells.

To understand whether Bcl6 is necessary for T_{FH} cell development, we used a previously reported Bcl6 knockout mouse (*Bcl6*^{-/-}) (14) and crossed it with OT-II T cell receptor (TCR) trans-

genic mice. The OT-II TCR is specific for a peptide derived from chicken ovalbumin presented by major histocompatibility complex class II; thus, the majority of T cells in these mice are CD4⁺. Naïve CD4⁺ T cells were first differentiated to promote T_{FH} cell differentiation in vitro (4). Bcl6 deficiency resulted in substantial

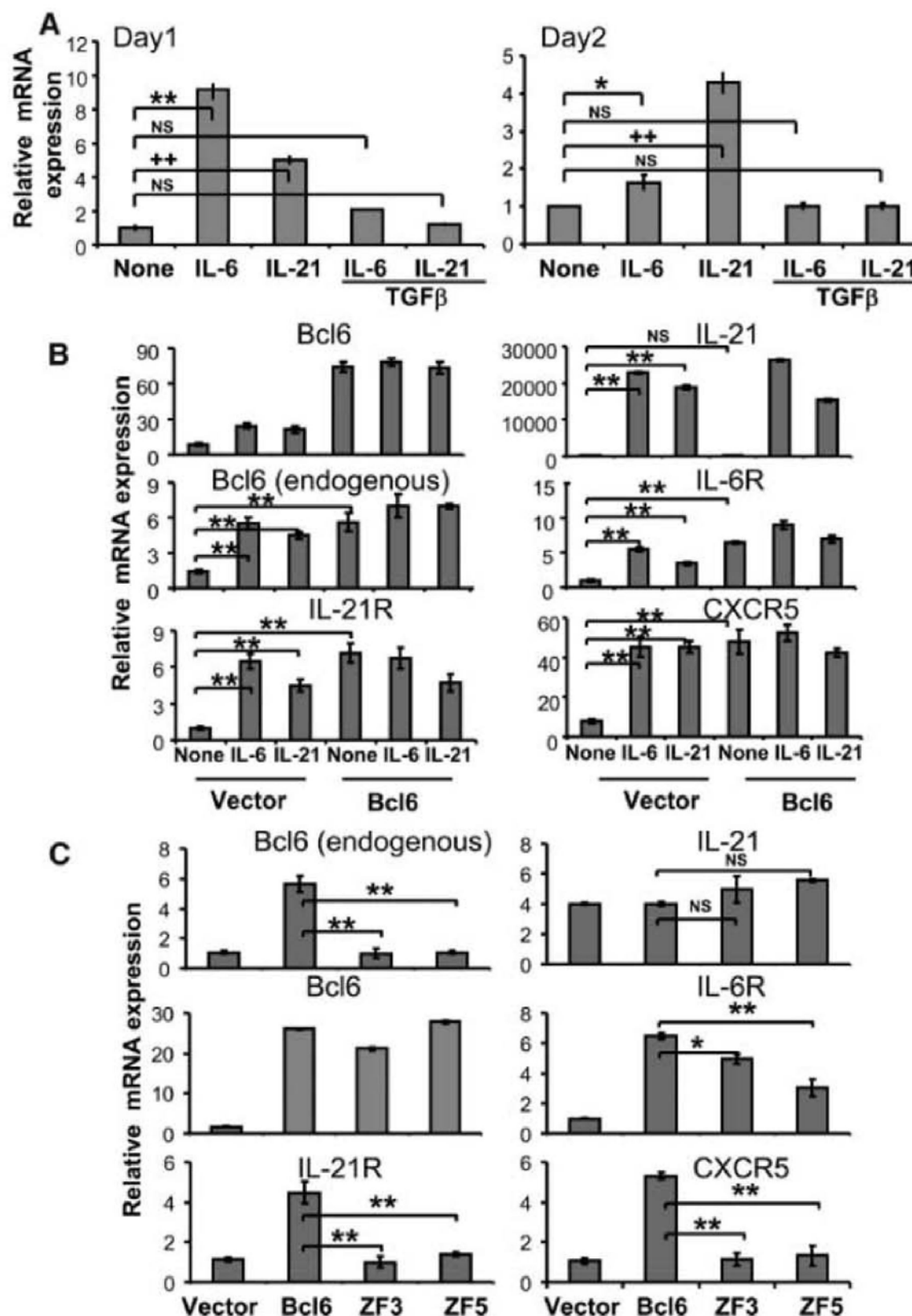


Fig. 1. Bcl6 regulates T_{FH}-specific gene expression. **(A)** Naïve T cells were activated with antibodies to CD3 and CD28, and with or without indicated cytokines for 1 or 2 days. Bcl6 mRNA expression was analyzed by real-time RT-PCR. The graph shows means \pm SD. * P < 0.005; ** P < 0.001 when comparing IL-6 and IL-6 plus TGF β to nontreated sample, analysis of variance (ANOVA) test. *** P < 0.001 when comparing IL-21 and IL-21 plus TGF β to nontreated sample, ANOVA test. **(B)** Naïve OT-II T cells were activated with antibodies to CD3 and CD28 alone or together with IL-6 or IL-21 and with antibodies to IL-4, IFN γ , and TGF β , and infected with a bicistronic retrovirus containing internal ribosomal entry site green fluorescent protein (GFP) expressing Bcl6 or a vector control virus. mRNA expression of indicated genes was assessed by real-time RT-PCR. **(C)** Naïve OT-II T cells were activated with antibodies to CD3 and CD28 alone and infected with retroviruses expressing Bcl6, Bcl6 mutants (ZF3 and ZF5), or vector alone. GFP⁺ cells were sorted from (B) and (C) and restimulated for 4 hours with antibody to CD3. mRNA expression of indicated genes was analyzed by real-time RT-PCR. The data shown were normalized to the expression of a reference gene, *Actb*. The graph shows means \pm SD. * P < 0.005; ** P < 0.001, t test. The data represent at least three independent experiments with consistent results.

reduction of CXCR5 and IL-6R expression, although the expression of IL-21R and IL-21 was partially reduced (Fig. 3A).

We also subjected control and *Bcl6*^{-/-} naïve T cells to T_H1 and T_H17 differentiation. As ex-

pected, absence of Bcl6 resulted in enhanced T_H1 and T_H17 differentiation and increased expression of T-bet and RORγt, respectively (Fig. 3, B and C, and fig. S3). Interestingly, IL-21 mRNA expression in *Bcl6*^{-/-} cells differentiated

under T_H17 condition was enhanced, correlating with increased expression of IL-17 and RORγt (Fig. 3C). When activated in the presence of TGFβ to induce Foxp3 expression, *Bcl6*^{-/-} T cells exhibited reduced levels of Foxp3 expression but enhanced IL-4 and IFNγ expression. Moreover, Foxp3 expression was partially restored by treatment with antibodies to IFNγ and IL-4 (Fig. 3D).

To analyze the function of Bcl6 in T_{FH} cell generation in vivo, we first analyzed germline wild-type and *Bcl6*^{-/-} mice. We found that memory T cells from aged *Bcl6*^{-/-} mice produced significantly elevated amounts of IL-17, but their production of IFNγ and IL-4 was comparable to that of wild-type cells (fig. S4, A and B). IL-21 expression in IL-17⁺ T cells was also increased in these mice (fig. S4C). We then immunized wild-type and *Bcl6*^{-/-} mice with keyhole limpet hemocyanin (KLH) protein (4), which induces an immune response where B cell activation requires T cell help. *Bcl6*^{-/-} mice exhibited severely reduced CXCR5 expression on T cells and numbers of germinal center B cells (fig. S5) 7 days after immunization. Immunohistochemistry analysis also revealed that the germinal center B cells were greatly reduced in the *Bcl6*^{-/-} mice when compared with immunized wild-type mice (fig. S6A). The production of KLH-specific IgG, IgM, and IgG2a was also reduced in *Bcl6*^{-/-} mice, whereas IgE was enhanced (fig. S7A). In contrast, we observed increased expression of T_H1, T_H2, and T_H17 cytokines in *Bcl6*^{-/-} mice, whereas IL-21 production was not affected (fig. S5). To substantiate the above results, we also purified CD4⁺CD44^{high} cells from immunized mice and measured their cytokine secretion after activation ex vivo with KLH and irradiated wild-type splenic antigen-presenting cells. We observed greatly increased expression of IL-4, IFNγ, and IL-17 in *Bcl6*^{-/-} T cells when compared with wild-type T cells (fig. S8A). Furthermore, *Bcl6*^{-/-} T cells exhibited defective expression of T_{FH}-related genes, but their expression of T_H1, T_H2, and T_H17 genes was significantly enhanced (fig. S8B). Interestingly, Bcl6 deficiency did not result in defective IL-21 production, and T_H17 cells are likely the source of IL-21 in knockout mice.

To specifically analyze the function of Bcl6 in T cells, we mixed wild-type or *Bcl6*^{-/-} naïve CD4⁺ T cells with wild-type B cells and transferred them into *Rag1*^{-/-} mice, which lack T and B cells, and immunized the mice with KLH. Absence of Bcl6 in T cells again resulted in greatly reduced numbers of CXCR5⁺ T cells (Fig. 4A). Moreover, germinal center B cells (GL7⁺ FAS⁺) were greatly reduced in these animals (Fig. 4A), which was consistent with our immunohistochemistry analysis (fig. S6B). KLH-specific IgG, IgM, and IgG2a production was also reduced (fig. S7B). We also observed that Bcl6 deficiency resulted in enhanced pro-

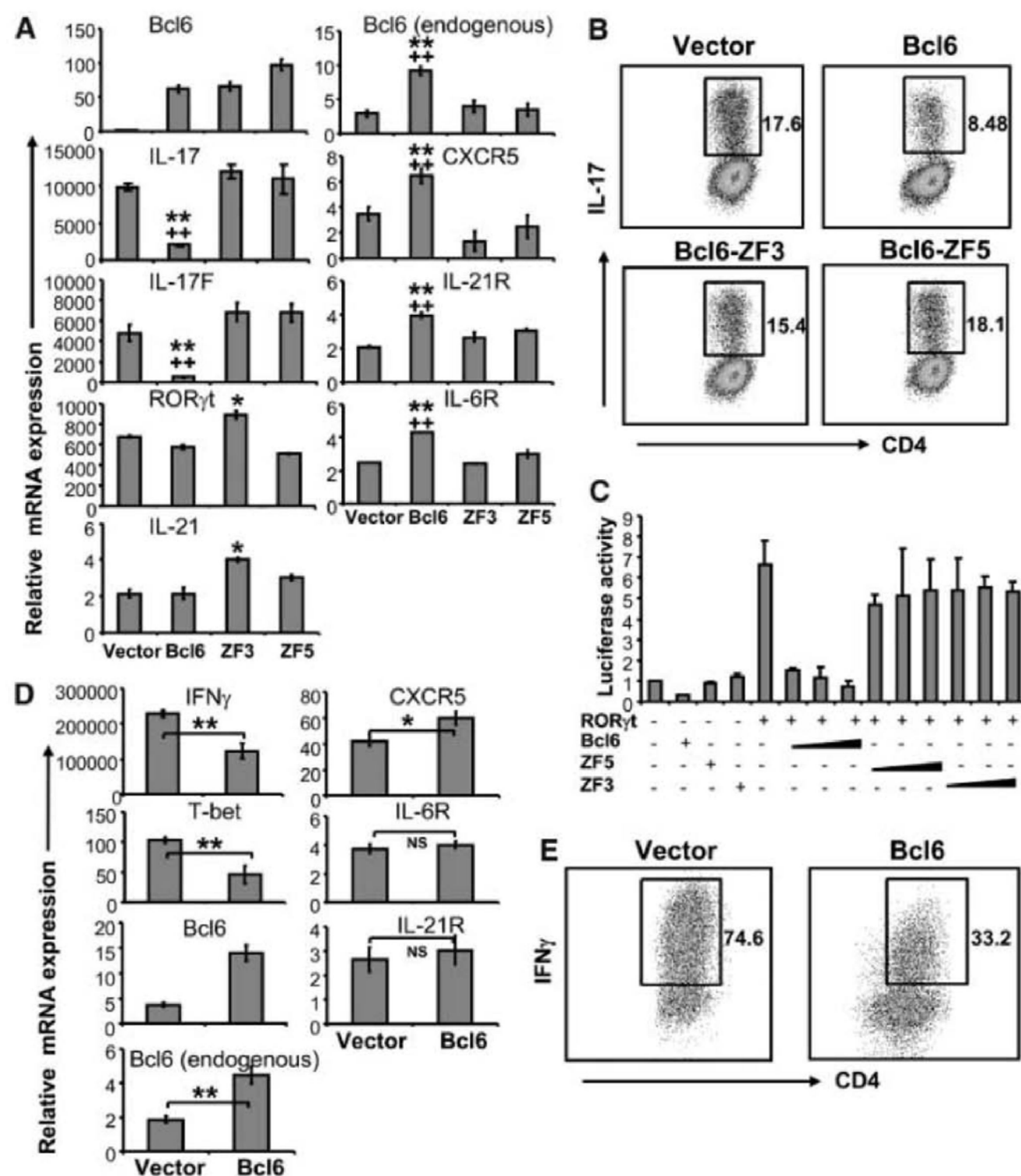
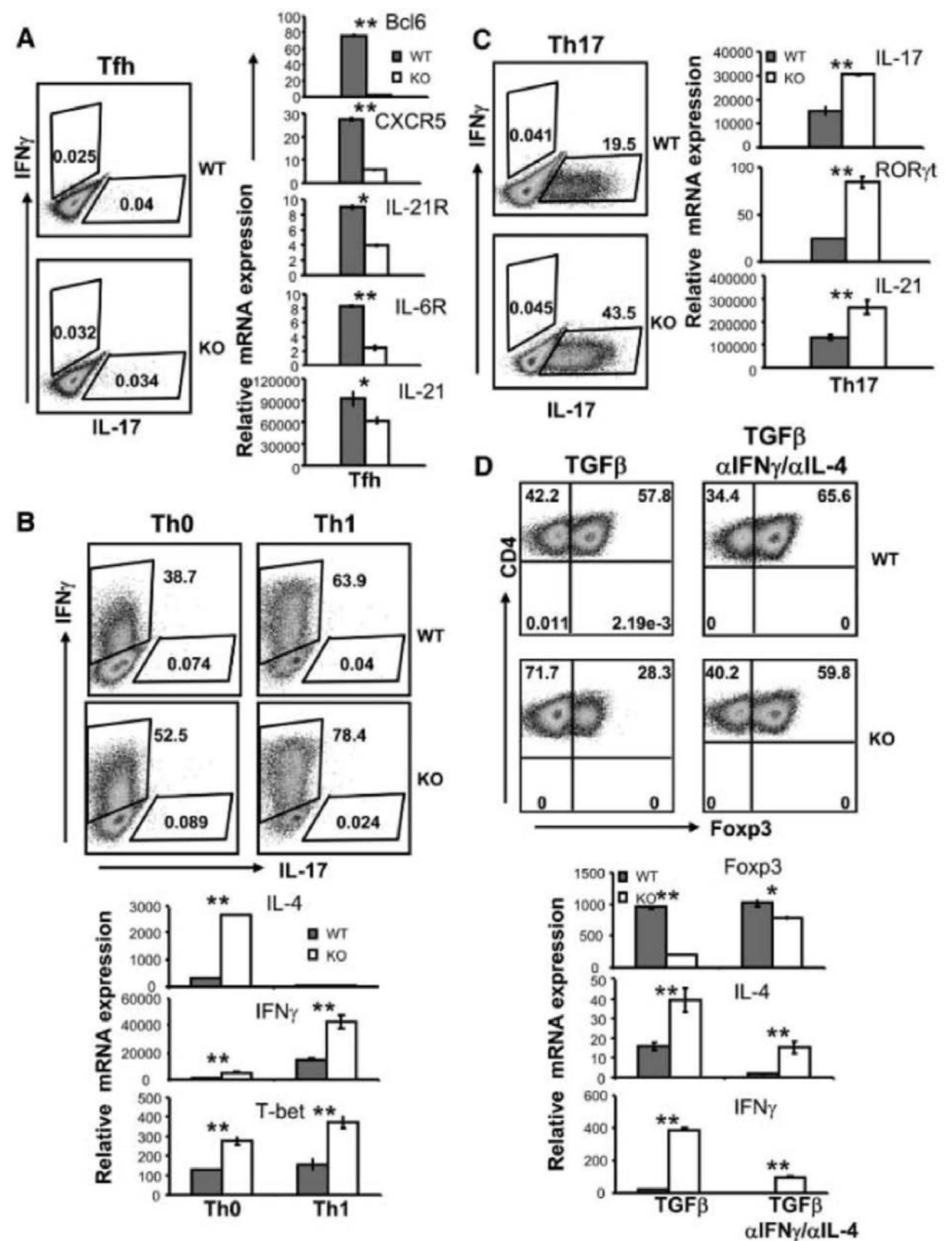


Fig. 2. Bcl6 suppresses T_H17 and T_H1 differentiation. (A and B) Naïve OT-II T cells were activated under T_H17 conditions and infected with retroviruses expressing Bcl6, Bcl6 mutants, or vector alone. GFP⁺ cells sorted by fluorescence-activated cell sorting (FACS) were restimulated with antibody to CD3, and mRNA expression of indicated genes was analyzed by real-time RT-PCR (A). The data shown were normalized to the expression of reference gene *Actb*. The graph shows means \pm SD. * P < 0.005; ** P < 0.001 when comparing Bcl6 and ZF3 to vector alone, ANOVA test. *** P < 0.001 when comparing Bcl6 and ZF5 to vector alone, ANOVA test. IL-17-expressing cells were measured by intracellular staining of the sorted GFP⁺ population (B). Numbers in dot-plot quadrants represent the percentages. (C) EL-4 cells were transfected with a vector containing the firefly luciferase gene under the control of the IL-17 promoter and the CNS2 region, a vector expressing Renilla luciferase, and vectors expressing RORγt, Bcl6 wild-type, various Bcl6 mutants, or vector alone. The firefly luciferase activity was determined and normalized to Renilla luciferase. Values were also normalized to vector alone. The graph shows means \pm SD. (D and E) Naïve OT-II T cells were activated under T_H1 conditions and infected with the indicated viruses. GFP⁺ cells were restimulated with antibody to CD3, and mRNA expression of the indicated genes was analyzed by real-time RT-PCR (D). The data shown were normalized to the expression of reference gene *Actb*. The graph shows means \pm SD. * P < 0.005; ** P < 0.001, t test. IFNγ expression was analyzed by intracellular staining on FACS-sorted GFP⁺ cells (E). Numbers in dot-plot quadrants represent the percentages. The data represent at least three independent experiments with consistent results.

Fig. 3. Bcl6 deficiency causes defective T cell differentiation in vitro. Naïve CD4⁺ T cells from *Bcl6*^{-/-} mice and their littermate control mice carrying the OT-II TcR transgene were activated under T_{FH} (A), T_{H0} and T_{H1} (B), T_{H17} (C), and T_{reg} (TGFβ or TGFβ with antibodies to IL-4 and IFNγ) (D) conditions. Five days later, cells were assessed for IFNγ and IL-17 production [(A) to (C)] or Foxp3 expression (D) using intracellular staining. Numbers in FACS plot quadrants represent the percentages. mRNA expression of various genes was analyzed by real-time RT-PCR, and the data shown were normalized to the expression of reference gene β-actin. The graph shows means ± SD. *P* values were calculated using a *t* test comparing wild-type and *Bcl6*^{-/-} CD4⁺ T cells and are indicated as follows: **P* < 0.005; ***P* < 0.001. The experiments were repeated three times with consistent results.



duction of IL-4 by T cells and KLH-specific IgE by B cells, but only moderately decreased IL-17 and IL-21 expression by knockout T cells (Fig. 4A and fig. S7B). In another experiment, we transferred wild-type and *Bcl6*^{-/-} total CD4⁺ T cells with wild-type B cells into *Rag1*^{-/-} mice and immunized them with KLH. The analysis of sorted effector-phenotype CD4⁺CD44^{high} cells from the immunized mice revealed that Bcl6 deficiency in T cells resulted in the reduction of mRNA expression of most of the T_{FH}-related genes except for IL-21 (fig. S9), which was increased together with IL-17 and RORγt, suggesting that the source of IL-21 may be T_{H17} cells.

Because Bcl6 deficiency also caused hyper-IL-4 production in the above experiment, we examined the effect of IL-4 neutralization. Treatment with antibody to IL-4 almost com-

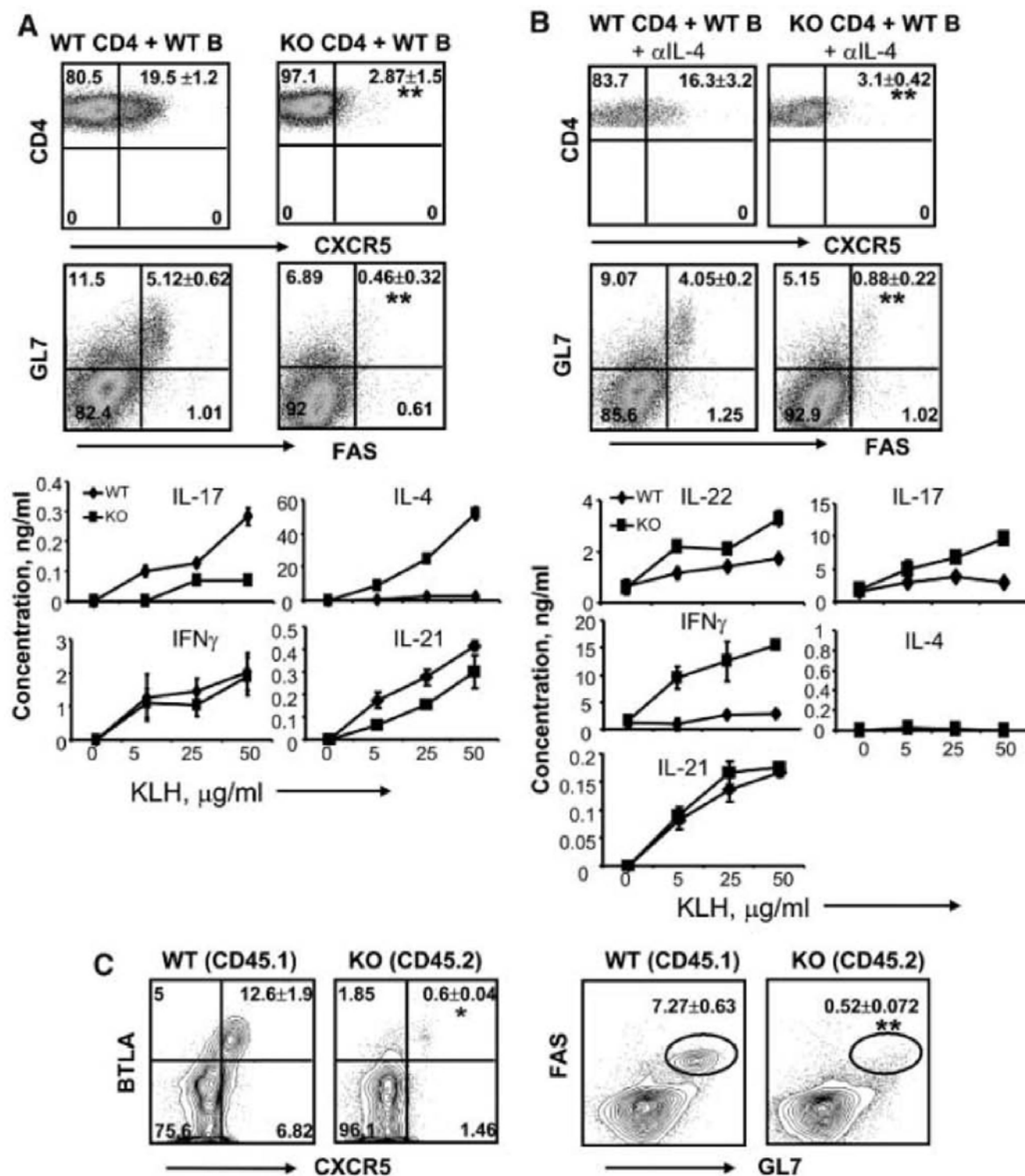
pletely blocked IL-4 production by T cells, whereas defective CXCR5 expression was still observed in *Bcl6*^{-/-} T cells (Fig. 4B). We also observed reduced generation of germinal center B cells and KLH-specific IgG, IgM, and IgG2a production (Fig. 4B, fig. S6C, and fig. S7C). In addition, *Bcl6*^{-/-} T cells also exhibited increased IL-22, IL-17, and IFNγ production (Fig. 4B). Despite the absence of T_{FH} cells in *Bcl6*^{-/-} mice, we detected IL-21 production that was comparable to wild-type mice, likely derived from T_{H17} cells.

To further demonstrate the role of Bcl6 in T and B cells, we generated mixed bone marrow chimeras by transferring a mixture of congenic CD45.1⁺ wild-type and CD45.2⁺ *Bcl6*-deficient bone marrow cells into sublethally irradiated *Rag1*^{-/-} mice. Eight weeks after reconstitution, we immunized the mice with KLH. *Bcl6*^{-/-}

CD4⁺ T cells did not mature into CXCR5⁺ T_{FH} cells that also express B and T lymphocyte attenuator (BTLA) (Fig. 4C), and did not exhibit germinal center B cells. CD4⁺CD44^{high} *Bcl6*^{-/-} cells exhibited greatly reduced T_{FH} gene expression; however, the expression of T_{H1}, T_{H2}, and T_{H17} genes were all increased when compared with wild-type cells (fig. S10). Moreover, Bcl6-deficient B cells did not produce germinal center B cells. On the basis of the above data, we conclude that Bcl6 expression in both T and B cells is required for the germinal center reactions.

In summary, we have demonstrated that Bcl6 is regulated by IL-6 and IL-21 but that, similar to RORγt in T_{H17} cells, it does not regulate the expression of IL-21. Bcl6 deficiency in vivo did not inhibit IL-21 expression, likely by T_{H17} cells. Thus, IL-21 expression by non-

Fig. 4. Bcl6 is necessary for the generation of T_{FH} cells in vivo. **(A and B)** Naïve $CD4^+$ cells from wild-type (WT) or *Bcl6*^{-/-} mice were mixed with WT B cells and transferred into *Rag1*^{-/-} mice (3 mice per group). The recipient mice were immunized subcutaneously with KLH emulsified in Freund's complete adjuvant (FCA). In **(B)**, recipient mice were also treated with antibody to IL-4. Seven days after the immunization, germinal center B cells were determined by staining with GL-7, FAS and B220 antibodies, and T_{FH} cells by CD4 and CXCR5 antibodies. Numbers in dot-plot quadrants represent the percentages in gated T and B cells, respectively. Spleen cells from immunized mice were stimulated with the indicated concentration of KLH. Effector cytokines were measured after 4 days of treatment. The graph shows means \pm SD. *P* values were calculated using a *t* test comparing CXCR5 expression on T cells or GL7/Fas expression on B cells between mice transferred with WT or *Bcl6*-deficient T and B cells, respectively, and are indicated as follows: **P* < 0.005; ***P* < 0.001. The results are representative of multiple mice (*n* = 6 per group) from two independent experiments with similar results. **(C)** Mixed-bone marrow chimeric mice (*n* = 15) were generated and immunized with KLH in FCA. Spleen cells were stained with antibody to CD45.2 to distinguish WT and *Bcl6* knockout compartments and then analyzed for the germinal center B cells and T_{FH} cells. *P* values were calculated using a *t* test comparing CXCR5 and GL7/Fas expression between WT and *Bcl6*-deficient T and B cells, respectively, and are indicated as follows: **P* < 0.005; ***P* < 0.001. The results are a representative of multiple mice (*n* = 15) from three independent experiments with similar results.



T_{FH} cells is not sufficient to induce germinal center reactions. Our data overall indicate that Bcl6, selectively induced by IL-21 or IL-6 in the absence of TGF β signaling, serves as a master transcriptional factor in T_{FH} cell differentiation, analogous to ROR γ t and ROR α , both of which are induced by IL-6 or IL-21 in the presence of TGF β and function to promote T_{H17} differentiation (fig. S11). IL-6 alone induces the expression of ROR γ t (15), whose function is inhibited by Bcl6, similar to regulatory T cells (T_{reg}), where the function of TGF β -induced ROR γ t is suppressed by Foxp3 (13, 16). The combination of TGF β and IL-6 not only induces ROR γ t expression in T cells, but in the meantime, Foxp3 and Bcl6 expression is suppressed by IL-6 and TGF β signaling, respectively, allowing ROR γ t to function properly in promoting T_{H17} cell differentiation.

Although we proposed in the past year that T_{FH} cell differentiation mediated by IL-6 and IL-21 is a novel lineage of T_H cell differentiation, subsequently several groups reported that CXCR5⁺ T cells also express T_{H2} or T_{H17} cytokines in vivo (17, 18). Our current study

indicates that Bcl6 promotes the expression of T_{FH} -related genes but inhibits the differentiation of T_{H1} , T_{H2} , and T_{H17} cells. Our data thus support Bcl6-dependent T_{FH} cell generation as a pathway that is independent of other T_H cell lineages.

References and Notes

- C. G. Vinuesa, S. G. Tangye, B. Moser, C. R. Mackay, *Nat. Rev. Immunol.* **5**, 853 (2005).
- N. Fazilleau, L. Mark, L. J. McHeyzer-Williams, M. G. McHeyzer-Williams, *Immunity* **30**, 324 (2009).
- C. King, S. G. Tangye, C. R. Mackay, *Annu. Rev. Immunol.* **26**, 741 (2008).
- R. I. Nurieva *et al.*, *Immunity* **29**, 138 (2008).
- A. Vogelzang *et al.*, *Immunity* **29**, 127 (2008).
- A. L. Dent, A. L. Shaffer, X. Yu, D. Allman, L. M. Staudt, *Science* **276**, 589 (1997).
- M. B. Harris *et al.*, *Mol. Cell. Biol.* **19**, 7264 (1999).
- B. H. Ye *et al.*, *Nat. Genet.* **16**, 161 (1997).
- U. Klein, R. Dalla-Favera, *Nat. Rev. Immunol.* **8**, 22 (2008).
- Materials and methods are available as supporting material on Science Online.
- X. Masclé, O. Albagli, C. Lemerrier, *Biochem. Biophys. Res. Commun.* **300**, 391 (2003).
- X. O. Yang *et al.*, *Immunity* **28**, 29 (2008).
- X. O. Yang *et al.*, *Immunity* **29**, 44 (2008).
- B. H. Ye *et al.*, *Nat. Genet.* **16**, 161 (1997).
- I. I. Ivanov *et al.*, *Cell* **126**, 1121 (2006).
- L. Zhou *et al.*, *Nature* **453**, 236 (2008).
- A. T. Bauquet *et al.*, *Nat. Immunol.* **10**, 167 (2009).
- R. L. Reinhardt, H.-E. Liang, R. M. Locksley, *Nat. Immunol.* **10**, 385 (2009).
- We thank R. Dalla-Favera for the generous gift of Bcl6-deficient mice, K. Murphy for the retrovirus vector, and members of the Dong laboratory for their help. The work is supported by research grants from NIH (to C.D. and R.I.N.), M. D. Anderson Cancer Center, and Leukemia and Lymphoma Society (to C.D.). G.J.M. is a Schisler Foundation Fellow in cancer research. Y.C. is a recipient of a postdoctoral fellowship from the Korea Science and Engineering Foundation. R.N. is a recipient of a Scientist Development Grant from the American Heart Association, and C.D. is a Leukemia and Lymphoma Society Scholar and a Trust Fellow of the M. D. Anderson Cancer Center.

Supporting Online Material

www.sciencemag.org/cgi/content/full/1176676/DC1

Materials and Methods

Figs. S1 to S11

References

22 May 2009; accepted 15 July 2009

Published online 23 July 2009;

10.1126/science.1176676

Include this information when citing this paper.

Bcl6 and Blimp-1 Are Reciprocal and Antagonistic Regulators of T Follicular Helper Cell Differentiation

Robert J. Johnston,^{1,2*} Amanda C. Poholek,^{3*} Daniel DiToro,¹ Isharat Yusuf,¹ Danelle Eto,¹ Burton Barnett,¹ Alexander L. Dent,⁴ Joe Craft,^{5,6} Shane Crotty^{1,2†}

Effective B cell-mediated immunity and antibody responses often require help from CD4⁺ T cells. It is thought that a distinct CD4⁺ effector T cell subset, called T follicular helper cells (T_{FH}), provides this help; however, the molecular requirements for T_{FH} differentiation are unknown. We found that expression of the transcription factor Bcl6 in CD4⁺ T cells is both necessary and sufficient for in vivo T_{FH} differentiation and T cell help to B cells in mice. In contrast, the transcription factor Blimp-1, an antagonist of Bcl6, inhibits T_{FH} differentiation and help, thereby preventing B cell germinal center and antibody responses. These findings demonstrate that T_{FH} cells are required for proper B cell responses in vivo and that Bcl6 and Blimp-1 play central but opposing roles in T_{FH} differentiation.

Each lineage of effector CD4⁺ T cells (T_H1, T_H2, T_H17, and T_{reg}) is defined and controlled by a unique master regulator transcription factor (T-bet, GATA3, RORγt, and Foxp3, respectively) (1). A proposed fifth effector subset, T follicular helper (T_{FH}) cells, is thought to provide help for the generation of B cell-mediated immune responses, including class switch recombination, germinal center differentiation, and affinity maturation (2). Here, we identified Bcl6 as a T_{FH} master regulator and found that germinal center formation does not occur in the absence of T_{FH} cells.

T_{FH} cells are well described phenotypically in humans, and more recently in mice, as expressing high levels of the chemokine receptor CXCR5 and molecules such as ICOS, PD1, interleukin-21 (IL-21), and BTLA (2–9). Given that CD4⁺ T cells can up-regulate CXCR5 and/or ICOS after activation (2, 10), it is important to phenotypically distinguish T_{FH} from highly activated CD4⁺ T cells. We identified T_{FH} cells in mice in the context of acute infection with lymphocytic choriomeningitis virus (LCMV) by adoptively transferring T cell receptor (TCR) transgenic T cells specific for the LCMV epitope gp66-77 in the context of major histocompatibility complex (MHC) class II molecule I-A^b (SMtg). T_{FH} cells were CXCR5^{high} ICOS^{high} PD1^{high} BTLA^{high} CD200^{high} SLAMF6^{low} (Fig. 1, A and B, and fig. S1) and capable of producing IL-21 (Fig. 1C). We con-

firmed these results for polyclonal LCMV-specific CD4⁺ T cell responses (fig. S2). CXCR5 is the receptor for the B cell follicle chemokine CXCL13 (11), and T_{FH} cells were selectively able to migrate in response to CXCL13 in vitro (Fig. 1D), consistent with the importance of CXCR5 for T_{FH} (6, 12).

To understand how T_{FH} differentiation is transcriptionally regulated, we performed gene expression microarray analysis of virus-specific T_{FH} and non-T_{FH} effector CD4⁺ T cells (Fig. 1E and figs. S3 and S4). Notably, the transcription factor B cell CLL/lymphoma 6 (Bcl6) was strongly up-regulated in T_{FH} (Fig. 1E). This is in agreement with previous reports of elevated Bcl6 expression in murine and human T_{FH} cells (3–5, 8). Furthermore, Blimp-1 (*prdm1*) was the most down-regulated transcription factor in T_{FH} cells (fig. S4), consistent with a recent report (13). Bcl6 is essential for germinal center B cell differentiation (14–16), and Blimp-1 is well characterized as an antagonist of Bcl6 that can also be directly repressed by Bcl6 (16–20). Up-regulation of Bcl6 mRNA (Fig. 1F) and down-regulation of Blimp-1 mRNA (Fig. 1G) were confirmed by quantitative polymerase chain reaction (qPCR). Bcl6 protein expression was detected in germinal center CD4⁺ T cells (fig. S2), consistent with previous observations in human lymphoid tissue (4, 21).

Although Bcl6 mRNA expression has been correlated with T_{FH}, no experimental data supporting a specific role for Bcl6 in T_{FH} differentiation have been reported. We expressed Bcl6 in SMtg CD4⁺ T cells via a retroviral vector (RV) with a bicistronic mRNA coexpressing green fluorescent protein (GFP) (fig. S5). Transduced Bcl6-RV⁺ SMtg and control untransduced SMtg CD4⁺ T cells were transferred into naïve C57BL/6 hosts, which were subsequently infected with LCMV, and T_{FH} differentiation was examined (Fig. 2, A to E). Bcl6 expression drove nearly absolute T_{FH} differentiation in vivo (80 to 90%; Fig. 2, B and C), in contrast to T_{FH} differentiation in control untransduced (GFP[−]) SMtg cells in the same mice (Fig. 2B) or mice that received SMtg transduced

with a control retrovirus expressing only GFP (GFP-RV⁺) and untransduced SMtg in equal proportions (Fig. 2C). Comparably striking results were seen in studies where only Bcl6-RV⁺ or GFP-RV⁺ SMtg CD4⁺ T cells were transferred into host mice (fig. S6). Bcl6 overexpression did not affect T cell expansion in vivo (fig. S5). Constitutive expression of Bcl6 drove up-regulation of CXCR5, PD-1, ICOS, CD200, and BTLA expression (Fig. 2, D and E, and fig. S6), as well as the inhibition of SLAMF6 and Blimp-1 (fig. S6; see below). These results indicate that Bcl6 expression drives full T_{FH} differentiation in vivo.

T_{FH} differentiation is known to require the presence of B cells and is thought to require the presence of antigen-specific B cells (6). We thus hypothesized that Bcl6 expression induced by interaction with antigen-specific B cells could be the event that commits a T cell to T_{FH} differentiation. To test this, we examined whether Bcl6 expression in CD4⁺ T cells was sufficient to drive T_{FH} differentiation in μMT B cell-deficient mice and in B cell receptor (BCR) transgenic mice of an irrelevant specificity (MD4, specific for hen egg lysozyme). GFP-RV⁺ SMtg CD4⁺ T cells failed to differentiate into T_{FH} in μMT or MD4 mice infected with LCMV (Fig. 2, F and G), which demonstrates that T_{FH} differentiation in the context of a viral infection is dependent on the presence of antigen-specific B cells. In contrast, Bcl6-RV⁺ SMtg cells differentiated into T_{FH} in the absence of antigen-specific B cells or even in the total absence of B cells (Fig. 2, F and G). These results indicate that cognate T-B interactions induce Bcl6 expression in CD4⁺ T cells and that Bcl6 is sufficient to drive T_{FH} differentiation, even in the absence of such interactions.

T_{FH} cells are thought to provide B cell help in vivo (2, 22). We assessed the capacity of Bcl6-RV⁺ SMtg CD4⁺ T cells to help B cells in vivo by examining germinal center development in LCMV-infected mice. Overexpression of Bcl6 increased the already robust frequency of germinal center B cells after LCMV infection (Fig. 3, A and B). As an additional measure of B cell help, we also examined the role of Bcl6 in T cell-dependent antibody production. Constitutive expression of Bcl6 in OT-II CD4⁺ T cells enhanced NP-Ova serum immunoglobulin G (IgG) responses (Fig. 3C and fig. S7), which were sustained (Fig. 3C). Our results suggest that Bcl6 was specifically enhancing T_{FH} differentiation and not skewing the T_H1/T_H2 profile of the CD4⁺ T cells, because all IgG isotypes were enhanced in the mice receiving Bcl6-expressing OT-II CD4⁺ T cells, with the strong IgG1 dominance maintained (fig. S7).

The results of these experiments showed that Bcl6 expression was sufficient to drive the differentiation of functional T_{FH}. To test whether Bcl6 was also necessary for T_{FH} differentiation, we examined *Bcl6*^{−/−} CD4⁺ T cells. *Bcl6*^{−/−} mice have an abundance of highly activated CD4⁺ T cells (fig. S8) and succumb to early mortality (14, 15). To circumvent these issues, we transferred *Bcl6*^{+/+} or *Bcl6*^{−/−} OT-II bone marrow into

¹Division of Vaccine Discovery, La Jolla Institute for Allergy and Immunology (LIAI), 9420 Athena Circle, La Jolla, CA 92037, USA. ²Department of Medicine, University of California, San Diego School of Medicine, La Jolla, CA 92037, USA. ³Department of Cell Biology, Yale University School of Medicine, New Haven, CT 06520, USA. ⁴Department of Microbiology and Immunology and Walther Oncology Center, Indiana University School of Medicine, Indianapolis, IN 46202, USA. ⁵Department of Immunobiology, Yale University School of Medicine, New Haven, CT 06520, USA. ⁶Section of Rheumatology, Department of Internal Medicine, Yale School of Medicine, New Haven, CT 06520, USA.

*These authors contributed equally to this work.

†To whom correspondence should be addressed. E-mail: shane@liai.org

Fig. 1. Bcl6 is a T_{FH} -specific transcription factor. Naïve SMtg $CD4^+$ T cells were transferred into B6 mice. In all panels, splenocytes were analyzed 8 days after infection with LCMV. (A and B) SMtg expression of CXCR5 and PD-1 (A) or SLAM (CD150) (B). SMtg $^+$ ($CD45.1^+$) $CD4^+$ gated cells are shown. CXCR5 high T_{FH} cells are boxed in fluorescence-activated cell sorter (FACS) plots. Histogram overlays depict T_{FH} cells (red) as well as naïve $CD4^+$ T cells (gray) and CXCR5 low non- T_{FH} SMtg cells (black). Data are representative of more than 10 independent experiments. (C) IL-21 mRNA in SMtg $CD4^+$ T cells, normalized to the β -actin mRNA level ($\times 10^{-4}$). $^{**}P = 0.008$. (D) In vitro chemotaxis toward CXCL13 (BLC) by ex vivo SMtg $CD4^+$ T cells. Results are expressed as percentages of SLAM low T_{FH} SMtg (solid circles) and SLAM high non- T_{FH} SMtg (open circles) that migrated in a transwell assay. $^{***}P \leq 0.001$. 1 μ g, $P = 0.001$; 2 μ g, $P = 0.0006$; 4 μ g, $P = 0.0006$. Data are representative of three independent experiments; $n = 2$ per group. (E) Scatterplot of the average signal of biological replicates of T_{FH} versus non- T_{FH} SMtg gene expression microarray data. Blue lines indicate changes in gene expression by a factor of 3; 386 gene probes exhibited a factor of >3.0 increase in T_{FH} . Data from one of two independent experiments are shown; $n = 2$ per group. (F and G) Quantitative reverse transcription PCR of Bcl6 (F) and Blimp-1 (G) mRNA expression, normalized to β -actin ($\times 10^{-4}$). $^{***}P < 0.0001$. Data are representative of four independent experiments; $n = 2$ per group. Error bars in all graphs are SEM.

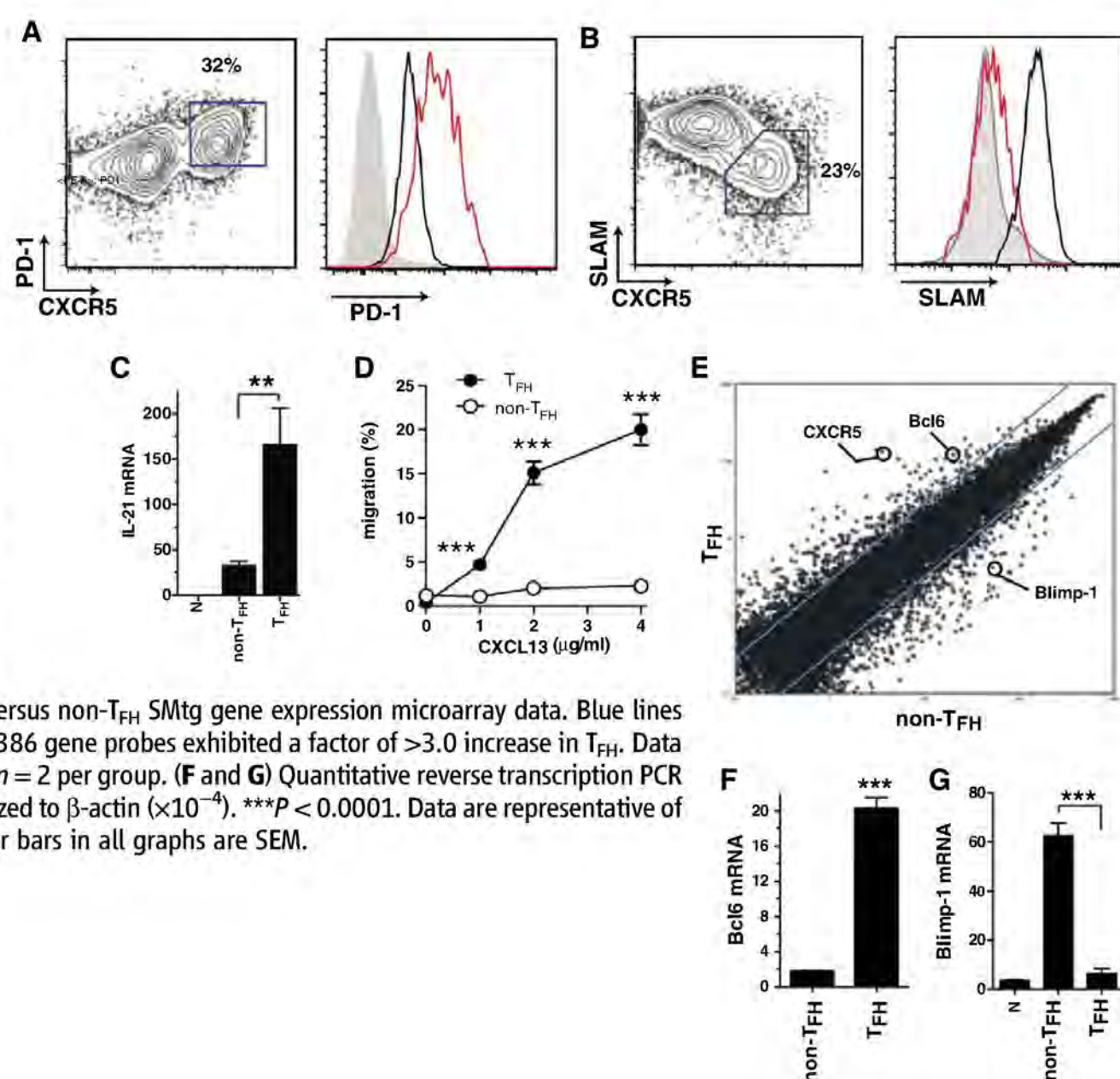
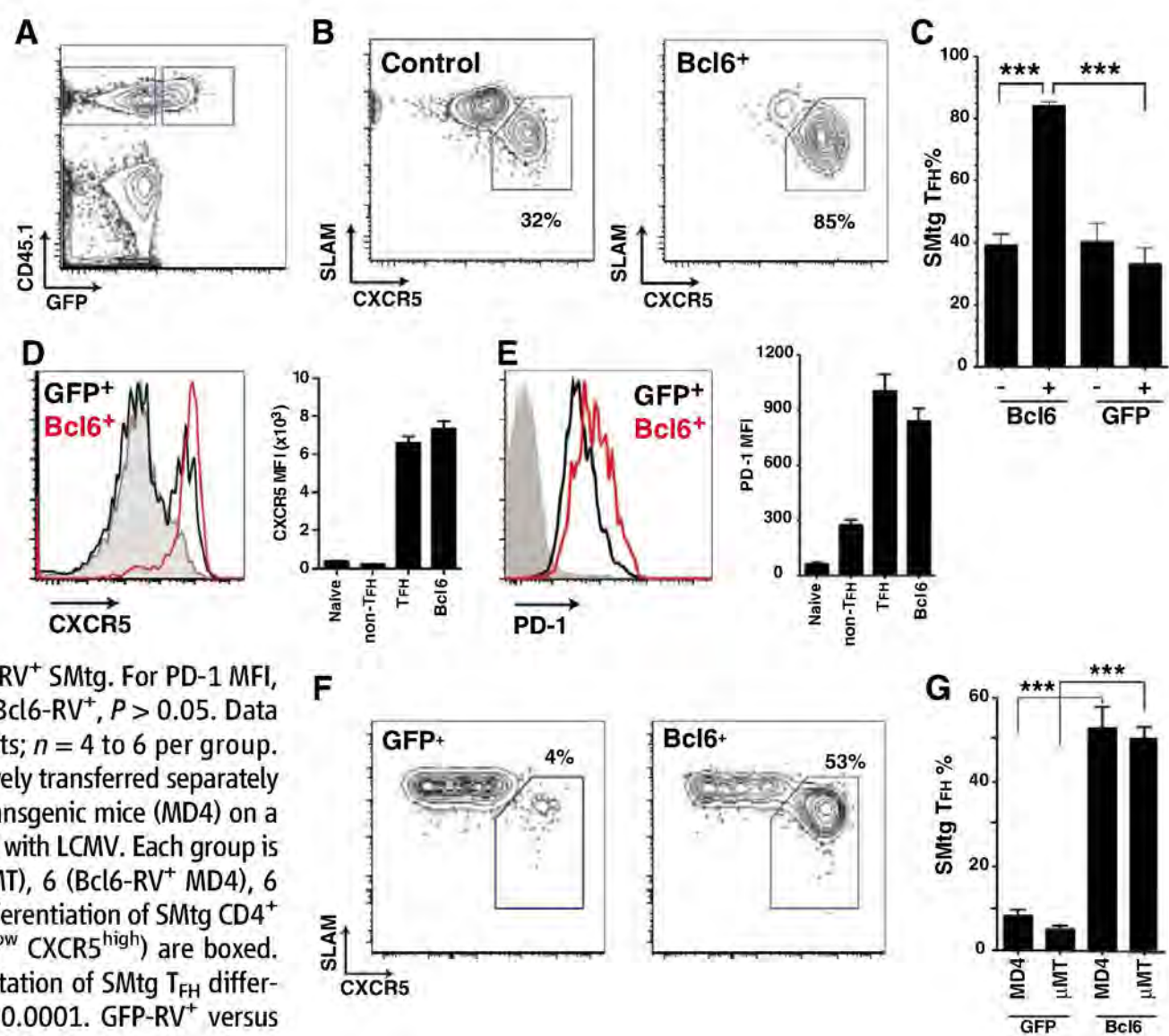


Fig. 2. Bcl6 expression is sufficient for T_{FH} differentiation in vivo. (A to E) Naïve SMtg $CD4^+$ T cells were transduced with Bcl6-RV (Bcl6 $^+$) or left untransduced (control) and transferred into B6 mice subsequently infected with LCMV. (A) Gating of $CD45.1^+$ untransduced SMtg (GFP $^+$) and Bcl6-RV $^+$ SMtg (GFP $^+$) in the same host. $CD4^+$ B220 $^-$ gate is shown. (B) T_{FH} (SLAM low CXCR5 high , boxed) and non- T_{FH} (SLAM high CXCR5 low) differentiation of untransduced SMtg (left) and Bcl6-RV $^+$ SMtg (right). (C) Quantitation of SMtg T_{FH} differentiation. Mice received Bcl6-RV $^+$ SMtg and untransduced SMtg, or GFP-RV $^+$ and untransduced SMtg. “–,” untransduced; “+,” transduced with indicated RV. $^{***}P < 0.0001$. Data are representative of three independent experiments; $n = 4$ per group. (D and E) CXCR5 expression (D) and PD-1 expression (E) on naïve $CD4^+$ T cells (gray), GFP-RV $^+$ SMtg (black), and Bcl6-RV $^+$ SMtg (red). Bar graphs show mean fluorescence intensity (MFI) of naïve $CD4^+$ T cells, GFP-RV $^+$ SMtg non- T_{FH} , GFP-RV $^+$ SMtg T_{FH} , and Bcl6-RV $^+$ SMtg. For PD-1 MFI, non- T_{FH} versus T_{FH} or Bcl6-RV $^+$, $P < 0.05$; T_{FH} versus Bcl6-RV $^+$, $P > 0.05$. Data are representative of three independent experiments; $n = 4$ to 6 per group. (F and G) GFP-RV $^+$ or Bcl6-RV $^+$ SMtg cells were adoptively transferred separately into B cell-deficient mice (μ MT) or HEL-specific BCR transgenic mice (MD4) on a μ MT background. Host mice were subsequently infected with LCMV. Each group is a composite of three experiments; $n = 2$ (GFP-RV $^+$ μ MT), 6 (Bcl6-RV $^+$ MD4), 6 (Bcl6-RV $^+$ μ MT), or 8 (GFP-RV $^+$ MD4) per group. (F) Differentiation of SMtg $CD4^+$ T cells in MD4 BCR transgenic mice. T_{FH} cells (SLAM low CXCR5 high) are boxed. $CD4^+$ B220 $^-$ $CD45.1^+$ GFP $^+$ gate is shown. (G) Quantitation of SMtg T_{FH} differentiation. GFP-RV $^+$ versus Bcl6-RV $^+$ in MD4, $^{***}P < 0.0001$. GFP-RV $^+$ versus Bcl6-RV $^+$ in μ MT, $^{***}P < 0.0001$.

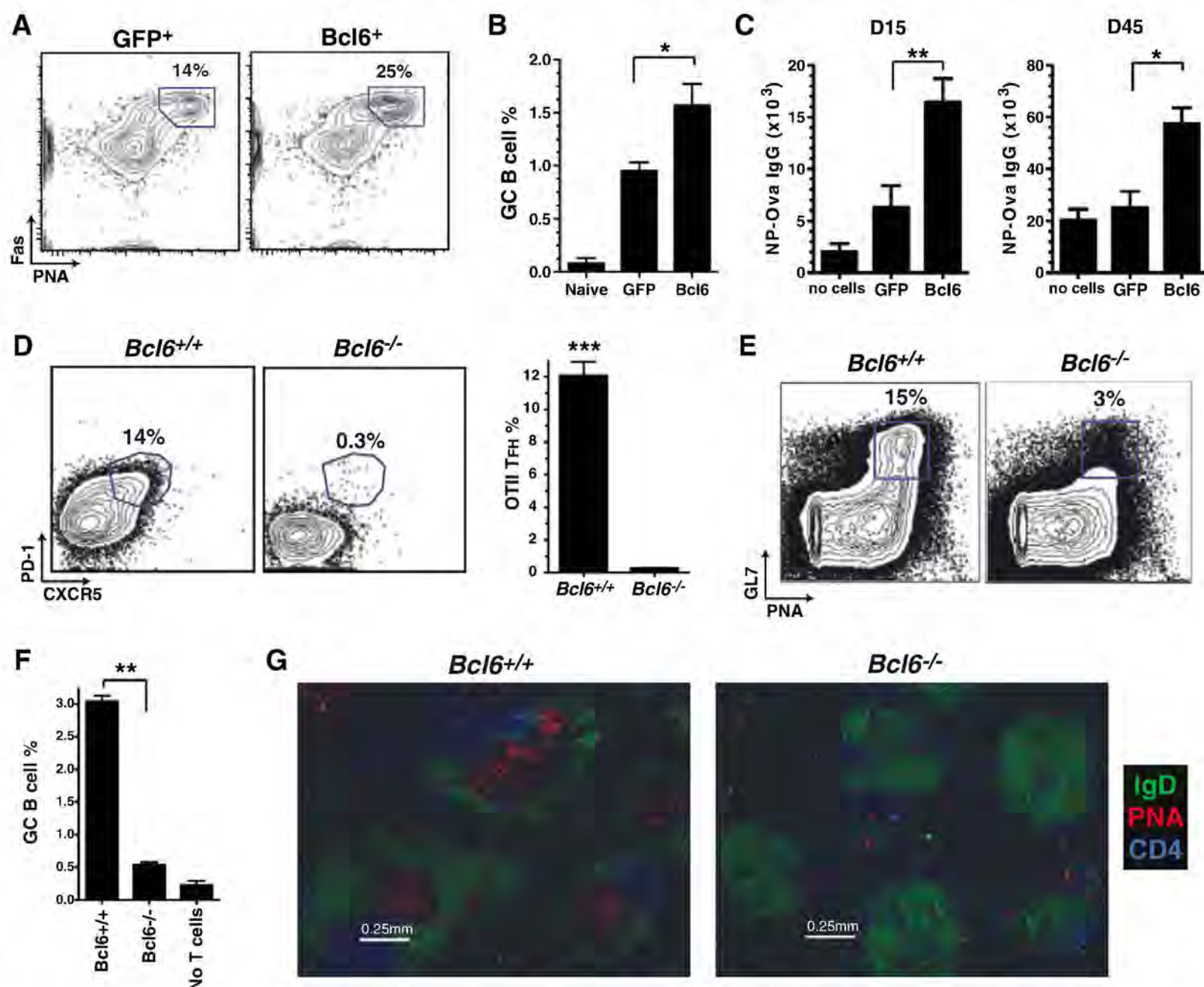


irradiated C57BL/6 recipients (fig. S8). *Bcl6*^{-/-} OT-II CD4⁺ T cells obtained from chimeric mice did not exhibit lymphoproliferation or spontaneous activation upon transfer into C57BL/6 mice (fig. S8, D to F). *Bcl6*^{-/-} or *Bcl6*^{+/-} OT-II recipient mice were subsequently immunized with Ova in alum. Strikingly, *Bcl6*^{-/-} OT-II CD4⁺ T cells did not differentiate into T_{FH} cells (Fig. 3D). We hypothesized that if T_{FH} cells are necessary for B cell help in vivo, a cell-intrinsic CD4⁺ T cell block in T_{FH} differentiation should result in a failure to generate antigen-specific B cell responses such as germinal center formation. To test this hypothesis, we transferred *Bcl6*^{-/-} or *Bcl6*^{+/-} OT-II CD4⁺ T cells into *Icos*^{-/-} mice, which have ineffective B cell help (2, 23). After NP-Ova immunization, *Icos*^{-/-} mice that received *Bcl6*^{-/-} OT-II CD4⁺ T cells were unable to form germinal centers, in contrast to mice that received wild-type OT-II CD4⁺ T cells (Fig. 3, E to G, and fig. S9). These data demonstrate that Bcl6 is necessary for T_{FH} differentiation and that T_{FH} cells are necessary for germinal center formation. Together, these results indicate that Bcl6 is a bona fide master regulator of T_{FH} differentiation in vivo.

Blimp-1 is a known antagonist of Bcl6, capable of directly inhibiting Bcl6 expression in B and T cells (17, 18). Conversely, Blimp-1 expression can be inhibited by Bcl6 (16–18, 20). On the basis of our observations that Bcl6 drives T_{FH} cell differentiation and function, and because Blimp-1 was the single most down-regulated transcription factor in T_{FH} cells by gene expression array analysis (Fig. 1E and fig. S4) and qPCR (Fig. 1G), we hypothesized a role for Blimp-1 in blocking T_{FH} differentiation in vivo. We constructed a Blimp-1 retroviral expression vector, Blimp1-RV (fig. S5), designed to express physiological levels of Blimp-1. Only CD4⁺ T cells expressing low levels of the GFP reporter were used for in vivo experiments (fig. S10A). Blimp-1 blocked Bcl6 protein expression in activated antigen-specific CD4⁺ T cells in vivo (Fig. 4A). To determine the effects of Blimp-1 on T_{FH} differentiation, we mixed Blimp1-RV⁺ SMtg CD4⁺ T cells and untransduced control SMtg cells in equal proportions and transferred them into host mice subsequently infected with LCMV. We observed normal proliferation of Blimp-1-expressing SMtg CD4⁺ T cells (fig. S10); however, T_{FH} differentiation was severely abrogated, with an 80%

reduction in T_{FH} frequency (Fig. 4, B and C). Blockade of T_{FH} differentiation by Blimp-1 was also observed when mice separately received Blimp1-RV⁺ versus GFP-RV⁺ SMtg cells (fig. S10, F and G). Constitutive expression of Blimp-1 inhibited acquisition of the T_{FH} phenotype: SLAM expression was increased (Fig. 4D), whereas CXCR5, ICOS, and PD-1 expression were all decreased (Fig. 4D and fig. S10). Inhibition of T_{FH} differentiation by Blimp-1 was physiological and specific, because the expression levels of SLAM, ICOS, and PD-1 by Blimp1-RV⁺ SMtg CD4⁺ T cells were equivalent to the expression levels seen in wild-type activated non-T_{FH} SMtg CD4⁺ T cells, and not naïve cells (fig. S10I). Blimp1-RV⁺ and wild-type non-T_{FH} SMtg cells also expressed comparable amounts of the cytokines interferon-γ (IFN-γ) and IL-2 (fig. S11). High amounts of Blimp-1 expression can inhibit proliferation in B and T cells (17, 24, 25). The moderate level of Blimp-1 expression used in our experiments (fig. S10E) did not affect proliferation in vivo (fig. S10, C, D, and H), in agreement with previous in vitro studies (26) and our observation that non-T_{FH} CD4⁺ T cells express 20 times as much Blimp-1 as do T_{FH} cells

Fig. 3. Bcl6 expression is necessary for inducing T_{FH} B cell help in vivo. (A) Germinal center B cells (PNA⁺ Fas⁺, gated) in mice that received GFP-RV⁺ or Bcl6-RV⁺ SMtg CD4⁺ T cells and were subsequently infected with LCMV, analyzed at day 8 and gated on activated B cells (B220⁺ IgD^{low}). (B) Frequency of germinal center B cells of total splenocytes; *n* = 4 per group. Data are representative of three independent experiments. **P* = 0.029. (C) GFP-RV⁺ or Bcl6-RV⁺ OT-II CD4⁺ T cells were transferred into B6 mice subsequently immunized with NP-Ova in alum. Control mice were immunized but received no OT-II cells. NP-Ova enzyme-linked immunosorbent assay (ELISA) was performed at day 15 and day 45; *n* = 6 per group. Data are representative of two independent experiments. Day 15 endpoint ELISA titers, ***P* = 0.008; day 45 endpoint ELISA titers, **P* = 0.017. (D) *Bcl6*^{+/-} or *Bcl6*^{-/-} OT-II CD4⁺ T cells were transferred into congenically mismatched B6 mice subsequently immunized with Ova in alum. Splenocytes were analyzed 6 days after immunization; *n* = 4 per group. Data are representative of four independent experiments. OT-II⁺ CD44^{high} gate is shown. Quantitation of OT-II T_{FH} differentiation is also shown. ****P* < 0.0001. (E to G) *Bcl6*^{+/-} or *Bcl6*^{-/-} OT-II CD4⁺ T cells were cotransferred with B1-8 B cells into *Icos*^{-/-} mice sub-



sequently immunized with NP-Ova in alum; *n* = 2 per group. Data are representative of two independent experiments. (E) Germinal center B cells (PNA⁺ GL7⁺, boxed) 7 days after immunization. TCRβ⁻ IgD^{low} gate is shown. (F) Quantitation of GC B cells as percent of spleen. ***P* = 0.0015. (G) Germinal center histology. Spleen sections were stained with IgD (green), PNA (red), and CD4 (blue).

and are still proliferative. Blimp-1 expression did not affect expression of the T helper lineage-specific transcription factors Foxp3, GATA3, and ROR γ t (fig. S11), which indicates that Blimp-1 did not induce differentiation into other helper lineages. Collectively, these data suggest that Blimp-1 acts specifically to repress Bcl6 and thus blocks T_{FH} differentiation.

Given that Blimp-1 is a physiological inhibitor of Bcl6 expression and T_{FH} differentiation in vivo, we performed an additional test of the necessity of T_{FH} for B cell help by transferring Blimp1-RV⁺ OT-II and GFP-RV⁺ OT-II CD4⁺ T cells into SAP-deficient (*sh2d1a*^{-/-}) mice [SAP-deficient mice exhibit a CD4⁺ T cell-intrinsic defect in germinal center formation (27–29)] subsequently immunized with NP-Ova. We observed germinal centers and anti-NP-Ova serum IgG in GFP-RV⁺ OT-II CD4⁺ T cell recipient mice after immunization (Fig. 4, E and F). Strikingly, although OT-II cell numbers were normal in Blimp1-RV⁺ OT-II recipient mice (fig. S12), germinal centers were reduced by 90% (Fig. 4E). Constitutive Blimp-1 expression also inhibited the NP-Ova-specific IgG response, reducing the serum antibody concentration to only 16% of normal levels (Fig. 4F). All IgG isotypes were reduced (fig. S12), confirming that Blimp-1 was

specifically inhibiting T_{FH} differentiation. These results demonstrate both that Blimp-1 inhibits CD4⁺ T cell help to B cells and that T_{FH} cells are required for B cell help in vivo.

To confirm the biological role of Blimp-1 in inhibiting T_{FH} differentiation in vivo, we tested the ability of Blimp-1-deficient CD4⁺ T cells to differentiate into T_{FH}. To avoid autoimmunity complications (30, 31), we deleted Blimp-1 (*prdm1*) in vitro in mature *prdm1*^{fl/fl} CD4⁺ T cells (32) by means of a Cre-expressing RV. We transferred Cre⁺ SMtg⁺ *prdm1*^{fl/fl} and control Cre⁻ SMtg⁺ *prdm1*^{fl/fl} CD4⁺ T cells into mice subsequently infected with LCMV. Deletion of *prdm1* substantially enhanced T_{FH} differentiation in vivo (Fig. 4G) without altering proliferation (fig. S13). These data indicate that Blimp-1 expression in vivo normally restricts Bcl6 expression and T_{FH} differentiation. In sum, our results reveal that Bcl6 and Blimp-1 are reciprocal master regulators of T_{FH} differentiation, with T_{FH} differentiation in vivo requiring the presence of Bcl6 and the absence of Blimp-1.

There has been extensive speculation about a role for Bcl6 in T_{FH} differentiation, based on gene expression data from human (2, 4) and murine T_{FH} studies (3, 8, 9, 13). Our data directly show that Bcl6 specifically drives T_{FH} differen-

tiation and is a bona fide master regulator. The relationship between T_{FH} and other CD4⁺ T cell lineages has been a long-standing problem. The predominant CD4⁺ T cell response to LCMV is T_H1 (fig. S14), and it is notable that T-bet and IFN- γ were still expressed in the T_{FH} in vivo, although at lower levels than in T_H1/non-T_{FH} LCMV-specific CD4⁺ T cells (fig. S14). These observations are consistent with a model in which T_{FH} cells follow their own differentiation pathway but are not an isolated lineage and can exhibit partial characteristics of T_H1/T_H2 polarization depending on environmental conditions. This overlapping differentiation model would resolve the conundrum in the literature that neither T_H1, T_H2, nor T_H17 are required for B cell help in vivo (8, 33, 34), but that cells with T_H1, T_H2, or T_H17 phenotypes can provide B cell help in vivo (9, 35–39).

The capacity for B cell help is a central attribute of CD4⁺ T cells and is a cornerstone of protective immunity. It is well known that in B cells, Bcl6 and Blimp-1 are powerful antagonistic master regulators of germinal center B cell differentiation and plasma cell differentiation. Our findings that Bcl6 and Blimp-1 also control T_{FH} differentiation illustrate the elegant use of the same antagonistic transcription factors to drive

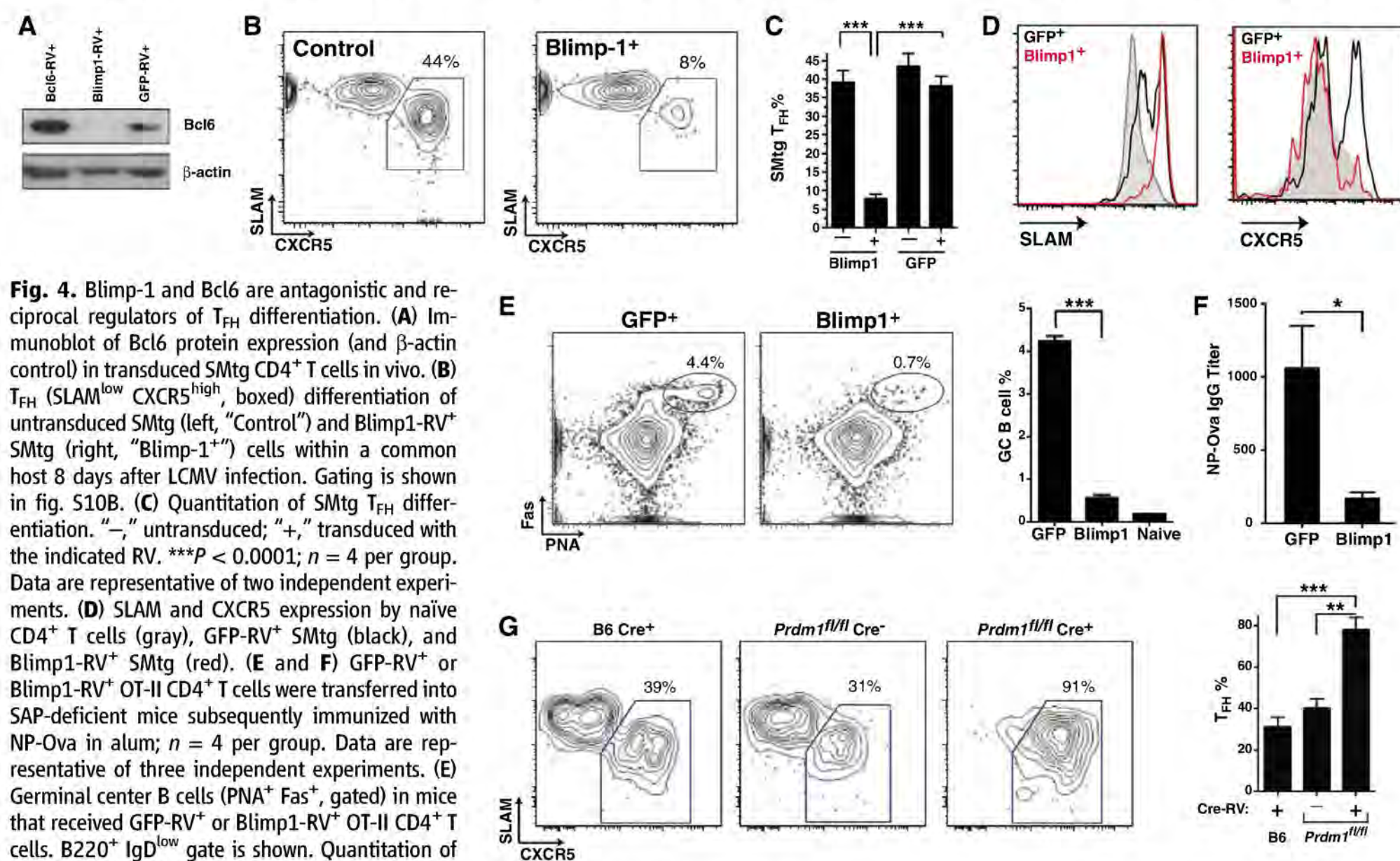


Fig. 4. Blimp-1 and Bcl6 are antagonistic and reciprocal regulators of T_{FH} differentiation. (A) Immunoblot of Bcl6 protein expression (and β -actin control) in transduced SMtg CD4⁺ T cells in vivo. (B) T_{FH} (SLAM^{low} CXCR5^{high}, boxed) differentiation of untransduced SMtg (left, "Control") and Blimp1-RV⁺ SMtg (right, "Blimp-1⁺") cells within a common host 8 days after LCMV infection. Gating is shown in fig. S10B. (C) Quantitation of SMtg T_{FH} differentiation. "–," untransduced; "+," transduced with the indicated RV. ****P* < 0.0001; *n* = 4 per group. Data are representative of two independent experiments. (D) SLAM and CXCR5 expression by naïve CD4⁺ T cells (gray), GFP-RV⁺ SMtg (black), and Blimp1-RV⁺ SMtg (red). (E and F) GFP-RV⁺ or Blimp1-RV⁺ OT-II CD4⁺ T cells were transferred into SAP-deficient mice subsequently immunized with NP-Ova in alum; *n* = 4 per group. Data are representative of three independent experiments. (E) Germinal center B cells (PNA⁺ Fas⁺, gated) in mice that received GFP-RV⁺ or Blimp1-RV⁺ OT-II CD4⁺ T cells. B220⁺ IgD^{low} gate is shown. Quantitation of germinal center B cells in the spleen is also shown. ****P* < 0.0001. (F) NP-Ova IgG ELISA endpoint titers at day 10. **P* = 0.016. (G) Purified naïve B6 and *prdm1*^{fl/fl} CD45.2⁺ CD4⁺ T cells were transduced with SMtg-RV, with or without Cre-RV (Cre⁺ or Cre⁻), sorted, and transferred into CD45.1⁺ mice subsequently infected with LCMV. FACS plots depict T_{FH} (CXCR5^{high} SLAM^{low}, boxed) differentiation of control Cre⁺ SMtg⁺ B6 cells

(left), Blimp-1-sufficient Cre⁻ SMtg⁺ *prdm1*^{fl/fl} cells (center), and Blimp-1-deficient Cre⁺ SMtg⁺ *prdm1*^{fl/fl} cells (right). CD4⁺ CD45.1⁻ CD44^{high} 7AAD⁻ gate is shown. Quantitation of T_{FH} differentiation is also shown. Data are representative of two independent experiments. ***P* = 0.002, ****P* = 0.0006; *n* = 4 to 5 per group.

different functions in two lymphocyte populations differentiating in parallel: antigen-specific B cells and the T_{FH} cells that provide their help. Manipulation of these signaling pathways in vivo may have substantial therapeutic benefit for enhancing vaccines or, conversely, blocking auto-antibody responses.

References and Notes

1. J. Zhu, W. E. Paul, *Blood* **112**, 1557 (2008).
2. C. King, S. Tangye, C. Mackay, *Annu. Rev. Immunol.* **26**, 741 (2008).
3. C. G. Vinuesa *et al.*, *Nature* **435**, 452 (2005).
4. T. Chtanova *et al.*, *J. Immunol.* **173**, 68 (2004).
5. A. U. Rasheed, H. P. Rahn, F. Sallusto, M. Lipp, G. Müller, *Eur. J. Immunol.* **36**, 1892 (2006).
6. N. M. Haynes *et al.*, *J. Immunol.* **179**, 5099 (2007).
7. A. Vogelzang *et al.*, *Immunity* **29**, 127 (2008).
8. R. I. Nurieva *et al.*, *Immunity* **29**, 138 (2008).
9. R. L. Reinhardt, H. E. Liang, R. M. Locksley, *Nat. Immunol.* **10**, 385 (2009).
10. K. M. Ansel, L. J. McHeyzer-Williams, V. N. Ngo, M. G. McHeyzer-Williams, J. G. Cyster, *J. Exp. Med.* **190**, 1123 (1999).
11. K. M. Ansel *et al.*, *Nature* **406**, 309 (2000).
12. S. Hardtke, L. Ohl, R. Förster, *Blood* **106**, 1924 (2005).
13. N. Fazilleau, L. J. McHeyzer-Williams, H. Rosen, M. G. McHeyzer-Williams, *Nat. Immunol.* **10**, 375 (2009).
14. B. H. Ye *et al.*, *Nat. Genet.* **16**, 161 (1997).
15. A. L. Dent, A. L. Shaffer, X. Yu, D. Allman, L. M. Staudt, *Science* **276**, 589 (1997).
16. U. Klein, R. Dalla-Favera, *Nat. Rev. Immunol.* **8**, 22 (2008).
17. G. Martins, K. Calame, *Annu. Rev. Immunol.* **26**, 133 (2008).
18. L. Cimmino *et al.*, *J. Immunol.* **181**, 2338 (2008).
19. A. L. Shaffer *et al.*, *Immunity* **17**, 51 (2002).
20. A. L. Shaffer *et al.*, *Immunity* **13**, 199 (2000).
21. G. Cattoretti *et al.*, *Blood* **86**, 45 (1995).
22. C. G. Vinuesa, S. Tangye, B. Moser, C. Mackay, *Nat. Rev. Immunol.* **5**, 853 (2005).
23. H. Akiba *et al.*, *J. Immunol.* **175**, 2340 (2005).
24. R. Reljic, S. D. Wagner, L. J. Peakman, D. T. Fearon, *J. Exp. Med.* **192**, 1841 (2000).
25. G. A. Martins, L. Cimmino, J. Liao, E. Magnusdottir, K. Calame, *J. Exp. Med.* **205**, 1959 (2008).
26. D. Gong, T. R. Malek, *J. Immunol.* **178**, 242 (2007).
27. S. Crotty, E. N. Kersh, J. Cannons, P. L. Schwartzberg, R. Ahmed, *Nature* **421**, 282 (2003).
28. C. S. Ma, K. E. Nichols, S. Tangye, *Annu. Rev. Immunol.* **25**, 337 (2007).
29. P. L. Schwartzberg, K. L. Mueller, H. Qi, J. L. Cannons, *Nat. Rev. Immunol.* **9**, 39 (2009).
30. A. Kallies *et al.*, *Nat. Immunol.* **7**, 466 (2006).
31. G. A. Martins *et al.*, *Nat. Immunol.* **7**, 457 (2006).
32. M. Shapiro-Shelef *et al.*, *Immunity* **19**, 607 (2003).
33. V. K. Tsiagbe, G. J. Thorbecke, in *The Biology of Germinal Centers*, G. J. Thorbecke, V. K. Tsiagbe, Eds. (Springer-Verlag, Berlin, 1998), pp. 1–103.
34. M. Kopf, G. Le Gros, A. J. Coyle, M. Kosco-Vilbois, F. Brombacher, *Immunol. Rev.* **148**, 45 (1995).
35. I. L. King, M. Mohrs, *J. Exp. Med.* **206**, 1001 (2009).
36. A. G. Zaretsky *et al.*, *J. Exp. Med.* **206**, 991 (2009).
37. H. C. Hsu *et al.*, *Nat. Immunol.* **9**, 166 (2008).
38. K. M. Smith, J. M. Brewer, C. M. Rush, J. Riley, P. Garside, *J. Immunol.* **173**, 1640 (2004).
39. K. M. Smith *et al.*, *J. Immunol.* **165**, 3136 (2000).
40. We thank R. Kageyama, L. Crickard, K. Hansen, C. Kim, and K. Van Gunst for technical assistance; S. Kaech for helpful discussions; A. Haberman and S. Kerfoot for technical help; and the NIH Tetramer Core for providing MHC class II tetramer reagents. Supported by LIAI institutional funds, a Pew Scholar Award, a Cancer Research Institute Award, and National Institute of Allergy and Infectious Diseases grants R01 072543 and NIAID R01 063107 (S.C.); Rheuminations Inc., the Arthritis Foundation, the Connecticut Chapter of the Lupus Foundation of America, and NIH grants AR40072, AR44076, and P30 AR053495 (J.C.); and fellowships from the UCSD/LIAI Immunology NIH Training Grant (I.Y. and R.J.J.). R.J.J. is a member of the UCSD Biomedical Sciences (BMS) graduate program. Microarray data have been deposited at the NCBI Gene Expression Omnibus (GSE16697). Author contributions are as follows: LCMV T_{FH} identification and microarrays, I.Y. and S.C.; Bcl6-RV and Blimp1-RV experiments, R.J.J., D.D., B.B.; T_{FH} migration, D.E.; Blimp-1 conditional knockout experiments, D.D.; Bcl6^{-/-} mice, A.L.D.; Bcl6^{-/-} experiments, A.C.P.; writing, S.C. (with intellectual and editorial contributions from the other authors); project conception and experimental design, S.C. and J.C.

Supporting Online Material

www.sciencemag.org/cgi/content/full/1175870/DC1

Methods

Table S1

Figs. S1 to S14

References

5 May 2009; accepted 2 July 2009

Published online 16 July 2009;

10.1126/science.1175870

Include this information when citing this paper.

Structure and Mechanism of a Na⁺-Independent Amino Acid Transporter

Paul L. Shaffer,¹ April Goehring,¹ Aruna Shankaranarayanan,¹ Eric Gouaux^{1,2}

Amino acid, polyamine, and organocation (APC) transporters are secondary transporters that play essential roles in nutrient uptake, neurotransmitter recycling, ionic homeostasis, and regulation of cell volume. Here, we present the crystal structure of apo-ApcT, a proton-coupled broad-specificity amino acid transporter, at 2.35 angstrom resolution. The structure contains 12 transmembrane helices, with the first 10 consisting of an inverted structural repeat of 5 transmembrane helices like the leucine transporter LeuT. The ApcT structure reveals an inward-facing, apo state and an amine moiety of lysine-158 located in a position equivalent to the sodium ion site Na2 of LeuT. We propose that lysine-158 is central to proton-coupled transport and that the amine group serves the same functional role as the Na2 ion in LeuT, thus demonstrating common principles among proton- and sodium-coupled transporters.

Amino acid, polyamine, and organocation (APC) transporters are members of a large family of secondary transport proteins that catalyze the uniport, symport, and antiport of a broad range of substrates across the membrane bilayer (1). Present throughout the kingdom of life, APC transporters are integral

to cellular physiology and in humans include multiple solute carrier (SLC) families (Fig. 1A and table S1) (2). Canonical APC transporters include the SLC7 glutamate/cystine antiporter (xCT), a sodium-independent antiporter that exchanges extracellular cystine for intracellular glutamate (3, 4). Cationic amino acid transporters (CATs) are also members of the SLC7 family, and they supply arginine for nitric oxide synthesis, a major contributor to asthma pathogenesis (5). In cancer, the APC L-type amino acid transporter 1 provides amino acids required for tumor growth, is up-regulated in tumor cells (6), and mediates the uptake of melphalin, a chemotherapy drug (7). Both cystinuria, the most com-

mon primary inherited aminoaciduria, and lysinuric protein intolerance are the consequence of mutations in SLC7 genes (8–10).

The SLC12 family cation chloride cotransporters (CCCs) are subsumed under the APC mantle, are targets for several classes of therapeutic diuretics, and are involved in active Cl⁻ absorption in the kidney, blood pressure maintenance, and cell volume homeostasis (11); in the central nervous system, these transporters play an essential role in setting the resting chloride concentration and in γ -amino butyric acid (GABA)- and glycine-mediated neurotransmission (12). Other APC transporters participate in manifold biochemical processes in the nervous system, including the packaging of inhibitory neurotransmitters into synaptic vesicles (13) and the sodium- or proton-dependent symport of glutamine, a crucial step in the recycling of glutamate and GABA (14). In epithelial cells, SLC36 transporters drive the absorption of amino acids at the apical membrane of intestinal epithelial cells through coupling to a proton gradient (15). Remarkably, some APC transporters serve as “transceptors,” transporter-substrate complexes that transduce signals to the inside of the cell in a receptor-like fashion (16).

To deepen our understanding of APC transporters as a whole and to understand the molecular commonalities and distinctions between proton-coupled and sodium-coupled transporters, we have studied the atomic structure and mechanism of a proton-dependent APC transporter. We initiated this effort by precrystallization screen-

¹Vollum Institute, Oregon Health and Science University, 3181 Southwest Sam Jackson Park Road, Portland, OR 97239, USA. ²Howard Hughes Medical Institute, Oregon Health and Science University, 3181 Southwest Sam Jackson Park Road, Portland, OR 97239, USA.

*To whom correspondence should be addressed. E-mail: gouauxe@ohsu.edu

ing of bacterial orthologs of the glutamate/cysteine antiporter by fluorescence detection, size exclusion chromatography (FSEC) (17). Analysis of several thermophilic orthologs revealed that a 435 amino acid integral membrane protein from *Methanocaldococcus jannaschii* (ApcT; GI:1591319) (Fig. 1A) possessed a sharp symmetrical elution profile, both alone and in complex with an anti-ApcT Fab fragment (fig. S1), and was thus a promising APC transporter for studies of function and structure.

We discovered the function of ApcT by examining the uptake of four ^3H -labeled amino acids—L-Ser, L-Gln, L-Ala, and Gly—using purified ApcT reconstituted into lipid vesicles. Several APC transporters are exchangers that are active over a range of pH values (3, 18, 19); thus, we loaded vesicles with cold substrate and explored various internal and external proton

concentrations. At low external pH, transport of L- ^3H -Ser, L- ^3H -Gln, L- ^3H -Ala, and ^3H -Gly is robust; at neutral pH, however, transport is negligible (fig. S2). Because ApcT efficiently transports ^3H -Ala (fig. S3), we chose alanine for further experiments. Substrate uptake does not require internal Ala, although uptake activity is trans-stimulated by a factor of about 3 in the presence of internal substrate (fig. S4). A time course of ^3H -Ala uptake under conditions of a proton gradient and in the absence of internal Ala is demonstrated (Fig. 1B). Ala exchange is dependent on acidic pH values (fig. S5), yet uptake does not require sodium or a sodium gradient (fig. S6). Inclusion of proton and potassium ionophores, which collapse the pH gradient, dramatically diminish transport activity to approximately the level measured in the absence of a proton gradient (Fig. 1C and fig. S7).

To probe the substrate specificity of ApcT, we employed the canonical 20 L-amino acids, D-Ala, β -Ala, and GABA as cold competitive inhibitors in a ^3H -Ala uptake assay. Uptake of ^3H -Ala is inhibited by almost all L-amino acids except Lys, Arg, and Pro (fig. S8). Transport is stereo-specific, as D-Ala does not effectively compete for L-Ala transport. β -Ala does inhibit transport, demonstrating that an α -amino group is not required for inhibition. On the basis of the cold competition experiment, we selected a subset of amino acids to test as bona fide substrates, finding that ApcT transports a range of amino acids (L-Glu, L-Ala, >L-Ser, L-Gln, and >L-Phe) but transports the smallest (Gly) or largest (Trp) amino acids very slowly, if at all (Fig. 1D). Taken together, our data demonstrate that ApcT is a sodium-independent, broad-specificity amino acid transporter active at acidic pH. We suggest that ApcT couples substrate uptake to one or more protons, although conclusive determination of this coupling, as well as the substrate to proton stoichiometry, requires further study.

ApcT solubilized in *n*-octyl- β -D-thioglucoside forms crystals that diffract to high resolution both alone and in complex with the 7F11 Fab fragment. We solved the crystal structure of ApcT by a combination of molecular replacement, using a known Fab structure as a search probe (tables S2 and S3) and single-wavelength anomalous scattering, using selenomethionine-labeled ApcT. Because the crystals of ApcT alone, grown at pH ~ 9 , diffract to higher resolution than those of the Fab complex, and the conformation of ApcT is similar in both crystal forms, we employed the former structure for analysis. The well-resolved electron density maps of ApcT allowed for a complete tracing of the polypeptide chain, the accurate positioning of almost all side chains, and the faithful fitting of ~ 180 water molecules. We found no evidence for bound ions or substrate molecules and have not yet grown crystals of a substrate complex. The present structure therefore represents a high pH, apo state.

The structure of ApcT reveals an overall cylindrical shape, intracellular amino and carboxyl termini, short cytoplasmic and extracellular loops, and 12 transmembrane (TM) helices (Fig. 2, A and B, and fig. S9). Within the first 10 TM helices, segments 1 to 5 and 6 to 10 share a similar conformation and are related by a pseudo 2-fold axis of symmetry oriented parallel to the membrane and positioned between TMs 1 and 6, about halfway across the putative bilayer (Fig. 2, A and B, and fig. S10). The two 5-helix repeats superimpose, with not only the “scaffold” helices 3 to 5 and 8 to 10 superimposing well but also the “bundle” helices 1 and 2 and 6 and 7 and the intracellular and extracellular loops IL1 and EL4 (Fig. 2, A and B). Together, the two penta-helical repeats form a cylindrical barrel on the outside of which reside TMs 11 and 12. The protein fold and pseudo symmetry of ApcT is similar to that of LeuT (20), a sodium-coupled amino acid transporter, and superposition confirms that the two

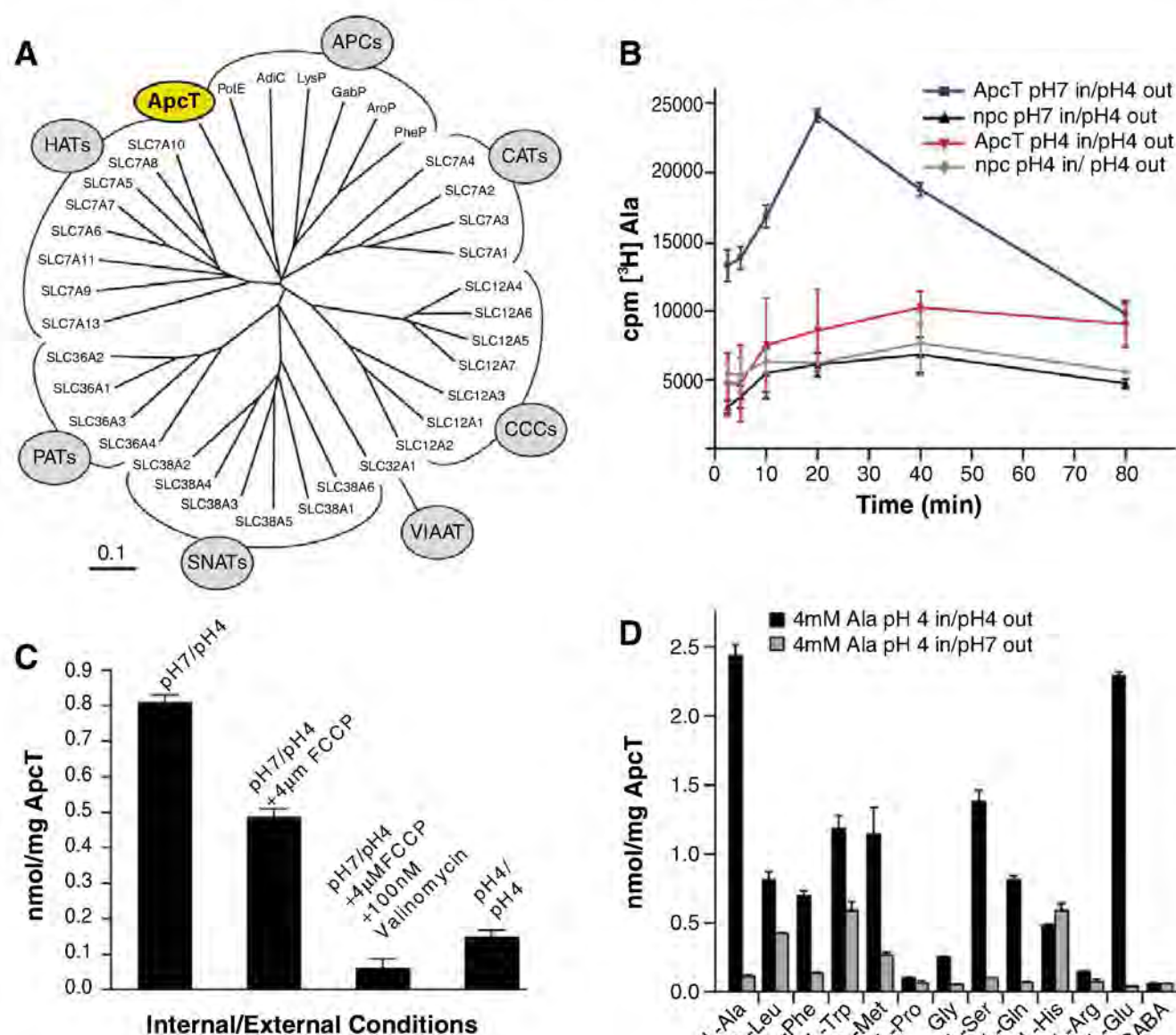


Fig. 1. ApcT is a broad-specificity amino acid transporter. (A) Dendrogram of human and selected bacterial APC transporters. Branches corresponding to prokaryotic APC transporters, CATs, CCCs, vesicular inhibitory amino acid transporter (VIAT), system A/N amino acid transporters (SNATs), proton-coupled amino acid transporters (PATs), and heterodimeric amino acid transporters (HATs) are defined in table S1. (B) ^3H -Ala uptake is pH dependent. ApcT and no-protein control proteoliposomes were loaded with buffer at pH 7 (blue and black, respectively) or pH 4 (red and gray, respectively). Uptake experiment was performed by diluting these liposomes in a pH 4 buffer supplemented with 500 nM ^3H -Ala. Error bars represent SEM of triplicate measurements. (C) Effect of carbonyl cyanide *p*-trifluoromethoxyphenylhydrazone (FCCP) and valinomycin treatment on ^3H -Ala uptake. Proteoliposomes were loaded with 100 mM KCl, and either pH 7 or pH 4 20 mM citrate buffer. Uptake experiment was performed at 30°C in 20 mM citrate buffer pH 4, 100 mM KCl, 750 nM L- ^3H -Ala, and in the presence or absence of 4 μM FCCP and/or 100 nM valinomycin. Time points were taken at 20 min. (D) Ala and Glu are the preferred substrates of ApcT in counterflow experiments. Proteoliposomes were loaded with 4 mM Ala, pH 4, and uptake of the particular ^3H amino acid, at 500 nM concentration, was measured. Estimates of uptake together with nonspecific transport or binding are defined by the experiments at pH 4 (external; black bars) whereas estimates of nonspecific transport or binding are defined by experiments at pH 7 (external; gray bars).

transport proteins harbor a remarkable kinship, in agreement with hydropathy profile analysis (21). Other LeuT-like sodium-coupled transporters, including vSGLT (22), Mph1 (23), and BetP (24), do not superimpose on ApcT as well as LeuT (see supporting online material).

The arginine/agmatine antiporter from *Escherichia coli* (19) (AdiC) is a member of the APC transporter family. Recently, Gao *et al.* reported its crystal structure (25). Because ApcT is related to AdiC in amino acid sequence and in biochemical function, we compared our structure of ApcT, determined at 2.35 Å resolution, to the structure of AdiC, solved at ~3.6 Å resolution (PDB code 3H5M). As anticipated from the relationships in amino acid sequence, the protein folds of ApcT and AdiC are similar. We found significant discrepancies, however, between the superpositions of the ApcT and AdiC structures and the independently aligned amino acid sequences in the transmembrane segments 6, 7, and 8 (figs. S11 and S12). Analysis of the structures and the sequence alignments leads us to conclude that in the AdiC structure, in the regions of TMs 6, 7, and 8, and perhaps to the C terminus, the amino acid sequence is off register by several amino acid residues relative to ApcT, beginning at the “loop” between TMs 5 and 6. This means that many residues after the end of TM5, including key residues such as Glu²⁰⁸, Tyr²³⁹, and Trp²⁹³, are “frame shifted” by ~4 residues or about one turn of α -helix (25) (figs. S11 to S13). Because of this frame shift, we have not used the AdiC structure in our analysis of APC transporters.

Analysis of the ApcT structure using three different criteria suggests that it adopts a substrate-free, inward-facing yet occluded conformation. First, there is a solvent-accessible path from the cytoplasmic solution to Lys¹⁵⁸, between TMs 1 and 5 (Fig. 2C). Second, analysis of the conformation of TM1 from the LeuT, vSGLT, and ApcT structures, an element of structure that plays a key role in allowing access to the substrate binding pocket, demonstrates that TM1 adopts a conformation that completely occludes access to the outside but only partially occludes access to the inside (Fig. 2D, fig. S14, and table S4). Third, mapping of bound water molecules onto the transporter clearly shows a belt of solvent at the extracellular face of the transporter, a solvent-free swath about 8 Å thick between the extracellular boundary and the putative substrate binding pocket, and a wide belt of solvent sites within and around the cytoplasmic “half” of the transporter (fig. S15). This apo conformation of ApcT is most similar to that of the substrate-bound, occluded conformation of the ~3.3 Å resolution BetP structure (fig. S14) (24), thus demonstrating, by way of our high-resolution structure, that formation of this occluded state is not dependent on the presence of bound substrate.

There is a water-filled pocket in ApcT about halfway across the membrane bilayer that overlaps with the substrate site of LeuT (Fig. 3, A and B). This putative substrate binding

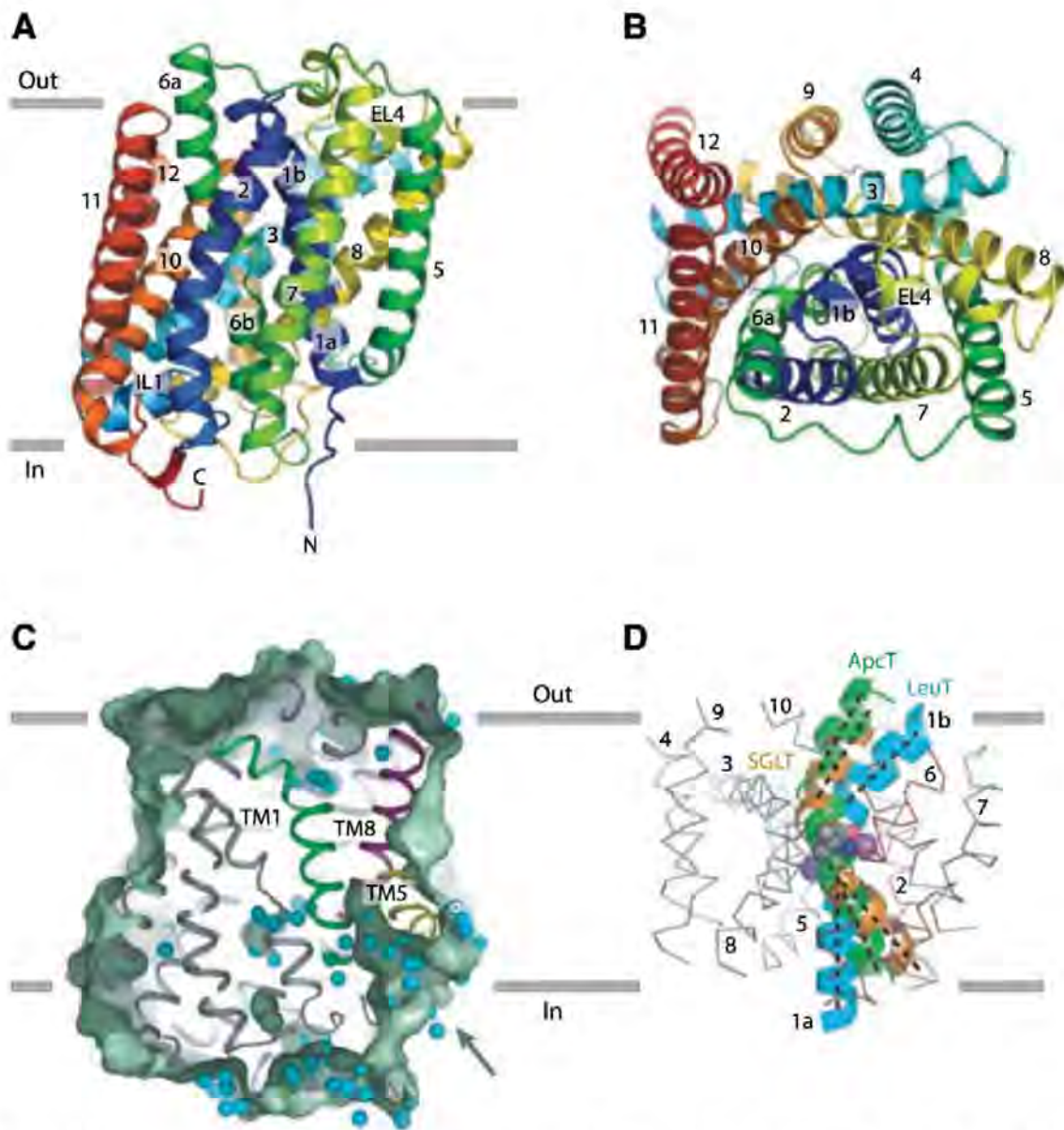


Fig. 2. Architecture of ApcT. **(A)** Ribbon diagram of the ApcT structure, viewed parallel to the membrane, along the pseudo 2-fold axis of molecular symmetry. **(B)** “Top” down view of ApcT from the outside. **(C)** Slice through a solvent-accessible surface of ApcT showing a solvent-accessible pathway reaching deep into the transporter. Water molecules are shown as cyan spheres. **(D)** Superposition of the scaffold helices TMs 3 to 5 and 8 to 10 of ApcT and vSGLT onto the equivalent elements of LeuT shows that in ApcT, TM1b is closed to the outside and TM1a is partially open to the inside. TMs 2 to 10 of LeuT are shown as an α -carbon trace.

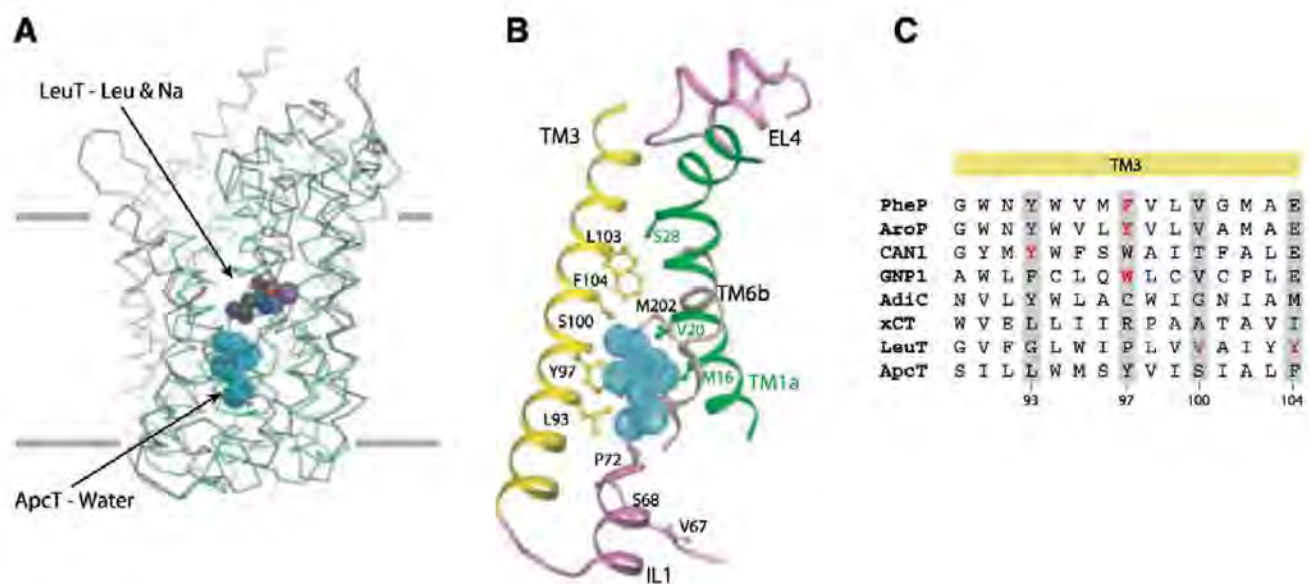


Fig. 3. Substrate pocket. **(A)** Structural superposition of TMs 1 to 10 of LeuT (gray) and ApcT (green). TMs 1 to 10 of LeuT were superposed on that of ApcT using the DaliLite program, and their C α traces are shown. The substrate leucine and two sodium ions in LeuT are shown as spheres. C, N, O, and Na atoms are gray, blue, red, and violet, respectively. The water molecules buried in the middle of the TM regions in ApcT are shown in cyan. **(B)** A closeup view of the putative solvent pocket in ApcT. TM helices 1, 3, and 6 and the IL1 and EL4 loops surrounding the solvent pocket are shown. Key residues predicted to be involved in substrate binding are shown as ball-and-stick models. **(C)** Role of TM3 in substrate binding. The sequence alignment shown is a composite of independent alignments generated by PROMALS 3D of the prokaryotic transporters (PheP, AroP, CAN1, GNP1, AdiC, LeuT, and ApcT) and of ApcT alone with xCT orthologs. Residues implicated in substrate binding are highlighted in red, and equivalent residues in other orthologs are highlighted by gray shading.

site is adjacent to non- α -helical regions of TMs 1 and 6, residues from TMs 3 and 8, and amino acids from IL1 and EL4 on the “bottom” and “top,” respectively (Fig. 3B and fig. S9). The volume of the water-filled pocket is $\sim 195 \text{ \AA}^3$ and is large enough to accommodate phenylalanine (191.9 \AA^3) but not tryptophan (228.2 \AA^3) (26), consistent with our determination that Phe is a better substrate than Trp (Fig. 1D) (27). The pocket is lined by a combination of polar, aromatic, and aliphatic amino acids and thus, like LeuT (20), the ionic interactions between the substrate's amino and carboxyl groups are probably satisfied by hydrogen bonding interactions with polar side-chain atoms and with main-chain carbonyl and amide moieties.

In related APC transporters, residues in TMs 3 and 8, as well as IL1, play important roles in substrate binding. In TM3, Phe¹¹¹ in PheP and Tyr¹⁰³ in AroP of *E. coli* and the equivalent Trp²³⁹ in yeast Gnp1 mediate substrate specificity (28). The corresponding residue in ApcT, Tyr⁹⁷ of TM3, lines part of the putative substrate binding site. In the human glutamate/cystine exchanger, the residue equivalent to Tyr⁹⁷ of ApcT is Arg¹³⁵, and we suggest that this residue interacts with the substrate's γ -carboxylate entity. Additional residues in TM3 that line the water-filled pocket—Leu⁹³, Ser¹⁰⁰, and Phe¹⁰⁴—correspond to residue Tyr¹⁷³ of yeast Can1 and Val¹⁰⁴ and Tyr¹⁰⁸ of LeuT, amino acids that also play central roles in substrate specificity (Fig. 3C) (20, 28). In TM8, Ala²⁸⁷ and Thr²⁹¹ of ApcT correspond to substrate binding residues Ser³⁵⁵ and Ile³⁵⁹ in LeuT (20), whereas Trp²⁹³ of AdiC (TM8) is crucial for substrate binding and transport (29). Together, these observations substantiate the water-filled pocket as a plausible substrate binding site.

ApcT is a proton-coupled amino transporter, and thus we asked if there were any titratable

groups in functionally conspicuous regions. Remarkably, the well-ordered, primary amine group of Lys¹⁵⁸ (TM5) is situated between TMs 1 and 8 (Fig. 4A and fig. S19) and forms hydrogen bonds to the main-chain carbonyl oxygen atom of G19 (TM1) and hydroxyl of S283 (TM8) (Fig. 4B). On the basis of a structural alignment with LeuT, the amine of Lys¹⁵⁸ (ApcT) superimposes on the Na2 ion (LeuT) (fig. S16). Consistent with the buried location of the Lys¹⁵⁸ amine group, calculations predict a pK_a (logarithm of acid dissociation constant) that is 3 to 4 pH units below that of an unperturbed lysine residue (30). To test the hypothesis that Lys¹⁵⁸ is important for ApcT transport activity we made the Lys to Ala substitution (K158A) and found that the mutant had no measurable [³H]-Ala transport activity (fig. S17).

The wild-type ApcT crystal structure was determined at alkaline pH, where the transporter is not active, and thus we reasoned that if Lys¹⁵⁸ undergoes reversible protonation and deprotonation during the transport cycle, the present structure may represent the neutral, non-protonated state of the amine group, i.e., the functional state of the transporter after unbinding of substrate and proton(s) to the cytoplasm. To assess the structural consequences of removing the lysine residue, we solved the ApcT K158A crystal structure. In agreement with our hypothesis that the wild-type structure represented the neutral, non-protonated state of Lys¹⁵⁸, the ApcT K158A crystal structure showed neither rearrangement to the overall fold of the protein nor significant changes in the positions of residues surrounding residue 158 (fig. S18).

Structural alignments of ApcT, LeuT, vSGLT (SLC5), Mhp1 (NCS-1), and BetP show that the ammonium group of the lysine occupies a position very similar to the predicted sodium sites in Mhp1, vSGLT, and BetP. Moreover, the crucial

oxygen atoms defining these essential sodium or ammonium ion binding sites between TM1 and TM8 are also conserved in sodium-potassium-chloride cotransporters (fig. S16), revealing that this monovalent cation binding site is broadly conserved across many different secondary transporters. Lys¹⁵⁸ and its hydrogen bonding partners in TM1 and TM8 of ApcT are also conserved in the glutamate/cystine antiporter (SLC7).

The structure of ApcT provides an atomic resolution view of an APC transporter captured in an inward-facing, yet occluded, apo state (Fig. 4C). We suggest that this state may represent the conformation of the transporter after substrate and proton have unbound to the intracellular solution, via an open-to-the-inside state, and the intracellular gate has partially closed. Upon protonation of the Lys¹⁵⁸ amine group, we speculate that ApcT will isomerize from this inward facing state to an open-to-the-outside conformation, ready to bind substrate and return to an inward-facing conformation.

How might protonation and deprotonation of Lys¹⁵⁸ in ApcT, or sodium binding and unbinding to the Na2 site in LeuT modulate the conformation of the transporter? We suggest that proton binding and unbinding to Lys¹⁵⁸ toggles the conformation of TM1 and changes the position of the kink in the helix, opening and closing the extracellular gate, respectively (Fig. 4C). How might this happen? If we compare the structures of LeuT and ApcT (fig. S16), we see that the Na2 ion is fully coordinated by five ligands from TMs 1 and 8. By contrast, the primary amine group of Lys¹⁵⁸, which we assert is neutral in the present structure, is only coordinated by two hydrogen bond donors, one each in TM1 and TM8. Because ApcT and LeuT are closely related in structure and in the sequences of their TM1 helices, we suggest that when Lys¹⁵⁸ of ApcT binds a proton, the coordination

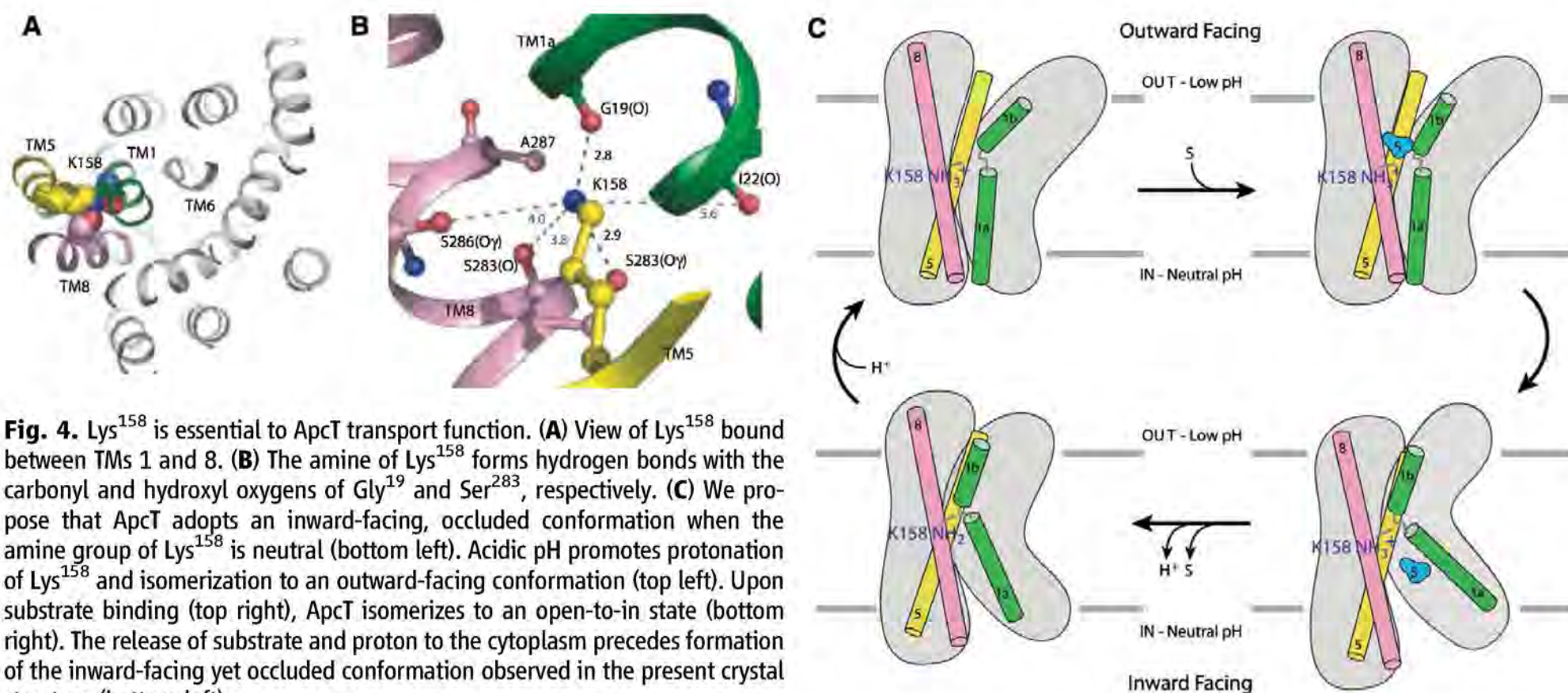


Fig. 4. Lys¹⁵⁸ is essential to ApcT transport function. (A) View of Lys¹⁵⁸ bound between TMs 1 and 8. (B) The amine of Lys¹⁵⁸ forms hydrogen bonds with the carbonyl and hydroxyl oxygens of Gly¹⁹ and Ser²⁸³, respectively. (C) We propose that ApcT adopts an inward-facing, occluded conformation when the amine group of Lys¹⁵⁸ is neutral (bottom left). Acidic pH promotes protonation of Lys¹⁵⁸ and isomerization to an outward-facing conformation (top left). Upon substrate binding (top right), ApcT isomerizes to an open-to-in state (bottom right). The release of substrate and proton to the cytoplasm precedes formation of the inward-facing yet occluded conformation observed in the present crystal structure (bottom left).

of the now positively charged amine group changes, with TM1 forming a kink at a position similar to the kink in LeuT, recruiting the carbonyl oxygen of Ile²² (TM1) and the hydroxyl groups of Ser²⁸³ and Ser²⁸⁶ (TM8). Proton binding and unbinding to the amine group of Lys¹⁵⁸ may not only modulate the local conformation of TM1 but in doing so may also promote the movement of TMs 1a, 1b, 6a, and 6b, thus facilitating the opening and closing of the extracellular and intracellular gates.

References and Notes

1. D. L. Jack, I. T. Paulsen, M. H. J. Saier, *Microbiology* **146**, 1797 (2000).
2. M. A. Hediger *et al.*, *Pflugers Arch.* **447**, 465 (2004).
3. H. Sato, M. Tamba, T. Ishii, S. Bannai, *J. Biol. Chem.* **274**, 11455 (1999).
4. S. Bannai, E. Kitamuri, *J. Biol. Chem.* **255**, 2372 (1980).
5. N. Zimmermann *et al.*, *J. Clin. Invest.* **111**, 1863 (2003).
6. O. Yanagida *et al.*, *Biochim. Biophys. Acta* **1514**, 291 (2001).
7. N. Harada *et al.*, *Acta Haematol.* **103**, 144 (2000).
8. M. J. Calonge *et al.*, *Nat. Genet.* **6**, 420 (1994).
9. D. Torrents *et al.*, *Nat. Genet.* **21**, 293 (1999).
10. G. Borsani *et al.*, *Nat. Genet.* **21**, 297 (1999).
11. S. C. Hebert, D. B. Mount, G. Gamba, *Pflugers Arch. Eur. J. Physiol.* **447**, 580 (2004).
12. P. Blaesse, M. S. Airaksinen, C. Rivera, K. Kaila, *Neuron* **61**, 820 (2009).
13. S. L. McIntire, R. J. Reimer, K. Schuske, R. H. Edwards, E. M. Jorgensen, *Nature* **389**, 870 (1997).
14. F. A. Chaudhry, R. J. Reimer, R. H. Edwards, *J. Cell Biol.* **157**, 349 (2002).
15. M. Boll, H. Daniel, B. Gasnier, *Pflugers Arch. Eur. J. Physiol.* **447**, 776 (2004).
16. P. M. Taylor, *Biochem. Soc. Trans.* **37**, 237 (2009).
17. T. Kawate, E. Gouaux, *Structure* **14**, 673 (2006).
18. N. Reig *et al.*, *J. Biol. Chem.* **282**, 13270 (2007).
19. R. Iyer, C. Williams, C. Miller, *J. Bacteriol.* **185**, 6556 (2003).
20. A. Yamashita, S. K. Singh, T. Kawate, Y. Jin, E. Gouaux, *Nature* **437**, 215 (2005).
21. J. S. Lolkema, D.-J. Slotboom, *Mol. Membr. Biol.* **25**, 567 (2008).
22. S. Faham *et al.*, *Science* **321**, 810 (2008).
23. S. Weyand *et al.*, *Science* **322**, 709 (2008).
24. S. Ressler, A. C. Terwisscha van Scheltinga, C. Vonnrhein, V. Ott, C. Ziegler, *Nature* **458**, 47 (2009).
25. X. Gao *et al.*, *Science* **324**, 1565 (2009).
26. J. Tsai, R. Taylor, C. Chothia, M. Gerstein, *J. Mol. Biol.* **290**, 253 (1999).
27. S. K. Singh, C. L. Piscitelli, A. Yamashita, E. Gouaux, *Science* **322**, 1655 (2008).
28. A. J. Cosgriff *et al.*, *J. Bacteriol.* **182**, 2207 (2000).
29. F. Casagrande *et al.*, *J. Biol. Chem.* **283**, 33240 (2008).
30. H. Li, A. D. Robertson, J. H. Jensen, *Proteins* **61**, 704 (2005).
31. We appreciate the beamtime and support of the staffs at beamlines 8.2.1, 8.2.2, and 5.0.2 at the Advanced Light Source. We thank Z. Zhang for initial screening efforts, J. Michel for cloning of the 7F11 gene, L. Vaskalis for assistance with preparation of figures, and C. Piscitelli for analysis of the AdiC structure. P.L.S. was supported by an individual NIH National Research Service Award postdoctoral fellowship. This work was supported by the New York Consortium for Membrane Protein Structure, a NIH-supported Protein Structure Initiative (E.G.). E.G. is an investigator with the Howard Hughes Medical Institute. Coordinates and structure factors of the apo ApcT, ApcT-7F11 Fab complex, and ApcT K158A-7F11 Fab complex have been deposited in the Protein DataBank with accession codes 3GIA, 3GI9, and 3GI8, respectively.

Supporting Online Material

www.sciencemag.org/cgi/content/full/1176088/DC1

Materials and Methods

Figs. S1 to S19

Tables S1 to S4

References

11 May 2009; accepted 2 July 2009

Published online 16 July 2009;

10.1126/science.1176088

Include this information when citing this paper.

Structures of the Ribosome in Intermediate States of Ratcheting

Wen Zhang,^{1*} Jack A. Dunkle,^{1*} Jamie H. D. Cate^{1,2†}

Protein biosynthesis on the ribosome requires repeated cycles of ratcheting, which couples rotation of the two ribosomal subunits with respect to each other, and swiveling of the head domain of the small subunit. However, the molecular basis for how the two ribosomal subunits rearrange contacts with each other during ratcheting while remaining stably associated is not known. Here, we describe x-ray crystal structures of the intact *Escherichia coli* ribosome, either in the apo-form (3.5 angstrom resolution) or with one (4.0 angstrom resolution) or two (4.0 angstrom resolution) anticodon stem-loop tRNA mimics bound, that reveal intermediate states of intersubunit rotation. In the structures, the interface between the small and large ribosomal subunits rearranges in discrete steps along the ratcheting pathway. Positioning of the head domain of the small subunit is controlled by interactions with the large subunit and with the tRNA bound in the peptidyl-tRNA site. The intermediates observed here provide insight into how tRNAs move into the hybrid state of binding that precedes the final steps of mRNA and tRNA translocation.

Protein biosynthesis requires many large-scale rearrangements in the ribosome as each amino acid is added to a growing polypeptide chain. Positioning of tRNA on the ribosome is proposed to occur through a ratcheting mechanism. Central to this mechanism is a rotation of the small ribosomal subunit relative to the large subunit (Fig. 1A) (*1, 2*) that occurs in all stages of translation—initiation, elongation, termination, and ribosome recycling (*1*)—and is

targeted by clinically useful antibiotics (*3, 4*). For example, after each peptide bond is formed an $\sim 8^\circ$ intersubunit rotation results in tRNAs bound in the aminoacyl-tRNA and peptidyl-tRNA binding sites (A site and P site, respectively), moving into the P site and exit-tRNA site (E site) on the large ribosomal subunit (Fig. 1B). From this hybrid state of tRNA binding (Fig. 1B) (*1, 5*), the tRNAs are then translocated to the P site and E site on the small subunit.

In addition to intersubunit rotation, ratcheting also involves a nearly orthogonal rotation of the head domain of the small ribosomal subunit (Fig. 1C) that plays a role in controlling the position of tRNAs within the ribosome (*1, 6, 7*). As with intersubunit rotation, movement of the head domain is a target for clinically useful anti-

biotics (*8*). Swiveling of the head domain relative to the body of the small subunit may also be required for the intrinsic helicase activity of the ribosome in unwinding secondary structure in mRNA (*8, 9*). Rotations of up to 14° allow the head domain to change its position by 20 Å or more at the ribosomal subunit interface, or the width of a tRNA substrate (*7*).

The molecular basis for how the ribosomal subunits rotate with respect to each other while remaining stably associated remains unknown (*1, 10*). Furthermore, the precise timing of movements of the small subunit head domain during ratcheting are not clear because the head domain can move independently of the body and platform domains of the small subunit (*1, 6, 7*). Here, we present three x-ray crystal structures of the *Escherichia coli* 70S ribosome that reveal intermediates along the ratcheting pathway. These structures show that the ribosome can rearrange the interface between the ribosomal subunits in discrete steps and suggest how these rearrangements may direct tRNAs into hybrid states of binding that are essential for mRNA and tRNA translocation.

Using new crystal forms, we determined x-ray crystal structures of the *E. coli* 70S ribosome in the absence of ligands, with mRNA and an anticodon stem-loop mimic of tRNA^{Met} (ASL^{Met}) bound in the P site of the small (30S) subunit, or with mRNA and two ASL mimics of tRNA^{Phe} (ASL^{Phe}) bound in the A and P sites of the 30S subunit (*11*) (3.5 Å, 4.0 Å, and 4.0 Å resolution, respectively) (tables S1 and S2). One of the two copies of the ribosome in each crystal structure resembles previously determined high-resolution structures of the ribosome (*7, 12*). In the other copies of the ribosome in each structure, the small

¹Departments of Molecular and Cell Biology and Chemistry, University of California at Berkeley, Berkeley, CA 94720, USA.

²Physical Biosciences Division, Lawrence Berkeley National Laboratory, Berkeley, CA 94720, USA.

*These authors contributed equally to this work.

†To whom correspondence should be addressed. E-mail: jcate@lbl.gov

Fig. 1. Rotated states of the ribosome. **(A)** View of the bacterial 70S ribosome, composed of the small (30S) ribosomal subunit and the large (50S) ribosomal subunit. The small subunit of the ribosome (blue) can rotate from a starting conformation seen in post-initiation and termination states (state R_0 , black outline) (12, 13, 18) to a fully rotated conformation seen in elongation, termination, and recycling steps of translation (state R_F , red outline) (1, 15–17). 30S features include the head, platform, and body. The 50S subunit is shown in gray. Letters indicate the positions of the aminoacyl (A), peptidyl (P), and exit (E) tRNA-binding sites. **(B)** Schematic of tRNA-binding states on the ribosome. In the transition of the ribosome to the fully rotated state, tRNAs shift from binding in the A/A and P/P sites (30S subunit and 50S subunit, respectively) to occupy hybrid binding sites (A/P and P/E for

30S/50S sites). The view of the ribosome is rotated 90° from that in (A). **(C)** Rotations of the head domain of the small ribosomal subunit. Letters indicate the locations of the aminoacyl (A), peptidyl (P), and exit (E) tRNA binding sites on the large subunit. In state R_0 (black), the head domain is centered over the P site (~0° rotation). Rotations of the head domain toward the E site of up to 14° (red) have been observed (1, 6, 7). The 5' to 3' direction of mRNA, which threads around the neck region of the 30S subunit, is also indicated.

subunit of the ribosome is rotated to an intermediate position with respect to the large subunit when compared with structures of the ribosome determined previously. In the new conformation, the small subunit is rotated by 3° to 6° relative to its position in a post-initiation state of the ribosome, in which initiator tRNA is bound in the P site (defined here as state R_0) (Fig. 2, A and B, and table S3) (12, 13), and 2° to 3° relative to the ribosome with tRNAs bound in the P/P and E/E sites (here denoted state R_1) (Fig. 2C and table S3) (14). In ribosomes in which tRNA occupies a hybrid P/E binding site (here called state R_F) (Fig. 1, A and B) (1, 15–17), the small subunit is rotated by an additional 2° to 4° relative to the rotational state described here (Fig. 2D and table S3), which we term state R_2 . The ribosome can therefore adopt at least four stable states of intersubunit rotation, R_0 , R_1 , R_2 , and R_F .

In state R_2 , the central contacts or “bridges” between the ribosomal subunits (1, 7) are nearly indistinguishable from those observed in ribosomes in states R_0 and R_1 (Fig. 3A) (7, 12, 14, 18–20). These bridges include contacts between ribosomal RNA (rRNA) elements in the small and large subunits (16S rRNA and 23S rRNA, respectively) that are near the tRNA binding sites. The largest change in the central bridges occurs in bridge B2a, which is adjacent to the mRNA decoding site (Fig. 3A). In this region, nucleotide A1913 in 23S rRNA and nucleotides A1492 to A1493 in helix h44 of 16S rRNA adopt different conformations depending on the tRNA occupancy of the A site, as observed in other structures (7, 12, 14). To maintain contacts in bridges at the center of the interface (Fig. 3A) during subunit rotation, helix h44 in the small subunit bends near 16S rRNA helix h14 (Fig. 3B).

In contrast, key bridges between the platform of the 30S subunit and the 50S subunit (B4 and B7a) are shifted halfway to their position in the R_F state (Figs. 2 and 3A) (1, 15, 16). In the structures observed here, the platform of the 30S subunit rotates about the helical axis of the top

Fig. 2. Structure of the apo-70S ribosome in an intermediate state of intersubunit rotation, state R_2 . **(A)** Comparison of the ribosome in state R_2 with the ribosome in state R_0 (12, 13), with the 50S subunit serving as reference (1). Arrows indicate the direction of movement in the transition from state R_0 to state R_2 . The distance changes in 30S subunit positions are color-coded in Å units, as shown, in this and the subsequent panels. Ribosomal RNA and proteins in the 50S subunit are colored gray and magenta, respectively. 30S features include the head, neck, platform, body, shoulder, and spur. 50S features include protein L1/rRNA arm (L1), central protuberance (CP), protein L11/rRNA arm (L11), and protein L9 (L9). The approximate location of proteins L7/L12 and L1, not observed in the structure, are noted in gray. **(B)** Comparison of the ribosome in state R_2 with the ribosome in state R_0 , viewed from the perspective of the 50S subunit. Difference vectors between phosphorous and C α atoms are shown to the right, with arrows indicating the direction of the change. **(C)** Comparison of the ribosome in state R_2 with the ribosome in state R_1 (14). **(D)** Comparison of the ribosome in state R_2 with the ribosome in the fully rotated state R_F (15, 16).

of helix h44 in 16S rRNA. The rotation exposes nucleotide A702 in 16S rRNA to solvent, whereas it is buried in the minor groove of H68 in 23S rRNA in high-resolution structures of states R_0 and R_1 (Fig. 3C and fig. S1) (12, 14, 18–20). In 16S rRNA, nucleotide A702 is protected from chemical probes when tRNAs are bound in the A/A and P/P sites (5). However, when tRNAs occupy hybrid binding sites (A/P and P/E) (Fig. 1B), nucleotide A702 becomes exposed to chemical probes (5) and bridge B7a is rearranged (1, 11, 15, 16). Exposure of A702 to solvent suggests that the conformation of the ribosome in state R_2 is at least partway to the fully rotated state (R_F) that accommodates tRNA binding in hybrid A/P and P/E sites (Fig. 1B). Apart from protein

S15 in bridge B4, which is also shifted halfway to its position in state R_F (fig. S2) (1, 11, 15, 16), most of the remainder of the 30S platform does not make direct contact with the large subunit (Fig. 3A). Limited contacts probably allow large shifts in the position of the interface in this region.

Contacts between the 30S subunit head domain and the 50S subunit have been shown to adopt many different configurations. In states R_0 and R_1 , protein L5 in the central protuberance of the 50S subunit contacts the N-terminal lobe of protein S13 in the 30S head domain when it is centered over the 30S P site (bridge B1b) (Figs. 1C and 4A) (1, 12, 14). In the R_F state of the ribosome, the head domain of the 30S subunit is shifted so that protein S13 forms a key interac-

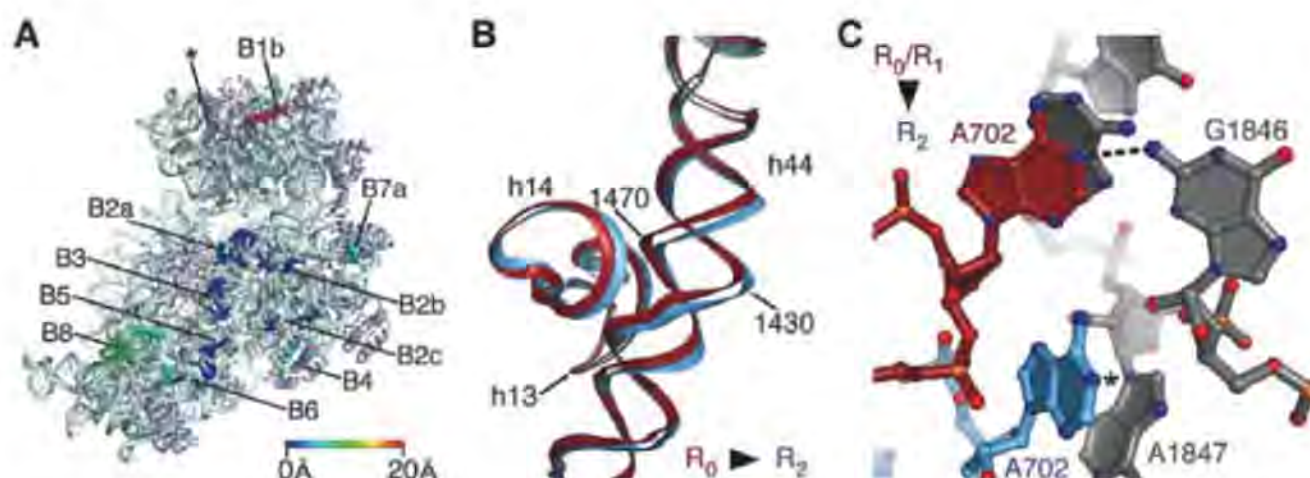
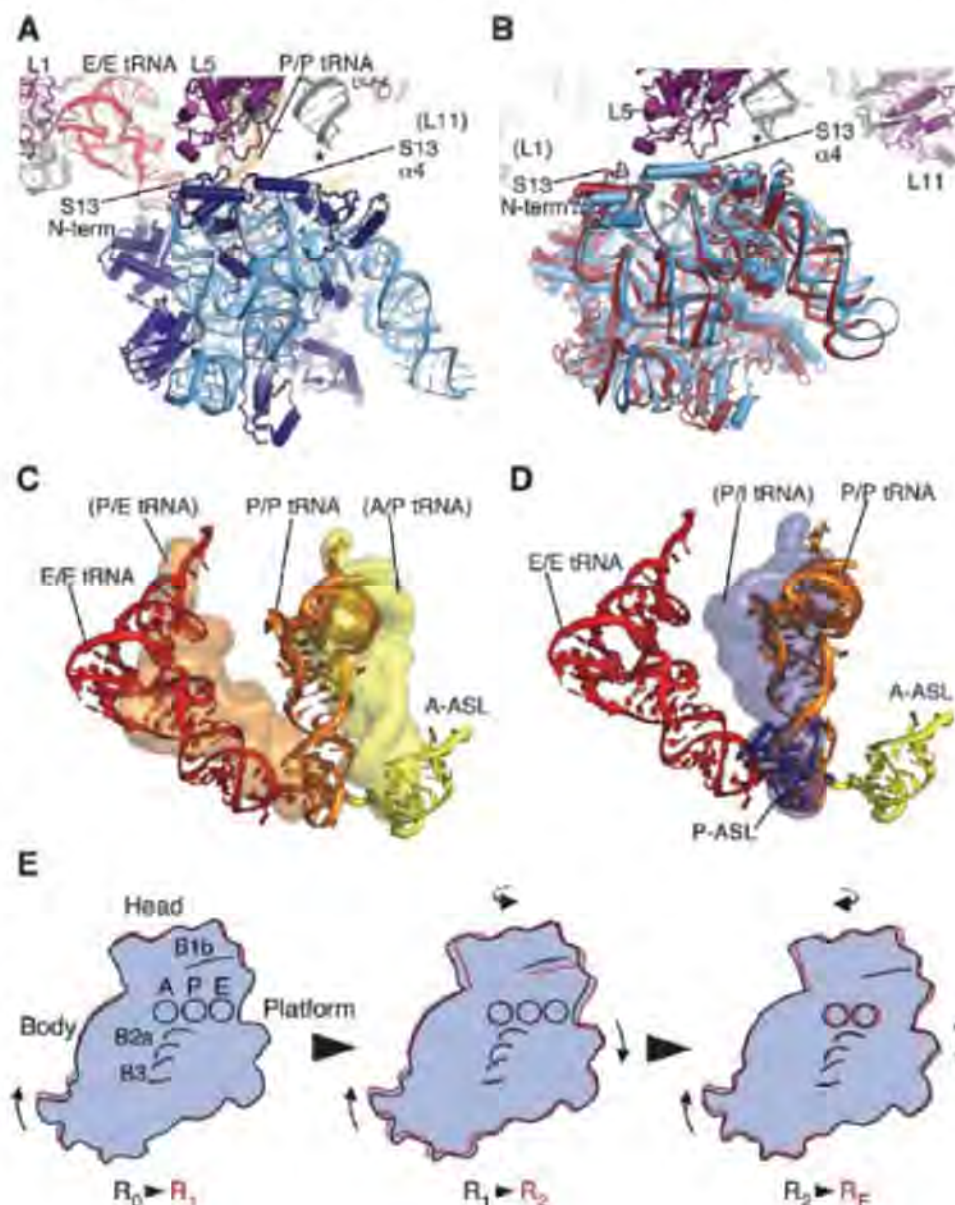


Fig. 3. Contacts, or bridges, between the ribosomal subunits in the apo-70S ribosome in state R_2 . **(A)** The position of bridges in state R_2 compared with those in state R_0 (12, 13). Bridge numbering is the same as in (7). The direction of view and color coding are the same as in Fig. 2C. Bridge B1a (asterisk) includes the A-site finger (H38 in 23S rRNA), which spans the subunit interface parallel to the A and P sites (29). This contact is not visible in the present structures because of disorder at the end of H38 in both states of the ribosome. **(B)** Bend in rRNA helix h44 in 16S rRNA that accommodates rotated state R_2 . Nucleotides and 16S rRNA helices are marked. The view is the same as in Fig. 2B. **(C)** Bridge B7a in state R_2 compared with that in states R_0 (12, 18–20) and R_1 (14). Nucleotide A702 in 16S rRNA in the 30S subunit (light blue) and nucleotides in H68 of 23S rRNA in the 50S subunit (gray) are shown for state R_2 . Nucleotide A702 in state R_0 or R_1 is shown in red. The N1 position of A702 that would be methylated by dimethylsulfate is marked with an asterisk (5).

Fig. 4. Changes in the position of the head domain in the 30S subunit in state R_2 . **(A)** Bridge B1 in ribosomes in state R_1 (14). The tRNAs bound in the 30S subunit A site (yellow), and in the P/P (orange) and E/E sites (red), are shown. Domains in protein S13 in the 30S subunit head domain (blue) and protein L5 in the 50S subunit (purple) are marked. An asterisk marks the approximate location of the A-site finger (ASF) helix H38 in 23S rRNA, the tip of which is disordered in the crystal structure (14). Protein L31, not seen in *E. coli* 70S ribosome structures, has been removed for clarity. **(B)** Bridge B1 in the apo-70S ribosome in state R_2 (light blue) compared with state R_F (red). Domains in protein S13 in the 30S subunit head domain and protein L5 in the 50S subunit are marked. Asterisk indicates the same as in (A). **(C)** Position of full-length tRNAs modeled onto the apo-70S ribosome in state R_2 . The superposition used the head domain of the 30S subunit in the fully rotated state R_F (16) for reference (1, 11). Surfaces of the modeled tRNAs (yellow and orange) are compared with the position of tRNAs in state R_1 (14), as described in (A), and shown as ribbons. **(D)** Position of full-length tRNA in the P site of state R_1 (14) modeled onto the ribosome complexed with ASL^{Met_f} in the P site in state R_2 (11), with the 30S subunit body and platform of the ribosome in state R_1 used as a reference. Surface of the modeled tRNA (blue) is compared with the position of the P-site ASL^{Met_f} in state R_2 (blue), and tRNAs in state R_1 (described above) are shown as ribbons. **(E)** Stepwise rearrangements in the ribosome along the ratcheting pathway. The molecular envelope of the 30S subunit is shown for clarity. Domains of the 30S subunit (head, body, and platform), tRNA binding sites (A, P, and E, respectively), and bridges B1b, B2a, and B3 are shown. The view is the same as in Fig. 2B. Arrows indicate the direction of movement from one state to the next.



(C) Position of full-length tRNAs modeled onto the apo-70S ribosome in state R_2 . The superposition used the head domain of the 30S subunit in the fully rotated state R_F (16) for reference (1, 11). Surfaces of the modeled tRNAs (yellow and orange) are compared with the position of tRNAs in state R_1 (14), as described in (A), and shown as ribbons. **(D)** Position of full-length tRNA in the P site of state R_1 (14) modeled onto the ribosome complexed with ASL^{Met_f} in the P site in state R_2 (11), with the 30S subunit body and platform of the ribosome in state R_1 used as a reference. Surface of the modeled tRNA (blue) is compared with the position of the P-site ASL^{Met_f} in state R_2 (blue), and tRNAs in state R_1 (described above) are shown as ribbons. **(E)** Stepwise rearrangements in the ribosome along the ratcheting pathway. The molecular envelope of the 30S subunit is shown for clarity. Domains of the 30S subunit (head, body, and platform), tRNA binding sites (A, P, and E, respectively), and bridges B1b, B2a, and B3 are shown. The view is the same as in Fig. 2B. Arrows indicate the direction of movement from one state to the next.

tion between its long central α -helix and protein L5 in the large subunit (1, 21, 22). In the structure of the ribosome in state R_2 with no bound ligands, the key interaction between proteins L5 and S13 (21, 22) is essentially indistinguishable from that in the fully rotated ribosome (Fig. 4B) (1, 15, 16). To enable the contact, the head of the small subunit is swiveled toward the E site by 11° relative to its conformation when the head domain is aligned with the 30S subunit P site (Figs. 1C and 4A) (14), whereas the head domain is swiveled by only 5° in the R_F state when tRNAs are bound in the hybrid A/P and P/E sites (Figs. 1B and 4B) (1, 11, 15, 16). Cryogenic electron microscopy (cryo-EM) reconstructions of the yeast ribosome in the R_F state reveal that tRNA bound in the P/E site remains associated with the head domain of the small subunit as the head domain adopts an “open” configuration required for tRNA transit to the small subunit E site (1). Using the head domain of the small subunit as a guide, we modeled full-length A/P and P/E tRNAs (11, 16) in the ribosome in state R_2 . Based on the model, tRNAs could bind in the hybrid A/P and P/E sites in the R_2 state because of swiveling of the head domain of the small subunit by $\sim 11^\circ$, as observed in the apo-70S structure (Fig. 4C).

Contacts between the ribosome and the ASL portion of tRNA may oppose movement of tRNAs into the hybrid state of binding. The ASL portion of P-site tRNA has been proposed to stabilize the 30S subunit head domain centered over the P site (0° rotation) (table S3) and prevent frame-shifting (12). ASL binding to the ribosome in state R_2 also centers the head domain of the small subunit over the P site (11), as seen in state R_0 (12). This is true regardless of whether an ASL is bound in the A site or not (11). In state R_2 , centering of the head domain over the P site would leave the acceptor end of P-site tRNA positioned partway between the P and E sites on the large subunit (Fig. 4D), which is presumably an unstable configuration except for translation initiation (23). To counterbalance the stabilizing effect of the ASL on the positioning of the head domain, bridge B1b between proteins S13 and L5 and contacts between the large subunit and the elbow and acceptor ends of tRNA (1, 24–27) may favor 30S subunit head rotation and P-site tRNA movement into the hybrid P/E site in states R_2 and R_F , which is in agreement with the in vivo importance of the α -helical region of S13 involved in the bridge (21, 22) and the requirement of full-length P-site tRNA in order for translocation to occur (25). Also consistent with our structural model of hybrid state formation, single-molecule fluorescence resonance energy transfer (FRET) experiments have shown that ribosomes lacking substrates or complexed with a P-site ASL^{Met_f} exhibit spontaneous subunit rotation, but not with the same rate or efficiency as when full-length P-site tRNA is bound (10).

The structures of the *E. coli* 70S ribosome presented here reveal that in addition to the known

R_0 , R_1 , and R_F states, the ribosome can adopt an intermediate state of subunit rotation, state R_2 . This state would likely occur transiently, before the ribosome adopts a fully rotated conformation (1, 10, 16). Based on the structures presented above, we propose that during ratcheting, which combines inter-subunit rotation and rotation of the small subunit head domain, key bridges between the ribosomal subunits rearrange in a step-wise manner. Ratcheting likely begins with the 30S subunit body, continuing with the 30S platform and head domains, and completes with rearrangement of the central bridges (Fig. 4E, table S3, and movies S1 and S2). Such a step-wise rearrangement would assist the ribosome in making large shifts at the interface without fully destabilizing the subunit interface. In addition, the multiple conformations of the head domain of the 30S subunit would help to position tRNAs on the ribosome during ratcheting (1, 6, 7). Intriguingly, single-molecule FRET studies have shown that P-site tRNA fluctuates between the P/P and P/E sites at a faster rate than intersubunit rotation (10, 26). The ability of tRNAs to adopt a hybrid state of binding in state R_2 may in part explain the different rates between these processes. Fluctuation of tRNAs between the P/P and P/E states would not require the full extent of intersubunit rotation but could occur in state R_2 because of swiveling of the 30S subunit head domain and the inherent flexibility of P-site tRNA (14, 28). High-resolution structures of the ribosome in different rotated states with intact tRNAs will be required to complete our molecular understanding of the large-scale con-

formational rearrangements in the ribosome that allow ratcheting and protein synthesis to occur.

References and Notes

1. J. Frank, H. Gao, J. Sengupta, N. Gao, D. J. Taylor, *Proc. Natl. Acad. Sci. U.S.A.* **104**, 19671 (2007).
2. L. H. Horan, H. F. Noller, *Proc. Natl. Acad. Sci. U.S.A.* **104**, 4881 (2007).
3. S. K. Johansen, C. E. Maus, B. B. Plikaytis, S. Douthwaite, *Mol. Cell* **23**, 173 (2006).
4. D. N. Ermolenko *et al.*, *Nat. Struct. Mol. Biol.* **14**, 493 (2007).
5. D. Moazed, H. F. Noller, *Nature* **342**, 142 (1989).
6. C. M. Spahn *et al.*, *EMBO J.* **23**, 1008 (2004).
7. B. S. Schuwirth *et al.*, *Science* **310**, 827 (2005).
8. M. A. Borovinskaya, S. Shoji, J. M. Holton, K. Fredrick, J. H. Cate, *ACS Chem. Biol.* **2**, 545 (2007).
9. S. Takyar, R. P. Hickerson, H. F. Noller, *Cell* **120**, 49 (2005).
10. P. V. Cornish, D. N. Ermolenko, H. F. Noller, T. Ha, *Mol. Cell* **30**, 578 (2008).
11. Materials and methods are available as supporting material on Science Online.
12. V. Berk, W. Zhang, R. D. Pai, J. H. Cate, *Proc. Natl. Acad. Sci. U.S.A.* **103**, 15830 (2006).
13. I. S. Gabashvili *et al.*, *Cell* **100**, 537 (2000).
14. M. Selmer *et al.*, *Science* **313**, 1935 (2006).
15. S. R. Connell *et al.*, *Mol. Cell* **25**, 751 (2007).
16. X. Agirrezabala *et al.*, *Mol. Cell* **32**, 190 (2008).
17. P. Julian *et al.*, *Proc. Natl. Acad. Sci. U.S.A.* **105**, 16924 (2008).
18. M. Laurberg *et al.*, *Nature* **454**, 852 (2008).
19. A. Weixlbaumer *et al.*, *Science* **322**, 953 (2008).
20. A. Korostelev *et al.*, *Proc. Natl. Acad. Sci. U.S.A.* **105**, 19684 (2008).
21. A. R. Cukras, R. Green, *J. Mol. Biol.* **349**, 47 (2005).
22. L. Hoang, K. Fredrick, H. F. Noller, *Proc. Natl. Acad. Sci. U.S.A.* **101**, 12439 (2004).
23. G. S. Allen, A. Zavialov, R. Gursky, M. Ehrenberg, J. Frank, *Cell* **121**, 703 (2005).
24. R. Lill, J. M. Robertson, W. Wintermeyer, *EMBO J.* **8**, 3933 (1989).
25. S. Joseph, H. F. Noller, *EMBO J.* **17**, 3478 (1998).
26. J. B. Munro, R. B. Altman, N. O'Connor, S. C. Blanchard, *Mol. Cell* **25**, 505 (2007).
27. D. Pan, S. V. Kirillov, B. S. Cooperman, *Mol. Cell* **25**, 519 (2007).
28. A. Korostelev, S. Trakhanov, M. Laurberg, H. F. Noller, *Cell* **126**, 1065 (2006).
29. M. Valle *et al.*, *Cell* **114**, 123 (2003).
30. We thank K. Frankel, S. Classen, and G. Meigs for help with data measurement at the 12.3.1 and 8.3.1 beamlines at the Advanced Light Source (ALS); R. Kanagalaghatta, D. Neau, and F. Murphy for help with data measurement at 24-ID at the Advanced Photon Source (APS); P. Afonine and P. Adams for help with Phenix refinement; S.-H. Kim, P. Adams, and J. Holton for useful crystallographic discussions; and J. Frank for providing the cryo-EM reconstructions of the *E. coli* 70S ribosome. We also thank J. Doudna, S. Blanchard, H. Noller, A. Korostelev, and D. Ermolenko for helpful discussions and comments on the manuscript. Atomic coordinates and structure factors are deposited in the Protein Data Bank (accession codes 3I1M, 3I1N, 3I1O, 3I1P, 3I1Q, 3I1R, 3I1S, 3I1T, 3I1Z, 3I2O, 3I21, 3I22). This work was funded by NIH (grant GM65050 to J.H.D.C., National Cancer Institute grant CA92584 for the SIBYLS and 8.3.1 beamlines at the ALS, and National Center for Research Resources grant RR-15301 for the Northeastern Collaborative Access Team beamlines at 24-ID at the APS) and by the Department of Energy (grants DE-AC03 76SF00098 for the 12.3.1 and 8.3.1 beamlines at the ALS and DE-AC02-06CH11357 for the APS).

Supporting Online Material

www.sciencemag.org/cgi/content/full/325/5943/1014/DC1
Materials and Methods

Figs. S1 and S2

Tables S1 to S3

References

Movies S1 and S2

21 April 2009; accepted 1 July 2009

10.1126/science.1175275

Dopamine Controls Persistence of Long-Term Memory Storage

Janine I. Rossato,^{1,2} Lia R. M. Bevilacqua,^{1,2} Iván Izquierdo,^{1,2}
Jorge H. Medina,^{1,3,4} Martín Cammarota^{1,2,3*}

The paradigmatic feature of long-term memory (LTM) is its persistence. However, little is known about the mechanisms that make some LTM last longer than others. In rats, a long-lasting fear LTM vanished rapidly when the D1 dopamine receptor antagonist SCH23390 was injected into the dorsal hippocampus 12 hours, but not immediately or 9 hours, after the fearful experience. Conversely, intrahippocampal application of the D1 agonist SK38393 at the same critical post-training time converted a rapidly decaying fear LTM into a persistent one. This effect was mediated by brain-derived neurotrophic factor and regulated by the ventral tegmental area (VTA). Thus, the persistence of LTM depends on activation of VTA/hippocampus dopaminergic connections and can be specifically modulated by manipulating this system at definite post-learning time points.

Relevant environmental changes trigger transient dopamine-dependent states in the hippocampus that favor memory encoding and synaptic potentiation, perhaps by attaching motivational connotations to experiences (1–4). The ventral tegmental area (VTA) is critical for assessing the significance of punishments and rewards (5), and it has been postulated that a VTA/hippocampus dopaminergic loop controls the entry

of information into long-term memory (LTM) (6). Dopamine regulates the expression of proteins essential for the establishment of lasting neuronal plasticity, such as brain-derived neurotrophic factor (BDNF) (7). In rats, we recently demonstrated that in order to persist, fear LTM requires BDNF expression in the hippocampus 12 hours after training (8). We have now investigated the role of hippocampal dopamine and the VTA on LTM persistence.

The effect of hippocampal dopamine on neuronal plasticity and LTM formation is mainly mediated by D1 receptors (4, 9). To test whether D1 receptors are also involved in LTM persistence, we used a one-trial, step-down, inhibitory avoidance task (IA) in rats (10). IA training can be attuned to induce short- or long-lasting LTM. Training with a weak footshock generated a LTM lasting 2 days or less. Conversely, training with a strong footshock induced a persistent LTM, lasting over 14 days [Fig. 1A; $t_{(18)} = 4.40$, $t_{(18)} = 12.16$, $t_{(18)} = 6.60$, $P < 0.001$]. Immediately or 9 or 12 hours after strong training, rats received the D1 receptor antagonist SCH23390 (1.5 μ g per side) in the CA1 region of the dorsal hippocampus. LTM was tested 2, 7, or 14 days later. SCH23390 had no effect on LTM when given immediately or 9 hours after training. However,

¹Centro de Memória, Instituto do Cérebro, Pontifícia Universidade Católica do Rio Grande do Sul, Porto Alegre, Brazil.

²Instituto Nacional de Neurociência Translacional, Conselho Nacional de Desenvolvimento Científico e Tecnológico, Brazil.

³Instituto de Biología Celular y Neurociencias "Prof. Dr. Eduardo de Robertis," Universidad de Buenos Aires, Buenos Aires, Argentina. ⁴Departamento de Fisiología, Universidad de Buenos Aires, Buenos Aires, Argentina.

*To whom correspondence should be addressed. E-mail: mcammaro@terra.com.br or martin.cammarota@puccs.br

when administered 12 hours after training, SCH23390 induced amnesia 7 and 14 but not 2 days later [Fig. 1B; $t_{(14)} = 5.30$, $P < 0.001$, and $t_{(14)} = 3.59$, $P < 0.01$]. In accordance with this result, when injected 12 hours after weak training, the D1 receptor agonist SKF38393 (12.5 μg per side) enhanced LTM 7 and 14 but not 2 days later [Fig. 1C; $t_{(14)} = 3.84$ and $t_{(14)} = 3.03$, $P < 0.01$]. Intra-CA1 infusion of SKF38393 immediately or 9 hours after weak training did not affect LTM. Co-infusion of SCH23390 12 hours after weak training antagonized the facilitatory effect of intra-CA1 SKF38393 (fig. S1).

Hippocampal D1 receptors are coupled to cyclic adenosine monophosphate (cAMP)-dependent protein kinase (PKA) activation. Thus, we investigated the role of this kinase on LTM persistence. Intra-CA1 infusion of 8-bromoadenosine-3',5'-cyclic monophosphate (8Br-cAMP) immediately after weak training increased LTM at all post-training times analyzed. Application of 8Br-cAMP (2.5 μg per side) 12 hours after training enhanced retention 7 and 14 but not 2 days later [Fig. 1D; $t_{(14)} = 2.40$ and $t_{(14)} = 2.68$, $P < 0.05$]. Similarly, intra-CA1 infusion of the PKA inhibitor PKI (6.5 μg per side) immediately after strong training hindered LTM 2, 7, and 14 days after training, but when infused 12 hours after training it only hampered retention 7 and 14 days thereafter [Fig. 1E; $t_{(18)} = 11.48$ and $t_{(18)} = 4.57$, $P < 0.001$]. Co-infusion of SKF38393 did not prevent the amnesia induced by PKI [Fig. 1F; $t_{(18)} = 4.08$, $P < 0.001$].

The firing pattern of midbrain dopamine neurons changes across the sleep/wake cycle

(11), and LTM persistence may depend on the circadian reactivation of PKA (12). However, the effects of SCH23390, SKF38393, PKI, and 8Br-cAMP on LTM were independent of the time of the day at which training was performed (fig. S2).

We next analyzed whether late post-training activation of hippocampal D1 receptors controlled the increase in BDNF required for LTM persistence (8). Strong but not weak IA training increased BDNF levels in dorsal CA1 12 hours after training [Fig. 2A; $F_{(2,11)} = 14.41$, $P < 0.001$; $q = 4.51$]. When given into CA1 11.5 hours after strong training, SCH23390 (1.5 μg per side) blocked the training-induced increase in BDNF [Fig. 2B; $F_{(2,10)} = 8.30$, $P < 0.01$; $q = 3.75$]. Concurring with this, intra-CA1 infusion of SKF38393 (12.5 μg per side) 11.5 hours after weak training increased BDNF levels [Fig. 2C; $F_{(2,12)} = 7.12$, $P < 0.01$; $q = 3.59$]. Intra-CA1 administration of BDNF (0.25 μg per side) 12 hours after weak training increased LTM persistence, whereas infusion of function-blocking antibody to BDNF (1 μg per side) at the same time after strong training induced its rapid decay (fig. S3). Co-infusion of BDNF reversed the amnesic effect of SCH23390 and PKI given into CA1 12 hours after strong training [Fig. 2D; $F_{(4,36)} = 24.21$, $P < 0.001$; $t = 5.81$ and $t = 5.21$], whereas co-infusion of function-blocking antibody to BDNF impaired the increase in persistence caused by SKF38393 and 8Br-cAMP given 12 hours after weak training [Fig. 2E; $F_{(4,34)} = 13.73$, $P < 0.001$; $t = 5.47$ and $t = 3.98$], indicating that the action of hippocampal BDNF

on LTM persistence is downstream D1 receptors. Amnesia caused by intra-CA1 administration of function-blocking antibody to BDNF 12 hours after strong training was unaffected by co-infusion of SKF38393 or 8Br-cAMP. Neither SCH23390 nor PKI affected the facilitation induced by BDNF infused into CA1 12 hours after weak training (fig. S3).

Tyrosine hydroxylase (TH) catalyzes the rate-limiting step in catecholamine biosynthesis. Phosphorylation at Ser⁴⁰ (pSer⁴⁰) increases TH activity to allow for replenishment of neurotransmitter stores during increased catecholamine signaling (13). To investigate whether LTM maintenance is indeed associated with activation of the hippocampal dopaminergic system late after acquisition, we measured TH phosphorylation. Strong but not weak IA training increased pSer⁴⁰-TH in dorsal CA1 12 hours after training and this increase was blocked by intra-VTA infusion of lidocaine (10 μg per side) 11.5 hours after training (fig. S4).

It has been proposed that VTA/hippocampus connections gate relevant information into LTM through a D1/D5-dependent mechanism (6). Dopamine modulates late long-term potentiation (LTP) in CA1 (14), whereas VTA *N*-methyl-D-aspartate receptors (NMDARs) regulate the development of dopamine-mediated long-term changes in the brain reward circuitry, control the establishment of persistent behaviors, and cause burst discharge of dopamine neurons (15–17). Therefore, we examined whether LTM persistence requires NMDAR activation in the VTA late after training. Intra-VTA infusion of the NMDAR antagonist AP5 (1 μg per side) 12 hours after

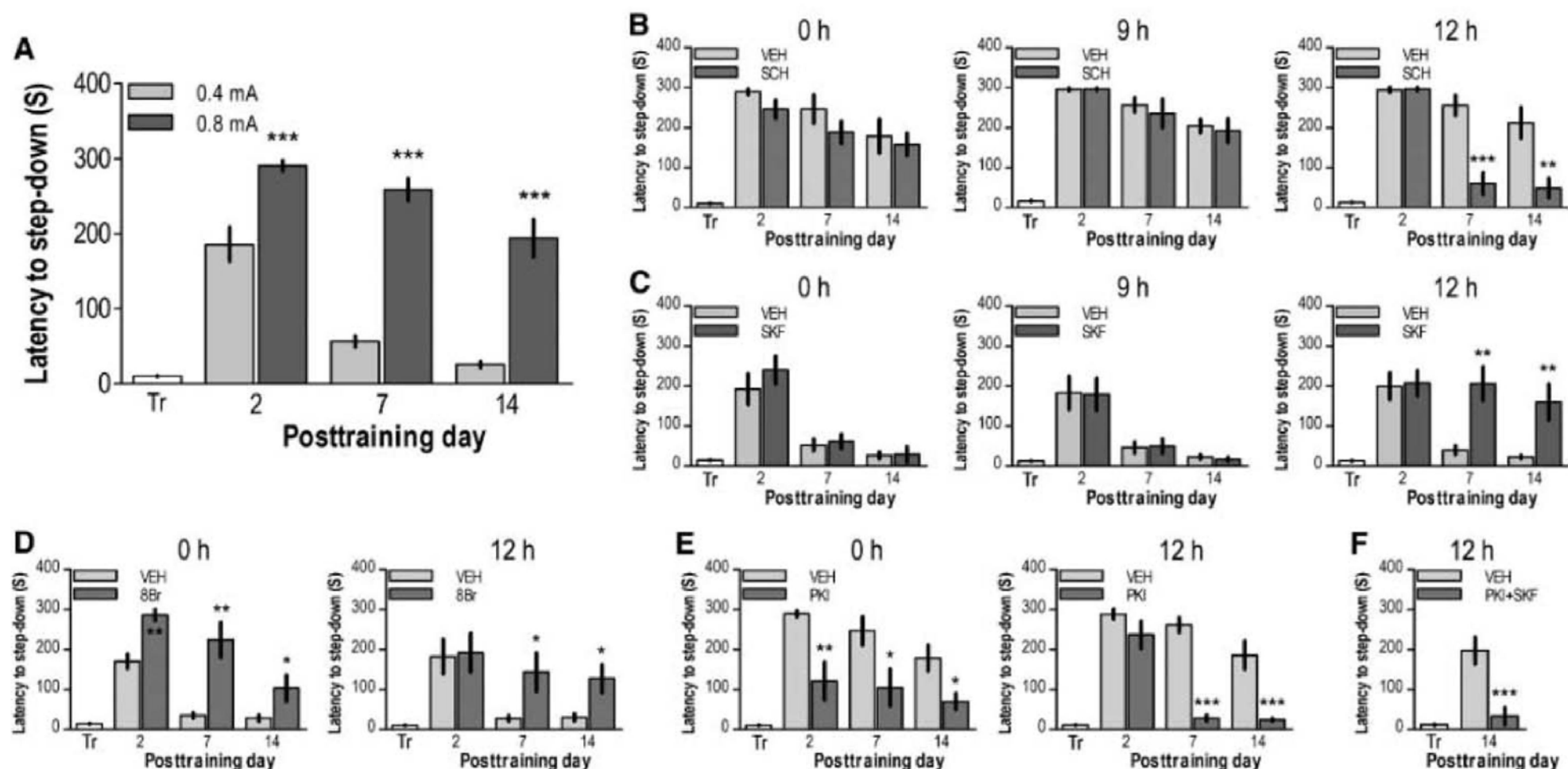


Fig. 1. Activation of D1 receptors in dorsal CA1 12 hours after training modulates LTM persistence. (A) Animals were trained in IA with a weak (0.4 mA for 2 s) or a strong (0.8 mA for 2 s) footshock. (B to E) Animals were trained in IA with a strong [(B) and (E)] or a weak [(C) and (D)] footshock and immediately or 9 or 12 hours later received SCH23390 (B), SKF38393 (C), 8Br-cAMP (D), or PKI (E) into CA1. VEH, vehicle. (F) Animals trained in IA with a strong footshock received SKF38393 plus PKI into CA1 12 hours after training. LTM was assessed either 2, 7, or 14 days after training. $n = 8$ to 10 rats per group.

strong training hindered LTM 14 but not 2 days later [Fig. 3A; $t_{(18)} = 5.15$, $P < 0.001$]. This was prevented by co-infusion of SKF38393 (12.5 μ g per side) or BDNF (0.25 μ g per side) into dorsal CA1 [Fig. 3B; $F_{(3,38)} = 10.93$, $P < 0.001$; $t = 4.36$ and $t = 4.92$]. Amnesia by intra-VTA AP5 was not reversed by co-infusion of SKF38393 into

the nucleus accumbens 12 hours after training (fig. S5). NMDA (0.1 μ g per side) given into the VTA 12 hours after weak training enhanced LTM retention 14 but not 2 days after training [Fig. 3C; $t_{(16)} = 3.59$, $P < 0.01$], an effect blocked by co-injection of SCH23390 (1.5 μ g per side) or antibody to BDNF (1 μ g per side) into CA1

[Fig. 3D; $F_{(3,38)} = 8.86$, $P < 0.001$; $t = 3.74$ and $t = 3.90$]. The increase in CA1 BDNF and pSer⁴⁰-TH caused by strong IA training was blocked by AP5 given into the VTA 11.5 hours after training [Fig. 3E; $F_{(2,11)} = 7.90$, $P < 0.01$; $t = 3.58$ and $F_{(2,9)} = 6.42$, $P < 0.05$; $t = 3.20$], whereas intra-VTA infusion of NMDA 11.5 hours after weak training increased BDNF and pSer⁴⁰-TH in dorsal CA1 30 min later [Fig. 3F; $F_{(2,11)} = 10.97$, $P < 0.01$, $t = 4.41$; and $F_{(2,8)} = 15.36$, $P < 0.01$, $t = 3.41$]. Thus, NMDAR activation in the VTA around 12 hours after training up-regulates the hippocampal dopaminergic system which, through a D1-dependent mechanism, controls the expression of BDNF required for LTM persistence.

A strong footshock is more salient than a weak one. Footshock strength correlates with LTM persistence (Fig. 1A). Because the VTA modulates the fear-arousing properties of footshock (18), we asked whether VTA inactivation immediately after training also affected LTM maintenance. AP5 (1 μ g per side) given into the VTA right after strong training hampered LTM retention 14 but not 2 days after training [Fig. 4A; $t_{(18)} = 3.58$, $P < 0.01$] and blocked the increase in BDNF and pSer⁴⁰-TH that happens in dorsal CA1 12 hours later [Fig. 4B; $F_{(2,11)} = 9.55$, $P < 0.01$, $t = 3.95$; and $F_{(2,9)} = 16.14$, $P < 0.01$, $t = 5.55$]. Conversely, intra-VTA infusion of NMDA (0.1 μ g per side) immediately after weak training enhanced LTM 14 but not 2 days after training [Fig. 4C; $t_{(16)} = 2.12$, $P < 0.05$] and increased BDNF and pSer⁴⁰-TH in dorsal CA1 12 hours thereafter [Fig. 4D; $F_{(2,11)} = 3.95$, $P < 0.05$, $t = 2.45$; and $F_{(2,9)} = 9.39$, $P < 0.01$, $t = 4.12$]. Neither AP5 nor NMDA affected LTM persistence when given into the VTA 9 hours after training (fig. S6). Intra-VTA infusion of the AMPAR antagonist 6-cyano-7-nitroquinoxaline-2,3-dione (0.07 μ g per side) or the γ -aminobutyric acid type A receptor agonist muscimol (0.05 μ g per side) 9 hours after strong training had no effect on retention (fig. S7). Thus, early post-training activation of the VTA is also essential to determine the duration of LTM storage. However, this role is different from that played by the VTA 12 hours later, because it does not involve hippocampal D1 receptors (Fig. 1).

Is there any functional relationship between the early post-training activation of the VTA and the delayed VTA/CA1 dopaminergic interaction relevant for LTM persistence? Intra-CA1 infusion of SKF38393 or BDNF 12 hours after strong training reversed the amnesic effect of the immediate post-training intra-VTA administration of AP5 [Fig. 4E; $F_{(3,33)} = 5.19$, $P < 0.01$; $t = 3.33$ and $t = 3.53$]. Moreover, when given into dorsal CA1 12 hours after weak training, SCH23390 or function-blocking antibody to BDNF hindered the promnesic action of the immediate post-training intra-VTA administration of NMDA [Fig. 4F; $F_{(3,28)} = 5.12$, $P < 0.01$; $t = 3.01$ and $t = 3.29$]. Intra-VTA infusion of NMDA 12 hours after strong training did not reverse the decrease in LTM persistence induced by the

Fig. 2. Late post-training activation of D1 receptors in dorsal CA1 controls the increase in BDNF required for LTM persistence. (A) Animals trained in IA with a weak or a strong footshock were killed 12 hours thereafter; NAI, naïve. (B and C) Rats trained in IA with a strong (B) or a weak (C) footshock received intra-CA1 SCH23390 (B) or SKF38393 (C) 11.5 hours after training and were killed 30 min later. In all cases, the dorsal CA1 was dissected out, and total homogenates were analyzed by immunoblotting with antibodies to BDNF. $n = 4$ or 5 rats per group. (D and E) Animals were trained in IA with a strong (D) or a weak (E) footshock and 12 hours later received SCH23390 plus BDNF (D), PKI plus BDNF (D), SKF38393 plus antibody to BDNF (E), or 8Br-cAMP plus antibody to BDNF (E) into dorsal CA1. LTM was assessed 14 days after training. $n = 7$ to 11 rats per group.

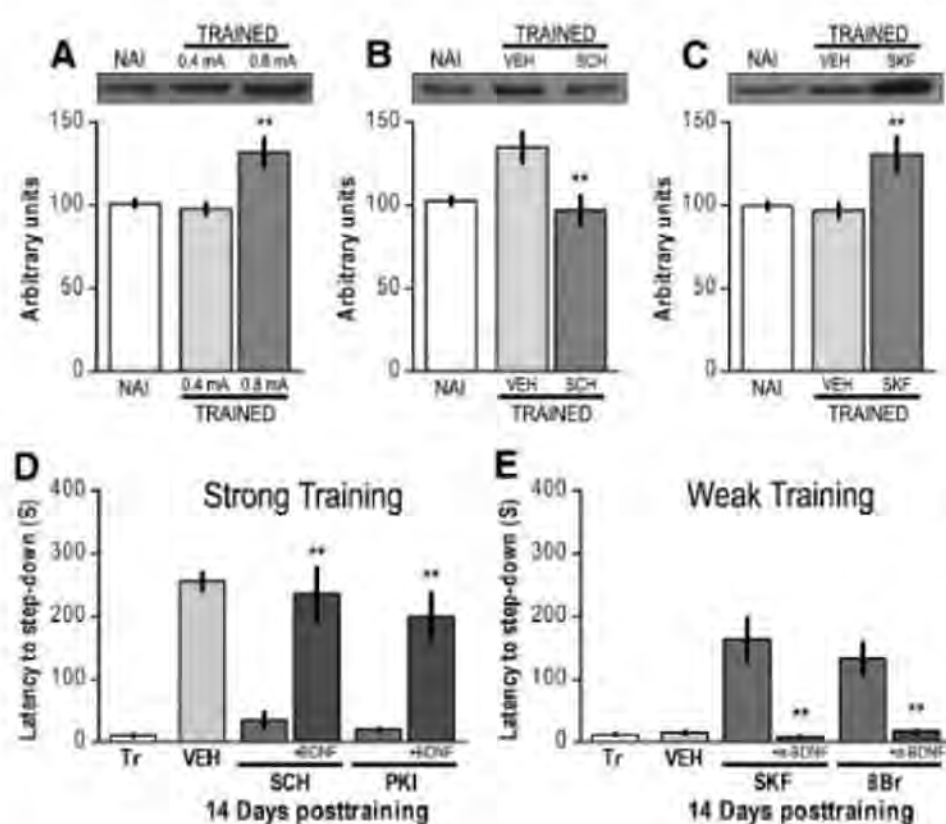
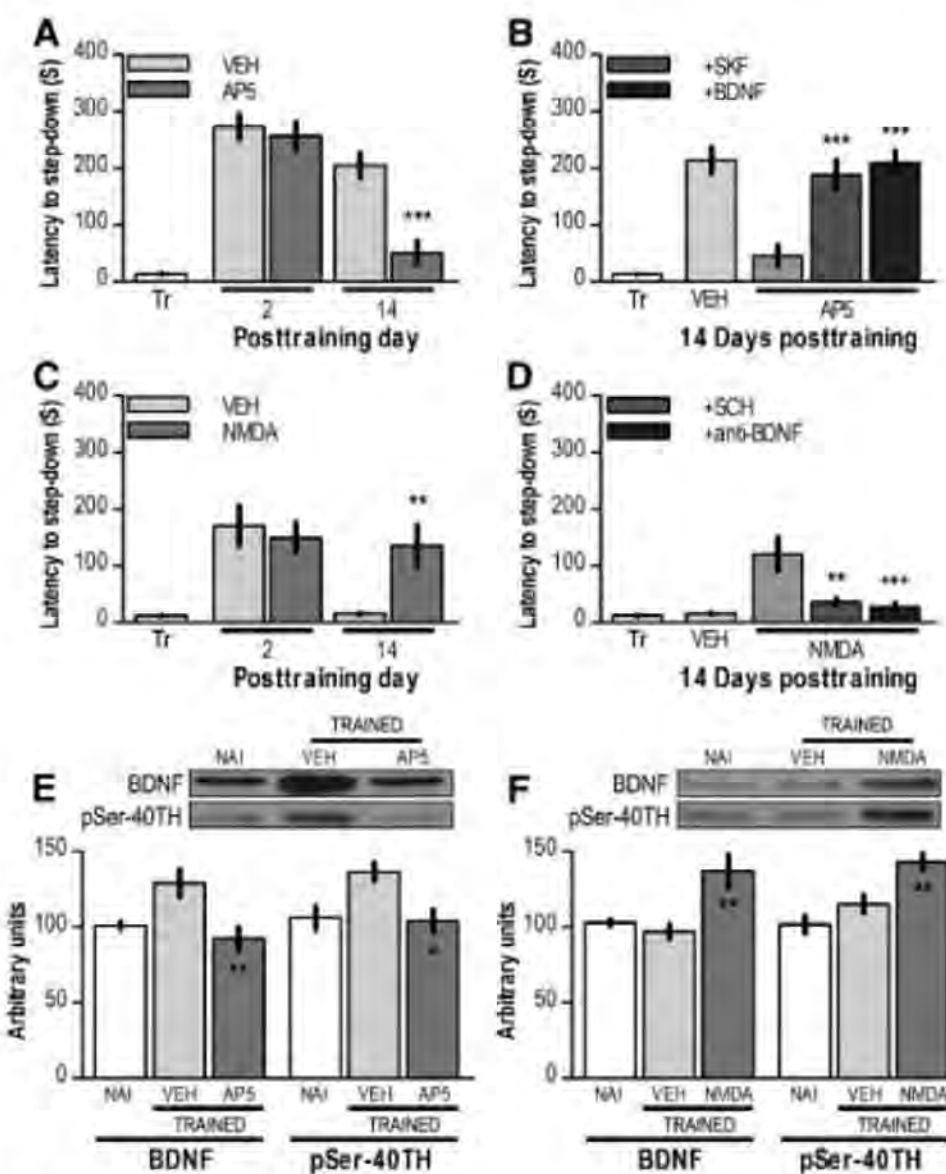


Fig. 3. LTM persistence requires NMDAR activation in the VTA late after training. Animals submitted to strong (A and B) or weak (C and D) IA training received intra-VTA infusions of AP5 (A); intra-VTA AP5 plus intra-CA1 infusions of vehicle, SKF38393, or BDNF (B); intra-VTA NMDA (C); or intra-VTA NMDA plus intra-CA1 infusions of vehicle, SCH23390, or function-blocking antibody to BDNF (D) 12 hours after training. LTM was assessed 2 or 14 days later. $n = 8$ to 11 rats per group. Animals submitted to strong (E) or weak (F) IA training received intra-VTA infusions of AP5 (E) or NMDA (F) 11.5 hours after training and were killed 30 min later. The dorsal CA1 was dissected out, and total homogenates were analyzed by immunoblotting with antibodies to BDNF or pSer⁴⁰-TH. $n = 4$ or 5 rats per group.



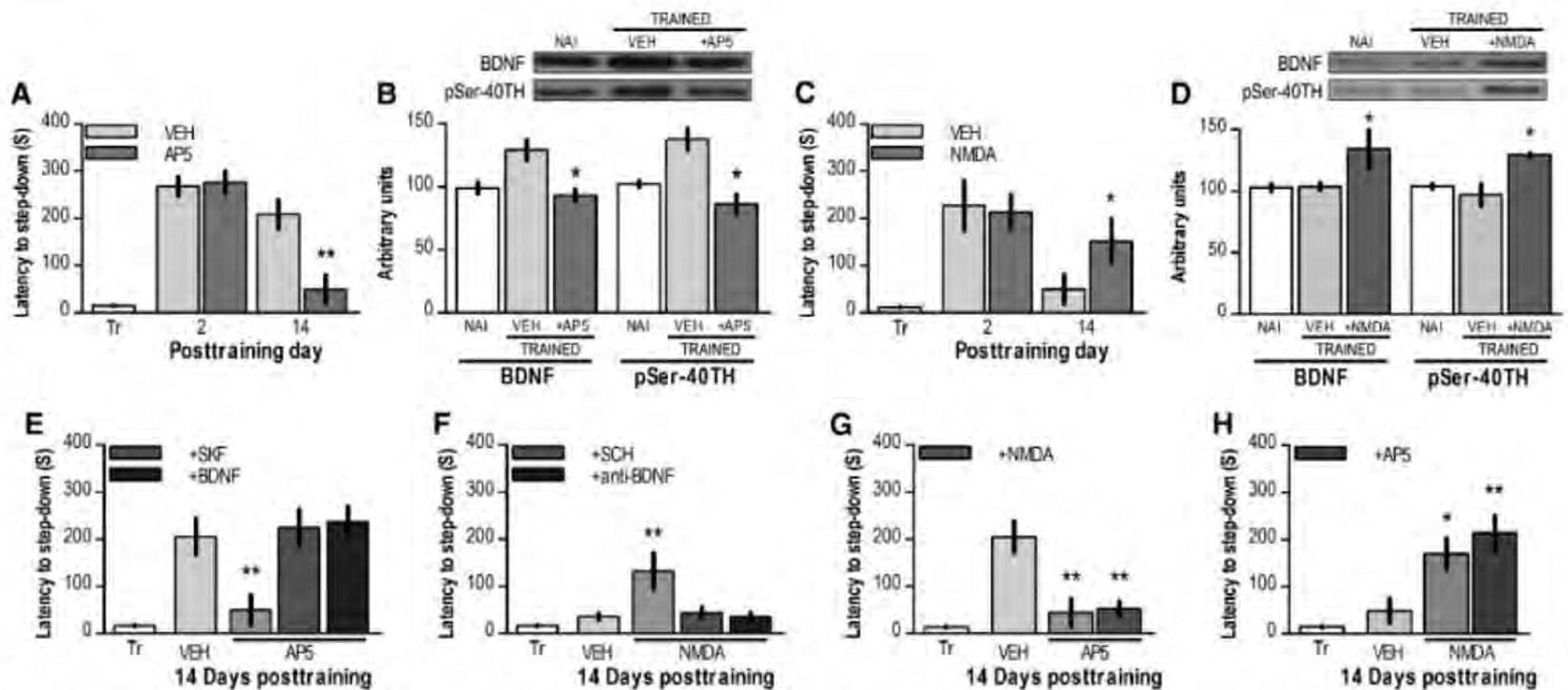


Fig. 4. Early post-training activation of the VTA determines LTM duration. (A) Animals submitted to strong IA training received intra-VTA vehicle or AP5 immediately after training. LTM was tested 2 or 14 days later. (B) Animals were trained and treated as in (A) but killed 12 hours later. The dorsal CA1 was dissected out, and total homogenates were immunoblotted with antibodies to BDNF or pSer⁴⁰-TH. (C) Animals submitted to weak IA training received intra-VTA vehicle or NMDA immediately after training. LTM was tested as in (A). (D) Animals trained and treated as in (C) were killed 12

hours later, and total homogenates were immunoblotted as in (B). Animals submitted to strong (E and G) or weak (F and H) IA training received AP5 [(E) and (G)] or NMDA [(F) and (H)] into the VTA immediately after training and 12 hours later were given intra-CA1 SKF38393 or BDNF (E), intra-CA1 SCH23390 or function-blocking antibody to BDNF (F), intra-VTA NMDA (G), or intra-VTA AP5 (H). LTM was tested 14 days after training. $n = 4$ or 5 or 8 to 10 rats per group for the biochemical and pharmacological experiments, respectively.

immediate post-training administration of AP5 into the VTA [Fig. 4G; $F_{(2,24)} = 11.13$, $P < 0.001$; $t = 4.18$ and $t = 3.98$]. Intra-VTA infusion of AP5 12 hours after weak IA training did not affect the increase in LTM persistence induced by the immediate post-training administration of NMDA into the VTA [Fig. 4H; $F_{(2,21)} = 6.96$, $P < 0.01$; $t = 2.63$ and $t = 3.60$].

Most findings suggest that dopamine modulates LTM encoding and consolidation during or early after training (4, 9). Our data indicate that dopamine also controls the maintenance of LTM storage through a late post-acquisition mechanism involving D1 receptors signaling in dorsal CA1. This regulates the expression of BDNF necessary for LTM persistence and requires NMDAR activity in the VTA immediately and 12 hours after training. Pharmacological activation of NMDAR in the VTA at these critical time points induces BDNF expression in CA1 and converts a rapidly decaying LTM into a persistent one. Moreover, the fact that the reduction in LTM persistence caused by AP5 in the VTA is reversed by intra-CA1 infusion of SKF38393 or BDNF 12 hours after training indicates that long-term maintenance of the learned response depends on a hierarchic sequential process involving VTA-hippocampus dopamine connections.

We propose that the VTA, or the VTA/hippocampus loop (6), is specifically activated during motivationally relevant experiences and, through a process that culminates with a D1-dependent increase of BDNF in the dorsal hip-

pocampus, determines LTM duration. The two periods during which the VTA is required for LTM persistence are linked by a mechanism that does not require the continuous participation of its main excitatory and inhibitory inputs. NMDAR-dependent phenomena that initiate delayed and long-lasting modifications in the efficacy of excitatory synapses on VTA dopamine neurons, probably underlying persistent behaviors, have been described (19, 20), and evidence indicates that activation of D1/D5 receptors in the hippocampus is necessary for the persistence but not induction of synaptic potentiation (21–24).

The idea that the entrance of new information into LTM depends on dopamine mechanisms controlled by VTA/hippocampus interactions has been postulated on the basis of theoretical considerations (2, 6) and is partially supported by empirical data (4). Our findings suggest that the role of these interactions is broader than previously thought. This is important for understanding the neural basis of persistent behaviors and for the development of treatments able to modulate not merely the entry but also maintenance of learned information into LTM.

References and Notes

1. L. P. Sugrue, G. S. Corrado, W. T. Newsome, *Nat. Rev. Neurosci.* **6**, 363 (2005).
2. R. A. Wise, *Nat. Rev. Neurosci.* **5**, 483 (2004).
3. S. Li, W. K. Cullen, R. Anwyl, M. J. Rowan, *Nat. Neurosci.* **5**, 526 (2003).
4. C. M. O'Carroll, S. J. Martin, J. Sandin, B. Frenguelli, R. G. Morris, *Learn. Mem.* **13**, 760 (2006).

5. D. A. Carter, H. C. Fibiger, *Neuroscience* **2**, 569 (1977).
6. J. E. Lisman, A. A. Grace, *Neuron* **46**, 703 (2005).
7. E. Küppers, C. Beyer, *Neuroreport* **12**, 1175 (2001).
8. P. Bekinschtein et al., *Neuron* **53**, 261 (2007).
9. T. M. Jay, *Prog. Neurobiol.* **69**, 375 (2003).
10. I. Izquierdo et al., *Trends Neurosci.* **29**, 356 (2006).
11. L. Dahan et al., *Neuropsychopharmacology* **32**, 1232 (2007).
12. K. L. Eckel-Mahan et al., *Nat. Neurosci.* **11**, 1074 (2008).
13. T. H. Joh, D. H. Park, D. J. Reis, *Proc. Natl. Acad. Sci. U.S.A.* **75**, 4744 (1978).
14. Y. Y. Huang, E. R. Kandel, *Learn. Mem.* **13**, 298 (2006).
15. D. B. Carr, P. W. Kalivas, *Neuron* **59**, 353 (2008).
16. K. Chergui et al., *Eur. J. Neurosci.* **5**, 137 (1993).
17. G. Mereu et al., *Neuroscience* **77**, 1029 (1997).
18. A. Gifkins, Q. Greba, L. Kokkinidis, *Behav. Neurosci.* **116**, 785 (2002).
19. E. Argilli, D. R. Sibley, R. C. Malenka, P. M. England, A. Bonci, *J. Neurosci.* **28**, 9092 (2008).
20. D. Engblom et al., *Neuron* **59**, 497 (2008).
21. N. Lemon, D. Manahan-Vaughan, *J. Neurosci.* **26**, 7723 (2006).
22. Y. Y. Huang, E. R. Kandel, *Proc. Natl. Acad. Sci. U.S.A.* **92**, 2446 (1995).
23. S. Navakkode, S. Sajikumar, J. U. Frey, *Neuropharmacology* **52**, 1547 (2007).
24. U. Frey, H. Schroeder, H. Matthies, *Brain Res.* **522**, 69 (1990).
25. This work was supported by the Conselho Nacional de Desenvolvimento Científico e Tecnológico and Coordenação de Aperfeiçoamento de Pessoal de Nível Superior (Brazil) and the Consejo Nacional de Investigaciones Científicas y Técnicas and Agencia Nacional de Promoción Científica y Tecnológica (Argentina).

Supporting Online Material

www.sciencemag.org/cgi/content/full/325/5943/1017/DC1
Materials and Methods
Figs. S1 to S7
References

20 February 2009; accepted 9 July 2009
10.1126/science.1172545

Protein Precipitation Cartridge

The 1ml Protein Precipitation Cartridge combines the proven operational benefits of the proprietary p3 technology with the low cost and convenience of a cartridge-based separation method. Incorporating a novel, treated dual matrix frit, the new cartridge eliminates the wetting out and leaking of sample associated with many traditional protein precipitation products before the application of vacuum. The treated frit matrix also maintains high flow rates enabling quick sample preparation times.

Porvair Sciences

For information +44-1372-824290
www.porvair.com



Vascular Research Tools

EndoGRO products for vascular research include human umbilical vein endothelial cells (HUVEC) and advanced media formulations for endothelial cell culture. EndoGRO advanced media products include four uniquely optimized formulations for large vessel and microvascular endothelial cells, as well as low-passage HUVEC. These formulations have lower serum concentrations than standard endothelial cell culture media, yet have been shown to support endothelial cell growth rates that exceed other commercially available serum-containing media, while maintaining excellent cell morphology. In addition, the media have no phenol red or antimicrobials, which can cause cell stress and mask natural biological processes.

Millipore

For information 800-548-7853
www.millipore.com

General Purpose Centrifuge

The Sorvall lines are 3-liter, general purpose centrifuges. The Sorvall ST 40 series provides ergonomic advancements for everyday sample preparations. The Sorvall Legend XT centrifuges offer high throughput processing. Both lines feature the Auto-Lock III rotor system, which enables 5-second rotor exchange without the need for tools for fast switching between applications. Operation is further simplified by the motorized lid latch and the ClickSeal bucket sealing system with its glove-friendly, one-handed open/close capability for certified biocontainment of samples. Rotor management SMART-Spin technology optimizes acceleration, braking, temperature control, and load balance for smooth runs and reproducible data. The user-friendly, backlit interface provides detailed information on operating parameters and the dedicated fast-keys enable immediate access to frequently used programs.

Thermo Fisher Scientific

For information 508-742-5254
www.thermofisher.com

Chemometric Software

The WITec Project Plus software package for advanced data evaluation and chemometric image processing features various tools for multivariate analysis in the fields of confocal Raman imaging and scanning probe microscopy, such as cluster analysis and principal component analysis. Thus, hidden structures in the images can be visualized automatically, leading to quick and consistent data interpretation. In addition, a variety of advanced patent-pending analysis

tools and algorithms enable comprehensive and user-friendly computerized data evaluation and image generation. The speed with which the extensive calculations behind the various algorithms and procedures can be executed provides a new level of analytical capability. WITec Project Plus can be obtained as an add-on package for the WITec Project data evaluation software.

WITec

For information +49-(0)-731-140-70-0
www.witec.de

Microplates

New Polypropylene Microplates 96 and 384 feature a high level of transparency, OptiTrack high-contrast alphanumeric labeling matrix, and innovative RecoverMax well geometry for maximum sample recovery. The ultraclear wells, combined with the OptiTrack labeling, make sample and well identification faster and less error-prone than conventional polypropylene microplates. The plates are also available in high contrast white or black for improved signal-to-noise ratio for fluorescence and luminescence readings and in LoBind DNA and LoBind Protein.

Eppendorf North America

For information 800-645-3050
www.eppendorfnna.com

Particle Size Measurement

A particle size measurement principle called induced grating (IG) allows users to measure nanoparticles with high sensitivity and reproducibility. Shimadzu's new IG-1000 particle size analyzer applies the IG method to measuring single nanoparticles. The IG-1000 offers advantages over the dynamic light scattering methods typically used. The sensitivity is the same when measuring a 1-nm particle or a 100-nm particle. Interference from clustering or contamination is significantly reduced or eliminated. The IG method eliminates interferences by using optical signals emitted by the diffraction grating formed by the particles. Even in the single nano region, users can obtain a satisfactory signal-to-noise ratio and stable measurement. The instrument's workflow involves three simple steps: inject the sample, insert the electrode, and begin analysis. It can measure particles in the 0.5 to 200 nm range in about 30 seconds.

Shimadzu

For information 800-477-1227
www.shimadzu.com

Electronically submit your new product description or product literature information! Go to www.sciencemag.org/products/newproducts.dtl for more information.

Newly offered instrumentation, apparatus, and laboratory materials of interest to researchers in all disciplines in academic, industrial, and governmental organizations are featured in this space. Emphasis is given to purpose, chief characteristics, and availability of products and materials. Endorsement by *Science* or AAAS of any products or materials mentioned is not implied. Additional information may be obtained from the manufacturer or supplier.

Release The Power of Science



Science Careers Classified Advertising

For full advertising details, go to ScienceCareers.org and click For Employers, or call one of our representatives.

UNITED STATES & CANADA

E-mail: advertise@sciencecareers.org
Fax: 202-289-6742

Daryl Anderson
US Sales Manager
Phone: 202-326-6543

Tina Burks
Midwest/Canada
Phone: 202-326-6577

Alexis Fleming
East Coast
Phone: 202-326-6578

Nicholas Hintibidze
West Coast/South Central
Phone: 202-326-6533

Online Job Posting Questions
Phone: 202-326-6577

EUROPE & INTERNATIONAL

E-mail: ads@science-int.co.uk
Fax: +44 (0) 1223 326532

Tracy Holmes
Associate Director, Science Careers
Phone: +44 (0) 1223 326525

Alex Palmer
Phone: +44 (0) 1223 326527

Dan Pennington
Phone: +44 (0) 1223 326517

Susanne Kharraz Tavakol
Phone: +44 (0) 1223 326529

Lisa Patterson
Phone: +44 (0) 1223 326528

To subscribe to Science:

In US/Canada call
202-326-6417 or 1-800-731-4939.
In the rest of the world call
+44 (0) 1223 326515.

Science makes every effort to screen its ads for offensive and/or discriminatory language in accordance with US and non-US law. Since we are an international journal, you may see ads from non-US countries that request applications from specific demographic groups. Since US law does not apply to other countries we try to accommodate recruiting practices of other countries. However, we encourage our readers to alert us to any ads that they feel are discriminatory or offensive.

Science Careers

From the journal Science



POSITIONS OPEN

UNIVERSITY OF WYOMING

CONSERVATION BIOLOGIST University of Wyoming

The Department of Botany and the Department of Zoology and Physiology at the University of Wyoming invite applications for a full-time, nine-month, tenure-track faculty position at the **ASSISTANT PROFESSOR** level, starting August 2010. Truly exceptional candidates at the **ASSOCIATE** or **FULL PROFESSOR** level may be considered. We seek candidates holding a Ph.D. and who demonstrate a track record of excellence in applied and conceptual aspects of conservation biology. Areas of research emphasis are open, and could include aquatic or terrestrial work, genetic or ecological analysis, and work in tropical, temperate, or arctic biomes. The successful candidate's taxonomic focus will determine whether the primary appointment for this position will be made in botany or zoology and physiology. Responsibilities include development of an active research program, teaching a conservation biology course, and affiliation with the interdepartmental Program in Ecology and the Berry Biodiversity Center. Research strengths in the two departments include ecology, conservation biology, wildlife/fisheries biology, evolutionary biology and systematics, comparative physiology, cell biology/physiology, and neuroscience. The successful candidate will have access to outstanding stable isotope, nucleic acid, microscopy and macromolecular facilities, the Red Buttes Environmental Research Laboratory, and the Rocky Mountain Herbarium.

Interested applicants should send PDF files of their curriculum vitae, a statement of research and teaching interests, three publications that represent their best work, and three letters of recommendation to: **e-mail: zprequest@uwyo.edu**. Further information is available at the Botany Department **website: <http://uwyo.edu/Botany/>** or the Department of Zoology and Physiology **website: <http://uwyo.edu/Zoology/>**. Review of applications will begin 1 October 2009 and continue until a suitable candidate is found. *The University of Wyoming is a Carnegie Foundation Research/Doctoral Extensive Institution, and is an Affirmative Action/Equal Employment Opportunity Employer.*

ASSISTANT PROFESSOR Molecular Arthropod-Host Interactions

The University of Nebraska-Lincoln, through the Institute of Agriculture and Natural Resources, seeks applications to fill a nine-month, tenure-track research (80 percent) and teaching (20 percent) position at the Assistant Professor rank in the Department of Entomology. The successful candidate will be expected to develop a nationally recognized program in stress biology emphasizing the molecular basis of arthropod interactions with plant or animal hosts. Visit **website: <http://entomology.unl.edu>** for complete job description. The position requires a Ph.D. in entomology or related field with emphasis in the molecular investigations of arthropod interactions with plant or animal hosts as they relate to stress biology. Preference will be given to applicants who show experience and commitment to research and teaching, have strong communication skills, ability to bring in extramural funding, and an interest and desire to work cooperatively on multidisciplinary projects.

To apply, go to **website: <http://employment.unl.edu>** (requisition #090448) and complete the faculty academic administrative information form. Attach a letter of application; curriculum vitae; and two personal statements, one describing your research focus/interest and one describing your teaching expertise/experience. Arrange for three letters of reference to be submitted to **e-mail: mweidner1@unl.edu**. Review of applications will begin September 28, 2009, and continue until the position has been filled or the search is closed.

The University of Nebraska has an active National Science Foundation ADVANCE gender equity program, and is committed to a pluralistic campus community through Affirmative Action, Equal Opportunity, work-life balance, and dual careers.

POSITIONS OPEN

FORENSIC BIOLOGIST, ASSISTANT PROFESSOR

The Departments of Entomology (**website: <http://entomology.unl.edu/>**), Biochemistry (**website: <http://biochem.unl.edu/>**), and Food Science and Technology (**website: <http://foodsci.unl.edu/>**) at the University of Nebraska-Lincoln invite applications for a nine-month (academic year), tenure-track faculty position with a 60 percent teaching and 40 percent research appointment supporting the undergraduate Forensic Science degree program. Responsibilities include teaching forensic biology and developing a research program with a focus on forensic DNA analysis and collaborations with faculty in the home department(s).

Ph.D. or equivalent in biochemistry, molecular biology, or related fields required. Preference will be given to applicants who show experience and commitment to research and teaching, have strong communication skills, ability to bring in extramural funding, and an interest and desire to work cooperatively on multidisciplinary projects.

To apply go to **website: <http://employment.unl.edu>** (requisition #090461) and complete the faculty academic administrative information form. Attach a letter of application, curriculum vitae, and two personal statements describing research and teaching interests. Have three letters of reference sent electronically by October 5, 2009, to **e-mail: forensicchair@unl.edu**. Review of applications will begin October 5, 2009, and continue until the position has been filled or the search is closed.

Lincoln, Nebraska, boasts an outstanding quality of life that includes fine culinary and artistic treasures, a budding live music scene, and numerous parks, golf courses, and bike trails. In 2008, WebMD reported that Lincoln was the healthiest city in the United States.

The University of Nebraska has an active National Science Foundation ADVANCE gender equity program, and is committed to a pluralistic campus community through affirmative action, equal opportunity, work-life balance, and dual careers.

ASSISTANT/ASSOCIATE PROFESSOR

The Department of Neural and Behavioral Sciences, The Pennsylvania State University College of Medicine, invites applications for a tenure-track faculty position at the Assistant or Associate Professor level. The successful candidates will be expected to have, or to establish, an active research program in neuroscience. Although candidates in all areas of the subject will be considered, we are particularly interested in candidates investigating either issues of plasticity at the cellular and molecular levels or aspects of neural development. The Department of Neural and Behavioral Sciences provides a competitive startup package and excellent core facilities. There are also opportunities for collaborative research and participation in graduate training programs. Candidates should hold a Ph.D., M.D., or equivalent degree, and should send curriculum vitae, statement of research interests and goals, and contact information for three references to: **Search Committee, Department of Neural and Behavioral Sciences, H109, Penn State College of Medicine, Box 850, 500 University Drive, Hershey, PA 17033**. Materials accepted until position is filled. *Penn State is committed to Affirmative Action, Equal Opportunity and the diversity of its work force.*

NEUROINFORMATICIAN

Department of Neurology, University at Buffalo

Full-time Faculty Position at State University of New York, Buffalo for Ph.D.-level with training in informatics/computer science and interest in the application of advanced computational expertise in clinical research. Focus on multidisciplinary translational research for neurological disease in areas including biomedical ontology, neurological disease phenotypes, measures of brain functioning, and neuroimage analysis. May include teaching. For more information or to apply, please visit: **website: <http://www.ubjobs.buffalo.edu>**. Posting #0900290.

FACULTY POSITION DEVELOPMENTAL GENETICS

The Department of Biological Sciences at Vanderbilt University seeks candidates to fill an open rank faculty position in developmental genetics. Research of candidates will be considered in all areas of development, with emphasis on early development in vertebrates (including stem cell research) or plant developmental genetics. We desire candidates whose interests broadly overlap the interests of our current faculty. Central criteria for the position are excellence in research and the ability to teach undergraduate and graduate students with a high level of effectiveness. For information about the Department, visit our website: <http://sitemason.vanderbilt.edu/biosci>. For information about developmental biology at Vanderbilt, see <http://www.mc.vanderbilt.edu/devbio/>.

Applicants should send a letter of application together with a curriculum vitae, a statement of current and future research interests, three letters of recommendation, teaching evaluations, if available, and selected reprints to: **Developmental Genetics Search Committee, Department of Biological Sciences, Vanderbilt University, VU Station B 351634, Nashville, TN 37235-1634 U.S.A.** Review of applicants will begin **October 1, 2009**, and will continue until the position has been filled.

Vanderbilt University is an Affirmative Action/Equal Opportunity Employer. Women and under-represented minority candidates are especially encouraged to apply.



The RIKEN Initiative Research Unit Program Unit Leader

Targeted Research Areas:

Environment and energy science or bioengineering research

Contract Period:

Maximum of five years
Upon completion of the initial five-year term and following a midterm evaluation, the unit leader may be recommended for a limited-term or permanent PI position as Associate Chief Scientist, allowing continuation of research, if desired.

Remuneration and Allowances, Research Budget:

(1) Salary will be 10.9 million yen/year (pre-tax) and commuting and housing allowances will be provided per RIKEN policy.
(2) A research budget of approximately 38.5 million yen/year from which the unit leader is expected to recruit and hire several research and technical staff persons will be provided. Depending on the circumstances, the first year budget may be supplemented with 10 million yen as startup funds.

Application Deadline: 5 pm on 30 October 2009, Japan Standard Time

Details can be found at: <http://www.riken.go.jp/engn/r-world/info/recruit/index.html>

If you have questions regarding application, please send an email to iru@riken.jp.

Boehringer Ingelheim ranks among the world's 20 leading pharmaceutical corporations. Our vision drives us forward. It helps us to foster value creation through innovation in our company and to look to the future with constantly renewed commitment and ambition.



Boehringer Ingelheim RCV Vienna is home to **Boehringer Ingelheim's dedicated drug discovery center for innovative cancer medicines.** A team of **more than 200 scientists and technicians, joining their expertise in cancer biology and genomics, pharmacology, medicinal chemistry, structural research, high-throughput screening and Discovery ADME,** drive our effort to identify and profile **novel oncology drugs.** In our Department of Lead Discovery we are currently looking for a highly motivated and independent scientist as:



Group Leader/Associate Director (m/f) Cancer Drug Discovery

Your responsibilities:

- Target selection and validation for new cancer drug discovery projects
- Joint effort with medical experts to define distinct therapeutic concepts for novel cancer targets, capitalizing on our expertise and capabilities for chemically synthesized "small-molecule drugs" as well as protein therapeutics
- Discovery of lead compounds using state-of-the-art technologies: high throughput screening, fragment-based screening, structural research, computational methods
- Profiling of small molecule leads and drug candidates in cellular cancer models
- Identification and management of external alliances with academia and biotech companies

Your qualifications:

- Ph.D. in biology, biochemistry, chemistry, pharmacology or related discipline; or M.D.-Ph.D. degree
- Post-doctoral experience with strong publication record, expertise in cancer biology and cancer genomics essential
- 3+ years experience in a successful pharmaceutical or biotech company with hands-on experience and documented leadership role in project work; or 3+ years of independent work in academia, with focus on cutting-edge cancer research (stellar publication record essential)
- Proven management skills relating to inter-disciplinary project work and team building
- Excellent communication skills

As Group Leader you will head a research team of 12-15 scientists and technicians working in 3-4 laboratories. In addition to the above you will contribute to in-licensing evaluations, participate in multi-disciplinary project teams and foster close interactions with **Boehringer Ingelheim's** independently operating basic research institute in Vienna, the I.M.P. (Institute of Molecular Pathology). Our working language is English.

If you are looking for an intellectual challenge, state-of-the-art facilities and a research driven environment please apply for this position on our homepage and send us your application including a CV with a detailed description of your relevant experience quoting our **reference number 531:**

www.boehringer-ingelheim.at

Boehringer Ingelheim RCV GmbH & Co KG
Human Resources
Personnel Development & Recruiting
Dr.-Boehringer-Gasse 5-11
1121 Wien

Informal inquiries may be directed to Prof. Dr. Norbert Kraut (telephone +43 1 80105 2783, E-Mail Norbert.Kraut@boehringer-ingelheim.com)

Positions @ NIH

THE NATIONAL INSTITUTES OF HEALTH

Help Us Help Millions

Staff Scientist

The National Institute of Allergy and Infectious Diseases (NIAID), a major component of the National Institutes of Health, is recruiting a **staff scientist** in the **Cellular Biology Section (CBS)** of the **Laboratory of Viral Diseases (LVD)** in the **Division of Intramural Research (DIR)**.

The principal scientific goal of the section is to extend basic understanding of virus-host interactions at the level of cells and animals. Major research projects include 1) real-time imaging of virus-host interactions using multiphoton intravital microscopy, 2) understanding generation of MHC class I peptide ligands from endogenous and exogenous viral antigens, and 3) understanding influenza A virus pathogenicity. The laboratory is well equipped with a number of state-of-the-art, laser-based microscopes and associated equipment and has access to the outstanding NIAID microscope core facility.

For additional information about CBS/LVD/DIR, visit: www.niaid.nih.gov/labs/aboutlabs/LVD/CellBiologyAndViralImmunologySection.

Qualifications:

We are seeking a highly motivated, independent, and creative individual with a Ph.D. and/or M.D. and 5 years or more of light microscopy experience. Preference will be given to candidates experienced in confocal live cell imaging techniques such as FRET, FRAP, FLIP, FLIM, and microinjection, as well as intravital multiphoton microscopy. Experience with electron microscopy and/or cryo- and vibratome-based light microscopy is a plus.

National Institute of Allergy and Infectious Diseases

Application Information:

Provide curriculum vitae, letter of research interests, and names and addresses of three references to Jonathan W. Yewdell, M.D., Ph.D., Chief, CBS, LVD, NIAID at jyewdell@nih.gov.

For further information about NIAID and to view additional career opportunities, visit us on the Web at www.niaid.nih.gov/careers/ssd.



U.S. DEPARTMENT OF HEALTH AND HUMAN SERVICES
National Institutes of Health



National Institute of Allergy and Infectious Diseases

Proud to be Equal Opportunity Employers

THE NIH IS DEDICATED TO BUILDING A DIVERSE COMMUNITY IN ITS TRAINING AND EMPLOYMENT PROGRAMS



WWW.NIH.GOV

NIAID needs you because the world needs us!

Announcing the NIAID Malaria Infection Biology Research and Postdoctoral and Graduate Training Program

Offering top young scientists opportunities to explore the complex interactions between *Plasmodium falciparum* and the host immune system

Infection biology is an emerging field that brings together immunologists and microbiologists to explore the complex set of feedback loops between pathogens and host immune systems.

The National Institute of Allergy and Infectious Diseases (NIAID) created the NIAID Malaria Infection Biology (MIB) Research and Training Program to improve understanding of the interplay among the human innate and adaptive immune systems, the mosquito's innate immune system, and the most deadly malaria parasite, *Plasmodium falciparum*.

The MIB Program aims to uncover critical new knowledge about these cellular and molecular interactions and to train the next generation of research scientists in this new and exciting field.

Program Benefits

- Conduct independent, cutting-edge research in a mentored environment in the United States and in malaria-endemic regions of the world.
- Access the outstanding research resources and facilities at NIH and at NIAID's International Centers for Excellence in Research.
- Receive mentoring from senior immunologists, malaria and vector biologists, and vaccinologists.
- Attend weekly seminars given by distinguished scientists.
- Develop public-speaking and other skills crucial to advancing your scientific career.

Help Us Help Millions



Microinjection of adult female mosquito.
Credit: J. Rodrigues

NIAID

National Institute of Allergy and Infectious Diseases

Eligibility

The MIB program is open to postdoctoral fellows and graduate students. Applications are accepted throughout the year, and decisions on admission to the program are made in a timely fashion after application receipt.

For instructions on how to apply, visit the NIAID MIB Program Web site at www.niaid.nih.gov/labs/training/mibProgram.



U.S. DEPARTMENT OF HEALTH AND HUMAN SERVICES
National Institutes of Health



National Institute of Allergy and Infectious Diseases

Proud to be Equal Opportunity Employers

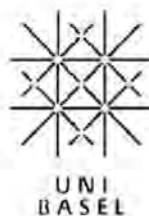
UNIVERSITÄT BASEL

Professor in Structural Biology

The Biozentrum of the University of Basel invites applications for a Professorship (open rank) in its Core Program «Structural Biology and Biophysics». The ideal candidate will combine X-ray crystallography with a broad range of biophysical, biochemical and cell biological techniques to solve biological problems related to complex nanomachines and/or communication systems. With a strong research record and proven communication skills, the successful candidate will strengthen the research portfolio of the Biozentrum and actively participate in teaching at the undergraduate and postgraduate level. In addition, he/she is invited to interact with other Life Science institutions in Basel as well as the Paul-Scherrer Institute (Swiss Light Source). The Biozentrum offers an outstanding scientific environment, a competitive salary and an attractive research endowment, while Basel provides a high standard of living and a superb cultural atmosphere.

Applications, including CV, list of publications and a short research summary, should be addressed to Prof. Dr. Eberhard Parlow, Dean, Faculty of Science, University of Basel, Klingelbergstrasse 50, 4056 Basel, Switzerland, and also be provided in electronic form (pdf or zip) to Dekanat-Philnat@unibas.ch. For informal enquiries please contact Prof. Dr. Erich A. Nigg (erich.nigg@unibas.ch, phone: +41 (0)61 267 16 56).

The deadline for receipt of applications is 30 October 2009. The University of Basel is an equal opportunity employer and encourages applications from female candidates.



TRANSLATIONAL HEALTH SCIENCE AND TECHNOLOGY INSTITUTE (THSTI)

(An autonomous institute of the Department of Biotechnology, Govt. of India)

Present location at the National Institute of Immunology, JNU Complex, Aruna Asaf Ali Marg, New Delhi-110067, INDIA

Advertisement for Scientific Positions

The Department of Biotechnology, Ministry of Science & Technology (Government of India) has established the Translational Health Science and Technology Institute (THSTI), an autonomous institution, as a part of the interdisciplinary Health Biotech Science Cluster, located in Faridabad, Haryana, in the National Capital Region. Major Indian and overseas institutions are mentoring the development of the THSTI. The THSTI is designed to be a dynamic and interactive organization with a mission to conduct innovative translational research and develop research collaborations across disciplines and professions to accelerate the extension of concepts to the improvement of human health. The other members of the cluster include the Regional Center for Biotechnology (RCB) under the aegis of UNESCO, with which THSTI will have seamless scientific collaboration to achieve interdisciplinary expertise. The cluster institutions will have access to state of the art experimental animal facility and platform technology resources.

THSTI intends to set up programs of research in a number of interface areas of relevance to translational research. One major area planned is the biology of childhood diseases and developmental health. This interdisciplinary research programme will be expected to conduct hypothesis-generating and hypothesis-driven research on the biological basis of childhood health and diseases. The generated knowledge will be incorporated in THSTI institutional networks developing diagnostic and therapeutic modalities. Such an interdisciplinary effort will need to knit together expertise from the fields of pediatrics, infectious disease, microbiology, immunology, cell and molecular biology, systems biology, imaging studies, clinical trials and epidemiology, among others. THSTI is looking for highly motivated individuals with expertise in any relevant areas with interests in the child biology domain.

Appointments in this programme will be offered Assistant Professor upwards at various levels depending on the quantum of experience and the quality of the scientific productivity. Candidates must have an MD or PhD degree from a recognized university in any area of natural sciences. A demonstrated record of scientific output in the form of recent peer-reviewed publications in scientific journals of high international repute and/or internationally valid and productive patents is essential. Post-doctoral experience with some indication of independent scientific thinking is a prerequisite. Appropriate levels of experience and scientific accomplishment will be considered for appointments at various levels of seniority. Investigators will be provided shared laboratory space and adequate start-up resources. They are expected eventually to generate extramural project-based funding for their research programmes.

The permanent laboratories of THSTI will come up at Faridabad over the next three years. Interim laboratories will function from Gurgaon in the South Delhi area which has adequate housing, transportation and schooling facilities. Campus housing may be made available when the institution moves to the Faridabad campus.

Interested scientists holding Indian citizenship are requested to send their bio-data containing details of qualification, positions held, professional experience/distinctions and copies of notable publications, with names and email addresses of three potential referees, to the Manager (A&F), Translational Health Science and Technology Institute (THSTI), c/o National Institute of Immunology, Aruna Asaf Ali Marg, New Delhi 110067, and a soft copy by email to thsti@nii.res.in. The application should also be accompanied by a two-page note on the proposed scientific programme with particular reference to its connection with child biology. Candidates working in public sector institutions within India are required to have their applications forwarded through proper channels. Applications will be accepted round the year. The first round of appointments is expected to be offered by December 2009, for which applications would be appreciated by the end of September 2009.



ÉCOLE POLYTECHNIQUE
FÉDÉRALE DE LAUSANNE

Faculty Positions in Basic and Translational Cancer Science Swiss Institute for Experimental Cancer Research (ISREC) at Ecole polytechnique fédérale de Lausanne (EPFL)

We seek several outstanding individuals to join the faculty of the Swiss Institute for Experimental Cancer Research (ISREC), one of the four institutes of the School of Life Sciences in the Swiss Federal Institute of Technology Lausanne (EPFL). ISREC intends to expand from its strong foundation in cancer-related research by appointing faculty focused on frontiers in the biology and therapy of cancer. ISREC is based in a new building on the shore of Lake Geneva amidst the EPFL campus and its interactive faculty in life sciences, chemistry and physics, computer science, and engineering. Additionally, ISREC is establishing a division proximal to the new Department of Oncology at the University of Lausanne's medical campus to nucleate translational oncology research. Both divisions of ISREC will pursue innovative approaches to reveal mechanisms of human cancers. An ancillary agenda will involve applying such knowledge to function-based therapeutic targeting of critical pathways and capabilities, in preclinical trials involving mouse models of selected human cancers, linked in due course to proof-of-concept clinical trials in those cancers. Topics of interest for new faculty include: functions and regulation of the tumor microenvironment; mechanisms of angiogenesis, invasion and metastasis; the roles of inflammation in cancer; metabolomics and energetics of tumors and applications of chemical biology and bioengineering to basic and applied cancer research. Appointments into both divisions of ISREC are anticipated.

ISREC faculty members receive core generous support (salary and research funds) with the expectation that their research programs will be complemented by extramural grant support. Participation in undergraduate and graduate teaching is anticipated. ISREC and the School of Life Sciences have an excellent infrastructure, including a number of technology core facilities.

We anticipate appointing a number of tenure track assistant professors of exceptional promise over the next few years into both divisions of ISREC, and are prepared to consider accomplished, ascendant mid-career cancer researchers for appointment as senior faculty.

Candidates are requested to submit via the website below, in separate PDF files, a curriculum vitae with a list of mentors who can provide letters of recommendation, a list of publications (annotated to indicate the candidate's contributions), a brief statement of teaching interests, and a 2–3 page research synopsis that both summarizes current/past research accomplishments and presents a strategic vision for development of the candidate's research program over the next 5–10 years.

While the ISREC faculty search will be ongoing, we will initially consider applications received by **November 1st, 2009**, with the aim to invite a few top candidates for interviews in early 2010.

Applications should be uploaded at
<http://isrecfac.epfl.ch>

Inquiries and questions may be addressed to:

Professor Douglas Hanahan, Director, ISREC
School of Life Sciences, EPFL, Room SV2.816
CH-1015 Lausanne, Switzerland, EM: dh@epfl.ch

For additional information on ISREC, the School of Life Sciences, and EPFL, please consult <http://isrec.epfl.ch/>, <http://sv.epfl.ch>, and <http://www.epfl.ch>, respectively.

EPFL is committed to expanding the ranks of women on its faculty, and qualified women are enthusiastically encouraged to apply.

COLLEGE of CHARLESTON

SCHOOL OF SCIENCES
AND MATHEMATICS

GENOMICS - ASSISTANT PROFESSOR

The Department of Biology, College of Charleston, invites applications for a tenure-track position in Genomics at the Assistant Professor level to begin August, 2010. Candidates must possess a Ph.D. in the biological sciences or a closely related field, a strong commitment to teaching, and an active research program. The particular area of research in genomics and the organism(s) are open, but the selected candidate will be expected to assist with the training of graduate students in the Marine Biology program. Teaching responsibilities may include undergraduate courses in genetics and molecular biology, and a graduate course that complements current genomics offerings in the Marine Biology master's program (<http://www.cofc.edu/marine>). The College of Charleston is a public liberal arts and sciences institution of 12,000 students, with MS degrees in Marine Biology and Environmental Studies, and a commitment to excellence in teaching and research. Information about the Biology Department is available at <http://www.cofc.edu/biology>. Applicants should submit a curriculum vitae, statement of teaching and research interests, copies of relevant publications, and three letters of reference to: **Chair, Genomics Search Committee, Department of Biology, College of Charleston, Charleston, SC 29424**; or (preferred) electronically to genomicssearch@cofc.edu. Screening of applications will begin **September 15, 2009**.

*The College of Charleston is an Equal Opportunity/
Affirmative Action Employer and encourages
applications from women and minorities.*



Ontario Institute
for Cancer Research

Director, Transformative Pathology

The Ontario Institute for Cancer Research (OICR) is seeking a Director of Transformative Pathology to develop an innovative research program in molecular pathology and cytopathology. The Director will join OICR's senior management team which oversees OICR's research plan.

OICR is a new research institute, created by the Government of Ontario to enhance cancer research, particularly translation of new discoveries into effective interventions that impact cancer and promote knowledge-based industries in Ontario.

Qualifications

- An MD with a proven track record in molecular pathology or related discipline(s);
- A relevant international reputation and strong publication record;
- Proven leadership, management experience and communications skills;
- Previous experience in leading multidisciplinary, multi-institutional teams;
- Proven ability to recruit outstanding clinical and basic scientists;
- Excellent and broad understanding of the field of molecular diagnostics and/or therapeutics, genomics, biomarkers, informatics and imaging in oncology;
- Eligible to hold the rank of associate or full professor at an Ontario university.

Conditions of Employment

The Director will devote at least 80 per cent of time to research and may devote up to 20 per cent of time to clinical duties. Academic and clinical appointments may be obtained at the University of Toronto and its affiliated hospitals. The initial appointment is for five years, renewable pending satisfactory review. A competitive salary and benefits package will be negotiated.

Application Process

Candidates are invited to submit a curriculum vitae, a vision statement on the opportunities for OICR to play a lead role in transforming pathology in the health care system and names of three references, electronically to search@oicr.on.ca. For more information about OICR please visit the website at www.oicr.on.ca.

The position will remain open until a suitable candidate is found, however applications are preferred by **November 15, 2009**.



Faculty Leadership Position in Cancer Immunology

The Hollings Cancer Center and the Division of Basic Sciences, Department of Microbiology and Immunology at the Medical University of South Carolina (MUSC) are excited to announce an opening for a mid to senior level

faculty leader to develop the Cancer Immunology Program. Candidates should have a national reputation in cancer immunology, a solid record of collaborative, peer-reviewed funded research, and evidence of leadership ability. This position will allow for additional junior recruitments, and have a leadership role both in the Department and the Cancer Center. The Hollings Cancer Center has recently received designation by the National Cancer Institute, and with its state-of-the-art clinical, research and shared resource facilities, including a new \$5M Center for Cellular Therapy, it has a strong culture of promoting translational research. MUSC has also just recently been awarded the NIH Clinical and Translational Award. MUSC/HCC is looking for an individual who will complement and expand its existing expertise in cancer immunology, which has a strong emphasis in head and neck oncology and T-cell immunology.

Located on the Atlantic coast in South Carolina, Charleston boasts one of the nation's most historic downtown areas and offers a superb quality of life including easy access to ocean beaches, extensive outdoor recreation, and internationally renowned arts and cultural events.

Interested individuals should send their CV, a summary of future research plans and three references to:

Andrew Kraft, M.D.
Director, Hollings Cancer Center
Medical University of
South Carolina
MSC 955
Charleston, SC 29425
campbetb@musc.edu

James Norris, PhD
Chair Department of Microbiology
and Immunology
Medical University of
South Carolina
MSC 504
Charleston, SC 29425
borckadm@musc.edu

MUSC is an Equal Opportunity Employer, promoting workplace diversity.



Technische Universität München

The TECHNISCHE UNIVERSITÄT MÜNCHEN is creating a new core competence in its strategic development through trans-disciplinary teaching and research activities. New professorships are being created to stimulate activity across the faculties. To this end, these professorships will require teaching and research in two or more faculties.

TUM Center for Electrical Mobility Chair for Technical Electrochemistry

A research center for electrical mobility is being developed in the MUNICH SCHOOL OF ENGINEERING with the participation of several faculties of engineering and natural sciences. In this context a new chair for Technical Electrochemistry will be created under the leadership of the faculty for chemistry. A complete concept for an economically and technologically promising electric vehicle of the future will be developed in the Center for Electrical Mobility.

The scientific emphasis of the professorship will be the fundamentals of electrochemistry, in particular in the development of new electrochemical storage for electrical mobility. The professorship is intended to strengthen existing activities in storage cell technology by improving the current technologies as well as developing completely new storage systems. We are looking for an internationally distinguished individual with research achievements in the area of electrochemical systems.

The teaching activity will cover the complete range of electrochemistry as well as energy sciences. The professorship will also include participation in the planned master course of studies for electrical mobility, as well as related courses of studies which will be set up. Appointment is planned at the level of Full Professor (W3).

Formal requirements for the professorship are a university diploma, teaching qualifications and a PhD degree. Excellent research accomplishments are obligatory; these may have been gained outside of academia. Postdoctoral teaching experience or a formal lecturing qualification is required. Applicants should not have passed the age of 52 at the time of their nomination. Well justified exceptions to the age limit are possible.

Persons with disabilities will be given preference over other applicants with comparable qualifications.

The TECHNISCHE UNIVERSITÄT MÜNCHEN is striving to increase the proportion of women in research and education. Female scientists are therefore especially encouraged to apply for this position.

Applications including CV, credentials, publication list, a short overview of research interests and relevant documents should be sent by **September 30, 2009** to **Prof. Dr. Thorsten Bach, Dean of the Faculty of Chemistry, TECHNISCHE UNIVERSITÄT MÜNCHEN, Lichtenbergstr. 4, D-85747 Garching, Germany.**



3M Harry Heltzer Multidisciplinary Chair in Science and Technology

University of Minnesota,
Minneapolis, MN USA

The Graduate School and the Institute of Technology at the University of Minnesota—Twin Cities invites applications and nominations for the position of 3M Harry Heltzer Multidisciplinary Chair in Science and Technology. This is a tenured and endowed position at the rank of associate or full professor (dependent upon qualifications and experience) in the area of physical and biological structures characterization using microscopy and imaging. Candidates must have outstanding academic and research records, with several years of successful research and teaching experience. A Ph.D. degree and dedication to teaching, graduate student advising, and regular and sustained interaction with industry are required. Candidates are sought whose research agenda will contribute to building cross-disciplinary and cross-college collaboration in one or more areas of strategic importance university-wide, including within the Institute of Technology and with other units at the University of Minnesota. This endowed chair is intended to foster industry-university research interaction and collaboration while advancing scientific and technological expertise in new frontiers of knowledge relevant to the Institute of Technology and 3M. Candidates with a background in any relevant areas of science or engineering are encouraged to apply. Department affiliation will depend on the candidate's area of expertise, with the possibility of a joint appointment with one or more units in the Institute of Technology or elsewhere in the University.

Applications should be submitted online at: <https://employment.umn.edu>, under Req. # 154636, and include a cover letter, curriculum vitae (including list of publications), research description/plan, statement of teaching interest, and contact information for three references. Review of applications will begin immediately and continue until the position is filled. For further information, contact **Douglas Ernie** at ernie@umn.edu.

*The University of Minnesota is an
Equal Opportunity Educator and Employer.*



Faculty Position

The North Dakota State University Department of Chemistry and Molecular Biology is accepting applications for a tenure-track faculty position available Fall 2010 in the broadly defined area of **theoretical or computational chemistry/biochemistry**. Appointment at the assistant professor rank is anticipated, but exceptional candidates may be considered for a more senior rank.

Candidates must have a Ph.D. in chemistry, biochemistry or a related field, strong potential to develop an externally funded, nationally competitive research program, demonstrated commitment to teaching at the undergraduate and graduate levels, and strong oral and written communication skills. See <http://www.ndsu.nodak.edu/chemistry/> for information about chemistry and biochemistry at NDSU.

Qualified applicants should apply online at <https://jobs.ndsu.edu> and use posting #0900167. Applications must include a cover letter, curriculum vitae, statement of research and teaching plans, and list at least three professional references. Review of applications will begin **November 1, 2009**, and will continue until the position is filled.

NDSU is an Equal Opportunity Institution.



**The European Commission is recruiting for a
Principal Adviser
for the Research Directorate-General
(COM/2009/10211)**

The European Commission is looking to recruit a
**Principal Adviser for the Research Directorate-General
from the EU Member States – COM/2009/10211**

The Directorate-General for Research (DG RTD) draws up, develops and monitors Commission policy initiatives aimed at creating a European Research Area. Through its efforts, European research contributes to achieving the objectives of these policies and, at the same time, the needs of research policy are taken into account in other Community policies. The DG devises and implements the Community measures needed to establish the European research area, notably the research and technological development framework programmes. DG RTD contributes to the implementation of the Lisbon strategy for employment, international competitiveness, economic reform and social cohesion in the European Union, in particular in connection with the establishment of an area of education, training, research and innovation.

Candidates should have: a solid scientific background; a good knowledge of Community policies in general; thorough knowledge and proven experience in the field of European research policy and a good knowledge of the existing instruments

for putting it into practice, in particular the framework programmes; a good knowledge of EU decision making; the ability to represent the Commission in European and international political and scientific bodies; good negotiation and communication skills. The working languages of the DG are English and French. A thorough knowledge of these languages will be an advantage.

A full job description, selection criteria and application details can be found in the Official Journal C 194 A of 18 August 2009 or on the EUROPA website:

http://ec.europa.eu/dgs/personnel_administration/working_senior_mgt_en.htm

If you want to apply, you must register via the internet by going to the website:

https://ec.europa.eu/dgs/personnel_administration/seniormanagementvacancies/CV_Encadext/index.cfm

The closing date for applications is 25 September 2009.

On-line application will not be possible after 12.00 noon Brussels time.



EUROPEAN COMMISSION

<http://ec.europa.eu>



**FACULTY POSITIONS
IN BIOLOGY**

**The Scripps Research Institute
(TSRI), La Jolla, CA**

TSRI is seeking outstanding applicants for multiple tenure-track and tenured faculty positions at all levels. Applicants in all areas of Biology will be considered, and we encourage candidates in Genetics, Neuroscience, Stem Cell Biology, and Chemical Biology conducting innovative basic science that contributes to translational medical research. Applicants should be leaders in their field, or demonstrate such potential.

By **November 1, 2009**, applicants should send an electronic version of their CV, a brief statement of research interests, and three letters of recommendation to:

**facultyjobs@scripps.edu
Attention: ADI Biology**

**TSRI Faculty Search Committee
c/o Laurie Colum
The Scripps Research Institute
10550 N Torrey Pines Road, BCC460B
La Jolla, CA 92037**



**ÉCOLE POLYTECHNIQUE
FÉDÉRALE DE LAUSANNE**

**Faculty Position in Organic Chemistry
at the Ecole polytechnique
fédérale de Lausanne (EPFL)**

EPFL anticipates making a faculty appointment at the level of tenure-track Assistant Professor or tenured Associate/Full Professor in its Institute of Chemical Sciences and Engineering (ISIC).

The successful applicant is expected to build up an internationally recognized research program in the areas of synthetic organic chemistry, chemical biology or medicinal chemistry. It is expected that the candidate will teach organic chemistry within the undergraduate and graduate curriculum at the EPFL.

We offer internationally competitive salaries, benefits, start-up resources for scientific equipment and annual resources for PhD students, scientific staff and consumables.

Applications including curriculum vitae, publications list, concise statement of research and teaching interests as well as the names and addresses (including email) of at least five references should be submitted in PDF format via the website **<http://sb.epfl.ch/chemsearch>** by **October 15, 2009**.

For additional information, please contact **Professor Paul Dyson** (paul.dyson@epfl.ch) or consult the following websites:

**<http://www.epfl.ch/Eplace.html>,
<http://sb.epfl.ch/en> and <http://isic.epfl.ch>**

The EPFL School of Basic Sciences aims for a strong presence of women amongst its faculty, and qualified female candidates are strongly encouraged to apply.

POSITIONS OPEN



POSTDOCTORAL POSITIONS
Colorado State University

We are looking for highly motivated person(s) with research experience in the areas of immunology and virology to participate in research projects on HIV/AIDS, dengue pathogenesis, and immunity. Candidates with experience in cellular immunology of viral infections are preferred. State-of-the-art technologies encompassing novel humanized mouse models, lentiviral vectors, RNAi, and stem cells are put to use to solve important problems. (Representative work: Anderson et al., *Molecular Therapy* 15:1182-88, 2007; Kuruvilla et al., *Virology* 369:143-152, 2007; Bandi and Akkina, *AIDS Research and Therapy* 5:1, 2008; Berges et al., *Virology* 373:342-351, 2008; Zhou et al., *Nucleic Acids Res.* 37:3094-3109, 2009). Capacity for problem solving, drive to succeed, and ability to interact productively with colleagues are important.

Please apply before September 10, 2009, for full consideration, although applications will be processed until suitable candidates are identified. Please send a letter of application together with a list of three references to the e-mail address below mentioning Akkina laboratory.

Ramesh Akkina, D.V.M., Ph.D.
Department of Microbiology, Immunology,
and Pathology
1619 Campus Delivery
Colorado State University
Fort Collins, CO 80523-1619
Telephone: 970-491-1009
E-mail: remling@colostate.edu

CSU is an Equal Opportunity Employer.



POSTDOCTORAL/RESEARCH ASSOCIATE POSITIONS are available in the area of mechanism-based cancer prevention using plant-derived compounds and molecular mechanism of metal carcinogenesis in the laboratory of Xianglin Shi, Graduate Center for Toxicology, University of Kentucky. Send curriculum vitae to e-mail: xianglin.shi@uky.edu.

COGNITIVE NEUROSCIENTIST
Department of Neurology, University at Buffalo

Full-time Faculty Position at State University of New York, Buffalo for M.D.- or Ph.D.-level training in cognitive neuroscience. Candidate will focus on multidisciplinary translational research in biomedical informatics and clinical, cognitive, social, and behavioral neuroscience. May include teaching and clinical service. For more information or to apply, please visit website: <http://www.ubjobs.buffalo.edu>. Posting # 0900291.

☒ More scientists agree — we are the most useful website.



www.ScienceCareers.org

Download
your free
copy today.

ScienceCareers.org/
booklets



From technology specialists to patent attorneys to policy advisers, learn more about the types of careers that scientists can pursue and the skills needed in order to succeed in nonresearch careers.



Your
career
is our
cause.

Get help
from the
experts.

www.sciencecareers.org

- Job Postings
- Job Alerts
- Resume/CV Database
- Career Advice
- Career Forum



Get your questions answered.
Careers Forum
www.ScienceCareers.org

MARKETPLACE

Oligo Synthesis Columns

- Columns For All Synthesizers
 - Bulk Column Pricing Available
 - Call for Free Column Samples
- BIOSEARCH TECHNOLOGIES**
Advancing Nucleic Acid Technology™
- +1.800.GENOME.1
www.btcicolumns.com

Custom Peptide Synthesis

- High quality peptide from mg to kg
- Deeply discounted price
- An extensive list of modification & labeling
- Peptide library construction
- ¹⁵N/¹³C labeled peptides for NMR

EZBiolab www.ezbiolab.com

Promab Biotechnologies Inc.
Custom Monoclonal Antibody \$4,200

>3,000 CLONES WILL BE SCREENED

1-866-339-0871

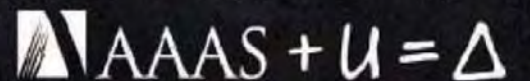
www.promab.com info@promab.com



AAAS is here.

Geospatial Technologies
Human Rights

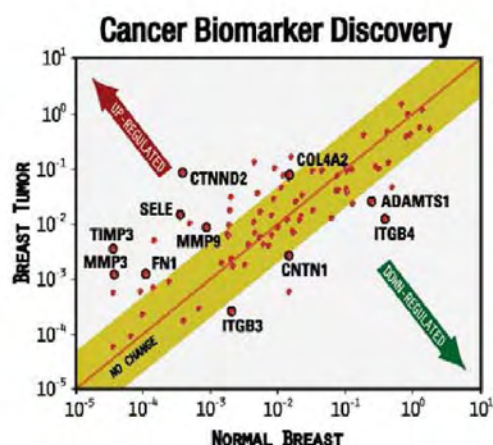
Remote, isolated, catastrophic events occur across the globe that affect civilians, the environment, indigenous rights, and more. The AAAS Science and Human Rights Program is the application of geospatial technologies to broaden the ability of non-governmental organizations to rapidly gather, analyze, and disseminate information in these times of crisis. And this is just one of the ways that AAAS is committed to advancing science to support a healthy and prosperous world. Join us. Together we can make a difference. aaas.org/plusyou/humanrights



FREE PCR ARRAYS*

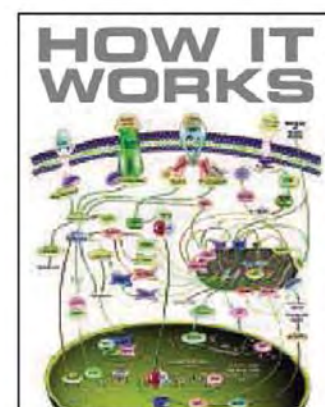


Gene Expression and Epigenomic Analysis



FREE PCR ARRAYS OFFER

* Visit Online for Details & Complete PCR ARRAY List
www.SABiosciences.com/Science6.php
ACT NOW! Offer Ends September 15th 2009



Find >100 Pathway
PCR Arrays Online:
www.SABiosciences.com

 **SABiosciences**TM